Redesign and Reparameterization of the DFT/MRCI Hamiltonian and its Application to Electronically Excited Linear Polyenes

---

HEINRICH HEINE
UNIVERSITÄT DÜSSELDORF

INAUGURAL-DISSERTATION

zur

Erlangung des Doktorgrades der
Mathematisch-Naturwissenschaftlichen Fakultät
der Heinrich-Heine-Universität Düsseldorf

vorgelegt von

IGOR LYSKOV

aus Zlatoust

Düsseldorf 2016

Aus dem Institut für Theoretische Chemie und Computerchemie
der Heinrich-Heine-Universität Düsseldorf

Gedruckt mit der Genehmigung der Mathematisch-Naturwissenschaftlichen Fakultät
der Heinrich-Heine-Universität Düsseldorf

Referentin: Frau Prof. Dr. Christel M. Marian
Korreferent: Herr Prof. Dr. Walter Thiel

Tag der mündlichen Prüfung: 22/12/2016

Zusammenfassung

Die vorliegende Arbeit handelt von einer semiempirischen multikonfigurellen Methode, namens DFT/MRCI, welche auf spezielle Weise die Ergebnisse der Dichtefunktionaltheorie mit Multireferenz-Konfigurationswechselwirkung kombiniert. Auf Grundlage der ursprünglichen Publikation von Grimme und Waletzke [J. Chem. Phys. **111**, 5645 (1999)] wird ein neues Parametrisierungsschema für angeregte Zustände mit ausgeprägtem Doppelanregungscharakter vorgeschlagen. Durch die Einführung einer individuellen energetischen Verschiebung für jede Zustandsfunktion in einer Konfiguration ist der modifizierte DFT/MRCI-Hamiltonoperator weniger empirisch, ohne dabei die hohe Effizienz des Standardoperators zu verlieren. Er beinhaltet vier globale spin-invariante Parameter, welche eine ausgewogene und konsistente Beschreibung für Excimere mit Singulett-, Triplett- und Quintett-Multiplizität liefern.

Diese Arbeit ist wie folgt strukturiert. Im ersten Kapitel werden die Definitionen von dynamischer und nicht-dynamischer Elektronenkorrelation als Korrekturen der Hartree-Fock Theorie eingeführt. Die mathematischen Konzepte hinter dem Kohn-Sham-Ansatz, der die korrelierte Elektronenbewegung berücksichtigt, und der Konfigurationswechselwirkung, die die statische Korrelation erfasst, werden ausführlich dargestellt. Kapitel 2 beinhaltet eine Übersicht vorheriger Versuche, beide Theorien zu verbinden, sowie eine allgemeine Diskussion über den neuen Hybrid-Hamiltonoperator. Kapitel 3 und 4 beurteilen hauptsächlich die Leistungsfähigkeit des neu konzipierten Hamiltonoperators. Ergebnisse der Berechnungen von Eigenschaften elektronisch angeregter Zustände kleiner und mittlerer organischer Moleküle werden kritisch mit denen aus Grimmes Ansatz sowie aus aufwändigen störungstheoretischen *ab-initio*-Methoden verglichen. Besondere Aufmerksamkeit bekommen dabei energetisch niedrig liegende doppelt angeregte Zustände. Darüber hinaus wird die Methode hinsichtlich ihrer Fähigkeit, die Relaxationsdynamik angeregter Zustände einiger kurzkettiger Polyene zu beschreiben, getestet. In diesen Systemen bestimmt die vibronische Wechselwirkung zwischen multidimensionalen Potentialflächen kovalenter und ionischer Zustände an und in der Nähe der Franck-Condon-Region die Kinetik des primären Schrittes der Anregungslöschung und die Feinstruktur des hochaufgelösten Absorptionsspektrums.

Insgesamt beschreibt der neu konzipierte DFT/MRCI-Hamiltonoperator Einelektronen-Übergangsenergien im UV/vis-Bereich für die untersuchten organischen Systeme mit einem mittleren quadratischen Fehler von < 0.2 eV. Berechnete Ein- und Zweielektroneneigenschaften der betrachteten Zustände, wie Übergangswahrscheinlichkeiten und Spin-Bahn-Matrixelemente, weisen auf die Robustheit der Parametrisierung hin. Weiterhin stimmen die Positionen größerer Banden und ihrer Obertöne im Absorptionsspektrum der Polyene mit experimentellen Ergebnissen gut überein. Der hier präsentierte Weg, die Hamiltonmatrix zu modifizieren, sollte die Standardwahl sein bei der Untersuchung photophysikalischer Prozesse gekoppelter bi-chromophorer Systeme.

Summary

The present work deals with a semi-empirical multiconfigurational method which combines in a special way the results of density functional theory with multireference configuration interaction, namely DFT/MRCI. On the basis of the original work by Grimme and Waletzke [J. Chem. Phys. **111**, 5645 (1999)] a new parameterization scheme is proposed for treating excited states with pronounced double excitation character. By constructing an individual energy shift for each of the state functions in a configuration, the modified DFT/MRCI Hamiltonian has less empiricism and at the same time preserves the high computational efficiency of the standard approach. It incorporates four global spin-invariant parameters which provide a balanced description for excimers with regard to singlet, triplet and quintet multiplicity.

This thesis is structured as follows: in Chapter (1), the definitions of dynamic and non-dynamic electron correlation are introduced as the corrections to the mean-field Hartree-Fock theory. The mathematical concept behind the Kohn-Sham approach which captures the effects of correlated electron motion and a computational scheme of configuration interaction which encompasses the static electron correlation are rigorously presented. Chapter (2) contains an overview of previous attempts to merge the theories together and discusses the novel hybrid Hamiltonian in detail. Chapter (3) and Chapter (4) are mainly dedicated to the assessment of the redesigned parameterization. Calculation results of electronically excited state properties for small and medium sized organic molecules are critically compared with Grimme's ansatz and high level *ab initio* methods based on a perturbative treatment. Special attention is given to the energetically low-lying doubly excited states. Besides that, the method is tested for its capability to describe the excited state relaxation dynamics in some short-chain polyenes. In these systems, the vibronic interaction between multidimensional potential energy surfaces of the covalent and ionic states at and near the Franck-Condon region governs the kinetics of the primary step of the excitation quenching and the fine structure of the high-resolution absorption spectrum.

Overall the redesigned DFT/MRCI Hamiltonian accurately delivers one-electron transition energies in the UV/vis range for a benchmark set of organic systems with a RMS error <0.2 eV. Computed one-electron properties of the states such as transition probability and spin-orbit matrix elements support the robustness of the parameterization. Furthermore, the position of major bands and their overtones in the absorption spectra of polyenes agree well with experimental findings. The presented way of modifying the Hamiltonian matrix shall be considered as default choice when investigating the photophysical processes of coupled bi-chromophoric systems.

List of papers included in the thesis

I *Redesign of the DFT/MRCI Hamiltonian.*
Igor Lyskov, Martin Kleinschmidt and Christel M. Marian,
J. Chem. Phys., **144**, 034104 (2016)
Own contribution: design, implementation, assessment of the Hamiltonian, wrote a first draft of the publication.

II *On the performance of DFT/MRCI-R and MR-MP2 in spin-orbit coupling calculations on diatomic and polyatomic organic molecules.*
Vladimir Jovanović, **Igor Lyskov**, Martin Kleinschmidt and Christel M. Marian,
Mol. Phys., **online** (2016) DOI: 10.1080/00268976.2016.1201600
Own contribution: calculations related to CASSCF/CASPT2 level, participated in the analysis and discussion of the results.

III *Singlet fission in quinoidal oligothiophenes.*
Nikolai Elfers, **Igor Lyskov**, J. Dominik Spiegel and Christel M. Marian,
J. Phys. Chem. C, **120**, 13901 (2016)
Own contribution: calculations related to intramolecular singlet fission.

IV *Nonadiabatic photodynamics and UV absorption spectrum of all-trans-octatetrane.*
Igor Lyskov, Horst Köppel and Christel M. Marian,
Phys. Chem. Chem. Phys., **submitted** (2016)
Own contribution: set up the vibronic Hamiltonian, carried out the DFT/MRCI and MCTDH calculations, wrote the manuscript.

V *Ab initio benchmark study of nonadiabatic S_1-S_2 photodynamics of cis- and trans-hexatriene.*
Adrian Komainda, **Igor Lyskov**, Christel M. Marian and Horst Köppel,
J. Phys. Chem. A, **120**, 6541 (2016)
Own contribution: calculations related to DFT/MRCI potential energy surfaces, wrote the technical section related to DFT/MRCI.

List of papers not included in the thesis

VI *Charge-transfer contributions to the excitonic coupling matrix element in BODIPY-based energy transfer cassettes.*
J. Dominik Spiegel, **Igor Lyskov**, Martin Kleinschmidt and Christel M. Marian,
Chem. Phys., **online** (2016) DOI: 10.1016/j.chemphys.2016.10.004

Contents

Glossary

BO — Born-Oppenheimer
WF — Wave Function
MO — Molecular Orbital
HF — Hartree-Fock
SAF — Spin-Adapted Function
CSF — Configuration State Function
AO — Atomic Orbital
SCF — Self-Consistent Field
CI — Configuration Interaction
TF — Thomas-Fermi
DFT — Density Functional Theory
KS — Kohn-Sham
XC — Exchange-Correlation
DFA — Density Functional Approximation
LDA — Local Density Approximation
GGA — Generalized Gradient Approximation
RI — Resolution of the Identity
eV — Electronvolt
RMSD — Root-Mean-Square Deviation
MAE — Mean Absolute Error
GS — Ground State
SO — Spin-Orbit
SF — Singlet Fission
PES — Potential Energy Surface
FC — Franck-Condon
WP — Wave Packet

Abbreviations

$\hat{H}$ — electronic Hamiltonian
ψ — many-body wave function
ϕ_i — one-particle wave function
F_{ij} — Fock matrix element
ρ — one-electron density
E_{XC} — exchange-correlation energy
v_{XC} — exchange correlation potential
Γ^1 — reduced one-body density matrix
Γ^2 — reduced two-body density matrix
E_X^{HF} — Hartree-Fock exchange
$\hat{\varepsilon}_i^j$ — one-body excitation operator
$|n\rangle$ — configuration
$|n, \omega\rangle$ — configuration state function
$\boldsymbol{\eta}_i^j$ — one-body spin-coupling coefficients
$\boldsymbol{\eta}_{ik}^{jl}$ — two-body spin-coupling coefficients
V_{ijkl} — two-particle multicenter integral
$\mathbf{Q}_{tune}$ — set of tuning mode distortions
$\mathbf{Q}_{coup}$ — set of coupling mode distortions
$\mu^{(n)}$ — n-th order vibronic coupling strength

List of Figures

Introduction

Modern quantum chemistry of molecular excited states increasingly touches upon a subject of complex nanoscale systems such as light-emitting diodes, organic solar cells, biologically active sites and molecular aggregates. Often these systems comprise hundreds of electrons which must be correlated at some point to deliver a correct physical picture. At this instance there are only some well-tested computational methods which allow to conduct a study of excited state properties in many-electron systems. The calculation time for high-order post-Hartree-Fock methods such as configuration interaction, coupled-cluster and methods based on perturbation theory scales up steeply with the number of particles. In addition, they require an employment of a primitive-rich basis set that makes *ab initio* approaches even more tedious or impracticable on the whole. Nowadays, the popular workhorse is density functional theory (DFT) which offers moderate calculation time demands due to faster basis set convergence and acceptable system size dependence. Although its conceptual background was derived from first principles, it is often used in conjunction with semiempirical exchange-correlation functionals. However, the Kohn-Sham theory has its own drawbacks. As an approximation for the ground state electron density, it uses a one-determinant wave function which is insufficient when the ground state exhibits strong multireference character. Furthermore, the standard extension of DFT for the optical problems is built upon a time-dependent linear density response function covering only one-electron transitions for excited states and neglects higher excitation classes. For this reason, the theory is fundamentally blind for low-lying two-photon transitions unless the response function is modified appropriately. In this context, the employment of specially tuned semiempirical methods for electronic structure calculations have recommended themselves as a relatively fast way to obtain desirable molecular quantities. They are built on the assumption that some terms of the equations of an underlying first-principles theory can be omitted to alleviate the computational speed. Hereafter, to recover from a major part of the introduced error, the working equations are modified with empirical parameters which are calibrated against verified empirical or *ab initio* data. [1–5] Among the variety of semiempirical schemes there are some which statistically perform similar to density functional approximations on the excited state studies. [6, 7] One of the most successful approaches is DFT/MRCI which incorporates advantages of density functional theory and multireference configuration interaction. It has been extensively used for the description of organometallic complexes [8–12], extended systems [13–16], and biologically relevant chromophores [17–25] shedding light on the excited states nature.

Nevertheless, like all semiempirical methods, DFT/MRCI is not without shortcomings. For example, in weakly coupled bi-chromophoric π-systems by virtue of substantial exchange interaction between electron and hole the triplet $\pi \to \pi^*$ states are regularly lower by a few electronvolts than the corresponding singlets. This fact facilitates the formation of the low-lying singlet, triplet and quintet excitons bounded by the Coulomb and Fermi interparticle

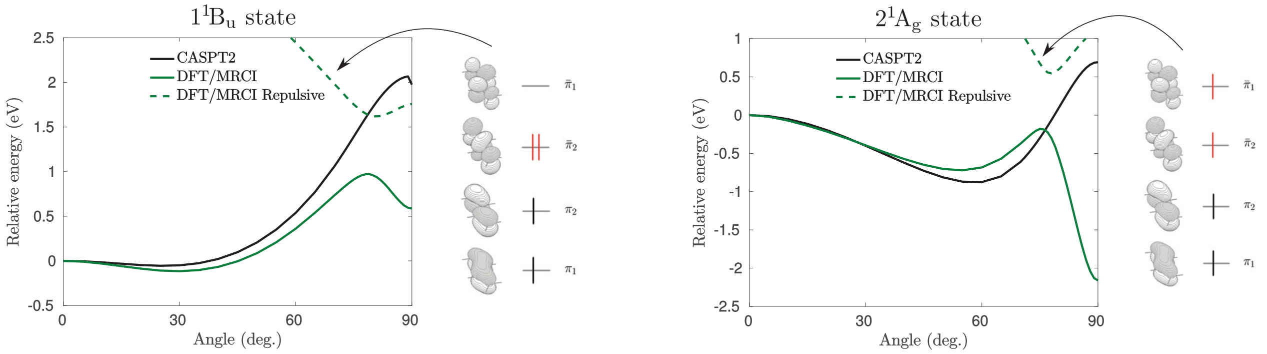

Figure I.1. Potential energy cuts of the 2^1A_g and 1^1B_u states in *all-s-trans*-butadiene along the disrotatory twist of –CH_2 groups.

terms spawned among two electrons and two holes. Although DFT/MRCI is able to account for two-photon transitions via the configuration expansion level, the vertical excitation energies for the coupled triplet pair states appear artificially much lower than expected. The main reason for this failure is the obvious underestimation of the interaction energy between four active orbitals involved in the configuration. It consequently hampers the elucidation of singlet fission where an optically accessible exciton is effectively split into two triplets yielding a four-open-shell configuration and its reverse process — triplet-triplet upconversion.

A simple and illustrative example of the effect of the problematic configurations is the adiabatic potential energy surface of the dark ($2\,^1A_g$) and bright (1^1B_u) states state in *s-trans*-butadiene along the simultaneous disrotatory methylene rotation about the double bonds. The configuration amplitudes of doubly excited configurations are gradually growing with an increasing of twisting angle and becomes dominant at ∼90°. Figure (I.1) depicts the significant change at 80° of the DFT/MRCI potential curves. Computed CASPT2 profile convinces that these kinks are attributed to methodological artifacts caused by the interaction with lowlying two-photon states. It is worth noting that even at the ground state geometry some aromatic compounds containing, for example, a nitro group tend to suffer from low-lying intruder states [26] which make the method inconvenient for the investigation of excited state relaxation processes where the performance of doubly excited configurations is essential.

The present work aims to improve the energetics of four-open-shell electron configurations using the main ideas of the original DFT/MRCI method. The resulting parameterization must be as fast as the original formulation while maintaining the excellent performance of the standard parameterization for singly excited states. Starting from the theoretical background, briefly explained in Chapter (1), the methodological framework of new hybrid Hamiltonian will be discussed in Chapter (2) and verified in subsequent Chapter (3) and Chapter (4).

Chapter 1

The many-body problem of electron correlation

The total non-relativistic Hamiltonian for an electronic system can be written as a sum of nuclear motions $\hat{T}_{nuc}$ with the electron-electron and electron-nuclear interaction term $\hat{H}_{el}$:

$$\begin{aligned}
\hat{H}_{tot} &= \hat{T}_{nuc}(\mathbf{R}) + \hat{H}_{el}(\mathbf{r}, \mathbf{R}) \\
\hat{T}_{nuc} &= -\sum_{\mu} \frac{1}{2m_{\mu}} \mathbf{\Delta}_{\mu} \\
\hat{H}_{el} &= -\sum_{i} \frac{1}{2} \mathbf{\Delta}_{i} - \sum_{\mu,i} \frac{Z_{\mu}}{|\mathbf{R}_{\mu} - \mathbf{r}_{i}|} + \sum_{i<j} \frac{1}{|\mathbf{r}_{i} - \mathbf{r}_{j}|} + \sum_{\mu<\nu} \frac{Z_{\mu} Z_{\nu}}{|\mathbf{R}_{\mu} - \mathbf{R}_{\nu}|}
\end{aligned} \tag{1.1}$$

where $\mathbf{r}$ and $\mathbf{R}$ denote the set of electronic and nuclear coordinates, respectively. The separation of $\mathbf{r}$ and $\mathbf{R}$ is an essential simplification of the molecular Schrödinger equation. Within the Born-Oppenheimer (BO) framework [27], the total wave function (WF) is represented as a product of the electronic and nuclear wave function:

$$\begin{aligned}
&\Psi_{tot}(\mathbf{r}, \mathbf{R}) = \psi_{nuc}(\mathbf{R}) \psi_{el}(\mathbf{r}, \mathbf{R}) \\
&\hat{H}_{el}(\mathbf{r}, \mathbf{R}) \psi_{el}(\mathbf{r}, \mathbf{R}) = E_{el}(\mathbf{R}) \psi_{el}(\mathbf{r}, \mathbf{R}) \\
&\left\{ \hat{T}_{nuc}(\mathbf{R}) + E_{el}(\mathbf{R}) \right\} \psi_{nuc}(\mathbf{R}) = E_{tot} \psi_{nuc}(\mathbf{R})
\end{aligned} \tag{1.2}$$

Taking into account the mass ratio of electron and nucleus, the electronic part of the problem (1.2) can be solved by fixing all nuclei at momentarily positions. In this spirit electrons follow the nuclear motions instantaneously (adiabatically). However, for systems of chemical interest, the electronic part is still too complicated to be treated exactly. Even for two electrons which orbit around a nucleus, a solution for $\psi_{el}(\mathbf{r}, \mathbf{R})$ is analytically inaccessible. Standard computational schemes are based on the iterative procedure of finding the extremum of the electronic energy as a function of $\mathbf{R}$. [28] The electronic wave function of an N-particle system is given by the normalized and anti-symmetrized linear combination of Hartree products built from one-electron wave functions, usually written in the form of a Slater determinant:

$$|\phi_1 \phi_2 \dots \phi_N| = \frac{1}{\sqrt{N!}} \begin{vmatrix} \phi_1(\mathbf{r}_1, \sigma_1) & \phi_1(\mathbf{r}_2, \sigma_2) & \dots & \phi_1(\mathbf{r}_N, \sigma_N) \\ \phi_2(\mathbf{r}_1, \sigma_1) & \phi_2(\mathbf{r}_2, \sigma_2) & \dots & \phi_2(\mathbf{r}_N, \sigma_N) \\ \vdots & \vdots & \ddots & \vdots \\ \phi_N(\mathbf{r}_1, \sigma_1) & \phi_N(\mathbf{r}_2, \sigma_2) & \dots & \phi_N(\mathbf{r}_N, \sigma_N) \end{vmatrix} \tag{1.3}$$

where $\phi(\mathbf{r}, \sigma)$ denote the molecular spin orbitals. [28] Therefore, the accuracy of the many-electron WF (1.3) and all its related properties critically relies on a rigorous description of the molecular orbitals (MO).

1.1. Hartree-Fock equations

Hartree-Fock (HF) theory is fundamental in the electronic structure calculations. It solves the electronic part of the Schrödinger equation (1.2) after invoking the BO approximation. For the sake of simplicity, let us rewrite the electronic Hamiltonian for a many-electron system as:

$$\begin{aligned} \hat{H} &= \sum_i \hat{h}_i + \sum_{i<j} \hat{g}_{ij} + \hat{h}_0 \\ \hat{h}_1 &= -\frac{1}{2}\mathbf{\Delta} - \sum_\mu \frac{Z_\mu}{|\mathbf{r}_1 - \mathbf{R}_\mu|} \qquad \hat{g}_{12} = \frac{1}{|\mathbf{r}_1 - \mathbf{r}_2|} \end{aligned} \tag{1.4}$$

and $\hat{h}_0$ is an additive constant for nuclei-nuclei repulsion at a fixed nuclear position. Evaluation of the total energy for the wave function in the form of Slater determinant (1.3) as an expectation value of the Hamiltonian (1.4) yields:

$$E_{el}[\Psi] = \langle\Psi|\hat{H}|\Psi\rangle = \sum_i h_i + \frac{1}{2}\sum_{i,j}\Big[V_{iijj} - V_{ijji}\Big] \tag{1.5}$$

where the two terms inside the double summation are the Coulomb and exchange interaction energy between two electrons, correspondingly written in short Mulliken notation:

$$V_{ijkl} = (\phi_i\phi_j|\hat{g}_{12}|\phi_k\phi_l) = \int \frac{d\mathbf{r}_1 d\mathbf{r}_2 d\sigma_1 d\sigma_2}{|\mathbf{r}_1 - \mathbf{r}_2|}\phi_i^*(\mathbf{r}_1,\sigma_1)\phi_j(\mathbf{r}_1,\sigma_1)\phi_k^*(\mathbf{r}_2,\sigma_2)\phi_l(\mathbf{r}_2,\sigma_2) \tag{1.6}$$

The first term in equation (1.4) includes the one-electron kinetic and potential energies:

$$h_1 = (\phi_i|\hat{h}_1|\phi_i) = \sum_\mu \int \phi_i(\mathbf{r}_1,\sigma_1)\Big(-\frac{1}{2}\mathbf{\Delta} - \frac{Z_\mu}{|\mathbf{r}_1 - \mathbf{R}_\mu|}\Big)\phi_i(\mathbf{r}_1,\sigma_1)d\mathbf{r}_1 d\sigma_1 \tag{1.7}$$

Now the task is to find a set of MO $\{\phi_i\}$ which minimizes the total electronic energy (1.5). The latter can be solved by applying the variational principle $\{\phi_i\} \to \{\phi_i + \delta\phi_i\}$ to the energy expression with the assumptions that the set of MO is orthonormal and the best orbitals lead to the lowest energy at a fixed $\mathbf{R}$ [28]. The result is a set of N one-body problems, written with introduction of the one-electron Fock operator $\hat{F}$, as:

$$\begin{aligned} \hat{F}(\mathbf{r}_1)\phi_i(\mathbf{r}_1) &= \epsilon_i\phi_i(\mathbf{r}_1) \\ \hat{F}(\mathbf{r}_1) &= \hat{h}(\mathbf{r}_1) + \sum_j \Big[\hat{J}_j(\mathbf{r}_1) - \hat{K}_j(\mathbf{r}_1)\Big] \end{aligned} \tag{1.8}$$

where $\hat{J}(\mathbf{r}_1)$ and $\hat{K}(\mathbf{r}_1)$ are local Coulomb and non-local exchange integral operators [28]:

$$\begin{aligned}
\hat{J}_j(\mathbf{r}_1)\phi_i(\mathbf{r}_1,\sigma_1) &= \left[\int \frac{d\mathbf{r}_2 d\sigma_2}{|\mathbf{r}_1-\mathbf{r}_2|}|\phi_j(\mathbf{r}_2,\sigma_2)|^2\right]\phi_i(\mathbf{r}_1,\sigma_1) \\
\hat{K}_j(\mathbf{r}_1)\phi_i(\mathbf{r}_1,\sigma_1) &= \left[\int \frac{d\mathbf{r}_2 d\sigma_2}{|\mathbf{r}_1-\mathbf{r}_2|}\phi_j^*(\mathbf{r}_2,\sigma_2)\phi_i(\mathbf{r}_2,\sigma_2)\right]\phi_j(\mathbf{r}_1,\sigma_1)
\end{aligned} \tag{1.9}$$

The important thing to note is that the summation over all occupied orbitals in the Fockian is resulting in mean-field terms. Therefore pairwise electron-electron interaction is not treated explicitly, instead the solution for every electron is given by the interaction of this electron with the effective potential generated by others.

The spin orbitals can be factorized to the product form of a function explicitly dependent on spatial coordinates of the electron and the spin coordinates σ. Within the Pauli principle, the $\phi(\mathbf{r},\sigma)$ can be classified as:

$$\phi^\alpha(\mathbf{r},\alpha) = \phi^\alpha(\mathbf{r})\cdot\alpha \qquad \phi^\beta(\mathbf{r},\beta) = \phi^\beta(\mathbf{r})\cdot\beta \tag{1.10}$$

Equation (1.10) accounts for the fact that the spatial part of a spin orbital depends on the electron spin. Two sets of spin orbitals are independent solutions of Hartree-Fock equations (1.8) adopted for each spin component $\hat{F}^\alpha$ and $\hat{F}^\beta$ (so called unrestricted HF method for different orbitals for different spins). Within UHF theory the wave function ψ_{el} for arbitrary electron occupation is expressed in the form of a single determinant, leading to the invariance of all physical properties (energy, charges, spin-densities etc.) of the system under the rotation of spin orbitals [29]. However, the use of spin orbitals constitutes the notorious problem of spin contamination for open-shell systems caused by the commutation disparity $[\hat{H},\hat{S}^2] \neq 0$. Thereby, the knowledge of the spin multiplicity of the electronic system is obscured and the UHF solution represents a mixing of high-spin and low-spin multiplets. It can be easily shown that a linear combination of determinants, built from one set of space functions for α- and β-electrons involving all possible spin arrangements of singly occupied orbitals associated with a given multiplicity, remedies the aforementioned problem. Because the resulting WF, built as linear combinations of factored determinants, is an eigenvalue of the $\hat{S}^2$ operator, such form is called a spin-adapted function or more often configuration state function (CSF). Note, that the high-spin component of the WF necessarily represents a single determinant, and the solution for its energy is given by the restricted open-shell HF equation (ROHF). Both UHF and ROHF schemes for open-shells system slightly modify the Fockian (1.8) and energy expression (1.5) due to the presence of unpaired electrons [28].

The Hartree-Fock approach for the Slater wave function represents an immense simplification with regard to the original Schrödinger equation. The resulting self-consistent field (SCF) equations (1.8) can be simplified by decomposing a spatial molecular orbital $\phi(\mathbf{r})$ to the linear combination of atomic orbitals (MO-LCAO) [30, 31]. In turn, atomic orbitals (AO) represent the linear sum of primitives or their contractions centered on nuclear positions $\mathbf{R}$.

The form of AO (analytic functions, all kinds of local potentials) is then a matter of the task under consideration. For molecular purposes, the well-established way is to use Gaussian functions leading eventually to Hartree-Fock-Roothaan equation [32, 33]:

$$\mathbf{FC} = \mathbf{SC}\epsilon \tag{1.11}$$

where $\mathbf{F}$ is the Fock matrix, $\mathbf{C}$ is the matrix of coefficients, ϵ is the matrix of orbital energies, $\mathbf{S}$ is the primitive overlap matrix. The Gaussian form of primitives provides a physically intuitive picture of the one-electron density decaying to zero by moving away from the nuclei and predicts the maximum of the single-particle probability at the region close to a nucleus. From a chemical point of view, the Gaussian basis can be easily adapted to various kinds of problems. For example, the description of radicals requires an introduction of polarized functions. Properties of charged systems and van der Waals complexes are highly dependent on the diffuseness of the basis set. One-electron wave functions and one-electron energies as defined in Equation (1.11) are the solution of the secular equation. Such a set of orbitals which diagonalizes the Fock matrix is called canonical. To this end, the machinery task is to find coefficients in front of Gaussian contractions or stand-alone functions using iterative methods of the self-consistent field (SCF) approach to achieve a minimum of the electronic energy at a given nuclear potential.

The assumption that electrons do not really recognize each other as unit charges in HF is a pretty severe approximation. Imagine two particles with opposite spin occupying the same or neighboring atomic shells. At the moment when the electrons are spatially located apart from each other, a small magnitude of the electron-electron repulsion force causes a small kinetic component. Another extreme is when two electrons are relatively nearby with a large Coulomb energy which must be contracted with the fast electron motions as clearly seen from Equation (1.5). The different electron velocities at different pair coordinates create an intuitive picture that the particle motions must be correlated. The effect that electrons tend to avoid each other inducing an instantaneous fluctuation of the density is usually called the dynamic electron correlation. As it has been discussed above, in the mean-field formalism each electron motion is described by a single-particle function which does not depend on the motions and instant coordinates of the other electrons. Therefore the HF approach neglects the dynamic correlation, and the probability to find opposite-spin particles at the same coordinate is given by the product of probabilities of independent events. It is common to say that there is no Coulomb hole for keeping a probe electron away from the reference one. It can be shown that the probability to find both electrons with same spin coordinate at the same place is zero due to the non-local exchange term in Equation (1.8). This exclusion satisfies the Pauli principle and it is said that there is a Fermi hole which correlates two electrons of equal spin in HF. The pairwise Coulomb and Fermi correlations are parts of many-body effects associated with the movement of the particles.

Often the use of a one-determinant wave function leads to a poor description of some chemical processes. Bond breaking, transition states on potential energy surfaces and near-degeneracy effects are among the instances which require additional electronic configurations to be considered in general. An error associated with the use of a single-determinant approach is attributed to non-dynamic or static electron correlation. The most trivial solution for the treatment of this error is to exploit a linear connection between the electronic configurations, thereby the wave function is written as follows:

$$\psi_{el} = c_0\psi_0 + \sum_{ai} c_i^a \psi_i^a + \sum_{abij} c_{ij}^{ab}\psi_{ij}^{ab} + \sum_{abcijk} c_{ijk}^{abc}\psi_{ijk}^{abc} \ldots \tag{1.12}$$

The first term in Equation (1.12) is the HF wave function, the second term is a sum over singly excited configurations with respect to the ground state ψ_0, the third term consists of a sum over doubly excited configurations and so on. Different schemes of configuration interaction (CI) incorporate different excitation orders resulting in the exact WF, and therefore exact molecular properties within the basis set error, upon complete configuration expansion. All coefficients c_0, c_i^a, c_{ij}^{ab} and so on are variationally optimized, filling up the configuration vector $\mathbf{V}$ of the equation:

$$(\mathbf{H} - \mathrm{E}\mathbf{1})\mathbf{V} = 0 \tag{1.13}$$

where $\mathbf{1}$ is unit matrix, E is the configuration interaction energy and $\mathbf{H}$ is the Hamiltonian matrix. One of the advantages of the CI is that Equation (1.13) is universal and applicable for the ground and electronically excited states. For these purposes, the energies of all CSF in the configuration space together with the inter-configuration couplings need to be computed. This can be legibly done using the formalism of second quantization.

1.2. Coulomb hole and density function theory

Density functional theory starts from the Thomas-Fermi (TF) model [34, 35] as an approximate method to find electronic properties of atoms using the one-electron density $\rho(\mathbf{r})$ neglecting relativity corrections. The model provides a functional form for the kinetic energy of uniform electronic gas as follow:

$$T[\rho] = C_F \int \rho^{5/3}(\mathbf{r})d\mathbf{r} \qquad C_F = \frac{3}{10}\left(3\pi^2\right)^{2/3} \tag{1.14}$$

The result shows that in combination with the classical expression for electrostatic repulsion $J[\rho]$,

$$J[\rho] = \frac{1}{2}\int \frac{\rho(\mathbf{r})\rho(\mathbf{r}')}{|\mathbf{r} - \mathbf{r}'|} d\mathbf{r}d\mathbf{r}' \tag{1.15}$$

the interaction of electrons in an atom is exhaustively given in terms of the electron density. Expressions (1.15) and (1.14) can be supplemented with the exchange energy of the free electron gas [36, 37]:

$$E_X[\rho] = -C_X \int \rho^{4/3}(\mathbf{r}) d\mathbf{r} \qquad C_X = \frac{3}{4}\Big(\frac{3}{\pi}\Big)^{1/2} \tag{1.16}$$

resulting in the Thomas-Fermi-Dirac model. Although Equation (1.14) was deduced from phase space consideration within the assumption that particles do not interact, it serves as a good starting point in modern Density Functional Theory (DFT).

The core of the DFT are two statements formulated and proven by Hohenberg and Kohn. Consider the Slater determinant (1.3) $\psi(\mathbf{r}_1, \cdots, \mathbf{r}_N)$ which is built from integrally occupied orthonormal single-particle orbitals, then the total electron density is defined as:

$$\rho(\mathbf{r}) = N \int \psi^*(\mathbf{r}, \mathbf{r}_2, \mathbf{r}_3, \ldots)\psi(\mathbf{r}, \mathbf{r}_2, \mathbf{r}_3, \ldots) d\mathbf{r}_2 d\mathbf{r}_3 \ldots \tag{1.17}$$

and this is the central quantity in DFT. The first theorem postulates that the external potential $v_{ext}(\mathbf{r})$ generated by the nuclear framework, and hence the total energy, is uniquely defined by the electron density $\rho(\mathbf{r})$ [38]. Thus,

$$E[\rho] = T_0[\rho] + J[\rho] + \int v_{ext}(\mathbf{r})\rho(\mathbf{r}) d\mathbf{r} + E_{XC}[\rho] \tag{1.18}$$

where the first term is the kinetic energy of non-interacting particles, the second is due to Coulomb repulsion of electrons and the last is the exchange and correlation (XC) energy. The second theorem states that the energy of an electronic system, written as a functional of the electron density, has a minimum, which corresponds to the ground state energy. Expression of an electron density via a set of occupied orbitals with an imposed constraint for an N-body system

$$\rho(\mathbf{r}) = \sum_i^N |\phi_i(\mathbf{r})|^2 \qquad N = \int \rho(\mathbf{r}) d\mathbf{r} \tag{1.19}$$

leads to well-known Kohn-Sham (KS) equations [39] of energy-minimizing orbitals:

$$\begin{gathered} \Big(-\frac{1}{2}\boldsymbol{\Delta} + v_{KS}(\mathbf{r})\Big)\phi_i(\mathbf{r}) = \epsilon_i \phi_i(\mathbf{r}) \\ v_{KS}(\mathbf{r}) = v_{ext}(\mathbf{r}) + \int \frac{\rho(\mathbf{r}')d\mathbf{r}'}{|\mathbf{r}-\mathbf{r}'|} + v_{XC}(\mathbf{r}) \end{gathered} \tag{1.20}$$

with $v_{XC}(\mathbf{r}) = \delta E_{XC}[\rho]/\delta\rho(\mathbf{r})$. So, electrons in atoms, molecules and solids are viewed in DFT formalism as independent particles, moving in the common effective Kohn-Sham potential $v_{KS}(\mathbf{r})$. One can read the KS theory as an attempt to do something wrong ($T_0[\rho]$ and $J[\rho]$ in Equation (1.18) are derived from the TF model) and then recover an error by an additional term $E_{XC}[\rho]$ which encodes the many-body contributions:

$$E_{XC}[\rho] = \Big(T[\rho] - T_0[\rho]\Big) + \Big(V_{ee}[\rho] - J[\rho]\Big) \tag{1.21}$$

The introduction of an exchange-correlation potential in Equation (1.20) is the point where all electron correlation effects are acquired. The fact that the true $T[\rho]$ and $V_{ee}[\rho]$ are still unreachable means that some density functional approximation (DFA) should be brought into play, opening a zoo of various kinds of E_{XC}. The robustness of the correction (1.21) determines the quality of the theory on the whole, and failures of DFT are considered due to the spurious formulation of XC.

Certainly, E_{XC} should include both exchange and correlation factors to be passable for solving different chemical problems by overcoming the shortcomings of the independent particle approximation. The concept of pair density needs to be introduced for the correlation treatment purpose. The one-particle density matrix normalized to N electrons is given as:

$$\Gamma^{(1)}(\mathbf{x}_1|\mathbf{x}_1') = N\int d\mathbf{x}_2\dots d\mathbf{x}_N \psi^*(\mathbf{x}_1', \mathbf{x}_2, \dots, \mathbf{x}_N)\psi(\mathbf{x}_1, \mathbf{x}_2, \dots, \mathbf{x}_N) \tag{1.22}$$

where $\mathbf{x}$ shall be understood as a combination of spin-space coordinate $\mathbf{x} = (\mathbf{r}, \sigma)$. The diagonal elements of the one-particle density $\Gamma^{(1)}(\mathbf{x}_1|\mathbf{x}_1)$ matrix are interpreted as the probability that an electron is at position $\mathbf{r}_1$ with spin σ_1, which is $\rho(\mathbf{x}_1)$ by definition. Next, the two-body reduced density matrix normalized to $N(N-1)$ electron pairs is:

$$\Gamma^{(2)}(\mathbf{x}_1, \mathbf{x}_2|\mathbf{x}_1', \mathbf{x}_2') = N(N-1)\int d\mathbf{x}_3\dots d\mathbf{x}_N \psi^*(\mathbf{x}_1', \mathbf{x}_2', \mathbf{x}_3, \dots, \mathbf{x}_N)\psi(\mathbf{x}_1, \mathbf{x}_2, \mathbf{x}_3, \dots, \mathbf{x}_N) \tag{1.23}$$

The quantity of diagonal elements of the two-particle density matrix (1.23) (so called pair-density) measures the probability density of finding one electron at spin-space point $\mathbf{x}_1$ and another at $\mathbf{x}_2$ [40]. The pair-density encodes dynamical two-particle correlation and can be viewed as follow:

$$\begin{aligned}\Gamma^{(2)}(\mathbf{x}_1, \mathbf{x}_2|\mathbf{x}_1, \mathbf{x}_2) = \Gamma^{(1)}(\mathbf{x}_1|\mathbf{x}_1)\cdot \Gamma^{(1)}(\mathbf{x}_2|\mathbf{x}_2) + \Gamma^{(2)}_{XC}(\mathbf{x}_1, \mathbf{x}_2|\mathbf{x}_1, \mathbf{x}_2) = \\ = \rho(\mathbf{x}_1)\rho(\mathbf{x}_2) + \Gamma^{(2)}_{XC}(\mathbf{x}_1, \mathbf{x}_2) = \Gamma^{(2)}(\mathbf{x}_1, \mathbf{x}_2)\end{aligned} \tag{1.24}$$

Here in Equation (1.24), the first term is a probability product of the independent particle approximation as following from HF theory. The last term describes the correlation of the electrons due to Fermi and Coulomb interactions which reduces the probability amplitude of finding them close to each other. By other words, a quality of $\Gamma^{(2)}_{XC}|_{ij}(\mathbf{x}_1, \mathbf{x}_2)$ tells how strongly motions of two electrons $\phi_i(\mathbf{x}_1)$ and $\phi_j(\mathbf{x}_2)$ are correlated [40]. The many-body correlation in the DFA is treated in an approximate way as a set of independent electron pairs leading to the expression for the XC energy:

$$E_{XC} = \frac{1}{2}\int \frac{d\mathbf{r}_1 d\mathbf{r}_2}{|\mathbf{r}_1 - \mathbf{r}_2|}\left[\Gamma^{(2)}(\mathbf{r}_1, \mathbf{r}_2) - \rho(\mathbf{r}_1)\rho(\mathbf{r}_2)\right] \tag{1.25}$$

where the integrand is the difference between the correlated and uncorrelated pair-densities. KS-DFT operates with an exchange-correlation hole function which gives an intuitive picture to show how the Fermi and Coulomb correlation affects the electron density distribution. It has the following form with imposed normalization:

$$h_{XC}(\mathbf{r}_1,\mathbf{r}_2)=\frac{\Gamma^{(2)}(\mathbf{r}_1,\mathbf{r}_2)}{\rho(\mathbf{r}_1)}-\rho(\mathbf{r}_2)\qquad\int h_{XC}(\mathbf{r}_1,\mathbf{r}_2)d\mathbf{r}_2=-1\tag{1.26}$$

The XC can be partitioned into the sum of exchange E_X and correlation E_C contributions, each of which are related to their respective holes $h_X(\mathbf{r}_1,\mathbf{r}_2)$ and $h_C(\mathbf{r}_1,\mathbf{r}_2)$:

$$E_{X/C}[\rho(\mathbf{r})]=\frac{1}{2}\int\frac{\rho(\mathbf{r}_1)}{|\mathbf{r}_1-\mathbf{r}_2|}h_{X/C}(\mathbf{r}_1,\mathbf{r}_2)d\mathbf{r}_1d\mathbf{r}_2\tag{1.27}$$

The Fermi hole $h_X(\mathbf{r}_1,\mathbf{r}_2)$ is due to the antisymmetry of the wave function the electronic density is constructed from. This exceptional factor in HF theory prevents the like-spin electrons from occupying the same region in space as the consequence of Pauli exclusion and reduces the probability density of finding a probe electron at $\mathbf{r}_2$ close to the reference electron $\mathbf{r}_1$. The Fermi hole can be expressed with help of the one-particle density matrix:

$$h_X(\mathbf{r}_1|\mathbf{r}_2)=-\frac{1}{2}|\Gamma^{(1)}(\mathbf{r}_1|\mathbf{r}_2)|^2/\rho(\mathbf{r}_1)\tag{1.28}$$

resulting in the exact HF-exchange expression. If one assumes that the h_X is symmetric and centered around the reference electron with constant density, one can at arrive to the already mentioned Dirac formula:

$$E_X^{LDA}[\rho(\mathbf{r})]=-\frac{3}{4}\left(\frac{3}{\pi}\right)^{1/3}\int\rho^{4/3}(\mathbf{r})d\mathbf{r}\tag{1.29}$$

with slightly modified prefactor, however, known as Slater-exchange [41]. Replacing the computationally complicated non-local exchange term (1.28) by this simple approximation (1.29), which depends on the local density only, is the first type of DFA, namely local density approximation (LDA). It turns out that the spin-independent Coulomb correlation, which was obscured in the mean-field approach, has no explicit expression as yet and, therefore, accurate numerical Monte-Carlo simulations are used to interpolate an analytic expression for h_C [42]. Correlation effects can be treated in LDA either by VWN [43] or PW [44] formulation. Nowadays, the most popular exchange functionals contain suitably tuned gradient corrections as the second term of the Taylor expansion to the $\rho(\mathbf{r})$ in order to account for weak density fluctuations. This opens a second family of DFA — generalized gradient approximations (GGA). As an example

$$\begin{aligned}E_X^{B88}[\rho]&=E_X^{LDA}[\rho]-\beta\int\rho^{4/3}(\mathbf{r})\frac{x^2d\mathbf{r}}{(1+6\beta x\cdot\sinh^{-1}x)}\\x=x(\rho,\nabla\rho)&=\frac{|\nabla\rho(\mathbf{r})|}{\rho^{4/3}(\mathbf{r})}\end{aligned}\tag{1.30}$$

is known as B88 exchange functional with the single parameter β optimized by a fit to the atomic exchange energy of the noble gas atoms [45]. It can be effectively combined with LYP [46–48] correlation and has no relation to the uniform electron gas. For a closed-shell systems it reads:

$$\begin{aligned} E_C^{LYP}[\rho] &= -a\int\frac{\rho(\mathbf{r})d\mathbf{r}}{1+e\rho^{-1/3}(\mathbf{r})}- \\ &- ab\int\omega\rho^2(\mathbf{r})\Big[C_F\rho^{8/3}(\mathbf{r})+|\nabla\rho(\mathbf{r})|^2(\frac{5}{12}-\delta\frac{7}{72})-\frac{11}{24}|\nabla\rho(\mathbf{r})|^2\Big]d\mathbf{r} \\ \omega &= \frac{\exp(-c\rho^{-1/3}(\mathbf{r}))}{1+e\rho^{-1/3}(\mathbf{r})}\rho^{-11/3}(\mathbf{r}) \qquad \delta = c\rho^{-1/3}(\mathbf{r})+\frac{e\rho^{-1/3}(\mathbf{r})}{1+e\rho^{-1/3}(\mathbf{r})} \end{aligned} \tag{1.31}$$

with a set of empirical parameters $\{a, b, c, e\}$ yielding together with B88 exchange (1.30) to the BLYP functional of the GGA approximation.

One of the important note in KS-DFT is an apparent disconnect between the interacting particle picture which is described by the true $T[\rho]$ and $V_{ee}[\rho]$ and non-interacting particles with $T_0[\rho]$ and $J[\rho]$. From one site, these two cases have the same external potential and thus, as follows from the first Hohenberg-Kohn theorem, the same density. From another — they have different Hamiltonian, which should lead to the different solutions. The latter discontinuity is remedied by the adiabatic connection [49, 50] of two extreme cases controlled by the interaction strength λ:

$$\hat{H}_\lambda = \sum_i\Big(-\frac{1}{2}\mathbf{\Delta}_i+v_{ext}^\lambda(\mathbf{r})\Big)+\frac{\lambda}{2}\sum_{j\neq i}\sum_i\frac{1}{|\mathbf{r}_j-\mathbf{r}_i|} \tag{1.32}$$

Here, v_{ext}^λ is the external potential that delivers the electron density for the scaled electron-electron interaction. The key result is that the corresponding pair-density and hence the exchange-correlation energy are expressed through the exchange-correlation hole integrated over the coupling constant:

$$\bar{\Gamma}^{(2)}(\mathbf{x}_1,\mathbf{x}_2) = \int_0^1\Gamma^{(2)^\lambda}(\mathbf{x}_1,\mathbf{x}_2)d\lambda \quad \text{or} \quad \bar{h}_{XC}(\mathbf{r}_1,\mathbf{r}_2) = \int_0^1 h_{XC}^\lambda(\mathbf{r}_1,\mathbf{r}_2)d\lambda \tag{1.33}$$

Equation (1.33) connects the KS independent particle reference ($\lambda = 0$) with the fully interacting picture ($\lambda = 1$) via a continuum of partially interacting particles. Now one should define the XC energy for the boundaries and connect them by interelectronic coupling. At the lower limit of λ, the electrons experience no dynamic correlation whatsoever, and practically it is desirable to evaluate the exchange energy in the exact way:

$$E_X^{HF} = -\frac{1}{4}\int\frac{|\Gamma^{(1)}(\mathbf{r}_1|\mathbf{r}_2)|^2}{|\mathbf{r}_1-\mathbf{r}_2|}d\mathbf{r}_1 d\mathbf{r}_2 \tag{1.34}$$

Equation (1.34) is nothing else than the HF exchange E_X^{HF} evaluated using KS orbitals. The upper limit of the integration (1.33) opens a flexibility for a functional form by which particle motions are correlated. The first attempt of constructing hybrid XC was done by Becke, who mixed the non-local exchange with LDA.

$$E_{XC}[\rho] = \frac{1}{2}E_X^{HF}[\rho] + \frac{1}{2}E_{XC}^{LDA}[\rho] \tag{1.35}$$

is known as Becke half-and-half functional [51].

Nowadays there are tens of different general-purpose XC functionals designed for various applications in chemistry, physics and material science [52–54]. Density functional theory is not viewed as rigorous many-body theory only due to the fact that it exploits the effective KS potential yielding to the mean-field formalism again. The solution of self-consistent Kohn-Sham equation can be viewed as the result for non-interacting pseudo-particles moving in the KS potential. However, DFT orbitals contain two-body Coulomb correlation terms, which are omitted in the HF theory. For each two KS-particles the pair-density is not given by the product of individual densities, but instead, the probability of finding a particle at a certain position in space correlates with the coordinate of the reference particle by the DFA. So, the one-particle wave functions are reconciled with the actual true electronic density to derive all the following molecular properties. For this reason, KS-orbitals represent non-interacting fictitious particles with no particular physical meaning, which are mapped to the physical characteristic $\rho(\mathbf{r})$ via a mathematical construct.

1.3. The second quantization and non-dynamic effects

The formalism of second quantization starts with the introduction of the Fock space in a basis of occupation vectors $|n\rangle$. For a system with m spin orbitals, the Slater wave function (1.3) in second quantization notation is represented by the Fock vector $|n\rangle$ with components defined by the occupation number n_k of one-electron spin-orbital ϕ_k:

$$|n\rangle = |n_1, n_2, \ldots, n_m\rangle, n_k = \begin{cases} 1 & \text{if } \phi_k \text{ is occupied} \\ 0 & \text{if } \phi_k \text{ is unoccupied} \end{cases} \tag{1.36}$$

We introduce a creation operator $\hat{b}_i^\dagger$ through the definition that $\hat{b}_i^\dagger$ acting on an occupation number vector gives zero if spin-orbital ϕ_i is occupied and non-zero if ϕ_i is vacant:

$$\begin{aligned} &\hat{b}_i^\dagger|n_1, n_2, \ldots 0_i \ldots n_m\rangle = (-1)^{(\sum_{j=1}^{i-1} n_j)}|n_1, n_2, \ldots 1_i \ldots n_m\rangle \\ &\hat{b}_i^\dagger|n_1, n_2, \ldots 1_i \ldots n_m\rangle = 0 \end{aligned} \tag{1.37}$$

The annihilation operator $\hat{b}_i$ is defined as the Hermitian adjoint of the creation operator and has the opposite meaning of $\hat{b}_i^\dagger$ — to reduce the occupation number of the i-th component of $|n\rangle$. The product of these two operators $\hat{b}_i^\dagger\hat{b}_j$ acting on arbitrary occupation vector represents a one particle-hole excitation from ϕ_i to ϕ_j, producing a new vector. The complete set of vectors in Fock space is grown by one-body generators $\hat{b}_i^\dagger \hat{b}_j$, two-body generators $\hat{b}_i^\dagger \hat{b}_j^\dagger \hat{b}_k \hat{b}_l$ and so on, therefore the solution of Equation (1.13) of such an expansion gives full-CI accuracy. For a given spin-orbital basis, there is a one-to-one mapping between the set of Slater determinants Δ_i and the occupation number vectors $|n\rangle_i$. This defines the simplicity of working with linear generators — if a reference vector is built from the orthonormal single particle functions they produce an orthonormal set of vectors which are eigenvalues of the number operator $\hat{b}_i^\dagger \hat{b}_i$.

The second quantization analogue for any one-electron operator in the coordinate representation $\hat{f}(\mathbf{r}, \sigma)$ has the following structure:

$$\hat{f} = \sum_{ij} f_{ij} \hat{b}_i^\dagger \hat{b}_j \qquad f_{ij} = \int \phi_i^*(\mathbf{r}, \sigma) \hat{f}(\mathbf{r}, \sigma) \phi_j(\mathbf{r}, \sigma) d\mathbf{r} d\sigma \tag{1.38}$$

where the constant f_{ij} is identified by calculating the matrix elements of $\hat{f}$ between two spin-orbitals. Equation (1.38) in a like manner can be adapted for any arbitrary two-electron operator. Thus, one arrives at the electronic Hamiltonian in terms of creation and annihilation operators obeying Fermi statistics through anti-commutation relations:

$$\begin{gathered} \hat{H} = \sum_{ij} h_{ij} \sum_{\sigma} \hat{b}_{i\sigma}^\dagger \hat{b}_{j\sigma} + \frac{1}{2} \sum_{ijkl} V_{ijkl} \sum_{\sigma\tau} \hat{b}_{i\sigma}^\dagger \hat{b}_{k\tau}^\dagger \hat{b}_{l\tau} \hat{b}_{j\sigma} \\ \left[\hat{b}_{i\sigma}^\dagger, \hat{b}_{j\tau}\right]_+ = \delta_{ij}\delta_{\sigma\tau} \qquad \left[\hat{b}_{i\sigma}^\dagger, \hat{b}_{j\tau}^\dagger\right]_+ = \left[\hat{b}_{i\sigma}, \hat{b}_{j\tau}\right]_+ = 0 \end{gathered} \tag{1.39}$$

Here Greek letters σ, τ denote the spin component and Latin letters i, j, k, l — the spatial component of spin-orbitals [28]. It is convenient to define two new operators $\hat{\varepsilon}_i^j$ and $\hat{\epsilon}_\sigma^\tau$ which act only on space and spin coordinates, respectively. They allow to rewrite the electronic Hamiltonian in the form:

$$\begin{gathered} \hat{H} = \sum_{ij} h_{ij} \hat{\varepsilon}_i^j + \frac{1}{2} \sum_{ijkl} V_{ijkl} \left(\hat{\varepsilon}_i^j \hat{\varepsilon}_k^l - \delta_{jk} \hat{\varepsilon}_i^l \right) \\ \hat{S}^2 = \frac{1}{2} \sum_{\sigma\tau} (\hat{\epsilon}_\sigma^\tau \hat{\epsilon}_\tau^\sigma - \frac{1}{2} \hat{\epsilon}_\sigma^\sigma \hat{\epsilon}_\tau^\tau) \qquad \hat{S}_z = \frac{1}{2} (\hat{\epsilon}_\alpha^\alpha - \hat{\epsilon}_\beta^\beta) \end{gathered} \tag{1.40}$$

The operators $\hat{\varepsilon}_i^j$ commute with $\hat{S}^2$ and $\hat{S}_z$, and hence $\hat{H}$ conserves the spin state [55, 56]. In this form the occupation vector $|n\rangle$ refers to individual MOs rather than to spin-orbitals, thus the allowed occupation elements are 0, 1 and 2. If ω indexes a linear combination of open-shell spins corresponding to a particular eigenfunction of $\hat{S}^2$, then an eigenfunction of $\hat{S}^2$ with total spin S and m_s component may be defined as:

$$|S, m_s, n, \omega\rangle = \sum_i c_i(S, m_s, \omega) \Delta_i(m_s, n) \tag{1.41}$$

Here the Slater determinants are related to each other by permutation of the spin functions among the various singly occupied MOs. In this basis, the matrix elements of the spin independent Hamiltonian (1.40) will depend solely on the spin eigenfunctions ω and occupation vectors:

$$\langle S, m_s, n, \omega|\hat{H}|S', m_s', n', \omega'\rangle = \delta_{SS'}\delta_{m_s m_s'}\langle n, \omega|\hat{H}|n', \omega'\rangle \tag{1.42}$$

The functions $|n, \omega\rangle$ form the complete antisymmetrized basis for the calculation.

The fundamental problem lies in efficient evaluation of pairwise interaction terms (1.42) encompassing various spin arrangements. In general, a number of spin states ω exist for a particular spatial occupation $|n\rangle$ and given $\langle\hat{S}^2\rangle$. When the excitation operator acts on a state $|n, \omega\rangle$, it produces a new occupation vector with a new spin occupation $|n', \omega'\rangle$. Likewise, for the parent vector there are a number of spin states compatible with the final occupation allowed by permutation of spins among the open shells. The final spin function must be expressible as a linear combination of weighted coefficients η which explicitly depend on the initial and final total functions:

$$\hat{\varepsilon}_i^j|n, \omega\rangle = \sum_{\omega'} \eta_i^j(n, \omega, n', \omega')|n', \omega'\rangle = \boldsymbol{\eta}_i^j|n', \omega'\rangle \tag{1.43}$$

where the sum runs over all possible CSF of $|n'\rangle$, and $\boldsymbol{\eta}$ is vector of weighted spin coefficients to represent a result of different interactions between the parent CSF and the ω' set [55, 56]. In evaluating of the expectation value of two-body operators in the Hamiltonian (1.40), the combination of two terms can be split into the product of individual results of one-electron operators acting on the bra- and ket-vectors as follows:

$$\begin{aligned}\langle n, \omega|\hat{\varepsilon}_i^j\hat{\varepsilon}_k^l|n'', \omega''\rangle =& \big(\hat{\varepsilon}_j^i|n, \omega\rangle\big)^\dagger\big(\hat{\varepsilon}_k^l|n'', \omega''\rangle\big) = \\ & \sum_{\omega'} \eta_j^i(n', \omega', n, \omega)^\dagger \eta_k^l(n', \omega', n'', \omega'') = \boldsymbol{\eta}_{ik}^{jl}\end{aligned} \tag{1.44}$$

Here in Equation (1.44) an intermediate configuration $|n'\rangle$ is involved to couple two states $|n, \omega\rangle$ and $|n'', \omega''\rangle$.

The self-consistent field energy E^{SCF} and Fock matrix elements F_{ij} for a given reference occupation vector $|\bar{n}\rangle$ are:

$$\begin{aligned} E^{SCF} &= \sum_i F_{ii}\bar{n}_i - \frac{1}{2}\sum_{ij}\Big(V_{iijj} - \frac{1}{2}V_{ijji}\Big)\bar{n}_i\bar{n}_j \\ F_{ij} &= h_{ij} + \sum_k \Big(V_{ijkk} - \frac{1}{2}V_{ikkj}\Big)\bar{n}_k \end{aligned} \tag{1.45}$$

When combining together the results of Equation (1.45) and the second quantization Hamiltonian (1.40), one arrives to:

$$\begin{aligned} \hat{\mathcal{H}} - E^{SCF} =& -\sum_i F_{ii}\bar{n}_i + \frac{1}{2}\sum_{ij}\Big(V_{iijj} - \frac{1}{2}\sum_{ij} V_{ijji}\Big)\bar{n}_i\bar{n}_j + \sum_{ij} F_{ij}\hat{\varepsilon}_i^j - \\ & -\sum_{ijk}\Big(V_{ijkk} - \frac{1}{2}V_{ikkj}\Big)\bar{n}_k\hat{\varepsilon}_i^j + \frac{1}{2}\sum_{ijkl} V_{ijkl}\Big(\hat{\varepsilon}_i^j\hat{\varepsilon}_k^l - \delta_{jk}\hat{\varepsilon}_i^l\Big) \end{aligned} \tag{1.46}$$

The easiest way of working with the latter equation is to derive individual formulae for separate cases. Applying two arbitrary occupation vectors $|n\rangle$ and $|n'\rangle$ to the left- and right-hand side of the Hamiltonian (1.46), all matrix elements are effectively split into three separated cases: Diagonal case $|n\rangle = |n'\rangle$:

$$\begin{aligned}\langle n,\omega|\hat{H} - E^{SCF}|n,\omega'\rangle &= \sum_i F_{ii}\Delta n_i + \frac{1}{2}\sum_{i\neq j} V_{iijj}\Delta n_i \Delta n_j + \\ +\frac{1}{2}\sum_{i\neq j} V_{ijji}\Big(-\frac{1}{2}\Delta n_i \Delta n_j + \frac{1}{2}n_i n_j - n_i + \boldsymbol{\eta}^{ji}_{ij}\Big) &+ \frac{1}{2}\sum_i V_{iiii}\Big(\frac{1}{2}\Delta n_i \Delta n_i + \frac{1}{2}n_i n_i - n_i\Big)\end{aligned} \tag{1.47}$$

One electron-hole difference between configurations $|n\rangle$ and $|n'\rangle$:

$$\begin{aligned}\langle n,\omega|\hat{H}|n',\omega'\rangle = F_{ij}\boldsymbol{\eta}^j_i + \sum_{k\neq i,j} V_{ijkk}\Delta n'_k \boldsymbol{\eta}^j_i + \sum_{k\neq i,j} V_{ikkj}\Big(-\frac{1}{2}\Delta n'_k \boldsymbol{\eta}^j_i + \\ +\frac{1}{2}n'_k \boldsymbol{\eta}^j_i - \boldsymbol{\eta}^j_i + \boldsymbol{\eta}^{kj}_{ik}\Big) + V_{iiij}\Big(\frac{1}{2}\Delta n'_i + \frac{1}{2}n'_i\Big)\boldsymbol{\eta}^j_i - V_{ijjj}\Big(\frac{1}{2}\Delta n'_j + \frac{1}{2}n'_j - 1\Big)\boldsymbol{\eta}^j_i\end{aligned} \tag{1.48}$$

Two electron-hole difference between configurations $|n\rangle$ and $|n'\rangle$:

$$\langle n,\omega|\hat{H}|n',\omega'\rangle = \frac{1}{(1+\delta_{ik})(1+\delta_{ij})}\Big(V_{ijkl}\boldsymbol{\eta}^{jl}_{ik} + V_{ilkj}\boldsymbol{\eta}^{lj}_{ik}\Big) \tag{1.49}$$

where Δn_i is the occupation number difference of the i-th MO between parent and actual configurations, V_{ijkl} is the two-particle electrostatic energy as defined in Equation (1.6). The Hamiltonian expression (1.46) contains only one- and two body generators, so no coupling arise between configurations which differ by more than two electrons in their occupation. As soon as the Hamiltonian matrix (1.13) is built with the help of the latter equations, the WF and its state energy are determined employing a diagonalization scheme.

Each new configuration to be added in the CI space possesses a nodal plane with zero probability of finding correlated electrons and holes. High-order excited states are not directly coupled to the reference, but rather affect those configurations which interact with a reference through Equation (1.48) and (1.49). This leads to one noticeable feature of the CI matrix — its sparseness. Therefore, to retrieve the dynamic electron correlation, the CI expansion requires to be quite large going beyond singly and doubly excited configurations with respect to the reference vector. Solving the full CI matrix is computationally tedious even for small organic systems. The latter can be alleviated by the truncation of the configuration space resulting in various configuration interaction levels. In this regard, a use of multireference ansatz (MRCI) alleviates demands for time consuming triple- and quadruple electron-hole permutations.

Chapter 2

Combined MRCI and DFT

As it is been discussed in Chapter (1), let us distinct between static and dynamic electron correlations which correct the errors of the Hartree-Fock approximation stabilizing the total electronic energy. On the one hand, the short-range correlation associated with electron motions can be recovered in the KS formalism, but one the other hand DFT is one-determinant theory in general. The non-dynamic part can in turn be captured within the configuration interaction ansatz. The first attempt to merge these two theories was done by Grimme who confined the CI expansion by accounting all singly excited configurations. The DFT/SCI equations are:

$$\begin{aligned}\langle\psi_a^r|\hat{H}-E^{KS}|\psi_a^r\rangle &= F_{rr}^{KS}-F_{aa}^{KS}-p_1V_{aarr}+2V_{arra}+\Delta\\ \langle\psi_a^r|\hat{H}|\psi_b^s\rangle &= -p_1V_{abrs}+2V_{arbs}\end{aligned} \tag{2.1}$$

with

$$\Delta = -0.025\epsilon + p_2\mathrm{exp}(-p_3V_{arra}) \tag{2.2}$$

where an empirical shift (2.2) helps to properly describe core excitations and excited states with small overlap between electron and hole densities [57]. F^{KS} in Equation (2.1) represent a one-particle KS wave function optimized in the B3LYP $v_{XC}(\mathbf{r})$ potential:

$$F_{ij}^{KS} = h_{ij} + (\phi_i|v_{XC}|\phi_j) + \sum_k \bar{n}_k V_{ijkk} \tag{2.3}$$

Three global empirical parameters were determined by a least-squares fit of selected reference data. It was found that the computational scheme described above yields an error for vertical excitations not exceeding 0.2-0.3 eV for closed-shell molecules. The valence and Rydberg-type excited states are calculated with the same accuracy for singlet and triplet multiplets.

The DFT/CIS method represents an improvement compared to the HF/CIS. However, the capability of the method does not surpass the time-dependent variation of DFT based on a linear density response function, which is a conceptual extension of KS theory used for excited states. Despite being a single reference theory, TD-DFT allows to reconstruct CIS-like wave functions using variationally optimized field amplitudes. A remarkable disadvantage of TD-DFT is the single reference wave function for the ground state (GS) delivering an inadequate description of molecular properties in certain circumstances. In contrast, the entire set of excited configurations in the DFT/CIS is evaluated by the modified CI Equations (2.1), (2.2) which remedy the aforementioned problem for describing the near-degeneracy of the GS.

2.1. Original formulation of semiempirical DFT/MRCI

A further improvement of the DFT/CIS model is straightforward at a first glance — to extend configuration expansion level. The DFT/MRCI approach, formulated by Grimme and Waletzke [58, 59], allows to account for doubly excited configurations in an approximate manner to depict their influence on low-lying excited states, for example in carotenoids, polyenes etc. Likewise DFT/CIS, the second generation employs the KS one-particle basis for building configuration space. It incorporates the BHLYP functional with 50% fraction of exact exchange. An employment of an exchange-rich DFA leads to better accuracy compared to B3LYP [58]. BHLYP reads as,

$$E_{XC}^{BHLYP}[\rho] = 0.5E_X^{HF}[\rho] + 0.5\Big(E_X^{B88}[\rho] + E_X^{LDA}[\rho]\Big) + E_C^{LYP}[\rho] \tag{2.4}$$

where the exchange terms $E_X^{HF}[\rho]$,$E_X^{B88}[\rho]$ and $E_X^{LDA}[\rho]$ are given by Equations (1.34), (1.30), (1.29), correspondingly, and the correlation functional $E_C^{LYP}[\rho]$ — by Equation (1.31). The principal extension of the DFT/MRCI over the DFT/CIS scheme is modified interaction terms, originating from the idea, that multiple electron excitations can be viewed as averaged sum of single excitation contributions:

$$\begin{aligned}
&\langle n,\omega|\hat{H}^{DFT} - E^{KS}|n,\omega\rangle = \langle n,\omega|\hat{H}^{HF} - E^{HF}|n,\omega\rangle - \\
&- \sum_c \left(F_{cc}^{HF} - F_{cc}^{KS}\right) + \sum_a \left(F_{aa}^{HF} - F_{aa}^{KS}\right) + \frac{1}{n_{ex}}\sum_a\sum_c \Big[p_1 V_{aacc} - p_2 V_{acac}\Big] \\
&\langle n,\omega|\hat{H}^{DFT}|n',\omega'\rangle = \langle n,\omega|\hat{H}^{HF}|n',\omega'\rangle f_{damp} \qquad f_{damp} = p_3 \cdot \exp\big(-p_4 \Delta E_{nn'}^4\big)
\end{aligned} \tag{2.5}$$

where a and c refer to annihilation and creation indices of excitation operators used to obtain an actual configuration, and n_{ex} is the excitation class of $|n\rangle$ with respect to the reference $|\bar{n}\rangle$ occupation. Thus, the Fock matrix F^{HF} is replaced by its KS counterpart F^{KS} and the diagonal elements are supplemented by scaled Coulomb and exchange energies over the whole set of electron-hole pairs. The exchange parameter p_2 explicitly depends on the number of open shells N in $|n\rangle$ as:

$$\begin{aligned}
{}^1p_2(N) &= p(0) + N \cdot {}^1\alpha \\
{}^3p_2(N) &= N \cdot {}^3\alpha
\end{aligned} \tag{2.6}$$

leading to different parameter sets for singlet and triplet states. It is noteworthy that in most cases the energy difference of spin-functions in a configuration is already included in the HF term $\langle n,\omega|\hat{H}^{HF} - E^{HF}|n,\omega\rangle$ and therefore all CSFs are shifted by the same energy, however, inconsistently with respect to different spin multiplets owing to the linear relation of p_2 and the open-shells number N. The couplings between different CSFs within one configuration are left unchanged. The interconfiguration coupling is required to be damped in order avoid overcounting of dynamic correlation arising from large CI expansions. Therefore, off-diagonal elements are scaled by factor p_1 by further multiplication on a damping function, magnitude of which is regulated by the configuration energy difference $\Delta E_{nn'}$. Because the main part of dynamic electron correlation is captured by DFT, all energetically high-lying configurations can be effectively discarded from the Hamiltonian matrix. The damping function f_{damp} smoothly reduces the interaction between energetically distant CSFs to zero, which makes it feasible to introduce a simple procedure for selecting the most important configurations to be included in the CI matrix. It is based on an estimate of the configuration energy gap as the difference of orbital energies with respect to the parent configuration:

$$E_{n\omega} - E_{n'\omega'} \approx \sum_c F_{cc}^{KS} - \sum_a F_{aa}^{KS} \tag{2.7}$$

If this difference is less then the sum of the highest-energy root among the desired states in the reference space and the δ cutoff parameter, a configuration is included in the eigenvalue problem. This preselection of the CI space mitigates the computational time of the method compared to the standard post-HF *ab initio* approaches significantly reducing the CI expansion.

Throughout Equation (2.5), the KS one-particle functions are used to calculate one- and two-electron integrals. Due to high storage demands for the direct evaluation of four-index MO integrals $(ij|kl)$, the resolution of the identity (RI) approach [60] is used to compute the two-electron integrals:

$$(ij|kl) \simeq \sum_P b_{ij}^P b_{kl}^P \qquad b_{ij}^P = \sum_Q (ij|Q) V_{PQ}^{-1/2} \tag{2.8}$$

Here, P and Q list auxiliary basis functions, and V_{PQ} in Equation (2.8) is the Coulomb metric.

Besides capturing the dynamic correlation effects, another advantage of KS orbitals is that the electronic potential is generated consistently for occupied and virtual orbitals unlike in HF theory. Each of the occupied orbitals is treated in an averaged field generated by $N-1$ particles, contrary to virtual orbitals, which are optimized for an N-electron potential. Therefore, the occupied set appears to be more compact compared to the unoccupied orbitals in HF theory. This effect is avoided in DFT due to the density normalization (1.19) and the entire set of KS orbitals is solved consistently in the mean-field of all electrons. A disadvantage of KS-DFT is the so-called self-interaction error — the result of a non-zero interaction term between an electron and its own density. This pathological problem does not arise in HF because the obvious cancellation of the self-interaction by the construction of the Fock Equations (1.8). As a consequence, each KS-particle feels a net charge generated by N electrons and reduced by electron-nuclei attraction, yielding a wrong electrostatic potential in the outer region. The self-interaction error is partly diminished in hybrid DFAs which explicitly contain a residual exchange counterpart to the unphysical Coulomb term. From this point of view, it is favorable to use a functional for DFT/MRCI which comprises a large fraction of exact exchange in XC

Table 2.1. DFT/MRCI $\pi \rightarrow \pi^*$ vertical excitation energies of ethylene $|s_1, 0\rangle$, tetrafluoroethylene $|s_2, 0\rangle$ and their $\pi_1\pi_2 \rightarrow \pi_1^*\pi_2^*$ dimer states $|S, 0, s_1, s_2\rangle$ energies.

		Singlet (eV)		Triplet (eV)		Quintet (eV)	
		computed	expected	computed	expected	computed	expected
Monomer	$\|s_1, 0\rangle$	8.05		4.42			
	$\|s_2, 0\rangle$	8.99		4.90			
Dimer	$\|s_1, 0\rangle$	7.84	8.05	4.29	4.42		
	$\|s_2, 0\rangle$	8.72	8.99	4.79	4.90		
	$\|S, 0, 1, 1\rangle$	2.19	9.32	4.21	9.32	—	9.32
	$\|S, 0, 0, 1\rangle$			9.56	12.95		
	$\|S, 0, 1, 0\rangle$			10.26	13.41		
	$\|S, 0, 0, 0\rangle$	13.56	17.04				

(0.5 in BHLYP) if one wants to stick with conventional hybrids.

Overall DFT/MRCI shows great efficiency for the evaluation of excited-state energies which mainly originate from one-electron transitions. [6] Furthermore, the method has been shown to perform well in extended π-systems such as polyenes [13, 61] and mini-carotenes [62] where doubly excited configurations of HOMO,HOMO→LUMO,LUMO type are essential for the proper description of the $2^1\mathrm{A}_g$ state. However, it fails for electronic states where four-open-shell configurations play a leading role in the CI vector. Consider, for example, local excitations in ethylene $\pi_1 \rightarrow \pi_1^*$ and tetrafluoroethylene $\pi_2 \rightarrow \pi_2^*$ which are spatially well separated. If the molecules are excited simultaneously, the various orientations of individual spin moments m_1 and m_2 of the monomers define the eigenstates of the dimer as components of $|s_1, m_1\rangle \otimes |s_2, m_2\rangle$. This product is generally reducible and can be decomposed into sixteen $|S, M, s_1, s_2\rangle$ components each of which is represented as a linear sum of weighted products $|s_1, m_1\rangle|s_2, m_2\rangle$ of local excitations. The genealogical coupling coefficients are determined by the Clebsch-Gordan decomposition with normalization requirement. All possible states can be grouped into two/three/one singlet/triplet/quintet multiplets within the framework of a spin-free Hamiltonian. In a similar fashion, the $\pi_1\pi_2 \rightarrow \pi_1^*\pi_2^*$ transition energies of the dimer states $|S, 0, m_1, m_2\rangle$ can be expressed as a sum of the energies of the local transitions. The first two dimer states of singlet and triplet multiplicity, respectively, shown in Table (2.1) correspond to one-electron local excitations on one monomer in the presence of the unperturbed second one. Among all states of non-interacting monomers there is a symmetry which manifests itself in the degeneracy of one singlet, one triplet and the quintet composed of the monomer triplet states. As it is seen from Table (2.1), this symmetry is not retained by DFT/MRCI. Instead, the energies of the spin-coupled triplet pairs are vastly underestimated. Let us also point out that the second singlet component $|0, 0, 0, 0\rangle$ must be isoenergetic to the sum of the singlet energies of the monomers. Likewise, the second $|1, 0, 0, 1\rangle$ and the third $|1, 0, 1, 0\rangle$ triplets correspond to combinations of singlet and triplet energies of the monomers, respectively. This is a very pictorial example to show the drastic DFT/MRCI errors in the energy of four-open-shell configurations.

A later modification of a combined density functional theory and CI expansion was done by Beck and coworkers [63, 64]. In their graphical unitary group approach-based DFT/MRCI code, the authors used series of 'update' and 'remove' operations for the KS correlation to incorporate it in the HF ansatz. The diagonal elements of the Hamiltonian matrix are computed like in HF-based MRCI and only two spin-invariant parameters are employed to adjust off-diagonal elements. This way of parameterization allows to calculate odd multiplicity systems exploiting correlation potential and correlation energy for α-electrons. However, the main application of the method was related to the calculation of spin-orbit effects of uranium complexes and the scheme is not well tested so far for medium or small sized systems. The hybrid formulation of Roemelt et. al. [65, 66] exploits the open-shell variation of DFT to incorporate them into DFT/ROCIS. To overcome a barrier 'occupied-orbitals-only' of standard DFT, two different KS equations are used to obtain orbital sets for paired and unpaired electrons. In this way, the authors have arrived at a universal three-parameter expression accounting only one-electron excitations from the reference of arbitrary multiplicity. Due to the shortened configuration expansion, DFT/ROCIS estimates energies for organic compounds at UV/vis excitation range remarkably worse than compared to DFT/MRCI. In contrast, it has been shown to perform well in describing L-edge spectra of X-ray absorption of transition metal compounds in various spin states.

2.2. Redesign of the DFT/MRCI Hamiltonian

The DFT/MRCI parameterization of Grimme and Waletzke (called as DFT/MRCI-S hereinafter) looks consistent with DFT/CIS for one-electron excitations. Both exploit KS one-particle energies and one-particle WFs, and scale electron-hole Coulomb interactions by a factor which is closely related to the amount of HF exchange in the DFT part. The orbital energy gap and the Coulomb integral are the dominant contributions to a CSF energy in most cases, especially when the density clouds of electron and hole overlap a little or do not overlap whatsoever. The example of the ethylene-tetrafluoroethylene dimer reveals a methodological artifact of DFT/MRCI-S which is apparently connected to an incorrect parameterization for four-open-shell state energies. One can easily see it by considering only the classical electrostatic terms of interacting particles. Assigning π-orbitals as 1 and 2 and unoccupied orbitals as 3 and 4, so that pairs $(1,3)$ and $(2,4)$ belong to different monomers, the Coulomb term for the $(12 \rightarrow 34)$ configuration reads:

$$V_{1122} + V_{3344} - V_{1133} - V_{1144} - V_{2233} - V_{2244} \tag{2.9}$$

Here in Equation (2.9), the first two terms describe the electron-electron and hole-hole interaction and the remaining four electron-hole attraction. Because the monomers are situated far apart, two of the four integrals are close to zero due to the long distance and only $(-V_{1133} - V_{2244})$ survives. The DFT/MRCI-S shift, introduced in Equation (2.5), is taking care of these two integrals consistently for one-electron transitions. However, the excitation factor n_{ex} reduces the correction by a factor 2. As consequence, the total energy of the resulting configuration suffers from the excess of Coulomb energy.

Another important aspect to consider is that the symmetry conservation of the ethylene-tetrafluoroethylene dimer in Tab. (2.1) requires to design an identical parameterization for different spin states. In HF-based MRCI, the Fermi correlation is accounted via the HF exchange energy between interacting orbitals producing the state function, thus making the multiplicity dependency of the exchange parameters (2.6) unsuitable. The energy splitting between CSFs $|n, \omega\rangle$ and $|n, \omega'\rangle$ is determined by the structural constants (1.44) in front of the exchange integrals according to Equation (1.47):

$$\langle n, \omega|\hat{H}|n, \omega\rangle - \langle n, \omega'|\hat{H}|n, \omega'\rangle = \sum_{i,j} \left[\boldsymbol{\eta}_{ij}^{ji}(\omega) - \boldsymbol{\eta}_{ij}^{ji}(\omega')\right] V_{ijji} \tag{2.10}$$

Due to the symmetry in the summation of the two-electron integrals in Equation (1.47), only the spin constants for orbitals of unpaired electrons in the Fock vector $|n\rangle$ are in the focus of interest. All other contributions are either zero or vanish due to cancellation by other parts of the matrix element. Therefore, a correction of the exchange energy part in a CSF should obviously account for spin-coefficients arising from the application of one-body operators with indices running over all singly occupied MOs in the actual configuration as follows from Equation (1.44). They explicitly contain all possible spin arrangements the unpaired electrons can adopt for a given multiplicity. The same arguments hold for the coupling energy between CSFs within a configuration. In order to maintain a consistent energy splitting between states of different multiplicities in the ethylene-tetrafluoroethylene dimer, similar exchange corrections must be applied for this case, too. Worthwhile to note, these matrix elements are built only from exchange integrals between all combinations of open-shell orbitals o. Accordingly, the resulting parameterization for diagonal Hamiltonian blocks is (Paper **I**):

$$\begin{aligned}
&\langle n, \omega|\hat{H}^{DFT} - E^{KS}|n, \omega\rangle = \langle n, \omega|\hat{H}^{HF} - E^{HF}|n, \omega\rangle - \\
&- \sum_{c} \left(F_{cc}^{HF} - F_{cc}^{KS}\right) + \sum_{a} \left(F_{aa}^{HF} - F_{aa}^{KS}\right) - p_2 \sum_{\substack{i,j \in o \\ i>j}} V_{ijji} \boldsymbol{\eta}_{ij}^{ji} - \\
&- p_1 \sum_{\substack{i,j \in a \\ i>j}} V_{iijj} - p_1 \sum_{\substack{i,j \in c \\ i>j}} V_{iijj} + \sum_{i \in a} \sum_{j \in c} \left(p_1 V_{iijj} - \frac{p_2}{2} V_{ijji}\right) \\
&\langle n, \omega|\hat{H}^{DFT}|n, \omega'\rangle = (1 - p_2)\langle n, \omega|\hat{H}^{HF}|n, \omega'\rangle
\end{aligned} \tag{2.11}$$

All integrals calibrated by p_1 in Equation (2.11) are attributed to the correction of electrostatic interaction which, in general, is exact for arbitrary occupation vectors. As usual, an issue is the nonclassical exchange part to be supplied for diagonal elements. Preliminary results revealed a lack of exchange energy in some circumstances if we link an exchange contribution to be added together with $\boldsymbol{\eta}$-factors only. Among the critical cases are the triplet $\pi \rightarrow \pi^*$ energies where the exchange integral is significant although the spin-coefficient is zero. A second example for which an exchange correction is not addressed, too, comprises states which exhibit large contributions from excited closed-shell configurations. In both instances, the excitation energy was exorbitantly overestimated indicating a desire to add a spin-invariant fraction of exchange. Test calculations showed that, to improve the energetics of the states, it is sufficient to introduce an additional exchange shift connecting created-annihilated orbital pairs only, as it is given in Equation (2.11).

To retain the high computational efficiency of the original parameterization and reduce the overcounting of dynamical correlation arising in the DFT part, the configuration coupling needs to be damped off. By examining the effects of various damping functions on the vertical energies of extended π-systems, the optimal shape was found to be:

$$\begin{aligned} \langle n,\omega|\hat{H}^{DFT}|n',\omega'\rangle &= \langle n,\omega|\hat{H}^{HF}|n',\omega'\rangle \cdot f_{damp} \\ f_{damp} &= \frac{p_3}{1+\gamma\cdot \mathrm{atan}\gamma} \qquad \gamma = \left(p_4\cdot \Delta E_{nn'}\right)^5 \end{aligned} \tag{2.12}$$

Similar to DFT/MRCI-S, the interconfiguration coupling is reduced with respect to the energy difference of two configurations, unless they are near degenerate. In case an electron configuration has more than one CSF, the factor $E_{nn'}$ in Equation (2.12) is estimated as the difference between the mean values of the CSF energies.

Table 2.2. Optimized DFT/MRCI-R Hamiltonian parameters.

δ (E_h)	p_1	p_2	p_3	p_4 (E_h^{-1})	RMSD (eV)	MAE (eV)
1.0†	0.5079	0.3559	0.5682	1.788	0.17	0.54
0.8†	0.5035	0.3681	0.5798	2.187†	0.20	0.63

† kept fixed during optimization.

Four global spin-invariant parameters entering the Hamiltonian (2.11), (2.12) (called hereafter as DFT/MRCI-R) were optimized with respect to the smallest root-mean-square deviation (RMSD) against experimentally well-studied singlet and triplet excited-state energies of small organic compounds. The results of the minimization employing different values of the damping decay parameter p_4 is presented in Table (2.2). The decay of the damping function as function of the energy difference between two coupled configurations is presented in Figure (2.1). As long as $E_{nn'}$ is smaller than 0.4 E_h, the configuration coupling is modified according to the scaling parameter p_3. Excited configurations of higher energies are giving a contribution to the dynamical correlation in MRCI, and the curve steeply goes down by prompt convergence to zero mitigating their effects. It implies that at 1.0 E_h almost all static correlation (>97%) for the actual configuration is already encompassed and it is not necessary to evaluate the entire MRCI matrix. Thereby, the optimized damping constant p_4 allows

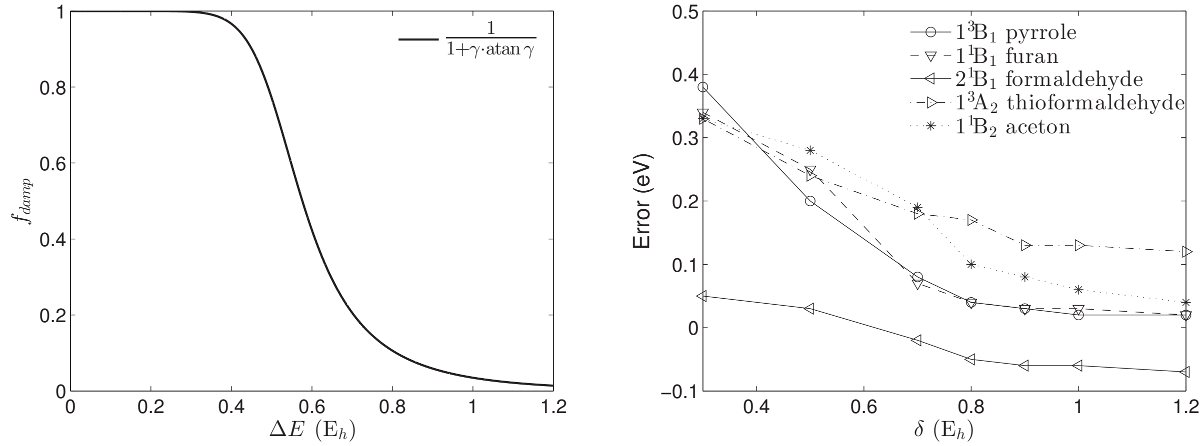

Figure 2.1. DFT/MRCI-R damping function (left) and DFT/MRCI-R error (right) for different energy cutoffs with respect to the experimental values taken from Paper **I**.

to use a similar preselection of important configurations (2.7) as in DFT/MRCI-S ignoring energetically high-lying CSFs. The right side of Figure (2.1) shows the convergence of the electronic transition energy for some small systems with regard to the selection threshold δ. Confirming previous arguments, the results of the calculations are found to be converged at values of 0.9-1.0 E_h for the energy cutoff parameter. In large molecular systems, for example organic light-emitting diodes, it is often required to solve secular equations with the size of billions of configurations. A steeper damping alleviates the dimensional demands of the Hamiltonian matrix resulting in a different parameter set to be used in conjunction with a smaller selection threshold, however with slightly worse statistical balance as is seen in Table (2.2). The incorporation of the energy cutoff δ tremendously accelerates the computational speed compared to *ab initio* multireference methods.

Table 2.3. DFT/MRCI-R results for ethylene-tetrafluoroethylene dimer.

		Singlet (eV)		Triplet (eV)		Quintet (eV)	
		computed	expected	computed	expected	computed	expected
Monomer	$\|s_1, 0\rangle$	7.82		4.38			
	$\|s_2, 0\rangle$	8.70		4.81			
Dimer	$\|s_1, 0\rangle$	7.82	7.82	4.38	4.38		
	$\|s_2, 0\rangle$	8.70	8.70	4.81	4.81		
	$\|S, 0, 1, 1\rangle$	9.17	9.19	9.18	9.19	9.20	9.19
	$\|S, 0, 0, 1\rangle$			12.66	12.63		
	$\|S, 0, 1, 0\rangle$			13.13	13.08		
	$\|S, 0, 0, 0\rangle$	16.59	16.52				

By the end, let us emphasize that DFT/MRCI-R parameterization accurately delivers the energy of four-open-shell states, which are reproduced with fairly good precision for the ethylene-tetraflyoroethylene dimer (Table (2.3)). By the mathematical construct of the corrections, all symmetry considerations, with respect to the excited states of the critical case, are retained for different multiplets as discussed in Section (2.1).

Chapter 3

Assessment of DFT/MRCI-R

3.1. Excited state properties of small organic systems

For a judgement on the performance of the DFT/MRCI-R Hamiltonian, the method was tested against a benchmark set of excitation energies measured by electron impact spectroscopy in gas phase [67] (Paper **I**). Similar to the fitting set, this benchmark set contains $\pi \rightarrow \pi^*$, $n \rightarrow \pi^*$ as well as valence-to-Rydberg transition energies of oxides and small organic compounds. The comparison of the performance of two parameterizations with respect to vertical excitation energies of singlet and triplet states is graphically illustrated in Figure (3.1). The error distributions over the sample shows the same statistical results for both methods. The mean deviations from the 160 experimental data (0.02 eV for DFT/MRCI-S, 0.06 for DFT/MRCI-R) are extremely gratifying. Also the standard (0.16 eV for DFT/MRCI-S, 0.14 for DFT/MRCI-R) and root-mean-square deviations (0.16 eV for DFT/MRCI-S, 0.15 for DFT/MRCI-R) are very satisfactory. DFT/MRCI-R maintains the high quality of the original formulation DFT/MRCI-S for states produced by the promotion of one electron out of the KS closed-shell reference. The biggest error was observed for triplet states in systems with a triple bond (acetylene, propyne, 1-butyne, 3,3,3-trifluoropropyne). The wave functions of these systems exhibit strong multiconfigurational character dominated by six CSFs. By analyzing the second triplet transition arising from their linear combination we concluded that the error originates from the way of parameterizing off-diagonal elements. Another general trend shifts $n \rightarrow \pi^*$ states toward lower excitation energies as computed by DFT/MRCI-S. In the majority of cases, results for these states obtained with the redesigned Hamiltonian are in better agreement with experiment than those computed with the standard parameterization.

The DFT/MRCI-S has been shown to be a useful approach for the treatment of elec-

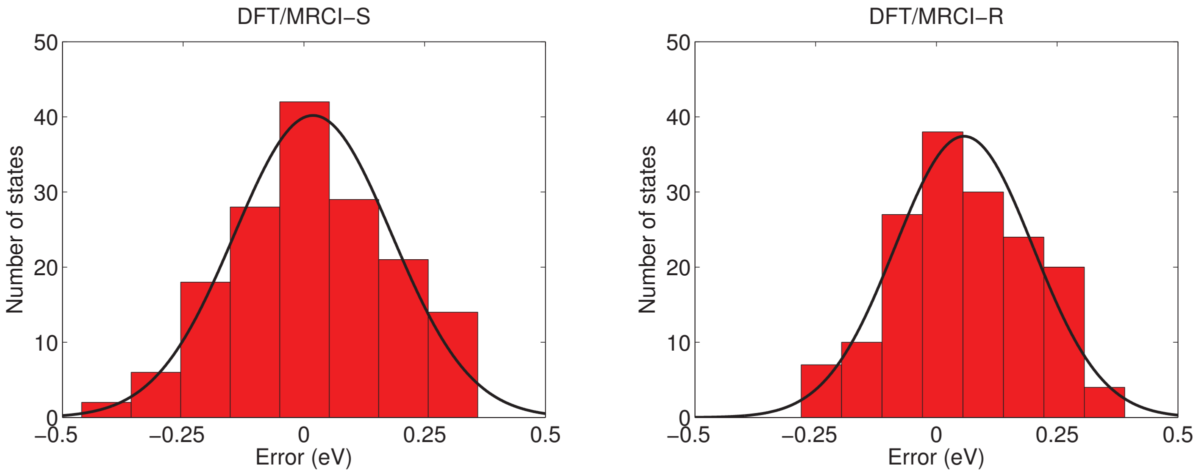

Figure 3.1. DFT/MRCI-S and DFT/MRCI-R error distribution.

tronic spin-orbit (SO) interaction [68–72]. In combination with SPOCK [68, 73, 74], which uses an effective mean-field operator for representing the two-electron SO terms in the Breit-Pauli operator and neglects differential multicenter integrals, the new parameterization was critically compared to DFT/MRCI-S and MR-MP2 results against a set of diatomic and polyatomic systems (Paper **II**). The states selected for the comparison are mainly the ground and low-lying photophysically and photochemically important excited states with $\pi \rightarrow \pi^*$ and $n \rightarrow \pi^*$ character. Because both parameterizations use identical one-electron bases for the CSF construction, the difference in LS coupling originates only from the composition of the CI vectors. As usual, the non-trivial cases are those which involve states with a non-negligible diffuse character and those which exhibit significant weights of doubly excited configurations. Particular interest attracts the energetics of two-electron transitions from the HF reference listed in Table (3.1). Because the states are not detectable in experimental spectra, the multireference methods based on perturbation theory (MRMP2 and CASPT2) were applied with similar AO basis sets for the quality validation of the DFT/MRCI energies.

For two-photon transitions, caused mainly by electron-hole interaction from the π-framework, the redesigned Hamiltonian shows good agreement with *ab initio* results (see o-benzyne, thioformaldehyde, dithiin in Table (3.1)). However, the striking difference between DFT/MRCI-R and the reference values is the prominent underestimation of state energies with a leading configuration produced by the annihilation of two electrons from lone-pair orbitals (formaldehyde, dithiosuccinimide, nitromethane). Moreover, the discrepancy is enhanced by a rising number of open shells in the resulting configuration. Although DFT/MRCI-R looks convincing for one-photon $n \rightarrow \pi^*$ state, this is something that has been overlooked in Paper **I**.

Table 3.1. Energy (in eV) of doubly excited states of molecules taken from Paper **II**.

System	State	Character	DFT/ MRCI-S	DFT/ MRCI-R	MRMP2	CASPT2
o-Benzyne	2^1A_1	$\pi\pi \rightarrow \pi^*\pi^*$	4.24	6.50	6.43	
	2^1B_1	$\pi\pi \rightarrow \pi^*\pi^*$	5.74	7.25	7.22	
	2^3A_1	$\pi\pi \rightarrow \pi^*\pi^*$	5.69	6.37	6.27	
Formaldehyde	5^1A_1	$n^2 \rightarrow \pi^{*2}$	11.06	9.20	10.67	10.29
Thioformaldehyde	3^1A_2	$n\pi \rightarrow \pi^{*2}$	7.19	7.70	7.61	7.66
	5^1A_1	$n^2 \rightarrow \pi^{*2}$	7.84	6.06	7.27	7.11
	4^3A_2	$n\pi \rightarrow \pi^{*2}$	7.77	7.28	7.11	7.19
Dithiin	3^1A_1	$\pi^2 \rightarrow \pi^{*2}$	4.80	4.69	4.39	
Dithiosuccinimide	2^1A_1	$nn \rightarrow \pi^*\pi^*$	4.71	3.40	>6.0	
	5^1A_1	$n^2 \rightarrow \pi^{*2}$	6.07	5.08	5.51	
	2^3B_2	$nn \rightarrow \pi^{*2}$	4.60	3.87	5.70	
	2^3A_1	$nn \rightarrow \pi^*\pi^*$	4.68	3.36	6.67	
Nitromethane	$2^3A'$	$nn \rightarrow \pi^{*2}$	7.31	6.12	8.70	8.97

The fact that the method shows remarkable data for the first group of transitions (usually π-orbitals are delocalized over several atomic centers) and inadequate for the second group (n-orbitals are strongly localized) implies that, likely, some part of dynamic correlation needs to be adjusted in the semi-empirical Hamiltonian as well. Also, the dependence on the number of open-shells can not be ignored in severe cases, pointing toward the needs of deep insight to the origin of the error. The doubly-excited states in these systems energetically appear in the range of one-electron transition energies. Their small energetic distance allows them to interact with each other and mix the configurations in their CI vectors. It results in pronounced outliers in the correlation plot of spin-orbit coupling components, which is directly related to the unbalanced description of the critical cases by the DFT/MRCI-R and DFT/MRCI-S parameterizations. Besides this, good agreement between the excitation energies and the LS coupling elements was found for the benchmark set, which is also corroborated by MRMP2 results (see Paper **II**).

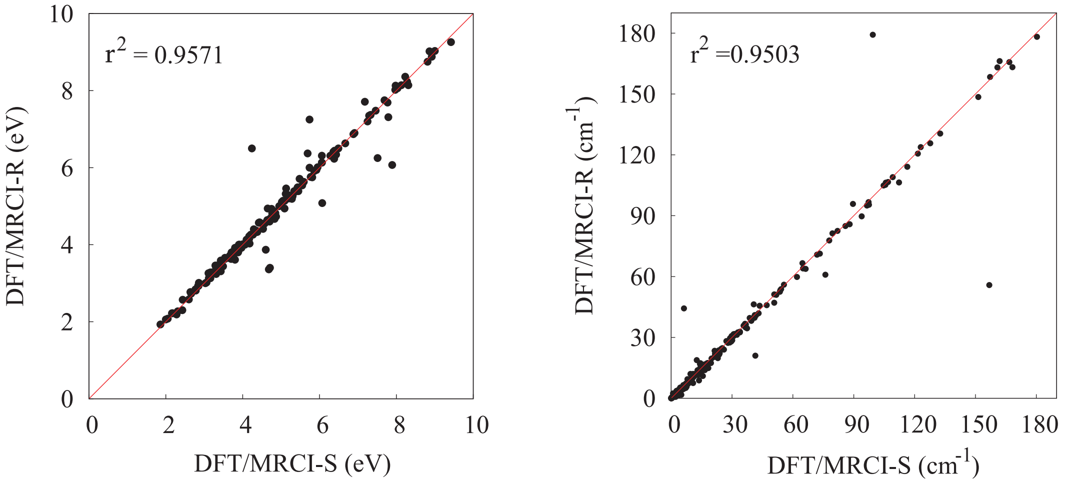

Figure 3.2. Correlation plot of excitation energies (left) and spin-orbit matrix elements (right) for polyatomic molecules as calculated with DFT/MRCI-S and DFT/MRCI-R levels.

3.2. Bridged-naphthalene systems

One of the test cases for the performance of the DFT/MRCI-R methods was the excitonic splitting of bridged naphthalene (N2) dimer states (Paper **I**). In these systems, two naphthalene units are held at fixed distance and orientation by a rigid bridge of variable length (Figure (3.3)). The absorption band of N2 with maximum at about ~44000 cm^{-1} (5.45 eV) originates from the most intense transition of naphthalene perturbed by the σ-framework of the norbornene fragment. Due to the bridge, the N2 peak is blue shifted by ~0.45 eV with respect to the $^1\mathrm{B}_\mathrm{b}$ transition in naphthalene. Like the $^1\mathrm{L}_\mathrm{b}$ state, the $^1\mathrm{B}_\mathrm{b}$ state of naphthalene is dominated by the two HOMO→LUMO+1 and HOMO-1→LUMO excitations. The $^1\mathrm{A}_1 \rightarrow {}^1\mathrm{B}_\mathrm{b}$ transition moment of N2 is located in the naphthalene plane which is oriented almost perpendicular (~90°) to another naphthalene in the dimers. Therefore, positive and negative linear

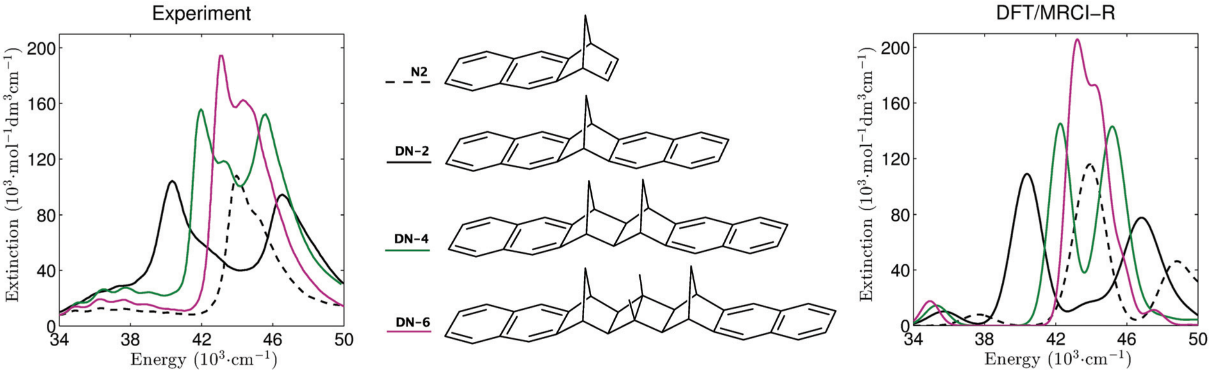

Figure 3.3. Measured and DFT/MRCI-R absorption spectra of bridged naphthalene dimers. The experimental spectrum was reprinted and adopted with permission from J. Am. Chem. Soc. **115**, 4345 (1993). Copyright 2016 American Chemical Society.

combinations

$$ {}^1\mathrm{B}_\mathrm{b}^{\pm} = \frac{1}{\sqrt{2}}(\psi_A^*\psi_B \pm \psi_A\psi_B^*) $$

yield peaks of approximately equal intensities, where ψ_A^* denotes the Frenkel exciton ${}^1\mathrm{B}_\mathrm{b}$ on monomer A, etc. [75, 76] Through-space and through-bond interaction mechanisms of monomers cause a splitting between the resulting states in the dimer, i.e. $\mathrm{E}({}^1\mathrm{B}_\mathrm{b}^+) - \mathrm{E}({}^1\mathrm{B}_\mathrm{b}^-)$, which is governed by the interchromophore distance. Thus, the two states must energetically approach the peak of N2 from the red- and blue-shifted zones when increasing the length of the bridge. Apparently, this is the case, indeed, as may be seen from Figure (3.3), where the simulated and experimental absorption spectra of the bridged naphthalene series are shown. The fact, that the positions and intensities of the simulated peaks coincide well with the experimental results tells about robustness of the DFT/MRCI-R excited-state WFs.

3.3. Singlet fission in quinoidal oligothiophenes

Singlet fission (SF) is a spin-allowed sub-picosecond process in multichromophoric systems, where one singlet Frenkel exciton undergoes delocalization onto surrounded monomers and can be converted into two triplet excitons thereafter. To be efficient, SF must mainly obey a two-step scheme:

$$ {}^1S_1 + S_0 \xrightarrow{k_{-1}} {}^1(T_1T_1) \xrightarrow{k_{-2}} {}^3T_1 + {}^3T_1 \qquad (3.1) $$

Excitation from the GS leads to the formation of a Frenkel exciton ${}^1S_1$, which should exhibit a large transition probability. Upon geometry relaxation on the singlet potential manifold, a system should proceed to a triplet pair overall coupled to the singlet ${}^1(T_1T_1)$ as the state of minimum energy with rate constant k_{-1} in Scheme (3.1). By this reason, the k_{-1} (and, therefore, feasibility of the SF) fatefully depends on a cofacial orientation of the neighbors [77–80] often favoring a slip-stacked geometry configuration of monomers for the initial exciton delocalization [81]. Because of the multi-exciton character of resulting state, the light emission is hindered and the coupled triplets can be split with k_{-2} into two independent triplets. Triplets offer a longer excited-state lifetime of the electron-hole pair compared to the singlet and provide more opportunities for injection which ideally double the photocurrent per photon. However the k_{-2} decoherence, which thermalizes the population of uncorrelated triplets due to their vibronic coupling to bath modes, is not well studied computationally as yet. It is clear, that the latter process should be exoergic, therefore, imposing an energy requirement for the high-yield fission to suppress all recombination mechanisms.

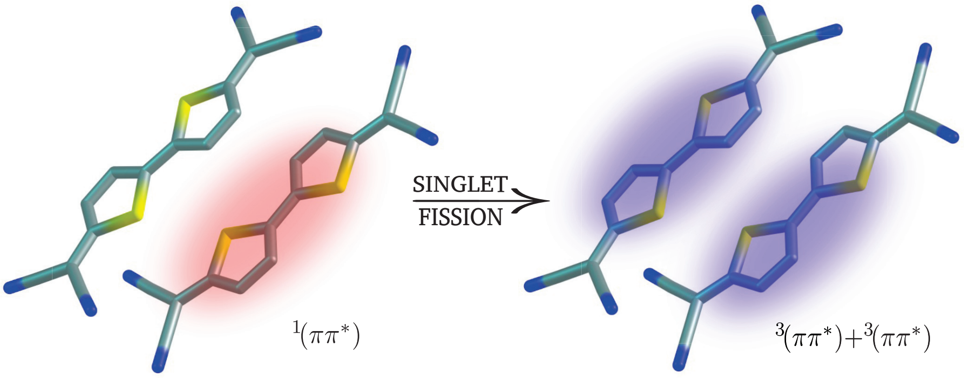

Figure 3.4. Slip-stacked conformation of quinoidal oligothiophenes.

Similar as in linear polyenes, the first two excited states in quinodal bithiophene (QBT) are seen as ionic $1^1\mathrm{B_u}$ (at 2.03 eV) and covalent $2^1\mathrm{A_g}$ (at 2.17 eV) in nature. The bright $1^1\mathrm{B_u}$ originates from the HOMO→LUMO transition and, therefore, a large exchange interaction between the frontier π-orbitals locates the corresponding triplet substantially lower than the singlet (at 0.61 eV vertically). The energetic position of the states motivated a study for intramolecular singlet fission, all the more so since time-resolved spectroscopy of a QBT in dilute solution revealed the ultrafast formation of a long-lived species with high quantum yield [82]. The authors of the experimental study claimed the SF to be an intramolecular process, but subsequent theoretical studies [83] involving spin-flip RAS methods could not locale a reasonable pathway for reaching the $^1(T_1T_1)$ state. In our group, possible intra- and intermolecular pathways were studied employing the DFT/MRCI-R method (Paper **III**). One dimensional cuts of the DFT/MRCI-R potential energy surfaces (PES) along coordinates which break the conjugation, and, therefore, localize covalently linked π-fragments, namely the potentials along the twisting about the central C=C bond and PES along the conrotatory twist of the dicyano groups, showed a crossing between the bright and dark states mediating the population of $2^1\mathrm{A_g}$ upon geometry relaxation. However, no indication for the formation of a coupled-triplet-pair state at large twisting angles was found in the monomer calculations. Due to the energetic proximity of the excited singlet states and $1^3\mathrm{A_g}$, even small SO coupling could give rise to fast inter-system crossing, which rise the population of triplet states. A torsion of QBT about the central bond by 20° requires only 370 cm^{-1} of activation energy and generates 2.3 cm^{-1} and 1.4 cm^{-1} of LS coupling energy for the $x-$ and $y-$component, correspondingly, between $1^3\mathrm{A_g}$ and $1^1\mathrm{B_u}$. Then, the lowest triplet state $1^3\mathrm{B_u}$ can be populated by internal conversion. Both $1^3\mathrm{B_u}$ and $1^1\mathrm{A_g}$ are long-lived and the excited-state absorption from these states resembles well the brightest experimental peak. Taking into account the energy gap between the bright and $^1(T_1T_1)$ states on the PESs of $\sim$0.3 eV for a conrotatory twist of the dicyano end groups, and $>$2.0 eV gap for torsion about the central bond, no evidence for intermolecular singlet fission in QBT was found.

The ground state geometry of the slip-stacked conformation of QBTs places the monomers at 3.5 Å apart due to weak van der Waals forces. Interestingly, the energy requirement for SF is met already at the Franck-Condon point — 1.98 eV for coupled triplets and 0.94 eV for the first and second triplet states. Moreover, the bright singlet state (2.00 eV) is almost adiabatically degenerate to the two-exciton state which may result in fast population of the latter by the displacement of GS geometry. Although quantitative rates were not calculated, the rigid scans of PESs along the normal distortions revealed two active modes describing symmetric and antisymmetric elongation of the double bonds of the monomers. These two vibrations mediate the intermolecular singlet fission dynamics in the slip-stacked dimer.

Chapter 4

Ab initio excited states dynamics of linear polyenes

Linear polyenes have been the subject of various spectroscopical and theoretical investigations due to their non-trivial photophysical properties of electronically excited states and relaxation processes. A biologically important class of polyenes are the carotenoids which play a big role in light harvesting complexes [84–86] and chemical quenching of singlet oxygen [87–89]. Also, the knowledge on linear π-systems with alternating single and double bonds can serve as a basis for elucidating mechanisms of photodynamics in visual pigments [89–92].

It is well known that for short polyenes with two and three double bonds the ionic $1\,^1\mathrm{B}_\mathrm{u}$ state is located vertically lower than the valence $2\,^1\mathrm{A}_\mathrm{g}$ state. These two states describe the electron-hole interaction of the π-manifold and possess different physical natures from the point of view of static correlation. The dark multiconfigurational $2\,^1\mathrm{A}_\mathrm{g}$ state manifests itself as a two-photon state which is characterized by three electronic CSFs, whereas the optically bright $1^1\mathrm{B}_\mathrm{u}$ is generated by a one-electron excitation from the highest bonding orbital to the lowest unoccupied antibonding orbital. The amplitude of the bosonic configuration $\pi^2 \rightarrow \pi^{*2}$ in the wave function of the valence state is enhanced relative to two other CSFs upon increasing the number of double bonds [93, 94]. Absorption spectra of polyenes show non-trivial band structures as a result of the interaction between the $1\,^1\mathrm{B}_\mathrm{u}$ and $2^1\mathrm{A}_\mathrm{g}$ states. An extension of the π-framework gradually reduces the $\mathrm{E}(2^1\mathrm{A}_\mathrm{g})-\mathrm{E}(1^1\mathrm{B}_\mathrm{u})$ energy gap and shifts the absorption spectrum toward the infrared region [13, 94–96]. The primary step of the mechanism of excitation quenching $\mathrm{S}_2 \rightsquigarrow \mathrm{S}_0$ involves a coherent population of S_1 caused by vibronic interactions. The energetic position and the coupling strength between two low-lying states $1\,^1\mathrm{B}_\mathrm{u}$ and $2^1\mathrm{A}_\mathrm{g}$ guide the wave packet (WP) evolution after the excitation at UV/vis range. As has been shown in previous experimental and computational studies on butadiene [97, 98], hexatriene [98–100] and octatetraene [101–103], the depopulation time of the $1\,^1\mathrm{B}_\mathrm{u}$ becomes longer when going from a two- to four-double-bond system. In this chapter, the results of quantum dynamics simulations for some short-chain polyenes employing DFT/MRCI potential energy surfaces are presented (Papers **IV** and **V**).

4.1. Vibronic Hamiltonian

All linear polyenes belong to the $\mathrm{C}_{2\mathrm{h}}$ molecular point group and its entire set of vibrational modes $\mathbf{Q}$ spans over the a_g, b_g, a_u and b_u irreducible representations (irreps). Apparently, the light absorption populates the bright $1\,^1\mathrm{B}_\mathrm{u}$ state at first. However, a model for the calculation of a vibronically resolved excitation spectrum needs to be adjusted in a way that it should be able to account for non-Condon effects due to the presence of the close-lying $2\,^1\mathrm{A}_\mathrm{g}$ dark state. Generally speaking, the quantum Hamiltonian must encompass both the interaction of electronic states with itself (intrastate) as well as the coupling between two electronic states

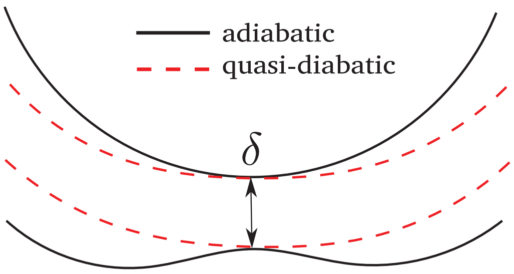

Figure 4.1. Quasi-diabatic states along a coupling mode in LVC model.

caused by nuclear motions (interstate). Following the well-established notations, all vibrations of the first type will be called tuning $\mathbf{Q}_{tune}$ and vibrations of the second type as coupling $\mathbf{Q}_{coup}$ modes. Use of symmetry-adapted internal coordinates makes the definition of two sets $\mathbf{Q}_{tune}$ and $\mathbf{Q}_{coup}$ feasible and straightforward. The non-vanishing interstate coupling modes are those for which the product of the irreps yields the totally symmetric representation:

$$\Gamma_1 \otimes \Gamma_2 \otimes \Gamma_{\mathbf{Q}_{coup}} \supset \Gamma_{\text{sym}} \tag{4.1}$$

where Γ_1 and Γ_2 are the irreps of the two electronic states considered and $\Gamma_{\mathbf{Q}_{coup}}$ is a perturbation irrep to couple the electronic states. By analogy, the intrastate coupling motions for each of the states (Γ_1=Γ_2) must obey following relationship:

$$\Gamma_{\mathbf{Q}_{tune}} = \Gamma_{\text{sym}} \tag{4.2}$$

In the context of this paper, $\mathbf{V}_{coup}$ and $\mathbf{V}_{tune}$ are considered as electronic potentials along the distortion of the nuclear framework, $\mathbf{Q}_{coup}$ and $\mathbf{Q}_{tune}$ correspondingly. By the symmetry constraint imposed in Equation (4.1), it is clear that all $\mathbf{Q}_{coup}$ modes should possess $\mathrm{b_u}$ symmetry. Such vibrations break the $\mathrm{C_2}$ generator of $\mathrm{C_{2h}}$ and retain the molecular plane. An interaction of electronic configurations with $\mathrm{b_u}$ distortions reduces the symmetry of the wave functions, such that the $1^1\mathrm{B_u}$ and $2^1\mathrm{A_g}$ states transform under the same irrep $\mathrm{A'}$ of the $\mathrm{C_s}$ point group. The evaluation of electronic potentials $\mathbf{V}_{tune}$ along the $\mathbf{Q}_{tune}$ set appears to be trivial and does not require additional computational work, unlike the $\mathbf{V}_{coup}$ potentials. One of the simplest solutions to overcome the diabatization problem is the linear vibronic coupling scheme (LVC) [104–106].

At the ground state geometry ($\mathbf{Q}_0$), the wave functions of the states transform under different irreps and it is assumed that diabatic and adiabatic state energies are identical. The LVC model [106] postulates that in a two-level system, in the presence of a $\mathrm{b_u}$ deformation generated by the coupling mode $q_i \subset \mathbf{Q}_{coup}$, the quasi-diabatic potentials can be expressed with the help of a coupling function $\mu(q_i)$ as:

$$\mathbf{V}_{coup}(q_i) = \begin{bmatrix} \overline{\mathrm{U}}(q_i) + \frac{\delta}{2} & \mu(q_i) \\ \mu(q_i) & \overline{\mathrm{U}}(q_i) - \frac{\delta}{2} \end{bmatrix} \qquad \epsilon_{1,2}(q_i) \in \operatorname{spec}(\mathbf{V}_{coup}(q_i)) \tag{4.3}$$

where δ is the interstate energy spacing between two levels at $\mathbf{Q}_0$. The solution of the secular Equation (4.3) brings back the adiabatic potentials $\epsilon_{1,2}(q_i)$ as a function of an applied distortion q_i:

$$\epsilon_{1,2}(q_i) = \overline{\mathrm{U}}(q_i) \pm \sqrt{\frac{\delta^2}{4} + \mu^2(q_i)} \tag{4.4}$$

From Equation (4.4) it is seen that $\overline{\mathrm{U}}(q_i)$ represents an average curve of two adiabatic potentials. In this way, two surfaces are topologically nested and shifted with respect to each other by δ in the quasi-diabatic representation. They remain equidistant along the complete range of the coupling coordinate q_i as graphically represented in Figure (4.1). The knowledge of $\epsilon_{1,2}(q_i)$ allows to estimate the quasi-coupling $\mu(q_i)$ by the least-square-fit of Equation (4.4).

For setting up the vibronic Hamiltonian, the kinetic energy operator which describes the nuclear motions needs to be set up. Employment of the GF technique [107, 108] yields the full Hamiltonian:

$$\mathbf{H} = \mathrm{T}\mathbf{1}_2 + \mathbf{V}_{tune}(\mathbf{Q}_{tune}) + \mathbf{V}_{coup}(\mathbf{Q}_{coup}) + \epsilon_v(\mathbf{Q}_0) \tag{4.5}$$

with the kinetic energy

$$2\mathrm{T} = \sum_{i,j} \mathbf{p}_j^{\top} \mathbf{G}_{ij} \mathbf{p}_i \tag{4.6}$$

where $\mathbf{p}_i$ refers to the momentum conjugate to the symmetry coordinate q_i. The last term ϵ_v of Equation (4.5) denotes a two-by-two diagonal matrix with elements of vertical energies at the Franck-Condon (FC) point. The second and third terms describe the sum of 1D-cuts of diabatic potential energy surfaces (PESs) of the two considered states along the tuning ($\mathrm{a_g}$) and the coupling ($\mathrm{b_u}$) modes, respectively:

$$\mathbf{V}_{tune} = \sum_{\mathbf{Q}_{tune}} \begin{bmatrix} \mathrm{U}_1(q_i) & 0 \\ 0 & \mathrm{U}_2(q_i) \end{bmatrix} \qquad \mathbf{V}_{coup} = \sum_{\mathbf{Q}_{coup}} \begin{bmatrix} \overline{\mathrm{U}}(q_i) & \mu(q_i) \\ \mu(q_i) & \overline{\mathrm{U}}(q_i) \end{bmatrix} \tag{4.7}$$

The kinetic energy in Equation (4.6) was built with the help of the $\mathbf{G}_{ij}$-matrix, the elements of which are analytically tabulated in Ref. [109]. Kinetic energy coefficients for momenta $\mathbf{p}_i$ and $\mathbf{p}_j$ conjugate to two distinct symmetric internal coordinates q_i and q_j (as will be defined later) represent a sum of factored pairwise interactions of all local momenta the $\mathbf{p}_i$ and $\mathbf{p}_j$ are composed from. The Hamiltonian (4.5) for the two-level system was treated within the fully quantal, time-dependent scheme of wave packet propagation as formulated in MCTDH.

4.2. All-trans-octatetraene

Numerous theoretical works have reported the results of semiempirical schemes [7, 13, 95], *ab initio* multireference [93, 94, 110, 116, 117] and density functional based [6, 118] methods (see the surveys in Ref. [6, 7, 116]) and often ambiguously predict the order and energy of the first two excited singlet states of *all-trans*-octatetraene (OT). Besides the fact that the excitation energy is highly dependent on the ground-state geometry [13], the challenge is the

Table 4.1. Excitation energies (in eV) of first valence states in *all-trans*-octatetraene. Experimental values for vertical excitations are estimated.

	CASPT2[a]	MRMP[b]	DFT/MRCI-R	DFT/MRCI-S	Exp.
			vertical transitions		
$1^1\mathrm{B_u}$	4.42	4.66	4.05	4.16	∼4.4
$2^1\mathrm{A_g}$	4.38	4.47	4.10	3.85	∼4.1
			0-0 transitions		
$1^1\mathrm{B_u}$	4.35	4.34	3.67	3.80	3.98[c,k] 4.40[d] 4.41[f,h,l]
$2^1\mathrm{A_g}$	3.61	3.50	3.44	3.30	3.55[c] 3.59[e] 3.54[k]
			emission maxima		
$1^1\mathrm{B_u}$	4.14	3.80	3.74	3.87	4.12[h] 4.20[d] 4.31[g]
$2^1\mathrm{A_g}$	2.95	2.80	2.92	2.60	∼3.1[l]

[a] CASPT2 from Ref. [110]
[b] MRMP form Ref. [94]
[c] 77K in hexane from Ref. [112]
[d] gas phase from Ref. [112]
[e] jet from Ref. [115]
[f] jet from Ref. [102]
[g] 4.2K in n-hexane from Ref. [111]
[h] jet from Ref. [113]
[k] 4.2K in n-octane from Ref. [114]
[l] vapor from Ref. [103]

different nature of these states, which deserves a different consideration in the computational treatment. The DFT/MRCI-R vertical excitation of 4.05 eV is somewhat too small for the dipole allowed state when compared to the best estimated value by at least 0.35 eV. The calculated position of the 0-0 origin and the emission energy are also red shifted by the same energy. The fact, that a perfect match of the DFT/MRCI-R with the experiment was found for $1^1\mathrm{B_u}$ in *trans*-butadiene, and the slightly worse agreement (0.2 eV below the experiment) in linear hexatriene suggests, that the latter method is unable to accurately describe the properties of the bright state upon extending the conjugation length. Presumably, the DFT/MRCI-R inherits the methodological drawbacks from DFT, which is known to systematically underestimate the energies of ionic states for polyenes of longer chain length [119]. Apart from this, the DFT/MRCI-R yields a qualitatively good energy of 4.10 eV for $2^1\mathrm{A_g}$, which is indeed close to what is expected. The mapping of the calculated transition origin with measured values also corroborates this finding (see Table (4.1)). As a result, the two states are almost isoenergetic at $\mathbf{Q_0}$ with a gap $\mathrm{E}(1^1\mathrm{B_u})-\mathrm{E}(2^1\mathrm{A_g})$ of -0.05 eV. Although both states are offset by 0.25 eV in the DFT/MRCI-S with regard to the experiment, they are both shifted downward consistently. Thus, contrary to the DFT/MRCI-R, the standard parameterization perfectly maintains the experimental splitting of 0.3 eV for the CASPT2 geometry.

At the ground-state geometry, the vibrational modes of *all-trans*-octatetraene transform under

$$\Gamma_{\mathbf{Q}} = 17\mathrm{a_g} \oplus 8\mathrm{a_u} \oplus 7\mathrm{b_g} \oplus 16\mathrm{b_u} \tag{4.8}$$

By incorporating ten in-plane and two out-of-plane nuclear degrees of freedom in the underlying Hamiltonian, adapted to the LVC model, the results of the time evolution of the excited WP are discussed (Paper **IV**). The absorption spectra of OT in the 3.5-5.0 eV region, shifted to the location of the 0-0 band, are shown in Figure (4.2). The intensities of all peaks are normalized to the maximum peak height corresponding to the origin. For comparison, the high-resolution absorption spectrum, recorded in a jet-cooled experiment, is also presented in Figure (4.2). The most prominent mode (denoted by v_2) with the most intense progression is associated with the carbon-carbon double-bond stretching q_2 and q_6. DFT/MRCI-R places the peak at 1727 cm^{-1} to the right of the origin (denoted by v_0), whereas DFT/MRCI-S — at 1736 cm^{-1}. Both methods here overshoot by ~70 cm^{-1} the reported values of 1645 cm^{-1} measured in the jet-cooled experiment [102] and 1666 cm^{-1} in the gas phase [112]. The peak displayed in the experimental spectrum at 1235 cm^{-1} (denoted to v_1) gives rise to the secondary vibrational progression, and is attributed to the symmetric single C-C bond alternations q_1 and q_4. This band appears with very low intensity in both the DFT/MRCI-R spectrum and the DFT/MRCI-S spectrum. Despite the almost dark v_1 peak, the DFT/MRCI-R and the DFT/MRCI-S outline the $v_{1,1}$ overtone at 2846 cm^{-1} and 2839 cm^{-1} respectively, whilst the

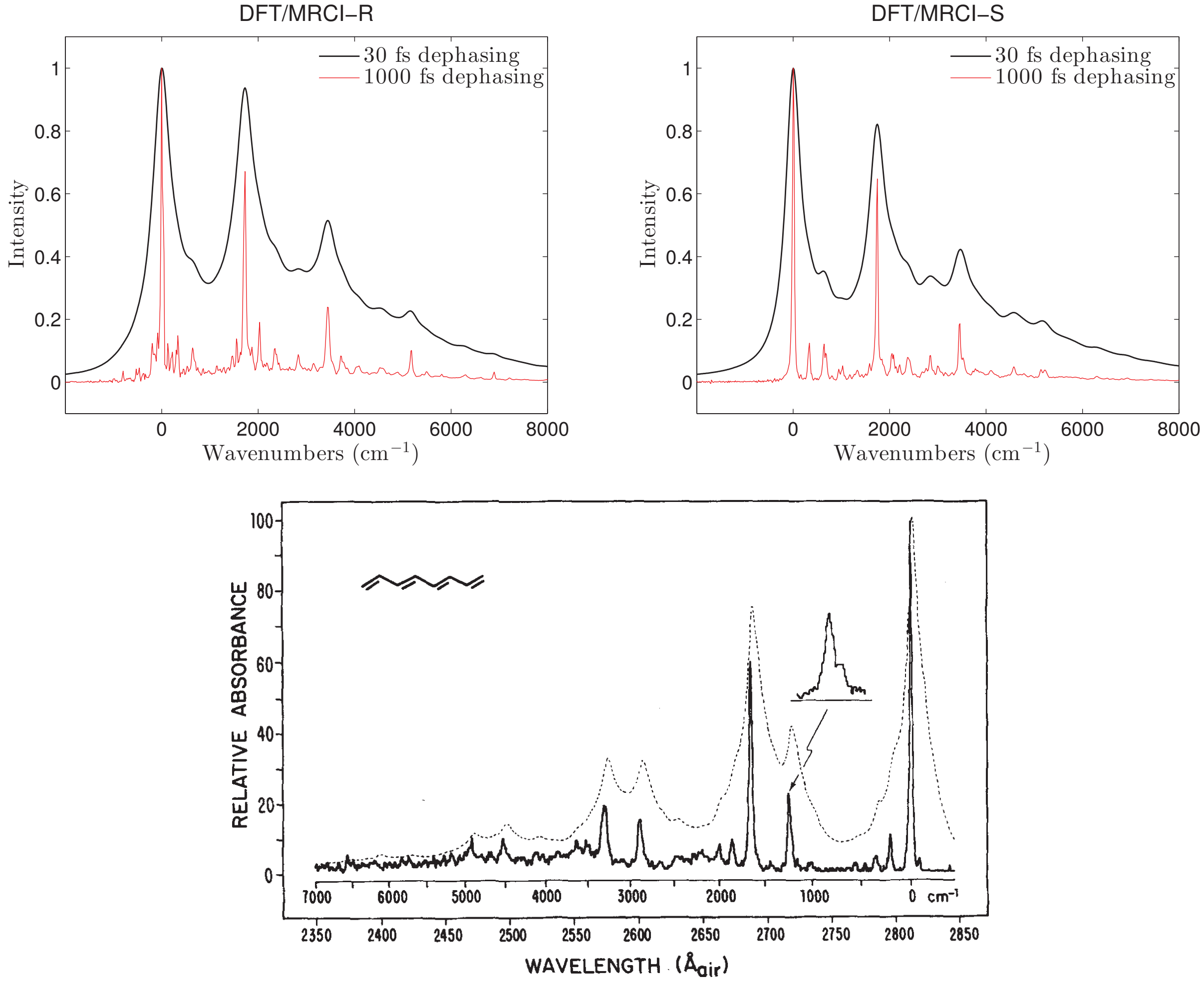

Figure 4.2. Calculated $1^1B_u \leftarrow 1^1A_g$ absorption spectra of *all-trans*-octatetraene (upper panels). Experimental spectra was reprinted from J. Chem. Phys. **81**, 4210 (1984) with the permission of AIP Publishing.

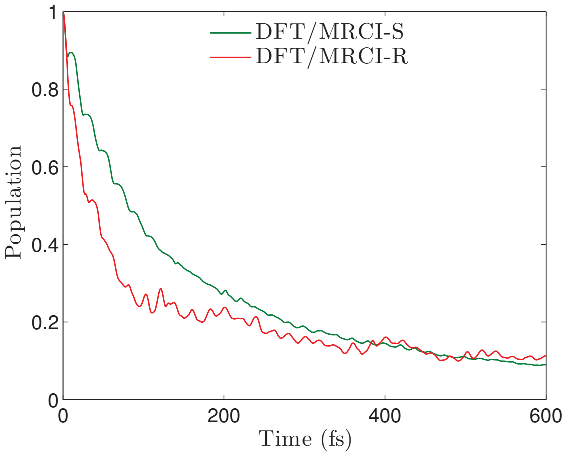

Figure 4.3. Population decay followed by the 1^1B_u excitation.

low-temperature experimental value is 2872 cm^{-1}. All overtones of v_1 and v_2 bands appear with low frequency shoulders, which are likely caused by symmetric in-plane angle bending q_8, q_{10} and q_{12} motions detected experimentally at 197 cm^{-1}, 348 cm^{-1}, 547 cm^{-1} [102]. The activity of these modes is also apparent in the simulated spectra, however the positions of minor bands are difficult to precisely locate due to the intricate low-intensity structure.

The initially excited wave packet was propagated over 600 femtoseconds in the $1\,^1B_u$ and 2^1A_g potential manifolds. Figure (4.3) shows the population dynamics of the bright state utilizing DFT/MRCI-R and DFT/MRCI-S PESs. Like in the *all-s-trans*-butadiene and *trans*-hexatriene, the energy transfer to 2^1A_g in octatetraene proceeds on the sub-picosecond time scale. DFT/MRCI-S completes the first step of photodynamics within τ=157 fs after the excitation to the bright state, as estimated from the curve fit to the exponential function $exp(-t/\tau)$. The population curve of the ionic state decays monotonously, with 10% of the entire wave packet remaining localized on the $1\,^1B_u$ surfaces. This outcome is in good agreement with the value of ~0.3 ps deduced from the experimentally observed 0-0 bandwidth for excitation at the origin [102, 103]. The DFT/MRCI-R predicts a slightly different picture with exponentially fitted lifetime τ=95 fs. The $1\,^1B_u$ population abruptly sweeps down and the wave packet reaches its meta-stable localization among the two manifolds after 100 fs of the propagation time, yielding 70% of its density to the dark state. Hereafter, the remaining half is lost in the next 200 fs. This is somewhat too fast for OT compared to what is experimentally estimated and the results for *trans*-hexatriene dynamics (see Section (4.3)). However, one can anticipate such effect appealing to the negligible energy splitting between the states at the Franck-Condon point as the pivotal quantity in the internal conversion process. This explains the very steep slope of DFT/MRCI-R curve, and, therefore, the nonradiative lifetime of the bright state is clearly underrated.

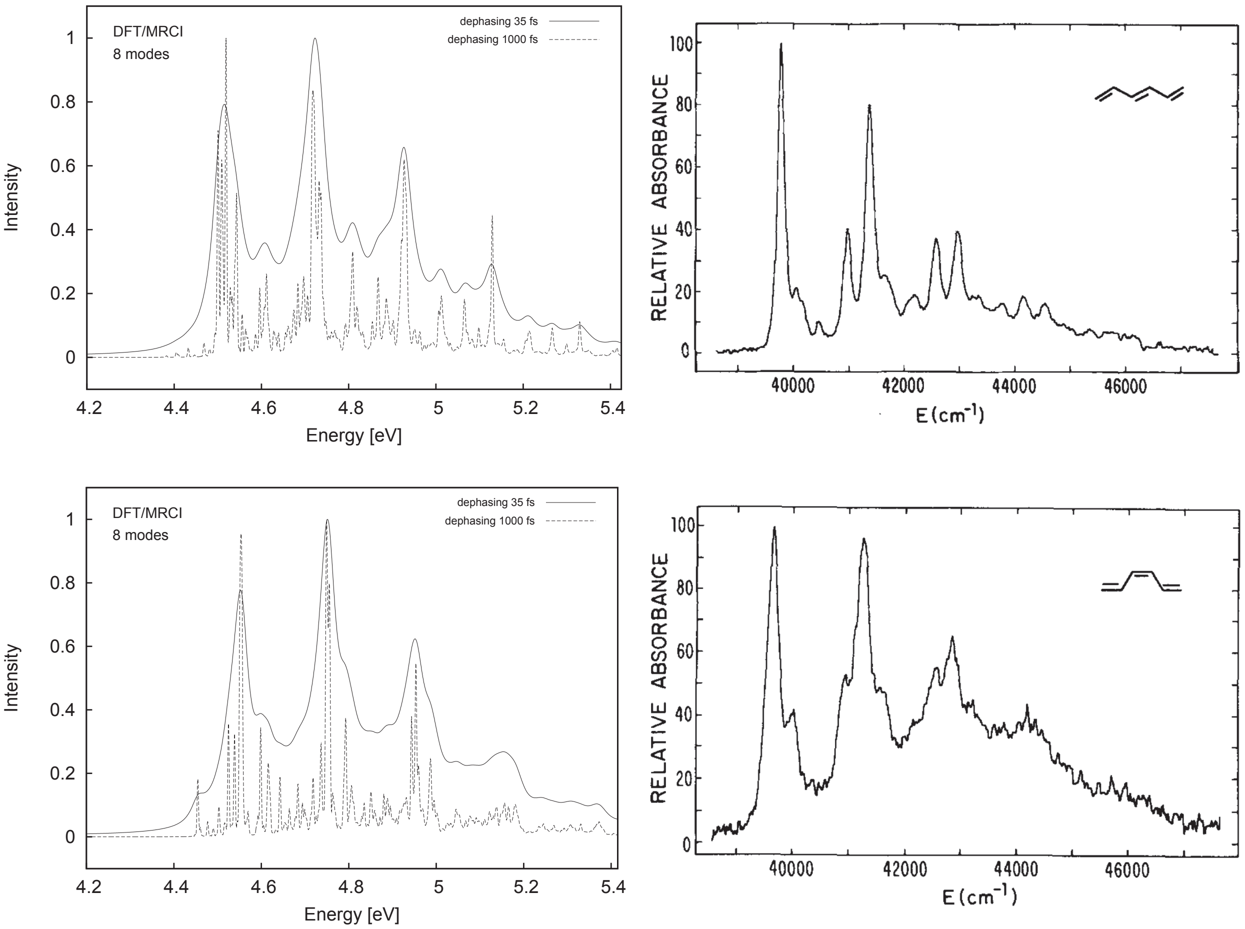

Figure 4.4. Calculated DFT/MRCI-R absorption spectra in UV range of *trans*-hexatriene (upper) and *cis*-hexatriene (lower). Jet absorption spectra (right panels) was reprinted from J. Chem. Phys. **81**, 4218 (1984) with the permission of AIP Publishing.

4.3. Trans- and cis-hexatriene

The dynamics of the nonadiabatically coupled lowest singlet excited states of *cis*- and *trans*-hexatriene were also studied theoretically employing DFT/MRCI-R potentials. For the *trans*- isomer the bright $1^1\mathrm{B_u}$ is found at 4.84 eV and the dark $2^1\mathrm{A_g}$ — at 5.22 eV, whilst the experiment locates the states at 5.08 eV and 5.21 eV, correspondingly [120]. An effect of underestimating the ionic state energy is also observed here, although the discrepancy is smaller ~0.2 eV compared to *all-trans*-octatetraene. The same holds for *cis*-hexatriene: 4.87 eV for the bright state and 5.15 eV for the dart state from the theory and 5.16 eV for the experimentally assigned $1^1\mathrm{B_2}$ [121, 122]. Here the energetic positions agree, however, the DFT/MRCI-R overshoots the energy gap at the Franck-Condon center again. Vibrational modes transform as follow:

$$\begin{aligned}\Gamma_{\mathbf{Q}}^{\mathrm{trans}} &= 13\mathrm{a_g} \oplus 6\mathrm{a_u} \oplus 5\mathrm{b_g} \oplus 12\mathrm{b_u}\\ \Gamma_{\mathbf{Q}}^{\mathrm{cis}} &= 13\mathrm{a_1} \oplus 6\mathrm{a_2} \oplus 5\mathrm{b_1} \oplus 12\mathrm{b_2}\end{aligned} \tag{4.9}$$

For the construction of the underlying vibronic Hamiltonian (4.5), up to nine curvilinear degrees of freedom were included in the simulations. Among them are four totally symmetric internal coordinates, namely the stretching of the two terminal double bonds, the stretching of the single bonds, the stretching of the central double bond and the last relevant distortion is the deformation of terminal angles. $\mathbf{Q}_{coup}$ includes the antisymmetric stretching of the single bonds and the antisymmetric bending of the inner angles. In addition, three out-of-plane motions were included: disrotatory and conrotatory twists of CH_2 groups and the skeletal torsion about the middle bond.

The DFT/MRCI-R absorption spectra of *trans*- and *cis*-hexatriene in the 5 eV range, incorporating eight modes to the potential energy matrix, is shown on Figure (4.4). Due to the high coupling strength between two nonadiabatic surfaces (see Paper **V**), the high-resolution spectra dephased by 1000 fs depict rather a non-trivial structure for any kind of interpretation. In contrast, the vibronic bands in the low-resolution 35 fs picture are quite diffuse, similar to the jet-cooled spectra. For comparison, the spectra recorded in a jet experiment by Leopold et. al. [98] is illustrated in Figure (4.4). Similar to the OT, spectra of hexatrienes show three most prominent bands arising from vibronic progressions of bond deformations [98] each of which appears with a fine structure in experiment. However, the shoulders are hardly visible in the simulated spectra for the same reason as in OT, namely — no intensity for the fundamental single-bond alternation mode at 1200 cm^{-1} from the right of the origin. This causes an intensity disbalance of the major peaks when comparing to the experimental finding, although their position with respect to the origin agrees well with experiment.

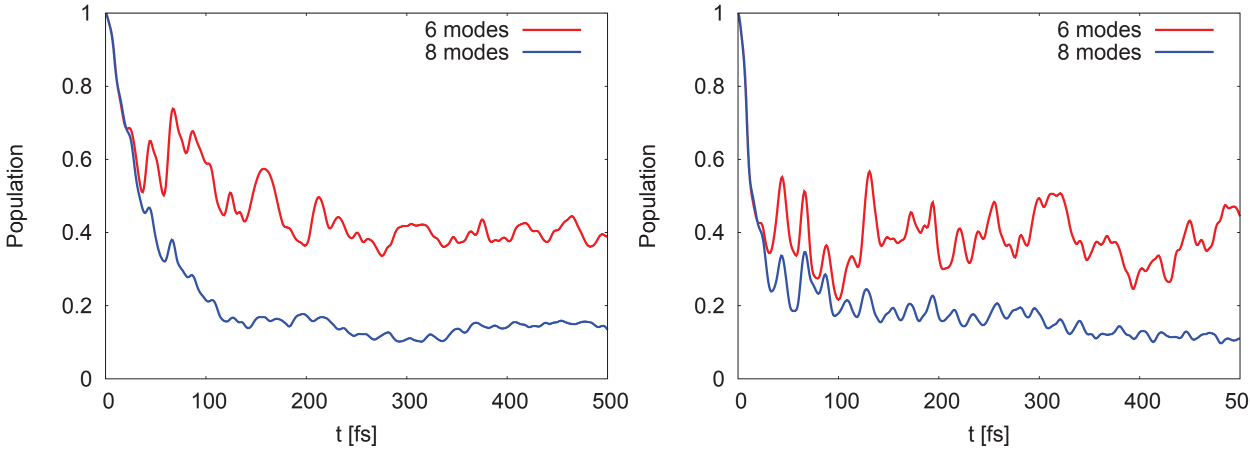

Figure 4.5. Population decay of the bright excited state of *trans*-hexatriene (left) and *cis*-hexatriene (right) using DFT/MRCI-R potentials.

The time-dependent electronic population of the $1\,^1B_u/1^1B_2$ state for *trans-/cis*-hexatriene following the energy absorption is displayed in Figure (4.5) as calculated using only in-plane modes (6 modes curve) and in-plane modes combined with CH_2 twists potentials (8 modes curve). The population transfer proceeds in the ultra-fast regime and appears to be more complete with inclusion of out-of-plane modes, which also reduces the fluctuations for both isomers. The short-time dynamics of the WP is much faster than the time scale of dipole-allowed emission, which is supported by experimental findings. However, a long-time average leaves ~15% and ~10% of entire density on the surfaces of the ionic states for the *trans*- and *cis*-isomer, correspondingly. It somewhat contradicts the experimental findings for *trans*-hexatriene as a nonfluorescent system, and, although under special conditions, *cis*-hexatriene as weakly emissive [123, 124]. For further discussion and nine modes spectra see Paper **V**.

Conclusions

A new way of parameterizing the semiempirical DFT/MRCI Hamiltonian was developed and implemented. As in the original approach, it incorporates dynamic and static electron correlation through a combination of KS-DFT and tuned configuration interaction. By separate calibration of spin-independent and exchange-like integrals in the diagonal matrix elements, the new DFT/MRCI-R was shown to be suitable for the description of the excimeric states. By construction, it yields consistent results for singlet, triplet, and quintet states in monomers and dimers, which is essential for the quantum chemical treatment of singlet fission. Through introduction of off-diagonal damping, for avoiding dynamic electron correlation contribution arising from the configuration expansion, the calculations can be performed at relatively low computational cost. Benchmark analysis on low-lying one-electron vertical transition energies of valence-to-valence and valence-to-Rydberg types in organic molecules gave a similar statistical picture as the original formulation of Grimme and Waletzke. The result of the DFT/MRCI-R assessment showed a root-mean-square deviation of 0.15 eV with the maximum error not exceeding 0.40 eV, which surpasses a convenient TD-DFT performance. Furthermore, one-electron interstate properties such as oscillator strength and spin-orbit coupling demonstrate the reliability of the DFT/MRCI-R singlet and triplet excited state wave functions. The application of DFT/MRCI-R potentials for the $1^1\mathrm{B}_\mathrm{u}$ and $2^1\mathrm{A}_\mathrm{g}$ states in *cis*-hexatriene, *trans*-hexatriene and *all-trans*-octatetraene describes well the main vibronic progressions due to Franck-Condon effects. However, the band associated with carbon-carbon single bond deformations is lacking intensity, which might be the result of the additivity assumption of the multidimensional potential energy surface. One shall bear in mind, that the family of polyenes represents a big challenge for computational chemistry due to the different nature of two low-lying valence states. They require an accurate and balanced description to model the absorption spectra and nonradiative internal conversion dynamics, which might be another explanation for the low intensity of the C–C activities in DFT/MRCI-R results.

Currently the method is being tested with regard to its performance in metal organic systems. Of particular interest are spin crossover complexes containing a transition metal where singlet-quintet and quintet-quintet transition energies are experimentally available. Although the DFT/MRCI-R Hamiltonian was not parameterized against quintet spin states, one might rely on the proposed spin-independent parameterization in elucidating the latter optical phenomenon. Another work in progress is the construction of a hybrid calculation scheme for even multiplicity systems. The difficulty here is that the standard Kohn-Sham approach limits itself to occupied orbitals and is intractable for the ground state with unpaired electrons.

It turns out that DFT/MRCI-R inherits all asymptotical drawbacks from the underlying BHLYP functional. One may clearly see this in the test calculation of the first charge-transfer state energy in the ethylene dimer (Figure (C.1)). When the interchromophore distance R is large enough, the charge-transfer state is seen as the interaction of a positively charged

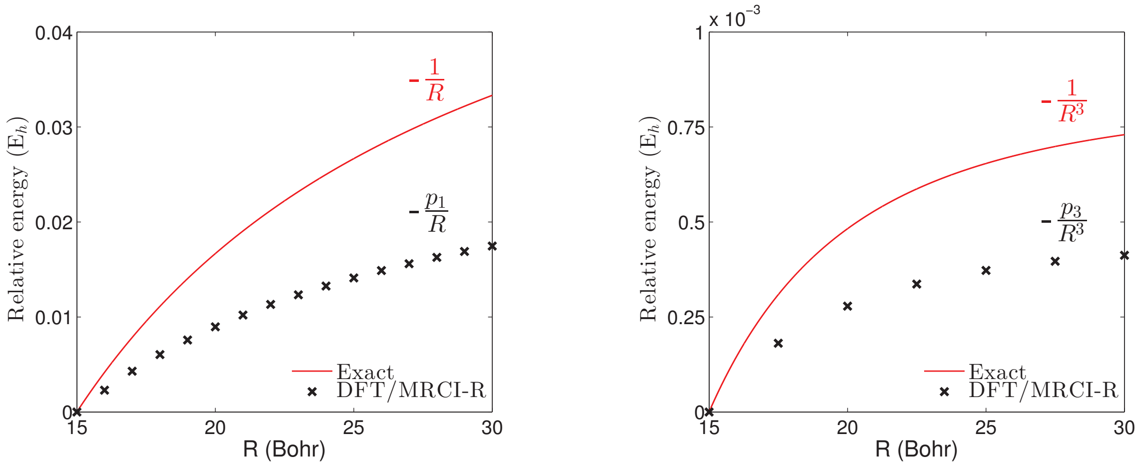

Figure C.1. DFT/MRCI-R energy of the first charge-transfer state (left) and half of the energy gap between first two localized transitions in ethylene dimer.

electron density located on one monomer and a negatively charged density on the other side. Thereby, the state energy must asymptotically approach with $-1/R$ to the difference of the monomeric energies of the ionization potential and electron affinity with respect to the ground state of the dimer. Contrary to this, as Figure (C.1) implies, the outer-range DFT/MRCI-R potential is reduced by a factor of p_1 owing to the scaled Coulomb interaction in the diagonal matrix elements of the Hamiltonian. It necessarily leads to the underestimation of the energetics of charge-transfer and high-lying Rydberg excitations. A similar effect is illustratively observed by deducing the excitonic coupling between two localized Frenkel excitations from the DFT/MRCI-R outcome. At large spatial distance, as the first approximation, two local transitions are part of a 2x2 eigenvalue problem with degenerate configuration energies. In this case, the interstate gap is given by a double off-diagonal term of the Hamiltonian. Assuming that the molecules are situated on a parallel plane with face-to-face conformation, the interaction of two local transitions is reduced to the interaction of local transition moments with known asymptotic behavior, which must obey $-1/R^3$ dependency. However, this is again not the case for DFT/MRCI-R, which underestimates the excitonic splitting with regard to the off-diagonal scaling parameter p_3 (Figure (C.1)). The Coulomb calibration by p_1 and p_3 for local excitations is essential in the context of DFT/MRCI and is playing a counterpart to the small KS-orbital energy gap. Fortunately, there is a known solution to remedy the latter problems. It lies in the partitioning of the Coulomb operator into a short-range interaction, where some portion of the exact exchange is preferred, and a long-range part, which must comprise the entire nonlocal integral in the KS equations. The most simple form reads as:

$$\frac{1}{r_{ij}} \rightarrow \frac{\alpha + \beta \cdot \mathrm{erf}(\mu r_{ij})}{r_{ij}} + \frac{1 - \left[\alpha + \beta \cdot \mathrm{erf}(\mu r_{ij})\right]}{r_{ij}} \tag{4.10}$$

where μ is the damping parameter, whilst α and $\alpha + \beta$ define the percentage of the HF exchange at $r_{ij} \rightarrow 0$ and $r_{ij} \rightarrow \infty$, respectively. It is expected, that the condition $\alpha + \beta = 1$

shall be imposed in Equation (4.10) in order to enforce the correct asymptotic behavior. The different fraction of exchange at different interparticle distances is widely used in the family of range-separated hybrid functionals [125, 126]. The latter could be integrated into the DFT/MRCI Hamiltonian with apparent needs to encounter both long-range and short--range terms at the configuration interaction level. It requires to evaluate an additional set of RI-assisted integrals of the attenuated Coulomb operator and its metrics in Equation (2.8). Another fact pointing toward the use of a different density functional approximation is that the DFT/MRCI scheme exploits the KS-SCF energy for the initial Hartree-Fock reference. Therefore, all excited state potentials rely on the rigorous ground state performance of the incorporated functional, whereas short-range electron correlation in BHLYP is far from being supreme in thermodynamical tasks. All these issues — related to the pathological tendency of energy underestimation for states involving two electrons annihilated from n-orbitals, unpaired electrons at the ground state problem, the choice of density functional approximation for the next DFT/MRCI generation and some more — are intensively studied in our group.

Acknowledgements

I am grateful to Prof. Dr. C.M. Marian for the formulation and coordination of the project, her mentoring support and countless discussions regarding modern topics of molecular excited states. My gratitude goes to Dr. M. Kleinschmidt for his immense help with the MRCI routines and principles of excited-state calculations in the beginning of my work. I am thankful to Prof. Dr. H. Köppel and Dr. A. Komainda for the fruitful collaboration on the excited polyene research and the introduction to the field of quantum dynamics calculations. I would like to thank Prof. Dr. W. Thiel and Prof. Dr. S. Grimme for helpful discussions and reviewing the current work. Shoutout to my friends up in Düsseldorf, Germany and EU, without you all my life here would be pale. I appreciate a warm ambience and the rich library of the Theoretische Chemie und Computerchemie group, and A. Heil personally for taking care of the Zusammenfassung and stylistic issues of the text. Financial support by Heinrich-Heine Universität Düsseldorf and the Deutsche Forschungsgemeinschaft (DFG) Project No. MA1051/14-1 is gratefully acknowledged.

Bibliography

1. R. Pariser and R. G. Parr, J. Chem. Phys. **21**, 466 (1953).
2. G. M. Zhidomirov, N. U. Zhanpeisov, I. L. Zilberberg, and I. V. Yudanov, Int. J. Quantum Chem. **58**, 175 (1996).
3. J. J. P. Stewart, J. Mol. Model. **19**, 1 (2013).
4. W. Thiel, WIREs Comput. Mol. Sci. **4**, 145 (2014).
5. A. A. Voityuk, WIREs Comput. Mol. Sci. **3**, 515 (2013).
6. M. R. Silva-Junior, M. Schreiber, S. P. A. Sauer, and W. Thiel, J. Chem. Phys. **129**, 104103 (2008).
7. M. R. Silva-Junior and W. Thiel, J. Chem. Theory Comput. **6**, 1546 (2010).
8. R. Crespo-Otero and M. Barbatti, J. Chem. Phys. **134**, 164305 (2011).
9. D. Escudero and W. Thiel, J. Chem. Phys. **140**, 194105 (2014).
10. M. Kleinschmidt, C. van Wüllen, and C. M. Marian, J. Chem. Phys. **142**, 094301 (2015).
11. A. Heil, K. Gollnisch, M. Kleinschmidt, and C. M. Marian, Mol. Phys. **114**, 407 (2016).
12. J. Föller, M. Kleinschmidt, and C. M. Marian, Inorg. Chem. **55**, 7508 (2016).
13. C. M. Marian and N. Gilka, J. Chem. Theory Comput. **4**, 1501 (2008).
14. S. Siegert, F. Vogeler, C. M. Marian, and R. Weinkauf, Phys. Chem. Chem. Phys. **13**, 10350 (2011).
15. M. Kleinschmidt, C. M. Marian, M. Waletzke, and S. Grimme, J. Chem. Phys. **130**, 044708 (2009).
16. D. Escudero, W. Thiel, and B. Champagne, Phys. Chem. Chem. Phys. **17**, 18908 (2015).
17. J. P. Götze, D. Kröner, S. Banerjee, B. Karasulu, and W. Thiel, ChemPhysChem **15**, 3392 (2014).
18. J. P. Götze and W. Thiel, Chem. Phys. **415**, 247 (2013).
19. M. R. Silva-Junior, M. Mansurova, W. Gärtner, and W. Thiel, ChemBioChem **14**, 1648 (2013).
20. J. P. Götze, B. Karasulu, M. Patil, and W. Thiel, Biochim. Biophys. Acta **1847**, 1509 (2015).
21. O. Andreussi, S. Knecht, C. M. Marian, J. Kongsted, and B. Mennucci, J. Chem. Theory Comput. **11**, 655 (2015).
22. I. Dokukina and O. Weingart, Phys. Chem. Chem. Phys. **17**, 25142 (2015).
23. C. M. Marian, S. Nakagawa, V. Rai-Constapel, B. Karasulu, and W. Thiel, J. Phys. Chem. B **118**, 1743 (2014).
24. N. H. List, C. Curutchet, S. Knecht, B. Mennucci, and J. Kongsted, J. Chem. Theory Comput. **9**, 4928 (2013).
25. S. Salzmann and C. M. Marian, Photochem. Photobiol. Sci. **8**, 1655 (2009).
26. J.-M. Mewes, V. Jovanovic, C. M. Marian, and A. Dreuw, Phys. Chem. Chem. Phys. **16**, 12393 (2014).

27. M. Born and R. Oppenheimer, Annalen der Physik **389**, 457 (1927).
28. R. Bast and E. Per-Olof Widmark, *European Summerschool in Quantum Chemistry 2013, Book I-III* (ESQC committee, 2013).
29. A. T. Amos and G. G. Hall, Proc. R. Soc. Lond. A **263**, 483 (1961).
30. R. S. Mulliken, Phys. Rev. **32**, 186 (1928).
31. R. S. Mulliken, Phys. Rev. **41**, 49 (1932).
32. C. C. J. Roothaan, Rev. Mod. Phys. **23**, 69 (1951).
33. G. G. Hall, Proc. R. Soc. Lond. A **205**, 541 (1951).
34. L. H. Thomas, Proc. Camb. Philos. Soc. **23**, 542 (1927).
35. E. Fermi, Z. Phys. **48**, 73 (1928).
36. P. A. M. Dirac, Proc. R. Soc. Lond. A **123**, 714 (1929).
37. P. A. M. Dirac, Proc. Camb. Philos. Soc. **26**, 376 (1930).
38. P. Hohenberg and W. Kohn, Phys. Rev. **136**, B864 (1964).
39. W. Kohn and L. J. Sham, Phys. Rev. **140**, A1133 (1965).
40. M. A. Buijse, *Electron Correlation. Fermi and Coulomb Holes, Dynamical and Nondynamical Correlation*, Ph.D. thesis, Vrije Universiteit (1991).
41. J. C. Slater, Phys. Rev. **81**, 385 (1951).
42. W. Koch and M. C. Holthausen, *A Chemist's Guide to Density Functional Theory, Second Edition* (Wiley-VCH Verlag GmbH, 2001).
43. S. H. Vosko, L. Wilk, and M. Nusair, Can. J. Phys. **58**, 1200 (1980).
44. J. P. Perdew and Y. Wang, Phys. Rev. B **45**, 13244 (1992).
45. A. D. Becke, Phys. Rev. A **38**, 3098 (1988).
46. R. Colle and O. Salvetti, Theor. Chim. Acta **37**, 329 (1975).
47. C. Lee, W. Yang, and R. G. Parr, Phys. Rev. B **37**, 785 (1988).
48. B. Miehlich, A. Savin, H. Stoll, and H. Preuss, Chem. Phys. Lett. **157**, 200 (1989).
49. D. Langreth and J. Perdew, Solid State Commun. **17**, 1425 (1975).
50. O. Gunnarsson and B. I. Lundqvist, Phys. Rev. B **13**, 4274 (1976).
51. A. D. Becke, J. Chem. Phys. **98**, 1372 (1993).
52. A. J. Cohen, P. Mori-Sánchez, and W. Yang, Chem. Rev. **112**, 289 (2012).
53. E. S. Kryachko and E. V. Ludena, Phys. Rep. **544**, 123 (2014).
54. R. Peverati and D. G. Truhlar, Phil. Trans. R. Soc. A **372**, 20120476 (2014).
55. G. A. Segal, R. W. Wetmore, and K. Wolf, Chem. Phys. **30**, 269 (1978).
56. R. W. Wetmore and G. A. Segal, Chem. Phys. Lett. **36**, 478 (1975).
57. S. Grimme, Chem. Phys. Lett. **259**, 128 (1996).
58. S. Grimme and M. Waletzke, J. Chem. Phys. **111**, 5645 (1999).
59. M. Waletzke, *Implementation und Anwendung von Multireferenz-DFT und ab initio Methoden für große Moleküle*, Ph.D. thesis, Rheinischen Friedrich-Wilhelms-Universität Bonn (2001).
60. F. Weigend and M. Häser, Theor. Chem. Acc. **97**, 331 (1997).

61. R. L. Christensen, M. G. I. Galinato, E. F. Chu, J. N. Howard, R. D. Broene, and H. A. Frank, J. Phys. Chem. A **112**, 12629 (2008).
62. M. Kleinschmidt, C. M. Marian, M. Waletzke, and S. Grimme, J. Chem. Phys. **130**, 044708 (2009).
63. E. V. Beck, *A Multireference Density Functional Approach to the Calculation of the Excited States of Uranium Ions*, Ph.D. thesis, Air Force Institute of Technology, Dayton (2007).
64. E. V. Beck, E. A. Stahlberg, L. W. Burggraf, and J.-P. Blaudeau, Chem. Phys. **349**, 158 (2008).
65. M. Roemelt and F. Neese, J. Phys. Chem. A **117**, 3069 (2013).
66. M. Roemelt, D. Maganas, S. DeBeer, and F. Neese, J. Chem. Phys. **138**, 204101 (2013).
67. A. Kuppermann, W. M. Flicker, and O. A. Mosher, Chem. Rev. **79**, 77 (1979).
68. M. Kleinschmidt, J. Tatchen, and C. M. Marian, J. Comput. Chem. **23**, 824 (2002).
69. S. Salzmann, M. Kleinschmidt, J. Tatchen, R. Weinkauf, and C. M. Marian, Phys. Chem. Chem. Phys. **10**, 380 (2008).
70. J. Tatchen, M. Waletzke, C. M. Marian, and S. Grimme, Chem. Phys. **264**, 245 (2001).
71. S. Salzmann, J. Tatchen, and C. M. Marian, J. Photochem. Photobiol. A: Chemistry **198**, 221 (2008).
72. C. M. Marian, WIREs Comput. Mol. Sci. **2**, 187 (2012).
73. M. Kleinschmidt and C. M. Marian, Chem. Phys. **311**, 71 (2005).
74. M. Kleinschmidt, J. Tatchen, and C. M. Marian, J. Chem. Phys. **124**, 124101 (2006).
75. G. D. Scholes, K. P. Ghiggino, A. M. Oliver, and M. N. Paddon-Row, J. Am. Chem. Soc. **115**, 4345 (1993).
76. S. Tretiak, W. M. Zhang, V. Chernyak, and S. Mukamel, Proc. Natl. Acad. Sci. **96**, 13003 (1999).
77. R. J. Dillon, G. B. Piland, and C. J. Bardeen, J. Am. Chem. Soc. **135**, 17278 (2013).
78. E. G. Fuemmeler, S. N. Sanders, A. B. Pun, E. Kumarasamy, T. Zeng, K. Miyata, M. L. Steigerwald, X.-Y. Zhu, M. Y. Sfeir, L. M. Campos, and N. Ananth, ACS Cent. Sci. **2**, 316 (2016).
79. D. H. Arias, J. L. Ryerson, J. D. Cook, N. H. Damrauer, and J. C. Johnson, Chem. Sci. **7**, 1185 (2016).
80. X. Feng and A. I. Krylov, Phys. Chem. Chem. Phys. **18**, 7751 (2016).
81. M. B. Smith and J. Michl, Chem. Rev. **110**, 6891 (2010).
82. O. Varnavski, N. Abeyasinghe, J. Aragó, J. J. Serrano-Pérez, E. Ortí, J. T. L. Navarrete, K. Takimiya, D. Casanova, J. Casado, and I. Theodore Goodson, J. Phys. Chem. Lett. **6**, 1375 (2015).
83. A. D. Chien, A. R. Molina, N. Abeyasinghe, O. P. Varnavski, I. Theodore Goodson, and P. M. Zimmerman, J. Phys. Chem. C **119**, 28258 (2015).
84. G. Cerullo, D. Polli, G. Lanzani, S. De Silvestri, H. Hashimoto, and R. J. Cogdell,

Science **298**, 2395 (2002).
85. X. Hu, A. Damjanović, T. Ritz, and K. Schulten, Proc. Natl. Acad. Sci. **95**, 5935 (1998).
86. X. Hu and K. Schulten, Phys. Today **50**, 28 (1997).
87. R. Schmidt, J. Phys. Chem. A **108**, 5509 (2004).
88. P. D. Mascio, S. Kaiser, and H. Sies, Arch. Biochem. Biophys. **274**, 532 (1989).
89. O. Hirayama, K. Nakamura, S. Hamada, and Y. Kobayasi, Lipids **29**, 149 (1994).
90. R. S. Becker, Photochem. Photobiol. **48**, 369 (1988).
91. O. Weingart, J. Am. Chem. Soc. **129**, 10618 (2007).
92. D. Polli, P. Altoe, O. Weingart, K. M. Spillane, C. Manzoni, D. Brida, G. Tomasello, G. Orlandi, P. Kukura, R. A. Mathies, M. Garavelli, and G. Cerullo, Nature **467**, 440 (2010).
93. J. H. Starcke, M. Wormit, J. Schirmer, and A. Dreuw, Chem. Phys. **329**, 39 (2006).
94. K. Nakayama, H. Nakano, and K. Hirao, Int. J. Quantum Chem. **66**, 157 (1998).
95. P. Tavan and K. Schulten, J. Chem. Phys. **70**, 5407 (1979).
96. R. Mcdiarmid, Adv. Chem. Phys. **110**, 177 (2007).
97. A. Komainda, B. Ostojić, and H. Köppel, J. Phys. Chem. A **117**, 8782 (2013).
98. D. G. Leopold, R. D. Pendley, J. L. Roebber, R. J. Hemley, and V. Vaida, J. Chem. Phys. **81**, 4218 (1984).
99. A. B. Myers and K. S. Pranata, J. Phys. Chem. **93**, 5079 (1989).
100. X. Ci and A. B. Myers, J. Chem. Phys. **96**, 6433 (1992).
101. Z. Qu and C. Liu, J. Chem. Phys. **139**, 244304 (2013).
102. D. G. Leopold, V. Vaida, and M. F. Granville, J. Chem. Phys. **81**, 4210 (1984).
103. W. G. Bouwman, A. C. Jones, D. Phillips, P. Thibodeau, C. Friel, and R. L. Christensen, J. Phys. Chem. **94**, 7429 (1990).
104. L. Cederbaum, W. Domcke, H. Köppel, and W. V. Niessen, Chem. Phys. **26**, 169 (1977).
105. L. S. Cederbaum and W. Domcke, Adv. Chem. Phys. **36**, 205 (2007).
106. H. Köppel, W. Domcke, and L. S. Cederbaum, Adv. Chem. Phys. **57**, 59 (1984).
107. E. B. Wilson, J. Chem. Phys. **7**, 1047 (1939).
108. E. B. Wilson, J. C. Decius, and P. C. Cross, *Molecular Vibrations - the Theory of Infrared and Raman Vibrational Spectra* (McGraw-Hill Book Company, Inc, 1955).
109. J. H. Frederick and C. Woywod, J. Chem. Phys. **111**, 7255 (1999).
110. L. Serrano-Andres, R. Lindh, B. O. Roos, and M. Merchan, J. Phys. Chem. **97**, 9360 (1993).
111. J. R. Ackerman, B. E. Kohler, D. Huppert, and P. M. Rentzepis, J. Chem. Phys. **77**, 3967 (1982).
112. R. M. Gavin, C. Weisman, J. K. McVey, and S. A. Rice, J. Chem. Phys. **68**, 522 (1978).
113. L. A. Heimbrook, B. E. Kohler, and I. J. Levy, J. Chem. Phys. **81**, 1592 (1984).
114. M. F. Granville, G. R. Holtom, and B. E. Kohler, J. Chem. Phys. **72**, 4671 (1980).
115. H. Petek, A. J. Bell, Y. S. Choi, K. Yoshihara, B. A. Tounge, and R. L. Christensen, J.

Chem. Phys. **98**, 3777 (1993).

116. M. Schreiber, M. R. Silva-Junior, S. P. A. Sauer, and W. Thiel, J. Chem. Phys. **128**, 134110 (2008).
117. C. Angeli and M. Pastore, J. Chem. Phys. **134**, 184302 (2011).
118. J. Catalán and J. L. G. de Paz, J. Chem. Phys. **124**, 034306 (2006).
119. M. Wanko, M. Garavelli, F. Bernardi, T. A. Niehaus, T. Frauenheim, and M. Elstner, J. Chem. Phys. **120**, 1674 (2004).
120. T. Fujii, A. Kamata, M. Shimizu, Y. Adachi, and S. Maeda, Chem. Phys. Lett. **115**, 369 (1985).
121. R. J. Hemley, A. C. Lasaga, V. Vaida, and M. Karplus, J. Phys. Chem. **92**, 945 (1988).
122. B. Amstrup, F. W. Langkilde, K. Bajdor, and R. Wilbrandt, J. Phys. Chem. **96**, 4794 (1992).
123. H. Petek, A. J. Bell, R. L. Christensen, and K. Yoshihara, J. Chem. Phys. **96**, 2412 (1992).
124. W. J. Buma, B. E. Kohler, and K. Song, J. Chem. Phys. **94**, 6367 (1991).
125. R. Baer, E. Livshits, and U. Salzner, Annu. Rev. Phys. Chem. **61**, 85 (2010).
126. M. Casida and M. Huix-Rotllant, Annu. Rev. Phys. Chem. **63**, 287 (2012).

Related publications

THE JOURNAL OF CHEMICAL PHYSICS **144**, 034104 (2016)

Redesign of the DFT/MRCI Hamiltonian

Igor Lyskov, Martin Kleinschmidt, and Christel M. Marian[a]
Institute of Theoretical and Computational Chemistry, Heinrich-Heine-University Düsseldorf, Universitätsstraße 1, 40225 Düsseldorf, Germany

(Received 3 December 2015; accepted 5 January 2016; published online 19 January 2016)

The combined density functional theory and multireference configuration interaction (DFT/MRCI) method of Grimme and Waletzke [J. Chem. Phys. **111**, 5645 (1999)] is a well-established semi-empirical quantum chemical method for efficiently computing excited-state properties of organic molecules. As it turns out, the method fails to treat bi-chromophores owing to the strong dependence of the parameters on the excitation class. In this work, we present an alternative form of correcting the matrix elements of a MRCI Hamiltonian which is built from a Kohn-Sham set of orbitals. It is based on the idea of constructing individual energy shifts for each of the state functions of a configuration. The new parameterization is spin-invariant and incorporates less empirism compared to the original formulation. By utilizing damping techniques together with an algorithm of selecting important configurations for treating static electron correlation, the high computational efficiency has been preserved. The robustness of the original and redesigned Hamiltonians has been tested on experimentally known vertical excitation energies of organic molecules yielding similar statistics for the two parameterizations. Besides that, our new formulation is free from artificially low-lying doubly excited states, producing qualitatively correct and consistent results for excimers. The way of modifying matrix elements of the MRCI Hamiltonian presented here shall be considered as default choice when investigating photophysical processes of bi-chromophoric systems such as singlet fission or triplet-triplet upconversion. © *2016 AIP Publishing LLC.* [http://dx.doi.org/10.1063/1.4940036]

I. INTRODUCTION

Methods of combining dynamic and static electron correlation are powerful tools in the hands of quantum chemists for studying molecular excited-state processes. One of them, the so-called complete active space second-order perturbation theory (CASPT2),[1,2] treats static correlation in a rather small electron-orbital space (usually the complete active space configuration interaction treatment does not exceed 16 electrons in 16 orbitals) adding second-order perturbation corrections to the total energy afterwards for accounting dynamic correlation. The method appears to be robust for exploring vertical excitation energies and excited-state dynamics of molecular systems,[3] but it is computationally time demanding due to the tremendous rise of configurations when increasing the active space. The restricted active space (RAS)[4] scheme alleviates the demands on the size of the active space to some extent, but this remains the bottleneck for the treatment of electronically excited states in extended heteroaromatic compounds. Another concept of looking at this issue is to combine results of density functional theory (DFT) calculations for treating dynamic correlation with a multi-reference configuration interaction (MRCI) approach which takes care in turn of non-dynamic effects.[5–8] The methodological idea behind DFT/MRCI is to employ a Kohn-Sham orbital set for constructing configuration state functions (CSFs) and to dress the MRCI matrix elements by appropriate portions of Coulomb- and exchange-like integrals. In the original work by Grimme and Waletzke,[5] different parameter sets were employed for singlet and triplet state calculations.

DFT/MRCI shows great efficiency for the evaluation of excited-state energies which mainly originate from one-electron transitions.[9] Furthermore, the method has been shown to perform well in extended π-systems such as polyenes[10] and mini-carotenes[11] where doubly excited configurations of HOMO, HOMO→LUMO, LUMO type are essential for the proper discussion of the 2^1A_g state. However, it fails for electronic states where four-open-shell configurations play a leading role in the CI vector. Consider, for example, local excitations in ethylene $\pi_1 \rightarrow \pi_1^*$ and tetrafluoroethylene $\pi_2 \rightarrow \pi_2^*$ which are spatially well separated (Figure 1). If the molecules are excited simultaneously, the various orientations of individual spin moments m_1 and m_2 of the monomers define the eigenstates of the dimer as components of $|s_1,m_1\rangle \otimes |s_2,m_2\rangle$. This product is generally reducible and can be decomposed into sixteen components $|S,M,s_1,s_2\rangle$ of the state wave functions, each of which is represented by linear combinations of local one-electron excitations

$$|S,M,s_1,s_2\rangle = \sum_{m_1 m_2} c^{S,M}_{m_1,m_2} |s_1,m_1\rangle |s_2,m_2\rangle.$$

As long as $|s_i,m_i\rangle$ are solutions of the spin-free Hamiltonian in the absence of external electromagnetics fields, all components M of a total spin-moment S with fixed s_1 and s_2 are energetically degenerate. Thus, the sixteen possible product states can be grouped into two/three/one singlet/triplet/quintet multiplets. In a similar fashion, the $\pi_1\pi_2 \rightarrow \pi_1^*\pi_2^*$ transition

---

[a] E-mail: Christel.Marian@hhu.de. Tel.: +49-211-8113209. Fax: +49-211-8113446.

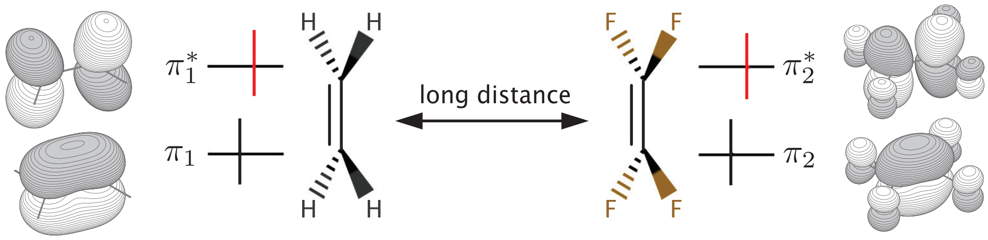

FIG. 1. Simultaneous local $\pi \rightarrow \pi^*$ excitations on ethylene and tetrafluoroethylene in a model dimer system.

energies of the dimer states $|S,0,m_1,m_2\rangle$ can be expressed as a sum of the energies of the local transitions $\pi_1 \rightarrow \pi_1^*$ and $\pi_2 \rightarrow \pi_2^*$ (Table I). The first two dimer states of singlet and triplet multiplicity, respectively, shown in Table I correspond to one-electron local excitations on one monomer in the presence of the unperturbed second one. Among all states of non-interacting monomers there is a symmetry which manifests itself in the degeneracy of one singlet, one triplet and the quintet composed of the monomer triplet states. As it is seen from Table I, this symmetry is not retained by DFT/MRCI. Instead, the energies of the spin-coupled triplet pairs are vastly underestimated. Let us also point out that the second singlet component $|0,0,0,0\rangle$ must be isoenergetic to the sum of the singlet energies of the monomers. Likewise, the second $|1,0,0,1\rangle$ and the third $|1,0,1,0\rangle$ triplets correspond to combinations of singlet and triplet energies of the monomers, respectively.

These failures are apparently linked to an incorrect parameterization of the Hamiltonian. Due to this fact, aromatic compounds containing, for example, a nitro group tend to suffer from low-lying intruder states[12] which makes the method inconvenient for the investigation of excited-state relaxation processes. Other obstacles are related to bichromophores and singlet fission. In the latter process, an optically accessible exciton is effectively split into two triplets, thereby generating a four-open-shell state in the dimer. In the present work, an alternative way of designing a hybrid DFT/MRCI Hamiltonian is presented. The challenge is to enhance the energetics of doubly excited configurations with varying number of open shells and multiplicity while maintaining the perfect performance of the standard parameterization for singly excited CSFs.

II. THEORY

Let $\bar{\wp}_i$ be the i-th component of the reference occupation vector $|\bar{\wp}\rangle$ in Fock space. The second-quantization form of the electronic Hamilton operator in terms of one-electron operators $\hat{\varepsilon}_i^j$ is then given by

$$\begin{aligned}\hat{\mathcal{H}} - E^{scf} = &-\sum_i F_{ii}\overline{\wp}_i + \frac{1}{2}\sum(V_{iijj} - \frac{1}{2}V_{ijji})\overline{\wp}_i\overline{\wp}_j \\ &+ \sum_{ij} F_{ij}\hat{\varepsilon}_i^j - \sum_{ijk}(V_{ijkk} - \frac{1}{2}V_{ikkj})\overline{\wp}_k\hat{\varepsilon}_i^j \\ &+ \frac{1}{2}\sum_{ijkl} V_{ijkl}(\hat{\varepsilon}_i^j\hat{\varepsilon}_k^l - \delta_{jk}\hat{\varepsilon}_i^l),\end{aligned} \tag{1}$$

where we have used the Mulliken notation of the four-index integral V_{ijkl}. In the formulation according to Eq. (1), a high degree of symmetry exists in the summation of two-electron integrals. Also the use of a closed-shell anchor configuration for configuration comparison and matrix element evaluation is wise in this context. The general case for systems with an even number of electrons will always be the Hartree-Fock (HF) reference. So an arbitrary occupation vector $|\wp\rangle$ will be considered as N-tuple electron-hole permutation of the closed-shell HF configuration. The energies of the states in $|\wp\rangle$ are then determined with regard to the HF energy by the interaction of all active orbitals and their Fock matrix elements. For configuration-based CI, the complete Hamiltonian can be split up into three separate cases: diagonal elements, one electron-hole and two electron-hole differences between two coupled configurations $|\wp_1\rangle$ and $|\wp_2\rangle$. Their mathematical expressions can be found in the work by Wetmore and Segal.[13,14]

TABLE I. DFT/MRCI $\pi \rightarrow \pi^*$ vertical excitation energies of ethylene $|s_1,0\rangle$, tetrafluoroethylene $|s_2,0\rangle$ and their $\pi_1\pi_2 \rightarrow \pi_1^*\pi_2^*$ dimer state $|S,0,s_1,s_2\rangle$ energies.

		Singlet (eV)		Triplet (eV)		Quintet (eV)	
		Computed	Expected	Computed	Expected	Computed	Expected
Monomer	$\lvert s_1,0\rangle$	8.05		4.42			
	$\lvert s_2,0\rangle$	8.99		4.90			
Dimer	$\lvert s_1,0\rangle$	7.84	8.05	4.29	4.42		
	$\lvert s_2,0\rangle$	8.72	8.99	4.79	4.90		
	$\lvert S,0,1,1\rangle$	2.19	9.32	4.21	9.32	…	9.32
	$\lvert S,0,0,1\rangle$			9.56	12.95		
	$\lvert S,0,1,0\rangle$			10.26	13.41		
	$\lvert S,0,0,0\rangle$	13.56	17.04				

In the original DFT/MRCI ansatz, the Becke *half-and-half* functional (BHLYP[15]) with 50% of Hartree-Fock exchange was found to be appropriate if mainly excited states are considered,[6]

$$E_{xc}^{bhlyp} = 0.5E_x^{hf} + 0.5(E_x^{b88} + E_x^{lda}) + E_c^{lyp}. \tag{2}$$

For conceptual reasons, it is convenient to choose canonical orbitals as the one-particle basis for generating the configuration space, although the Fock matrix in DFT has a different form compared to HF,

$$F_{ij}^{ks} = h_{ij} + \langle i|\frac{\delta E_{xc}[\rho]}{\delta \rho}|j\rangle + \sum_k \bar{\wp}_k V_{ijkk}. \tag{3}$$

Thereby, diagonal elements of the Fock matrix are replaced by KS orbital energies in the DFT/MRCI formalism and off-diagonal elements are zero.

A. Matrix element adjustment

The symmetry conservation of the ethylene-tetrafluoroethylene dimer in Table I requires to design identical parameterization for different spin states. In HF-based MRCI, the Fermi correlation is accounted via the HF exchange energy between interacting orbitals producing the state function. In terms of CI matrix elements, the energy splitting between CSFs in $|\wp\rangle$ is determined by the structural constants in front of the exchange integrals V_{ijji},

$${}^{\sigma_1}\mathcal{H}_{\wp\wp} - {}^{\sigma_2}\mathcal{H}_{\wp\wp} = \sum_{i,j}({}^{\sigma_1}\eta_{ij}^{ji} - {}^{\sigma_2}\eta_{ij}^{ji})V_{ijji}. \tag{4}$$

Herein, σ_i is a spin part of $|\wp\rangle$ and the η_{ij}^{ij} arise from the dot product of one-electron operators over the spin states σ' of the intermediate spatial occupation $\wp'$ produced by the promotion of an electron from orbital i to orbital j,

$$\begin{aligned}\eta_{ij}^{ji} &= \langle\wp\sigma_1|\hat{\varepsilon}_i^j\hat{\varepsilon}_j^i|\wp\sigma_2\rangle = (\hat{\varepsilon}_j^i|\wp\sigma_1\rangle)^\dagger \cdot (\hat{\varepsilon}_j^i|\wp\sigma_2\rangle)\\ &= \sum_{\sigma'}(\eta_j^i(\wp',\sigma',\wp,\sigma_1))^\dagger \cdot (\eta_j^i(\wp',\sigma',\wp,\sigma_2)).\end{aligned} \tag{5}$$

The coefficients $\eta(\wp,\sigma,\wp',\sigma')$ represent the weights associated with all possible combinations of spin functions σ and σ' for a given pair of space occupations $|\wp\rangle \otimes |\wp'\rangle$.[13] Numerical algebra for the evaluation spin-coefficients in Eq. (5) between CSFs of, in general case, an arbitrary number of open shells can be found elsewhere.[13,14] As was pointed out before, due to the symmetry in the summation of the two-electron integrals in Eq. (1), only the structural constants for singly occupied orbitals are in the focus of interest. All other contributions are either zero or vanish due to cancelation by other parts of the matrix element. The number of unpaired electrons n_o dictates the multiplicity manifold m_i an electronic system can adopt $|\frac{n_o}{2}, m_i\rangle$. It is useful to analyze the singlet-triplet energy splitting of a two open-shell state where non-dynamic correlation effects can be disregarded at first approximation. The difference of the two-electron spin integral parameters $\Delta\eta_{ij}^{ji}$ in Eq. (4) brings about a factor of 2 for this case. Fig. 2 shows that the HF exchange integral between created and annihilated BHLYP orbitals correlates nearly linearly with the experimental singlet-triplet splitting and can thus be reasonably scaled. This fact makes it possible to introduce an exchange-dependent parameter p_F as the prefactor of the weighted coefficients η_{ij}^{ji}. Based on this result, p_F is found to be near 0.3. In case of multiple excitations, configurations with more than a single CSF can be generated. In order to maintain a consistent energy splitting between states of one multiplicity, p_F must be applied for off-diagonal elements of the configuration as well. Worthwhile to note, these elements contain only exchange integrals over all combinations of open-shell orbitals. Hence, they can be simply scaled by $(1 - p_F)$.

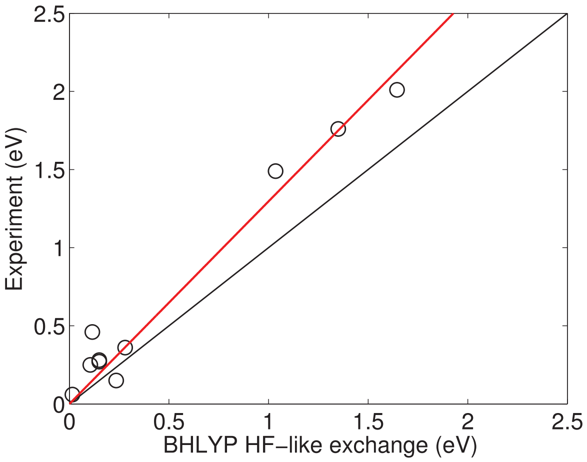

FIG. 2. Correlation between the exchange energy of BHLYP annihilated-created orbital pairs and experimental singlet-triplet splittings. For details see Table 1 of the supplementary material.[16]

The magnitude of one-electron excitation energies of valence-Rydberg or charge-transfer transitions is usually dominated by the electron-hole orbital energy gap reduced by the Coulomb interaction. In DFT theory, the orbital gap of the Kohn-Sham eigenvalues is much smaller compared to HF theory. Thus, a complementary Coulomb portion for diagonal elements is required.[6] In TDDFT, such scaling factor p_J depends on the contribution of pure exchange in the KS functional $p_J = 1 - x_{hf}$, i.e., 0.5 for BHLYP. By analyzing matrix elements of various configurations generated from the HF reference and generalizing the results for multiple excitations, a concise form of the spin-independent energy shift for diagonal elements is given by

$$\Delta E_c = p_J\Big(-\sum_{\substack{i,j\in a\\ i>j}} V_{iijj} - \sum_{\substack{i,j\in c\\ i>j}} V_{iijj} + \sum_{i\in a}\sum_{j\in c} V_{iijj}\Big), \tag{6}$$

where c and a denote created and annihilated orbitals, correspondingly. The first and the second terms in Eq. (6) basically represent electron-electron and hole-hole repulsion while the third term is about electron-hole attraction. ΔE_c can be associated with a correction for electrostatic Coulomb interaction. However, we detected cases where the use the energy shift ΔE_c does not lead to satisfactory results. The first case relates to triplet $\pi \rightarrow \pi^*$ transitions where the exchange integral between π-electrons is significant although $\eta_{\pi\pi^*}^{\pi^*\pi}$, defined in Eq. (5), is zero for triplet multiplets. The second critical type of states exhibits large contributions from closed-shell configurations where no Fermi hole is observed and hence the exchange interaction is not properly treated by the η-coefficients either. The omission of an exchange correction has a drastical impact on the excitation energies of these states, i.e., they are exorbitantly overestimated. Therefore, an additional spin-invariant fraction of exchange is desired. Our test calculations showed that, to improve the energetics of the states, it is sufficient to introduce an additional exchange shift for the corresponding created-annihilated orbital pairs only. Moreover, the scaling parameter was found to be almost equal to half the value of p_F. On these grounds, we decided to have one parameter for all exchange loops in the diagonal elements. In this way, the diagonal matrix elements for different spin components of a configuration become

$$\begin{aligned}\sigma = \sigma' : \hat{\mathcal{H}}_{\wp\wp} = \hat{\mathcal{H}}^{ci}_{\wp\wp} &- \sum_{i\in c}(F_i^{hf} - F_i^{ks}) \\ &+ \sum_{i\in a}(F_i^{hf} - F_i^{ks}) + \Delta E_c \\ &- p_F\Big(\frac{1}{2}\sum_{i\in a}\sum_{j\in c} V_{iijj} + \sum_{\substack{i,j\in o\\ i>j}} V_{ijji}\eta^{ji}_{ij}\Big) \qquad (7)\end{aligned}$$

$$\sigma \neq \sigma' : \hat{\mathcal{H}}_{\wp\wp} = (1 - p_F)\hat{\mathcal{H}}^{ci}_{\wp\wp}. \qquad (8)$$

As in the original parameterization of DFT/MRCI, the orbital energies of HF are replaced by their Kohn-Sham counterparts which contain information about dynamic electron correlation effects (Eqs. (2) and (3)). The summation indices in the last term in Eq. (7) run over all singly occupied orbitals o. Herein, the effects of Pauli electron repulsion are contained in the spin-coupling coefficients η^{ji}_{ij}.

Generally speaking, the same parameters p_J and p_F need to be adjusted for off-diagonal elements in a similar fashion as in the diagonal case. Unfortunately, four-index integrals become ambiguous in the sense that spin-dependent and spin-independent parts of the interaction between two doubly excited CSFs cannot easily be distinguished. Here, one shall note that an inconsistent application of the parameters inevitably leads to asymmetric excited-state wave functions for systems with a high degree of spatial symmetry. For a further discussion of this topic see the supplementary material.[16]

Large parts of the dynamic correlation are treated by the Kohn-Sham operators at the DFT level, thus the configuration coupling needs to be damped off in order to avoid its double counting. One way to judge the effect of damping is to look at conjugated systems. Upon increasing the length of the conjugation, the number of valence electrons which have to be correlated at the CI level is rising. Simultaneously, the correlation energy of the excited states is gradually increased and the magnitude of the increment is subject to the shape of the applied damping (see Sec. III C). By examining the effect of various damping functions on the vertical energies of n-acenes and mini-n-carotenes, the optimal form for off-diagonal matrix elements was found to be

$$\wp \neq \wp' : \hat{\mathcal{H}}_{\wp\wp'} = \frac{p_1}{1 + (p_2 \cdot \delta\epsilon)^5 \arctan(p_2 \cdot \delta\epsilon)^5}\hat{\mathcal{H}}^{CI}_{\wp\wp'}. \qquad (9)$$

As in the original DFT/MRCI, an interaction between two coupled configurations is damped with respect to its energy difference $\delta\epsilon$, unless they are degenerate and thus their coupling is only scaled by the p_1 parameter. In case an electron configuration has more than one CSF, $\delta\epsilon$ is computed as the mean value of its state energies. It is feasible to introduce configuration selection based on $\delta\epsilon$ criteria. Only those configurations which play an important role for the reference wave functions are kept in the CI space for solving the eigenvalue problem. In this work, we use the same selection procedure for important configurations as in the original version.[6] It is based on a simple estimate of the configuration energy as the energy gap between the sum of created and the sum of annihilated orbitals with respect to the reference configuration

$$\delta\epsilon \approx \sum_{i\in c} F^{ks}_{ii} - \sum_{i\in a} F^{ks}_{ii}. \qquad (10)$$

So, if $\delta\epsilon$ in Eq. (10) is less than the sum of the computed excitation energy of the highest root in the reference space and the energy cutoff δE_{sel}, the configuration is included in the secular equation. Such truncated MRCI technique, combined with the implemented parallel multi-processor calculation algorithm,[11] yields an enormous gain in computational speed compared to standard Hartree-Fock based multi-reference methods.

B. Computational details

The ground-state geometry of all complexes has been obtained by the DFT branch of TURBOMOLE[17] employing the semi-local B3LYP[18] exchange-correlation functional. Herein, we have made use of the full point-group symmetry. Two- and three-body dispersion terms were taken into account by means of Grimme's D3 correction[19] that incorporates Becke and Johnson (BJ) damping.[20] Valence split triple zeta basis sets with polarisation functions def2-TZVPP[21] were applied for all atomic centers unless noted otherwise.

In order to evaluate excitations of valence-Rydberg type, single-point BHLYP calculations for all systems were carried out with the TZVP atomic orbital (AO) basis augmented by diffuse functions for all non-hydrogen atoms. Their exponents were taken from the aug-cc-pVTZ[22] set. The resolution-of-the-identity approach[6,23] for calculating four-index two-electron molecular orbital (MO) integrals V_{ijkl} was performed with TZVP auxiliary basis[24] sets from the standard RI-MP2 Turbomole library. The reference space for DFT/MRCI was generated by including all electron configurations having expansion coefficients greater than 0.003 in intermediately generated wave functions of probe DFT/MRCI runs within the reference space of 10 electrons in 10 orbitals. Based on the selector Eq. (10), all configurations with an energy higher than $\delta E_{sel} = 1.0$ E$_h$ were discarded.

CASPT2 energies for the disrotatory twist of s-*trans*-butadiene in Section III D were calculated with MOLPRO.[25] Both CASPT2 and DFT/MRCI energies were obtained using Dunning's correlation-consistent valence triple zeta (cc-pVTZ)[26] basis set. The active space for the calculation of the CASSCF wave functions included all π-type orbitals. The reference wave functions for RAS2[27] were determined by averaging equally weighted densities of the 1^1A ground state and the first two valence excited-state wave functions

2^1A and 1^1B. The suggested ipea shift of 0.25[28] together with an energy level shift 0.1[29] was used in the perturbative treatment.

C. Parameter optimization

The four global Hamiltonian parameters were optimized as follows. First, we collected experimentally well-studied vertical excitation energies for small compounds with highly resolved transition peaks. Second, we carried out standard DFT/MRCI runs (later denoted as DFT/MRCI-S) and assigned the states which are of particular interest. Then we performed DFT/MRCI runs with a redesigned Hamiltonian as described above (DFT/MRCI-R) and compared the CI vectors by calculating their scalar product. Besides the assignment, this procedure ensures that the wave function of DFT/MRCI-R does not change drastically compared to DFT/MRCI-S. In fact, this is important for the states with strong multi-reference character where the standard parameterization has proved to be effective. The set of molecules together with selected transitions used as the reference data for the fitting are listed in Table 3 in the supplementary material.[16] In addition, problematic cases of dimers $(C_2H_4)\cdot(C_2H_4)$ and $(H_2CO)\cdot(H_2CO)$ were included in the parameterization. Herein, the monomers are spatially separated by approximately 40 Bohr, thus well enough to consider them as ideally coupled spin moments upon local excitations. The parameter optimization has been done by utilizing the simplex algorithm[30] for root-mean-square error function minimization. The chemical structures of the molecular compounds in the fitting set are presented in the supplementary material.[16]

III. RESULTS AND DISCUSSION

A. DFT/MRCI-R parameters

The set of four empirical parameters shown in Table II minimizes the root-mean-square deviation (RMSD) of the calculated energies with respect to their reference data. The parameter p_2 deserves special attention because it is linked to the shape of the damping function. The damping of off-diagonal CI matrix elements shown in Fig. 3 implies that the DFT/MRCI-R matrix can be effectively truncated at $\delta\epsilon = 1.0$ E$_h$. In conjunction with the selection threshold of $\delta E_{sel} = 1.0$ E$_h$, a RMSD of 0.17 eV could be achieved on the fitting set, with a maximum absolute error (MAE) of 0.54 eV. The correlation with the reference data is shown pictorially in Fig. 4. For comparison, we computed excitation energies for the fitting set also with the original DFT/MRCI approach. Due to inability of the DFT/MRCI-S Hamiltonian to appropriately describe four-open-shell configurations, all dimer state energies appear at much lower energies than expected. In Fig. 4, the DFT/MRCI-S dimer energies show up as outliers of the otherwise good correlation with experimental energies. In the case of DFT/MRCI-R all outliers vanish on the correlation plot. So, in addition to single-electron transitions and excited states of multi-configurational character, DFT/MRCI-R accurately evaluates the energy of four-open-shell states which are reproduced with the same precision as for non-critical cases. Furthermore, all symmetry considerations with respect to the excited states of the ethylene-tetrafluoroethylene dimer (Fig. 1) are retained for different multiplets (Table III) as discussed in the introduction.

TABLE II. Optimized DFT/MRCI-R Hamiltonian parameters.

δE_{sel} (E$_h$)	p_J	p_F	p_1	p_2 (E$_h^{-1}$)	RMSD (eV)	MAE (eV)
1.0	0.5079	0.3559	0.5682	1.788	0.17	0.54
0.8	0.5035	0.3681	0.5798	2.187[a]	0.20	0.63

[a] Kept fixed during optimization.

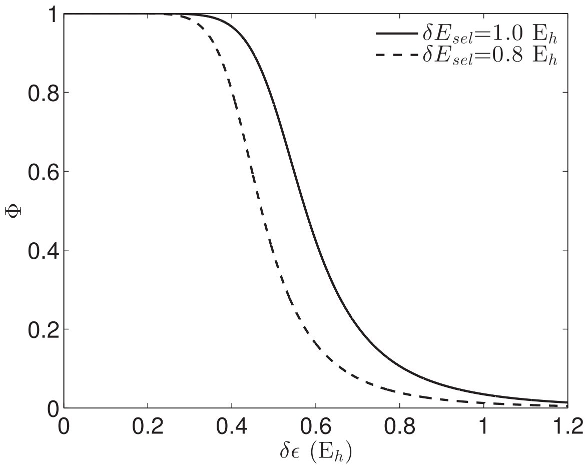

FIG. 3. Damping decay as function of the energy difference $\delta\epsilon$ between configurations.

Due to its moderate computational cost and its good performance, the DFT/MRCI method is ideal for calculating the photophysical properties of emitters. However, the large number of correlated electrons and holes in extended systems requires sometimes to solve a Hamiltonian matrix with a dimension of billions of configurations, even if a minimal basis set is employed. To reduce the size of the CI matrix in severe cases, the damping parameter p_2 was fixed at the value $p_2^5 = 50$ E$_h^{-5}$ and the remaining three parameters were fitted in a similar way as before, resulting in another set of four parameters to be used in conjunction with a tighter selection threshold. By employing this parameter set, the damping decay becomes steeper in the intermediate region. Thereby, converged results can be reached at $\delta\epsilon = 0.8$ E$_h$. When the parameter set in conjunction with the tighter selection threshold of $\delta E_{sel} = 0.8$ E$_h$ is employed, slightly larger statistical errors are obtained. With regard to the excitation energies in the fitting set, a RMSD of 0.20 eV is found, with a maximum absolute error (MAE) of 0.63 eV (see also Table II).

B. Assessment of the DFT/MRCI-R parameterization

For a fair judgement on the performance of the original and redesigned DFT/MRCI Hamiltonians, we have chosen a benchmark set of excitation energies not contained in the

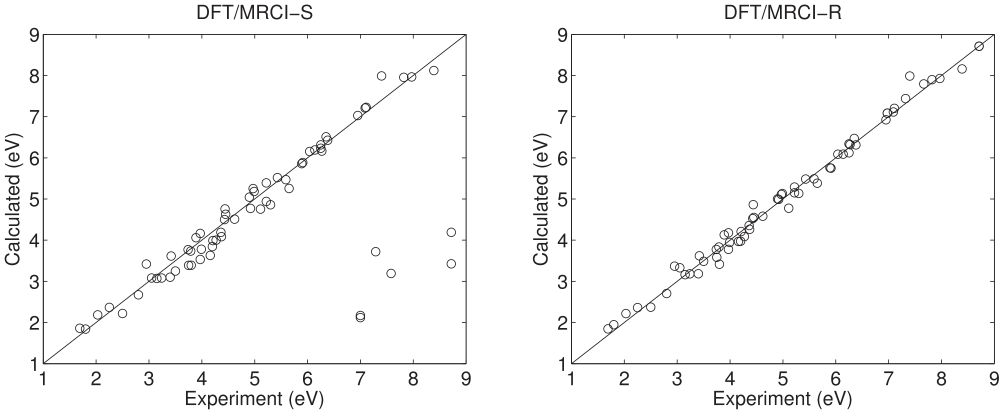

FIG. 4. Correlation between calculated and experimental vertical transition energies of the fitting set listed in Table 3 of Ref. 16.

fitting set. Similar to the fitting set, this benchmark set contains $\pi \rightarrow \pi^*$, $n \rightarrow \pi^*$ as well as valence-to-Rydberg transition energies of oxides and small organic compounds (see Table 4 in the supplementary material[16]). The chemical structures and molecular geometries of the compounds are presented in Ref. 16 as well.

In a first step, it seems reasonable to investigate whether DFT/MRCI-R does maintain the high quality of the original DFT/MRCI-S approach for states produced by the promotion of one electron out of the Kohn-Sham closed-shell reference. We have compared the performance of the two parameterizations with respect to vertical excitation energies of singlet and triplet states as obtained by electron impact spectroscopy in the gas phase.[31] Several $n \rightarrow \pi^*$ states of this set were omitted due to their low spectroscopic resolution. Instead, we added $n \rightarrow \pi^*$ transition energies from other experimental sources.[32–37] The error distributions over the sample (Fig. 5) in principle show the same statistical results for the DFT/MRCI-S and DFT/MRCI-R methods. The mean deviations from the 160 experimental data (0.02 eV for DFT/MRCI-S, 0.06 for DFT/MRCI-R) are extremely gratifying. Also the standard (0.16 eV for DFT/MRCI-S, 0.14 for DFT/MRCI-R) and root-mean-square deviations (0.16 eV for DFT/MRCI-S, 0.15 for DFT/MRCI-R) are very satisfactory. In the following, we shall discuss only the states with a tendency to deteriorate the DFT/MRCI-R statistics.

The biggest error compared to the experimental results is observed for triplet multiplets in systems with a triple bond (acetylene, propyne, 1-butyne, 3,3,3-trifluoropropyne). The wave functions of these systems have strong multi-reference character and are represented dominantly by six CSFs with almost equal CI coefficients. Inspection of Table 4 of Ref. 16 shows that the energies of the lowest excited triplet states are overestimated by DFT/MRCI-R whereas the energies of the second states almost hit the experimental values. Using DFT/MRCI-S instead, the energetic splitting of the two triplet states remains nearly constant while their barycenter is shifted toward lower energies. As the consequence, the first transitions are in a good agreement with experiment whereas the second ones are not. We also note that valence-to-Rydberg excitations of these compounds are slightly underestimated by both parameterizations. However, the equivalent first $\pi \rightarrow 3s$ states in methylated ethylenes and fluoroethylenes are well represented energetically. Hence, errors in this case can be attributed to the statistical distribution.

Second, let us address fluorobenzenes. The computed DFT/MRCI-R and DFT/MRCI-S energies of the first singlet and first triplet $\pi \rightarrow \pi^*$ states tend to overestimate the experimental values. These states arise from the interaction of two degenerate CSFs. Thereby, the configuration coupling is scaled by p_1 in Eq. (9) and Eq. (8) of Ref. 6, respectively. The most likely reason for these errors is the artificial exchange adjunct in Eq. (7), which is substantial for these systems

TABLE III. DFT/MRCI-R $\pi \rightarrow \pi^*$ vertical excitation energies of ethylene $|s_1, 0\rangle$, tetrafluoroethylene $|s_2, 0\rangle$, and their $\pi_1\pi_2 \rightarrow \pi_1^*\pi_2^*$ dimer state $|S, 0, s_1, s_2\rangle$ energies.

		Singlet (eV)		Triplet (eV)		Quintet (eV)	
		Computed	Expected	Computed	Expected	Computed	Expected
Monomer	$\|s_1, 0\rangle$	7.82		4.38			
	$\|s_2, 0\rangle$	8.70		4.81			
Dimer	$\|s_1, 0\rangle$	7.82	7.82	4.38	4.38		
	$\|s_2, 0\rangle$	8.70	8.70	4.81	4.81		
	$\|S, 0, 1, 1\rangle$	9.17	9.19	9.18	9.19	9.20	9.19
	$\|S, 0, 0, 1\rangle$			12.66	12.63		
	$\|S, 0, 1, 0\rangle$			13.13	13.08		
	$\|S, 0, 0, 0\rangle$	16.59	16.52				

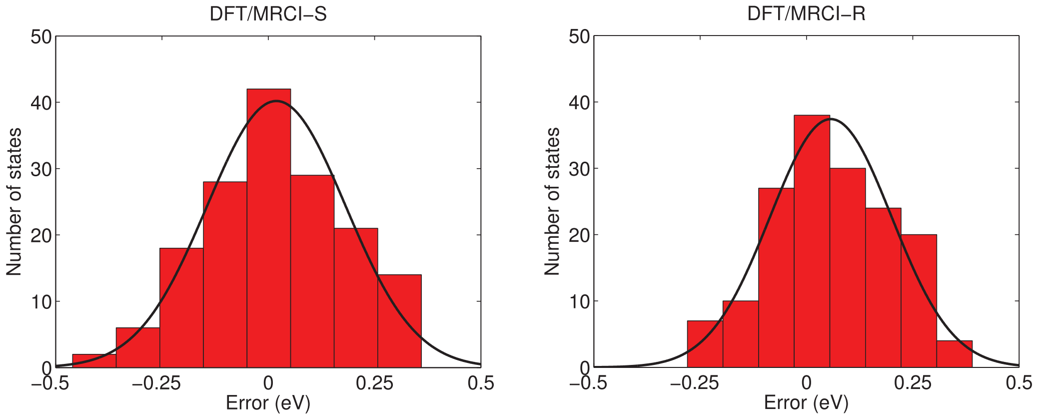

FIG. 5. DFT/MRCI-S and DFT/MRCI-R error distributions ($E_{calc} - E_{exp}$) from a sample of 160 data points from the benchmark set presented in Table 4 of Ref. 16.

(~0.3 eV), in combination with the parameterization of the off-diagonal elements.

On one hand it is obvious that the highest energy deviation is caused by the fact that a constant global parameter p_1 is introduced in Eq. (9) instead of decorating the off-diagonal elements with different portions of Coulomb- and exchange-like integrals. On the other hand, an individually tailored damping of the off-diagonal coupling elements might increase the computational cost of the CI matrix construction dramatically since the number of off-diagonal elements is much bigger than the number of diagonal elements. We leave this question open for later refurbishment, all the more because the root-mean-square error of 0.15 eV for the DFT/MRCI-R Hamiltonian looks convincing. Further, it seems that the DFT/MRCI-S has a general trend to shift $n \to \pi^*$ states toward lower excitation energies (see Tables 3 and 4 of Ref. 16). In the majority of all cases, the vertical excitation energies for $n \to \pi^*$ states obtained with the redesigned Hamiltonian are in better agreement with experiment than those computed with the standard parameterization. For some of the nitrogen containing heteroaromatic compounds (pyridine, pyrazine, pyrimidine, and triazine) we obtain higher excitation energies than the experimental ones by 0.2-0.3 eV and the DFT/MRCI-R excitation energies are even higher. The only exception is found in s-tetrazine where the DFT/MRCI-R energies of the $n \to \pi^*$ states are marginally lower (by at most 0.05 eV) than for DFT/MRCI-S.

C. Extended π systems

In practice, the adequate description of $\pi \to \pi^*$ states demands much more correlation compared to $n \to \pi^*$ and Rydberg states. The effect is enhanced upon extending the conjugation length because the number of $\pi \to \pi^*$ CSFs within one irreducible representation is increased. In DFT/MRCI this fact is important since the coupling between configurations is damped in Eq. (9) and the shape of the applied damping governs the total correlation energy of the states.

One of the simplest aromatic molecules with six π-electrons is benzene. Due to its high spatial symmetry, the two lowest optically allowed transitions are inherently different from the viewpoint of static correlation. The wave function of the first state (${}^1L_b$) requires at least two CSFs which are degenerate and with regard to the high spatial symmetry have to appear with equal CI coefficient in the state vector. The second state (${}^1L_a$) can efficiently be described by the interaction of the corresponding electron-hole pair, similar to the 1^1A_u state in mini-carotenoids and polyenes. Figure 6 shows the dependence of the first valence excited state energies on the π-conjugation length

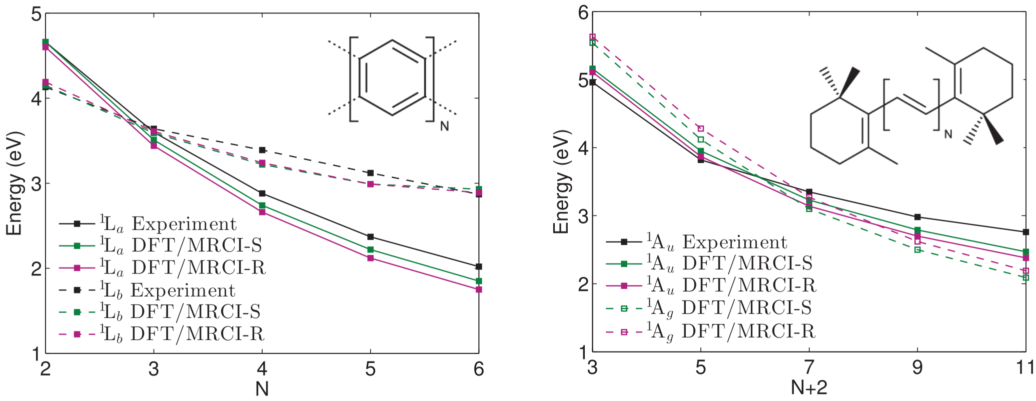

FIG. 6. DFT/MRCI-S and DFT/MRCI-R vertical excited-state energies of n-acenes and mini-n-carotenes as function of the conjugation length N. Polyacenes: TZVP AO-basis for B3LYP geometry, TZVP AO-basis for DFT/MRCI, experimental values were taken from Ref. 10; Mini-carotenes: TZVP AO-basis for B3LYP geometry, def-SV(P)[48] AO-basis for DFT/MRCI, experimental values were taken from Ref. 11.

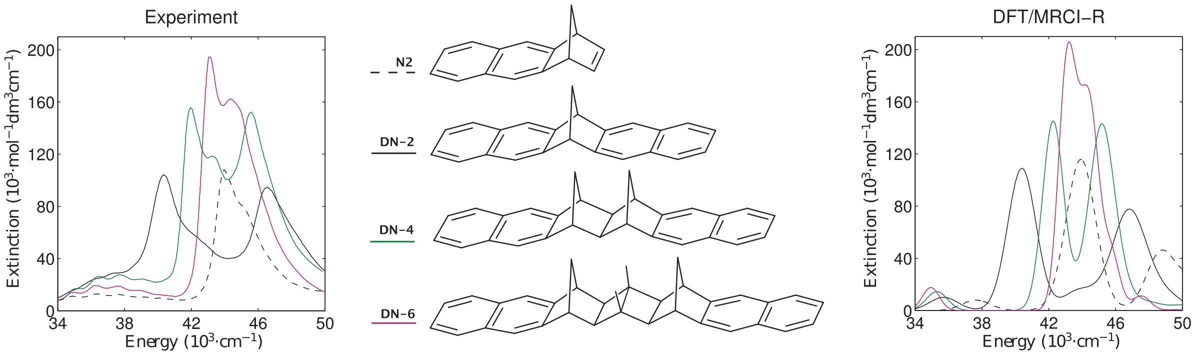

FIG. 7. Measured and DFT/MRCI-R absorption spectra of bridged naphthalene dimers. The experimental data were read from Figure 3 of Ref. 40.

for *n*-acenes (going from naphthalene to pentacene) and mini-*n*-carotenes (going from mini-3 to mini-11). It is clearly seen that the two parameterizations perform equally well for the $^1\mathrm{L}_b$ state of polyacenes which are dominated by HOMO−1→LUMO and HOMO→LUMO+1 excitations. This state remains covalent in character and can be well described also by TDDFT.[10,38] In valence bond theory, the $^1\mathrm{L}_a$ state exhibits large contributions from ionic components. It results mainly from a HOMO→LUMO excitation and is substantially underestimated by TDDFT.[38] With regards to the DFT/MRCI parameterizations, we see that both perform well, with a slight tendency to underestimate the excitation energies. Due to selection rules, the $2^1\mathrm{A}_g$ state of carotenes and polyenes cannot be reached from the electronic ground state by one-photon absorption. Vertical excitation energies are therefore not observable from experiment in all the series. However, its presence has been proven by transient excited-state absorption and resonance Raman spectroscopy.[39] The state is known to have significant contributions of doubly excited CSFs, similar to the corresponding state in linear polyenes. It is important to note that the excitation energies of $2^1\mathrm{A}_g$ and $1^1\mathrm{A}_u$ at N=7 are almost identical ~3.3 eV.

Next, we address the family of bridged naphthalene dimers. In these systems, two naphthalene units are held at fixed distance and orientation by a rigid bridge of variable length (Fig. 7). The absorption band of N2 with maximum at about ~44 000 cm^{-1} (5.45 eV) originates from the most intense transition of naphthalene perturbed by the σ-framework of the norbornene fragment. Due to the bridge, the N2 peak is blue shifted by ~0.45 eV with respect to the $^1\mathrm{B}_b$ transition in naphthalene. Like the $^1\mathrm{L}_b$ state, the $^1\mathrm{B}_b$ state of naphthalene is dominated by the two HOMO→ LUMO+1 and HOMO−1→LUMO excitations. In contrast to $^1\mathrm{L}_b$, the phases are such that the transition dipole moments add up instead of canceling each other. Through-space and through-bond interaction mechanisms of the monomers cause a splitting between the resulting states in the dimer,

$$^1\mathrm{B}_b^{\pm} = \frac{1}{\sqrt{2}}(\psi_A^*\psi_B \pm \psi_A\psi_B^*),$$

where ψ_A^* denotes the Frenkel exciton $^1\mathrm{B}_b$ on monomer *A*, etc.[40,41] In principle, the excitonic splitting, i.e., $\mathrm{E}(^1\mathrm{B}_b^+) - \mathrm{E}(^1\mathrm{B}_b^-)$, is governed by the interchromophore distance. Thus, the two states must energetically approach the peak of N2 from the red- and blue-shifted zones when increasing the length of the bridge. In Table IV, we summarize the corresponding transition energies and their calculated oscillator strengths. Besides $^1\mathrm{B}_b^{\pm}$, there are other intense peaks which were not resolved by the measurements and therefore the comparison of their splitting gap is hindered. Instead, we show the simulated absorption spectra of the bridged naphthalene series in Figure 7 which incorporate large Gaussian broadening. It is seen that the positions and intensities of the DFT/MRCI-R peaks coincide well with the experimental results. This is also the case for the DFT/MRCI-S spectrum of DN-2 (not shown). When the interchromophore separation increases, we observe a substantial change of the oscillator strengths (Table IV), however. In DN-6, for example, the intensity ratio between the lower- and higher-energetic peak is reversed in the DFT/MRCI-S spectrum.

TABLE IV. Vertical excitation energies and oscillator strengths of bridged naphthalenes series calculated by DFT/MRCI with TZVP AO-basis. Experimental energies were taken from Ref. 40. States corresponding to the bright $^1\mathbf{B}_b$ state of naphthalene are marked in boldface.

		DFT/MRCI-S		DFT/MRCI-R		
		E (eV)	f (L)	E (eV)	f (L)	Expt. (eV)
Naphthalene	$^1\mathrm{C}_b$	5.73	0.0	5.78	0.0	
	$^1\mathbf{B}_b$	5.94	1.75	5.83	1.75	5.89[a]
	$^1\mathrm{B}_a$	6.25	0.32	6.15	0.35	
N2[b]	$^1\mathrm{B}_a$	5.33	0.04	5.31	0.05	
	$^1\mathbf{B}_b$	5.49	0.98	5.44	1.41	5.45
	$^1\mathrm{C}_b$	5.51	0.29	5.54	0.11	
DN-2	$^1\mathbf{B}_b^+$	5.04	2.04	5.01	2.14	5.00
	$^1\mathrm{C}_b^+$	5.38	0.30	5.41	0.23	~5.3
	$^1\mathrm{B}_a^-$	5.83	0.45	5.78	0.50	5.76
	$^1\mathbf{B}_b^-$	5.89	0.80	5.80	0.68	
DN-4	$^1\mathbf{B}_b^+$	5.27	1.81	5.24	2.03	5.21
	$^1\mathrm{C}_b^+$	5.43	0.47	5.49	0.23	~5.4
	$^1\mathbf{B}_b^-$	5.67	1.78	5.60	1.49	5.65
	$^1\mathrm{B}_a^-$	5.72	0.48	5.70	0.52	
DN-6	$^1\mathbf{B}_b^+$	5.35	1.08	5.34	2.09	5.34
	[c]	5.38	0.05	5.44	0.72	5.54
		5.42	1.30	5.49	0.22	
	$^1\mathbf{B}_b^-$	5.55	1.95	5.53	1.27	
	$^1\mathrm{B}_a^-$	5.67	0.48	5.68	0.43	

[a] From Ref. 47.

[b] For the nomenclature of the compounds see Fig. 7.

[c] Due to the high density of states both can be attributed to $^1\mathrm{C}_b^+$.

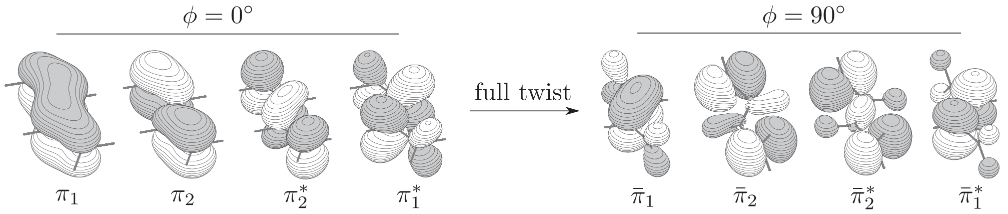

FIG. 8. BHLYP π-orbitals of s-*trans*-butadiene at 0 and 90° of disrotatory methylene twisting.

A case when four-open-shell configurations play an important role may sometimes be disclosed in the task of theoretically investigating the light-induced molecular photodynamics of molecules. However, in applications such as excitation-energy transfer from one chromophore to another, the study of dimers is inevitable. As shown in Table III, the newly designed DFT/MRCI correctly predicts the energy of four-open-shell configurations for spatially separated monomers. Note, however, that the two-electron integrals between the two annihilated and two created orbital pairs located on different monomers vanish due to the long distance between the chromophores. This is different for a single compact molecule such as, for example, *trans*-butadiene which will be discussed in the following.

D. Butadiene twisting

Next, we examined the performance of DFT/MRCI-R on the disrotatory twist about the s-*trans*-1,3-butadiene double bonds. The first spin-allowed transition 1^1B_u of s-*trans*-butadiene is well known by means of various measurements.[42–44] It features a strong peak in the experimental absorption spectrum at ~6.0 eV and is predominantly described by a valence $\pi_2 \rightarrow \pi_2^*$ single excitation. The corresponding orbitals are displayed in Fig. 8. The second valence transition $1^1A_g \rightarrow 2^1A_g$ is dipole forbidden. The state is known to exhibit strong multi-reference character. At the ground-state geometry, its wave function shows large contributions from the doubly excited configuration $\pi_2\pi_2 \rightarrow \pi_2^*\pi_2^*$ in addition to the two leading $\pi_1 \rightarrow \pi_2^*$ and $\pi_2 \rightarrow \pi_1^*$ single excitations. Because of its nature and symmetry, it is very difficult to precisely locate the optically dark state experimentally. However, ~6.4 eV may serve as an estimate for the vertical absorption energy.[3,45,46] To demonstrate the improvement, we model the cuts through the adiabatic potential energy surfaces (PESs) in s-*trans*-butadiene along a symmetry-adapted internal coordinate as described in Ref. 46, namely, along the simultaneous disrotatory methylene twisting about the double bonds.

Upon twisting of the CH_2 groups, the π_2- and π_2^*-orbitals of s-*trans*-butadiene are transformed to σ-like ones locating in the skeleton plane ($\bar{\pi}_2$ and $\bar{\pi}_2^*$ in Fig. 8), whereas the pair of σ-orbitals turns into π. It seems reasonable to include the corresponding orbital pairs in the active space for a CASPT2 treatment, but we noticed that the contribution of the determinants produced by $\sigma - \pi^*$ interactions in the 1^1A, 1^1B, and 2^1A CAS wave functions is fairly small and can be recovered in a perturbative manner. The ground state (1^1A state in Fig. 9) is naturally contaminated by the closed-shell doubly excited configuration (D0) $\bar{\pi}_2\bar{\pi}_2 \rightarrow \bar{\pi}_2^*\bar{\pi}_2^*$ upon the twist. As already mentioned in the introduction, the standard parameterization shows satisfactory results for D0 configurations, therefore all three curves exhibit similar behavior. Our particular interest focuses on the PESs of the 1^1B and 2^1A states. The weight of $\bar{\pi}_1\bar{\pi}_2 \rightarrow \bar{\pi}_2^*\bar{\pi}_2^*$ (D2) and $\bar{\pi}_1\bar{\pi}_2 \rightarrow \bar{\pi}_2^*\bar{\pi}_1^*$ (D4) in 1^1B and 2^1A, respectively, is gradually growing with increasing twisting angle and becomes prominent at $\phi \sim 90°$. As shown in Fig. 9, the 1^1B and 2^1B states come energetically close at $\phi \sim 80°$ and repel each other which is contradictory to the CASPT2 result. While the D2 weight is increased in the CI expansion of 1^1B, the DFT/MRCI-S state energy drops dramatically. In contrast, the DFT/MRCI-R curve keeps rising and imitates the CASPT2 result. An even more pronounced effect was found for 2^1A where a D4 configuration in the DFT/MRCI-S expansion causes a drastic change of the PES. As a consequence, the 2^1A state energy falls off even steeper than the 1^1B state, giving rise to an energy difference of ~3 eV between CASPT2 and DFT/MRCI-S at 90°. Again, the redesigned DFT/MRCI-R produces a qualitatively correct shape of the PES.

Concluding, we would like to emphasize that the appearance of energetically low-lying D2 and D4 states in

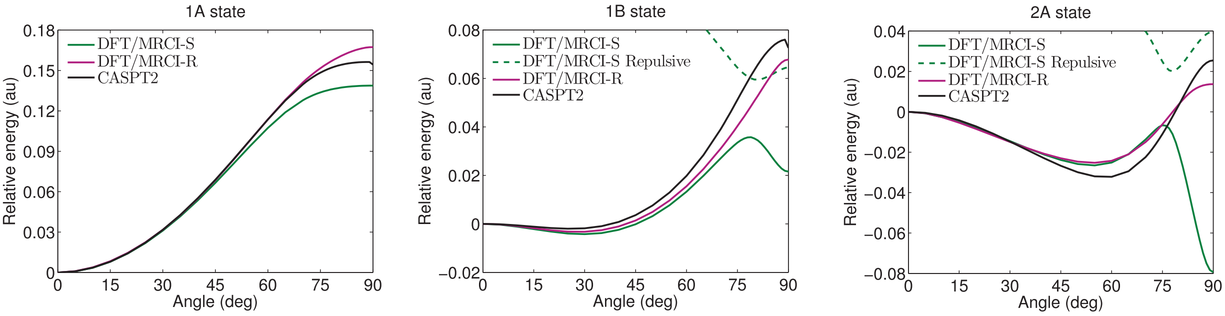

FIG. 9. Potential energy profiles of the simultaneous disrotatory twisting of the methylene groups in butadiene. Energies of different cuts are normalized to their ground state values.

DFT/MRCI-S wave functions is by no means a rare event. In nitrobenzene and nitronaphthalene, for example, a strong admixture of such configurations occurs even at the ground-state geometry, messing up the DFT/MRCI-S excited-state spectrum. As may be seen from the plots, DFT/MRCI-R is free from these artificial features, more or less matching the CASPT2 curve for all three states. These results corroborate the robustness of the new parametrization, making the method suitable for studying excited-state relaxation processes where the performance of doubly excited configurations is essential.

IV. CONCLUSIONS

We have presented a new way of modifying MRCI matrix elements between configuration state functions which are built from a one-particle BHLYP orbitals basis. Maintaining the good performance for standard excitations, the new scheme has been shown to be applicable for doubly excited configurations with varying number of open shells. The new parameterization yields good qualitative agreement with experiment for systems with an even number of electrons in their singlet and triplet spin states with statistical errors not exceeding 0.2 eV. Furthermore, the utilization of four global spin- and seniority-invariant parameters predicts consistent energetics of different multiplets for dimer systems of spatially separated molecules. The truncation scheme of the MRCI space retains the low computational cost of the original parameterization for large molecules where post-Hartree-Fock methods are computationally tedious.

The proposed parameterization extends the applicability of the standard DFT/MRCI approach beyond one-electron excitations, making the method convenient for exploring light-induced processes such as singlet fission and triplet-triplet up conversion within moderate time limits. The scheme is in principle general and can be applied for any combination of MRCI with hybrid density functionals.

ACKNOWLEDGMENTS

Financial support by the *Deutsche Forschungsgemeinschaft* (DFG) Project No. MA1051/14-1 is gratefully acknowledged. The authors thank Stefan Grimme for helpful discussions.

[1] K. Andersson, P. Å. Malmqvist, B. O. Roos, A. J. Sadlej, and K. Wolinski, J. Phys. Chem. **94**, 5483 (1990).
[2] K. Andersson, P. Å. Malmqvist, and B. O. Roos, J. Chem. Phys. **96**, 1218 (1992).
[3] M. Schreiber, M. R. Silva-Junior, S. P. A. Sauer, and W. Thiel, J. Chem. Phys. **128**, 134110 (2008).
[4] P. Å. Malmqvist, A. Rendell, and B. O. Roos, J. Phys. Chem. **94**, 5477 (1990).
[5] S. Grimme, Chem. Phys. Lett. **259**, 128 (1996).
[6] S. Grimme and M. Waletzke, J. Chem. Phys. **111**, 5645 (1999).
[7] M. Roemelt, D. Maganas, S. DeBeer, and F. Neese, J. Chem. Phys. **138**, 204101 (2013).
[8] E. V. Beck, E. A. Stahlberg, L. W. Burggraf, and J.-P. Blaudeau, Chem. Phys. **349**, 158 (2008).
[9] M. R. Silva-Junior, M. Schreiber, S. P. A. Sauer, and W. Thiel, J. Chem. Phys. **129**, 104103 (2008).
[10] C. M. Marian and N. Gilka, J. Chem. Theory Comput. **4**, 1501 (2008).
[11] M. Kleinschmidt, C. M. Marian, M. Waletzke, and S. Grimme, J. Chem. Phys. **130**, 044708 (2009).
[12] J.-M. Mewes, V. Jovanović, C. M. Marian, and A. Dreuw, Phys. Chem. Chem. Phys. **16**, 12393 (2014).
[13] R. W. Wetmore and G. A. Segal, Chem. Phys. Lett. **36**, 478 (1975).
[14] G. A. Segal, R. W. Wetmore, and K. Wolf, Chem. Phys. **30**, 269 (1978).
[15] A. D. Becke, J. Chem. Phys. **98**, 1372 (1993).
[16] See supplementary material at http://dx.doi.org/10.1063/1.4940036 for geometry parameters, chemical structures, and experimental data of all molecules used in the fitting and assessment as well as additional information on MRCI matrix element formulas.
[17] TURBOMOLE V6.5 2013, a development of University of Karlsruhe and Forschungszentrum Karlsruhe GmbH, 1989-2007, TURBOMOLE GmbH, since 2007, available from http://www.turbomole.com.
[18] A. D. Becke, J. Chem. Phys. **98**, 5648 (1993).
[19] S. Grimme, J. Antony, S. Ehrlich, and H. Krieg, J. Chem. Phys. **132**, 154104 (2010).
[20] S. Grimme, S. Ehrlich, and L. Goerigk, J. Comput. Chem. **32**, 1456 (2011).
[21] F. Weigend and R. Ahlrichs, Phys. Chem. Chem. Phys. **7**, 3297 (2005).
[22] R. A. Kendall, T. H. Dunning, and R. J. Harrison, J. Chem. Phys. **96**, 6796 (1992).
[23] O. Vahtras, J. Almlöf, and M. Feyereisen, Chem. Phys. Lett. **213**, 514 (1993).
[24] F. Weigend, M. Häser, H. Patzelt, and R. Ahlrichs, Chem. Phys. Lett. **294**, 143 (1998).
[25] H.-J. Werner, P. J. Knowles, G. Knizia, F. R. Manby, and M. Schütz, WIREs: Comput. Mol. Sci. **2**, 242 (2012).
[26] T. H. Dunning, J. Chem. Phys. **90**, 1007 (1989).
[27] H.-J. Werner, Mol. Phys. **89**, 645 (1996).
[28] G. Ghigo, B. O. Roos, and P.-Å. Malmqvist, Chem. Phys. Lett. **396**, 142 (2004).
[29] B. O. Roos and K. Andersson, Chem. Phys. Lett. **245**, 215 (1995).
[30] J. A. Nelder and R. Mead, Comput. J. **7**, 308 (1965).
[31] A. Kuppermann, W. M. Flicker, and O. A. Mosher, Chem. Rev. **79**, 77 (1979).
[32] Y. Okuzawa, M. Fujii, and M. Ito, Chem. Phys. Lett. **171**, 341 (1990).
[33] A. Bolovinos, P. Tsekeris, J. Philis, E. Pantos, and G. Andritsopoulos, J. Mol. Spectrosc. **103**, 240 (1984).
[34] W. M. St. John, R. C. Estler, and J. P. Doering, J. Chem. Phys. **61**, 763 (1974).
[35] E. B. Nielsen and J. A. Schellman, J. Phys. Chem. **71**, 2297 (1967).
[36] S. Nagakura, M. Kojima, and Y. Maruyama, J. Mol. Spectrosc. **13**, 174 (1964).
[37] S. C. J. Meskers, T. Polonski, and H. P. J. M. Dekkers, J. Phys. Chem. **99**, 1134 (1995).
[38] M. Parac and S. Grimme, Chem. Phys. **292**, 11 (2003).
[39] T. Polívka and V. Sundström, Chem. Rev. **104**, 2021 (2004).
[40] G. D. Scholes, K. P. Ghiggino, A. M. Oliver, and M. N. Paddon-Row, J. Am. Chem. Soc. **115**, 4345 (1993).
[41] S. Tretiak, W. M. Zhang, V. Chernyak, and S. Mukamel, Proc. Natl. Acad. Sci. U. S. A. **96**, 13003 (1999).
[42] K. R. Asmis, "Electron-molecule collisions: A novel instrument for measuring inelastic differential cross sections at 180° angle and applications," Ph.D. thesis, University of Freiburg, Switzerland, 1996.
[43] J. P. Doering, J. Chem. Phys. **70**, 3902 (1979).
[44] O. A. Mosher, W. M. Flicker, and A. Kuppermann, J. Chem. Phys. **59**, 6502 (1973).
[45] M. A. Watson and G. K.-L. Chan, J. Chem. Theory Comput. **8**, 4013 (2012).
[46] A. Komainda, B. Ostojić, and H. Köppel, J. Phys. Chem. A **117**, 8782 (2013).
[47] G. George and G. Morris, J. Mol. Spectrosc. **26**, 67 (1968).
[48] A. Schäfer, H. Horn, and R. Ahlrichs, J. Chem. Phys. **97**, 2571 (1992).

Redesigned of the DFT/MRCI Hamiltonian: Supplementary material

Igor Lyskov, Martin Kleinschmidt, and Christel M. Marian*

Institute of Theoretical and Computational Chemistry,
Heinrich-Heine-University Düsseldorf, Universitätsstraße 1,
40225 Düsseldorf, Germany,
Tel.: +49-211-8113209. Fax: +49-211-8113446.
E-mail: Christel.Marian@hhu.de

January 4, 2016

1. Cartesian coordinates of all systems listed in table 3, table 4 as well as geometry of bridged naphthalenes are to be found in geometry.txt file.

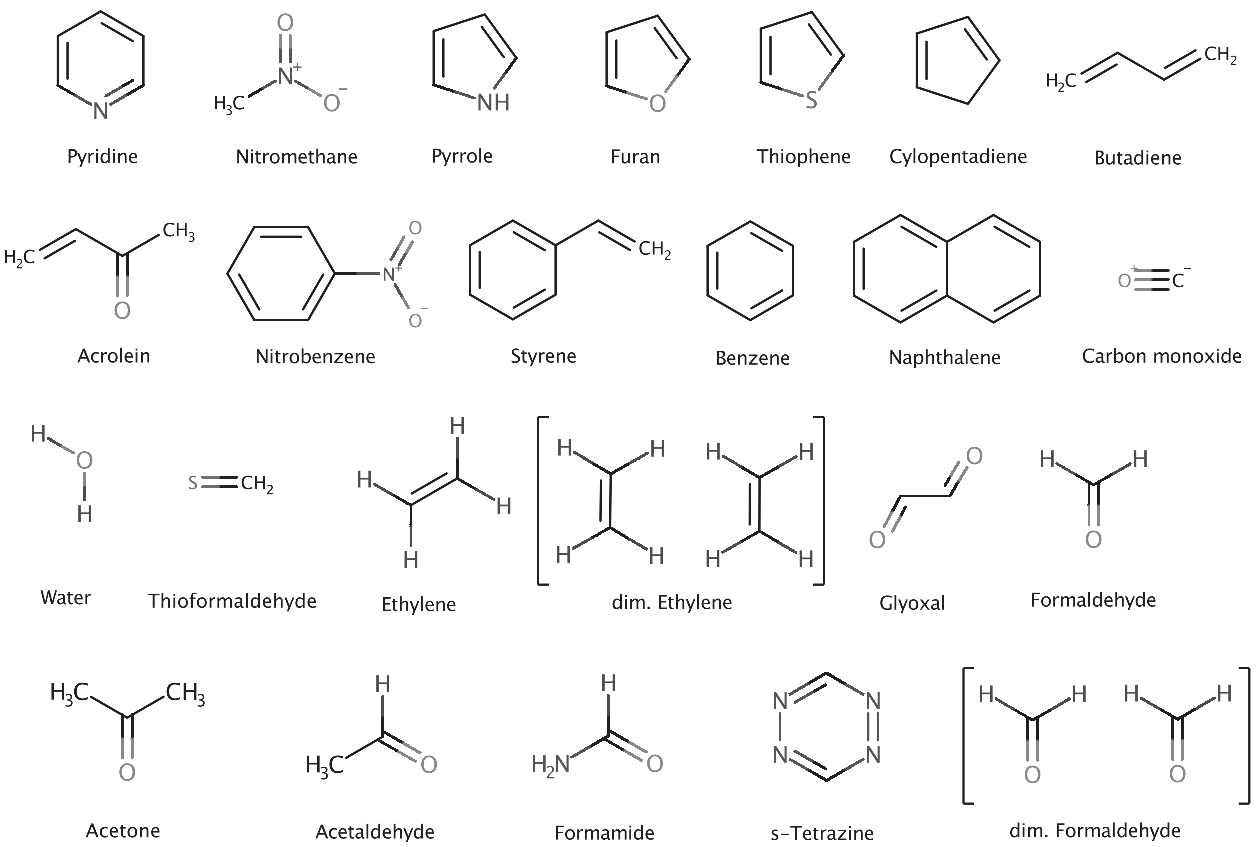

Figure 1: Chemical structure of the molecules used in parameters optimization.

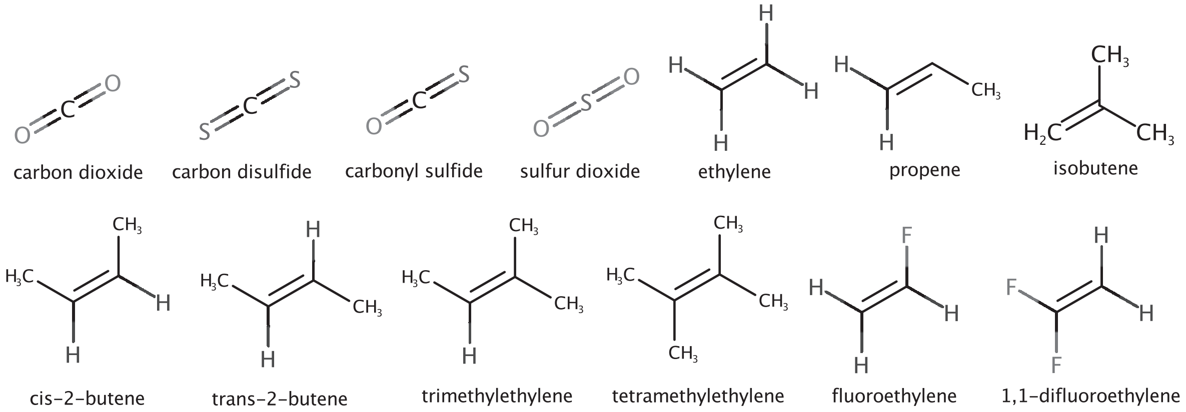

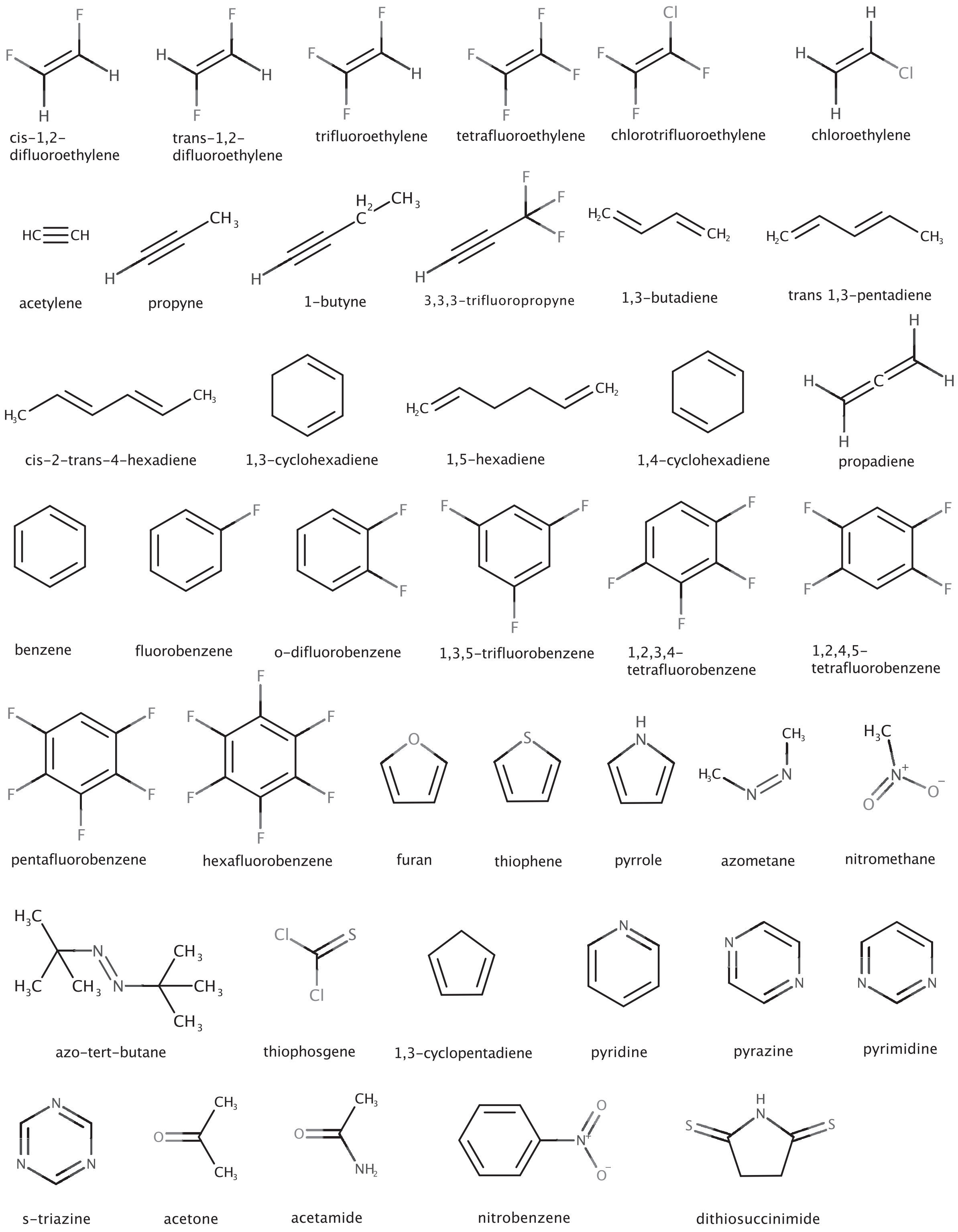

Figure 2: Chemical structures of the molecules used in the DFT/MRCI-R assessment.

2. The data points of Figure 2 are presented in Table 1.

3. Here we shall briefly discuss an effect of scaling parameter p_1. The MRCI matrix elements are given by the following expressions:
   Diagonal case:

$$\begin{aligned}\hat{\mathcal{H}}_{\wp\wp} - \mathcal{E}^{scf} &= \sum_i F_{ii}\Delta\wp_i + \frac{1}{2}\sum_{i\neq j} V_{iijj}\Delta\wp_i\Delta\wp_j + \\ &+\frac{1}{2}\sum_{i\neq j} V_{ijji}(-\frac{1}{2}\Delta\wp_i\Delta\wp_j + \frac{1}{2}\wp_i\wp_j - \wp_i + \eta^{ji}_{ij}) + \\ &+\frac{1}{2}\sum_i V_{iiii}(\frac{1}{2}\Delta\wp_i\Delta\wp_i + \frac{1}{2}\wp_i\wp_i - \wp_i)\end{aligned} \tag{1}$$

One electron difference between configurations:

$$\begin{aligned}\hat{\mathcal{H}}_{\wp\wp'} &= F_{ij}\eta^j_i + \sum_{k\neq i,j} V_{ijkk}\Delta\wp'_k\eta^j_i + \\ &+\sum_{k\neq i,j} V_{ikkj}(-\frac{1}{2}\Delta\wp'_k\eta^j_i + \frac{1}{2}\wp'_k\eta^j_i - \eta^j_i + \eta^{kj}_{ik}) + \\ &+V_{iiij}(\frac{1}{2}\Delta\wp'_i + \frac{1}{2}\wp'_i)\eta^j_i - V_{ijjj}(\frac{1}{2}\Delta\wp'_j + \frac{1}{2}\wp'_j - 1)\eta^j_i\end{aligned} \tag{2}$$

Two electron difference between configurations:

$$\hat{\mathcal{H}}_{\wp\wp''} = \frac{1}{(1+\delta_{ik})(1+\delta_{ij})}(V_{ijkl}\eta^{jl}_{ik} + V_{ilkj}\eta^{lj}_{ik}) \tag{3}$$

Lets now focus on Eq. 2 and Eq. 3. Obviously, in the case where the configurations differ by a one-electron excitation V_{ijkk} plays a role of a Coulomb-like integral, meanwhile V_{ikkj} is exchange-like. In the case of a double excitation, the main trick is to separate the spin-invariant part out of the spin-dependent terms in Eq. 3. Let us consider the extreme case, namely an interaction of two degenerate CSFs. Then the damping function turns to unity and the inter-configuration coupling is scaled simply by a factor of p_1. Within this model (Fig. 3), the total wave function of the states is given by the positive/negative linear combination of CSFs. Their interaction, of course, results in an energy splitting between ϕ_+ and ϕ_-, where Δ denotes to the absolute value of off-diagonal element in the secular equation of rank 2. In Table 2, the some electron transitions matching to the model with Δ computed according Eq. 3 are summarized. Now we represent $\mathcal{H}_{\wp\wp''}$ as following:

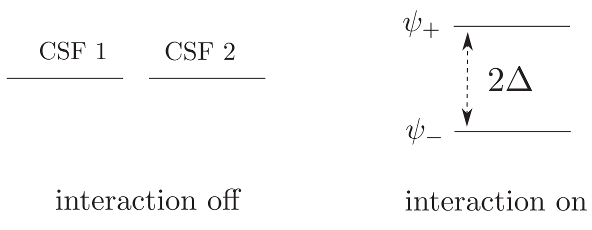

Figure 3: *two-degenerate-CSFs* model

$$\Delta = |\mathcal{H}_{\wp\wp''}| = |\eta_a V_a + \eta_b V_b| \tag{4}$$

Similar to the diagonal case, the eta-coefficients (η_a;η_b) are found to be (-1;2) for singlet and (-1;0) for triplet multiplets, which makes the distinction of the spin-dependent part apparent. We shall now apply the approximate Coulomb correction parameter p_J=0.5 and exchange parameter p_F=0.3 to these simple cases. Figure 4 implies that without loss of accuracy the use of the scaling parameter p_1 can be avoided by utilizing the same parameters p_J and p_F as in diagonal elements. Besides less-empirism, such parameterization form has another advantage. The gradual increase of the number of singly excited configuration in CI space in highly symmetric molecules (benzene as an example) leads to a symmetric wave function of states:

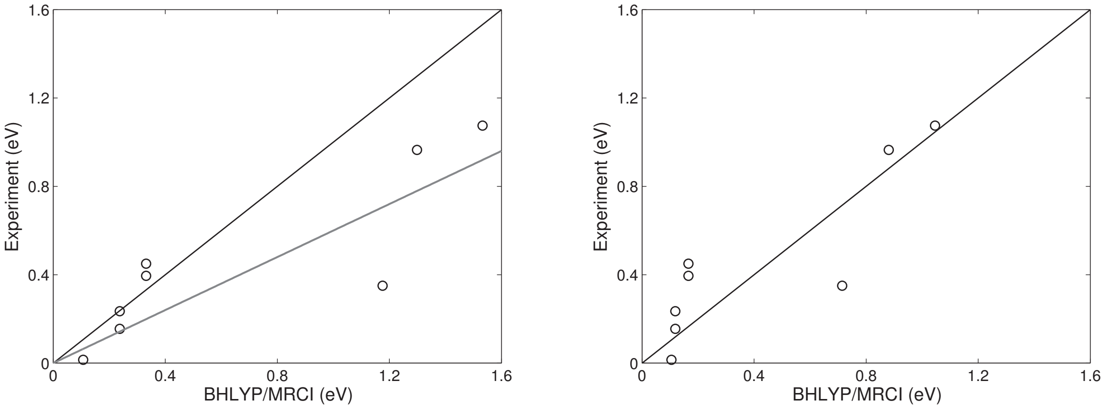

Figure 4: Left plot: Off-diagonal elements are scaled by p_1 =0.6 (slope of red line); Right plot: applied consistent parameters p_J=0.5 and p_F=0.3.

$$\phi_{\pm} = b_{\pm}|\mathrm{CSF}\ 1\rangle \pm b_{\pm}|\mathrm{CSF}\ 2\rangle + \ldots \tag{5}$$

so the total wave function $\phi_{\pm}$ is given then by equal contributions of the degenerate configurations with weight $b_{\pm}$, as it is in HF-based CI. It is indeed cumbersome to generalize this way of parameterizing off-diagonal elements for CI-SD which retains the symmetry of Eq 5. All the more so since this symmetry is demolished by utilizing a damping function for the off-diagonal elements in Eq. 2 and Eq. 3 even for CI-S which plays a major role in DFT/MRCI ansatz.

Table 1: Comparison of the BH-LYP/MRCI exchange integral of a creator-annihilator pair K_{ac} and the experimental singlet-triplet splitting δ_{exp}. DFT/MRCI data (configuration weight in parentheses) is given for original parameterization.

state type	exp, eV	DFT/MRCI-S, eV	δ_{exp}, eV	K_{ac}, eV
butadiene				
B_{1u} $\pi \to \pi^*$	5.92[1] 3.22[1]	5.85 (0.95) 3.08 (0.88)	2.70	1.76
cyclopentadiene				
B_2 $\pi \to \pi^*$	5.22[2] 3.15[2]	5.36 (0.95) 3.07 (0.90)	2.07	1.49
glyoxal				
A_u $n \to \pi^*$	2.8[3] 2.5[3]	2.63 (0.90) 2.22 (0.91)	0.3	0.27
thioformaldehyde				
A_2 $n \to \pi^*$	2.03[4] 1.80[4]	2.14 (0.91) 1.83 (0.95)	0.23	0.46
aceton				
A_2 $n \to \pi^*$	4.37[5] 4.16[5]	4.11 (0.87) 3.73 (0.88)	0.21	0.25
acetaldehyde				
A'' $n \to \pi^*$	4.27[6] 3.97[6]	3.95 (0.88) 3.53 (0.89)	0.30	0.28
tetrazine				
B_{1u} $n \to \pi^*$	2.25[7] 1.69[7]	2.37 (0.92) 1.86 (0.93)	0.56	0.36
A_u $n \to \pi^*$	3.42[8] 2.95[9]	3.64 (0.87) 3.42 (0.86)	0.47	0.15
ethylene				
B_{2u} $\pi \to \pi^*$	7.65[10] 4.36[10]	7.60 (0.95) 4.19 (0.83)	3.29	2.01
pyridine				
A_2 $n \to \pi^*$	5.43[11] 5.40[11]	5.39 (0.88) 5.30 (0.89)	0.03	0.06

Table 2: Comparison of the experimental splitting δ_{exp} between degenerate CSFs and the absolute value of the BHLYP/MRCI matrix element $|\mathcal{H}_{\wp\wp''}|$. SiO vertical transition energies have been taken from RKR curves.

states type	exp, eV	δ_{exp}, eV	$\mathcal{H}_{\wp\wp''}$, eV	V_a, eV	V_b, eV
benzene					
$^1(\mathrm{B}_{3u}/\mathrm{B}_{3u})$ $\pi \rightarrow \pi^*$, $\pi \rightarrow \pi^*$	4.80[12] 6.95[12]	2.15	-1.5325	-0.3316	-0.9321
$^1(\mathrm{B}_{2u}/\mathrm{B}_{2u})$ $\pi \rightarrow \pi^*$, $\pi \rightarrow \pi^*$	6.25[12] 6.95[12]	0.70	1.1758	-0.3316	0.4221
$^3(\mathrm{B}_{2u}/\mathrm{B}_{2u})$ $\pi \rightarrow \pi^*$, $\pi \rightarrow \pi^*$	3.90[12] 4.80[12]	0.90	0.3316	-0.3316	—
$^3(\mathrm{B}_{3u}/\mathrm{B}_{3u})$ $\pi \rightarrow \pi^*$, $\pi \rightarrow \pi^*$	4.80[12] 5.59[12]	0.79	0.3316	-0.3316	—
naphthalene					
$^1(\mathrm{B}_{3u}/\mathrm{B}_{3u})$ $\pi \rightarrow \pi^*$, $\pi \rightarrow \pi^*$	3.97[13] 5.89[13]	1.93	1.2992	0.2453	0.7723
SiO					
$^1(\Delta/\Sigma^-)$ $\pi \rightarrow \pi^*$, $\pi \rightarrow \pi^*$	5.55[14] 5.52[14]	0.03	0.1069	0.2375	0.1722
$^3(\Delta/\Sigma^-)$ $\pi \rightarrow \pi^*$, $\pi \rightarrow \pi^*$	5.17[14] 5.48[14]	0.31	-0.2375	0.2375	—
$^3(\Delta/\Sigma^+)$ $\pi \rightarrow \pi^*$, $\pi \rightarrow \pi^*$	5.17[14] 4.70[14]	0.47	-0.2375	0.2375	—

Table 3: Molecular states employed in the parameters optimization. Vertical excitation energies for optimal-parameters DFT/MRCI-S (δE_{sel}=1.0 E$_h$), DFT/MRCI-R (δE_{sel}=1.0 E$_h$), tight DFT/MRCI-R (δE_{sel}=0.8 E$_h$) in comparison with experimental data (reference values used in fitting are set in bold face). All energies are given in eV.

State	Type	Experiment	DFT/MRCI-S	DFT/MRCI-R	tight DFT/MRCI-R
Pyridine C_5H_5N					
1^1B_2	$n \rightarrow \pi^*$	**4.44**[a], 4.45[b]	4.75	4.86	4.86
1^1B_1	$\pi \rightarrow \pi^*$	4.99[a], **4.99**[c]	5.10	5.13	5.12
2^1A_1	$\pi \rightarrow \pi^*$	6.38[a], **6.38**[c], 6.32[d]	6.37	6.31	6.13
Nitromethane $H_3C—NO_2$					
$2^1A'$	$\pi \rightarrow \pi^*$	**6.25**[e], 6.23[e], 6.23[f]	6.18	6.34	6.49
$1^3A''$	$n \rightarrow \pi^*$	**3.80**[f]	3.49[†]	3.42[†]	3.27[†]
Pyrrole C_4H_4NH					
1^3B_1	$\pi \rightarrow$ Ry	**4.21**[g], 4.21[h], 4.2[i]	3.99	4.21	4.16
Furan C_4H_4O					
1^1B_1	$\pi \rightarrow \pi^*$	**6.04**[g], 6.06[h] 6.04[j]	6.12	6.09	6.09
3^1A_1	$\pi \rightarrow \pi^*$	**7.82**[h], 7.8[j]	7.91	7.90	7.98
1^3B_1	$\pi \rightarrow \pi^*$	4.0[i], **3.99**[h]	3.78	3.94	3.89
1^3A_1	$\pi \rightarrow \pi^*$	5.2[i], **5.22**[h]	4.94	5.15	5.09
Thiophene C_4H_4S					
2^1A_1	$\pi \rightarrow \pi^*$	5.48[h], **5.43**[g], 5.52[k]	5.46	5.48	5.47
1^3B_1	$\pi \rightarrow \pi^*$	3.7[i], **3.74**[g], 3.75[h]	3.77	3.77	3.73
1^3A_1	$\pi \rightarrow \pi^*$	**4.62**[h], 4.6[i], 4.7[k]	4.51	4.58	4.52
Cyclopentadiene C_5H_6					
1^1B_2	$\pi \rightarrow \pi^*$	**5.22**[g], 5.26[l], 5.33[m]	5.36	5.29	5.23
1^3B_2	$\pi \rightarrow \pi^*$	**3.15**[g], 3.10[l]	3.07	3.16	3.13
s-trans Butadiene C_4H_6					
1^1B_u	$\pi \rightarrow \pi^*$	**5.91**[g], 5.9[n], 5.92[o]	5.85	5.75	5.67
2^1A_g	$\pi \rightarrow \pi^*$	**6.27**[p]	6.08	6.32	6.26
1^3B_u	$\pi \rightarrow \pi^*$	**3.24**[g], 3.22[o], 3.2[n]	3.08	3.18	3.13
1^3A_g	$\pi \rightarrow \pi^*$	**4.92**[g], 4.91[o] 4.95[n]	4.77	4.99	4.94
Acrolein C_3H_4O					

$1^1A''$	$n \rightarrow \pi^*$	3.76^q, **3.75**^{r}, 3.71^s	3.34	3.58	3.59
$1^3A''$	$n \rightarrow \pi^*$	3.08^s, **3.05**^{t}	3.08	3.33	3.33
Nitrobenzene $C_6H_5NO_2$					
2^1A_1	$\pi \rightarrow \pi^*$	5.17^u, **5.11**^{v}	4.63	4.78	4.72
Styrene $H_5C_6CH{=}CH_2$					
$2^1A'$	$\pi \rightarrow \pi^*$	**4.43**^{w}, 4.43^x	4.43	4.53	4.53
$1^3A'$	$\pi \rightarrow \pi^*$	**3.40**^{w}	3.10	3.19	3.17
Benzene C_6H_6					
1^1B_{3u}	$\pi \rightarrow \pi^*$	4.80^y, **4.90**^{z}, 4.89^A	4.97	5.00	4.72
1^1B_{2u}	$\pi \rightarrow \pi^*$	**6.25**^{y}, 6.03^z	6.19	6.12	5.94
2^1B_{3u}	$\pi \rightarrow \pi^*$	**6.95**^{y,A}, 6.87^z	6.97	6.92	6.97
1^3B_{2u}	$\pi \rightarrow \pi^*$	3.90^y, **3.89**^{A}	4.06	4.13	4.10
2^3B_{3u}	$\pi \rightarrow \pi^*$	**5.59**^{y}, 5.69^A	5.47	5.49	5.36
Naphthalene $C_{10}H_8$					
1^1B_{3u}	$\pi \rightarrow \pi^*$	4.0^B, **3.97**^{C}	4.10	4.18	4.18
1^1B_{2u}	$\pi \rightarrow \pi^*$	4.45^B **4.45**^{C}	4.58	4.55	4.48
2^1B_{3u}	$\pi \rightarrow \pi^*$	5.89^B **5.89**^{C}	5.81	5.76	5.84
2^1B_{2u}	$\pi \rightarrow \pi^*$	**6.14**^{C}	6.13	6.09	6.10
Carbon monoxide CO					
2^1A	$n \rightarrow \pi^*$	**8.39**^{D}	8.02	8.16	8.14
Water H_2O					
1^1B_2	$n \rightarrow$ Ry	7.5^E, **7.4**^{F}	7.93	7.99	8.03
Thioformaldehyde $H_2C{=}S$					
1^1A_2	$n \rightarrow \pi^*$	**2.03**^{G}	2.15	2.22	2.13
1^3A_2	$n \rightarrow \pi^*$	**1.80**^{G}	1.84	1.95	1.88
Ethylene $H_2C{=}CH_2$					
1^1B_{1u}	$\pi \rightarrow$ Ry	**7.11**^{H}, 7.11^I	7.19	7.20	7.20
1^3B_{2u}	$\pi \rightarrow \pi^*$	**4.36**^{J}	4.19	4.36	4.29
Ethylene Dimer $2\times[H_2C{=}CH_2]$					
2^1A	$\pi\pi \rightarrow \pi^*\pi^*$	$2\times E(1^3B_{2u})$	3.29	8.71	8.64
3^3A	$\pi\pi \rightarrow \pi^*\pi^*$	$2\times E(1^3B_{2u})$	4.59	8.71	8.65

s-trans Glyoxal HOC—COH					
$1^1\mathrm{A}_u$	$n \rightarrow \pi^*$	$\mathbf{2.8}^K$	2.62	2.71	2.74
$1^1\mathrm{B}_g$	$n \rightarrow \pi^*$	$\mathbf{4.2}^K$	3.74	3.97	4.00
$1^3\mathrm{A}_u$	$n \rightarrow \pi^*$	$\mathbf{2.5}^K$	2.22	2.37	2.41
Formaldehyde $\mathrm{H_2C{=}O}$					
$1^1\mathrm{A}_2$	$n \rightarrow \pi^*$	$\mathbf{3.79}^L$, 3.94^M	3.69	3.83	3.85
$1^1\mathrm{B}_1$	$n \rightarrow$ Ry	$\mathbf{7.09}^N$, 7.09^O, 7.10^P	7.20	7.11	7.22
$2^1\mathrm{B}_1$	$n \rightarrow$ Ry	$\mathbf{7.97}^N$, 7.97^O, 7.98^P	7.95	7.93	8.00
$1^3\mathrm{A}_2$	$n \rightarrow \pi^*$	$\mathbf{3.50}^L$, 3.50^M	3.25	3.49	3.50
Formaldehyde Dimer $2\times[\mathrm{H_2C{=}O}]$					
$2^1\mathrm{A}$	$nn \rightarrow \pi^*\pi^*$	$2\times\mathrm{E}(1^3\mathrm{A}_2)$	2.05	7.09	7.15
$5^1\mathrm{A}$	$nn \rightarrow \pi^*\pi^*$	$2\times\mathrm{E}(1^1\mathrm{A}_2)$	3.12	7.80	7.90
$1^3\mathrm{A}$	$nn \rightarrow \pi^*\pi^*$	$2\times\mathrm{E}(1^3\mathrm{A}_2)$	2.17	7.09	7.15
$4^3\mathrm{A}$	$nn \rightarrow \pi^*\pi^*$	$\mathrm{E}(1^3\mathrm{A}_2)+\mathrm{E}(1^1\mathrm{A}_2)$	3.72	7.44	7.52
$5^3\mathrm{A}$	$nn \rightarrow \pi^*\pi^*$	$\mathrm{E}(1^3\mathrm{A}_2)+\mathrm{E}(1^1\mathrm{A}_2)$	3.72	7.44	7.52
Acetone $\mathrm{C_3H_6O}$					
$1^1\mathrm{A}_2$	$n \rightarrow \pi^*$	4.38^L, $\mathbf{4.37}^Q$	4.07	4.26	4.31
$1^1\mathrm{B}_2$	$n \rightarrow$ Ry	6.36^L, $\mathbf{6.35}^Q$, 6.36^R	6.53	6.47	6.66
$1^3\mathrm{A}_2$	$n \rightarrow \pi^*$	4.18^L, $\mathbf{4.16}^Q$	3.63	3.97	4.00
Acetaldehyde $\mathrm{C_2H_4O}$					
$1^1\mathrm{A}''$	$n \rightarrow \pi^*$	$\mathbf{4.27}^L$	3.95	4.09	4.12
$1^3\mathrm{A}''$	$n \rightarrow \pi^*$	$\mathbf{3.97}^L$, 3.91^R	3.53	3.78	3.81
Formamide $\mathrm{HCONH_2}$					
$1^1\mathrm{A}''$	$n \rightarrow \pi^*$	$\mathbf{5.65}^S$	5.22	5.38	5.44
$1^3\mathrm{A}''$	$n \rightarrow \pi^*$	$\mathbf{5.30}^T$	4.86	5.14	5.17
s-Tetrazine $\mathrm{C_2H_2N_4}$					
$1^1\mathrm{B}_{1u}$	$n \rightarrow \pi^*$	2.35^U, $\mathbf{2.25}^{X,Y}$, 2.34^W	2.39	2.36	2.35
$1^1\mathrm{A}_u$	$n \rightarrow \pi^*$	3.60^U, $\mathbf{3.42}^V$	3.64	3.62	3.63
$1^1\mathrm{B}_{3u}$	$\pi \rightarrow \pi^*$	$\mathbf{4.97}^U$ 5.0^W	5.15	5.11	5.16
$1^3\mathrm{B}_{1u}$	$n \rightarrow \pi^*$	$\mathbf{1.69}^{U,X}$ 1.70^Y	1.86	1.85	1.82
$1^3\mathrm{A}_u$	$n \rightarrow \pi^*$	$\mathbf{2.95}^X$	3.42	3.37	3.32

[a] Ref. [11], [b] Ref. [15], [c] Ref. [16], [d] Ref. [17], [e] Ref. [18], [f] Ref. [19], [g] Ref. [2], [h] Ref. [20], [i] Ref. [21], [j] Ref. [22]
[k] Ref. [23], [l] Ref. [24], [m] Ref. [25], [n] Ref. [26], [o] Ref. [1], [p] Ref. [27], [q] Ref. [28], [r] Ref. [29], [s] Ref. [30], [t] Ref. [31]
[u] Ref. [32], [v] Ref. [33], [w] Ref. [34], [x] Ref. [35], [y] Ref. [12], [z] Ref. [36], [A] Ref. [37], [B] Ref. [38], [C] Ref. [13], [D] Ref. [39]
[E] Ref. [40], [F] Ref. [41], [G] Ref. [4], [H] Ref. [42], [I] Ref. [43], [J] Ref. [44], [K] Ref. [3], [L] Ref. [6], [M] Ref. [45] [N] Ref. [46]
[O] Ref. [47], [P] Ref. [48], [Q] Ref. [5], [R] Ref. [49], [S] Ref. [50], [T] Ref. [51], [U] Ref. [9], [V] Ref. [8], [W] Ref. [52], [X] Ref. [7]

^{Y} Ref. [53]

† Accidentally, the first calculated triplet transition 1^3A′ was used in the fitting procedure, whilst the experimental energy shown in the table denotes to 1^3A″ state and corresponds to 3.69 eV for DFT/MRCI-S, 3.79 eV for DFT/MRCI-R and 3.75 eV for tight DFT/MRCI-R.

Table 4: Selected molecules and vertical absorption energies (in eV) used for benchmarking.

State	Experiment[a]	DFT/MRCI-S	DFT/MRCI-R
carbon dioxide			
$^1\Delta_u$ ($\pi \rightarrow \pi^*$)	8.6	8.75	8.80
carbon disulfide			
$^3\Delta_u$ ($\pi \rightarrow \pi^*$)	3.36	3.39	3.37
$^1\Delta_u$ ($\pi \rightarrow \pi^*$)	3.91	4.02	4.02
$^1\Pi_g$ ($\pi \rightarrow \pi^*$)	6.79	6.71	6.69
carbonyl sulfide			
$^3\Sigma_u^+$ ($\pi \rightarrow \pi^*$)	4.94	4.86	4.95
$^1\Delta_u$ ($\pi \rightarrow \pi^*$)	5.53	5.57	5.59
$^1\Pi_g$ ($\pi \rightarrow 3s$)	7.36	7.29	7.31
$^1\Sigma_u^+$ ($\pi \rightarrow \pi^*$)	8.02*	8.26	8.11
sulfur dioxide			
$^3B_2$ ($n \rightarrow \pi^*$)	3.40	3.23	3.27
$^1A_2$ ($n \rightarrow \pi^*$)	4.31	4.28	4.29
ethylene			
$^3B_{3u}$ ($\pi \rightarrow \pi^*$)	4.32	4.25	4.35
$^1B_{1u}$ ($\pi \rightarrow 3s$)	7.28*	7.23	7.20
$^1B_{3u}$ ($\pi \rightarrow \pi^*$)	7.6	7.64	7.51
$^1B_{3g}$ ($\sigma \rightarrow \pi^*$)	8.25	8.21	8.25
$^1B_{1u}$ ($\pi \rightarrow 3d$)	8.91*	8.94	8.89
propene			
$^3A'$ ($\pi \rightarrow \pi^*$)	4.28	4.14	4.35
$^1A''$ ($\pi \rightarrow 3s$)	6.6	6.61	6.64
$^1A'$ ($\pi \rightarrow \pi^*$)	7.17	7.22	7.16
isobutene			
$^3A_1$ ($\pi \rightarrow \pi^*$)	4.22	4.04	4.30
$^1B_1$ ($\pi \rightarrow 3s$)	6.1	6.26	6.29
$^1A_1$ ($\pi \rightarrow \pi^*$)	6.71*	6.69	6.67
$^1A_1$ ($\pi \rightarrow \pi^*$)	7.78	7.88	7.88
cis-2-butene			
$^3B_2$ ($\pi \rightarrow \pi^*$)	4.21	4.27	4.41
$^1B_2$ ($\pi \rightarrow \pi^*$)	7.10	7.40	7.32
trans-2-butene			
^3B_u ($\pi \rightarrow \pi^*$)	4.24	4.18	4.37
^1A_u ($\pi \rightarrow 3s$)	6.3	6.31	6.33
^1B_u ($\pi \rightarrow \pi^*$)	6.95	7.12	7.06
trimethylethylene			
$^3A'$ ($\pi \rightarrow \pi^*$)	4.16	4.02	4.31
$^1A''$ ($\pi \rightarrow 3s$)	5.76	5.87	5.91
$^1A'$ ($\pi \rightarrow \pi^*$)	6.47	6.59	6.60
$^1A'$ ($\pi \rightarrow \pi^*$)	6.97*	7.20	7.19
tetramethylethylene			

^{3}A ($\pi \to \pi^*$)	4.10	4.07	4.27
^{1}A ($\pi \to 3s$)	5.55	5.67	5.70
^{1}A ($\pi \to \pi^*$)	6.57	6.65	6.64
fluoroethylene			
^{3}A$'$ ($\pi \to \pi^*$)	4.40	4.34	4.46
^{1}A$''$ ($\pi \to 3s$)	7.02	7.09	7.09
^{1}A$'$ ($\pi \to \pi^*$)	7.50	7.66	7.53
^{1}A$''$ ($\pi \to 3p$)	8.08	7.88	7.89
^{1}A$''$ ($\pi \to 3d$)	8.87	9.02	8.98
1,1-difluoroethylene			
^{3}A$_1$ ($\pi \to \pi^*$)	4.63	4.47	4.68
^{1}B$_2$ ($\pi \to 3s$)	6.95	6.98	6.99
^{1}A$_1$ ($\pi \to \pi^*$)	7.50	7.67	7.59
^{1}A$_2$ ($\pi \to 3p$)	8.23	7.93	7.98
cis-1,2-difluoroethylene			
^{3}B$_1$ ($\pi \to \pi^*$)	4.43	4.43	4.53
^{1}B$_2$ ($\pi \to 3s$)	6.52	6.43	6.48
^{1}B$_1$ ($\pi \to \pi^*$)	7.82	7.96	7.80
^{1}A$_1$ ($\pi \to 3p$)	8.38	8.29	8.24
^{1}B$_2$ ($\pi \to 3d$)	9.01	8.81	8.79
trans-1,2-difluoroethylene			
^{3}B$_u$ ($\pi \to \pi^*$)	4.18	4.27	4.37
^{1}B$_g$ ($\pi \to 3s$)	6.44	6.60	6.70
^{1}B$_u$ ($\pi \to \pi^*$)	7.39	7.68	7.53
trifluoroethylene			
^{3}A$'$ ($\pi \to \pi^*$)	4.43	4.39	4.61
^{1}A$''$ ($\pi \to 3s$)	6.56	6.47	6.56
^{1}A$'$ ($\pi \to \pi^*$)	7.65	7.85	7.77
^{1}A$''$ ($\pi \to 3p$)	7.98	7.79	7.78
^{1}A$''$ ($\pi \to 3d$)	8.74	8.77	8.78
tetrafluoroethylene			
^{3}B$_{2u}$ ($\pi \to \pi^*$)	4.68	4.85	4.84
^{1}B$_{1u}$ ($\pi \to 3s$)	6.62	6.81	6.80
^{1}B$_{2u}$ ($\pi \to \pi^*$)	8.84	8.79	8.58
chlorotrifluoroethylene			
^{3}A$'$ ($\pi \to \pi^*$)	4.43	4.41	4.51
^{1}A$''$ ($\pi \to 3s$)	6.51	6.54	6.59
chloroethylene			
^{3}A$'$ ($\pi \to \pi^*$)	4.08	4.08	4.22
^{1}A$'$ ($\pi \to \pi^*$)	6.72*	6.82	6.73
acetylene			
$^3\Sigma_u^+$ ($\pi \to \pi^*$)	5.2	5.23	5.43
$^3\Delta_u$ ($\pi \to \pi^*$)	6.0	5.72	5.87
$^1\Pi_u$ ($\pi \to 3s$)	8.16*	7.96	7.91
propyne			
^{3}A$'$ ($\pi \to \pi^*$)	5.2	5.16	5.48
^{3}A$'$ ($\pi \to \pi^*$)	5.8	5.62	5.89

$^{1}\mathrm{A}'$ ($\pi \rightarrow 3s$)	7.18	6.91	6.94
1-butyne			
$^{3}\mathrm{A}'$ ($\pi \rightarrow \pi^*$)	5.2	5.11	5.45
$^{3}\mathrm{A}'$ ($\pi \rightarrow \pi^*$)	5.8	5.57	5.85
3,3,3-trifluoropropyne			
$^{3}\mathrm{A}'$ ($\pi \rightarrow \pi^*$)	5.0	5.27	5.39
$^{3}\mathrm{A}'$ ($\pi \rightarrow \pi^*$)	5.8	5.75	5.81
$^{1}\mathrm{A}'$ ($\pi \rightarrow 3s$)	8.80	8.55	8.52
1,3-butadiene			
$^{3}\mathrm{B}_u$ ($\pi \rightarrow \pi^*$)	3.22	3.13	3.18
$^{3}\mathrm{A}_g$ ($\pi \rightarrow \pi^*$)	4.91	4.84	4.99
$^{1}\mathrm{B}_u$ ($\pi \rightarrow \pi^*$)	5.92*	5.88	5.75
trans-1,3-pentadiene			
$^{3}\mathrm{A}'$ ($\pi \rightarrow \pi^*$)	3.14	3.14	3.19
$^{3}\mathrm{A}'$ ($\pi \rightarrow \pi^*$)	4.87	4.83	4.99
$^{1}\mathrm{A}'$ ($\pi \rightarrow \pi^*$)	5.80	5.83	5.81
cis-2-trans-4-hexadiene			
$^{3}\mathrm{A}'$ ($\pi \rightarrow \pi^*$)	3.11	3.12	3.17
$^{3}\mathrm{A}'$ ($\pi \rightarrow \pi^*$)	4.8	4.93	5.02
$^{1}\mathrm{A}'$ ($\pi \rightarrow \pi^*$)	5.69	5.71	5.61
1,3-cyclohexadiene			
$^{3}\mathrm{B}$ ($\pi \rightarrow \pi^*$)	2.94	2.89	2.95
$^{1}\mathrm{B}$ ($\pi \rightarrow \pi^*$)	4.94	5.06	4.96
1,5-hexadiene			
$^{3}\mathrm{A}$ ($\pi \rightarrow \pi^*$)	4.25	4.00	4.29
1,4-cyclohexadiene			
$^{3}\mathrm{B}_{2g}$ ($\pi \rightarrow \pi^*$)	4.29	4.15	4.35
$^{1}\mathrm{B}_{3g}$ ($\pi \rightarrow \pi^*$)	6.15	6.27	6.30
$^{1}\mathrm{B}_{3g}$ ($\pi \rightarrow \pi^*$)	7.95	7.88	7.89
propadiene (allene)			
$^{3}\mathrm{A}_1$ ($\pi \rightarrow \pi^*$)	4.28	4.38	4.61
$^{1}\mathrm{A}_1$ ($\pi \rightarrow \pi^*$)	7.24	7.16	7.14
benzene			
$^{3}\mathrm{B}_{2u}$ ($\pi \rightarrow \pi^*$)	3.90	4.12	4.13
$^{3}\mathrm{B}_{3u}$ ($\pi \rightarrow \pi^*$)	5.59	5.51	5.49
$^{1}\mathrm{B}_{3u}$ ($\pi \rightarrow \pi^*$)	4.80	5.04	5.00
$^{1}\mathrm{B}_{2u}$ ($\pi \rightarrow \pi^*$)	6.25	6.23	6.12
fluorobenzene			
$^{3}\mathrm{A}_1$ ($\pi \rightarrow \pi^*$)	3.90	4.16	4.19
$^{3}\mathrm{B}_1$ ($\pi \rightarrow \pi^*$)	5.72	5.63	5.61
$^{1}\mathrm{B}_1$ ($\pi \rightarrow \pi^*$)	4.78	5.02	5.00
$^{1}\mathrm{A}_1$ ($\pi \rightarrow \pi^*$)	6.23	6.26	6.15
o-difluorobenzene			
$^{3}\mathrm{B}_1$ ($\pi \rightarrow \pi^*$)	3.92	4.17	4.19
$^{3}\mathrm{A}_1$ ($\pi \rightarrow \pi^*$)	5.67	5.65	5.63
$^{1}\mathrm{A}_1$ ($\pi \rightarrow \pi^*$)	4.76	5.04	5.01

$^1B_1$ ($\pi \to \pi^*$)	6.22	6.30	6.19
1,3,5-trifluorobenzene			
$^3A_1$ ($\pi \to \pi^*$)	3.95	4.23	4.25
$^3B_2$ ($\pi \to \pi^*$)	5.62	5.61	5.59
$^1B_2$ ($\pi \to \pi^*$)	4.87	5.13	5.12
$^1A_1$ ($\pi \to \pi^*$)	6.20	6.34	6.24
1,2,3,4-tetrafluorobenzene			
$^3A_1$ ($\pi \to \pi^*$)	3.95	4.19	4.20
$^1A_1$ ($\pi \to \pi^*$)	4.85	5.07	5.04
$^1B_1$ ($\pi \to \pi^*$)	6.43	6.37	6.27
1,2,4,5-tetrafluorobenzene			
$^3B_{2u}$ ($\pi \to \pi^*$)	4.0	4.18	4.18
$^1B_{3u}$ ($\pi \to \pi^*$)	4.69	4.97	4.95
$^1B_{2u}$ ($\pi \to \pi^*$)	6.3	6.40	6.28
pentafluorobenzene			
$^3A_1$ ($\pi \to \pi^*$)	3.90	4.26	4.22
$^1B_1$ ($\pi \to \pi^*$)	4.79	5.09	5.07
$^1A_1$ ($\pi \to \pi^*$)	6.36	6.44	6.33
hexafluorobenzene			
$^3B_{2u}$ ($\pi \to \pi^*$)	3.86	4.18	4.15
$^1B_{3u}$ ($\pi \to \pi^*$)	4.80	5.15	5.10
$^1B_{2u}$ ($\pi \to \pi^*$)	6.36	6.51	6.38
furan			
$^3B_1$ ($\pi \to \pi^*$)	3.99	3.82	3.94
$^3A_1$ ($\pi \to \pi^*$)	5.22	4.99	5.15
$^1B_1$ ($\pi \to \pi^*$)	6.06	6.15	6.09
$^1A_1$ ($\pi \to \pi^*$)	7.82	7.95	7.90
thiophene			
$^3B_1$ ($\pi \to \pi^*$)	$3.66^{\star}$	3.75	3.78
$^3A_1$ ($\pi \to \pi^*$)	4.62	4.55	4.56
$^1A_1$ ($\pi \to \pi^*$)	5.48	5.50	5.47
$^1A_1$ ($\pi \to \pi^*$)	7.05	7.10	7.11
pyrrole			
$^3B_1$ ($\pi \to \pi^*$)	4.21	4.04	4.21
$^1A_2$ ($\pi \to 3s$)	5.22	5.11	5.07
$^1B_1$ ($\pi \to \pi^*$)	5.98	6.01	5.98
azomethane			
^3B_g ($n \to \pi^*$)	2.75	2.62	2.79
^1B_g ($n \to \pi^*$)	3.50	3.44	3.48
^1B_u ($n \to 3p$)	6.71	6.92	6.97
^1B_u ($\pi \to \pi^*$)	7.8	8.07	8.02
azo-tert-butane			
^3B_g ($n \to \pi^*$)	2.67	2.30	2.61
^3B_u ($\pi \to \pi^*$)	4.9	4.70	5.08
^1B_g ($n \to \pi^*$)	3.37	3.10	3.28
^1B_u ($n \to 3p$)	7.3	7.39	7.53

nitromethane			
$^3\mathrm{A}''$ $(n \rightarrow \pi^*)$	3.8	3.69	3.79
$^1\mathrm{A}''$ $(n \rightarrow \pi^*)$	4.45	4.35	4.36
$^1\mathrm{A}'$ $(\pi \rightarrow \pi^*)$	6.23	6.31	6.34
thiophosgene			
$^3\mathrm{A}_1$ $(\pi \rightarrow \pi^*)$	3.1	3.08	3.10
$^1\mathrm{A}_2$ $(n \rightarrow \pi^*)$	2.61	2.65	2.68
$^1\mathrm{A}_1$ $(\pi \rightarrow \pi^*)$	4.89	4.91	4.88
1,3-cyclopentadiene			
$^3\mathrm{B}_2$ $(\pi \rightarrow \pi^*)$	3.1	3.11	3.16
$^1\mathrm{B}_2$ $(\pi \rightarrow \pi^*)$	5.26	5.39	5.29
pyridine[b]			
$^1\mathrm{A}_2$ $(n \rightarrow \pi^*)$	5.43	5.39	5.43
pyrazine[b]			
$^3\mathrm{B}_{1u}$ $(n \rightarrow \pi^*)$	3.33	3.55	3.61
$^3\mathrm{B}_{2g}$ $(n \rightarrow \pi^*)$	4.59	4.87	4.96
$^1\mathrm{B}_{1u}$ $(n \rightarrow \pi^*)$	3.83	4.03	4.04
$^1\mathrm{B}_{2g}$ $(n \rightarrow \pi^*)$	5.19	5.33	5.45
pyrimidine[c]			
$^1\mathrm{A}_2$ $(n \rightarrow \pi^*)$	4.62	4.83	4.86
s-triazine[c]			
$^1\mathrm{B}_2$ $(n \rightarrow \pi^*)$	4.59	4.62	4.66
acetone[d]			
$^3\mathrm{A}_2$ $(n \rightarrow \pi^*)$	4.16	3.70	3.97
$^1\mathrm{A}_2$ $(n \rightarrow \pi^*)$	4.37	4.11	4.26
acetamide[e]			
$^1\mathrm{A}''$ $(n \rightarrow \pi^*)$	5.44	5.27	5.43
nitrobenzene[f]			
$^1\mathrm{A}_2$ $(n \rightarrow \pi^*)$	3.65	3.32	3.52
dithiosuccinimide[g]			
$^3\mathrm{B}_1$ $(n \rightarrow \pi^*)$	2.63	2.44	2.58
$^1\mathrm{B}_1$ $(n \rightarrow \pi^*)$	2.77	2.65	2.73
$^1\mathrm{A}_2$ $(n \rightarrow \pi^*)$	3.04	2.84	2.93
max. error(+), eV		0.36	0.39
max. error(-), eV		–0.46	–0.28
standard dev., eV		0.16	0.14
RMS dev., eV		0.16	0.15

[a] For experimental energies see Ref. [54] and references therein.

[b] Ref. [55], [c] Ref. [16], [d] Ref. [5], [e] Ref. [56], [f] Ref. [32], [g] Ref. [57]

* Band maximum.

Bibliography

[1] Oren A. Mosher, Wayne M. Flicker, and Aron Kuppermann. Electronic spectroscopy of s-trans 1,3-butadiene by electron impact. *J. Chem. Phys.*, 59(12):6502–6511, 1973.

[2] Knut Roger Asmis. *Electron-Molecule Collisions: A Novel Instrument for Measuring Inelastic Differential Cross Sections at 180° Angle and Applications.* PhD thesis, University of Freiburg, Switzerland, 1996.

[3] G.J. Verhaart and H.H. Brongersma. Triplet n$\rightarrow \pi^\star$ and $\pi \rightarrow \pi^\star$ transitions in glyoxal and biacetyl by low-energy electron-impact spectroscopy. *Chem. Phys. Lett.*, 72(1):176 – 180, 1980.

[4] R.H. Judge, C.R. Drury-Lessard, and D.C. Moule. The far ultraviolet spectrum of thioformaldehyde. *Chem. Phys. Lett.*, 53(1):82 – 83, 1978.

[5] Willard M. St. John, Ron C. Estler, and John P. Doering. Low energy electron impact study of acetone. *J. Chem. Phys.*, 61(3):763–767, 1974.

[6] K. N. Walzl, C. F. Koerting, and A. Kuppermann. Electron-impact spectroscopy of acetaldehyde. *J. Chem. Phys.*, 87(7):3796–3803, 1987.

[7] K.K. Innes, I.G. Ross, and William R. Moomaw. Electronic states of azabenzenes and azanaphthalenes: A revised and extended critical review. *J. Mol. Spectrosc.*, 132(2):492 – 544, 1988.

[8] K.K Innes. Approximate energy of the 1au electronic state of s-tetrazine. *J. Mol. Spectrosc.*, 129(1):140 – 144, 1988.

[9] Michael H. Palmer, Hamish McNab, David Reed, Anne Pollacchi, Isobel C. Walker, Martyn F. Guest, and Michele R.F. Siggel. The molecular and electronic states of 1,2,4,5-tetrazine studied by {VUV} absorption, near-threshold electron energy-loss spectroscopy and ab initio multi-reference configuration interaction studies. *Chem. Phys.*, 214(23):191 – 211, 1997.

[10] Melvin B. Robin. *Higher Excited States of Polyatomic Molecules, Volume II.* Academic Press, Inc., 1975.

[11] Isobel C. Walker, Michael H. Palmer, and Andrew Hopkirk. The electronic states of the azines. ii. pyridine, studied by vuv absorption, near-threshold electron energy loss spectroscopy and ab initio multi-reference configuration interaction calculations. *Chem. Phys.*, 141(23):365 – 378, 1990.

[12] Robert P. Frueholz, Wayne M. Flicker, Oren A. Mosher, and Aron Kuppermann. Electronic spectroscopy of benzene and the fluorobenzenes by variable angle electron impact. *J. Chem. Phys.*, 70(6):3057–3070, 1979.

[13] G.A. George and G.C. Morris. The intensity of absorption of naphthalene from 30 000 cm^{-1} to 53 000 cm^{-1}. *J. Mol. Spectrosc.*, 26(1):67 – 71, 1968.

[14] R W Field, A Lagerqvist, and I Renhorn. *Phys. Scr.*, 14(6):298, 1976.

[15] Eliel Villa, Aviv Amirav, and Edward C. Lim. Single-vibronic-level and excitation-energy dependence of radiative and nonradiative transitions in jet-cooled s1 pyridine. *J. Phys. Chem.*, 92(19):5393–5397, 1988.

[16] A. Bolovinos, P. Tsekeris, J. Philis, E. Pantos, and G. Andritsopoulos. Absolute vacuum ultraviolet absorption spectra of some gaseous azabenzenes. *J. Mol. Spectrosc.*, 103(2):240 – 256, 1984.

[17] E.H. van Veen and F.L. Plantenga. Threshold electron-impact excitation spectrum of pyridine. *Chem. Phys. Lett.*, 30(1):28 – 31, 1975.

[18] Isobel C Walker and Malcolm A.D Fluendy. Spectroscopy and dynamics of nitromethane ($\mathrm{ch_3no_2}$) and its anionic states. *Int. J. Mass Spectrom.*, 205(13):171 – 182, 2001.

[19] Wayne M. Flicker, Oren A. Mosher, and Aron Kuppermann. Variable angle electron-impact excitation of nitromethane. *J. Chem. Phys.*, 72(4):2788–2794, 1980.

[20] Wayne M. Flicker, Oren A. Mosher, and Aron Kuppermann. Electron impact investigation of electronic excitations in furan, thiophene, and pyrrole. *J. Chem. Phys.*, 64(4):1315–1321, 1976.

[21] E.H. Van Veen. Triplet $\pi \to \pi^\star$ transitions in thiophene, furan and pyrrole by low-energy electron-impact spectroscopy. *Chem. Phys. Lett.*, 41(3):535 – 539, 1976.

[22] Michael H. Palmer, Isobel C. Walker, Charles C. Ballard, and Martyn F. Guest. The electronic states of furan studied by {VUV} absorption, near-threshold electron energy-loss spectroscopy and ab initio multi-reference configuration interaction calculations. *Chem. Phys.*, 192(2):111 – 125, 1995.

[23] Michael H. Palmer, Isobel C. Walker, and Martyn F. Guest. The electronic states of thiophene studied by optical (vuv) absorption, near-threshold electron energy-loss (eel) spectroscopy and ab initio multi-reference configuration interaction calculations. *Chem. Phys.*, 241(3):275 – 296, 1999.

[24] Robert P. Frueholz, Wayne M. Flicker, Oren A. Mosher, and Aron Kuppermann. Electronic spectroscopy of 1,3-cyclopentadiene, 1,3-cyclohexadiene and 1,3-cycloheptadiene by electron impact. *J. Chem. Phys.*, 70(4):2003–2013, 1979.

[25] Lucy W. Pickett, Eleanor Paddock, and Elinor Sackter. The ultraviolet absorption spectrum of 1,3-cyclopentadiene*. *J. Am. Chem. Soc.*, 63(4):1073–1077, 1941.

[26] J. P. Doering. Electron impact study of the energy levels of trans-1,3-butadiene. *J. Chem. Phys.*, 70(8):3902–3909, 1979.

[27] W. C. Price and A. D. Walsh. The absorption spectra of conjugated dienes in the vacuum ultra-violet (1). *Proc. R. Soc. Lond. A*, 174(957):220–234, 1940.

[28] A. D. Walsh. The absorption spectra of acrolein, crotonaldehyde and mesityl oxide in the vacuum ultra-violet. *Trans. Faraday Soc.*, 41(0):498–505, 1945.

[29] Ralph S. Becker, Kozo Inuzuka, and Jimmie King. Acrolein: Spectroscopy, photoisomerization, and theoretical considerations. *J. Chem. Phys.*, 52(10):5164–5170, 1970.

[30] Kozo Inuzuka. Calculation on the electronic states of the acrolein molecule by the semi-empirical molecular orbital method. *Bull. Chem. Soc. Jpn.*, 34(1):6–8, 1961.

[31] J.M. Hollas. The electronic absorption spectrum of acrolein vapour. *Spectrochim. Acta.*, 19(9):1425 – 1441, 1963.

[32] Saburo Nagakura, Maomi Kojima, and Yasuko Maruyama. Electronic spectra and electronic structures of nitrobenzene and nitromesitylene. *J. Mol. Spectrosc.*, 13(14):174 – 192, 1964.

[33] Tayfun Ari, Haluk Güven, and Necati Ecevit. Electron energy-loss spectroscopy in monosubstituted benzenes. *J. Electron Spectrosc. Relat. Phenom.*, 73(1):13 – 23, 1995.

[34] P. Swiderek, M.-J. Fraser, M. Michaud, and L. Sanche. Electron-energy-loss spectroscopy of the low-lying triplet states of styrene. *J. Chem. Phys.*, 100(1):70–77, 1994.

[35] Katsumi Kimura and Saburo Nagakura. Vacuum ultraviolet spectra of styrene, benzaldehyde, acetophenone, and benzonitrile. *Theor. Chim. Acta*, 3(2):164–173, 1965.

[36] Atsunari Hiraya and Kosuke Shobatake. Direct absorption spectra of jet-cooled benzene in 130-260 nm. *J. Chem. Phys.*, 94(12):7700–7706, 1991.

[37] J. P. Doering. Electronic energy levels of benzene below 7 ev. *J. Chem. Phys.*, 67(9):4065–4070, 1977.

[38] R.H. Huebner, S.R. Meilczarek, and C.E. Kuyatt. Electron energy-loss spectroscopy of naphthalene vapor. *Chem. Phys. Lett.*, 16(3):464 – 469, 1972.

[39] Edwin N. Lassettre and Ausma Skerbele. Absolute generalized oscillator strengths for four electronic transitions in carbon monoxide. *J. Chem. Phys.*, 54(4):1597–1607, 1971.

[40] S. Trajmar, W. Williams, and Aron Kuppermann. Detection and identification of triplet states of h_2o by electron impact. *J. Chem. Phys.*, 54(5):2274–2275, 1971.

[41] A. Chutjian, R. I. Hall, and S. Trajmar. Electron-impact excitation of h[sub 2]o and d[sub 2]o at various scattering angles and impact energies in the energy-loss range 4.2–12 ev. *J. Chem. Phys.*, 63(2):892–898, 1975.

[42] D G Wilden and J Comer. Rydberg states of c_2h_4 and c_2d_4 : assignments using the technique of low-energy electron energy-loss spectroscopy. *J. Phys. B: At. Mol. Phys.*, 13(5):1009, 1980.

[43] Ruth McDiarmid. A reinvestigation of the absorption spectrum of ethylene in the vacuum ultraviolet. *J. Phys. Chem.*, 84(1):64–70, 1980.

[44] Michael Allan. Measurement of absolute differential cross section for the excitation of the lowest triplet state of ethene. *Chem. Phys. Lett.*, 225(13):156 – 160, 1994.

[45] Steven Taylor, David G. Wilden, and John Comer. Electron energy-loss spectroscopy of forbidden transitions to valence and rydberg states of formaldehyde. *Chem. Phys.*, 70(3):291 – 298, 1982.

[46] Masako Suto, Xiuyan Wang, and L. C. Lee. Fluorescence from vuv excitation of formaldehyde. *J. Chem. Phys.*, 85(8):4228–4233, 1986.

[47] J. E. Mentall, E. P. Gentieu, M. Krauss, and D. Neumann. Photoionization and absorption spectrum of formaldehyde in the vacuum ultraviolet. *J. Chem. Phys.*, 55(12):5471–5479, 1971.

[48] M. J. Weiss, C. E. Kuyatt, and S. Mielczarek. Inelastic electron scattering from formaldehyde. *J. Chem. Phys.*, 54(10):4147–4150, 1971.

[49] E.H. Van Veen, W.L. Van Dijk, and H.H. Brongersma. Low-energy electron-impact excitation spectra of formaldehyde, acetaldehyde and acetone. *Chem. Phys.*, 16(3):337 – 345, 1976.

[50] Harold Basch, M. B. Robin, and N. A. Kuebler. Electronic states of the amide group. *J. Chem. Phys.*, 47(4):1201–1210, 1967.

[51] Ralph H. Staley, Lawrence B. Harding, W.A. Goddard III, and J.L. Beauchamp. Triplet states of the amide group. trapped electron spectra of formamide and related molecules. *Chem. Phys. Lett.*, 36(5):589 – 593, 1975.

[52] C. Fridh, L. Åsbrink, B.Ö. Jonsson, and E. Lindholm. Rydberg series in small molecules: Xviii. photoelectron, uv, mass, and electron impact spectra of s-tetrazine. *Int. J. Mass. Spectrom. Ion. Phys.*, 9(5):485 – 497, 1972.

[53] D.T. Livak and K.K. Innes. A triplet-singlet transition of s-tetrazine. *J. Mol. Spectrosc.*, 39(1):115 – 122, 1971.

[54] Aron. Kuppermann, Wayne M. Flicker, and Oren A. Mosher. Electronic spectroscopy of polyatomic molecules by low-energy, variable-angle electron impact. *Chem. Rev.*, 79(1):77–90, 1979.

[55] Yasuo Okuzawa, Masaaki Fujii, and Mitsuo Ito. Direct observation of second excited ^{1,3}(n,π^*) states of pyrazine by uvir double resonance dip spectroscopy. *Chem. Phys. Lett.*, 171(4):341 – 346, 1990.

[56] Eigil B. Nielsen and John A. Schellman. The absorption spectra of simple amides and peptides. *J. Phys. Chem.*, 71(7):2297–2304, 1967.

[57] Stefan C. J. Meskers, Tadeusz Polonski, and Harry P. J. M. Dekkers. Polarized absorption and phosphorescence spectra and magnetic circular dichroism of dithioimides: Assignment of the lower ^{1}nπ^* and ^{3}nπ^*. states. *J. Phys. Chem.*, 99(4):1134–1142, 1995.

MOLECULAR PHYSICS, 2016
http://dx.doi.org/10.1080/00268976.2016.1201600

OPEN SHELLS. OPEN QUESTIONS

On the performance of DFT/MRCI-R and MR-MP2 in spin–orbit coupling calculations on diatomics and polyatomic organic molecules

Vladimir Jovanović, Igor Lyskov, Martin Kleinschmidt and Christel M. Marian

Institute of Theoretical and Computational Chemistry, Heinrich-Heine-University Düsseldorf, Düsseldorf, Germany

ABSTRACT

We have investigated the performance of different multi-reference quantum chemical methods with regard to electronic excitation energies and spin–orbit matrix elements (SOMES). Among these methods are two variants of the combined density functional theory and multi-reference configuration interaction method (DFT/MRCI and DFT/MRCI-R) and a multi-reference second-order Møller–Plesset perturbation theory (MR-MP2) approach. Two variants of MR-MP2 have been tested based on either Hartree–Fock orbitals or Kohn–Sham orbitals of the BH-LYP density functional. In connection with the MR-MP2 approaches, the first-order perturbed wave functions have been employed in the evaluation of spin–orbit coupling. To validate our results, we assembled experimental excitation energies and SOMES of eight diatomic and fifteen polyatomic molecules. For some of the smaller molecules, we carried out calculations at the complete active space self-consistent field (CASSCF) level to obtain SOMEs to compare with. Excitation energies of the experimentally unknown states were assessed with respect to second-order perturbation theory corrected (CASPT2) values where available. Overall, we find a very satisfactory agreement between the excitation energies and the SOMEs obtained with the four approaches. For a few states, outliers with regard to the excitation energies and/or SOMEs are observed. These outliers are carefully analysed and traced back to the wave function composition.

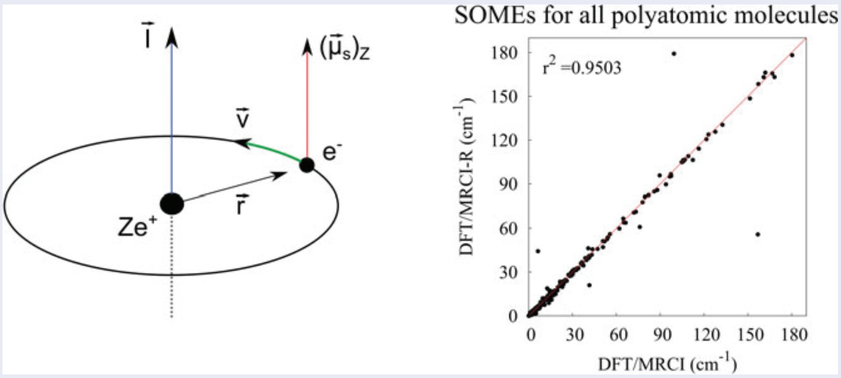

ARTICLE HISTORY
Received 1 February 2016
Accepted 2 June 2016

KEYWORDS
Spin–orbit coupling; multi-reference configuration interaction; multi-reference perturbation theory; assessment; benchmark

1. Introduction

The combined density functional theory and multi-reference configuration interaction (DFT/MRCI) method by Grimme and Waletzke [1] has proven itself as a very useful approach to an efficient treatment of static and dynamic correlation in larger molecules. In combination with SPOCK [2–4], which allows for the inclusion of electronic spin–orbit coupling, and VIBES [5–7], capable of treating the vibronic part of the problem, it has been used for the successful elucidation of many spin-dependent properties in molecules [2,8–15]. However, the DFT/MRCI method is not without shortcomings. The impetus for the present study came when we realised that the original DFT/MRCI method has some difficulties providing a balanced description of configurations with four open shells. Obviously, this is the case in electronically excited dimers and other weakly coupled bi-chromophores [16]. Less obvious are cases such as nitrobenzene where artificially low-lying excited singlet states with four open shells are encountered in the DFT/MRCI spectrum [17]. Recently, some of these shortcomings of the original DFT/MRCI were remedied by the parameterisation of

CONTACT Christel M. Marian ✉ Christel.Marian@hhu.de

Supplemental data for this article can be accessed at http://dx.doi.org/10.1080/00268976.2016.1201600.

a redesigned DFT/MRCI-R Hamiltonian [16], dubbed DFT/MRCI-R in the following. A completely different hybrid multi-configuration wave function and density functional theory (DFT) ansatz has been presented by Jensen and coworkers [18–22]. It combines a long-range multi-configuration self-consistent field (MCSCF) treatment with an adiabatic short-range DFT description of electron correlation. Time-dependent MCSCF short-range DFT (TD-MC-srDFT) has been implemented in the Dalton program package [23] and might, therefore, be used for computing spin-dependent properties. To our knowledge, spin–orbit coupling calculations based on this method have not yet been reported, however.

Alternative *ab initio* methods that are able to treat static and dynamic electron correlation in sizeable molecules and allow for the computation of spin–orbit matrix elements (SOMEs) are sparse. Spin–orbit coupling constants have been evaluated in a multi-configuration linear response approach a long time ago [24,25], but the amount of dynamic electron correlation that can the covered by MCSCF is very limited. State-averaged complete active space self-consistent field (SA-CASSCF) calculations followed by second-order perturbation theory (CASPT2) have become something like a gold standard for computing excited-state energies when the active space can be made large enough to include all important excitations [26–28]. Spin-dependent properties are then evaluated by the so-called CASPT2/CASSI-SO procedure where SA-CASSCF wave functions are employed for computing SOMEs while adapting the energies of the states by shifting them to their CASPT2 energies [29–31]. The same applies to CASSCF/NEVPT2 calculations of spin–orbit interactions [32]. In that way, the perturbation corrections to the CASSCF wave functions are not accounted for when computing SOMEs. A slightly more general multireference second-order Møller–Plesset perturbation theory (MR-MP2) approach, albeit with configuration selection, was devised by Grimme and Waletzke [33] and is implemented in their mrci code. In this approach, all configurations, whose interactions with one of the reference vectors exceed a user-defined threshold, are included in the first-order space and contribute to the first-order perturbed wave function that can subsequently be used to determine SOMEs. The discarded configurations contribute solely to the MR-MP2 energy.

In this work, we investigate how the DFT/MRCI-R and MR-MP2 wave functions perform in spin–orbit coupling calculations on light-element compounds. To validate our results, we assembled data on energies and SOMEs of eight diatomic and fifteen polyatomic organic molecules. For the diatomic molecules, the excitation energies and spin–orbit coupling constants can be checked directly against experimental data. Energies of the polyatomic molecules can be compared with experimental data to a limited extent only. In particular, experimental data on optically dark states – that are often essential for the photophysical behaviour of a molecule and in particular for intersystem crossing – are missing for comparison. For some of the smaller molecules (formaldehyde, thioformaldehyde, nitromethane, furan, and thiophene), we carried out benchmark calculations at the CASSCF/CASPT2 level to obtain SOMEs and excitation energies to compare with. Excitation energies of the experimentally unknown states of the other molecules were assessed with respect to CASPT2 values from the literature [28,34–38] where available.

Moreover, numerous examples exist in which the combination of DFT/MRCI and Spock yielded higher order spin-dependent properties such as phosphorescence and intersystem crossing rates in excellent agreement with experimental data [2,8–10,12,13]. Hence, these SOMEs are considered reliable and may serve as a reference.

Furthermore, we shed light on an earlier assumption that SOMEs are more robust with regard to the wave function quality than energies [17]. In that work, the relaxation pathways of photoexcited nitrobenzene were studied. As mentioned already above, artificially low-lying excited singlet states with four open shells were encountered in the DFT/MRCI spectrum. For that reason, energies from the algebraic diagrammatic construction scheme ADC(3) were combined with SOMEs from DFT/MRCI wave functions. The *ab initio* MR-MP2 method treats the four open-shell configurations in a qualitatively correct manner which allows us now to quantitatively address this assumption.

2. Methods and computational details

2.1. Geometries and general remarks

The ground-state geometries of all polyatomic molecules were optimised at the DFT level, employing Becke's three-parameter exchange functional combined with the Lee–Yang–Parr correlation functional (B3LYP) [39–41]. Throughout, a valence triple zeta basis set with polarisation function (TZVP) [42] was used with additional polarisation functions on sulphur atoms (TZVPP) [43]. These calculations were performed with the Turbomole program package, version 6.5 [44]. The ground-state geometries were employed in all computations of excited-state energies (which corresponds to vertical transitions) as well as the SOMEs. For some molecules with low-lying Rydberg states, we augmented the atomic orbital (AO) basis by a diffuse Gaussian *s*, *p*, and *d* function [45] after the geometry optimisation. These bases have been marked as *augmented* in contrast to *valence* for the pure TZVP/TZVPP basis sets.

For the diatomic molecules, experimental equilibrium bond distances of the ground and the first excited $^3\Pi$ (first $^3\Pi_g$ for P_2) states were used [46] to enable comparison with experimental fine-structure splitting constants. In these cases, adiabatic energies were calculated.

Excited-state energies and wave functions were obtained by methods capable of treating multi-reference character in an efficient way (see below). The MRCI program makes use of an interface to TURBOMOLE that provides spin-independent one-electron integrals and three-index-two-electron integrals. For the resolution-of-the-identity (RI) approximation of the four-index-two-electron integrals, optimised auxiliary basis sets (TZVP, TZVPP) from the TURBOMOLE library [43] were utilised.

2.2. Electron correlation

Electron correlation calculations were carried out in four different manners as described in more detail below. All methods are implemented in the MRCI code originally written by Grimme and Waletzke [1,33], later extended and parallelised in our laboratory [16,47].

In the electron correlation calculations, all electrons of the diatomic molecules and only the valence electrons of the polyatomic molecules were explicitly correlated. Unless noted otherwise, the initial reference space was generated in a restricted active space (RAS) manner with a maximum of two excitations out of ten electrons in ten orbitals. In total, 21 singlet and 20 triplet roots were obtained for all molecules. When molecular point-group symmetry is exploited, these roots do not necessarily relate to the lowest eigenvalues. In C_s symmetric molecules, we solved for 11 $^1A'$ and 10 $^3A'$ states as well as for 10 roots each of $^{1,3}A''$ symmetry. In C_{2v} point-group symmetry, we computed six totally symmetric roots with singlet multiplicity and five roots each for other combinations of spin and spatial symmetry.

2.2.1. DFT/MRCI calculations

The DFT/MRCI method designed by Grimme and Waletzke [1] is a combination of DFT (which gives information about dynamic correlation) and truncated MRCI expansions (to take the static correlation into account). It makes use of a semi-empirical Hamiltonian that has been parameterised in combination with the BH-LYP functional. In the original work, five parameters that depend on the multiplicity, the excitation class with respect to a closed-shell reference and the number of open shells of the configuration were fitted to experimental excitation energies. Only a small number of configuration state functions (CSFs), instead of the full MRCI space, is used in the actual calculation. Double counting of correlation is avoided by exponential scaling of the off-diagonal matrix elements. Configurations whose contributions would have been scaled away are discarded according to an energy gap criterion δE_{sel}. δE_{sel} was set to 0.8 E_h for constructing the final reference space where all configurations with a squared coefficient exceeding 0.003 in one of the roots were kept. In the subsequent DFT/MRCI calculations that generate wave functions and excitation energies, the threshold was increased to 1.0 E_h.

2.2.2. DFT/MRCI-R calculations

Recently, some of us presented an alternative form of the DFT/MRCI method [16]. The new parameterisation is spin-invariant and incorporates less empiricism compared to the original formulation while preserving its computational efficiency. The robustness of the redesigned Hamiltonian has been tested on experimentally known vertical excitation energies of organic molecules yielding similar statistics as for the original parameterisation. Besides that, the new formulation yields a consistent description of all multiplet components of a doubly excited configuration with four open shells. The DFT/MRCI-R method [16] is particularly well suited for studying photophysical processes in bi-chromophores. With regard to technical details, the DFT/MRCI-R calculations are carried out exactly in the same manner as the DFT/MRCI ones.

2.2.3. MR-MP2 calculations

The *ab initio* MR-MP2 method [33] is implemented in the same MRCI code, but not parallelised. It is based on a zeroth-order CI reference wave function. To make it feasible for applications on large molecules, extensive configuration selection is made in the construction of the first-order perturbed wave function. The second-order energy correction is evaluated then as the Hamiltonian matrix element of the first-order perturbed and the zeroth-order wave functions. Second-order energy contributions of configurations discarded in the selection procedure are added to the MR-MP2 energy. In the case of a single closed-shell reference and a selection threshold of zero, this approach is equivalent to the standard MP2 theory [33]. The first-order perturbed wave function generated in this procedure can be employed for evaluating properties.

If not stated otherwise, the initial reference space was generated with the same procedure and size (10-10-2) as for the DFT/MRCI case. To avoid cutting of the initial

RAS space between degenerate orbitals, in most of the diatomic molecules (AlCl, AlF, BCl, BF, P_2 and SiO), the 10-11-2 restricted active space was employed. Because of the same reason, AlBr needed the inclusion of yet another active orbital to obtain eventually a 10-12-2 RAS. In the MR-MP2 calculations, orbitals with energies larger than 10 E_h were discarded. After every iteration, all configurations with a squared coefficient exceeding 0.003 in one of the roots were added to the reference space. The threshold for the truncation of the first-order space was set to 10^{-7} E_h, as recommended in the original publication [33]. This general approach had to be altered for some difficult cases when using the augmented basis. The calculations on thiophene were performed with the 10-12-2 RAS and the admixture of HF Rydberg and valence orbitals in thioformaldehyde and nitromethane led to the use of 10-11-2 as the initial reference space. The biggest starting RAS (12-12-2) was chosen for bithiophene in order to include both linear combinations of the lone-pair n(S) orbitals.

We employed the g0 operator as the unperturbed zeroth-order Hamiltonian, which is given by a sum of generalised one-particle Fock operators [33]. The MO basis and Fock matrix elements were generated in two different ways. First, Hartree–Fock (HF) orbitals were used, but this approach has possible difficulties because of the diffuse character of the virtual orbitals since these are generated in the field of N (instead of $N-1$) electrons. In their original publication, Grimme and Waletzke recommended to employ improved virtual orbitals (IVOs) [33]. Instead, we use Kohn–Sham (BH-LYP) orbitals as a second set of one-particle basis which do not suffer from the same difficulties as the HF orbitals. This additionally allows for a direct comparison of the performance between the methods lifting the orbital influence.

2.2.4. CASSCF/CASPT2 calculations

State-averaged CASSCF and subsequent CASPT2 calculations were carried out with the MOLPRO package [48–51] using exactly the same AO basis sets as in the other calculations. We employed the minimum number of active electrons and active orbitals able to describe the desired molecular states appropriately. As the chosen active space varies from molecule to molecule, detailed specifications will be given below where the results for the individual molecules are presented.

2.3. Electronic spin–orbit coupling

Spin–orbit matrix elements for the DFT/MRCI and MR-MP2 wave functions were calculated using the spin–orbit coupling kit (Spock) developed in our laboratory [2–4]. It employs an effective one-electron mean-field approximation to the Breit–Pauli Hamiltonian [52]. A further simplification is introduced by neglecting all multicentre integrals, and atomic mean-field integrals are calculated with the AMFI program [53]. These approximations introduce errors which are usually lower than 5% [54,55]. To match the DFT/MRCI and MR-MP2 SOMEs as closely as possible, SOMEs of the CASSCF wave functions were computed with the one-centre approximation (als option) for the one- and two-electron Breit–Pauli spin–orbit integrals in MOLPRO [31].

The spin–orbit-free mrci code [1,33] computes only the $M_s = S$ sublevel of a multiplet state. This allows the calculation of triplet–triplet SOMEs in addition to singlet–triplet SOMEs which would not be possible if only the $M_s = 0$ wave function were available. To enable the fast determination of SOMEs between the other multiplet sublevels by means of the Wigner–Eckart theorem [56], Spock expresses the spin part of the Hamiltonian in terms of components of a first-rank tensor operator, i.e. $\hat{\mathcal{S}}_{+1}$, $\hat{\mathcal{S}}_0$, and $\hat{\mathcal{S}}_{-1}$. In contrast, the spatial part of the spin–orbit Hamiltonian is adapted to the point-group symmetry of the molecule which corresponds, in most cases, to a Cartesian representation. Because of the relations

$$\hat{\mathcal{S}}_{+1} = \frac{-1}{\sqrt{2}}(\hat{\mathcal{S}}_x + i\hat{\mathcal{S}}_y); \quad \hat{\mathcal{S}}_0 = \hat{\mathcal{S}}_z;$$
$$\hat{\mathcal{S}}_{-1} = \frac{1}{\sqrt{2}}(\hat{\mathcal{S}}_x - i\hat{\mathcal{S}}_y), \tag{1}$$

it is easy to transform the mixed representation of the Hamiltonian to a purely Cartesian one [57]. In the following, the x- and y-components of SOMEs between the $M_s = 1$ sublevel of a triplet state and a singlet state $\langle T, M_s = 1|\hat{\mathcal{H}}_{\mathrm{SO\,x/y}}|S\rangle$ are presented, while the z-component of the Hamiltonian couples a singlet state with the $M_s = 0$ sublevel of a triplet $\langle T, M_s = 0|\hat{\mathcal{H}}_{\mathrm{SO\,z}}|S\rangle$. The matrix elements between two triplet states are always given in the form $\langle T, M_s = 1|\hat{\mathcal{H}}_{\mathrm{SO\,x/y}}|T, M_s = 0\rangle$ and $\langle T, M_s = 1|\hat{\mathcal{H}}_{\mathrm{SO\,z}}|T, M_s = 1\rangle$. In the tables, the imaginary unit (i) has been omitted from the complex-valued matrix elements of the $\hat{\mathcal{H}}_{\mathrm{SO\,x}}$ and $\hat{\mathcal{H}}_{\mathrm{SO\,z}}$ operators and absolute values are presented instead. For details with regard to the transformation of the SOMEs, see the Supplemental Material (SM).

3. Results and discussion

3.1. Test set

The selected test molecules include eight diatomic molecules (AlBr, AlCl, AlF, BCl, BF, CS, P_2, SiO) and fifteen polyatomic molecules (see Figure 1). The diatomic

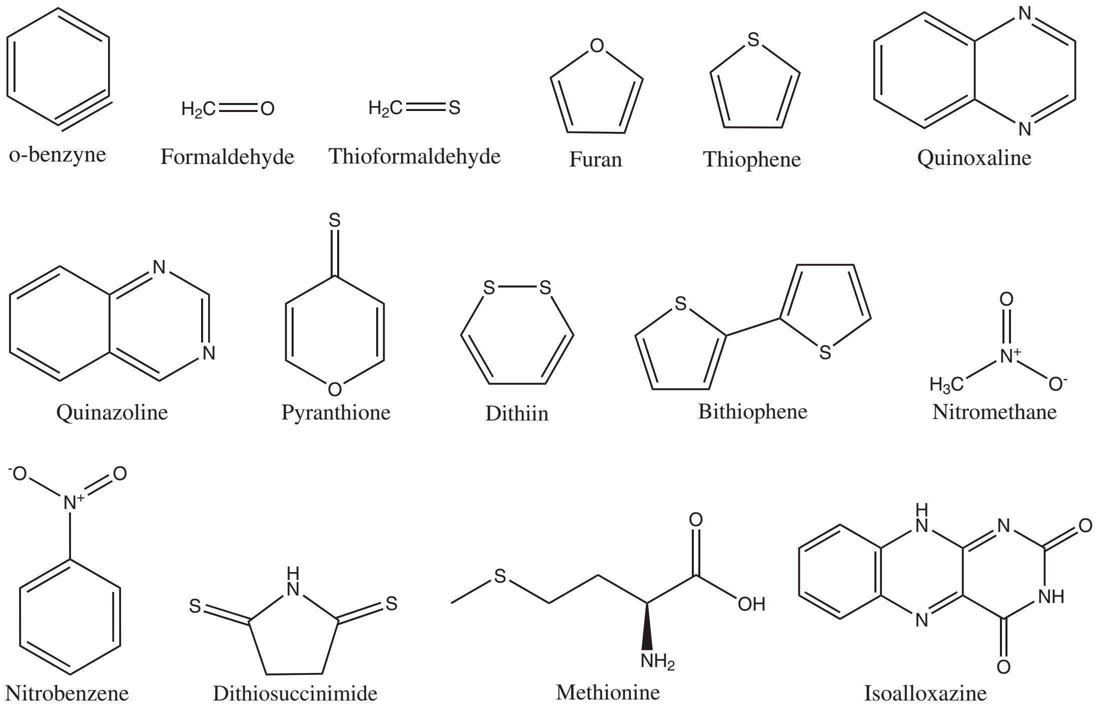

Figure 1. Test set of polyatomic molecules.

molecules primarily consist of first- and second-row elements, where first-order spin–orbit interactions still dominate the fine-structure splittings of spatially degenerate states. Their excitation energies and SOMEs will be compared directly to experimentally derived adiabatic transition energies and spin–orbit coupling constants.

Unfortunately, such a comparison is not possible for spatially non-degenerate states of polyatomic molecules. In these cases, only off-diagonal SOMEs may adopt significant values. However, numerous examples have been presented in which the combination of DFT/MRCI and Spock yielded higher order spin-dependent properties such as phosphorescence and intersystem crossing rates in excellent agreement with experimental data [2,8–10,12,13]. Hence, these results can serve as a reference. In addition, CASSCF/CASPT2 calculations on some of the smaller polyatomic molecules were carried out for comparison. The polyatomic molecules in the test set are chosen such that substantial spin–orbit coupling is expected which involves the presence of heteroatoms and states of different electronic characters. The states selected for comparison are mainly the ground and low-lying excited, photophysically and photochemically important states with $\pi\pi^*$ and $n\pi^*$ characters, which allows for an easier correspondence between the methods. In some cases, higher lying excited states with significant SOMEs are also included. Because their wave functions tend to be mixed with Rydberg excitations and contributions from doubly excited configurations, the correspondence is more difficult to determine. In the following, the singlet and triplet excitation energies and the computed SOMEs of all polyatomic are presented and analysed. Tables with detailed information on the experimental reference data, oscillator strengths for electric dipole-allowed transitions and the wave function composition, as well as the optimised geometries, are given in the SM. Additionally, statistical data for each molecule is shown there.

3.2. Diatomic molecules

Spatially degenerate states of diatomic molecules exhibit a first-order spin–orbit splitting. From spectral data involving different substates, the fine-structure parameter A_{SO} can be derived which quantitatively describes the first-order zero-field splitting at the equilibrium bond distance of the respective state [58]. A_{SO} can be correlated with calculated SOMEs and hence gives valuable reference data for testing theoretical predictions. From the axial symmetry of diatomic molecules, with the z-axis being the internuclear axis, it follows that only the z-component of the spin–orbit Hamiltonian couples the degenerate states. This simplifies the phenomenological SO Hamiltonian to the expression

$$\hat{\mathcal{H}}_{\mathrm{SO}} = a_{\parallel}\hat{\mathcal{L}}_0\hat{\mathcal{S}}_0 = A_{\mathrm{SO}}\hat{\mathcal{L}}_z\hat{\mathcal{S}}_z \tag{2}$$

Table 1. Calculated DFT/MRCI, DFT/MRCI-R, MR-MP2(HF) and MR-MP2(BH-LYP) adiabatic energies of the pure spin (unperturbed) 1 $^3\Pi$ (1 $^3\Pi_g$ for P_2) state in selected diatomic molecules, together with the experimental values of the $\Omega = 1$ component.

	Energies (cm^{-1})				
Molecule	DFT/MRCI	DFT/MRCI-R	MRMP2 (HF)	MRMP2 (BH-LYP)	Experiment [46]
AlBr	23,145	23,471	23,003	22,769	23,779
AlCl	24,206	24,506	24,195	23,957	24,594
AlF	27,135	27,302	27,132	27,445	27,241
BCl	19,961	20,503	19,821	19,752	20,200
BF	27,829	28,621	28,429	28,330	29,144
CS	27,848	28,078	25,301	25,543	27,661
P_2	28,105	27,915	26,974	27,189	28,197
SiO	32,594	32,263	31,431	31,664	33,947

and gives the fine-structure parameter for the equilibrium structure as [57]

$$A_e = \frac{1}{\Lambda\Sigma}\langle\Psi(\vec{r}, R_e)|\hat{\mathcal{H}}_{\mathrm{SO}}|\Psi(\vec{r}, R_e)\rangle. \qquad (3)$$

Here, Λ and Σ are projections of the total spatial and spin angular momenta on the internuclear axis, respectively. Our state of interest is the first triplet of Π symmetry, in which case $\Lambda = \Sigma = 1$. The spin–orbit coupling is introduced perturbatively. If we set up a matrix for the first-order degenerate perturbation theory in the basis of LS coupled states, we see that the fine-structure parameter A_{SO} is exactly equal to the off-diagonal matrix element between the $M_s = 1$ components of the degenerate Π_x and Π_y sublevels, i.e. $A_{\mathrm{SO}} = \langle {}^3\Pi_x, M_s = 1|\hat{\mathcal{H}}_{\mathrm{SO}\,z}|{}^3\Pi_y, M_s = 1\rangle$.

The first triplet state of Π symmetry in the considered molecules is a regular state with configuration $\sigma^1\pi^1$. In P_2, it is symmetric with respect to inversion, Π_g, and its configuration is $\sigma_g^1\pi_u^4\pi_g^1$. For a straightforward comparison with experimental data, adiabatic energies are calculated using the experimental values for the bond lengths. Tables 1 and 2 summarise the calculated and experimental energies and fine-structure parameters of the 1 $^3\Pi_r$ states, while Tables 3 and 4 present the corresponding statistical data. As a general trend, we notice from the graphs in Figure 2 that all methods underestimate the excitation energies of the 1 $^3\Pi_r$ state on the average. With correlation coefficients of 0.9856 (DFT/MRCI-R) and 0.9834 (DFT/MRCI), the MRCI methods perform somewhat better than the MR-MP2 methods (0.9629 for MR-MP2(HF) and 0.9658 for MR-MP2(BH-LYP)) when it comes to $^3\Pi_r$ excitation energies. The maximum negative deviations are observed for the SiO molecule. A reason may be the unusually strong Si=O bond with at least double bond character (bond length 1.509739 Å [46]) in the electronic ground state which poses a challenge for the quantum chemical description.

The correlation plots for the SOMEs of the diatomic molecules are presented in Figure 3. (Note that the experimentally derived zero-field splittings may contain also higher order spin–orbit interactions and contributions from electronic spin–spin coupling which are assumed to be small.) The agreement with the experimental splittings is excellent for all four methods, with equal RMSD of 2 cm^{-1}, and maximal positive/negative deviations of 3.1/2.6, 3.0/2.7, 2.1/3.5 and 3.8/1.6 cm^{-1} for

Table 2. Fine-structure splitting of the 1 $^3\Pi$ (1 $^3\Pi_g$ for P_2) state with the configuration $\sigma^1\pi^1$ ($\sigma_g^1\pi_u^4\pi_g^1$) in selected diatomic molecules, characterised by the presented spin–orbit coupling coefficient A_{SO}(cm^{-1}). Experimental values are given for comparison.

Molecule	DFT/MRCI	DFT/MRCI-R	MRMP2 (HF)	MRMP2 (BH-LYP)	Experiment [46]
AlBr	135.1	135.0	134.1	135.8	132.0
AlCl	64.6	63.1	62.3	64.2	65.8
AlF	48.1	47.1	46.1	47.4	47.0
BCl	46.8	46.3	47.3	48.9	
BF	24.0	23.6	24.9	25.5	24.2
CS	90.2	92.0	91.0	93.1	92.8
P_2	130.7	129.9	126.4	127.4	128.9
SiO	74.1	72.3	69.5	71.4	73.0

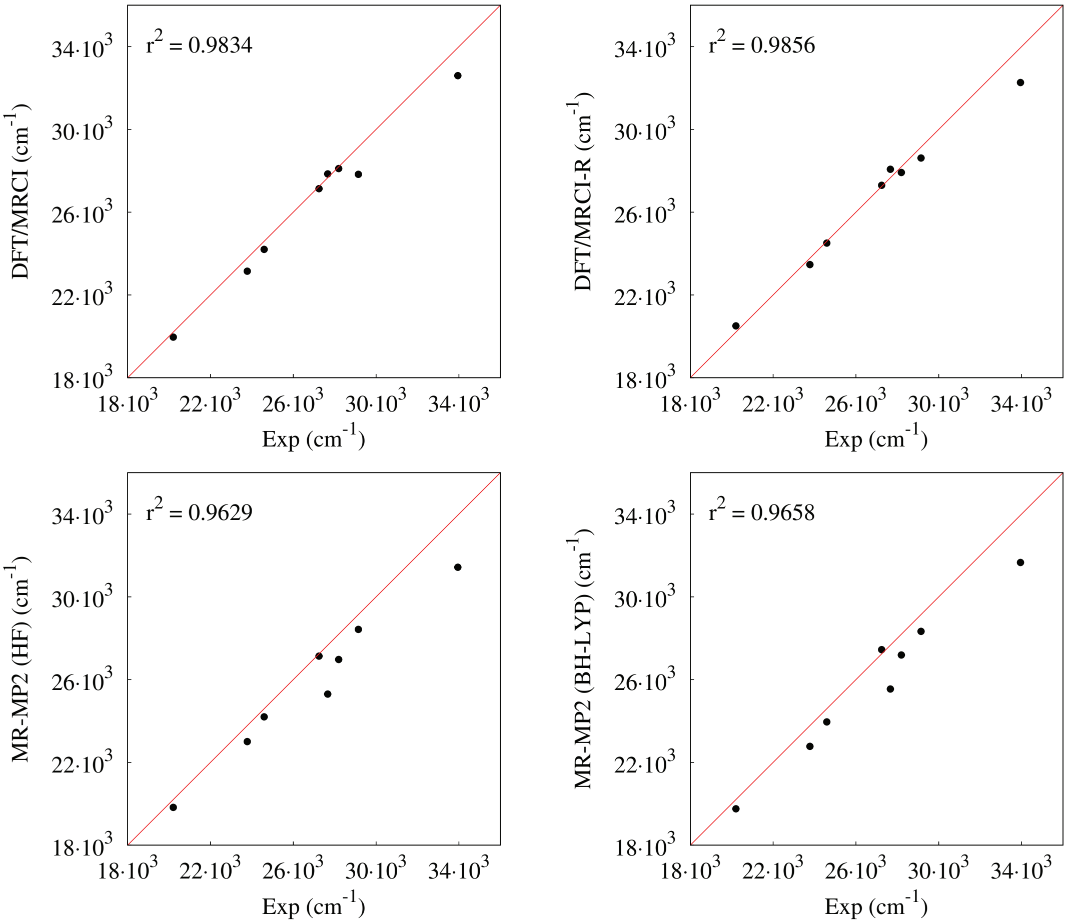

Figure 2. Correlation plots for adiabatic energies of the $1\,^3\Pi$ ($1\,^3\Pi_g$ for P_2) state in selected diatomic molecules, calculated with DFT/MRCI, DFT/MRCI-R, MR-MP2(HF) and MR-MP2(BH-LYP) methods vs. experimental data.

Table 3. Deviations in adiabatic excitation energies for the $1\,^3\Pi$ state of diatomic molecules calculated with DFT/MRCI, DFT/MRCI-R, MR-MP2(HF) and MR-MP2(BH-LYP) with respect to the experimental data. The values are given in cm^{-1}.

Method	RMSD	Max. (+)	Max. (−)
DFT/MRCI	727	187	1353
DFT/MRCI-R	667	417	1684
MR-MP2(HF)	1361		2516
MR-MP2(BH-LYP)	1277	204	2283

Table 4. Deviations in fine-structure splittings for the $1\,^3\Pi$ state of diatomic molecules calculated with DFT/MRCI, DFT/MRCI-R, MR-MP2(HF) and MR-MP2(BH-LYP) with respect to the experimental data. The values are given in (cm^{-1}).

Method	RMSD	Max. (+)	Max. (−)
DFT/MRCI	2	3.1	2.6
DFT/MRCI-R	2	3.0	2.7
MR-MP2(HF)	2	2.1	3.5
MR-MP2(BH-LYP)	2	3.8	1.6

DFT/MRCI, DFT/MRCI-R, MR-MP2(HF), and MR-MP2(BH-LYP), respectively. This shows that SOMEs are less sensitive to the level of correlation treatment than excitation energies.

3.3. Polyatomic molecules

3.3.1. Vertical energies

Individual data regarding computed vertical excitation energies of all polyatomic molecules are compiled in Tables 5 and 6. Where available, also CASPT2 and experimentally determined values are given there for comparison. Note that the data for formaldehyde, thioformaldehyde, furan, thiophene, and nitromethane, shown in Tables 5 and 6, have been obtained with the *augmented* AO basis sets containing diffuse functions. The corresponding data computed in the *valence* AO bases may be found in the SM.

Table 5. Vertical singlet excitation energies ΔE (eV).

Molecule (AO basis)	State	Dominant character	DFT/MRCI	DFT/MRCI-R	MRMP2 (HF)	MRMP2 (BH-LYP)	CASPT2	Experiment
o-Benzyne (*valence*)	1^1A_2	$\pi \rightarrow \pi_{\parallel}^*$	3.89	3.83	4.22	4.20		
	1^1B_2	$\pi \rightarrow \pi_{\parallel}^*$	3.97	3.92	4.27	4.21		
	2^1A_1	$\pi_{\parallel}, \pi \rightarrow \pi_{\parallel}^*, \pi^*$	4.24	6.50	6.43	6.44		
	1^1B_1	$\pi_{\parallel} \rightarrow \pi_{\parallel}^*$	5.09	4.94	5.12	5.01		5.08
	3^1A_1	$\pi \rightarrow \pi^*$	5.28	5.19	4.75	4.64		
	2^1B_2	$\pi_{\parallel} \rightarrow \pi^*$	5.38	5.38	5.54	5.47		
	2^1B_1	$\pi_{\parallel}, \pi \rightarrow \pi_{\parallel}^*, \pi^*$	5.74	7.25	7.22	7.22		
	3^1B_1	$\pi \rightarrow \pi^*$	6.38	6.23	6.34	6.08		6.25
Formaldehyde (*augmented*)	1^1A_2	$n \rightarrow \pi^*$	3.67	3.81	3.88	3.93	3.90, 3.99	3.79, 3.94
	1^1B_2	$n \rightarrow 3s$	7.02	6.93	6.99	6.99	6.77, 6.87	7.09
	2^1B_2	$n \rightarrow 3p_z$	7.86	7.84	7.92	8.17	7.68, 7.76	8.13
	2^1A_1	$n \rightarrow 3p_y$	7.96	7.88	7.99	8.04	7.78, 7.84	7.98
	2^1A_2	$n \rightarrow 3p_x$	8.40	8.26	8.14	8.24	7.95, 8.00	8.37
	1^1B_1	$\sigma \rightarrow \pi^*$	8.81	8.90	9.12	9.20	9.21, 9.43	9.00
	4^1A_1	$\pi \rightarrow \pi^*$	9.51	9.50	9.64	9.64	9.33, 10.41	
	5^1A_1	$n^2 \rightarrow \pi^{*2}$	11.06	9.20	10.67	10.75	10.29, 10.87	
Thioformaldehyde (*augmented*)	1^1A_2	$n \rightarrow \pi^*$	2.16	2.20	2.10	2.16	2.11	2.03
	1^1B_1	$n \rightarrow 4s$	5.67	5.67	6.07	5.99	5.84	5.84
	2^1B_1	$n \rightarrow 4p_z$	6.35	6.35	6.83	6.73	6.57	6.59
	2^1A_1	$\pi \rightarrow \pi^*$	6.46	6.48	6.30	6.50	6.29	6.2
	3^1A_1	$n \rightarrow 4p_x$	6.53	6.53	7.04	6.45	6.78	6.84
	2^1A_2	$n \rightarrow 4p_y$	6.67	6.65	7.19	7.08	6.94	
	1^1B_2	$\sigma \rightarrow \pi^*$	6.89	6.89	6.72	6.78	7.15	
	3^1A_2	$\pi, n \rightarrow \pi^{*2}$	7.19	7.70	7.61	7.58	7.66	
	5^1A_1	$n^2 \rightarrow \pi^{*2}$	7.84	6.06	7.27	7.26	7.11	
Furan (*augmented*)	1^1A_2	$\pi \rightarrow 3s$	5.91	5.90	6.10	6.00	5.98	5.91
	1^1B_1	$\pi \rightarrow \pi^*$	6.05	6.04	6.47	6.48	6.11	6.04, 6.06
	2^1A_1	$\pi \rightarrow \pi^*$	6.29	6.30	6.11	5.93	6.22	
	1^1B_2	$\pi \rightarrow 3p_x$	6.38	6.36	6.59	6.48	6.51	6.48
	2^1A_2	$\pi \rightarrow 3p_z$	6.55	6.54	6.89	6.74	6.70	6.61
	2^1B_1	$\pi \rightarrow 3p_y$	6.80	6.77	6.92	6.92	6.63	6.75
	4^1A_1	$\pi \rightarrow \pi^*$	8.13	8.09	8.31	8.12	7.87	7.82, 7.80
Thiophene (*augmented*)	2^1A_1	$\pi \rightarrow \pi^*$	5.43	5.43	5.23	5.18	5.47	5.43
	1^1B_1	$\pi \rightarrow \pi^*$	5.65	5.62	6.14	5.62	5.47	5.61
	1^1B_2	$\pi \rightarrow \sigma^*/4p_x$	5.83	5.88	6.29	6.21	6.28	
	1^1A_2	$\pi \rightarrow 4s$	5.85	5.84	6.11	6.16	6.03	5.93
	2^1A_2	$\pi \rightarrow \sigma^*/4p_x$	6.06	6.10	6.25	6.21	6.33	
	3^1A_1	$\pi \rightarrow \pi^*$	7.08	7.02	7.04	6.89	6.99	7.05
Quinoxaline (*valence*)	1^1B_1	$n \rightarrow \pi^*$	3.54	3.63	3.24	3.24		
	2^1A_1	$\pi \rightarrow \pi^*$	4.14	4.13	3.75	3.61		3.96
	1^1B_2	$\pi \rightarrow \pi^*$	4.36	4.33	4.68	4.57		
	1^1A_2	$n \rightarrow \pi^*$	4.75	4.93	4.68	4.56		
	2^1A_2	$n \rightarrow \pi^*$	5.05	5.14	4.47	4.28		
Quinazoline (*valence*)	$1^1A''$	$n \rightarrow \pi^*$	3.80	3.92	3.49	3.39		
	$2^1A'$	$\pi \rightarrow \pi^*$	4.27	4.26	3.90	3.55		4.07
	$3^1A'$	$\pi \rightarrow \pi^*$	4.72	4.68	4.86	4.62		4.66
	$2^1A''$	$n \rightarrow \pi^*$	4.76	4.89	4.35	4.13		
	$3^1A''$	$n \rightarrow \pi^*$	5.18	5.29	4.72	4.42		
Pyranthione (*valence*)	1^1A_2	$n \rightarrow \pi^*$	2.16	2.22	2.26	2.25		2.25
	1^1B_2	$n \rightarrow \pi^*$	3.76	3.66	3.95	3.85		
	2^1A_1	$\pi \rightarrow \pi^*$	3.92	3.90	3.76	3.71		3.78
	1^1B_1	$\pi \rightarrow \pi^*$	4.32	4.35	4.39	4.30		
	2^1B_1	$\pi \rightarrow \pi^*$	5.59	5.63	5.54	5.37		
Dithiin (*valence*)	1^1B	$\pi \rightarrow \pi^*$	2.60	2.58	2.38	2.33		2.74
	2^1A	$\pi \rightarrow \pi^*$	4.36	4.36	4.17	4.01		4.44
	2^1B	$\pi \rightarrow \pi^*$	4.54	4.52	4.26	4.14		5.00
	3^1B	$\pi \rightarrow \pi^*$	4.73	4.69	4.20	3.97		
	3^1A	$\pi^2 \rightarrow \pi^{*2}$	4.80	4.69	4.39	4.23		
Bithiophene (*valence*)	1^1B	$\pi \rightarrow \pi^*$	4.17	4.15	4.02	3.93		3.86, 4.11
	2^1A	$\pi \rightarrow \pi^*$	4.81	4.87	4.66	4.39		
	2^1B	$\pi \rightarrow \pi^*$	4.95	5.00	4.58	4.18		5.02
	3^1A	$\pi \rightarrow \pi^*$	5.02	5.11	4.69	4.28		
	4^1A	$\pi \rightarrow \sigma^*$	5.34	5.39	5.27	4.81		
	3^1B	$\pi \rightarrow \sigma^*$	5.42	5.46	5.44	4.92		
Nitromethane	$1^1A''$	$n \rightarrow \pi^*$	3.83	3.92	3.64	3.71	3.92	4.25

(*Continued*)

Table 5. (*Continued*)

Molecule (AO basis)	State	Dominant character	DFT/MRCI	DFT/MRCI-R	MRMP2 (HF)	MRMP2 (BH-LYP)	CASPT2	Experiment
(*augmented*)	$2^1A''$	$n' \rightarrow \pi^*$	4.26	4.28	3.97	4.03	4.32	4.50, 4.45, 4.51, 4.59
	$2^1A'$	$\pi \rightarrow \pi^*$	6.30	6.34	6.18	6.31	6.38	6.25, 6.23 6.29, 6.26
	$3^1A'$	$n \rightarrow 3s$	7.74	7.66	7.55	7.49	7.07	
	$4^1A'$	$n' \rightarrow 3s$	8.00	7.87	7.62	7.72	7.55	
Nitrobenzene	1^1A_2	$n \rightarrow \pi^*$	3.29	3.46	3.25	3.47	3.67[a]	3.65
(*valence*)	1^1B_2	$n' \rightarrow \pi^*$	3.88	3.91	3.82	3.76	4.32[a]	
	1^1B_1	$\pi \rightarrow \pi^*$	4.29	4.40	4.28	4.18	4.54[a]	
	2^1B_1	$\pi, \pi \rightarrow \pi^*, \pi^*$	4.63		7.19	7.00		
	2^1A_1	$\pi \rightarrow \pi^*$	4.77	4.81	5.33	5.08	5.10[a]	5.17
Dithiosuccinimide	1^1B_1	$n \rightarrow \pi^*$	2.66	2.73	2.58	2.45		2.77, 2.82
(*valence*)	1^1A_2	$n \rightarrow \pi^*$	2.85	2.93	2.80	2.66		3.04, 3.08
	1^1B_2	$\pi \rightarrow \pi^*$	4.13	4.09	3.85	3.75		3.96, 3.87
	2^1A_2	$n \rightarrow \pi^*$	4.64	4.64	4.37	4.00		
	2^1A_1	$n, n' \rightarrow \pi^*, \pi^{*'}$	4.71	3.40				
	2^1B_1	$n \rightarrow \pi^*$	4.83	4.80	4.55	4.20		
	5^1A_1	$n^2 \rightarrow \pi^{*2}$	6.07	5.08	5.51	5.26		
Methionine	2^1A	$\pi \rightarrow \sigma^*/Ry$	5.12	5.32	5.99	5.24		
(*valence*)	3^1A	$n_O \rightarrow \pi^*$	5.48	5.71	5.97	5.54		
Isoalloxazine	$2^1A'$	$\pi \rightarrow \pi^*$	3.03	3.00	2.84	2.64		2.85
(*valence*)	$1^1A''$	$n \rightarrow \pi^*$	3.16	3.28	3.52	3.85		
	$2^1A''$	$n \rightarrow \pi^*$	3.34	3.46	3.45	3.11		
	$3^1A''$	$n \rightarrow \pi^*$	3.90	4.00	3.87	3.76		
	$3^1A'$	$\pi \rightarrow \pi^*$	3.94	3.94	3.98	3.71		3.76

[a] CASPT2 (14,11) using an ANO-L-VDZP basis [38].

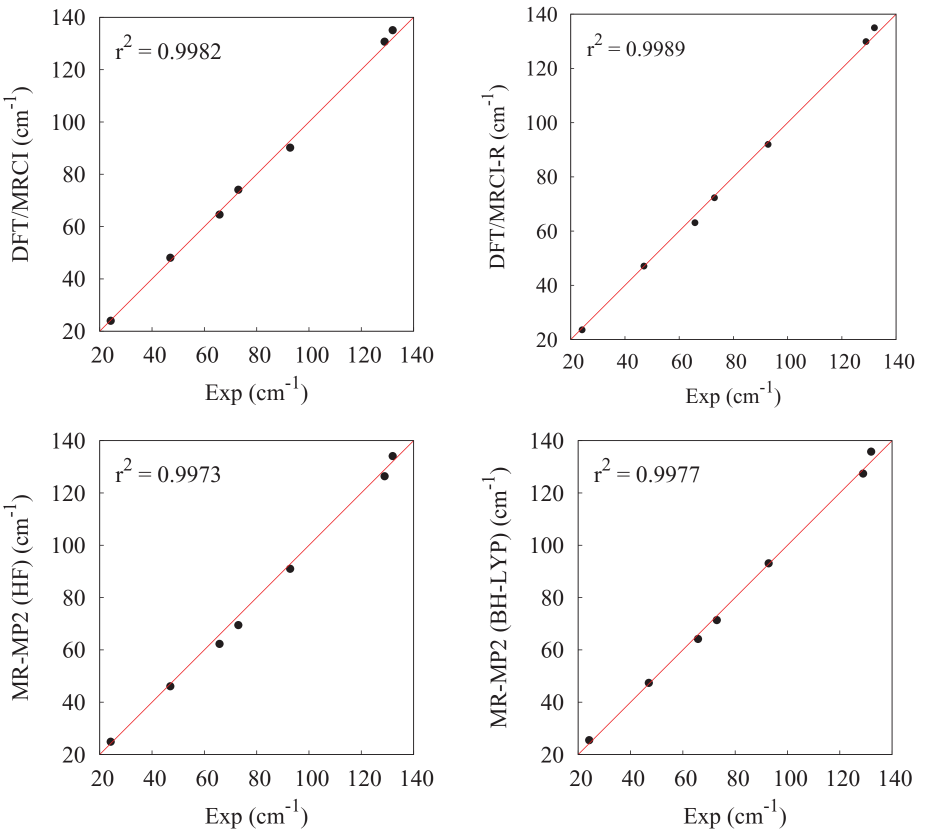

Figure 3. Correlation plots of spin–orbit coupling coefficient $A_{SO}(\mathrm{cm}^{-1})$ for the $1\,^3\Pi$ ($1\,^3\Pi_g$ for P_2) state in selected diatomic molecules, calculated with DFT/MRCI, DFT/MRCI-R, MR-MP2(HF) and MR-MP2(BH-LYP) methods vs. experimental data.

Table 6. Vertical triplet excitation energies ΔE (eV).

Molecule (AO basis)	State	Dominant character	DFT/MRCI	DFT/MRCI-R	MRMP2 (HF)	MRMP2 (BH-LYP)	CASPT2	Experiment
o-Benzyne	1^3B_1	$\pi_{\parallel} \rightarrow \pi^*_{\parallel}$	2.43	2.30	2.25	2.25		
(*valence*)	1^3A_2	$\pi \rightarrow \pi^*_{\parallel}$	3.49	3.44	3.68	3.64		
	1^3B_2	$\pi \rightarrow \pi^*_{\parallel}$	3.88	3.80	4.12	4.10		
	2^3B_1	$\pi \rightarrow \pi^*$	4.18	4.03	3.93	3.82		
	1^3A_1	$\pi \rightarrow \pi^*$	4.83	4.67	4.58	4.46		
	2^3B_2	$\pi_{\parallel} \rightarrow \pi^*$	5.30	5.26	5.38	5.43		
	2^3A_1	$\pi_{\parallel}, \pi \rightarrow \pi^*_{\parallel}, \pi^*$	5.69	6.37	6.27	6.26		
Formaldehyde	1^3A_2	$n \rightarrow \pi^*$	3.23	3.46	3.42	3.46	3.45, 3.56	3.50
(*augmented*)	1^3A_1	$\pi \rightarrow \pi^*$	5.58	5.71	6.13	6.18	6.04, 6.04	5.82, 5.86
	1^3B_2	$n \rightarrow 3s$	6.78	6.75	6.79	6.79	6.65, 6.75	
	2^3B_2	$n \rightarrow 3p_z$	7.67	7.71	7.82	7.86	7.57, 7.65	
	2^3A_1	$n \rightarrow 3p_y$	7.76	7.72	7.90	8.11	7.67, 7.73	
	1^3B_1	$\sigma \rightarrow \pi^*$	8.01	8.23	8.33	8.42	8.36, 8.56	
	2^3A_2	$n \rightarrow 3p_x$	8.32	8.20	8.20	8.23	7.97, 8.03	
Thioformaldehyde	1^3A_2	$n \rightarrow \pi^*$	1.84	1.92	1.81	1.89	1.84	1.80
(*augmented*)	1^3A_1	$\pi \rightarrow \pi^*$	3.29	3.23	3.33	3.37	3.34	
	1^3B_1	$n \rightarrow 4s$	5.54	5.54	5.93	5.85	5.75	
	1^3B_2	$\sigma \rightarrow \pi^*$	6.04	6.12	5.81	5.85	6.24	
	4^3A_2	$\pi, n \rightarrow \pi^{*2}$	7.77	7.28	7.11	7.24	7.19	
Furan	1^3B_1	$\pi \rightarrow \pi^*$	3.74	3.90	4.03	3.97	4.13	4.00, 3.99
(*augmented*)	1^3A_1	$\pi \rightarrow \pi^*$	5.03	5.15	5.15	5.10	5.25	5.20, 5.22
	1^3A_2	$\pi \rightarrow 3s$	5.80	5.83	6.00	5.90	5.93	5.8
	1^3B_2	$\pi \rightarrow 3p_x$	6.27	6.30	6.51	6.44	6.46	
	2^3A_2	$\pi \rightarrow 3p_z$	6.48	6.50	6.84	6.72	6.69	
Thiophene	1^3B_1	$\pi \rightarrow \pi^*$	3.62	3.71	3.73	3.75	3.75	3.75, 3.80
(*augmented*)	1^3A_1	$\pi \rightarrow \pi^*$	4.45	4.50	4.53	4.47	4.59	4.62, 4.70
	1^3B_2	$\pi \rightarrow \sigma^*/4p_x$	5.64	5.71	6.07	6.04	6.11	
	1^3A_2	$\pi \rightarrow 4s$	5.77	5.78	6.09	6.09	6.00	
	2^3A_2	$\pi \rightarrow \sigma^*/4p_x$	5.79	5.86	5.95	5.88	5.99	
	2^3A_1	$\pi \rightarrow \pi^*$	5.88	5.92	5.78	5.70	5.68	
Quinoxaline	1^3B_2	$\pi \rightarrow \pi^*$	3.06	3.02	3.00	2.88		
(*valence*)	1^3B_1	$n \rightarrow \pi^*$	3.16	3.25	2.83	2.74		
	1^3A_1	$\pi \rightarrow \pi^*$	3.70	3.63	3.72	3.59		
	1^3A_2	$n \rightarrow \pi^*$	4.42	4.57	4.32	4.17		
	2^3B_2	$\pi \rightarrow \pi^*$	4.53	4.41	4.22	4.10		
Quinazoline	$1^3A'$	$\pi \rightarrow \pi^*$	3.16	3.13	3.13	2.96		
(*valence*)	$1^3A''$	$n \rightarrow \pi^*$	3.54	3.66	3.16	3.10		
	$2^3A'$	$\pi \rightarrow \pi^*$	4.06	4.00	3.91	3.72		
	$3^3A'$	$\pi \rightarrow \pi^*$	4.38	4.33	4.50	4.27		
	$2^3A''$	$n \rightarrow \pi^*$	4.44	4.58	4.03	3.75		
Pyranthione	1^3A_2	$n \rightarrow \pi^*$	2.05	2.08	2.15	2.16		
(*valence*)	1^3A_1	$\pi \rightarrow \pi^*$	2.28	2.19	2.22	2.19		
	1^3B_1	$\pi \rightarrow \pi^*$	3.70	3.71	3.57	3.49		
	1^3B_2	$n \rightarrow \pi^*$	3.80	3.61	3.94	3.83		
	2^3A_1	$\pi \rightarrow \pi^*$	4.85	4.82	4.74	4.66		
Dithiin	1^3B	$\pi \rightarrow \pi^*$	2.00	2.06	1.86	1.84		
(*valence*)	2^3B	$\pi \rightarrow \pi^*$	3.31	3.40	2.88	2.85		
	1^3A	$\pi \rightarrow \pi^*$	3.75	3.82	3.74	3.68		
	3^3B	$\pi \rightarrow \pi^*$	4.36	4.36	3.91	3.81		
	2^3A	$\pi \rightarrow \pi^*$	4.77	4.88	4.37	4.24		
Bithiophene	1^3B	$\pi \rightarrow \pi^*$	2.78	2.81	2.62	2.44		2.32
(*valence*)	1^3A	$\pi \rightarrow \pi^*$	3.72	3.79	3.50	3.25		
	2^3A	$\pi \rightarrow \pi^*$	4.17	4.22	4.02	3.72		
	2^3B	$\pi \rightarrow \pi^*$	4.21	4.26	3.98	3.71		
	3^3B	$\pi \rightarrow \sigma^*$	5.09	5.14	5.03	4.55		
	3^3A	$\pi \rightarrow \sigma^*$	5.09	5.14	5.35	4.76		
	4^3B	$\pi \rightarrow \pi^*$	5.43	5.49	5.46	4.76		
	4^3A	$\pi \rightarrow \pi^*$	5.45	5.39	5.38	4.92		
Nitromethane	$1^3A'$	$\pi \rightarrow \pi^*$	3.36	3.30	3.54	3.57	3.65	
(*augmented*)	$1^3A''$	$n \rightarrow \pi^*$	3.61	3.72	3.42	3.52	3.66	
	$2^3A''$	$n' \rightarrow \pi^*$	4.01	4.06	3.80	3.93	4.15	
	$2^3A'$	$n, n' \rightarrow \pi^{*2}$	7.31	6.12	8.70	8.79	8.97	
	$3^3A'$	$n \rightarrow 3s$	7.65	7.56	7.50	7.46	7.43	
	$4^3A'$	$n' \rightarrow 3s$	7.91	7.79	7.51	7.57	7.73	

(*Continued*)

Table 6. (*Continued*)

Molecule (AO basis)	State	Dominant character	DFT/MRCI	DFT/MRCI-R	MRMP2 (HF)	MRMP2 (BH-LYP)	CASPT2	Experiment
Nitrobenzene	1^3B_1	$\pi \rightarrow \pi^*$	2.84	2.93	3.35	3.35		
(*valence*)	1^3A_2	$n \rightarrow \pi^*$	3.11	3.26	3.00	3.09		
	1^3A_1	$\pi \rightarrow \pi^*$	3.66	3.65	3.62	3.51		
	1^3B_2	$n' \rightarrow \pi^*$	3.67	3.72	3.63	3.62		
	2^3B_1	$\pi \rightarrow \pi^*$	4.01	4.01	4.34	4.18		
	4^3B_1	$\pi, \pi \rightarrow \pi^*, \pi^*$	5.88					
Dithiosuccinimide	1^3B_1	$n \rightarrow \pi^*$	2.44	2.57	2.42	2.42		2.63
(*valence*)	1^3A_2	$n \rightarrow \pi^*$	2.64	2.77	2.67	2.59		
	1^3B_2	$\pi \rightarrow \pi^*$	2.77	2.84	2.67	2.55		
	1^3A_1	$\pi \rightarrow \pi^*$	3.43	3.51	3.42	3.28		
	2^3B_2	$n, n' \rightarrow \pi^{*2}$	4.60	3.87	5.70	5.29		
	2^3A_1	$n, n' \rightarrow \pi^*, \pi^{*'}$	4.68	3.36	6.67	6.55		
	2^3A_2	$n \rightarrow \pi^*$	4.70	4.60	4.38	4.03		
	2^3B_1	$n \rightarrow \pi^*$	4.87	4.73	4.50	4.14		
Methionine	1^3A	$\pi \rightarrow \sigma^*/Ry$	4.65	4.94	5.62	4.77		
(*valence*)	2^3A	$n_O \rightarrow \pi^*$	5.13	5.46	5.77	5.26		
	3^3A	$\pi \rightarrow \sigma^*/Ry$	5.74	6.00	6.74	5.74		
	4^3A	$\pi_{H-4} \rightarrow \pi^*$	6.06	6.31	7.01	6.24		
Isoalloxazine	$1^3A'$	$\pi \rightarrow \pi^*$	2.31	2.27	2.60	2.29		
(*valence*)	$1^3A''$	$n \rightarrow \pi^*$	2.86	3.01	3.53	2.98		
	$2^3A'$	$\pi \rightarrow \pi^*$	3.12	3.13	3.31	2.84		
	$2^3A''$	$n \rightarrow \pi^*$	3.19	3.28	3.87	3.61		

Table 7. Deviations in vertical excitation energies for polyatomic molecules calculated with DFT/MRCI, DFT/MRCI-R, MR-MP2(HF) and MR-MP2(BH-LYP) with respect to the experimental data (50 excited states; experimental energies used for calculation are given in bold in the Supplementary Materials). The values are given in (eV).

Method	RMSD	Max. (+)	Max. (−)
DFT/MRCI	0.19	0.33	0.46
DFT/MRCI-R	0.17	0.29	0.48
MR-MP2(HF)	0.26	0.53	0.74
MR-MP2(BH-LYP)	0.29	0.44	0.86

General trends. Table 7 contains the RMSD values, maximum positive as well as negative deviations for the complete set of experimentally known excitation energies of electronic states studied in this work. (Please note that the total number of electronic states, for which SOMEs have been determined, is substantially larger.) Very good agreement between the computed and measured excitation energies is observed for all methods (Figure 4). All correlation coefficients are close to 1. As for the diatomic molecules, the semi-empirical DFT/MRCI methods perform slightly better than the MR-MP2 calculations that also show a broader scattering (Table 7). In contrast to our expectations, MR-MP2 is in somewhat better agreement with experiment on the average when HF orbitals are employed instead of BH-LYP KS orbitals.

If the excitation energies of all calculated states are compared among the different computation methods, the correlation deteriorates, of course. Excitation energies for low-lying Rydberg states have been computed for formaldehyde, thioformaldehyde, furan, thiophene, and nitromethane. For some of the singlet states, experimental reference data are available; in the other cases, CASPT2 energies may be used for comparison. Both DFT/MRCI parameterisations and the two MR-MP2 variants show very good agreement with the reference data. In general, the agreement for the valence-excited states is satisfactory, but in a few cases, larger deviations are recognised (Figure 5). Inspection of Tables 5 and 6 reveals that the deviations between the two DFT/MRCI parameterisations are all related to doubly excited states of one type or the other. These cases will be analysed in the following on an individual basis. Furthermore, we will address some cases where the different energy splittings between states of equal symmetry in MR-MP2, as compared to DFT/MRCI, result in different wave function compositions, which in turn lead to deviations of the corresponding SOMEs.

Special cases.

Formaldehyde. Being the smallest of the polyatomic molecules, formaldehyde represents the least demanding system for the MR-MP2 methods with regard to the size of the reference space and the first-order space selection threshold. The energy contribution arising from discarded configurations of the first-order space is less than one percent of the total correlation energy, making the results for formaldehyde nearly converged with respect to the selection procedures in the MR-MP2 approach. CASSCF/CASPT2 calculations were carried out for two different active

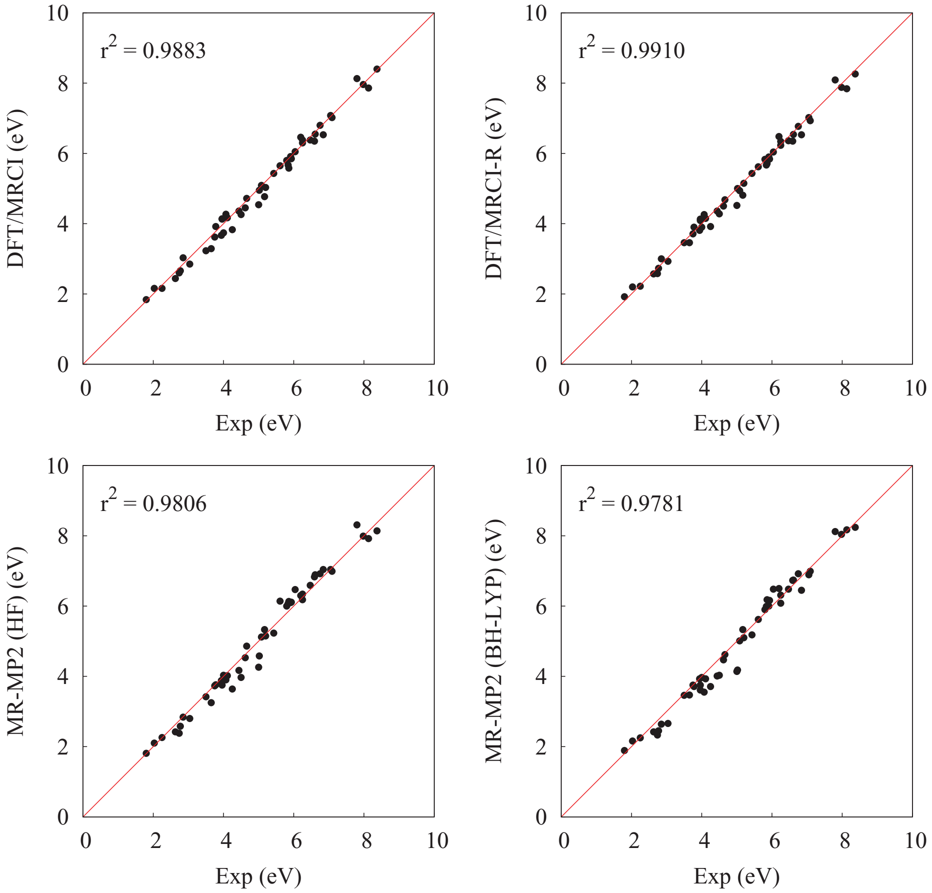

Figure 4. Correlation plots of excitation energies for all polyatomic molecules calculated with DFT/MRCI, DFT/MRCI-R, MR-MP2(HF) and MR-MP2(BH-LYP) methods vs. experimental band maxima.

spaces. The first active space where eight electrons were distributed in nine active orbitals comprised two σ MOs, the valence π and π^* MOs, the n orbital and the Rydberg 3s and 3p orbitals; in the larger (8,11) calculations, two σ^* MOs were added to the active space. The level shift of 0.2 that was used for CASPT2(8,9) had to be increased to 0.3 in the CASPT2(8,11) calculations due to problems with intruder states. In addition to our CASPT2 results, high-level *ab initio* values are available from the literature for comparison [34–37,59].

For all methods, the calculated excitation energies of the 1^1A_2 state (Table 5) are in good agreement with the experimentally observed energies of 3.79 [60] and 3.94 eV [61], respectively, for the energy-loss maximum

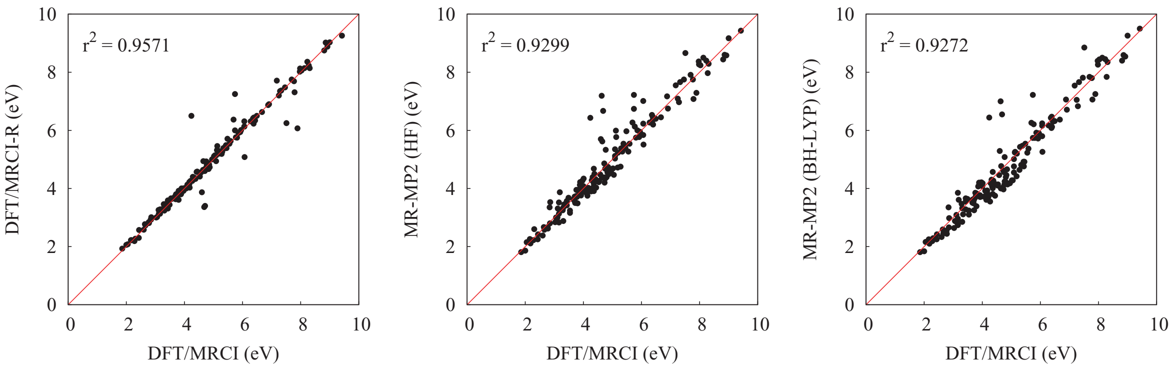

Figure 5. Correlation plots of excitation energies for all polyatomic molecules calculated with DFT/MRCI-R, MR-MP2(HF) and MR-MP2(BH-LYP) methods vs. excitation energies calculated with DFT/MRCI.

(vapour) of the $1^1\mathrm{A}_2$ state. Equally good correspondence (Table 6) with the experimentally measured value of 3.50 eV [60,61] is found for the first triplet state, $1^3\mathrm{A}_2$. The excitation energy of the $1^3\mathrm{A}_1$ $(\pi\pi^*)$ state is somewhat underestimated by the DFT/MRCI methods, whereas the results for the MR-MP2(HF) and MR-MP2(BH-LYP) are a bit higher than the energy-loss maximum at 5.82 eV [60] or 5.86 eV [61]. All methods find the Rydberg $n \rightarrow 3s_\mathrm{C}$ and $n \rightarrow 3p_\mathrm{C}$ excitations in good agreement with experimental data [62]. The DFT/MRCI and MR-MP2 approaches predict similar energies for the valence $4^1\mathrm{A}_1$ $(\pi\pi^*)$ state ($5^1\mathrm{A}_1$ in DFT/MRCI-R) which is experimentally not observed, but suspected to lie in the Rydberg region between 7 and 12 eV [60,61]. Nevertheless, there is one peculiarity with regard to the wave function of that state that gives rise to two outliers when correlating the SOMEs of the DFT/MRCI and DFT/MRCI-R methods. We recognise a pronounced weight of a doubly excited closed-shell configuration $(n^2 \rightarrow \pi^{*2})$ in the DFT/MRCI-R wave function which is not seen among the leading configurations of the DFT/MRCI and MR-MP2 wave functions (Tables S11 and S12 of the SM). The state with leading $(n^2 \rightarrow \pi^{*2})$ term shows up at 9.2 eV in DFT/MRCI-R, whereas DFT/MRCI and both MR-MP2 variants places it at markedly higher excitation energies. The CASSCF/CASPT2 results for the smaller (8,9) active space support the order found by the DFT/MRCI and MR-MP2 methods. The $(n^2 \rightarrow \pi^{*2})$ double excitation exhibits only a small coefficient in the CASSCF (8,9) wavefunction, and an optically very bright $\pi\pi^*$ state is obtained with an excitation energy of 9.33 eV after PT2 correction. The state with leading $(n^2 \rightarrow \pi^{*2})$ configuration is found at 10.29 eV in these calculations. Literature values of the vertical $4^1\mathrm{A}_1$ $(\pi\pi^*)$ excitation energies range between 9.47 eV for EOM-CCSD [35] over 9.77 eV for CASPT2 [37] and 9.80 for MR-CISD+Q [34] to 10.15 eV for MR-CISD [34]. For the doubly excited $n^2 \rightarrow \pi^{*2}$ state, MR-CISD(+Q) results are available for comparison [34] that place this state at 10.63 eV (10.54 eV). All these data point toward a problem of the redesigned DFT/MRCI-R in properly describing this closed-shell double excitation of type $(n^2 \rightarrow \pi^{*2})$. The mixture of these high-lying singly and doubly excited configurations is also an issue in the CASSCF/CASPT2 calculations. In the larger active space (8,11) that was primarily chosen to improve the description of the $(\sigma \rightarrow \pi^*)$ excitations, strong configuration interaction of the A_1 symmetric $(\pi \rightarrow \pi^*)$, $(n^2 \rightarrow \pi^{*2})$, and $(\pi \rightarrow 3p_x)$ excitations takes place leading to a substantially higher excitation energies for these states than the CASPT2(8,9) treatment (see Tables S10 and S12 in the SM).

Thioformaldehyde. Substitution of oxygen in formaldehyde by sulphur to obtain thioformaldehyde additionally lowers the energy of the zero-open shell doubly excited $^1\mathrm{A}_1$ state $(n_H^2 \rightarrow \pi_L^{*2})$. The effect is very pronounced in the case of the DFT/MRCI-R Hamiltonian which brings this state below the $^1\mathrm{A}_1$ $(\pi_{H-1} \rightarrow \pi_L^*)$ state and quite close to it (Table 5). The energetic proximity results in strong wave function mixing so that the $^1\mathrm{A}_1$ state with leading (54%) $(\pi_{H-1} \rightarrow \pi_L^*)$ term exhibits major contributions (22%) from the $(n_H^2 \rightarrow \pi_L^{*2})$ double excitation. In addition, contributions from the nearby $(n_H \rightarrow 4p_x)$ excitation are found in the wave function (Table S19 in the SM). In contrast, the admixture is quite small for the standard DFT/MRCI with minor configurations contributing by only 2% (Table S18 in the SM). All methods slightly overestimate the vertical energy of the bright $(\pi_{H-1} \rightarrow \pi_L^*)$ state of thioformaldehyde. With a value of 6.30 eV, MR-MP2(HF) is closest to the CASPT2 (8,11) value of 6.29 eV and the experimentally measured peak maximum which is located at 6.2 eV [63]. No experimental reference data are available for the doubly excited $^1\mathrm{A}_1$ state with leading $(n_H^2 \rightarrow \pi_L^{*2})$ term. The original DFT/MRCI parameterisation places this state about 0.7 eV above the CASPT2 value, whereas DFT/MRCI-R places it about 1 eV below the CASPT2 reference. The MR-MP2 methods yield energies in good agreement with CASPT2. Notice, however, that the CASSCF wave function shows configuration mixings very similar to the DFT/MRCI-R Hamiltonian (Table S19 in the SM).

We find also a pronounced difference for the excitation energy of another pair of dark states which are doubly excited with respect to the electronic ground state. The $(\pi_{H-1}^1 n_H^1 \pi_L^{*2})$ occupation gives rise to a singlet and a triplet state of A_2 spatial symmetry, $3^1\mathrm{A}_2$ and $4^3\mathrm{A}_2$. The energy of the $3^1\mathrm{A}_2$ state (7.19 eV) is markedly lower for the standard DFT/MRCI method than for all other methods employed (see Table 5). Since it is also substantially lower than the energy of the corresponding $4^3\mathrm{A}_2$ state, we consider this to be a problem of the original DFT/MRCI parameterisation. The energy shift of that configuration has almost no consequence with regard to the SOMEs, however, as there is no close-lying state of equal symmetry with which the wave function could mix.

o-Benzyne. The $2^1\mathrm{A}_1$ state of o-benzyne is dominated by a configuration with four open shells which arises from an excitation of the in-plane $\pi_\parallel$ orbital and the highest occupied out-of-plane π_H orbital to the corresponding antibonding $\pi_\parallel^*$ and π_{L+1}^* orbitals. In the standard DFT/MRCI calculations, it is located at 4.24 eV. A hint that there might be something wrong comes from the fact that the lowest triplet state with the same leading configuration appears at 5.69 eV. The other methods place this doubly excited $^1\mathrm{A}_1$ state more than 2 eV higher in energy (Table 5) while the corresponding triplet is shifted upwards by about 0.7 eV (Table 6). In all cases except for DFT/MRCI, it is located well below the respective singlet state. The reason for the problems of the standard DFT/MRCI method in describing doubly excited states with four open shells properly has been traced back to the parameterisation of the effective Hamiltonian [16]. In particular, the parameter that scales the exchange contributions to the diagonal elements depends strongly on the excitation class, the number of open shells, and the multiplicity [1]. Also for the second low-lying singlet state with four open shells, $2^1B_1\,(\pi_{\parallel}^1\pi_{H-1}^1\pi_{\parallel}^{*\,1}\pi_{L+1}^{*\,1})$, good agreement among the DFT/MRCI-R (7.25 eV) and the MR-MP2 methods (both 7.22 eV) is observed, whereas the standard DFT/MRCI value is substantially smaller (5.74 eV).

Nitrobenzene. The questionable description of doubly excited singlet and triplet states with four open shells by the DFT/MRCI method as manifested, for example, in large negative singlet–triplet energy splittings, actually was the reason why we started looking for an alternative method to compute SOMEs of nitrobenzene. Double excitations with four open shells play an important role even in low-lying excited states of this molecule. The standard DFT/MRCI parameterisation associates with them too low energies, and as a consequence, too high contributions in the state vector [17]. Our calculated singlet excitation energies of nitrobenzene can be compared with experimental data for an $(n \rightarrow \pi^*)$ transition and an optically bright $(\pi \rightarrow \pi^*)$ transition. In addition, high-level CASPT2 (14,11) excitation energies are available in the literature for comparison [38]. As a general trend, all methods employed in this work place the singlet states at too low excitation energies. Particularly problematic is the description of the B_1 states in the standard DFT/MRCI, where a configuration with spatial occupation $(\pi_{H-2}^1\pi_H^1\pi_L^{*\,1}\pi_{L+1}^{*\,1})$ dominates the wave function of the lowest $^1B_1$ state. The electron density in the π_{H-2} and π_L^* MOs of nitrobenzene is mainly localised on the NO_2 group, whereas π_H and π_{L+1}^* are pure benzene MOs (see Figure S6 in the SM). In this way, nitrobenzene exhibits a tendency towards a bi-chromophoric system for which the redesigned DFT/MRCI-R method [16] was developed. In the DFT/MRCI-R wave function, the two CSFs associated with this configuration contribute only with about 0.1% each. The MR-MP2 wave functions have this configuration contributing by less than 2%. The next DFT/MRCI vector (2^1B_1) has, as a dominant, the four open-shell configurations (33%). Its excitation energy of 4.63 eV is much lower than that of the corresponding triplet state (4^3B_1) which is found at 5.88 eV. For that reason, the DFT/MRCI description of the 2^1B_1 state is regarded as being unphysical. The MR-MP2 methods place the singlet state with leading $(\pi_{H-2}^1\pi_H^1\pi_L^{*\,1}\pi_{L+1}^{*\,1})$ configuration at 7.19 eV (MR-MP2(HF)) and 7.00 eV (MR-MP2(BH-LYP)). In the DFT/MRCI-R calculation, a state of that type does not appear among the five lowest roots of $^1B_1$ symmetry. Its energy must, therefore, be higher than that of 5^1B_1, i.e. >7.3 eV.

Dithiosuccinimide. DFT/MRCI-R finds a low-lying pair of A_1 states (1^3A_1 at 3.36 eV and 2^1A_1 at 3.40 eV) with a leading configuration that corresponds to a double excitation from the in-plane lone-pair orbitals on sulphur, i.e. n_{H-1} in the a_1 irreducible representation (irrep) and n_H in the b_2 irrep, to π_L^* and π_{L+1}^* which correspond to the a_2 symmetric (π_L^*) and b_1 symmetric (π_{L+1}^*) linear combination of the antibonding thiocarbonyl π^* orbitals. In addition, π_{L+1}^* exhibits contributions from nitrogen $p_\perp$. The standard DFT/MRCI places these states with leading $n_{H-1}^1 n_H^1 \pi_L^{*\,1}\pi_{L+1}^{*\,1}$ term at 4.68 eV (2^3A_1) and 4.71 eV (2^1A_1), about 1.3 eV higher in energy. Since the parameters of the redesigned DFT/MRCI-R Hamiltonian are spin independent, we carried out a calculation for the lowest quintet states, too. Not surprisingly, we find a state with leading $n_{H-1}^1 n_H^1 \pi_L^{*\,1}\pi_{L+1}^{*\,1}$ configuration as the 1^5A_1 state with an excitation energy of 3.24 eV. This means, that the 1^5A_1, 1^3A_1, and 2^1A_1 states of dithiosuccinimide, as obtained from DFT/MRCI-R calculations, originate from a rather loosely coupled pair of $^3(n \rightarrow \pi^*)$ excitations. While the multiplet splitting appears to be of similar size in the DFT/MRCI Hamiltonians, the Coulomb repulsion between the pairs is substantially larger in the original DFT/MRCI case. MR-MP2(HF) puts the corresponding triplet at 6.67 eV (4^3A_1) and the quintet at 6.47 (1^5A_1). In the singlet manifold, a state with such electronic structure is not found among the lowest six states of A_1 symmetry. We, therefore, performed an additional MR-MP2(HF) calculation where we solved for 10 roots in A_1 symmetry. In that calculation, the desired singlet-coupled wave function is found for the 5^1A_1 state with an energy of 6.37 eV. At present, it is not clear whether the DFT/MRCI methods, and in particular the redesigned DFT/MRCI-R method, have problems with a balanced description of this particular $(n, n' \rightarrow \pi^*\pi'^*)$ double excitation in dithiosuccinimide or whether the true problem lies rather in the truncation of the MR-MP2 first-order space.

Also, the 3^1A_1 state of the DFT/MRCI-R at 5.08 eV stems from a double excitation, in this case with two leading closed-shell configurations, i.e. $n_H^2\pi_L^{*\,2}$ and $n_{H-1}^2\pi_L^{*\,2}$. MR-MP2(BH-LYP) finds this state as 4^1A_1 at 5.26 eV, MR-MP2(HF) at 5.51 eV (MR-MP2(HF) with ten roots in $^1A_1$ symmetry yields 5.26 eV), whereas it is the fifth root of $^1A_1$ symmetry in the DFT/MRCI calculation with an energy of 6.07 eV. This finding is consistent with the observations made for $n^2 \rightarrow \pi^{*\,2}$ double excitations in formaldehyde and thioformaldehyde. The second pair of

A_2 states, 2^3A_2 and 2^1A_2, should be uncritical as their wave functions are primarily made up from single excitations with $n_H^1\pi_{L+1}^{*1}$ as the leading term. Their energies agree well among the DFT/MRCI and DFT/MRCI-R methods (Table 5 and 6). In this case, the MR-MP2 methods add stronger contributions from doubly excited configurations involving the π_{H-2} orbital (the b_1 symmetric combination of the bonding thiocarbonyl π orbitals) and one of the n orbitals. This brings their energy further down. While the MR-MP2 (HF) energies are in reasonable agreement with the DFT/MRCI results, MR-MP2 (BH-LYP) places these states at much lower energies. A similar observation is made for the second pair of B_1 states, 2^3B_1 and 2^1B_1 (see Tables S52 and S53 of the SM) which has a similar composition as the just described 2^3A_2 and 2^1A_2 states. In B_2 symmetry, we observe a triplet state, 2^3B_2 in DFT/MRCI and 3^3B_2 in MR-MP2, with a very large spread of excitation energies, ranging from 3.87 eV in DFT/MRCI-R over 4.60 eV in DFT/MRCI, 5.29 eV in MR-MP2 (BH-LYP) to 5.70 eV in MR-MP2(HF). Its leading configuration is a double excitation $n_{H-1}^1 n_H^1\pi_L^{*2}$ with two open shells, but again two n electrons are transferred to π shells.

Nitromethane. We performed CASSCF/CASPT2 calculations with various active spaces for this compound in the augmented basis. Unfortunately, we were not able to find an active space yielding a balanced description of the $\pi \rightarrow \pi^*$ and Rydberg transitions. Attempts to use a large active spaces, for example (12,11), were unsuccessful because the state-averaged CASPT2 calculations did not converge. The results presented here are for the (8,7) active space which comprise 2 π and 2 n orbitals, 1 π^* and 1 σ^* MO as well as a 3s orbital. The fact that the $n \rightarrow 3s$ excitations are stabilised so strongly by the CASPT2 corrections is caused by a mixture of 3s and σ^* character in the active orbitals. All methods, in particularly the MR-MP2 methods, predict too low energies for the first two singlet states of nitromethane (Table 5). The DFT/MRCI-R and CASPT2 excitation energies of these states are practically identical. Both states are of $n\pi^*$ character and A'' symmetry, with the electron energy-loss maximum of $1^1A''$ being measured at 4.25 eV in the gas phase and the absorption maximum of $2^1A''$ at 4.50 eV in the gas phase [64]. When Rydberg functions are not included in the basis set (Table S42 in the SM), the excitation energy of the first $\pi\pi^*$ singlet state ($2^1A'$) is overestimated, again in larger measure by the MR-MP2 method. Augmentation of the basis by diffuse functions brings the excitation energy of this state down for all methods and in good agreement with the expeirmental value of 6.25 eV [64] obtained as the maximum of absorption in the gas phase. In the triplet manifold, we observe one state that attracts our special attention. The leading term of the $2^3A'$ state is a double excitation with two open shells: from each of the in-plane n and n' orbitals of the nitro group, one electron is excited to the lowest lying π^* MO. The results of the MR-MP2 calculations agree well with the CASPT2 excitation energy, whereas DFT/MRCI and in particular DFT/MRCI-R places this double excitation at significantly lower energies.

Furan and thiophene. CASSCF/CASPT2 calculations of furan distributed six active electrons in nine active orbitals comprising five valence MOs (3 π, 2 π^*) and the 3s and 3p orbitals. For thiophene, one σ^* orbital was added to the active space. Very good consensus is achieved among the theoretical methods for furan and the agreement with the available experimental data is good. We, therefore, refrain from discussing this compound further. In thiophene, similar conclusions can be drawn with regard to the $^{1,3}(\pi \rightarrow \pi^*)$ excited states which are found in the A_1 and B_1 irreducible representations for our choice of coordinate system. There is one exception though. MR-MP2(HF) yields an excitation energy of 6.14 eV in the augmented basis while a value of 5.75 eV was obtained in the valence basis. In contrast, DFT/MRCI, DFT/MRCI-R, and MR-MP2(BH-LYP) excitation energies are lowered by about 0.15 eV upon adding diffuse functions to the basis set which brings them into excellent agreement with the experimental value of 5.61 eV determined by electron energy-loss spectroscopy [65]. The wave functions show some mixing with ($\pi \rightarrow 4p_y$) excitations, with the diffuseness increasing from DFT/MRCI over MR-MP2(BH-LYP) to MR-MP2(HF). Although barely visible from the wave function composition (Table S30 in the SM), the MR-MP2(HF) state must be considered significantly more Rydberg-like than the wave functions obtained by the other methods. To understand the trends observed for the SOMEs (see below), it is important to notice also that the 1^1B_2, 1^3B_2, 1^1A_2, and 2^3A_2 states are mixtures of ($\pi \rightarrow \sigma^*$) and ($\pi \rightarrow 4p_x$) excitations, with the DFT/MRCI and DFT/MRCI-R wave functions being more valence-like than their MR-MP2(HF), MR-MP2(BHLYP), and CASSCF counterparts. Furthermore, we note that the wave function composition of the 3^1A_1 differs dramatically between the DFT/MRCI and MR-MP2 methods in the augmented basis sets (Tables S30 and S31 in the SM), although the energy is nearly the same for all methods and in good agreement with the experimental value.

Quinoxaline and quinazoline. For these two naphthalene analogues, we observe a general trend that the MR-MP2(HF) singlet excitation energies are markedly lower than their DFT/MRCI counterparts (Table 5). The difference is even more pronounced for MR-MP2(BH-LYP). There is one exception from this trend, namely for the 1^1B_2 state of quinoxaline and the $3^1A'$ state of quinazoline. Both transitions are dominated by $(\pi_H \rightarrow \pi_L^*)$ excitations, thus representing L_a states. In quinoxaline, the L_b state which is characterised by a nearly equal mixture of $(\pi_{H-1} \rightarrow \pi_L^*)$ and $(\pi_H \rightarrow \pi_{L+1}^*)$ excitations can be identified unambiguously with the 2^1A_1 state, whereas the assignment to the $3^1A'$ state of quinazoline is not so clear-cut because of the lower symmetry of that compound. The reasons underlying these differences are not obvious. One might guess that the first-order interacting spaces in the MR-MP2 calculations were too small and that the PT2 corrections overshooted. In a previous work, DFT/MRCI has been shown to perform very well for the L_a and L_b states of polyacenes [66]. We, therefore, consider the DFT/MRCI energies trustworthy. As the energy shifts do not lead to substantial variations of the wave function composition, they do not have consequences with regard to the SOMEs.

Dithiin. All MR-MP2 excitation energies of dithiin are lower compared to the experimentally observed absorption maxima in dichloromethane. The measured transitions are at 2.74 eV ($\pi\pi^*$, 1^1B), 4.44 eV ($\pi\pi^*$, 2^1A) and 5.00 eV ($\pi\pi^*$, 2^1B) [67], while MR-MP2 places them at 2.38 eV and 2.33 eV (1^1B), 4.17 eV and 4.01 eV (2^1A), 4.26 eV and 4.14 eV (2^1B) on the basis of HF and KS MOs, respectively. The DFT/MRCI and DFT/MRCI-R values are closer to the experimental ones (Table 5). As a general trend, all DFT/MRCI excitation energies of this compound are higher than the MR-MP2 ones and the maximal negative deviations are 0.53 and 0.76 eV for the MR-MP2(HF) and MR-MP2(BH-LYP), respectively. With respect to the forthcoming analysis of the SOMEs, it is important to note that the energetic separation of the second and third $^3B_1$ states that are dominated by linear combinations of $(\pi \rightarrow \pi^*)$ and $(\pi \rightarrow \sigma^*)$ excitations is much smaller in the MR-MP2 calculations compared to the DFT/MRCI methods. The same is true for the second and third $^3A_1$ states. Remarkably, DFT/MRCI and DFT/MRCI-R yield very similar excitation energies for the doubly excited 3^1A_1 state. The leading term in the wave function of this state originates from the closed-shell $(\pi_H^2 \rightarrow \pi_L^{*2})$ excitation.

Bithiophene. The electronic structure of s-*trans* bithiophene has already been treated in our laboratory using the DFT/MRCI method [68]. Since the same basis and geometry have been used, the vertical excitation energies of S_1, S_2, T_1, T_2, T_3 and T_4 differ only marginally to the ones presented here due to a different choice of reference space. In the present study, higher lying states are added among which the $\pi\sigma^*$ ones (3^3B and 3^3A) are especially interesting, because of their strong SO interaction with the lower $\pi\pi^*$ states. The S_1 and T_1 energies of 3.86 and 2.32 eV, respectively, determined by Siegert et al. [68] in anion photodetachment studies in a jet stream, are 0-0 energies which are close to the adiabatic DFT/MRCI energies as shown by these authors. The computed vertical DFT/MRCI energy of 1^1B is in better agreement with the experimentally measured absorption maxima in apolar solvents (4.09 eV in dioxane, 4.11 eV in methylcyclohexane) [69]. There is a second, less intensive peak at 5.02 eV in the absorption spectrum in dioxane which can be assigned to the 2^1B state of bithiophene with corresponding DFT/MRCI energy of 4.95 eV. In order to include both linear combinations of the lone-pair n(S) orbitals, the 12-12-2 space was used in the first iteration. This is of importance only for the MR-MP2 method, since the DFT/MRCI results are not significantly different compared to the calculation with the initial 10-10-2 RAS. The MR-MP2 energies of S_1 are slightly lower than the DFT/MRCI values but all agree well with the experimental 1^1B absorption energy (Table 5). In contrast, the 2^1B MR-MP2 energies are significantly lower than the experimentally determined and the DFT/MRCI energies, especially when BH-LYP orbitals are employed. It appears that the first-order interacting space is too small in this case and that the PT2 corrections of the discarded configurations overshoot. Lowering the selection threshold for the inclusion of configurations in the first-order perturbed wave function to 5×10^{-9} E_h increases the MR-MP2(BH-LYP) energy of 2^1B to 4.29 eV. A further decrease of the threshold to test whether the results are converged was technically not feasible.

Methionine. To the best of our knowledge, there are no experimental data of excitation energies of methionine which could be used for comparison with our vertical energies. DFT/MRCI-R energies are consistently higher than the DFT/MRCI ones by about 0.2–0.3 eV. The striking result for methionine is the huge variation of the MR-MP2 energies regarding the employed type of MOs. MR-MP2(HF) energies are much higher than MR-MP2(BH-LYP), with the difference reaching 1 eV for the 3^3A state. On the other hand, MR-MP2(BH-LYP) excitation energies are very close to the DFT/MRCI values. Examination of the HF and BH-LYP MOs confirms that virtual orbitals obtained by HF and DFT procedure differ by such an extent that it is difficult to make a correspondence between them. This, of course, also leads to a quite different MR-MP2(HF) and MR-MP2(BH-LYP) state vectors (see Table S55, SM).

Isoalloxazine. Isoalloxazine is the photosensitive core of the flavin family of chromophores. They play an important role in blue-light sensing proteins. It is a heteroaromatic compound with four of its six heteroatoms carrying lone-pair orbitals. The photophysics of this chromophore is determined by the coupling between optically dark $n\pi^*$ and bright $\pi\pi^*$ states and their subtle interactions with the environment. The only available experimental data for comparison are absorption spectra of flavin derivatives in solution. 8-Methyl isoalloxazine in ethanol absorbs with peak maxima at 2.85 eV ($2^1A'$, $\pi\pi^*$) and 3.76 eV ($3^1A'$, $\pi\pi^*$) [70]. Theoretical studies on flavins in various solvent environments point out the small solvatochromicity of the first band (stabilisation with regard to vacuum by 0.06 eV in methanol) and a more pronounced red shift of the second maximum with increasing solvent polarity (stabilisation by 0.21 eV) [12]. Thus, the DFT/MRCI and DFT/MRCI-R vertical excitation energies of the first two $\pi\pi^*$ states (Table 5) are considered to be in good agreement with experimental evidences. No experimental data are available for the $n\pi^*$ states. For these states, we notice that the DFT/MRCI-R energies are systematically higher by approximately 0.1 eV. This finding is in line with the general trend for the DFT/MRCI-R energies of $n\pi^*$ states observed by Lyskov et al. [16]

Isoalloxazine is a challenging molecule for MR-MP2. The method, as implemented in the MRCI program, is at its limits here, since the code is not parallelised and allows only for a maximum number of 1000 reference configurations. The latter restriction is severe, because of the large number of active orbitals in isoalloxazine. The computed MR-MP2 excitation energies of isoalloxazine are strongly dependent on the selection threshold, the choice of reference space, and the employed orbital basis, with MR-MP2(HF) being more consistent with the experimental findings. Setting the selection threshold (Esel) for the inclusion of configurations in the first-order space to the standard value of 10^{-7} E_h leads to energy contributions from the discarded configurations of up to 45% of the total correlation energy in the case of isoalloxazine, while this contribution is lower than 20% for the other molecules (with exception of methionine). Unfortunately, a lowering of the Esel parameter is technically not feasible for the triplet multiplicity because of the large number of CSFs already needed for Esel $= 10^{-7}$ E_h. In the singlet manifold, the expansion length of the first-order perturbed wave function increases from 122,474,081 CSFs for 10^{-7} E_h to 348,025,394 CSFs for 10^{-8} E_h. Test calculations for the singlet states with Esel $= 10^{-8}$ E_h revealed that the excitation energies of the $n\pi^*$ states are lowered by up to 0.5 eV in comparison with the standard MR-MP2 calculations.

3.3.2. Spin–orbit coupling matrix elements

Since there are no experimental data which could be used to judge the quality of our SOMEs for polyatomic molecules, we adopted here the following approach. The matrix elements of the redesigned DFT/MRCI-R and this particular implementation of the MR-MP2 method are presented here for the first time. The standard DFT/MRCI has been successfully used in a number of studies on photophysical and photochemical processes such as intersystem crossing and phosphorescence that depend indirectly on the spin–orbit coupling between the involved states. Absolute values of the calculated SOMEs of all polyatomic molecules are compiled in Table 8. In addition, SOMEs calculated for CASSCF wave functions of formaldehyde, thioformaldehyde, furan, thiophene, and nitromethane in the *augmented* basis, as well as literature data on formaldehyde [59], have been used for comparison. The phase factors of the SOMEs have been omitted because they depend on the arbitrary phases of the underlying wave functions and MOs. They are relevant only when second-order spin-dependent properties such as phosphorescence probabilities are to be determined [13,57].

General trends. In order to examine whether the DFT/MRCI-R and the first-order MR-MP2 wave functions provide a reasonable description of the spin–orbit interaction, we have correlated the SOMEs obtained with these methods to the ones calculated with DFT/MRCI. The plots showing this correlation for all SOMEs of polyatomic molecules are presented in Figure 6. Correlation plots for the individual molecules as well as the wave function compositions of the involved states are provided in the SM together with statistical data for each molecule individually and for the complete set of selected SOMEs, 278 in total. Absolute values have been employed when computing the maximum positive and negative deviations of the SOMEs. Normalised RMSD (NRMSD), expressed as percentage, are given as the RMSD normalised by the range, i.e. the maximum value minus the minimum absolute value of the evaluated data.

Excellent agreement is observed between the SOMEs computed with the DFT/MRCI and DFT/MRCI-R wave functions, respectively, with two pairs of outliers that spoil the otherwise good correlation (Figure S1 of the SM). The outliers are associated with high-lying states of formaldehyde and thioformaldehyde, respectively. Their origin will be discussed in more detail below. The SOMEs obtained for the first-order MR-MP2 wave functions show larger scattering that is even increased when Rydberg functions are added to the AO basis. At first sight, there is not much difference to be found whether HF (Figure S2 of the SM) or KS orbitals (Figure S3 of the SM) have been employed. In these cases, the largest outliers are found for dithiin, bithiophene, and isoalloxazine.

Special cases. *Formaldehyde*. SOMEs have been calculated for the CASSCF(8,9) and CASSCF (8,11) wave

Table 8. Spin–orbit matrix elements (cm^{-1}).

Molecule (AO basis)	SOME	DFT/MRCI	DFT/MRCI-R	MRMP2 (HF)	MRMP2 (BH-LYP)	CASSCF
o-benzyne (*valence*)	$\langle 1^3A_2\|\hat{\mathcal{H}}_{\mathrm{SO\,z}}\|1^1A_1\rangle$	1.9	1.9	1.5	1.7	
	$\langle 1^3B_1\|\hat{\mathcal{H}}_{\mathrm{SO\,y}}\|1^1A_1\rangle$	4.3	4.3	4.1	4.4	
	$\langle 2^3B_2\|\hat{\mathcal{H}}_{\mathrm{SO\,x}}\|1^1A_1\rangle$	7.2	7.2	6.9	6.9	
	$\langle 1^3B_1\|\hat{\mathcal{H}}_{\mathrm{SO\,x}}\|1^1A_2\rangle$	3.5	3.6	3.2	3.3	
	$\langle 1^3A_1\|\hat{\mathcal{H}}_{\mathrm{SO\,y}}\|1^1B_1\rangle$	0.2	0.1	0.1	0.1	
	$\langle 1^3A_2\|\hat{\mathcal{H}}_{\mathrm{SO\,x}}\|1^1B_1\rangle$	6.7	6.5	7.8	7.5	
	$\langle 1^3A_1\|\hat{\mathcal{H}}_{\mathrm{SO\,x}}\|2^1B_2\rangle$	3.1	3.0	3.0	2.9	
	$\langle 1^3B_1\|\hat{\mathcal{H}}_{\mathrm{SO\,z}}\|1^1B_2\rangle$	2.8	2.6	2.4	2.6	
	$\langle 2^3B_1\|\hat{\mathcal{H}}_{\mathrm{SO\,y}}\|1^3A_1\rangle$	0.2	0.0	0.2	0.2	
	$\langle 1^3B_1\|\hat{\mathcal{H}}_{\mathrm{SO\,x}}\|1^3A_2\rangle$	4.4	4.4	4.2	4.4	
	$\langle 1^3B_2\|\hat{\mathcal{H}}_{\mathrm{SO\,z}}\|1^3B_1\rangle$	2.5	2.4	2.3	2.3	
Formaldehyde (*augmented*)	$\langle 1^3A_2\|\hat{\mathcal{H}}_{\mathrm{SO\,z}}\|1^1A_1\rangle$	62.0	60.2	65.0	65.0	69.2
	$\langle 1^3A_2\|\hat{\mathcal{H}}_{\mathrm{SO\,z}}\|4^1A_1\rangle$	32.1	57.2	29.0	23.8	21.8
	$\langle 1^3A_2\|\hat{\mathcal{H}}_{\mathrm{SO\,z}}\|5^1A_1\rangle$	55.0	31.5	54.1	56.5	31.6
	$\langle 1^3B_1\|\hat{\mathcal{H}}_{\mathrm{SO\,y}}\|1^1A_1\rangle$	43.1	42.0	45.3	45.4	46.5
	$\langle 1^3B_1\|\hat{\mathcal{H}}_{\mathrm{SO\,y}}\|4^1A_1\rangle$	18.7	16.7	17.8	17.9	17.5
	$\langle 1^3A_1\|\hat{\mathcal{H}}_{\mathrm{SO\,z}}\|1^1A_2\rangle$	52.8	52.4	56.9	57.0	57.1
	$\langle 1^3B_1\|\hat{\mathcal{H}}_{\mathrm{SO\,x}}\|1^1A_2\rangle$	36.2	36.2	37.6	37.5	38.8
	$\langle 1^3A_1\|\hat{\mathcal{H}}_{\mathrm{SO\,y}}\|1^1B_1\rangle$	30.2	30.6	31.7	32.5	33.0
	$\langle 1^3A_2\|\hat{\mathcal{H}}_{\mathrm{SO\,x}}\|1^1B_1\rangle$	35.7	35.7	36.8	36.8	37.4
	$\langle 1^3B_2\|\hat{\mathcal{H}}_{\mathrm{SO\,x}}\|1^1A_1\rangle$	6.4	6.3	5.5	5.8	6.6
	$\langle 1^3B_2\|\hat{\mathcal{H}}_{\mathrm{SO\,x}}\|4^1A_1\rangle$	1.1	1.3	1.0	0.9	3.0
	$\langle 1^3B_2\|\hat{\mathcal{H}}_{\mathrm{SO\,y}}\|1^1A_2\rangle$	5.2	5.0	4.4	4.8	5.7
	$\langle 1^3B_2\|\hat{\mathcal{H}}_{\mathrm{SO\,z}}\|1^1B_1\rangle$	1.3	1.2	1.9	2.9	2.7
	$\langle 1^3A_1\|\hat{\mathcal{H}}_{\mathrm{SO\,x}}\|1^1B_2\rangle$	0.2	0.2	0.3	0.4	0.7
	$\langle 1^3A_2\|\hat{\mathcal{H}}_{\mathrm{SO\,z}}\|1^3A_1\rangle$	50.6	51.2	53.8	54.2	54.5
	$\langle 1^3B_1\|\hat{\mathcal{H}}_{\mathrm{SO\,y}}\|1^3A_1\rangle$	28.8	29.6	30.7	31.6	32.0
	$\langle 1^3B_1\|\hat{\mathcal{H}}_{\mathrm{SO\,x}}\|1^3A_2\rangle$	35.9	36.0	37.1	37.2	38.6
Thioformaldehyde (*augmented*)	$\langle 1^3A_2\|\hat{\mathcal{H}}_{\mathrm{SO\,z}}\|1^1A_1\rangle$	180.1	177.8	163.3	168.3	180.7
	$\langle 1^3A_2\|\hat{\mathcal{H}}_{\mathrm{SO\,z}}\|2^1A_1\rangle$	100.1	166.1	71.7	56.4	6.0
	$\langle 1^3A_2\|\hat{\mathcal{H}}_{\mathrm{SO\,z}}\|5^1A_1\rangle$	156.4	55.9	123.5	145.2	171.9
	$\langle 1^3B_1\|\hat{\mathcal{H}}_{\mathrm{SO\,y}}\|1^1A_1\rangle$	40.0	37.2	28.7	28.7	26.9
	$\langle 1^3B_1\|\hat{\mathcal{H}}_{\mathrm{SO\,y}}\|2^1A_1\rangle$	8.4	6.2	6.5	3.7	5.2
	$\langle 1^3B_1\|\hat{\mathcal{H}}_{\mathrm{SO\,y}}\|5^1A_1\rangle$	3.0	3.9	2.7	2.5	4.6
	$\langle 1^3B_2\|\hat{\mathcal{H}}_{\mathrm{SO\,x}}\|1^1A_1\rangle$	105.3	104.9	97.8	101.3	102.9
	$\langle 1^3B_2\|\hat{\mathcal{H}}_{\mathrm{SO\,x}}\|2^1A_1\rangle$	75.2	55.9	66.6	46.7	66.9
	$\langle 1^3B_2\|\hat{\mathcal{H}}_{\mathrm{SO\,x}}\|5^1A_1\rangle$	5.9	43.9	13.3	14.6	54.0
	$\langle 1^3A_1\|\hat{\mathcal{H}}_{\mathrm{SO\,z}}\|1^1A_2\rangle$	168.1	163.2	157.4	162.8	169.7
	$\langle 1^3A_1\|\hat{\mathcal{H}}_{\mathrm{SO\,z}}\|3^1A_2\rangle$	87.9	93.5	60.2	67.5	83.1
	$\langle 1^3B_1\|\hat{\mathcal{H}}_{\mathrm{SO\,x}}\|1^1A_2\rangle$	20.2	18.9	13.9	14.5	16.0
	$\langle 1^3B_2\|\hat{\mathcal{H}}_{\mathrm{SO\,y}}\|1^1A_2\rangle$	105.7	106.2	96.7	102.4	107.4
	$\langle 1^3A_2\|\hat{\mathcal{H}}_{\mathrm{SO\,x}}\|1^1B_1\rangle$	13.7	13.3	9.7	10.0	12.0
	$\langle 1^3A_1\|\hat{\mathcal{H}}_{\mathrm{SO\,x}}\|1^1B_2\rangle$	88.1	85.9	81.3	79.6	78.2
	$\langle 1^3A_2\|\hat{\mathcal{H}}_{\mathrm{SO\,y}}\|1^1B_2\rangle$	104.7	104.6	94.2	95.1	104.0
	$\langle 1^3A_2\|\hat{\mathcal{H}}_{\mathrm{SO\,z}}\|1^3A_1\rangle$	157.3	158.4	152.8	157.2	161.4
	$\langle 1^3B_1\|\hat{\mathcal{H}}_{\mathrm{SO\,x}}\|1^3A_2\rangle$	18.4	16.9	12.5	12.6	13.3
	$\langle 1^3B_2\|\hat{\mathcal{H}}_{\mathrm{SO\,x}}\|1^3A_1\rangle$	81.9	82.4	77.7	82.1	80.5
	$\langle 1^3B_2\|\hat{\mathcal{H}}_{\mathrm{SO\,y}}\|1^3A_2\rangle$	106.7	106.4	97.1	103.2	109.1
Furan (*augmented*)	$\langle 1^3A_2\|\hat{\mathcal{H}}_{\mathrm{SO\,z}}\|1^1A_1\rangle$	4.8	4.6	3.1	3.3	4.3
	$\langle 1^3A_2\|\hat{\mathcal{H}}_{\mathrm{SO\,z}}\|2^1A_1\rangle$	0.4	0.3	0.1	0.1	0.1
	$\langle 1^3B_1\|\hat{\mathcal{H}}_{\mathrm{SO\,x}}\|1^1A_2\rangle$	1.6	0.2	0.8	0.7	1.2
	$\langle 1^3A_2\|\hat{\mathcal{H}}_{\mathrm{SO\,x}}\|1^1B_1\rangle$	1.3	1.3	0.3	0.2	0.4
	$\langle 1^3A_1\|\hat{\mathcal{H}}_{\mathrm{SO\,x}}\|1^1B_2\rangle$	1.7	1.7	1.5	1.5	1.8
	$\langle 1^3A_2\|\hat{\mathcal{H}}_{\mathrm{SO\,y}}\|1^1B_2\rangle$	0.1	0.1	0.1	0.1	0.2
	$\langle 1^3B_1\|\hat{\mathcal{H}}_{\mathrm{SO\,z}}\|1^1B_2\rangle$	4.6	4.5	3.3	3.4	3.7
	$\langle 1^3A_2\|\hat{\mathcal{H}}_{\mathrm{SO\,z}}\|1^3A_1\rangle$	0.3	0.2	0.3	0.3	0.2
	$\langle 1^3B_1\|\hat{\mathcal{H}}_{\mathrm{SO\,x}}\|1^3A_2\rangle$	1.6	1.5	0.6	0.7	1.1
	$\langle 1^3B_2\|\hat{\mathcal{H}}_{\mathrm{SO\,x}}\|1^3A_1\rangle$	1.7	1.7	1.4	1.4	1.9

(*Continued*)

Table 8. (*Continued*)

Molecule (AO basis)	SOME	DFT/MRCI	DFT/MRCI-R	MRMP2 (HF)	MRMP2 (BH-LYP)	CASSCF
Thiophene (*augmented*)	$\langle 2^3A_2\vert\hat{\mathcal{H}}_{\mathrm{SO}\,z}\vert 1^1A_1\rangle$	103.1	113.8	93.1	98.4	99.7
	$\langle 2^3A_2\vert\hat{\mathcal{H}}_{\mathrm{SO}\,z}\vert 2^1A_1\rangle$	43.9	50.1	34.7	38.3	26.8
	$\langle 2^3A_2\vert\hat{\mathcal{H}}_{\mathrm{SO}\,z}\vert 3^1A_1\rangle$	1.6	4.1	20.1	24.1	26.1
	$\langle 1^3B_1\vert\hat{\mathcal{H}}_{\mathrm{SO}\,y}\vert 1^1A_1\rangle$	0.1	0.3	0.1	0.0	0.1
	$\langle 1^3B_2\vert\hat{\mathcal{H}}_{\mathrm{SO}\,x}\vert 1^1A_1\rangle$	6.3	5.6	3.4	3.0	4.3
	$\langle 1^3B_2\vert\hat{\mathcal{H}}_{\mathrm{SO}\,x}\vert 2^1A_1\rangle$	1.6	1.9	3.0	3.3	0.9
	$\langle 1^3A_1\vert\hat{\mathcal{H}}_{\mathrm{SO}\,z}\vert 2^1A_2\rangle$	41.4	40.3	25.8	28.8	27.6
	$\langle 1^3A_1\vert\hat{\mathcal{H}}_{\mathrm{SO}\,y}\vert 1^1B_1\rangle$	0.5	0.4	0.1	0.2	0.0
	$\langle 2^3A_2\vert\hat{\mathcal{H}}_{\mathrm{SO}\,x}\vert 1^1B_1\rangle$	14.0	16.0	12.6	17.9	0.9
	$\langle 1^3B_1\vert\hat{\mathcal{H}}_{\mathrm{SO}\,z}\vert 1^1B_2\rangle$	53.2	52.1	26.5	25.7	30.9
	$\langle 2^3A_2\vert\hat{\mathcal{H}}_{\mathrm{SO}\,z}\vert 1^3A_1\rangle$	33.2	37.8	25.3	27.7	27.7
	$\langle 2^3A_2\vert\hat{\mathcal{H}}_{\mathrm{SO}\,z}\vert 2^3A_1\rangle$	9.1	9.5	15.8	14.9	18.1
	$\langle 1^3B_1\vert\hat{\mathcal{H}}_{\mathrm{SO}\,y}\vert 1^3A_1\rangle$	0.2	0.2	0.1	0.1	0.2
	$\langle 1^3B_1\vert\hat{\mathcal{H}}_{\mathrm{SO}\,x}\vert 2^3A_2\rangle$	1.0	1.9	2.2	2.2	1.1
	$\langle 1^3B_2\vert\hat{\mathcal{H}}_{\mathrm{SO}\,z}\vert 1^3B_1\rangle$	56.3	57.2	35.0	38.9	37.4
Quinoxaline (*valence*)	$\langle 1^3A_2\vert\hat{\mathcal{H}}_{\mathrm{SO}\,z}\vert 1^1A_1\rangle$	41.1	39.7	41.5	40.5	
	$\langle 1^3A_2\vert\hat{\mathcal{H}}_{\mathrm{SO}\,z}\vert 2^1A_1\rangle$	4.1	4.3	3.0	3.0	
	$\langle 1^3B_1\vert\hat{\mathcal{H}}_{\mathrm{SO}\,y}\vert 1^1A_1\rangle$	0.8	0.9	1.0	0.7	
	$\langle 1^3A_1\vert\hat{\mathcal{H}}_{\mathrm{SO}\,z}\vert 1^1A_2\rangle$	2.8	3.7	3.0	3.1	
	$\langle 1^3A_1\vert\hat{\mathcal{H}}_{\mathrm{SO}\,z}\vert 2^1A_2\rangle$	6.1	4.6	5.5	6.5	
	$\langle 1^3B_2\vert\hat{\mathcal{H}}_{\mathrm{SO}\,y}\vert 1^1A_2\rangle$	1.1	1.0	1.2	1.2	
	$\langle 1^3A_1\vert\hat{\mathcal{H}}_{\mathrm{SO}\,y}\vert 1^1B_1\rangle$	1.6	1.5	1.6	1.7	
	$\langle 1^3B_2\vert\hat{\mathcal{H}}_{\mathrm{SO}\,z}\vert 1^1B_1\rangle$	14.2	13.2	11.9	13.4	
	$\langle 1^3B_1\vert\hat{\mathcal{H}}_{\mathrm{SO}\,z}\vert 1^1B_2\rangle$	5.7	5.7	5.7	5.3	
	$\langle 1^3A_2\vert\hat{\mathcal{H}}_{\mathrm{SO}\,z}\vert 1^3A_1\rangle$	2.8	2.7	3.1	3.1	
	$\langle 1^3B_2\vert\hat{\mathcal{H}}_{\mathrm{SO}\,y}\vert 1^3A_2\rangle$	0.9	0.9	1.0	1.1	
	$\langle 1^3B_2\vert\hat{\mathcal{H}}_{\mathrm{SO}\,z}\vert 1^3B_1\rangle$	12.7	12.3	11.0	12.1	
Quinazoline (*valence*)	$\langle 1^3A'\vert\hat{\mathcal{H}}_{\mathrm{SO}\,z}\vert 1^1A'\rangle$	0.0	0.0	0.0	0.0	
	$\langle 1^3A''\vert\hat{\mathcal{H}}_{\mathrm{SO}\,x}\vert 1^1A'\rangle$	9.3	8.9	9.0	9.0	
	$\langle 1^3A''\vert\hat{\mathcal{H}}_{\mathrm{SO}\,y}\vert 1^1A'\rangle$	7.0	6.9	6.0	6.4	
	$\langle 1^3A'\vert\hat{\mathcal{H}}_{\mathrm{SO}\,x}\vert 1^1A''\rangle$	3.6	3.4	2.8	3.0	
	$\langle 1^3A'\vert\hat{\mathcal{H}}_{\mathrm{SO}\,x}\vert 2^1A''\rangle$	1.5	1.3	0.7	1.1	
	$\langle 1^3A'\vert\hat{\mathcal{H}}_{\mathrm{SO}\,y}\vert 1^1A''\rangle$	3.5	3.4	2.8	3.2	
	$\langle 1^3A'\vert\hat{\mathcal{H}}_{\mathrm{SO}\,y}\vert 2^1A''\rangle$	4.1	3.6	3.0	3.4	
	$\langle 1^3A''\vert\hat{\mathcal{H}}_{\mathrm{SO}\,z}\vert 3^1A''\rangle$	11.6	11.8	13.3	12.8	
	$\langle 1^3A''\vert\hat{\mathcal{H}}_{\mathrm{SO}\,x}\vert 3^1A'\rangle$	2.6	2.8	2.4	2.2	
	$\langle 2^3A''\vert\hat{\mathcal{H}}_{\mathrm{SO}\,x}\vert 1^1A'\rangle$	11.8	11.4	11.3	11.9	
	$\langle 1^3A''\vert\hat{\mathcal{H}}_{\mathrm{SO}\,y}\vert 3^1A'\rangle$	1.5	1.4	1.4	1.2	
	$\langle 2^3A''\vert\hat{\mathcal{H}}_{\mathrm{SO}\,y}\vert 1^1A'\rangle$	17.0	15.9	17.3	17.9	
	$\langle 1^3A'\vert\hat{\mathcal{H}}_{\mathrm{SO}\,x}\vert 3^1A''\rangle$	1.4	1.5	0.8	0.9	
	$\langle 1^3A'\vert\hat{\mathcal{H}}_{\mathrm{SO}\,y}\vert 3^1A''\rangle$	6.1	5.9	4.1	4.3	
	$\langle 1^3A''\vert\hat{\mathcal{H}}_{\mathrm{SO}\,z}\vert 2^1A''\rangle$	3.5	3.1	4.1	4.3	
	$\langle 1^3A''\vert\hat{\mathcal{H}}_{\mathrm{SO}\,x}\vert 1^3A'\rangle$	3.3	3.3	2.7	3.2	
	$\langle 1^3A''\vert\hat{\mathcal{H}}_{\mathrm{SO}\,y}\vert 1^3A'\rangle$	3.3	3.2	2.5	3.0	
	$\langle 2^3A''\vert\hat{\mathcal{H}}_{\mathrm{SO}\,z}\vert 1^3A''\rangle$	5.8	5.5	7.1	7.6	
Pyranthione (*valence*)	$\langle 1^3A_2\vert\hat{\mathcal{H}}_{\mathrm{SO}\,z}\vert 1^1A_1\rangle$	151.4	148.5	134.1	143.4	
	$\langle 1^3A_2\vert\hat{\mathcal{H}}_{\mathrm{SO}\,z}\vert 2^1A_1\rangle$	116.4	114.1	104.2	106.3	
	$\langle 1^3A_1\vert\hat{\mathcal{H}}_{\mathrm{SO}\,z}\vert 1^1A_2\rangle$	166.7	165.7	153.6	161.3	
	$\langle 1^3B_2\vert\hat{\mathcal{H}}_{\mathrm{SO}\,y}\vert 1^1A_2\rangle$	1.4	0.9	1.4	1.3	
	$\langle 1^3A_2\vert\hat{\mathcal{H}}_{\mathrm{SO}\,x}\vert 1^1B_1\rangle$	0.2	0.1	0.3	0.2	
	$\langle 1^3B_2\vert\hat{\mathcal{H}}_{\mathrm{SO}\,z}\vert 1^1B_1\rangle$	161.9	166.2	155.6	161.9	
	$\langle 1^3A_2\vert\hat{\mathcal{H}}_{\mathrm{SO}\,y}\vert 1^1B_2\rangle$	0.7	0.6	1.3	1.1	
	$\langle 1^3A_2\vert\hat{\mathcal{H}}_{\mathrm{SO}\,z}\vert 1^3A_1\rangle$	160.8	163.1	151.8	158.9	
	$\langle 1^3A_2\vert\hat{\mathcal{H}}_{\mathrm{SO}\,z}\vert 2^3A_1\rangle$	37.4	34.5	42.5	43.3	
	$\langle 1^3B_1\vert\hat{\mathcal{H}}_{\mathrm{SO}\,y}\vert 1^3A_1\rangle$	0.0	0.1	0.0	0.0	

(*Continued*)

Table 8. (*Continued*)

Molecule (AO basis)	SOME	DFT/MRCI	DFT/MRCI-R	MRMP2 (HF)	MRMP2 (BH-LYP)	CASSCF
Dithiin	$\langle 1^3A\|\hat{\mathcal{H}}_{\mathrm{SO}\,z}\|1^1A\rangle$	123.0	123.8	65.6	71.8	
(*valence*)	$\langle 1^3A\|\hat{\mathcal{H}}_{\mathrm{SO}\,z}\|2^1A\rangle$	10.6	10.0	16.5	17.5	
	$\langle 2^3A\|\hat{\mathcal{H}}_{\mathrm{SO}\,z}\|1^1A\rangle$	112.3	106.4	139.6	151.2	
	$\langle 2^3A\|\hat{\mathcal{H}}_{\mathrm{SO}\,z}\|2^1A\rangle$	15.5	14.9	5.7	5.8	
	$\langle 1^3B\|\hat{\mathcal{H}}_{\mathrm{SO}\,x}\|1^1A\rangle$	9.9	9.8	5.0	6.3	
	$\langle 1^3B\|\hat{\mathcal{H}}_{\mathrm{SO}\,x}\|2^1A\rangle$	36.4	36.7	27.6	29.0	
	$\langle 1^3B\|\hat{\mathcal{H}}_{\mathrm{SO}\,x}\|3^1A\rangle$	16.5	15.4	17.1	18.5	
	$\langle 2^3B\|\hat{\mathcal{H}}_{\mathrm{SO}\,x}\|1^1A\rangle$	9.7	9.6	7.7	7.2	
	$\langle 2^3B\|\hat{\mathcal{H}}_{\mathrm{SO}\,x}\|2^1A\rangle$	9.6	8.5	19.6	19.1	
	$\langle 2^3B\|\hat{\mathcal{H}}_{\mathrm{SO}\,x}\|3^1A\rangle$	3.8	3.2	12.5	11.9	
	$\langle 3^3B\|\hat{\mathcal{H}}_{\mathrm{SO}\,x}\|1^1A\rangle$	0.7	0.4	3.4	6.1	
	$\langle 3^3B\|\hat{\mathcal{H}}_{\mathrm{SO}\,x}\|2^1A\rangle$	8.5	8.0	15.9	18.1	
	$\langle 3^3B\|\hat{\mathcal{H}}_{\mathrm{SO}\,x}\|3^1A\rangle$	2.4	3.1	6.4	6.4	
	$\langle 1^3B\|\hat{\mathcal{H}}_{\mathrm{SO}\,y}\|1^1A\rangle$	32.9	32.5	21.1	22.5	
	$\langle 1^3B\|\hat{\mathcal{H}}_{\mathrm{SO}\,y}\|2^1A\rangle$	1.6	0.8	2.3	1.1	
	$\langle 1^3B\|\hat{\mathcal{H}}_{\mathrm{SO}\,y}\|3^1A\rangle$	30.8	31.6	23.1	25.0	
	$\langle 2^3B\|\hat{\mathcal{H}}_{\mathrm{SO}\,y}\|1^1A\rangle$	41.8	40.9	40.8	43.8	
	$\langle 2^3B\|\hat{\mathcal{H}}_{\mathrm{SO}\,y}\|2^1A\rangle$	13.4	13.9	7.7	8.8	
	$\langle 2^3B\|\hat{\mathcal{H}}_{\mathrm{SO}\,y}\|3^1A\rangle$	7.6	5.7	1.0	3.4	
	$\langle 3^3B\|\hat{\mathcal{H}}_{\mathrm{SO}\,y}\|1^1A\rangle$	5.2	4.1	19.7	22.4	
	$\langle 3^3B\|\hat{\mathcal{H}}_{\mathrm{SO}\,y}\|2^1A\rangle$	28.0	27.3	29.8	31.3	
	$\langle 3^3B\|\hat{\mathcal{H}}_{\mathrm{SO}\,y}\|3^1A\rangle$	5.3	4.2	11.4	11.8	
	$\langle 1^3A\|\hat{\mathcal{H}}_{\mathrm{SO}\,x}\|1^1B\rangle$	29.8	30.7	14.4	17.3	
	$\langle 1^3A\|\hat{\mathcal{H}}_{\mathrm{SO}\,x}\|2^1B\rangle$	9.8	9.3	6.6	8.0	
	$\langle 2^3A\|\hat{\mathcal{H}}_{\mathrm{SO}\,x}\|1^1B\rangle$	36.7	34.9	37.9	38.9	
	$\langle 2^3A\|\hat{\mathcal{H}}_{\mathrm{SO}\,x}\|2^1B\rangle$	2.6	3.6	2.1	4.0	
	$\langle 1^3A\|\hat{\mathcal{H}}_{\mathrm{SO}\,y}\|1^1B\rangle$	1.8	1.5	1.8	1.3	
	$\langle 1^3A\|\hat{\mathcal{H}}_{\mathrm{SO}\,y}\|2^1B\rangle$	14.4	15.1	7.5	8.6	
	$\langle 2^3A\|\hat{\mathcal{H}}_{\mathrm{SO}\,y}\|1^1B\rangle$	14.2	16.9	9.4	5.8	
	$\langle 2^3A\|\hat{\mathcal{H}}_{\mathrm{SO}\,y}\|2^1B\rangle$	7.1	5.4	14.1	19.0	
	$\langle 1^3B\|\hat{\mathcal{H}}_{\mathrm{SO}\,z}\|1^1B\rangle$	3.9	2.2	13.9	15.9	
	$\langle 1^3B\|\hat{\mathcal{H}}_{\mathrm{SO}\,z}\|2^1B\rangle$	77.9	77.8	57.6	61.9	
	$\langle 2^3B\|\hat{\mathcal{H}}_{\mathrm{SO}\,z}\|1^1B\rangle$	79.5	81.3	63.6	68.3	
	$\langle 2^3B\|\hat{\mathcal{H}}_{\mathrm{SO}\,z}\|2^1B\rangle$	50.8	47.1	62.7	72.9	
	$\langle 3^3B\|\hat{\mathcal{H}}_{\mathrm{SO}\,z}\|1^1B\rangle$	18.3	14.9	48.9	55.8	
	$\langle 3^3B\|\hat{\mathcal{H}}_{\mathrm{SO}\,z}\|2^1B\rangle$	8.9	8.0	25.0	30.5	
	$\langle 2^3A\|\hat{\mathcal{H}}_{\mathrm{SO}\,z}\|1^3A\rangle$	23.4	23.3	17.7	20.9	
	$\langle 1^3B\|\hat{\mathcal{H}}_{\mathrm{SO}\,x}\|1^3A\rangle$	27.2	28.2	13.2	15.6	
	$\langle 1^3B\|\hat{\mathcal{H}}_{\mathrm{SO}\,x}\|2^3A\rangle$	16.6	13.9	21.0	24.6	
	$\langle 2^3B\|\hat{\mathcal{H}}_{\mathrm{SO}\,x}\|1^3A\rangle$	2.6	2.2	4.1	5.4	
	$\langle 2^3B\|\hat{\mathcal{H}}_{\mathrm{SO}\,x}\|2^3A\rangle$	3.7	1.5	13.6	17.4	
	$\langle 3^3B\|\hat{\mathcal{H}}_{\mathrm{SO}\,x}\|1^3A\rangle$	3.4	2.8	5.4	6.6	
	$\langle 3^3B\|\hat{\mathcal{H}}_{\mathrm{SO}\,x}\|2^3A\rangle$	0.9	2.4	12.6	16.6	
	$\langle 1^3B\|\hat{\mathcal{H}}_{\mathrm{SO}\,y}\|1^3A\rangle$	0.8	0.7	2.0	2.3	
	$\langle 1^3B\|\hat{\mathcal{H}}_{\mathrm{SO}\,y}\|2^3A\rangle$	21.4	23.4	8.5	5.4	
	$\langle 2^3B\|\hat{\mathcal{H}}_{\mathrm{SO}\,y}\|1^3A\rangle$	13.0	13.8	4.7	5.2	
	$\langle 2^3B\|\hat{\mathcal{H}}_{\mathrm{SO}\,y}\|2^3A\rangle$	19.9	19.6	20.0	17.6	
	$\langle 3^3B\|\hat{\mathcal{H}}_{\mathrm{SO}\,y}\|1^3A\rangle$	12.5	12.4	8.5	11.1	
	$\langle 3^3B\|\hat{\mathcal{H}}_{\mathrm{SO}\,y}\|2^3A\rangle$	5.0	1.7	18.3	23.2	
	$\langle 2^3B\|\hat{\mathcal{H}}_{\mathrm{SO}\,z}\|1^3B\rangle$	9.5	12.0	7.0	7.0	
	$\langle 3^3B\|\hat{\mathcal{H}}_{\mathrm{SO}\,z}\|1^3B\rangle$	109.2	109.0	104.7	114.9	
	$\langle 3^3B\|\hat{\mathcal{H}}_{\mathrm{SO}\,z}\|2^3B\rangle$	13.7	8.8	56.4	60.4	
Bithiophene	$\langle 1^3A\|\hat{\mathcal{H}}_{\mathrm{SO}\,z}\|1^1A\rangle$	0.1	0.1	0.3	0.6	
(*valence*)	$\langle 2^3A\|\hat{\mathcal{H}}_{\mathrm{SO}\,z}\|1^1A\rangle$	1.8	1.8	0.6	1.3	
	$\langle 1^3B\|\hat{\mathcal{H}}_{\mathrm{SO}\,x}\|1^1A\rangle$	1.0	1.1	1.0	1.1	
	$\langle 1^3B\|\hat{\mathcal{H}}_{\mathrm{SO}\,x}\|2^1A\rangle$	1.9	2.0	0.6	0.2	
	$\langle 2^3B\|\hat{\mathcal{H}}_{\mathrm{SO}\,x}\|1^1A\rangle$	2.1	2.3	0.4	1.5	
	$\langle 3^3B\|\hat{\mathcal{H}}_{\mathrm{SO}\,x}\|1^1A\rangle$	14.7	13.8	6.9	8.5	

(*Continued*)

Table 8. (*Continued*)

Molecule (AO basis)	SOME	DFT/MRCI	DFT/MRCI-R	MRMP2 (HF)	MRMP2 (BH-LYP)	CASSCF
	$\langle 4^3B\|\hat{\mathcal{H}}_{\mathrm{SO\,x}}\|1^1A\rangle$	7.2	5.1	21.1	17.1	
	$\langle 1^3B\|\hat{\mathcal{H}}_{\mathrm{SO\,y}}\|1^1A\rangle$	1.0	1.3	0.7	0.6	
	$\langle 1^3B\|\hat{\mathcal{H}}_{\mathrm{SO\,y}}\|2^1A\rangle$	3.7	4.2	1.9	4.2	
	$\langle 2^3B\|\hat{\mathcal{H}}_{\mathrm{SO\,y}}\|1^1A\rangle$	4.4	5.2	2.2	4.0	
	$\langle 3^3B\|\hat{\mathcal{H}}_{\mathrm{SO\,y}}\|1^1A\rangle$	26.0	24.0	12.3	14.6	
	$\langle 4^3B\|\hat{\mathcal{H}}_{\mathrm{SO\,y}}\|1^1A\rangle$	15.6	11.0	31.3	28.3	
	$\langle 1^3A\|\hat{\mathcal{H}}_{\mathrm{SO\,x}}\|1^1B\rangle$	2.4	2.3	1.0	2.0	
	$\langle 1^3A\|\hat{\mathcal{H}}_{\mathrm{SO\,x}}\|2^1B\rangle$	2.2	2.4	3.1	4.0	
	$\langle 1^3A\|\hat{\mathcal{H}}_{\mathrm{SO\,y}}\|1^1B\rangle$	11.9	11.6	7.4	9.4	
	$\langle 1^3A\|\hat{\mathcal{H}}_{\mathrm{SO\,y}}\|2^1B\rangle$	5.2	5.5	6.4	6.4	
	$\langle 2^3A\|\hat{\mathcal{H}}_{\mathrm{SO\,z}}\|1^3A\rangle$	0.5	0.7	0.1	0.2	
	$\langle 1^3B\|\hat{\mathcal{H}}_{\mathrm{SO\,x}}\|2^3A\rangle$	2.0	2.0	2.0	1.9	
	$\langle 1^3B\|\hat{\mathcal{H}}_{\mathrm{SO\,x}}\|3^3A\rangle$	21.6	21.9	10.2	13.9	
	$\langle 1^3B\|\hat{\mathcal{H}}_{\mathrm{SO\,x}}\|4^3A\rangle$	2.2	0.7	11.7	12.5	
	$\langle 1^3B\|\hat{\mathcal{H}}_{\mathrm{SO\,y}}\|2^3A\rangle$	8.4	8.3	7.0	7.2	
	$\langle 1^3B\|\hat{\mathcal{H}}_{\mathrm{SO\,y}}\|3^3A\rangle$	38.7	39.6	15.8	23.0	
	$\langle 1^3B\|\hat{\mathcal{H}}_{\mathrm{SO\,y}}\|4^3A\rangle$	10.8	7.5	21.5	21.9	
Nitromethane (*augmented*)	$\langle 1^3A'\|\hat{\mathcal{H}}_{\mathrm{SO\,z}}\|1^1A'\rangle$	0.3	0.3	0.0	0.0	0.2
	$\langle 1^3A''\|\hat{\mathcal{H}}_{\mathrm{SO\,x}}\|1^1A'\rangle$	33.9	32.8	36.5	37.6	34.7
	$\langle 1^3A''\|\hat{\mathcal{H}}_{\mathrm{SO\,x}}\|2^1A'\rangle$	17.2	16.1	16.7	17.2	17.1
	$\langle 1^3A''\|\hat{\mathcal{H}}_{\mathrm{SO\,y}}\|1^1A'\rangle$	16.3	16.4	17.0	15.0	16.3
	$\langle 1^3A''\|\hat{\mathcal{H}}_{\mathrm{SO\,y}}\|2^1A'\rangle$	30.3	28.7	29.3	29.9	31.1
	$\langle 1^3A'\|\hat{\mathcal{H}}_{\mathrm{SO\,x}}\|1^1A''\rangle$	23.7	23.5	24.2	24.0	28.9
	$\langle 1^3A'\|\hat{\mathcal{H}}_{\mathrm{SO\,x}}\|2^1A''\rangle$	9.5	9.6	7.2	7.3	17.3
	$\langle 1^3A'\|\hat{\mathcal{H}}_{\mathrm{SO\,y}}\|1^1A''\rangle$	40.9	40.7	40.8	40.3	48.7
	$\langle 1^3A'\|\hat{\mathcal{H}}_{\mathrm{SO\,y}}\|2^1A''\rangle$	6.8	6.6	7.7	7.6	12.1
	$\langle 1^3A''\|\hat{\mathcal{H}}_{\mathrm{SO\,z}}\|2^1A''\rangle$	32.5	31.8	35.5	36.1	19.8
	$\langle 1^3A''\|\hat{\mathcal{H}}_{\mathrm{SO\,x}}\|1^3A'\rangle$	22.7	23.2	23.6	24.0	28.8
	$\langle 1^3A''\|\hat{\mathcal{H}}_{\mathrm{SO\,y}}\|1^3A'\rangle$	39.0	40.1	40.2	40.0	48.6
	$\langle 2^3A''\|\hat{\mathcal{H}}_{\mathrm{SO\,z}}\|1^3A''\rangle$	33.4	32.0	35.9	36.3	20.4
Nitrobenzene (*valence*)	$\langle 1^3A_2\|\hat{\mathcal{H}}_{\mathrm{SO\,z}}\|1^1A_1\rangle$	51.8	51.0	53.0	52.9	
	$\langle 1^3A_2\|\hat{\mathcal{H}}_{\mathrm{SO\,z}}\|2^1A_1\rangle$	14.7	12.7	9.7	9.7	
	$\langle 1^3B_1\|\hat{\mathcal{H}}_{\mathrm{SO\,y}}\|1^1A_1\rangle$	0.2	0.2	0.0	0.0	
	$\langle 1^3B_2\|\hat{\mathcal{H}}_{\mathrm{SO\,x}}\|1^1A_1\rangle$	53.8	53.3	55.3	55.6	
	$\langle 1^3B_2\|\hat{\mathcal{H}}_{\mathrm{SO\,x}}\|2^1A_1\rangle$	12.9	12.0	8.3	9.5	
	$\langle 1^3A_1\|\hat{\mathcal{H}}_{\mathrm{SO\,z}}\|1^1A_2\rangle$	9.9	11.7	10.1	9.8	
	$\langle 1^3B_1\|\hat{\mathcal{H}}_{\mathrm{SO\,x}}\|1^1A_2\rangle$	40.7	46.3	46.4	46.0	
	$\langle 1^3B_2\|\hat{\mathcal{H}}_{\mathrm{SO\,y}}\|1^1A_2\rangle$	23.6	21.5	23.7	24.0	
	$\langle 1^3A_2\|\hat{\mathcal{H}}_{\mathrm{SO\,x}}\|1^1B_1\rangle$	3.9	3.1	1.5	1.0	
	$\langle 1^3B_2\|\hat{\mathcal{H}}_{\mathrm{SO\,z}}\|1^1B_1\rangle$	1.5	1.3	0.6	0.5	
	$\langle 1^3A_1\|\hat{\mathcal{H}}_{\mathrm{SO\,x}}\|1^1B_2\rangle$	8.0	9.4	7.7	8.1	
	$\langle 1^3A_2\|\hat{\mathcal{H}}_{\mathrm{SO\,y}}\|1^1B_2\rangle$	23.8	21.9	24.6	23.9	
	$\langle 1^3B_1\|\hat{\mathcal{H}}_{\mathrm{SO\,z}}\|1^1B_2\rangle$	12.6	18.8	14.5	16.7	
	$\langle 1^3A_2\|\hat{\mathcal{H}}_{\mathrm{SO\,z}}\|1^3A_1\rangle$	12.1	11.5	9.8	10.0	
	$\langle 1^3B_1\|\hat{\mathcal{H}}_{\mathrm{SO\,y}}\|1^3A_1\rangle$	0.0	0.0	0.0	0.0	
	$\langle 1^3B_1\|\hat{\mathcal{H}}_{\mathrm{SO\,x}}\|1^3A_2\rangle$	43.6	45.6	45.6	46.5	
	$\langle 1^3B_2\|\hat{\mathcal{H}}_{\mathrm{SO\,x}}\|1^3A_1\rangle$	8.8	8.4	6.8	6.8	
	$\langle 1^3B_2\|\hat{\mathcal{H}}_{\mathrm{SO\,y}}\|1^3A_2\rangle$	23.9	22.3	24.4	24.1	
	$\langle 1^3B_2\|\hat{\mathcal{H}}_{\mathrm{SO\,z}}\|1^3B_1\rangle$	14.4	17.3	15.4	15.9	
Dithiosuccinimide (*valence*)	$\langle 1^3A_2\|\hat{\mathcal{H}}_{\mathrm{SO\,z}}\|1^1A_1\rangle$	71.9	70.8	64.2	68.4	
	$\langle 1^3B_1\|\hat{\mathcal{H}}_{\mathrm{SO\,y}}\|1^1A_1\rangle$	132.6	130.5	117.9	126.0	
	$\langle 1^3B_2\|\hat{\mathcal{H}}_{\mathrm{SO\,x}}\|1^1A_1\rangle$	0.1	0.1	0.1	0.2	
	$\langle 1^3A_1\|\hat{\mathcal{H}}_{\mathrm{SO\,z}}\|1^1A_2\rangle$	54.2	53.8	53.2	55.7	
	$\langle 1^3B_1\|\hat{\mathcal{H}}_{\mathrm{SO\,x}}\|1^1A_2\rangle$	9.9	9.9	7.6	7.9	
	$\langle 1^3B_2\|\hat{\mathcal{H}}_{\mathrm{SO\,y}}\|1^1A_2\rangle$	121.6	120.6	109.6	114.8	
	$\langle 1^3A_1\|\hat{\mathcal{H}}_{\mathrm{SO\,y}}\|1^1B_1\rangle$	97.5	95.4	97.0	101.5	
	$\langle 1^3A_2\|\hat{\mathcal{H}}_{\mathrm{SO\,x}}\|1^1B_1\rangle$	9.4	9.2	6.8	7.5	

(*Continued*)

Table 8. (*Continued*)

Molecule (AO basis)	SOME	DFT/MRCI	DFT/MRCI-R	MRMP2 (HF)	MRMP2 (BH-LYP)	CASSCF
	$\langle 1^3A_1\|\hat{\mathcal{H}}_{\mathrm{SO\,x}}\|1^1B_2\rangle$	0.1	0.0	0.1	0.1	
	$\langle 1^3A_2\|\hat{\mathcal{H}}_{\mathrm{SO\,y}}\|1^1B_2\rangle$	93.9	89.7	87.1	87.2	
	$\langle 1^3B_1\|\hat{\mathcal{H}}_{\mathrm{SO\,y}}\|1^3A_1\rangle$	96.5	95.0	96.6	100.5	
	$\langle 1^3B_2\|\hat{\mathcal{H}}_{\mathrm{SO\,x}}\|1^3A_1\rangle$	0.0	0.0	0.1	0.0	
	$\langle 1^3B_1\|\hat{\mathcal{H}}_{\mathrm{SO\,x}}\|1^3A_2\rangle$	9.6	9.5	7.1	8.0	
Methionine (*valence*)	$\langle 1^3A\|\hat{\mathcal{H}}_{\mathrm{SO\,x}}\|1^1A\rangle$	31.4	31.7	26.2	27.4	
	$\langle 2^3A\|\hat{\mathcal{H}}_{\mathrm{SO\,x}}\|1^1A\rangle$	39.6	38.9	38.3	37.6	
	$\langle 2^3A\|\hat{\mathcal{H}}_{\mathrm{SO\,x}}\|2^1A\rangle$	0.4	0.1	0.2	0.8	
	$\langle 3^3A\|\hat{\mathcal{H}}_{\mathrm{SO\,x}}\|1^1A\rangle$	73.3	71.3	59.8	63.8	
	$\langle 3^3A\|\hat{\mathcal{H}}_{\mathrm{SO\,x}}\|2^1A\rangle$	13.5	13.2	12.3	12.7	
	$\langle 4^3A\|\hat{\mathcal{H}}_{\mathrm{SO\,x}}\|3^1A\rangle$	25.2	24.7	24.9	26.2	
	$\langle 1^3A\|\hat{\mathcal{H}}_{\mathrm{SO\,y}}\|1^1A\rangle$	85.9	84.9	70.6	74.5	
	$\langle 2^3A\|\hat{\mathcal{H}}_{\mathrm{SO\,y}}\|1^1A\rangle$	14.2	14.0	13.5	14.6	
	$\langle 2^3A\|\hat{\mathcal{H}}_{\mathrm{SO\,y}}\|2^1A\rangle$	0.5	0.5	1.3	0.1	
	$\langle 3^3A\|\hat{\mathcal{H}}_{\mathrm{SO\,y}}\|1^1A\rangle$	36.8	36.4	32.3	32.9	
	$\langle 3^3A\|\hat{\mathcal{H}}_{\mathrm{SO\,y}}\|2^1A\rangle$	18.0	17.4	15.3	15.3	
	$\langle 4^3A\|\hat{\mathcal{H}}_{\mathrm{SO\,y}}\|3^1A\rangle$	13.4	13.1	12.7	13.4	
	$\langle 1^3A\|\hat{\mathcal{H}}_{\mathrm{SO\,z}}\|1^1A\rangle$	97.3	96.7	80.8	84.6	
	$\langle 2^3A\|\hat{\mathcal{H}}_{\mathrm{SO\,z}}\|1^1A\rangle$	14.8	14.3	15.6	15.6	
	$\langle 2^3A\|\hat{\mathcal{H}}_{\mathrm{SO\,z}}\|2^1A\rangle$	0.9	0.8	1.2	0.1	
	$\langle 3^3A\|\hat{\mathcal{H}}_{\mathrm{SO\,z}}\|1^1A\rangle$	21.3	20.4	17.4	18.0	
	$\langle 3^3A\|\hat{\mathcal{H}}_{\mathrm{SO\,z}}\|2^1A\rangle$	39.5	38.2	34.7	35.7	
	$\langle 4^3A\|\hat{\mathcal{H}}_{\mathrm{SO\,z}}\|3^1A\rangle$	23.6	23.6	23.5	24.4	
	$\langle 2^3A\|\hat{\mathcal{H}}_{\mathrm{SO\,x}}\|1^3A\rangle$	0.9	0.6	0.9	0.6	
	$\langle 3^3A\|\hat{\mathcal{H}}_{\mathrm{SO\,x}}\|1^3A\rangle$	14.1	13.8	12.6	12.3	
	$\langle 4^3A\|\hat{\mathcal{H}}_{\mathrm{SO\,x}}\|2^3A\rangle$	24.7	24.4	23.9	25.4	
	$\langle 2^3A\|\hat{\mathcal{H}}_{\mathrm{SO\,y}}\|1^3A\rangle$	0.2	0.2	0.1	0.4	
	$\langle 3^3A\|\hat{\mathcal{H}}_{\mathrm{SO\,y}}\|1^3A\rangle$	17.7	17.1	15.4	15.6	
	$\langle 4^3A\|\hat{\mathcal{H}}_{\mathrm{SO\,y}}\|2^3A\rangle$	13.2	13.0	12.2	13.2	
	$\langle 2^3A\|\hat{\mathcal{H}}_{\mathrm{SO\,z}}\|1^3A\rangle$	0.4	0.5	1.8	0.6	
	$\langle 3^3A\|\hat{\mathcal{H}}_{\mathrm{SO\,z}}\|1^3A\rangle$	39.5	38.3	35.5	36.4	
	$\langle 4^3A\|\hat{\mathcal{H}}_{\mathrm{SO\,z}}\|2^3A\rangle$	23.5	23.6	23.0	24.2	
Isoalloxazine (*valence*)	$\langle 1^3A''\|\hat{\mathcal{H}}_{\mathrm{SO\,x}}\|1^1A'\rangle$	8.4	7.2	11.4	12.0	
	$\langle 1^3A''\|\hat{\mathcal{H}}_{\mathrm{SO\,x}}\|2^1A'\rangle$	6.0	6.5	2.8	3.0	
	$\langle 1^3A''\|\hat{\mathcal{H}}_{\mathrm{SO\,x}}\|3^1A'\rangle$	4.2	4.1	4.0	3.6	
	$\langle 2^3A''\|\hat{\mathcal{H}}_{\mathrm{SO\,x}}\|1^1A'\rangle$	10.4	10.7	6.7	7.7	
	$\langle 1^3A''\|\hat{\mathcal{H}}_{\mathrm{SO\,y}}\|1^1A'\rangle$	10.8	12.0	5.1	5.9	
	$\langle 1^3A''\|\hat{\mathcal{H}}_{\mathrm{SO\,y}}\|2^1A'\rangle$	2.0	2.7	0.5	0.5	
	$\langle 1^3A''\|\hat{\mathcal{H}}_{\mathrm{SO\,y}}\|3^1A'\rangle$	2.5	3.2	1.9	2.0	
	$\langle 2^3A''\|\hat{\mathcal{H}}_{\mathrm{SO\,y}}\|1^1A'\rangle$	23.0	19.8	26.4	26.1	
	$\langle 1^3A'\|\hat{\mathcal{H}}_{\mathrm{SO\,x}}\|1^1A''\rangle$	11.2	10.7	2.5	0.9	
	$\langle 1^3A'\|\hat{\mathcal{H}}_{\mathrm{SO\,x}}\|2^1A''\rangle$	2.4	2.5	7.9	8.1	
	$\langle 1^3A'\|\hat{\mathcal{H}}_{\mathrm{SO\,y}}\|1^1A''\rangle$	9.8	9.8	9.3	9.9	
	$\langle 1^3A'\|\hat{\mathcal{H}}_{\mathrm{SO\,y}}\|2^1A''\rangle$	7.3	6.2	2.8	3.4	
	$\langle 1^3A''\|\hat{\mathcal{H}}_{\mathrm{SO\,z}}\|1^1A''\rangle$	1.9	1.9	4.8	5.7	
	$\langle 1^3A''\|\hat{\mathcal{H}}_{\mathrm{SO\,z}}\|2^1A''\rangle$	3.1	3.1	0.3	0.5	
	$\langle 1^3A''\|\hat{\mathcal{H}}_{\mathrm{SO\,x}}\|1^3A'\rangle$	9.8	9.8	7.3	7.5	
	$\langle 1^3A''\|\hat{\mathcal{H}}_{\mathrm{SO\,y}}\|1^3A'\rangle$	4.5	5.3	2.3	2.8	
	$\langle 2^3A''\|\hat{\mathcal{H}}_{\mathrm{SO\,x}}\|1^3A'\rangle$	2.3	2.3	0.9	1.2	
	$\langle 2^3A''\|\hat{\mathcal{H}}_{\mathrm{SO\,y}}\|1^3A'\rangle$	10.4	9.8	8.9	9.6	
	$\langle 2^3A''\|\hat{\mathcal{H}}_{\mathrm{SO\,z}}\|1^3A''\rangle$	4.1	4.0	5.9	5.7	

functions of formaldehyde. In addition, literature values for the spin–orbit coupling in formaldehyde are available for comparison. Formaldehyde has been studied intensively by Langhoff and Davidson by *ab initio* MRCI methods using the full Breit–Pauli spin–orbit Hamiltonian [59]. The SO coupling is relatively strong with SOMEs up to 70 cm^{-1} and very similar values for all four methods (see Table 8). The MR-MP2

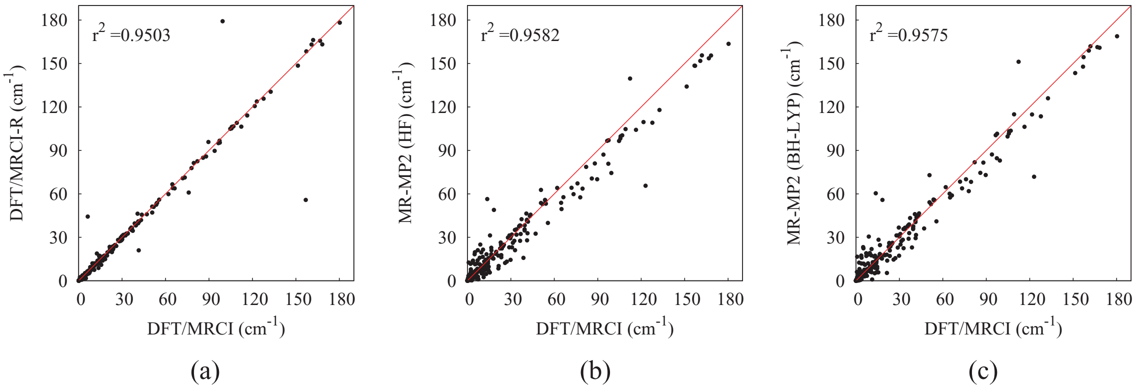

Figure 6. Correlation plots of SOMEs for all polyatomic molecules calculated with DFT/MRCI-R, MR-MP2(HF) and MR-MP2(BH-LYP) wave functions vs. SOMEs calculated with DFT/MRCI wave functions.

expansion based on HF orbitals gives results marginally closer to DFT/MRCI. The substantially larger statistical deviation of the DFT/MRCI-R is essentially caused by two outliers as will be discussed below. For several pairs of states, Langhoff and Davidson explicitly listed computed SOMEs which can serve as reference values for comparison [59]. For example, they obtained a value of 61.96 cm^{-1} for $\langle 1^3\mathrm{A}_2|\hat{\mathcal{H}}_{\mathrm{SO\,z}}|\mathrm{GS}\rangle$ at the MRCI level which agrees well with our values of 62.0, 60.2, 65.0 and 65.0 cm^{-1} for the DFT/MRCI, DFT/MRCI-R, MR-MP2(HF) and MR-MP2(BH-LYP), respectively. CASSCF gives a slightly larger value of 69.2 cm^{-1} for that SOME. Note that our singlet–triplet interaction matrix elements for the x (or y) Cartesian component of $\hat{\mathcal{H}}_{\mathrm{SO}}$ are of the form $\langle {}^3\Psi, M_S = 1|\hat{\mathcal{H}}_{\mathrm{SO\,x}}|{}^1\Psi', M_S = 0\rangle$. The corresponding integrals presented by Langhoff and Davidson have to be divided by a factor of $\sqrt{2}$ before they can be compared to the values listed in Table 8. Such an example is $\langle 1^3\mathrm{B}_1|\hat{\mathcal{H}}_{\mathrm{SO\,y}}|\mathrm{GS}\rangle$ for which we obtain values of 43.1, 42.0, 45.3, and 45.4 cm^{-1} for the DFT/MRCI, DFT/MRCI-R, MR-MP2(HF) and MR-MP2(BH-LYP), respectively. Dividing the value of 57.79 cm^{-1} given by the latter authors by $\sqrt{2}$ yields 40.86 cm^{-1}, in fair agreement with our results.

The only exceptions from the good agreement between the DFT/MRCI, MR-MP2, and CASSCF results for the SOMEs of formaldehyde, listed in Table 8, are the matrix elements of the $1^3\mathrm{A}_2$ state with the high-lying $4^1\mathrm{A}_1$ and $5^1\mathrm{A}_1$ states. The leading configuration of the $1^3\mathrm{A}_2$ state originates from an $(n_H \rightarrow \pi^*_L)$ $(1^3\mathrm{A}_2)$ with respect to the electronic ground state. As discussed at length in Section 3.3.1.2, the $4^1\mathrm{A}_1$ and $5^1\mathrm{A}_1$ arise from mixtures of the $(\pi_{H-1} \rightarrow \pi^*_L)$ and $(n^2_H \rightarrow \pi^{*2}_L)$ with weights varying from method to method. A further complication arises due to the energetic proximity of a third $^1\mathrm{A}_1$ state with Rydberg character which mixes with the valence states. The $(n_H \rightarrow \pi^*_L)$ excitation and the just mentioned valence-excited singlet A_1 configurations are coupled through the large $\langle n_H|\hat{\mathcal{H}}_{\mathrm{SO\,z}}|\pi_{H-1}\rangle$ and $\langle n_H|\hat{\mathcal{H}}_{\mathrm{SO\,z}}|\pi^*_L\rangle$ integrals, respectively. The latter is the same integral that dominates the matrix element between the $1^3\mathrm{A}_2$ state and the electronic ground state. The Rydberg configurations contribute little to the SOMEs. Depending on the size and phase of the wave function coefficients of the $4^1\mathrm{A}_1$ state, SOMEs varying between 22 cm^{-1} (CASSCF(8,11)) and 57 cm^{-1} (DFT/MRCI-R) are obtained (Table 8). To clarify this issue further, we can compare our SOMEs with the MRCI values presented by Langhoff and Davidson. These authors found two $^1A_1$ valence states, the energetic order of which depends on the chosen MO basis for the MRCI expansion. For the matrix element of the $1^3\mathrm{A}_2$ state and the $^1\mathrm{A}_1$ with leading $(\pi \rightarrow \pi^*)$ configuration, they obtain a value of 41.32 cm^{-1} which is a bit larger than our SOMEs, save for the DFT/MRCI-R value. For the other SOME involving the $1^3\mathrm{A}_2$ state and the $^1\mathrm{A}_1$ state with leading $(n^2 \rightarrow \pi^{*\,2})$ configuration, Langhoff and Davidson list a value of 53.08 cm^{-1} which compares favourably with the corresponding SOME of the DFT/MRCI wave functions (55.0 cm^{-1}). The DFT/MRCI-R wave function yields a SOME of 31.5 cm^{-1} in that case, in accidental coincidence with the CASSCF (8,11) value. The varying weight of the $(\pi \rightarrow \pi^*)$ excitation in the wave functions of the three densely spaced electronically excited singlet states is also reflected in the electric dipole moments for a radiative transition to the electronic ground state (see Table S10 of the SM). Concluding this discussion, we believe that it makes little sense to compare the matrix elements of energetically close-lying interacting electronic states on an individual basis. Rather, their contributions to spin-forbidden transitions such as the phosphorescence of the lowest lying triplet state should be considered as a whole.

Thioformaldehyde. Like in formaldehyde, very good agreement among the methods is observed with respect to the majority of the SOMEs (see Table 8). The above-mentioned large outliers in the DFT/MRCI vs. DFT/MRCI-R correlation of the SOMEs all involve the 2^1A_1 and 3^1A_1 states in the valence AO basis which relate to 2^1A_1 and 5^1A_1 in the augmented basis due to interjacent Rydberg states. They are coupled with the 1^3A_2 and 1^3B_2 states via very large MO integrals, $\langle n_H|\hat{\mathcal{H}}_{\mathrm{SO\,z}}|\pi_{H-1}\rangle$, $\langle n_H|\hat{\mathcal{H}}_{\mathrm{SO\,z}}|\pi_L^*\rangle$, and $\langle \sigma_{H-2}|\hat{\mathcal{H}}_{\mathrm{SO\,x}}|\pi_{H-1}\rangle$, which amount to 273.9, –236.1, and –215.2 cm^{-1}, respectively, for the BH-LYP MOs in the augmented basis. Such a strong SO interaction makes the above discussed differences in the DFT/MRCI and DFT/MRCI-R wave functions become apparent. The phase factors of the nearly equally large wave function coefficients of the $(\pi_{H-1} \rightarrow \pi_L^*)$ and $(n_H^2 \rightarrow \pi_L^{*2})$ excitations in the CASSCF leads to an almost perfect cancellation of their contributions to $\langle 1^3A_2|\hat{\mathcal{H}}_{\mathrm{SO\,z}}|2^1A_1\rangle$, whereas they add up in $\langle 1^3A_2|\hat{\mathcal{H}}_{\mathrm{SO\,z}}|5^1A_1\rangle$ (Table 8). Such a cancellation does not happen in $\langle 1^3B_2|\hat{\mathcal{H}}_{\mathrm{SO\,x}}|2^1A_1\rangle$ or $\langle 1^3B_2|\hat{\mathcal{H}}_{\mathrm{SO\,x}}|5^1A_1\rangle$. The leading term of the 1^3B_2 wave function $(\sigma_{H-2} \rightarrow \pi_L^*)$ connects solely to one of the major contributors to the 2^1A_1 and 5^1A_1 wave functions by a single excitation, namely to $(\pi_{H-1} \rightarrow \pi_L^*)$. Indirectly, the $\langle 1^3B_2|\hat{\mathcal{H}}_{\mathrm{SO\,x}}|2^1A_1\rangle$ and $\langle 1^3B_2|\hat{\mathcal{H}}_{\mathrm{SO\,x}}|5^1A_1\rangle$ SOMEs, therefore, reflect the weight of that configuration in the 2^1A_1 and 5^1A_1 wave functions of the various methods. The SOMEs of the 1^3B_1 state with the ground state and the first excited singlet state 1^1A_2 reflect the amount of valence character in the 1^3B_1 wave function. This state originates mainly from an $n \rightarrow 4s$ Rydberg excitation. As may be seen in Tables S18 and S19 of the SM, the coefficient of the $n_H \rightarrow \sigma^*$ excitation which is decisive for the magnitude of the spin–orbit interaction is larger for the DFT/MRCI methods compared to MR-MP2 and CASSCF. The size of the $\langle 1^3A_1|\hat{\mathcal{H}}_{\mathrm{SO\,z}}|3^1A_2\rangle$ SOME is controlled mainly by the weight of the $(\pi_{H-1}^1 n_H^1 \pi_L^{*2})$ configuration in the 3^1A_2 wave function which constitutes a $(n_H \rightarrow \pi_L^*)$ single excitation with respect to the leading $(\pi_{H-1}^1 \pi_L^*)$ term of the 1^3A_1 wave function.

Thiophene. The correspondence between the SOMEs obtained by the two flavours of DFT/MRCI is so close that the differences need not be discussed. Focusing instead on the MR-MP2 approaches, we see that the matrix elements involving $\pi \rightarrow \sigma^*$ excitations are systematically smaller for the MR-MP2(HF) method than for MR-MP2(BH-LYP) (Table 8). The largest SOME is obtained for the second triplet of A_2 symmetry with the ground state. The dominant configuration in the 2^3A_2 wave function arises from the $\pi_{H-1} \rightarrow \sigma_{L+10}^*$ excitation, but also substantial contributions from π_{H-1} to Rydberg excitations are recognised in the wave function expansions (Tables S30 and S31 of the SM). The π_{H-1} MO exhibits substantial electron density at the sulphur centre. This is true also for the σ_{L+10}^* orbital. As a consequence, the SOC integral $\langle \pi_{H-1}|\hat{\mathcal{H}}_{\mathrm{SO\,z}}|\sigma_{L+10}^*\rangle$ is large, 142.8 cm^{-1} (BH-LYP orbitals) and 105.2 cm^{-1} (HF orbitals), indicating that the electron density distributions of the σ_{L+10}^* orbitals differ significantly between the HF and BH-LYP one-particle basis. Most importantly, the electron density at the sulphur centre is lower in the σ_{L+10}^* HF orbital compared to the corresponding BH-LYP orbital. This is the reason for a lower value of $\langle \pi_{H-1}|\hat{\mathcal{H}}_{\mathrm{SO\,z}}|\sigma_{L+10}^*\rangle$ in the case of HF orbitals. The MR-MP2 SOMEs agree better with the CASSCF values in general. The DFT/MRCI approaches tend to exhibit larger valence character in the energetically lower lying states (1^1B_2, 2^1A_1 1^3B_2, 1^3A_1) and more Rydberg character in the higher lying ones (2^1B_2, 3^1A_1, 2^3A_1) (Tables S30 and S31 of the SM), thus explaining the shifts in the SOMEs. For example, the decrease of $\langle 2^3A_2|\hat{\mathcal{H}}_{\mathrm{SO\,z}}|2^1A_1\rangle$ and concomitant increase of $\langle 2^3A_2|\hat{\mathcal{H}}_{\mathrm{SO\,z}}|3^1A_1\rangle$ when going from DFT/MRCI to MR-MP2 are due to different valence-Rydberg mixings in the A_1 symmetric singlet states.

Pyranthione. Some of the states in pyranthione are coupled by the largest SOMEs presented in this paper (see Table 8). We should point out that a similarly strong coupling of the 1^3A_2 state with the GS (127.4 cm^{-1} [9]) and 2^1A_1 (126.1 cm^{-1} [9]) is predicted when HF/MRD-CI wave functions are employed, where MRD-CI stands for *ab initio* multi-reference singles and double excitation CI with individual configuration selection [71,72]. Very strong coupling could have been foreseen due to the observable absorption of the first triplet state. The correlation between the MR-MP2(BH-LYP) and DFT/MRCI SOMEs is very good, having one of the smallest values of NRMSD, only 3%. MR-MP2(HF) has SOMEs somewhat shifted toward lower values, with a relatively large maximum negative deviation of 17.3 cm^{-1}, but with still good NRMSD of 6%.

Dithiin. With regard to the treatment of SO interaction, dithiin is the most challenging molecule examined in the present study. The DFT/MRCI and DFT/MRCI-R SOMEs are so close that we refrain from discussing the DFT/MRCI-R values further. In contrast, the MR-MP2 methods show very large NRMSDs values for both variants. Inspection of Table S2 in the SM reveals that the maximum positive and negative deviations for the set of all presented SOMEs both come from dithiin. Large negative deviations arise from the coupling between the 1^3A and the ground state (Table 8). On the opposite side, there is a stronger coupling of 2^3A and the ground state in the case of MR-MP2. In Section 3.3.1.2, it was already noted that the energy separation of the 1^3A and 2^3A states is smaller in the MR-MP2 cases compared to DFT/MRCI (see also Table 6). Accordingly, the configuration mixing is more pronounced for the MR-MP2 methods (Table S39 in the SM). Due to the distortion from the planar symmetry, a strict characterisation of the MOs as σ, n or π is not possible anymore. This mixing of orbital characters, together with the two sulphur centres located next to each other, leads to very large spin–orbit coupling of all orbitals with electron densities at the sulphur centres. This applies, for example, to the π_{H-1} and π_L^* orbitals (see Figure S5, SM) so that the integral $\langle\pi_{H-1}|\hat{\mathcal{H}}_{\mathrm{SO\,z}}|\pi_L^*\rangle$ has a value of 143.8 cm^{-1} (BH-LYP orbitals) and 114.7 cm^{-1} (HF orbitals). In contrast, the π_{L+4}^* orbital has very little electron density at the sulphur atoms and the integrals involving it have very modest values. $\langle\pi_H|\hat{\mathcal{H}}_{\mathrm{SO\,z}}|\pi_{L+4}^*\rangle$ amounts to 25.1 cm^{-1} for the BH-LYP orbitals and 18.5 cm^{-1} for the HF orbitals. Likewise, $\langle\pi_{H-2}|\hat{\mathcal{H}}_{\mathrm{SO\,z}}|\pi_{L+4}^*\rangle$ is 34.5 cm^{-1} for the BH-LYP orbitals and 31.5 cm^{-1} for the HF orbitals. Many other configurations, even with small coefficients, contribute to the final values of the $\langle 1^3\mathrm{A}|\hat{\mathcal{H}}_{\mathrm{SO\,z}}|\mathrm{GS}\rangle$ and $\langle 2^3\mathrm{A}|\hat{\mathcal{H}}_{\mathrm{SO\,z}}|\mathrm{GS}\rangle$ matrix elements. Since the correspondence between the 1^3A and 2^3A states in the DFT/MRCI and MR-MP2 treatments is shadowed by their strong mixing, the correlation of their SOMEs leads to outliers on opposite sides (see Figures S2 and S3 of the SM), with the DFT/MRCI matrix elements larger for the coupling of 1^3A and the GS and smaller in the case of 2^3A.

The maximal positive deviations in the correlation of DFT/MRCI and MR-MP2 SOMEs of dithiin are introduced by the coupling between triplet states, 2^3B and 3^3B (Table 8). The state vectors are dominated by the negative and positive linear combinations arising from the ($\pi_{H-2} \rightarrow \pi_L^*$) and ($\pi_H \rightarrow \sigma_{L+1}^*$) excitations. As the two leading configurations in 2^3B and 3^3B are either the same or differ by more than one excitation, they do not interact by the here employed effective one-electron, mean-field SO Hamiltonian. Thus, the SO coupling is achieved by the involvement of configurations with minor coefficients in the state vectors. The 2^3B and 3^3B states are no exception from the usual trend that the dominant configurations have smaller coefficients in the MR-MP2 wave functions compared to DFT/MRCI. In the present case, the substantial admixture of minor configurations results in a stronger SO coupling of the MR-MP2 wave functions. Especially important are excitations from the n_{H-4} orbital which are more pronounced in the 3^3B state calculated by MR-MP2 (see Table S39 of the SM). The n_{H-4} orbital has most of its electron density located at the two sulphur centres (see Figure S5, SM) and SO coupling involving n_{H-4} is very strong. For example, the configurations obtained by the ($\pi_{H-2} \rightarrow \pi_L^*$) and ($n_{H-4} \rightarrow \pi_L^*$) excitations are strongly coupled via the $\langle n_{H-4}|\hat{\mathcal{H}}_{\mathrm{SO\,z}}|\pi_{H-2}\rangle$ integral which has values of 193.7 and 203.1 cm^{-1} for the BH-LYP and HF orbitals, respectively. Such large values of SOMEs between molecular orbitals are the reason why dithiin is a challenging case for the SO treatment, especially when comparing different theoretical methods, since all differences in calculated wave functions are amplified.

Bithiophene. Bithiophene has the smallest correlation coefficient of only 0.3280 for the MR-MP2(HF) and 0.5416 for the MR-MP2(BH-LYP), suggesting very poor correlation between MR-MP2 and DFT/MRCI SOMEs. Indeed, the graphs presented in Figures S2 and S3 of the SM show the occurrence of both positive and negative outliers. The outliers are in the region of stronger spin–orbit interaction, suggesting the involvement of the $\pi\sigma^*$ states. Note that bithiophene, like dithiin, is not planar but exhibits a *trans gauche* conformation in the electronic ground state. The $\pi\sigma^*$ states, 3^3A and 3^3B, can therefore mix with the close-lying 4^3A and 4^3B states and thus also have some $\pi\pi^*$ character. The mixing is stronger for the MR-MP2 triplet wave functions (compare Table S41 in the SM) so that the pair of SOMEs (x and y components) involving 3^3B has larger values for DFT/MRCI (more $\pi\sigma^*$ character) than for MR-MP2. The 4^3B has more $\pi\pi^*$ character in the case of DFT/MRCI and thus lower matrix elements (Table 8). A similar observation is made for 3^3A and 4^3A. This rotation of characters between the close-lying triplet states in MR-MP2 leads to correlated pairs of positive and negative outliers compared to DFT/MRCI. Again, DFT/MRCI and DFT/MRCI-R values agree nearly perfectly (Figure S1 of the SM).

Nitromethane. The agreement between SOMEs is quite good among the DFT/MRCI and MR-MP2 treatments (Table 8). We ascribe the deviations for the corresponding CASSCF SOMEs to the insufficient active space employed in the augmented basis (see Section 3.3.1.2).

Nitrobenzene. Despite the substantially different wave function compositions of the $1^1\mathrm{B}_1$ state, good agreement between the DFT/MRCI and MR-MP2 SOMEs are found. Maximum deviations are around 5 cm^{-1} and NRMSDs are approximately 4%. The correlation between DFT/MRCI and DFT/MRCI-R SOMEs is even better. Why is that? The reason is tracked back to the small size of the spin–orbit integrals involved in the coupling of the $1^1\mathrm{B}_1$ state with the low-lying $^3\mathrm{A}_1$, $^3\mathrm{A}_2$, and $^3\mathrm{B}_2$ states. At the planar ground-state geometry, the coupling between $1^1\mathrm{B}_1$ and $1^3\mathrm{A}_1$ is El-Sayed forbidden because both states represent ($\pi \rightarrow \pi^*$) excitations. The origin of the small values for $\langle 1^3\mathrm{A}_2|\hat{\mathcal{H}}_{\mathrm{SO}}|1^1\mathrm{B}_1\rangle$ and $\langle 1^3\mathrm{B}_2|\hat{\mathcal{H}}_{\mathrm{SO}}|1^1\mathrm{B}_1\rangle$ is more subtle. Their leading configurations differ by an El-Sayed allowed single excitation from π_H to n_{H-3} ($^3\mathrm{A}_2$) and n_{H-4}

($^3B_2$). However, the π_H orbital has very little electron density on the nitro group (see Figure S6 in the SM), whereas n_{H-3} and n_{H-4} represent predominantly the negative and positive linear combinations of the oxygen lone-pair orbitals. In addition, the n_{H-4} MO exhibits density along the C–N σ bond. Because of its r^{-3} dependence, the spin–orbit operator is near-sighted and has large matrix elements only for electronic wave functions located at the same centre. As a consequence, the spin–orbit integrals $\langle \pi_H | \hat{\mathcal{H}}_{SO} | n_{H-3} \rangle$ and $\langle \pi_H | \hat{\mathcal{H}}_{SO} | n_{H-4} \rangle$ have very small values. The photophysically relevant SOMEs of the 1^3B_1 and 1^3A_2 states with the electronic ground state as well as the coupling between the first excited singlet state (1^1A_2) and 1^3B_1 are free from complications due to four open-shell configurations. Hence, in nitrobenzene, the SOMEs are seen to be more robust with regard to the wave function quality than the energies. This observation is confirmed by good agreement between the DFT/MRCI and MR-MP2 SOMEs. Maximum deviations are around 5 cm^{-1} and NRMSDs are 4%.

Methionine. The large variation of the MR-MP2 energies with regard to the employed type of MOs seems to have no effect on the SO interaction since the net coupling between the states is almost equal for the MR-MP2(HF) and MR-MP2(BH-LYP) wave functions (Table 8). While the SOMEs of states connected by an ($n \rightarrow \pi^*$) excitation, $\langle 2^3A | \hat{\mathcal{H}}_{SO\,x} | 1^1A \rangle$ for example, are nearly equal for all methods, we observe systematically lower MR-MP2 SOMEs for states that are coupled by a $\pi \rightarrow \sigma^*$ excitation such as $\langle 1^3A | \hat{\mathcal{H}}_{SO\,y} | 1^1A \rangle$. Like in thiophene, DFT/MRCI and DFT/MRCI-R wave functions of the lower lying excited states tend to have more valence and less Rydberg character than the first-order perturbed wave functions of the MR-MP2 methods. Overall, the agreement between the DFT/MRCI and MR-MP2 SOMEs is satisfactory, especially considering the difference in energies between DFT/MRCI and MR-MP2(HF), with NRMSD of 7% and 5% for MR-MP2(HF) and MR-MP2(BH-LYP), respectively.

Isoalloxazine. The agreement between the DFT/MRCI and DFT/MRCI-R SOMEs (RMSD of 1 cm^{-1}, NRMSD of 5%) is satisfactory, considering the high density of states and the medium size of the selected SOMEs (ranging between 2 and 23 cm^{-1}). In contrast, the correlation of DFT/MRCI and MR-MP2 SOMEs is rather poor (see graphs in Figures S2 and S3 of the SM). We could not find any pattern in the scattering depicted in the graphs, as is it not caused by a simple 2 × 2 rotation of wave functions. Examination of the DFT/MRCI and MR-MP2 state vectors (Table S57 in the SM) reveals that the $n\pi^*$ states are heavy mixtures of excitations originating from lone-pair orbitals centred on N and O. Since the molecular orbitals located at O contribute with larger spin–orbit integrals, the size of the computed SOME is very sensitive with respect to wave function composition. In an effort to improve the results, we expanded the initial RAS space to 16-11-2 to include all the leading orbitals in the desired states. To this end, the number of excited states was reduced to five per irreducible representation, but Esel still could not be lowered. The computed excitation energies differ by up to ≈0.2 eV from the results of the corresponding calculations with an initial 10-10-2 RAS, but the changes of the SOMEs are relatively small (compare Table 8 and Table S58 in the SM). Thus, the bad correlation between DFT/MRCI and MR-MP2 SOMEs is retained. After all, it will be difficult to carry out MR-MP2 calculations on isoalloxazine that are converged with respect to the choice of first-order interacting space.

4. Conclusion

In this work, we have presented a thorough comparison of electronic excitation energies and spin–orbit matrix elements (SOMEs) of a representative set of molecules, obtained with different electronic structure methods. Among them are two variants of the DFT/MRCI method, the original parameterisation by Grimme and Waletzke [1] and the newer parameterisation of a redesigned DFT/MRCI-R Hamiltonian by Lyskov et al. [16]. While SOMEs of DFT/MRCI wave functions have been successfully employed in many photophysical studies, SOMEs of DFT/MRCI-R wave functions are presented here for the first time. Furthermore, we have tested the performance of the MR-MP2 method [33] with respect to spin–orbit coupling. Herein, a truncated first-order perturbed wave function is employed where the inclusion of configurations in the first-order interacting space is controlled by a selection threshold. Two variants have been employed, MR-MP2(HF) based on Hartree–Fock orbitals and MR-MP2(BH-LYP) based on Kohn–Sham orbitals using the BH-LYP density functional.

For the diatomic molecules, our quantum chemical results could be validated with respect to experimental data. For the polyatomic molecules, this was possible only to a limited extent. In particular, experimental data on optically dark states are missing for comparison. For some of the experimentally unknown states and their coupling matrix elements, we therefore carried out reference calculations at the CASSCF/CASPT2 levels.

Overall, we find very satisfactory agreement between the excitation energies and the SOMEs obtained with the four approaches. The correlation between the experimentally known adiabatic excitation energies of the first ${}^3\Pi$ state and the two variants of DFT/MRCI is very good (correlation coefficient above 0.98). Both MR-MP2 approaches seem to underestimate these energies somewhat but the correlation is still considered good (correlation coefficient above 0.96). The agreement between the experimentally derived fine-structure splitting constant A_{SO} and the computed SOME is excellent (correlation coefficient >0.997) for all four approaches. For the experimentally known excitation energies of the polyatomic test molecules, correlation coefficients of 0.9806 (MR-MP2(BH-LYP)), 0.9781 (MR-MP2(HF)), 0.9883 (DFT/MRCI), and 0.9910 (DFT/MRCI-R) are found. This correlation includes both valence and Rydberg excitations. With regard to the uncertainties arising from a spread of experimental values, the influence of solvent effects, and the more systematic question how well vertical excitation energies can be compared with peak maxima of absorption spectra, we are very satisfied with this correspondence.

Since our comparison of SOMEs also involves higher lying electronically excited states, the agreement among the four approaches deteriorates somewhat, with the correlation coefficients still extending 0.95. The correlation plots show some pronounced outliers that can be grouped into several types. The most innocuous one arises from rotations among the wave functions of close-lying electronic states in molecules with low spatial symmetry. These types of outliers are characterised by a good correlation of the corresponding excitation energies. An example is the 3^3A and 4^3A pair of states of bithiophene. The different mixing of $\pi\sigma^*$ and $\pi\pi^*$ in MR-MP2 as compared to DFT/MRCI leads to pairs of positive and negative outliers. Dithiin is a similar case with $\sigma - \pi$ mixing. Isoalloxazine also falls into this group although it is planar. Here, several $n\pi^*$ states are involved where the contribution of the lone-pair excitations on the oxygen and nitrogen centres to the wave function varies substantially among the states. In several thio compounds (thioformaldehyde, thiophene, pyranthione, methionine), we find systematically lower SOMEs between $(\pi \rightarrow \sigma^*)$ and $(\pi \rightarrow \pi^*)$ excited states in the MR-MP2 approaches compared to DFT/MRCR and DFT/MRCI-R. The analysis is complicated by the fact that the first-order perturbed wave functions of the MR-MP2 expansions often do not exhibit a few dominant terms plus many terms with small coefficients. In contrast to DFT/MRCI, the major wave function contributions are spread over many configurations with medium-sized coefficients. Since the deviation is more pronounced when HF orbitals are employed, we ascribe the main difference in the SOMEs to an orbital effect. The density distribution in the lowest lying σ^* HF MO is more diffuse than in the corresponding KS MO. Other reasons for large outliers are more serious as they involve the appearance of doubly excited configurations in the wave functions of (low-lying) electronic states. The large outliers observed in the correlation of the SOMEs of DFT/MRCI-R, on the one hand, and DFT/MRCI, on the other hand, arise from the interaction of the 2^1A_1 and 5^1A_1 states in thioformaldehyde with the ${}^3A_2$ state that stems from a $(n \rightarrow \pi^*)$ single excitation. In particular, a double excitation of the $n^2 \rightarrow \pi^{*2}$ type gains a much larger weight in the DFT/MRCI-R wave function of 2^1A_1 so that this becomes the leading configuration, whereas a $(\pi \rightarrow \pi^*)$ excitation dominates the 2^1A_1 wave functions of the other methods. Comparison with CASPT2 energies point toward a problem of the redesigned DFT/MRCI-R in properly describing this closed-shell double excitation of $(n^2 \rightarrow \pi^{*2})$ type. For such a small molecule, also the MR-MP2 method represents a good alternative because the reference and first-order interacting spaces can be converged.

Some of the different wave function compositions are not reflected in the SOMEs. In o-benzyne and nitrobenzene, for example, large negative singlet–triplet splittings (meaning that among states with equal spatial composition, the singlet has a substantially lower energy) point towards an unbalanced description of doubly excited configurations with four open shells by the original DFT/MRCI method. This problem is remedied by the redesigned DFT/MRCI-R Hamiltonian. However, since the spin–orbit integrals are close to zero, the changes in the wave function have almost no effect on the SOMEs. Closing the discussion on doubly excited states, a comparison of the higher lying electronic states of dithiosuccinimide suggests that it might be worthwhile to reinvestigate the performance of the DFT/MRCI-R method on n, $n' \rightarrow \pi^*\pi'^*$ and $n^2 \rightarrow \pi^{*2}$ double excitations. The difference between the two parameterisations arises predominantly from two integrals, i.e. $\langle o_1 o_2 || o_1 o_2 \rangle$ and $\langle v_1 v_2 || v_1 v_2 \rangle$ where o denotes an occupied and v a vacant orbital. When validating the DFT/MRCI-R approach, we computed energy profiles for a simultaneous rotation of the CH_2 end groups about the carbon–carbon double bonds of s-*trans*-butadiene [16]. Using this example, it was shown by us that such types of integrals play an important role for $(\pi_1\pi_2 \rightarrow \pi_1^*\pi_2^*)$ excitations, causing a large change of the adiabatic potential energy surfaces of the first excited states. Moreover, the good agreement with the present MR-MP2 results for the 2^1B_1 state of o-benzyne corroborates our conclusions that DFT/MRCI-R describes the interaction of π electrons properly. In cases in which electrons are annihilated from n orbitals (which are in general much more compact than π orbitals) and promoted to π orbitals, the change of correlation energy associated with the electron motion becomes more significant compared to a $(\pi_1\pi_2 \rightarrow \pi_1^*\pi_2^*)$ transition. Thus, the doubtful states in thioformaldehyde and dithiosuccinimide can be treated more accurately by addressing the correlation-exchange potential of the underlying density functional.

In cases of doubt, the use of MR-MP2 is a good alternative. Herein, the choice of orbitals seems to play a minor role. On the average, MR-MP2 energies are in slightly better agreement with experiment when Hartree–Fock orbitals are employed instead of Kohn–Sham (BH-LYP) orbitals, whereas the opposite is found for SOMEs. In connection with MR-MP2 calculations, it is recommended to solve for more roots than the minimum number, thereby improving the first-order interacting space. Otherwise, states with large perturbation corrections are easily missed, in analogy to CASSCF/CASPT2 treatments. For the photophysically important electronic states, SOMEs agree well with the corresponding coupling matrix elements from DFT/MRCI and DFT/MRCI-R calculations. The mapping of states among the methods becomes more and more difficult as we move up in energy. Concomitantly, the matching of the SOMEs deteriorates in these cases. Since MR-MP2 is computationally substantially more demanding than DFT/MRCI-R, the latter method is generally preferable. However, if doubly excited configurations appear in the wave function with large weights, we recommend the use of the MR-MP2 approach as a control that the semi-empirical DFT/MRCI-R approach is functioning properly.

Disclosure statement

No potential conflict of interest was reported by the authors.

Funding

This study is financially supported by the Deutsche Forschungsgemeinschaft (DFG) [project number MA 1051/12-1] and [project number MA 1051/14-1].

References

[1] S. Grimme and M. Waletzke, J. Chem. Phys. **111**, 5645 (1999).

[2] M. Kleinschmidt, J. Tatchen, and C.M. Marian, J. Comp. Chem. **23**, 824 (2002).

[3] M. Kleinschmidt and C.M. Marian, Chem. Phys. **311**, 71 (2005).

[4] M. Kleinschmidt, J. Tatchen, and C.M. Marian, J. Chem. Phys. **124**, 124101 (2006).

[5] J. Tatchen, N. Gilka, and C.M. Marian, Phys. Chem. Chem. Phys. **9**, 5209 (2007).

[6] M. Etinski, J. Tatchen, and C.M. Marian, J. Chem. Phys. **134**, 154105 (2011).

[7] M. Etinski, V. Rai-Constapel, and C.M. Marian, J. Chem. Phys. **140**, 114104 (2014).

[8] S. Salzmann, M. Kleinschmidt, J. Tatchen, R. Weinkauf, and C.M. Marian, Phys. Chem. Chem. Phys. **10**, 380 (2008).

[9] J. Tatchen, M. Waletzke, C.M. Marian, and S. Grimme, Chem. Phys. **264**, 245 (2001).

[10] J. Tatchen, M. Kleinschmidt, C.M. Marian, M. Parac, and S. Grimme, Z. Phys. Chem. **217**, 205 (2003).

[11] S. Perun, J. Tatchen, and C.M. Marian, ChemPhysChem **9**, 282 (2008).

[12] S. Salzmann, J. Tatchen, and C.M. Marian, J. Photochem. Photobiol. A Chem. **198**, 221 (2008).

[13] C.M. Marian, WIREs Comput. Mol. Sci. **2**, 187 (2012).

[14] V. Rai-Constapel, T. Villnow, G. Ryseck, P. Gilch, and C.M. Marian, J. Phys. Chem. A **118**, 11708 (2014).

[15] M. Kleinschmidt, C. van Wüllen, and C.M. Marian, J. Chem. Phys. **142**, 094301 (2015).

[16] I. Lyskov, M. Kleinschmidt, and C.M. Marian, J. Chem. Phys. **144**, 034104 (2016).

[17] J.M. Mewes, V. Jovanović, C.M. Marian, and A. Dreuw, Phys. Chem. Chem. Phys. **16**, 12393 (2014).

[18] E. Fromager and H.J.A. Jensen, Phys. Rev. A **78**, 022504 (2008).

[19] K. Sharkas, A. Savin, H.J.A. Jensen, and J. Toulouse, J. Chem. Phys. **137**, 044104 (2012).

[20] E. Fromager, S. Knecht, and H.J.A. Jensen, J. Chem. Phys. **138**, 084101 (2013).

[21] E.D. Hedegård, F. Heiden, S. Knecht, E. Fromager, and H.J.A. Jensen, J. Chem. Phys. **139**, 184308 (2013).

[22] E.D. Hedegård, J.M.H. Olsen, S. Knecht, J. Kongsted, and H.J.A. Jensen, J. Chem. Phys. **142**, 114113 (2015).

[23] K. Aidas, C. Angeli, K. Bak, R. Bast, V. Bakken, L. Boman, O. Christiansen, R. Cimiraglia, S. Coriani, P. Dahle, E. Dalskov, U. Ekström, T. Enevoldsen, J. Eriksen, P. Ettenhuber, B. Fernández, L. Ferrighi, H. Fliegl, L. Frediani, K. Hald, A. Halkier, C. Hättig, H. Heiberg, T. Helgaker, A. Hennum, H. Hettema, E. Hjertenaes, S. Høst, I.M. Høyvik, M. Iozzi, B. Jansík, T. Kjaergaard, D. Jonsson, P. Jørgensen, J. Kauczor, S. Kirpekar, W. Klopper, S. Knecht, R. Kobayashi, H. Koch, J. Kongsted, A. Krapp, K. Kristensen, A. Ligabue, O. Lutnaes, J. Melo, K. Mikkelsen, R. Myhre, C. Neiss, C. Nielsen, P. Norman, J. Olsen, P.F. Provasi, A. Osted, M. Packer, F. Pawlowski, T. Pedersen, P. Provasi, S. Reine, Z. Rinkevicius, T. Ruden, K. Ruud, V. Rybkin, P. Sałek, K. Sneskov, A. de Merás, T. Saue, P.R. Taylor, B. Schimmelpfennig, A. Steindal, K. Sylvester Hvid, P. Taylor, A. Teale, E. Tellgren, D. Tew, A. Thorvaldsen, L. Thøgersen, O. Vahtras, M. Watson, and M. Ziolkowsk, WIREs Comput. Mol. Sci. **4**, 269 (2014).

[24] O. Vahtras, H. Ågren, P. Jørgensen, H.J.A. Jensen, T. Helgaker, and J. Olsen, J. Chem. Phys. **96**, 2118 (1992).

[25] H. Ågren, O. Vahtras, and B. Minaev, Adv. Quantum Chem. **27**, 71 (1996).

[26] K. Andersson, P.Å. Malmqvist, and B.O. Roos, J. Chem. Phys. **96**, 1218 (1992).

[27] B.O. Roos, K. Andersson, M. Fülscher, P. Malmqvist, L. Serrano-Andrés, K. Pierloot, and M. Merchán, Adv. Chem. Phys. **93**, 219 (1996).

[28] M. Schreiber, M.R. Silva-Junior, S.P.A. Sauer, and W. Thiel, J. Chem. Phys. **128**, 134110 (2008).

[29] J. Finley, P.Å. Malmqvist, B.O. Roos, and L. Serrano-Andrés, Chem. Phys. Lett. **288**, 299 (1998).

[30] B.O. Roos and P. Malmqvist, Phys. Chem. Chem. Phys. **6**, 2919 (2004).

[31] A. Berning, M. Schweizer, H.J. Werner, P.J. Knowles, and P. Palmieri, Mol. Phys. **98**, 1823 (2000).

[32] C. Duboc, D. Ganyushin, K. Sivalingam, M.N. Collomb, and F. Neese, J. Phys. Chem. A **114**, 10750 (2010).

[33] S. Grimme and M. Waletzke, Phys. Chem. Chem. Phys. **2**, 2075 (2000).

[34] T. Müller and H. Lischka, Theor. Chem. Acc. **106**, 369 (2001).

[35] S.R. Gwaltney and R.J. Bartlett, Chem. Phys. Lett. **241**, 26 (1995).

[36] M.R.J. Hachey, P.J. Bruna, and F. Grein, J. Phys. Chem. **99**, 8050 (1995).

[37] M. Merchán and B.O. Roos, Theor. Chim. Acta **92**, 227 (1995).

[38] J.P. Zobel, J.J. Nogueira, and L. González, J. Phys. Chem. Lett. **6**, 3006 (2015).

[39] A.D. Becke, J. Chem. Phys. **98**, 5648 (1993).

[40] P.J. Stephens, F.J. Devlin, C.F. Chabalowski, and M.J. Frisch, J. Phys. Chem. **98**, 11623 (1994).

[41] C. Lee, W. Yang, and R.G. Parr, Phys. Rev. B **37**, 785 (1988).

[42] A. Schäfer, C. Huber, and R. Ahlrichs, J. Chem. Phys. **100**, 5829 (1994).

[43] F. Weigend, M. Häser, H. Patzelt, and R. Ahlrichs, Chem. Phys. Lett. **294**, 143 (1998).

[44] TURBOMOLE V6.5 2013, a development of University of Karlsruhe and Forschungszentrum Karlsruhe GmbH, 1989–2007, TURBOMOLE GmbH, since 2007. <http://www.turbomole.com>.

[45] T.H. Dunning, Jr. and P.J. Hay, in *Modern Theoretical Chemistry*, edited by H.F. Schaefer, III (Springer, New York, 1977), Vol. 3, pp. 1–27.

[46] K.P. Huber and G. Herzberg, *Molecular Spectra and Molecular Structure, IV, Constants of Diatomic Molecules* (Van Nostrand, New York, 1979).

[47] M. Kleinschmidt, C.M. Marian, M. Waletzke, and S. Grimme, J. Chem. Phys. **130**, 044708 (2009).

[48] H.J. Werner, P.J. Knowles, G. Knizia, F.R. Manby, and M. Schütz, WIREs Comput. Mol. Sci. **2**, 242 (2012).

[49] P.J. Knowles and H.J. Werner, Chem. Phys. Lett. **115**, 259 (1985).

[50] H. Werner and P.J. Knowles, J. Chem. Phys. **82**, 5053 (1985).

[51] H.J. Werner, Mol. Phys. **89**, 645 (1996).

[52] B.A. Heß, C.M. Marian, U. Wahlgren, and O. Gropen, Chem. Phys. Lett. **251**, 365 (1996).

[53] B. Schimmelpfennig, *AMFI – An Atomic Spin–Orbit Integral Program* (University of Stockholm, 1996).

[54] J. Tatchen and C.M. Marian, Chem. Phys. Lett. **313**, 351 (1999).

[55] D. Danovich, C.M. Marian, T. Neuheuser, S.D. Peyerimhoff, and S. Shaik, J. Phys. Chem. A **102**, 5923 (1998).

[56] E. Wigner, *Group Theory and Its Application to Quantum Mechanics of Atomic Spectra* (Academic Press, New York, 1995).

[57] C. Marian, in *Reviews in Computational Chemistry*, edited by K. Lipkowitz and D. Boyd (Wiley-VCH, Weinheim, 2001), Vol. 17, pp. 99–204.

[58] A. Carrington, *Microwave Spectroscopy of Free Radicals* (Academic Press, London, 1974).

[59] S.R. Langhoff and E.R. Davidson, J. Chem. Phys. **64**, 4699 (1976).

[60] K.N. Walzl, C.F. Koerting, and A. Kuppermann, J. Chem. Phys. **87**, 3796 (1987).

[61] S. Taylor, D.G. Wilden, and J. Comer, Chem. Phys. **70**, 291 (1982).

[62] J.E. Mentall, E.P. Gentieu, M. Krauss, and D. Neumann, J. Chem. Phys. **55**, 5471 (1971).

[63] C. Drury and D. Moule, J. Mol. Spectrosc. **92**, 469 (1982).

[64] I.C. Walker and M.A. Fluendy, Intern. J. Mass Spectrom. **205**, 171 (2001).

[65] K.R. Asmis, Ph. D. thesis, University of Freiburg, Switzerland, 1996.

[66] C.M. Marian and N. Gilka, J. Chem. Theory Comput. **4**, 1501 (2008).

[67] E. Block, M. Birringer, R. DeOrazio, J. Fabian, R.S. Glass, C. Guo, C. He, E. Lorance, Q. Qian, T.B. Schroeder, Z. Shan, M. Thiruvazhi, G.S. Wilson, and X. Zhang, J. Am. Chem. Soc. **122**, 5052 (2000).

[68] S. Siegert, F. Vogeler, C.M. Marian, and R. Weinkauf, Phys. Chem. Chem. Phys. **13**, 10350 (2011).

[69] R.S. Becker, J. Seixas de Melo, A.L. Maçanita, and F. Elisei, J. Phys. Chem. **100**, 18683 (1996).

[70] M. Sun, T.A. Moore, and P.S. Song, J. Am. Chem. Soc. **94**, 1730 (1972).

[71] R.J. Buenker and S.D. Peyerimhoff, Theor. Chim. Acta **35**, 33 (1974).

[72] R.J. Buenker and R.A. Phillips, J. Mol. Struct. THEOCHEM **123**, 291 (1985).

To appear in *Molecular Physics*
Vol. 00, No. 00, Month 200x, 1–75

Supplemental Material for

On the Performance of DFT/MRCI-R and MR-MP2 in Spin–Orbit Coupling Calculations in Diatomics and Polyatomic Organic Molecules

Vladimir Jovanović[a], Igor Lyskov[a], Martin Kleinschmidt[a], and Christel M. Marian[a*]

[a] *Institute of Theoretical and Computational Chemistry, Heinrich-Heine-University Düsseldorf, Universitätsstraße 1, 40225 Düsseldorf, Germany*

(*May 29, 2016*)

---

*Corresponding author. Email: Christel.Marian@hhu.de

ISSN: 0040-5167 print/ISSN 1754-2278 online

DOI: 10.1080/0040516YYxxxxxxxx
http://www.informaworld.com

S1. On the calculation of SOMEs

In the SPOCK program all SOMEs between singlet and triplet states are initially computed with the $\hat{S}_{+1}$ operator. In this paper, the Cartesian x- and y-components of SOMEs between the $M_s = 1$ sublevel of a triplet state and a singlet state ($\langle T, M_s = 1|\hat{\mathcal{H}}_{\mathrm{SO\ x/y}}|S\rangle$) are presented. The x-components could be obtained from the initially calculated mixed-representation matrix element ($\langle T, M_s = 1|\hat{L}_{\mathrm{x}}\hat{S}_{+1}|S\rangle$) by multiplication with $-1/\sqrt{2}$ which arises from the relationship between the Cartesian and tensor forms of the spin operator, $\hat{S}_{\mathrm{x}} = (\hat{S}_{-1} - \hat{S}_{+1})/\sqrt{2}$. The corresponding relationship for the $\hat{S}_{\mathrm{y}}$ operator, $\hat{S}_{\mathrm{y}} = i(\hat{S}_{-1} + \hat{S}_{+1})/\sqrt{2}$ leads to the same factor of $-1/\sqrt{2}$ for the y-component of SOMEs. One should note that this choice of the imaginary phase in the $\hat{S}_{\mathrm{y}}$ operator is the reason for the real values of the $\hat{\mathcal{H}}_{\mathrm{SOy}}$ matrix elements. The x and z-components are imaginary since the angular momentum operator is a purely imaginary operator. [1] The chosen z-component of the Hamiltonian couples a singlet state with the $M_s = 0$ sublevel of a triplet ($\langle T, M_s = 0|\hat{\mathcal{H}}_{\mathrm{SO\ z}}|S\rangle$). To arrive at $\langle T, M_s = 0|\hat{L}_{\mathrm{z}}\hat{S}_{\mathrm{z}}|S\rangle$ starting from the "wrong" combination $\langle T, M_s = 1|\hat{L}_{\mathrm{z}}\hat{S}_{+1}|S\rangle$, one first needs to obtain the reduced matrix element (RME) by dividing the initially calculated matrix element by a 3-j symbol (only for the spin part, $\langle T, M_s = 1|\hat{S}_{+1}|S\rangle$), and then multiplying the RME with the new, appropriate 3-j symbol (corresponding to the $\langle T, M_s = 0|\hat{S}_0|S\rangle$). The values of these 3-j symbols happen to be the same, $1/\sqrt{3}$, and since $\hat{S}_{\mathrm{z}} = \hat{S}_0$, the conversion factor between the calculated "wrong" SOMEs and the appropriate ones is 1. The presented matrix elements between two triplet states are always of the form: $\langle T, M_s = 1|\hat{\mathcal{H}}_{\mathrm{SO\ x/y}}|T, M_s = 0\rangle$ and $\langle T, M_s = 1|\hat{\mathcal{H}}_{\mathrm{SO\ z}}|T, M_s = 1\rangle$ and could be obtained from the computed matrix elements by multiplying them with $1/\sqrt{2}$ in the case of x and y-components while the z-component does not need to be modified. In the tables, the imaginary unit (i) is omitted from the complex-valued matrix elements of the $\hat{\mathcal{H}}_{\mathrm{SO\ x}}$ and $\hat{\mathcal{H}}_{\mathrm{SO\ z}}$ operators and absolute values are presented instead.

S2. Statistical data and correlation plots

Table S1 shows the statistical data with regard the excitation energies employing the valence basis obtained at the DFT/MRCI-R, MR-MP2(HF) and MR-MP2(BH-LYP) levels of theory with respect to DFT/MRCI. Table S2 contains the corresponding statistical data for the SOMEs of each molecule individually and for the complete set of selected SOMEs, 278 in total. As the sign of an individual SOME depends on the (arbitrary) phases of the molecular orbitals (MOs) and of the wave functions, absolute values have been employed when computing the maximum positive and negative deviations of the SOMEs. Normalized RMSD (NRMSD), expressed as percentage, are given as the RMSD normalized by the range, i.e. the maximum value minus the minimum absolute value of the evaluated data.

Table S1. Deviations in energies of polyatomic molecules calculated with DFT/MRCI-R, MR-MP2(HF) and MR-MP2(BH-LYP) with respect to DFT/MRCI. The values are given in eV and the normalized RMSD (NRMSD) is expressed as percentage.

	DFT/MRCI-R				MR-MP2(HF)				MR-MP2(BH-LYP)			
Molecule	RMSD	NRMSD	Max. (+)	Max. (-)	RMSD	NRMSD	Max. (+)	Max. (-)	RMSD	NRMSD	Max. (+)	Max. (-)
o-benzyne	0.73	15	2.26	0.16	0.73	15	2.19	0.53	0.75	15	2.20	0.64
Formaldehyde	0.12	2	0.16	0.17	0.17	3	0.36	0.02	0.23	4	0.44	
Thioformaldehyde	0.59	10	0.53	1.82	0.33	6	0.37	0.71	0.34	6	0.36	0.73
Furan	0.04	1	0.06	0.09	0.25	6	0.40	0.31	0.30	7	0.42	0.44
Thiophene	0.04	1	0.07	0.06	0.16	5	0.17	0.32	0.20	6	0.10	0.46
Quinoxaline	0.10	5	0.18	0.12	0.30	16	0.32	0.58	0.39	21	0.21	0.77
Quinazoline	0.09	4	0.14	0.06	0.31	18	0.14	0.46	0.50	30		0.76
Pyranthione	0.08	2	0.06	0.19	0.12	4	0.19	0.16	0.15	5	0.11	0.22
Dithiin	0.07	2	0.11	0.11	0.34	14		0.53	0.46	19		0.76
Bithiophene	0.05	2	0.09	0.06	0.19	7	0.26	0.37	0.52	21		0.77
Nitromethane	0.39	7	0.16	1.26	0.42	8	1.15	0.37	0.47	9	1.34	0.41
Nitrobenzene	0.09	5	0.17	0.01	0.85	20	2.56	0.11	0.78	20	2.37	0.15
Dithiosuccinimide	0.58	23	0.13	1.32	0.65	15	1.99	0.56	0.69	17	1.87	0.81
Methionine	0.26	19	0.33		0.84	61	1.00		0.12	8	0.18	
Isoalloxazine	0.09	5	0.15	0.04	0.37	27	0.68	0.19	0.34	22	0.69	0.39
All (161 exc states)	0.33	5	2.26	1.82	0.47	6	2.56	0.71	0.49	6	2.37	0.81

Table S2. Deviations in SOMEs of polyatomic molecules calculated with DFT/MRCI-R, MR-MP2(HF) and MR-MP2(BH-LYP) with respect to DFT/MRCI. The values are given in cm^{-1} and the normalized RMSD (NRMSD) is expressed as percentage.

	DFT/MRCI-R				MR-MP2(HF)				MR-MP2(BH-LYP)			
Molecule	RMSD	NRMSD	Max. (+)	Max. (-)	RMSD	NRMSD	Max. (+)	Max. (-)	RMSD	NRMSD	Max. (+)	Max. (-)
o-benzyne	0.1	2	0.1	0.2	0.4	6	1.1	0.4	0.3	4	0.8	0.3
Formaldehyde	5.2	9	0.6	20.5	2.7	4	2.9	8.7	3.1	5	3.4	9.9
Thioformaldehyde	30.2	18	79.8	100.9	10.4	7	5.5	25.0	7.5	5	4.7	16.6
Furan	0.2	2		0.3	0.8	8	0.4	1.6	0.6	7	0.6	1.1
Thiophene	1.1	1	2.0	2.0	9.6	9	5.1	18.6	7.4	7	7.2	14.6
Quinoxaline	0.7	2	0.9	1.5	0.9	2	0.4	2.3	0.5	1	0.4	1.0
Quinazoline	0.4	2	0.2	1.1	0.9	5	1.7	2.0	0.8	5	1.8	1.8
Pyranthione	2.2	1	4.3	2.9	8.8	6	5.1	17.3	4.8	3	6.0	10.0
Dithiin	1.7	1	2.7	5.9	14.1	10	42.7	57.4	15.2	10	46.6	51.2
Bithiophene	1.4	4	0.8	4.6	8.3	27	15.8	22.9	6.5	23	12.7	15.7
Nitromethane	0.8	2	0.5	1.5	2.6	6	6.3	5.5	1.6	4	3.0	1.6
Nitrobenzene	2.4	4	6.2	2.1	2.4	4	5.7	5.0	2.5	4	5.3	5.1
Dithiosuccinimide	1.5	1		4.2	6.1	5	0.1	14.7	3.8	3	4.0	6.8
Methionine	0.7	0	0.3	2.0	5.5	7	1.4	16.5	4.2	5	1.0	12.7
Isoalloxazine	1.0	5	1.2	3.2	3.7	14	5.4	8.7	3.7	14	5.7	10.3
All (278 SOMEs)	8.3	5	79.8	100.9	8.1	5	42.7	57.4	7.7	5	46.6	51.2

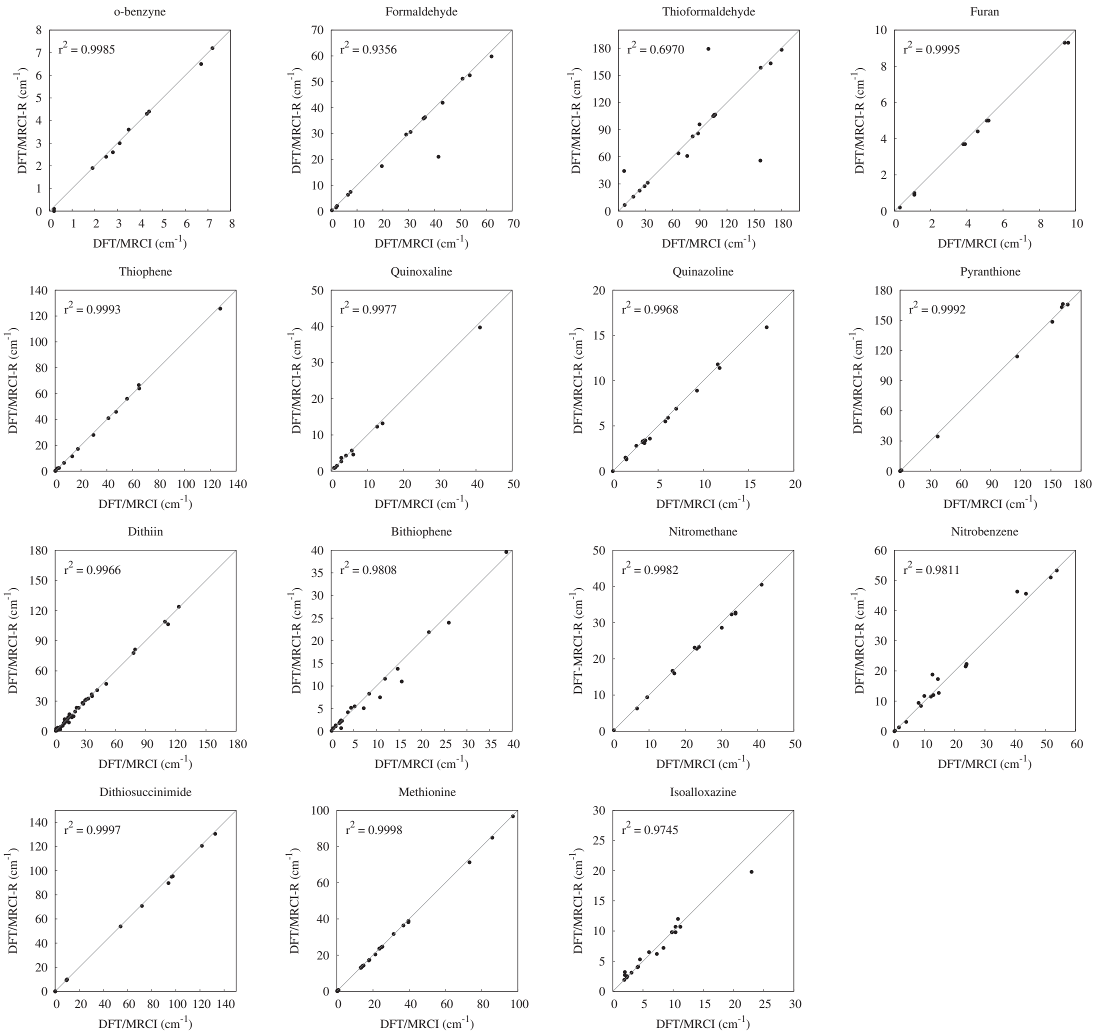

Figure S1. Correlation plots of SOMEs for individual polyatomic molecules calculated with DFT-MRCI-R method vs SOMEs calculated with DFT/MRCI.

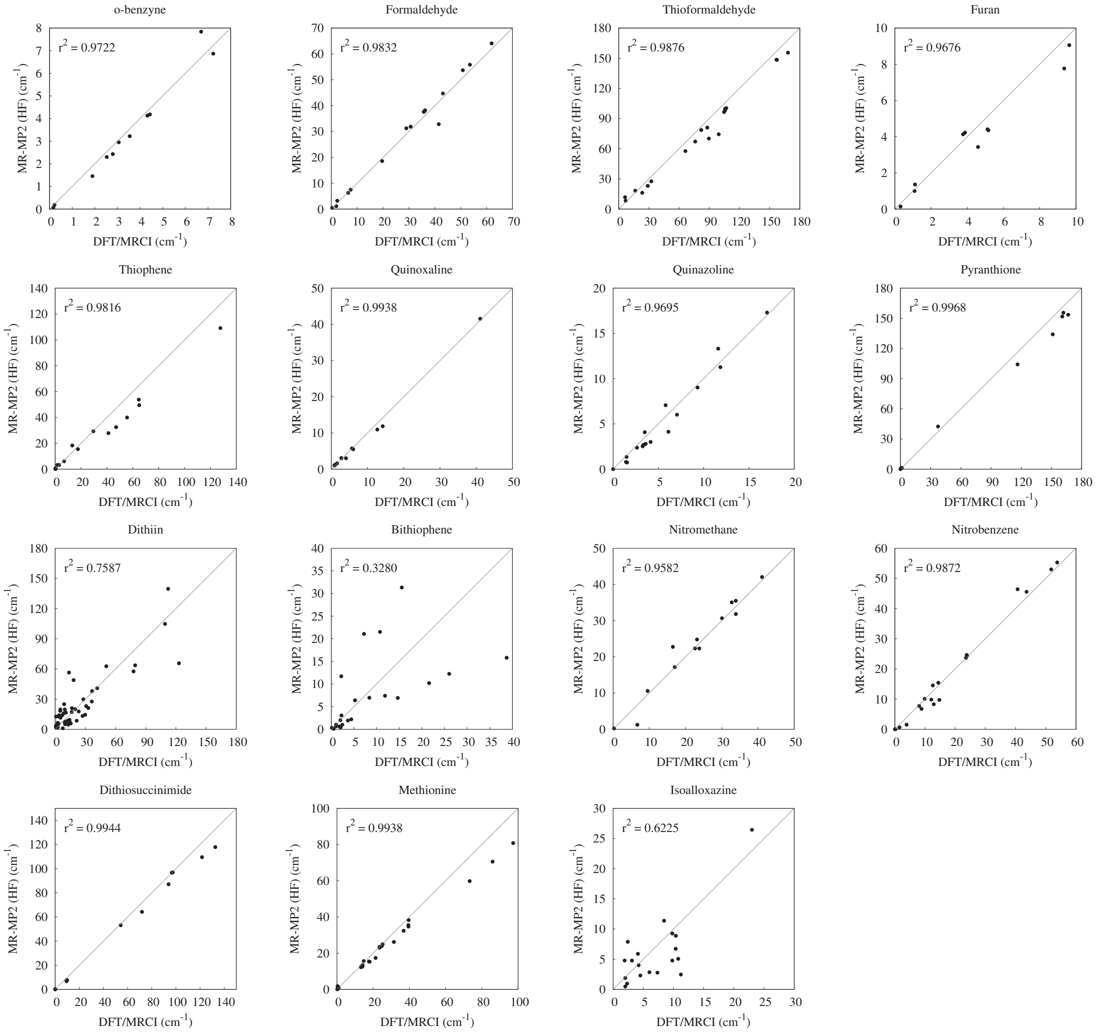

Figure S2. Correlation plots of SOMEs for individual polyatomic molecules calculated with MR-MP2(HF) method vs SOMEs calculated with DFT/MRCI.

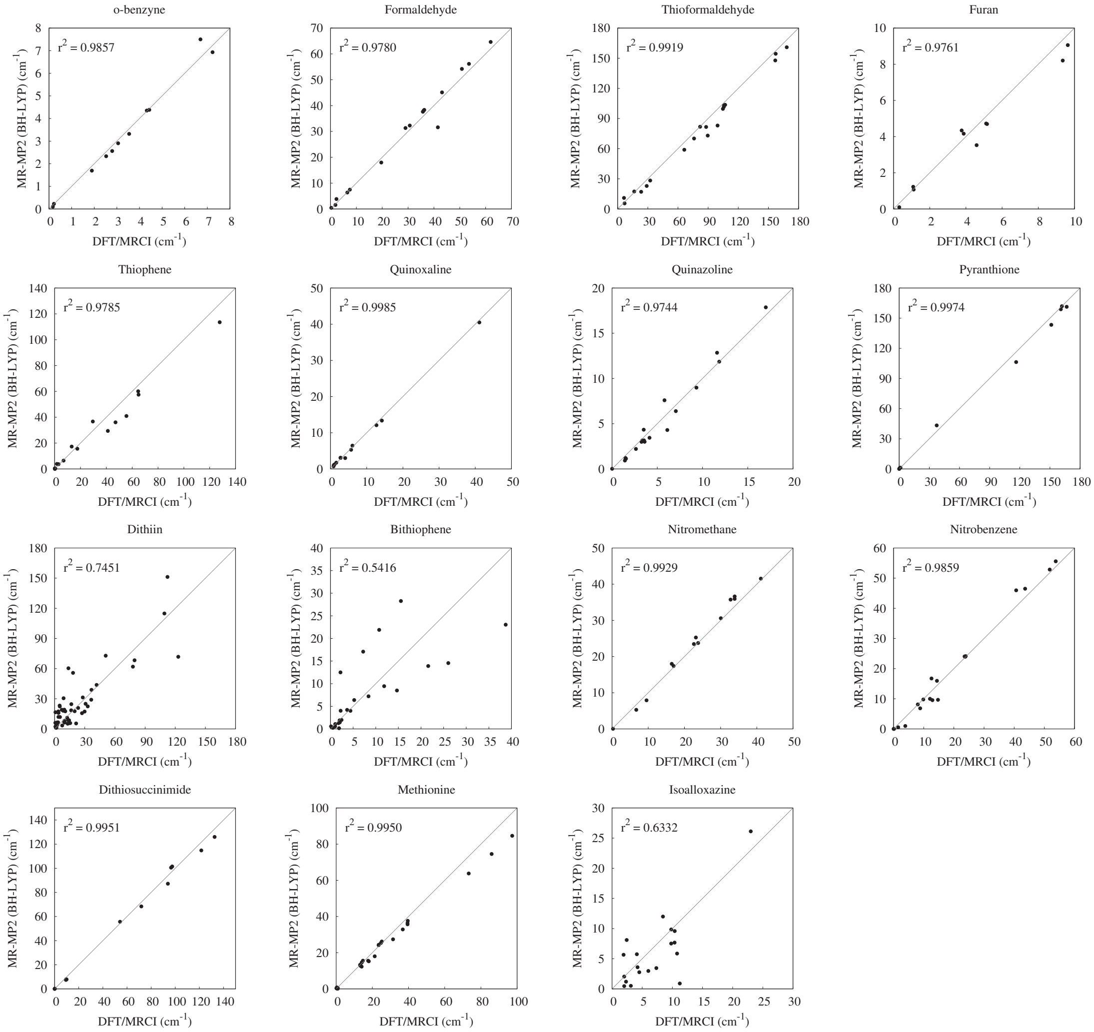

Figure S3. Correlation plots of SOMEs for individual polyatomic molecules calculated with MR-MP2(BH-LYP) method vs SOMEs calculated with DFT/MRCI.

S3. Molecular orbitals

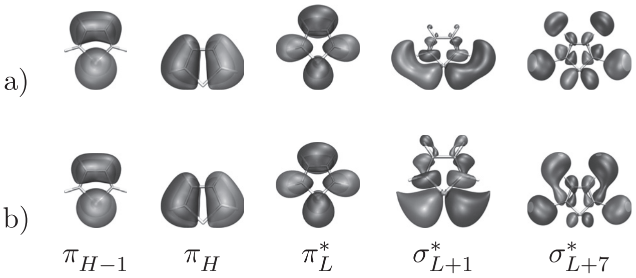

Figure S4. Molecular orbitals of thiophene, calculated employing the valence basis. a) HF orbitals, b) BH-LYP orbitals.

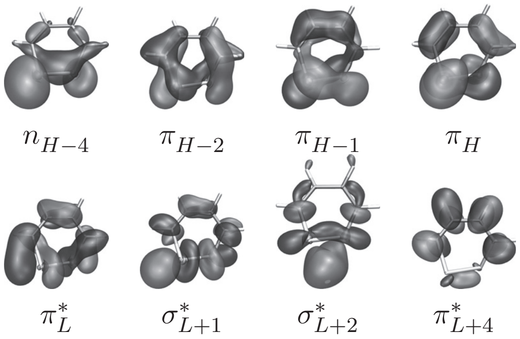

Figure S5. BH-LYP molecular orbitals of dithiin involved in the discussed states.

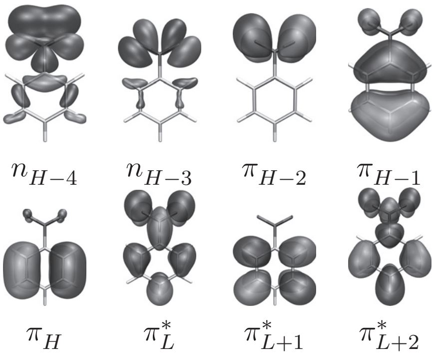

Figure S6. BH-LYP molecular orbitals of nitrobenzene involved in the discussed states.

S4. Individual molecules

S4.1. *o-benzyne*

Table S3. Experimental and computed DFT/MRCI, DFT/MRCI-R, MR-MP2(HF) and MR-MP2(BH-LYP) vertical excitation energies of **o-benzyne**. The oscillator strengths are given in the parentheses.

		Energies(eV)				
State	Dominant character	DFT/MRCI	DFT/MRCI-R	MRMP2 (HF)	MRMP2 (BH-LYP)	Experiment
$1^1\mathrm{A}_2$	$\pi \rightarrow \pi^*_{\parallel}$	3.89 (0)	3.83 (0)	4.22 (0)	4.20 (0)	
$1^1\mathrm{B}_2$	$\pi \rightarrow \pi^*_{\parallel}$	3.97 (0.002)	3.92 (0.002)	4.27 (0.002)	4.21 (0.002)	
$2^1\mathrm{A}_1$	$\pi_{\parallel}, \pi \rightarrow \pi^*_{\parallel}, \pi^*$	4.24 (0)	6.50 (0.003)[1]	6.43 (0)[1]	6.44 (0)[1]	
$1^1\mathrm{B}_1$	$\pi_{\parallel} \rightarrow \pi^*_{\parallel}$	5.09 (0.037)	4.94 (0.046)	5.12 (0.024)	5.01 (0.030)	**5.08**[a]
$3^1\mathrm{A}_1$	$\pi \rightarrow \pi^*$	5.28 (0.013)	5.19 (0.018)[2]	4.75 (0.006)[2]	4.64 (0.002)[2]	
$2^1\mathrm{B}_2$	$\pi_{\parallel} \rightarrow \pi^*$	5.38 (0.005)	5.38 (0.005)	5.54 (0.004)	5.47 (0.005)	
$2^1\mathrm{B}_1$	$\pi_{\parallel}, \pi \rightarrow \pi^*_{\parallel}, \pi^*$	5.74 (0)	7.25 (0.019)[3]	7.22 (0.001)[3]	7.22 (0.001)[3]	
⋮						
$3^1\mathrm{B}_1$	$\pi \rightarrow \pi^*$	6.38 (0.183)	6.23 (0.178)[4]	6.34 (0.106)[4]	6.08 (0.089)[4]	**6.25**[a]
$1^3\mathrm{B}_1$	$\pi_{\parallel} \rightarrow \pi^*_{\parallel}$	2.43	2.30	2.25	2.25	
$1^3\mathrm{A}_2$	$\pi \rightarrow \pi^*_{\parallel}$	3.49	3.44	3.68	3.64	
$1^3\mathrm{B}_2$	$\pi \rightarrow \pi^*_{\parallel}$	3.88	3.80	4.12	4.10	
$2^3\mathrm{B}_1$	$\pi \rightarrow \pi^*$	4.18	4.03	3.93	3.82	
$1^3\mathrm{A}_1$	$\pi \rightarrow \pi^*$	4.83	4.67	4.58	4.46	
$2^3\mathrm{B}_2$	$\pi_{\parallel} \rightarrow \pi^*$	5.30	5.26	5.38	5.43	
⋮						
$2^3\mathrm{A}_1$	$\pi_{\parallel}, \pi \rightarrow \pi^*_{\parallel}, \pi^*$	5.69	6.37[5]	6.27[5]	6.26[5]	

DFT/MRCI-R: [1] $3^1\mathrm{A}_1$, [2] $2^1\mathrm{A}_1$, [3] $3^1\mathrm{B}_1$, [4] $2^1\mathrm{B}_1$, [5] $3^3\mathrm{A}_1$
MR-MP2(HF): [1] $3^1\mathrm{A}_1$, [2] $2^1\mathrm{A}_1$, [3] $4^1\mathrm{B}_1$, [4] $2^1\mathrm{B}_1$, [5] $3^3\mathrm{A}_1$
MR-MP2(BH-LYP): [1] $3^1\mathrm{A}_1$, [2] $2^1\mathrm{A}_1$, [3] $4^1\mathrm{B}_1$, [4] $2^1\mathrm{B}_1$, [5] $3^3\mathrm{A}_1$
[a] (Absorption maximum (Ar matrix)) [2]

Table S4.: Calculated percentage of electron configurations in the excited states wave functions of **o-benzyne** obtained at the DFT/MRCI, MR-MP2(HF) and MR-MP2(BH-LYP) levels of theory. Only electron configurations with more than 2 percentage are presented.

	DFT/MRCI (BH-LYP)			MRMP2 (HF)			MRMP2 (BH-LYP)		
		Excitation			Excitation			Excitation	
State	%	from	to	%	from	to	%	from	to
1^1A_2	89	π_{H-1}	$\pi^*_{\parallel}$	65	π_{H-1}	$\pi^*_{\parallel}$	65	π_{H-1}	$\pi^*_{\parallel}$
	3	π_{H-3}	$\pi^*_{\parallel}$	4	π_{H-3}	$\pi^*_{\parallel}$	3	π_{H-3}	$\pi^*_{\parallel}$
	2	π_{H-1},π_H	$\pi^*_{\parallel}$,π^*_{L+2}	2	π_{H-1},π_H	$\pi^*_{\parallel}$,π^*_{L+2}	2	π_{H-1},π_H	$\pi^*_{\parallel}$,π^*_{L+2}
1^1B_2	88	π_H	$\pi^*_{\parallel}$	65	π_H	$\pi^*_{\parallel}$	64	π_H	$\pi^*_{\parallel}$
	4	π_{H-1},π_H	$\pi^*_{\parallel}$,π^*_{L+1}	3	π_{H-1},π_H	$\pi^*_{\parallel}$,π^*_{L+1}	4	π_{H-1},π_H	$\pi^*_{\parallel}$,π^*_{L+1}
	2	π_{H-3},π_H	$\pi^*_{\parallel}$,π^*_{L+1}	2	π_{H-3},π_H	$\pi^*_{\parallel}$,π^*_{L+1}	2	π_{H-3},π_H	$\pi^*_{\parallel}$,π^*_{L+1}
2^1A_1	88	$\pi_{\parallel}$,π_H	$\pi^*_{\parallel}$,π^*_{L+1}	59	$\pi_{\parallel}$,π_H	$\pi^*_{\parallel}$,π^*_{L+1}	61	$\pi_{\parallel}$,π_H	$\pi^*_{\parallel}$,π^*_{L+1}
	2	$\pi_{\parallel}$,π_{H-1}	$\pi^*_{\parallel}$,π^*_{L+2}	5	$\pi_{\parallel}$,π_{H-1}	$\pi^*_{\parallel}$,π^*_{L+2}	4	$\pi_{\parallel}$,π_{H-1}	$\pi^*_{\parallel}$,π^*_{L+2}
1^1B_1	79	$\pi_{\parallel}$	$\pi^*_{\parallel}$	53	$\pi_{\parallel}$	$\pi^*_{\parallel}$	54	$\pi_{\parallel}$	$\pi^*_{\parallel}$
	11	π_{H-1}	π^*_{L+2}	14	π_{H-1}	π^*_{L+2}	12	π_{H-1}	π^*_{L+2}
	2	π_{H-3}	π^*_{L+2}	2	π_{H-3}	π^*_{L+2}	2	π_{H-3}	π^*_{L+2}
2^1B_2	90	$\pi_{\parallel}$	π^*_{L+1}	66	$\pi_{\parallel}$	π^*_{L+1}	66	$\pi_{\parallel}$	π^*_{L+1}
	2	σ_{H-5},$\pi_{\parallel}$	$\pi^*_{\parallel}$,π^*_{L+1}	2	$\pi_{\parallel}$,π_H	π^*_{L+1},π^*_{L+2}	2	$\pi_{\parallel}$,π_H	π^*_{L+1},π^*_{L+2}
2^1B_1	62	$\pi_{\parallel}$,π_{H-1}	$\pi^*_{\parallel}$,π^*_{L+1}	42	$\pi_{\parallel}$,π_{H-1}	$\pi^*_{\parallel}$,π^*_{L+1}	42	$\pi_{\parallel}$,π_{H-1}	$\pi^*_{\parallel}$,π^*_{L+1}
	27	$\pi_{\parallel}$,π_H	$\pi^*_{\parallel}$,π^*_{L+2}	21	$\pi_{\parallel}$,π_H	$\pi^*_{\parallel}$,π^*_{L+2}	21	$\pi_{\parallel}$,π_H	$\pi^*_{\parallel}$,π^*_{L+2}
1^3B_1	94	$\pi_{\parallel}$	$\pi^*_{\parallel}$	69	$\pi_{\parallel}$	$\pi^*_{\parallel}$	69	$\pi_{\parallel}$	$\pi^*_{\parallel}$
1^3A_2	88	π_{H-1}	$\pi^*_{\parallel}$	62	π_{H-1}	$\pi^*_{\parallel}$	62	π_{H-1}	$\pi^*_{\parallel}$
	6	π_{H-3}	$\pi^*_{\parallel}$	7	π_{H-3}	$\pi^*_{\parallel}$	6	π_{H-3}	$\pi^*_{\parallel}$
1^3B_2	91	π_H	$\pi^*_{\parallel}$	65	π_H	$\pi^*_{\parallel}$	64	π_H	$\pi^*_{\parallel}$
	3	π_{H-1},π_H	$\pi^*_{\parallel}$,π^*_{L+1}	4	π_{H-1},π_H	$\pi^*_{\parallel}$,π^*_{L+1}	4	π_{H-1},π_H	$\pi^*_{\parallel}$,π^*_{L+1}
				2	π_{H-3},π_H	$\pi^*_{\parallel}$,π^*_{L+1}	2	π_{H-3},π_H	$\pi^*_{\parallel}$,π^*_{L+1}
2^3B_1	87	π_H	π^*_{L+1}	62	π_H	π^*_{L+1}	61	π_H	π^*_{L+1}
	5	π_{H-1}	π^*_{L+2}	6	π_{H-1}	π^*_{L+2}	6	π_{H-1}	π^*_{L+2}
1^3A_1	79	π_{H-1}	π^*_{L+1}	50	π_{H-1}	π^*_{L+1}	47	π_{H-1}	π^*_{L+1}
	12	π_H	π^*_{L+2}	16	π_H	π^*_{L+2}	18	π_H	π^*_{L+2}
				2	π_{H-3},π_H	π^*_{L+1},π^*_{L+2}	2	π_{H-3},π_H	π^*_{L+1},π^*_{L+2}
2^3B_2	92	$\pi_{\parallel}$	π^*_{L+1}	68	$\pi_{\parallel}$	π^*_{L+1}	67	$\pi_{\parallel}$	π^*_{L+1}
	2	σ_{H-5},$\pi_{\parallel}$	$\pi^*_{\parallel}$,π^*_{L+1}	2	$\pi_{\parallel}$,π_H	π^*_{L+1},π^*_{L+2}	2	$\pi_{\parallel}$,π_H	π^*_{L+1},π^*_{L+2}
2^3A_1	87	$\pi_{\parallel}$,π_H	$\pi^*_{\parallel}$,π^*_{L+1}	61	$\pi_{\parallel}$,π_H	$\pi^*_{\parallel}$,π^*_{L+1}	61	$\pi_{\parallel}$,π_H	$\pi^*_{\parallel}$,π^*_{L+1}
	3	$\pi_{\parallel}$,π_{H-1}	$\pi^*_{\parallel}$,π^*_{L+2}						

Table S5.: Calculated percentage of electron configurations in the excited states wave functions of **o-benzyne** obtained at the DFT/MRCI, and DFT/MRCI-R levels of theory. Only electron configurations with more than 2 percentage are presented.

	DFT/MRCI			DFT/MRCI-R		
		Excitation			Excitation	
State	%	from	to	%	from	to
1^1A_2	89	π_{H-1}	$\pi^*_{\parallel}$	90	π_{H-1}	$\pi^*_{\parallel}$
	3	π_{H-3}	$\pi^*_{\parallel}$	3	π_{H-3}	$\pi^*_{\parallel}$
	2	π_{H-1},π_H	$\pi^*_{\parallel}$,π^*_{L+2}	1	π_{H-1},π_H	$\pi^*_{\parallel}$,π^*_{L+2}
1^1B_2	88	π_H	$\pi^*_{\parallel}$	89	π_H	$\pi^*_{\parallel}$
	4	π_{H-1},π_H	$\pi^*_{\parallel}$,π^*_{L+1}	2	π_{H-1},π_H	$\pi^*_{\parallel}$,π^*_{L+1}
	2	π_{H-3},π_H	$\pi^*_{\parallel}$,π^*_{L+1}	2	π_{H-3},π_H	$\pi^*_{\parallel}$,π^*_{L+1}
2^1A_1	90	$\pi_{\parallel}$,π_H	$\pi^*_{\parallel}$,π^*_{L+1}	85	$\pi_{\parallel}$,π_H	$\pi^*_{\parallel}$,π^*_{L+1}
	2	$\pi_{\parallel}$,π_{H-1}	$\pi^*_{\parallel}$,π^*_{L+2}	3	$\pi_{\parallel}$,π_{H-1}	$\pi^*_{\parallel}$,π^*_{L+2}
1^1B_1	79	$\pi_{\parallel}$	$\pi^*_{\parallel}$	81	$\pi_{\parallel}$	$\pi^*_{\parallel}$
	11	π_{H-1}	π^*_{L+2}	11	π_{H-1}	π^*_{L+2}
	2	π_{H-3}	π^*_{L+2}	1	π_{H-3}	π^*_{L+2}
2^1B_2	90	$\pi_{\parallel}$	π^*_{L+1}	92	$\pi_{\parallel}$	π^*_{L+1}
	2	σ_{H-5},$\pi_{\parallel}$	$\pi^*_{\parallel}$,π^*_{L+1}			
2^1B_1	62	$\pi_{\parallel}$,π_{H-1}	$\pi^*_{\parallel}$,π^*_{L+1}	71	$\pi_{\parallel}$,π_{H-1}	$\pi^*_{\parallel}$,π^*_{L+1}
	27	$\pi_{\parallel}$,π_H	$\pi^*_{\parallel}$,π^*_{L+2}	15	$\pi_{\parallel}$,π_H	$\pi^*_{\parallel}$,π^*_{L+2}
1^3B_1	94	$\pi_{\parallel}$	$\pi^*_{\parallel}$	95	$\pi_{\parallel}$	$\pi^*_{\parallel}$
1^3A_2	88	π_{H-1}	$\pi^*_{\parallel}$	88	π_{H-1}	$\pi^*_{\parallel}$
	6	π_{H-3}	$\pi^*_{\parallel}$	5	π_{H-3}	$\pi^*_{\parallel}$
1^3B_2	91	π_H	$\pi^*_{\parallel}$	90	π_H	$\pi^*_{\parallel}$
	3	π_{H-1},π_H	$\pi^*_{\parallel}$,π^*_{L+1}	2	π_{H-1},π_H	$\pi^*_{\parallel}$,π^*_{L+1}
2^3B_1	87	π_H	π^*_{L+1}	89	π_H	π^*_{L+1}
	5	π_{H-1}	π^*_{L+2}	4	π_{H-1}	π^*_{L+2}
1^3A_1	79	π_{H-1}	π^*_{L+1}	80	π_{H-1}	π^*_{L+1}
	12	π_H	π^*_{L+2}	12	π_H	π^*_{L+2}
2^3B_2	92	$\pi_{\parallel}$	π^*_{L+1}	92	$\pi_{\parallel}$	π^*_{L+1}
	2	σ_{H-5},$\pi_{\parallel}$	$\pi^*_{\parallel}$,π^*_{L+1}			
2^3A_1	87	$\pi_{\parallel}$,π_H	$\pi^*_{\parallel}$,π^*_{L+1}	86	$\pi_{\parallel}$,π_H	$\pi^*_{\parallel}$,π^*_{L+1}
	3	$\pi_{\parallel}$,π_{H-1}	$\pi^*_{\parallel}$,π^*_{L+2}			

S4.2. *Formaldehyde*

Table S6. Experimental and computed DFT/MRCI, DFT/MRCI-R, MR-MP2(HF) and MR-MP2(BH-LYP) vertical excitation energies of **formaldehyde** using the valence basis. The oscillator strengths are given in the parentheses.

State	Dominant character	Energies(eV)				
		DFT/MRCI	DFT/MRCI-R	MRMP2 (HF)	MRMP2 (BH-LYP)	Experiment
1^1A_2	$n \to \pi^*$	3.86 (0)	3.94 (0)	3.97 (0)	4.07 (0)	3.79[a], **3.94**[b]
1^1B_2	$n \to Ryd$	8.31 (0.121)	8.14 (0.119)	8.29 (0.099)	8.35 (0.117)	
1^1B_1	$\sigma \to \pi^*$	9.00 (0.004)	9.03 (0.005)	9.17 (0.002)	9.26 (0.002)	9.0[c]
2^1A_1	$\pi \to \pi^*$	9.42 (0.079)	9.26 (0.077)	9.43 (0.063)	9.50 (0.031)	
1^3A_2	$n \to \pi^*$	3.43	3.59	3.57	3.66	3.50[a], **3.50**[b]
1^3A_1	$\pi \to \pi^*$	5.77	5.76	6.13	6.21	5.82[a], **5.86**[b]
1^3B_2	$n \to Ryd$	7.77	7.69	7.75	7.80	
1^3B_1	$\sigma \to \pi^*$	8.23	8.36	8.40	8.45	

[a] Energy-loss maximum (vapor) [3]

[b] Energy-loss maximum (vapor) [4]

[c] Energy-loss band origin (vapor) [5]

Table S7.: Calculated percentage of electron configurations in the excited states wave functions of **formaldehyde** obtained at the DFT/MRCI, MR-MP2(HF) and MR-MP2(BH-LYP) levels of theory using the valence basis. Only electron configurations with more than 2 percentage are presented.

	DFT/MRCI (BH-LYP)			MRMP2 (HF)			MRMP2 (BH-LYP)		
		Excitation			Excitation			Excitation	
State	%	from	to	%	from	to	%	from	to
1^1A_2	93	n_H	π^*_L	78	n_H	π^*_L	82	n_H	π^*_L
	3	π_{H-1},n_H	π^*_L,π^*_L	4	n_H	Ry_{L+5}	3	π_{H-1},n_H	π^*_L,π^*_L
	2	n_H	Ry_{L+5}	3	π_{H-3}	π^*_L	2	π_{H-3}	π^*_L
				3	π_{H-1},n_H	π^*_L,π^*_L			
1^1B_2	94	n_H	Ry_{L+1}	78	n_H	Ry_{L+1}	79	n_H	Ry_{L+1}
	3	π_{H-1},n_H	π^*_L,Ry_{L+1}	3	π_{H-1},n_H	π^*_L,Ry_{L+1}	4	π_{H-1},n_H	π^*_L,Ry_{L+1}
				3	n_H	Ry_{L+2}	2	n_H	Ry_{L+2}
1^1B_1	93	σ_{H-2}	π^*_L	78	σ_{H-2}	π^*_L	82	σ_{H-2}	π^*_L
	3	σ_{H-2},π_{H-1}	π^*_L,π^*_L	4	σ_{H-2}	Ry_{L+5}	5	σ_{H-2},π_{H-1}	π^*_L,π^*_L
	2	σ_{H-2}	Ry_{L+5}	3	σ_{H-2},π_{H-1}	π^*_L,π^*_L			
2^1A_1	67	π_{H-1}	π^*_L	59	π_{H-1}	π^*_L	53	π_{H-1}	π^*_L
	22	n_H	σ^*	13	n_H	σ^*	17	n_H	σ^*
	4	π_{H-1}, π_{H-1}	π^*_L,π^*_L	4	π_{H-1}, π_{H-1}	π^*_L,π^*_L	5	n_H, n_H	π^*_L,π^*_L
				4	n_H, n_H	π^*_L,π^*_L	5	π_{H-1}, π_{H-1}	π^*_L,π^*_L
1^3A_2	95	n_H	π^*_L	79	n_H	π^*_L	83	n_H	π^*_L
	2	n_H	Ry_{L+5}	4	n_H	Ry_{L+5}	2	π_{H-1},n_H	π^*_L,π^*_L
				3	π_{H-3}	π^*_L	2	π_{H-3}	π^*_L
1^3A_1	97	π_{H-1}	π^*_L	84	π_{H-1}	π^*_L	89	π_{H-1}	π^*_L
	2	π_{H-1}	Ry_{L+5}	6	π_{H-1}	Ry_{L+5}	2	π_{H-1}	Ry_{L+5}
				2	π_{H-1}	Ry_{L+10}			
1^3B_2	95	n_H	Ry_{L+1}	80	n_H	Ry_{L+1}	80	n_H	Ry_{L+1}
	2	π_{H-1},n_H	π^*_L,Ry_{L+1}	3	π_{H-1},n_H	π^*_L,Ry_{L+1}	3	π_{H-1},n_H	π^*_L,Ry_{L+1}
1^3B_1	95	σ_{H-2}	π^*_L	78	σ_{H-2}	π^*_L	83	σ_{H-2}	π^*_L
	2	σ_{H-2}	Ry_{L+5}	6	σ_{H-2}	Ry_{L+5}	3	σ_{H-2},π_{H-1}	π^*_L,π^*_L
				2	σ_{H-2},π_{H-1}	π^*_L,π^*_L			

Table S8.: Calculated percentage of electron configurations in the 2^1A_1 state wave function of **formaldehyde** obtained at the DFT/MRCI, and DFT/MRCI-R levels of theory using the valence basis. Only electron configurations with more than 2 percentage are presented.

	DFT/MRCI			DFT/MRCI-R		
		Excitation			Excitation	
State	%	from	to	%	from	to
2^1A_1	67	π_{H-1}	π^*_L	56	π_{H-1}	π^*_L
	22	n_H	σ^*	19	n_H	σ^*
	4	π_{H-1}, π_{H-1}	π^*_L,π^*_L	17	n_H, n_H	π^*_L,π^*_L
				2	π_{H-1}, π_{H-1}	π^*_L,π^*_L

Table S9. Selected matrix elements (cm^{-1}) for **formaldehyde** calculated with DFT/MRCI, DFT/MRCI-R, MR-MP2(HF) and MR-MP2(BH-LYP) methods using the valence basis.

	SOMEs(cm^{-1})			
	DFT/MRCI	DFT/MRCI-R	MRMP2 (HF)	MRMP2 (BH-LYP)
$\langle 1^3A_2 \vert \hat{\mathcal{H}}_{\mathrm{SO\ z}} \vert 1^1A_1 \rangle$	62.0	59.8	64.1	64.6
$\langle 1^3A_2 \vert \hat{\mathcal{H}}_{\mathrm{SO\ z}} \vert 2^1A_1 \rangle$	41.5	21.0	32.8	31.6
$\langle 1^3B_1 \vert \hat{\mathcal{H}}_{\mathrm{SO\ y}} \vert 1^1A_1 \rangle$	43.1	41.9	44.7	45.1
$\langle 1^3B_1 \vert \hat{\mathcal{H}}_{\mathrm{SO\ y}} \vert 2^1A_1 \rangle$	19.6	17.4	18.6	18.0
$\langle 1^3A_1 \vert \hat{\mathcal{H}}_{\mathrm{SO\ z}} \vert 1^1A_2 \rangle$	53.6	52.5	55.8	56.1
$\langle 1^3B_1 \vert \hat{\mathcal{H}}_{\mathrm{SO\ x}} \vert 1^1A_2 \rangle$	36.3	36.3	38.2	38.3
$\langle 1^3A_1 \vert \hat{\mathcal{H}}_{\mathrm{SO\ y}} \vert 1^1B_1 \rangle$	30.7	30.6	31.9	32.3
$\langle 1^3A_2 \vert \hat{\mathcal{H}}_{\mathrm{SO\ x}} \vert 1^1B_1 \rangle$	35.7	35.8	37.6	37.6
$\langle 1^3B_2 \vert \hat{\mathcal{H}}_{\mathrm{SO\ x}} \vert 1^1A_1 \rangle$	7.5	7.4	7.5	7.5
$\langle 1^3B_2 \vert \hat{\mathcal{H}}_{\mathrm{SO\ x}} \vert 2^1A_1 \rangle$	1.9	1.4	1.1	1.6
$\langle 1^3B_2 \vert \hat{\mathcal{H}}_{\mathrm{SO\ y}} \vert 1^1A_2 \rangle$	6.5	6.3	6.3	6.4
$\langle 1^3B_2 \vert \hat{\mathcal{H}}_{\mathrm{SO\ z}} \vert 1^1B_1 \rangle$	2.3	2.0	3.2	3.9
$\langle 1^3A_1 \vert \hat{\mathcal{H}}_{\mathrm{SO\ x}} \vert 1^1B_2 \rangle$	0.3	0.3	0.5	0.4
$\langle 1^3A_2 \vert \hat{\mathcal{H}}_{\mathrm{SO\ z}} \vert 1^3A_1 \rangle$	50.8	51.2	53.7	54.2
$\langle 1^3B_1 \vert \hat{\mathcal{H}}_{\mathrm{SO\ y}} \vert 1^3A_1 \rangle$	29.0	29.6	31.3	31.3
$\langle 1^3B_1 \vert \hat{\mathcal{H}}_{\mathrm{SO\ x}} \vert 1^3A_2 \rangle$	36.0	36.0	37.9	38.1

Table S10. Experimental and computed DFT/MRCI, DFT/MRCI-R, MR-MP2(HF), MR-MP2(BH-LYP) and CASPT2 vertical excitation energies of **formaldehyde** using the augmented basis. The CASPT2 (8,11) active space consists of fallowing occupied/unoccupied orbitals: 1/3 a_1, 1/2 b_1 and 2/2 b_2. The oscillator strengths are given in the parentheses.

State	Dominant character	Energies(eV)						
		DFT/MRCI	DFT/MRCI-R	MRMP2 (HF)	MRMP2 (BH-LYP)	CASPT2 (8,9)	CASPT2 (8,11)	Experiment
1^1A_2	$n \rightarrow \pi^*$	3.67 (0)	3.81 (0)	3.88 (0)	3.93 (0)	3.90	3.99 (0)	3.79[a], **3.94**[b]
1^1B_2	$n \rightarrow 3s$	7.02 (0.032)	6.93 (0.034)	6.99 (0.010)	6.99 (0.023)	6.77	6.87 (0.035)	**7.09**[c]
2^1B_2	$n \rightarrow 3p_z$	7.86 (0.039)	7.84 (0.032)	7.92 (0.026)	8.17 (0.034)	7.68	7.76 (0.027)	**8.13**[c]
2^1A_1	$n \rightarrow 3p_y$	7.96 (0.054)	7.88 (0.052)	7.99 (0.035)	8.04 (0.042)	7.78	7.84 (0.058)	**7.98**[c]
2^1A_2	$n \rightarrow 3p_x$	8.40 (0)	8.26 (0)	8.14 (0)	8.24 (0)	7.95	8.00 (0)	**8.37**[d]
1^1B_1	$\sigma \rightarrow \pi^*$	8.81 (0.004)	8.90 (0.005)	9.12 (0.006)	9.20 (0.002)	9.21	9.43 (0.014)	9.0[e]
⋮								
4^1A_1	$\pi \rightarrow \pi^*$	9.51 (0.193)	9.50 (0.197)†	9.64 (0.129)	9.64 (0.126)	9.33	10.41 (0.129)[n]	
⋮								
5^1A_1	$n^2 \rightarrow \pi^{*2}$	11.06 (0.008)	9.20 (0.022)‡	10.67 (0.007)	10.75 (0.016)	10.29[m]	10.87(0.030)[p]	
1^3A_2	$n \rightarrow \pi^*$	3.23	3.46	3.42	3.46	3.45	3.56	3.50[a], **3.50**[b]
1^3A_1	$\pi \rightarrow \pi^*$	5.58	5.71	6.13	6.18	6.04	6.04	5.82[a], **5.86**[b]
1^3B_2	$n \rightarrow 3s$	6.78	6.75	6.79	6.79	6.65	6.75	
2^3B_2	$n \rightarrow 3p_z$	7.67	7.71	7.82	7.86	7.57	7.65	
2^3A_1	$n \rightarrow 3p_y$	7.76	7.72	7.90	8.11	7.67	7.73	
1^3B_1	$\sigma \rightarrow \pi^*$	8.01	8.23	8.33	8.42	8.36	8.56	
2^3A_2	$n \rightarrow 3p_x$	8.32	8.20	8.20	8.23	7.97	8.03	

† 5^1A_1

‡ 4^1A_1

[m] Mixed with $\pi - 3p_x$, positive linear combination at 11.07

[n] Mixture of $\pi - \pi^*$ (51%), $\pi - 3p_x$ (32%), and $n^2 - \pi^{*2}$ (6%)

[p] Mixture of $n^2 - \pi^{*2}$ (43%), $\pi - 3p_x$ (39%), and $\pi - \pi^*$ (4%). There is another, almost degenerate state at 10.81 eV with oscillator strengths of 0.104, comprised of $n^2 - \pi^{*2}$ (31%), $\pi - \pi^*$ (25%) and $\pi - 3p_x$ (21%) excitations

[a] Energy-loss maximum (vapor) [3]

[b] Energy-loss maximum (vapor) [4]

[c] Absorption band origin (vapor) [6]

[d] Energy-loss band origin (vapor) [4]

[e] Energy-loss band origin (vapor) [5]

Table S11.: Calculated percentage of electron configurations in the excited states wave functions of **formaldehyde** obtained at the DFT/MRCI, MR-MP2(HF) and MR-MP2(BH-LYP) levels of theory using the augmented basis. Only electron configurations with more than 5 percentage are presented.

	DFT/MRCI (BH-LYP)			MRMP2 (HF)			MRMP2 (BH-LYP)		
		Excitation			Excitation			Excitation	
State	%	from	to	%	from	to	%	from	to
1^1A$_2$	81	n_H	π_L^*	67	n_H	π_L^*	74	n_H	π_L^*
	10	n_H	$3p_x(c)$	11	n_H	$3p_x(c)$	5	n_H	$3p_x(c)$
1^1B$_2$	85	n_H	$3s(c)$	58	n_H	$3s(c)$	75	n_H	$3s(c)$
	7	n_H	$3p_z(c)$	12	n_H	$3s(o)$	5	n_H	$3p_z(c)$
				12	n_H	$3p_z(c)$			
1^1B$_1$	82	σ_{H-2}	π_L^*	71	σ_{H-2}	π_L^*	74	σ_{H-2}	π_L^*
	11	σ_{H-2}	$3p_x(c)$	9	σ_{H-2}	$3p_x(c)$	7	σ_{H-2}	$3p_x(c)$
4^1A$_1$	53	π_{H-1}	π_L^*	43	π_{H-1}	π_L^*	61	π_{H-1}	π_L^*
	25	n_H	$3p_y(o)$	19	π_{H-1}	$3p_x(c)$	6	n_H	$3p_y(o)$
	5	π_{H-1}	$3p_x(c)$	7	n_H	$3p_y(o)$	6	π_H,π_H	π_L^*, π_L^*
							5	π_{H-1},π_{H-1}	π_L^*, π_L^*
5^1A$_1$	72	n_H^2	π_L^{2*}	54	n_H^2	π_L^{2*}	64	n_H^2	π_L^{2*}
	13	n_H^2	π_L^*,$3p_x$	17	n_H^2	π_L^*,$3p_x$	6	π_{H-1}	π_L^*
							5	n_H^2	π_L^*,$3p_x$
1^3A$_2$	83	n_H	π_L^*	70	n_H	π_L^*	75	n_H	π_L^*
	10	n_H	$3p_x(c)$	11	n_H	$3p_x(c)$	6	n_H	$3p_x(c)$
1^3A$_1$	84	π_{H-1}	π_L^*	75	π_{H-1}	π_L^*	78	π_{H-1}	π_L^*
	11	π_{H-1}	$3p_x(c)$	10	π_{H-1}	$3p_x(c)$	9	π_{H-1}	$3p_x(c)$
1^3B$_2$	84	n_H	$3s(c)$	58	n_H	$3s(c)$	75	n_H	$3s(c)$
	7	n_H	σ_{L+10}^*	10	n_H	$3p_z(c)$			
				8	n_H	$3s(o)$			
1^3B$_1$	82	σ_{H-2}	π_L^*	72	σ_{H-2}	π_L^*	75	σ_{H-2}	π_L^*
	11	σ_{H-2}	$3p_x(c)$	9	σ_{H-2}	$3p_x(c)$	7	σ_{H-2}	$3p_x(c)$

The orbitals presented in the table are labeled according to the order obtained within the DFT theory. In the following cases the ordering of the Hartree-Fock orbitals is different:
The π_L^* bh-lyp orbital corresponds to the π_{L+9}^* hf orbital.

Table S12.: Calculated percentage of electron configurations in the excited states wave functions of **formaldehyde** obtained at the DFT/MRCI-R and CASPT2 (8,11) levels of theory using the augmented basis. Only electron configurations with more than 5 percentage are presented.

	DFT/MRCI-R			CASPT2 (8,11)		
		Excitation			Excitation	
State	%	from	to	%	from	to
1^1A$_2$	83	n_H	π_L^*	95	n_H	π_L^*
	10	n_H	$3p_x(c)$			
1^1B$_2$	87	n_H	$3s(c)$	94	n_H	$3s(c)$
	4	n_H	$3p_z(c)$			
1^1B$_1$	82	σ_{H-2}	π_L^*	96	σ_{H-2}	π_L^*
	10	σ_{H-2}	$3p_x(c)$			
4^1A$_1$	53	π_{H-1}	π_L^*	51	π_{H-1}	π_L^*
	13	n_H^2	π_L^{2*}	32	π_{H-1}	$3p_x(c)$
	12	n_H	$3p_y(o)$	6	n_H^2	π_L^{2*}
5^1A$_1$	52	n_H^2	π_L^{2*}	43	n_H^2	π_L^{2*}
	17	n_H	$3p_y(o)$	39	π_{H-1}	$3p_x(c)$
	12	n_H^2	π_L^*,$3p_x$			
	5	π_{H-1}	π_L^*			
1^3A$_2$	84	n_H	π_L^*	94	n_H	π_L^*
	10	n_H	$3p_x(c)$			
1^3A$_1$	86	π_{H-1}	π_L^*	97	π_{H-1}	π_L^*
	10	π_{H-1}	$3p_x(c)$			
1^3B$_2$	85	n_H	$3s(c)$	94	n_H	$3s(c)$
	6	n_H	σ_{L+10}^*			
1^3B$_1$	83	σ_{H-2}	π_L^*	96	σ_{H-2}	π_L^*
	11	σ_{H-2}	$3p_x(c)$			

S4.3. *Thioformaldehyde*

Table S13. Experimental and computed DFT/MRCI, DFT/MRCI-R, MR-MP2(HF) and MR-MP2(BH-LYP) vertical excitation energies of **thioformaldehyde** using the valence basis. The oscillator strengths are given in the parentheses.

		Energies(eV)				
State	Dominant character	DFT/MRCI	DFT/MRCI-R	MRMP2 (HF)	MRMP2 (BH-LYP)	Experiment
1^1A_2	$n \rightarrow \pi^*$	2.18 (0)	2.22 (0)	2.11 (0)	2.10 (0)	
2^1A_1	$\pi \rightarrow \pi^*$	6.49 (0.213)	6.50 (0.177)†	6.40 (0.162)	6.32 (0.151)	**6.2**^{a}
1^1B_1	$n \rightarrow \sigma^*$	6.88 (0.001)	6.87 (0.001)	7.17 (0)	7.06 (0.001)	
1^1B_2	$\sigma \rightarrow \pi^*$	6.91 (0.019)	6.90 (0.021)	6.75 (0.010)	6.71 (0.008)	
2^1A_2	$\pi, n \rightarrow \pi^{*2}$	7.18 (0)	7.71 (0)	7.55 (0)	7.54 (0)	
3^1A_1	$n^2 \rightarrow \pi^{*2}$	7.89 (0.011)	6.07 (0.074)‡	7.29 (0.015)	7.25 (0.015)	
1^3A_2	$n \rightarrow \pi^*$	1.86	1.93	1.81	1.81	
1^3A_1	$\pi \rightarrow \pi^*$	3.31	3.24	3.34	3.32	
1^3B_2	$\sigma \rightarrow \pi^*$	6.06	6.13	5.84	5.80	
1^3B_1	$n \rightarrow \sigma^*$	6.36	6.41	6.53	6.43	
⋮						
2^3A_2	$\pi, n \rightarrow \pi^{*2}$	7.79	7.31	7.08	7.06	

[a] Peak maximum [7]

† 3^1A_1

‡ 2^1A_1

Table S14.: Calculated percentage of electron configurations in the excited states wave functions of **thioformaldehyde** obtained at the DFT/MRCI, MR-MP2(HF) and MR-MP2(BH-LYP) levels of theory using the valence basis. Only electron configurations with more than 2 percentage are presented.

	DFT/MRCI (BH-LYP)			MRMP2 (HF)			MRMP2 (BH-LYP)		
		Excitation			Excitation			Excitation	
State	%	from	to	%	from	to	%	from	to
1^1A_2	92	n_H	π^*_L	79	n_H	π^*_L	80	n_H	π^*_L
	7	π_{H-1},n_H	π^*_L,π^*_L	6	π_{H-1},n_H	π^*_L,π^*_L	7	π_{H-1},n_H	π^*_L,π^*_L
2^1A_1	89	π_{H-1}	π^*_L	72	π_{H-1}	π^*_L	72	π_{H-1}	π^*_L
	2	n_H, n_H	π^*_L,π^*_L	5	n_H, n_H	π^*_L,π^*_L	4	n_H, n_H	π^*_L,π^*_L
1^1B_1	88	n_H	σ^*_{L+1}	73	n_H	σ^*_{L+1}	76	n_H	σ^*_{L+1}
	4	n_H	σ^*_{L+4}	6	n_H	σ^*_{L+4}	3	π_{H-1},n_H	π^*_L,σ_{L+1}
	3	π_{H-1},n_H	π^*_L,σ_{L+1}	3	π_{H-1},n_H	π^*_L,σ_{L+1}	3	n_H	σ^*_{L+4}
1^1B_2	94	σ_{H-2}	π^*_L	78	σ_{H-2}	π^*_L	79	σ_{H-2}	π^*_L
	2	σ_{H-2},π_{H-1}	π^*_L,π^*_L	3	σ_{H-2},π_{H-1}	π^*_L,π^*_L	3	σ_{H-2},π_{H-1}	π^*_L,π^*_L
2^1A_2	72	π_{H-1},n_H	π^*_L,π^*_L	41	π_{H-1},n_H	π^*_L,π^*_L	43	π_{H-1},n_H	π^*_L,π^*_L
	18	σ_{H-3}	π^*_L	33	σ_{H-3}	π^*_L	32	σ_{H-3}	π^*_L
				5	σ_{H-3},π_{H-1}	π^*_L,π^*_L	5	σ_{H-3},π_{H-1}	π^*_L,π^*_L
	5	n_H	π^*_L	4	n_H	π^*_L	4	n_H	π^*_L
3^1A_1	86	n_H,n_H	π^*_L,π^*_L	70	n_H,n_H	π^*_L,π^*_L	70	n_H,n_H	π^*_L,π^*_L
	8	n_H,σ_{H-3}	π^*_L,π^*_L	7	n_H,σ_{H-3}	π^*_L,π^*_L	9	n_H,σ_{H-3}	π^*_L,π^*_L
	2	π_{H-1}	π^*_L	4	π_{H-1}	π^*_L	4	π_{H-1}	π^*_L
1^3A_2	96	n_H	π^*_L	82	n_H	π^*_L	83	n_H	π^*_L
1^3A_1	99	π_{H-1}	π^*_L	86	π_{H-1}	π^*_L	88	π_{H-1}	π^*_L
1^3B_2	97	σ_{H-2}	π^*_L	82	σ_{H-2}	π^*_L	82	σ_{H-2}	π^*_L
1^3B_1	78	n_H	σ_{L+1}	56	n_H	σ_{L+1}	64	n_H	σ_{L+1}
	9	n_H	σ_{L+4}	16	n_H	σ_{L+4}	10	n_H	σ_{L+4}
	7	n_H	σ_{L+3}	6	n_H	σ_{L+3}	5	n_H	σ_{L+3}
2^3A_2	51	σ_{H-3}	π^*_L	63	π_{H-1},n_H	π^*_L,π^*_L	64	π_{H-1},n_H	π^*_L,π^*_L
	44	π_{H-1},n_H	π^*_L,π^*_L	14	σ_{H-3}	π^*_L	14	σ_{H-3}	π^*_L

Table S15.: Calculated percentage of electron configurations in the discussed wave functions of **thioformaldehyde** obtained at the DFT/MRCI, and DFT/MRCI-R levels of theory using the valence basis. Only electron configurations with more than 2 percentage are presented.

	DFT/MRCI			DFT/MRCI-R		
		Excitation			Excitation	
State	%	from	to	%	from	to
2^1A_1	89	π_{H-1}	π^*_L	65	π_{H-1}	π^*_L
	2	n_H, n_H	π^*_L,π^*_L	28	n_H, n_H	π^*_L,π^*_L
2^1A_2	72	π_{H-1},n_H	π^*_L,π^*_L	63	π_{H-1},n_H	π^*_L,π^*_L
	18	σ_{H-3}	π^*_L	29	σ_{H-3}	π^*_L
	5	n_H	π^*_L	3	n_H	π^*_L
3^1A_1	86	n_H,n_H	π^*_L,π^*_L	66	n_H,n_H	π^*_L,π^*_L
	8	n_H,σ_{H-3}	π^*_L,π^*_L	28	π_{H-1}	π^*_L
	2	π_{H-1}	π^*_L	2	n_H,σ_{H-3}	π^*_L,π^*_L
2^3A_2	51	σ_{H-3}	π^*_L	79	π_{H-1},n_H	π^*_L,π^*_L
	44	π_{H-1},n_H	π^*_L,π^*_L	14	σ_{H-3}	π^*_L

Table S16. Selected matrix elements (cm^{-1}) for **thioformaldehyde** calculated with DFT/MRCI, DFT/MRCI-R, MR-MP2(HF) and MR-MP2(BH-LYP) methods using the valence basis.

	SOMEs(cm^{-1})			
	DFT/MRCI	DFT/MRCI-R	MRMP2 (HF)	MRMP2 (BH-LYP)
$\langle 1^3A_2\lvert\hat{\mathcal{H}}_{\mathrm{SO\ z}}\rvert 1^1A_1\rangle$	180.3	178.2	163.6	168.8
$\langle 1^3A_2\lvert\hat{\mathcal{H}}_{\mathrm{SO\ z}}\rvert 2^1A_1\rangle$	99.4	179.2	74.4	83.0
$\langle 1^3A_2\lvert\hat{\mathcal{H}}_{\mathrm{SO\ z}}\rvert 3^1A_1\rangle$	156.8	55.8	148.5	147.8
$\langle 1^3B_1\lvert\hat{\mathcal{H}}_{\mathrm{SO\ y}}\rvert 1^1A_1\rangle$	66.3	63.8	57.7	58.9
$\langle 1^3B_1\lvert\hat{\mathcal{H}}_{\mathrm{SO\ y}}\rvert 2^1A_1\rangle$	16.5	15.9	18.3	17.4
$\langle 1^3B_1\lvert\hat{\mathcal{H}}_{\mathrm{SO\ y}}\rvert 3^1A_1\rangle$	6.9	6.7	8.3	5.6
$\langle 1^3B_2\lvert\hat{\mathcal{H}}_{\mathrm{SO\ x}}\rvert 1^1A_1\rangle$	105.6	105.2	98.2	101.6
$\langle 1^3B_2\lvert\hat{\mathcal{H}}_{\mathrm{SO\ x}}\rvert 2^1A_1\rangle$	76.0	60.9	67.2	70.1
$\langle 1^3B_2\lvert\hat{\mathcal{H}}_{\mathrm{SO\ x}}\rvert 3^1A_1\rangle$	6.3	44.3	11.8	11.0
$\langle 1^3A_1\lvert\hat{\mathcal{H}}_{\mathrm{SO\ z}}\rvert 1^1A_2\rangle$	168.2	163.2	155.5	160.9
$\langle 1^3A_1\lvert\hat{\mathcal{H}}_{\mathrm{SO\ z}}\rvert 2^1A_2\rangle$	89.6	95.8	70.1	73.0
$\langle 1^3B_1\lvert\hat{\mathcal{H}}_{\mathrm{SO\ x}}\rvert 1^1A_2\rangle$	32.4	31.3	27.6	28.3
$\langle 1^3B_2\lvert\hat{\mathcal{H}}_{\mathrm{SO\ y}}\rvert 1^1A_2\rangle$	105.8	106.3	99.7	103.2
$\langle 1^3A_2\lvert\hat{\mathcal{H}}_{\mathrm{SO\ x}}\rvert 1^1B_1\rangle$	23.4	22.6	16.2	17.1
$\langle 1^3A_1\lvert\hat{\mathcal{H}}_{\mathrm{SO\ x}}\rvert 1^1B_2\rangle$	88.0	85.8	81.0	81.6
$\langle 1^3A_2\lvert\hat{\mathcal{H}}_{\mathrm{SO\ y}}\rvert 1^1B_2\rangle$	104.7	104.9	96.5	99.6
$\langle 1^3A_2\lvert\hat{\mathcal{H}}_{\mathrm{SO\ z}}\rvert 1^3A_1\rangle$	157.2	158.4	148.4	154.4
$\langle 1^3B_1\lvert\hat{\mathcal{H}}_{\mathrm{SO\ x}}\rvert 1^3A_2\rangle$	28.9	27.5	23.1	22.9
$\langle 1^3B_2\lvert\hat{\mathcal{H}}_{\mathrm{SO\ x}}\rvert 1^3A_1\rangle$	82.0	82.5	78.6	81.8
$\langle 1^3B_2\lvert\hat{\mathcal{H}}_{\mathrm{SO\ y}}\rvert 1^3A_2\rangle$	106.9	106.6	100.4	103.6

Table S17. Experimental and computed DFT/MRCI, DFT/MRCI-R, MR-MP2(HF), MR-MP2(BH-LYP) and CASPT2 vertical excitation energies of **thioformaldehyde** using the augmented basis. The CASPT2 (8,11) active space consists of fallowing occupied/unoccupied orbitals: 1/3 a_1, 1/2 b_2 and 2/2 b_1. The oscillator strengths are given in the parentheses.

State	Dominant character	Energies(eV)					
		DFT/MRCI	DFT/MRCI-R	MRMP2 (HF)	MRMP2 (BH-LYP)	CASPT2 (8,11)	Experiment
1^1A$_2$	$n \to \pi^*$	2.16 (0)	2.20 (0)	2.10 (0)	2.16 (0)	2.11 (0)	**2.03**^{a}
1^1B$_1$	$n \to 4s$	5.67 (0.009)	5.67 (0.009)	6.07 (0.015)	5.99 (0.016)	5.84 (0.027)	**5.84**^{b}
2^1B$_1$	$n \to 4p_z$	6.35 (0.039)	6.35 (0.039)	6.83 (0.030)	6.73 (0.033)	6.57 (0.024)	**6.59**^{b}
2^1A$_1$	$\pi \to \pi^*$	6.46 (0.243)	6.48 (0.216)^1	6.30 (0.178)	6.50 (0.146)^1	6.29 (0.126)^m	**6.2**^{c}
3^1A$_1$	$n \to 4p_x$	6.53 (0.014)	6.53 (0)^2	7.04 (0.003)	6.45 (0.046)^2	6.78 (0.019)	**6.84**^{b}
2^1A$_2$	$n \to 4p_y$	6.67 (0)	6.65 (0)	7.19 (0)	7.08 (0)	6.94 (0)	
1^1B$_2$	$\sigma \to \pi^*$	6.89 (0.016)	6.89 (0.018)	6.72 (0.008)	6.78 (0.002)	7.15 (0.058)	
3^1A$_2$	$\pi, n \to \pi^{*2}$	7.19 (0)	7.70 (0)^3	7.61 (0)	7.58 (0)	7.66 (0)	
⋮							
5^1A$_1$	$n^2 \to \pi^{*2}$	7.84 (0.006)	6.06 (0.076)^4	7.27 (0.010)^1	7.26 (0.019)^3	7.11 (0.086)^n	
1^3A$_2$	$n \to \pi^*$	1.84	1.92	1.81	1.89	1.84	**1.80**^{a}
1^3A$_1$	$\pi \to \pi^*$	3.29	3.23	3.33	3.37	3.34	
1^3B$_1$	$n \to 4s$	5.54	5.54	5.93	5.85	5.75	
1^3B$_2$	$\sigma \to \pi^*$	6.04	6.12	5.81	5.85	6.24	
⋮							
4^3A$_2$	$\pi, n \to \pi^{*2}$	7.77	7.28^5	7.11^2	7.24	7.19	

DFT-/MRCI-R: ^{1} 3^1A$_1$, ^{2} 4^1A$_1$, ^{3} 4^1A$_2$, ^{4} 2^1A$_1$, ^{5} 3^3A$_2$

MR-MP2(HF): ^{1} 4^1A$_1$,^{2} 2^3A$_2$

MR-MP2(BH-LYP): ^{1} 3^1A$_1$, ^{2} 2^1A$_1$, ^{3} 4^1A$_1$

[m] Mixture of $\pi - \pi^*$ (50%) and $n^2 - \pi^{*2}$ (37%)

[n] Mixture of $n^2 - \pi^{*2}$ (51%) and $\pi - \pi^*$ (36%)

[a] Vertical transition (absorption) [8]

[b] Absorption band origin [9]

[c] Absorption peak maximum (vapor) [7]

Table S18.: Calculated percentage of electron configurations in the excited states wave functions of **thioformaldehyde** obtained at the DFT/MRCI, MR-MP2(HF) and MR-MP2(BH-LYP) levels of theory using the augmented basis. Only electron configurations with more than 5 percentage are presented.

	DFT/MRCI (BH-LYP)			MRMP2 (HF)			MRMP2 (BH-LYP)		
		Excitation			Excitation			Excitation	
State	%	from	to	%	from	to	%	from	to
1^1A$_2$	91	n_H	π^*_L	51	n_H	π^*_L	78	n_H	π^*_L
	6	π_{H-1},n_H	π^*_L,π^*_L	28	n_H	π^*_{L+9} †	8	π_{H-1},n_H	π^*_L,π^*_L
2^1A$_1$	87	π_{H-1}	π^*_L	50	π_{H-1}	π^*_L	36	π_{H-1}	π^*_L
				21	π_{H-1}	π^*_{L+9}	36	n_H	$4px$
1^1B$_1$	86	n_H	$4s(c)$	52	n_H	$4s(c)$	73	n_H	$4s(c)$
	5	n_H	σ^*_{L+10}	24	n_H	$4s(s)$	7	n_H	$4p_z$
1^1B$_2$	92	σ_{H-2}	π^*_L	49	σ_{H-2}	π^*_L	73	σ_{H-2}	π^*_L
				29	σ_{H-2}	π^*_{L+9}	6	n_H	$3d_{xy}$
3^1A$_2$	66	π_{H-1},n_H	π^*_L,π^*_L	27	σ_{H-3}	π^*_L	38	π_{H-1},n_H	π^*_L,π^*_L
	18	σ_{H-3}	π^*_L	14	π_{H-1},n_H	π^*_L,π^*_L	34	σ_{H-3}	π^*_L
	6	n_H	π^*_L	13	π_{H-1},n_H	π^*_L,π^*_{L+9}	5	σ_{H-3},π_{H-1}	π^*_L,π^*_L
				16	σ_{H-3}	π^*_{L+9}			
5^1A$_1$	85	n^2_H	π^{2*}_L	28	n^2_H	π^{2*}_L	68	n_H,n_H	π^*_L,π^*_L
	8	n_H,σ_{H-3}	π^*_L,π^*_L	27	n^2_H	π^*_L,π^*_{L+9}	9	n_H,σ_{H-3}	π^*_L,π^*_L
		π_{H-1}	π^*_L				6	π_{H-1}	π^*_L
1^3A$_2$	95	n_H	π^*_L	52	n_H	π^*_L	82	n_H	π^*_L
				29	n_H	π^*_{L+9}			
1^3A$_1$	98	π_{H-1}	π^*_L	52	π_{H-1}	π^*_L	88	π_{H-1}	π^*_L
				34	π_{H-1}	π^*_{L+9}			
1^3B$_1$	81	n_H	$4s(c)$	48	n_H	$4s(c)$	71	n_H	$4s(c)$
	11	n_H	σ^*_{L+10}	23	n_H	$4s(S)$	5	n_H	p_z
				6	n_H	σ^*_{L+10}			
1^3B$_2$	96	σ_{H-2}	π^*_L	50	σ_{H-2}	π^*_L	82	σ_{H-2}	π^*_L
				32	σ_{H-2}	π^*_{L+9}			
4^3A$_2$	50	σ_{H-3}	π^*_L	19	π_{H-1},n_H	π^*_L,π^*_L	42	n_H	$3d_{yz}$
	41	π_{H-1},n_H	π^*_L,π^*_L	17	π_{H-1},n_H	π^*_L,π^*_{L+9}	28	π_{H-1},n_H	π^*_L,π^*_L
				21	σ_{H-3}	π^*_L	5	σ_{H-3}	π^*_L
				13	σ_{H-3}	π^*_{L+9}			
				5	n_H	π^*_{L+9}			

† HF orbital which valence part is the same as π^*_L(BH-LYP), but with the opposite phase.
The π^* and d_{yz} orbitals are mixed at the HF level.
The orbitals presented in the table are labeled according to the order obtained within the DFT theory.
In the following cases the ordering of the Hartree-Fock orbitals is different:
The π^*_L bh-lyp orbital corresponds to the π^*_{L+4} hf orbital.

Table S19.: Calculated percentage of electron configurations in the discussed wave functions of **thioformaldehyde** obtained at the DFT/MRCI-R, and CASPT2 (8,11) levels of theory using the augmented basis. Only electron configurations with more than 5 percentage are presented.

	DFT/MRCI-R			CASPT2 (8,11)		
		Excitation			Excitation	
State	%	from	to	%	from	to
1^1A_2	93	n_H	π^*_L	92	n_H	π^*_L
	5	π_{H-1},n_H	π^*_L,π^*_L			
2^1A_1	54	π_{H-1}	π^*_L	50	π_{H-1}	π^*_L
	22	n_H^2	π_L^{2*}	37	n_H^2	π_L^{2*}
	16	n_H	$4p_x$			
1^1B_1	87	n_H	$4s(c)$	92	n_H	$4s(c)$
	5	n_H	σ^*_{L+10}			
1^1B_2	94	σ_{H-2}	π^*_L	94	σ_{H-2}	π^*_L
3^1A_2	59	π_{H-1},n_H	π^*_L,π^*_L	60	π_{H-1},n_H	π^*_L,π^*_L
	28	σ_{H-3}	π^*_L	25	σ_{H-3}	π^*_L
		n_H	π^*_L			
5^1A_1	65	n_H^2	π_L^{2*}	51	n_H^2	π_L^{2*}
	28	π_{H-1}	π^*_L	36	π_{H-1}	π^*_L
	2	n_H,σ_{H-3}	π^*_L,π^*_L			
1^3A_2	95	n_H	π^*_L	95	n_H	π^*_L
1^3A_1	98	π_{H-1}	π^*_L	97	π_{H-1}	π^*_L
1^3B_1	83	n_H	$4s(c)$	93	n_H	$4s(c)$
	9	n_H	σ^*_{L+10}			
1^3B_2	96	σ_{H-2}	π^*_L	94	σ_{H-2}	π^*_L
4^3A_2	65	π_{H-1},n_H	π^*_L,π^*_L	75	π_{H-1},n_H	π^*_L,π^*_L
	12	σ_{H-3}	π^*_L	12	σ_{H-3}	π^*_L
	11	n_H	$3d_yz$			

S4.4. *Furan*

Table S20. Experimental and computed DFT/MRCI, DFT/MRCI-R, MR-MP2(HF) and MR-MP2(BH-LYP) vertical excitation energies of **furan** using the valence basis. The oscillator strengths are given in the parentheses.

State	Dominant character	Energies(eV)				
		DFT/MRCI	DFT/MRCI-R	MRMP2 (HF)	MRMP2 (BH-LYP)	Experiment
2^1A_1	$\pi \rightarrow \pi^*$	6.40 (0)	6.43 (0.001)	6.20 (0.001)	6.12 (0.002)	
1^1B_1	$\pi \rightarrow \pi^*$	6.43 (0.235)	6.34 (0.253)	6.42 (0.165)	6.30 (0.163)	**6.04**^{a,b}, 6.06^c
1^1A_2	$\pi \rightarrow Ryd$	7.46 (0)	7.48 (0)	7.75 (0)	7.81 (0)	
2^1A_2	$\pi \rightarrow Ryd$	8.03 (0)	8.06 (0)	8.24 (0)	8.44 (0)	
1^1B_2	$\pi \rightarrow Ryd$	8.13 (0.014)	8.14 (0.014)	8.50 (0.020)	8.50 (0.022)	
3^1A_1	$\pi \rightarrow \pi^*$	8.28 (0.698)	8.23 (0.772)	7.97 (0.415)	7.84 (0.390)	7.82^c, **7.80**^{a}
1^3B_1	$\pi \rightarrow \pi^*$	4.00	4.01	4.08	4.08	**4.00**^{d}, 3.99^c
1^3A_1	$\pi \rightarrow \pi^*$	5.19	5.20	5.23	5.20	**5.20**^{d} 5.22^c
2^3A_1	$\pi \rightarrow \pi^*$	6.67	6.63	6.45	6.37	
2^3B_1	$\pi \rightarrow \pi^*$	7.25	7.20	7.09	7.05	
1^3A_2	$\pi \rightarrow Ryd$	7.33	7.37	7.66	7.66	
2^3A_2	$\pi \rightarrow Ryd$	7.69	7.75	7.91	7.84	
1^3B_2	$\pi \rightarrow Ryd$	7.97	8.02	8.37^1	8.39^1	

MRMP2 (HF)$^1 2^3B_2$

MRMP2 (BH-LYP)$^1 2^3B_2$

[a] VUV maximum (gas) [10]

[b] Electron energy-loss maximum (gas) [11]

[c] Electron energy-loss maximum (gas) [12]

[d] Electron impact maximum (gas)[13]

Table S21.: Calculated percentage of electron configurations in the excited states wave functions of **furan** obtained at the DFT/MRCI, MR-MP2(HF) and MR-MP2(BH-LYP) levels of theory using the valence basis. Only electron configurations with more than 2 percentage are presented.

	DFT/MRCI			MRMP2			MRMP2		
	(BH-LYP)			(HF)			(BH-LYP)		
		Excitation			Excitation			Excitation	
State	%	from	to	%	from	to	%	from	to
2^1A_1	45	π_{H-1}	π^*_L	31	π_{H-1}	π^*_L	31	π_{H-1}	π^*_L
	37	π_H	π^*_{L+2}	26	π_H	π^*_{L+2}	27	π_H	π^*_{L+2}
	5	π_{H-1},π_H	π^*_L,π^*_{L+2}	6	π_H,π_H	π^*_L,π^*_L	6	π_H,π_H	π^*_L,π^*_L
	4	π_H,π_H	π^*_L,π^*_L	4	π_{H-1},π_H	π^*_L,π^*_{L+2}	5	π_{H-1},π_H	π^*_L,π^*_{L+2}
	2	π_H,π_H	π^*_{L+2},π^*_{L+2}	2	π_H,π_H	π^*_{L+2},π^*_{L+2}	2	π_H,π_H	π^*_{L+2},π^*_{L+2}
				2	π_{H-1},π_{H-1}	π^*_L,π^*_L	2	π_{H-1},π_{H-1}	π^*_L,π^*_L
1^1B_1	95	π_H	π^*_L	74	π_H	π^*_L	72	π_H	π^*_L
1^1A_2	89	π_H	Ry_{L+1}	68	π_H	Ry_{L+1}	71	π_H	Ry_{L+1}
	4	π_H	Ry_{L+6}	4	π_H	Ry_{L+6}			
				2	π_{H-1}	Ry_{L+4}			
1^1B_2	85	π_H	Ry_{L+4}	56	π_H	Ry_{L+4}	61	π_H	Ry_{L+4}
	9	π_{H-1}	Ry_{L+1}	10	π_H	Ry_{L+5}	11	π_{H-1}	Ry_{L+1}
				9	π_{H-1}	Ry_{L+1}	4	π_H	Ry_{L+5}
1^3B_1	92	π_H	π^*_L	69	π_H	π^*_L	70	π_H	π^*_L
	4	π_{H-1}	π^*_{L+2}	4	π_{H-1}	π^*_{L+2}	5	π_{H-1}	π^*_{L+2}
1^3A_1	51	π_{H-1}	π^*_L	36	π_{H-1}	π^*_L	37	π_H	π^*_{L+2}
	44	π_H	π^*_{L+2}	35	π_H	π^*_{L+2}	35	π_{H-1}	π^*_L
	2	π_{H-1},π_H	π^*_L,π^*_{L+2}	2	π_{H-1},π_H	π^*_L,π^*_{L+2}	3	π_{H-1},π_H	π^*_L,π^*_{L+2}
1^3A_2	89	π_H	Ry_{L+1}	68	π_H	Ry_{L+1}	69	π_H	Ry_{L+1}
	4	π_H	Ry_{L+6}	3	π_H	Ry_{L+6}	3	π_H	Ry_{L+6}
	2	π_{H-1}	Ry_{L+4}	2	π_{H-1}	Ry_{L+4}	2	π_{H-1}	Ry_{L+4}
1^3B_2	84	π_H	Ry_{L+4}	55	π_H	Ry_{L+4}	62	π_H	Ry_{L+4}
	11	π_{H-1}	Ry_{L+1}	11	π_{H-1}	Ry_{L+1}	12	π_{H-1}	Ry_{L+1}
				8	π_H	Ry_{L+5}			

The orbitals presented in the table are labeled according to the order obtained within the DFT theory.
In the following cases the ordering of the Hartree-Fock orbitals is different:
The π^*_{L+2} bh-lyp orbital corresponds to the π^*_{L+5} hf orbital;
The Ry_{L+4} bh-lyp orbital corresponds to the Ry_{L+2} hf orbital;
The Ry_{L+5} bh-lyp orbital corresponds to the Ry_{L+4} hf orbital.

Table S22. Selected matrix elements (cm^{-1}) for **furan** calculated with DFT/MRCI, DFT/MRCI-R, MR-MP2(HF) and MR-MP2(BH-LYP) methods using the valence basis.

	SOMEs(cm^{-1})			
	DFT/MRCI	DFT/MRCI-R	MRMP2 (HF)	MRMP2 (BH-LYP)
$\langle 1^3A_2 \vert \hat{\mathcal{H}}_{\mathrm{SO\ z}} \vert 1^1A_1 \rangle$	9.6	9.3	9.1	9.1
$\langle 1^3A_2 \vert \hat{\mathcal{H}}_{\mathrm{SO\ z}} \vert 2^1A_1 \rangle$	1.1	1.0	1.0	1.2
$\langle 1^3B_1 \vert \hat{\mathcal{H}}_{\mathrm{SO\ x}} \vert 1^1A_2 \rangle$	5.2	5.0	4.4	4.7
$\langle 1^3A_2 \vert \hat{\mathcal{H}}_{\mathrm{SO\ x}} \vert 1^1B_1 \rangle$	4.6	4.4	3.4	3.5
$\langle 1^3A_1 \vert \hat{\mathcal{H}}_{\mathrm{SO\ x}} \vert 1^1B_2 \rangle$	3.8	3.7	4.1	4.3
$\langle 1^3A_2 \vert \hat{\mathcal{H}}_{\mathrm{SO\ y}} \vert 1^1B_2 \rangle$	0.3	0.2	0.1	0.1
$\langle 1^3B_1 \vert \hat{\mathcal{H}}_{\mathrm{SO\ z}} \vert 1^1B_2 \rangle$	9.4	9.3	7.8	8.2
$\langle 1^3A_2 \vert \hat{\mathcal{H}}_{\mathrm{SO\ z}} \vert 1^3A_1 \rangle$	1.1	0.9	1.4	1.1
$\langle 1^3B_1 \vert \hat{\mathcal{H}}_{\mathrm{SO\ x}} \vert 1^3A_2 \rangle$	5.1	5.0	4.4	4.7
$\langle 1^3B_2 \vert \hat{\mathcal{H}}_{\mathrm{SO\ x}} \vert 1^3A_1 \rangle$	3.9	3.7	4.2	4.2

Table S23. Experimental and computed DFT/MRCI, DFT/MRCI-R, MR-MP2(HF), MR-MP2(BH-LYP) and CASPT2 (6,9) vertical excitation energies of **furan** using the augmented basis. The CASPT2 active space consists of fallowing occupied/unoccupied orbitals: 0/2 a_1, 0/1 b_1, 2/2 b_2 and 1/1 a_2. The oscillator strengths are given in the parentheses.

State	Dominant character	Energies(eV)					
		DFT/MRCI	DFT/MRCI-R	MRMP2 (HF)	MRMP2 (BH-LYP)	CASPT2 (6,9)	Experiment
1^1A_2	$\pi \rightarrow 3s$	5.91 (0)	5.90 (0)	6.10 (0)	6.00 (0)	5.98 (0)	**5.91**^{e}
1^1B_1	$\pi \rightarrow \pi^*$	6.05 (0.238)	6.04 (0.253)	6.47 (0.106)	6.48 (0.092)	6.11 (0.144)	**6.04**^{a,b}, 6.06^c
2^1A_1	$\pi \rightarrow \pi^*$	6.29 (0.006)	6.30 (0.004)	6.11 (0.001)	5.93 (0.001)	6.22 (0.003)	
1^1B_2	$\pi \rightarrow 3p_x$	6.38 (0.047)	6.36 (0.047)	6.59 (0.050)	6.48 (0.056)	6.51 (0.047)	**6.47**^{a}
2^1A_2	$\pi \rightarrow 3p_z$	6.55 (0)	6.54 (0)	6.89 (0)	6.74 (0)	6.70 (0)	**6.61**^{c}
2^1B_1	$\pi \rightarrow 3p_y$	6.80 (0)	6.77 (0)	6.92 (0.015)	6.92 (0.011)	6.63 (0.029)	**6.75**^{a}
$\vdots$							
4^1A_1	$\pi \rightarrow \pi^*$	8.13 (0.506)	8.09 (0.549)	8.31 (0.307)^1	8.12 (0.366)^1	7.87 (0.446)	7.82^c, **7.80**^{a}
1^3B_1	$\pi \rightarrow \pi^*$	3.74	3.90	4.03	3.97	4.13	**4.00**^{d}, 3.99^c
1^3A_1	$\pi \rightarrow \pi^*$	5.03	5.15	5.15	5.10	5.25	**5.20**^{d} 5.22^c
1^3A_2	$\pi \rightarrow 3s$	5.80	5.83	6.00	5.90	5.93	**5.8**^{f}
1^3B_2	$\pi \rightarrow 3p_x$	6.27	6.30	6.51	6.44	6.46	
2^3A_2	$\pi \rightarrow 3p_z$	6.48	6.50	6.84	6.72	6.69	

MRMP2 (HF)$^1 6^1A_1$

MRMP2 (BH-LYP)$^1 6^1A_1$

[a] VUV maximum (gas) [10]

[b] Electron energy-loss maximum (gas) [11]

[c] Electron energy-loss maximum (gas) [12]

[d] Electron impact maximum (gas)[13]

[e] Resonantly enhanced multiphoton ionization [14]

[f] Electron energy-loss maximum (gas) [10]

Table S24.: Calculated percentage of electron configurations in the excited states wave functions of **furan** obtained at the DFT/MRCI, MR-MP2(HF) and MR-MP2(BH-LYP) levels of theory using the augmented basis. Only electron configurations with more than 5 percentage are presented.

	DFT/MRCI (BH-LYP)			MRMP2 (HF)			MRMP2 (BH-LYP)		
		Excitation			Excitation			Excitation	
State	%	from	to	%	from	to	%	from	to
2^1A_1	32	π_H	π^*_{L+10}	30	π_{H-1}	π^*_{L+9}	26	π_H	π^*_{L+10}
	28	π_{H-1}	π^*_{L+3}/p_y	26	π_H	π^*_{L+10}	19	π_{H-1}	π^*_{L+3}/p_y
	23	π_{H-1}	π^*_{L+9}/p_y	6	π_H,π_H	π^*_{L+9},π^*_{L+9}	14	π_{H-1}	π^*_{L+9}/p_y
1^1B_1	71	π_H	π^*_{L+3}/p_y	59	π_H	$3p_y$	50	π_H	π^*_{L+3}/p_y
	24	π_H	π^*_{L+9}/p_y	14	π_H	π^*_{L+9}	26	π_H	$3p_y$
1^1A_2	90	π_H	$3s$	57	π_H	$3s$	68	π_H	$3s$
				13	π_H	$3p_z$			
1^1B_2	91	π_H	$3p_x$	66	π_H	$3p_x$	71	π_H	$3p_x$
		π_{H-1}	Ry_{L+1}	7	π_H	$3d_xz$			
1^3B_1	46	π_H	π^*_{L+3}/p_y	67	π_H	π^*_{L+9}	36	π_H	π^*_{L+9}/p_y
	46	π_H	π^*_{L+9}/p_y	5	π_{H-1}	π^*_{L+10}	36	π_H	π^*_{L+9}/p_y
1^3A_1	36	π_H	π^*_{L+10}	39	π_H	π^*_{L+10}	38	π_H	π^*_{L+10}
	30	π_{H-1}	π^*_{L+3}/p_y	32	π_{H-1}	π^*_{L+9}	18	π_{H-1}	π^*_{L+3}/p_y
	28	π_{H-1}	π^*_{L+9}/p_y				17	π_{H-1}	π^*_{L+9}/p_y
1^3A_2	89	π_H	$3s$	54	π_H	$3s$	67	π_H	$3s$
				17	π_H	$3p_z$			
1^3B_2	89	π_H	$3p_x$	65	π_H	$3p_x$	69	π_H	$3p_x$
		π_{H-1}	Ry_{L+1}	6	π_H	$3d_xz$	5	π_{H-1}	$3s$

π^*_{L+3}/p_y and π^*_{L+9}/p_y BH-LYP orbitals arise from combination of π^*_{L+9} and p_y orbitals. In HF and CASSCF calculations this orbitals do not mix.

Table S25.: Calculated percentage of electron configurations in the discussed wave functions of **furan** obtained at the DFT/MRCI-R, and CASPT2 (6,9) levels of theory using the augmented basis. Only electron configurations with more than 5 percentage are presented.

	DFT/MRCI-R			CASPT2 (6,9)		
		Excitation			Excitation	
State	%	from	to	%	from	to
$2^1\mathrm{A}_1$	33	π_H	π^*_{L+10}	38	π_{H-1}	π^*_{L+9}
	28	π_{H-1}	π^*_{L+3}/p_y	31	π_H	π^*_{L+10}
	22	π_{H-1}	π^*_{L+9}/p_y	8	π^2_H	π^{2*}_{L+9}
				7	π_H, π_{H-1}	π^*_{L+9}, π^*_{L+10}
$1^1\mathrm{B}_1$	73	π_H	π^*_{L+3}/p_y	78	π_H	π^*_{L+9}
	23	π_H	π^*_{L+9}/p_y	9	π_H	p_y
$1^1\mathrm{A}_2$	91	π_H	$3s$	91	π_H	$3s$
$1^1\mathrm{B}_2$	92	π_H	$3p_x$	90	π_H	$3p_x$
$1^3\mathrm{B}_1$	47	π_H	π^*_{L+3}/p_y	85	π_H	π^*_{L+9}
	46	π_H	π^*_{L+9}/p_y	7	π_{H-1}	π^*_{L+10}
$1^3\mathrm{A}_1$	39	π_H	π^*_{L+10}	44	π_H	π^*_{L+10}
	29	π_{H-1}	π^*_{L+3}/p_y	45	π_{H-1}	π^*_{L+9}
	26	π_{H-1}	π^*_{L+9}/p_y			
$1^3\mathrm{A}_2$	90	π_H	$3s$	91	π_H	$3s$
$1^3\mathrm{B}_2$	90	π_H	$3p_x$	88	π_H	$3p_x$
				5	π_{H-1}	$3s$

π^*_{L+3}/p_y and π^*_{L+9}/p_y BH-LYP orbitals arise from combination of π^*_{L+9} and p_y orbitals. In HF and CASSCF calculations these orbitals do not mix.

S4.5. *Thiophene*

Table S26. Experimental and computed DFT/MRCI, DFT/MRCI-R, MR-MP2(HF) and MR-MP2(BH-LYP) vertical excitation energies of **thiophene** using the valence basis. The oscillator strengths are given in the parentheses.

		Energies(eV)				
State	Dominant character	DFT/MRCI	DFT/MRCI-R	MRMP2 (HF)	MRMP2 (BH-LYP)	Experiment
2^1A_1	$\pi \rightarrow \pi^*$	5.55 (0.095)	5.54 (0.109)	5.27 (0.030)	5.23 (0.057)	**5.43**[a]
1^1B_1	$\pi \rightarrow \pi^*$	5.81 (0.109)	5.75 (0.120)	5.75 (0.074)	5.74 (0.078)	**5.61**[a]
1^1B_2	$\pi \rightarrow \sigma^*$	6.06 (0)	6.13 (0)	6.23 (0.001)	6.16 (0.001)	
1^1A_2	$\pi \rightarrow \sigma^*$	6.28 (0)	6.31 (0)	6.27 (0)	6.17 (0)	
3^1A_1	$\pi \rightarrow \pi^*$	7.29 (0.321)	7.35 (0.400)	6.97 (0.173)	6.83 (0.223)	**7.05**[b]
1^3B_1	$\pi \rightarrow \pi^*$	3.78	3.78	3.71	3.74	**3.75**[c], 3.80[d]
1^3A_1	$\pi \rightarrow \pi^*$	4.58	4.56	4.48	4.46	**4.62**[c], 4.70[d]
1^3B_2	$\pi \rightarrow \sigma^*$	5.86	5.91	6.00	5.92	
2^3A_1	$\pi \rightarrow \pi^*$	5.92	5.94	5.77	5.72	
1^3A_2	$\pi \rightarrow \sigma^*$	5.95	6.01	5.95	5.90	

[a] Electron energy-loss maximum (gas) [11]

[b] VUV absorption maximum (gas) [15]

[c] Electron impact maximum (gas) [12]

[d] Electron energy-loss maximum (gas) [15]

Table S27. Calculated percentage of electron configurations in the excited states wave functions of **thiophene** obtained at the DFT/MRCI, MR-MP2(HF) and MR-MP2(BH-LYP) levels of theory using the valence basis. Only electron configurations with more than 2 percentage are presented.

	DFT/MRCI			MRMP2			MRMP2		
	(BH-LYP)			(HF)			(BH-LYP)		
		Excitation			Excitation			Excitation	
State	%	from	to	%	from	to	%	from	to
2^1A_1	74	π_{H-1}	π^*_L	47	π_{H-1}	π^*_L	45	π_{H-1}	π^*_L
	15	π_H	π^*_{L+3}	16	π_H	π^*_{L+3}	17	π_H	π^*_{L+3}
	3	π_{H-1},π_H	π^*_L,π^*_{L+3}	3	π_{H-1},π_H	π^*_L,π^*_{L+3}	3	π_{H-1},π_H	π^*_L,π^*_{L+3}
	2	π_{H-3},π_{H-1}	π^*_L,π^*_L	3	π_{H-3},π_{H-1}	π^*_L,π^*_L	3	π_{H-3},π_{H-1}	π^*_L,π^*_L
							2	π_H,π_H	π^*_L,π^*_L
1^1B_1	89	π_H	π^*_L	66	π_H	π^*_L	66	π_H	π^*_L
	2	π_{H-1}	π^*_{L+3}	2	π_{H-1}	π^*_{L+3}	2	π_{H-3},π_H	π^*_L,π^*_L
	2	π_{H-1},π_H	π^*_L,π^*_L	2	π_{H-1},π_H	π^*_L,π^*_L	2	n_{H-2}	σ^*_{L+1}
	2	n_{H-2}	σ^*_{L+1}	2	π_{H-3},π_H	π^*_L,π^*_L			
1^1B_2	85	π_H	σ^*_{L+1}	54	π_H	σ^*_{L+1}	64	π_H	σ^*_{L+1}
	5	π_{H-1},π_H	π^*_L,σ^*_{L+1}	8	π_H	σ^*_{L+7}	6	π_{H-1},π_H	π^*_L,σ^*_{L+1}
	2	π_H	σ^*_{L+7}	6	π_H	Ry_{L+5}	2	π_{H-3},π_H	π^*_L,σ^*_{L+1}
	2	π_H	Ry_{L+5}	5	π_{H-1},π_H	π^*_L,σ^*_{L+1}			
1^1A_2	87	π_{H-1}	σ^*_{L+1}	57	π_{H-1}	σ^*_{L+1}	67	π_{H-1}	σ^*_{L+1}
	3	π_{H-1}	σ^*_{L+7}	9	π_{H-1}	σ^*_{L+7}	2	π_{H-1},π_H	σ^*_{L+1},π^*_{L+3}
	2	π_{H-1}	Ry_{L+5}	5	π_{H-1}	Ry_{L+5}			
3^1A_1	46	π_H	π^*_{L+3}	18	π_H	π^*_{L+3}	17	π_{H-1}	π^*_L
	15	π_{H-3}	π^*_L	16	π_{H-3}	π^*_L	16	π_H	π^*_{L+3}
	13	π_{H-1}	π^*_L	15	π_{H-1}	π^*_L	15	π_{H-3}	π^*_L
	12	π_H,π_H	π^*_L,π^*_L	14	π_H,π_H	π^*_L,π^*_L	14	π_H,π_H	π^*_L,π^*_L
	2	π_{H-1},π_{H-1}	π^*_L,π^*_L	3	π_{H-1},π_{H-1}	π^*_L,π^*_L	4	π_{H-1},π_{H-1}	π^*_L,π^*_L
	2	π_H,π_H	π^*_{L+3},π^*_{L+3}	2	π_H,π_H	π^*_{L+3},π^*_{L+3}	2	π_H,π_H	π^*_{L+3},π^*_{L+3}
	2	σ_{H-4}	σ^*_{L+1}				2	σ_{H-4}	σ^*_{L+1}
1^3B_1	93	π_H	π^*_L	70	π_H	π^*_L	69	π_H	π^*_L
	2	π_{H-1}	π^*_{L+3}	2	π_{H-3}	π^*_{L+3}	3	π_{H-1}	π^*_{L+3}
	2	π_{H-3}	π^*_{L+3}	2	π_{H-1}	π^*_{L+3}	2	π_{H-3}	π^*_{L+3}
1^3A_1	87	π_{H-1}	π^*_L	54	π_{H-1}	π^*_L	54	π_{H-1}	π^*_L
	9	π_H	π^*_{L+3}	17	π_H	π^*_{L+3}	16	π_H	π^*_{L+3}
				2	π_{H-3}	π^*_L	2	π_{H-3}	π^*_L
							2	π_{H-1},π_H	π^*_L,,π^*_{L+3}
1^3B_2	88	π_H	σ^*_{L+1}	53	π_H	σ^*_{L+1}	65	π_H	σ^*_{L+1}
	4	π_{H-1},π_H	π^*_L,σ^*_{L+1}	9	π_H	σ^*_{L+7}	5	π_{H-1},π_H	π^*_L,σ^*_{L+1}
	2	π_H	σ^*_{L+7}	5	π_H	Ry_{L+5}			
	2	π_H	Ry_{L+5}	5	π_{H-1},π_H	π^*_L,σ^*_{L+1}			
2^3A_1	74	π_H	π^*_{L+3}	42	π_H	π^*_{L+3}	45	π_H	π^*_{L+3}
	11	π_{H-3}	π^*_L	21	π_{H-1}	π^*_L	20	π_{H-1}	π^*_L
	10	π_{H-1}	π^*_L	9	π_{H-3}	π^*_L	9	π_{H-3}	π^*_L
1^3A_2	86	π_{H-1}	σ^*_{L+1}	53	π_{H-1}	σ^*_{L+1}	66	π_{H-1}	σ^*_{L+1}
	3	π_{H-1}	σ^*_{L+7}	11	π_{H-1}	σ^*_{L+7}	3	π_{H-3}	σ^*_{L+1}
	3	π_{H-1}	Ry_{L+5}	6	π_{H-1}	Ry_{L+5}			
	3	π_{H-3}	σ^*_{L+1}	2	π_{H-3}	σ^*_{L+1}			

The orbitals presented in the table are labeled according to the order obtained within the DFT theory.
In the following cases the ordering of the Hartree-Fock orbitals is different:
The σ^*_{L+1} bh-lyp orbital corresponds to the σ^*_{L+2} hf orbital;

Table S28. Selected matrix elements (cm^{-1}) for **thiophene** calculated with DFT/MRCI, DFT/MRCI-R, MR-MP2(HF) and MR-MP2(BH-LYP) methods using the valence basis.

	SOMEs(cm^{-1})			
	DFT/MRCI	DFT/MRCI-R	MRMP2 (HF)	MRMP2 (BH-LYP)
$\langle 1^3A_2\|\hat{\mathcal{H}}_{\mathrm{SO\ z}}\|1^1A_1\rangle$	127.7	125.7	109.1	113.5
$\langle 1^3A_2\|\hat{\mathcal{H}}_{\mathrm{SO\ z}}\|2^1A_1\rangle$	55.6	56.0	39.9	41.0
$\langle 1^3A_2\|\hat{\mathcal{H}}_{\mathrm{SO\ z}}\|3^1A_1\rangle$	29.6	28.0	29.3	36.7
$\langle 1^3B_1\|\hat{\mathcal{H}}_{\mathrm{SO\ y}}\|1^1A_1\rangle$	0.1	0.3	0.6	0.4
$\langle 1^3B_2\|\hat{\mathcal{H}}_{\mathrm{SO\ x}}\|1^1A_1\rangle$	6.9	6.4	6.1	6.5
$\langle 1^3B_2\|\hat{\mathcal{H}}_{\mathrm{SO\ x}}\|2^1A_1\rangle$	1.8	2.2	3.3	3.9
$\langle 1^3A_1\|\hat{\mathcal{H}}_{\mathrm{SO\ z}}\|1^1A_2\rangle$	47.1	45.9	32.5	36.1
$\langle 1^3A_1\|\hat{\mathcal{H}}_{\mathrm{SO\ y}}\|1^1B_1\rangle$	0.5	0.4	0.4	0.4
$\langle 1^3A_2\|\hat{\mathcal{H}}_{\mathrm{SO\ x}}\|1^1B_1\rangle$	17.6	17.2	15.5	15.7
$\langle 1^3B_1\|\hat{\mathcal{H}}_{\mathrm{SO\ z}}\|1^1B_2\rangle$	65.0	64.0	49.5	57.5
$\langle 1^3A_2\|\hat{\mathcal{H}}_{\mathrm{SO\ z}}\|1^3A_1\rangle$	41.2	41.0	27.9	29.4
$\langle 1^3A_2\|\hat{\mathcal{H}}_{\mathrm{SO\ z}}\|2^3A_1\rangle$	13.2	11.5	18.3	17.3
$\langle 1^3B_1\|\hat{\mathcal{H}}_{\mathrm{SO\ y}}\|1^3A_1\rangle$	0.2	0.2	0.1	0.0
$\langle 1^3B_1\|\hat{\mathcal{H}}_{\mathrm{SO\ x}}\|1^3A_2\rangle$	3.0	2.5	3.2	3.7
$\langle 1^3B_2\|\hat{\mathcal{H}}_{\mathrm{SO\ z}}\|1^3B_1\rangle$	64.7	66.6	53.9	60.1

Table S29. Experimental and computed DFT/MRCI, DFT/MRCI-R, MR-MP2(HF), MR-MP2(BH-LYP) and CASPT2 (6,10) vertical excitation energies of **thiophene** using the augmented basis. The CASPT2 active space consists of fallowing occupied/unoccupied orbitals: 0/2 a_1, 0/2 b_1, 2/2 b_2 and 1/1 a_2. The oscillator strengths are given in the parentheses.

State	Dominant character	Energies(eV)					
		DFT/MRCI	DFT/MRCI-R	MRMP2 (HF)	MRMP2 (BH-LYP)	CASPT2 (6,10)	Experiment
2^1A$_1$	$\pi \rightarrow \pi^*$	5.43 (0.114)	5.43 (0.124)	5.23 (0.270)	5.18 (0.063)	5.47 (0.080)	**5.43**^{a}
1^1B$_1$	$\pi \rightarrow \pi^*$	5.65 (0.102)	5.62 (0.115)	6.14 (0.086)	5.62 (0.042)	5.47 (0.124)	**5.61**^{a}
1^1B$_2$	$\pi \rightarrow \sigma^*/4p_x$	5.83 (0.004)	5.88 (0.005)	6.29 (0.016)	6.21 (0.014)	6.28 (0.015)	
1^1A$_2$	$\pi \rightarrow 4s$	5.85 (0)	5.84 (0)	6.11 (0)	6.16 (0)	6.03 (0)	**5.93**^{c}
2^1A$_2$	$\pi \rightarrow \sigma^*/4p_x$	6.06 (0)	6.10 (0)	6.25 (0)	6.21 (0)	6.33 (0)	
$\vdots$							
3^1A$_1$	$\pi \rightarrow \pi^*$	7.08 (0.167)	7.02 (0.114)	7.04 (0.150)	6.89 (0.158)	6.99 (0.332)	**7.05**^{b}
1^3B$_1$	$\pi \rightarrow \pi^*$	3.62	3.71	3.73	3.75	3.75	**3.75**^{c}, 3.80^d
1^3A$_1$	$\pi \rightarrow \pi^*$	4.45	4.50	4.53	4.47	4.59	**4.62**^{c}, 4.70^d
1^3B$_2$	$\pi \rightarrow \sigma^*/4p_x$	5.64	5.71	6.07	6.04	6.11	
1^3A$_2$	$\pi \rightarrow 4s$	5.77	5.78	6.09^1	6.09^1	6.00	
2^3A$_2$	$\pi \rightarrow \sigma^*/4p_x$	5.79	5.86	5.95^2	5.88^2	5.99	
2^3A$_1$	$\pi \rightarrow \pi^*$	5.88	5.92	5.78	5.70	5.68	

MR-MP2(HF): ^{1} 2^3A$_2$, ^{2} 1^3A$_2$

MR-MP2(BH-LYP): ^{1} 2^3A$_2$, ^{2} 1^3A$_2$

[a] Electron energy-loss maximum (gas) [11]

[b] VUV absorption maximum (gas) [15]

[c] Electron impact maximum (gas) [12]

[d] Electron energy-loss maximum (gas) [15]

Table S30. Calculated percentage of electron configurations in the excited states wave functions of **thiophene** obtained at the DFT/MRCI, MR-MP2(HF) and MR-MP2(BH-LYP) levels of theory using the augmented basis. Only electron configurations with more than 5 percentage are presented.

	DFT/MRCI			MRMP2			MRMP2		
	(BH-LYP)			(HF)			(BH-LYP)		
		Excitation			Excitation			Excitation	
State	%	from	to	%	from	to	%	from	to
2^1A_1	55	π_{H-1}	π^*_{L+4}	46	π_{H-1}	π^*_{L+4}	36	π_{H-1}	π^*_{L+4}
	21	π_{H-1}	$4p_y$	16	π_H	π^*_{L+11}	16	π_H	π^*_{L+11}
	13	π_H	π^*_{L+11}				9	π_{H-1}	$4p_y$
1^1B_1	66	π_H	π^*_{L+4}	44	π_H	π^*_{L+4}	39	π_H	π^*_{L+4}
	24	π_H	$4p_y$	20	π_H	$4p_y$	24	π_H	$4p_y$
1^1B_2	47	π_H	σ^*_{L+10}	53	π_H	$4p_x$	50	π_H	$4p_x$
	36	π_H	$4p_x$	16	π_H	σ^*_{L+10}	13	π_{H-1}	$4s$
	8	π_H	$3d_{xz}$				8	π_H	σ^*_{L+10}
2^1A_2	54	π_{H-1}	σ^*_{L+10}	34	π_{H-1}	σ^*_{L+10}	39	π_{H-1}	$4p_x$
	28	π_{H-1}	$4p_x$	27	π_{H-1}	$4p_x$	27	π_{H-1}	σ^*_{L+10}
	11	π_{H-1}	$3d_{xz}$	6	π_H	$4s$			
3^1A_1	55	π_{H-1}	$4p_y$	18	π_{H-1}	$3d_{yz}$	27	π_H	$3d_{xy}$
	19	π_H	π^*_{L+11}	12	π_{H-3}	π^*_{L+4}	10	π_{H-1}	π^*_{L+4}
				12	π_H	π^*_{L+11}	9	π_H	π^*_{L+11}
				10	π^2_H	π^{2*}_{L+4}	7	π_{H-3}	π^*_{L+4}
							5	π^2_H	π^{2*}_{L+4}
1^3B_1	72	π_H	π^*_{L+4}	69	π_H	π^*_{L+4}	57	π_H	π^*_{L+4}
	21	π_H	$4p_y$				14	π_H	$4p_y$
1^3A_1	70	π_{H-1}	π^*_{L+4}	53	π_{H-1}	π^*_{L+4}	44	π_{H-1}	π^*_{L+4}
	19	π_{H-1}	$4p_y$	17	π_H	π^*_{L+11}	17	π_H	π^*_{L+11}
	7	π_H	π^*_{L+11}				10	π_{H-1}	$4p_y$
1^3B_2	54	π_H	σ^*_{L+10}	42	π_H	$4p_x$	49	π_H	$4p_x$
	29	π_H	$4p_x$	28	π_H	σ^*_{L+10}	19	π_H	σ^*_{L+10}
	9	π_H	$3d_{xz}$						
2^3A_2	46	π_{H-1}	σ^*_{L+10}	48	π_{H-1}	σ^*_{L+10}	42	π_{H-1}	σ^*_{L+10}
	22	π_H	$4s$	17	π_{H-1}	$4p_x$	24	π_{H-1}	$4p_x$
	17	π_{H-1}	$4p_x$						
	7	π_{H-1}	$3d_{xz}$						
2^3A_1	73	π_H	π^*_{L+11}	41	π_H	π^*_{L+11}	43	π_H	π^*_{L+11}
	10	π_{H-3}	π^*_{L+4}	21	π_{H-1}	π^*_{L+4}	17	π_{H-1}	π^*_{L+4}
	6	π_{H-1}	π^*_{L+4}	10	π_{H-3}	π^*_{L+4}	7	π_{H-3}	π^*_{L+4}

The orbitals presented in the table are labeled according to the order obtained within the DFT theory. In the following cases the ordering of the Hartree-Fock orbitals is different:
The π^*_{L+4} bh-lyp orbital corresponds to the π^*_{L+9} hf orbital;

Table S31.: Calculated percentage of electron configurations in the discussed wave functions of **thiophene** obtained at the DFT/MRCI-R, and CASPT2 (6,10) levels of theory using the augmented basis. Only electron configurations with more than 5 percentage are presented.

	DFT/MRCI-R			CASPT2 (6,10)		
		Excitation			Excitation	
State	%	from	to	%	from	to
2^1A_1	56	π_{H-1}	π^*_{L+4}	46	π_{H-1}	π^*_{L+4}
	20	π_{H-1}	$4p_y$	19	π_H	π^*_{L+11}
	13	π_H	π^*_{L+11}	10	π_{H-1}	$4p_y$
1^1B_1	69	π_H	π^*_{L+4}	82	π_H	π^*_{L+4}
	22	π_H	$4p_y$	7	π_{H-1}	π^*_{L+11}
1^1B_2	44	π_H	σ^*_{L+10}	78	π_H	σ^*/p_x
	40	π_H	$4p_x$	5	π_H	$4p_x$
	7	π_H	$3d_{xz}$			
2^1A_2	53	π_{H-1}	σ^*_{L+10}	85	π_{H-1}	σ^*/p_x
	30	π_{H-1}	$4p_x$			
	11	π_{H-1}	$3d_{xz}$			
3^1A_1	66	π_{H-1}	$4p_y$	25	π_{H-1}	π^*_{L+4}
	11	π_H	π^*_{L+11}	25	π^2_H	π^{2*}_{L+4}
	9	π_{H-1}	π^*_{L+4}	21	π_{H-3}	π^*_{L+4}
				9	π_H	π^*_{L+11}
				7	π^2_{H-1}	π^{2*}_{L+4}
1^3B_1	74	π_H	π^*_{L+4}	87	π_H	π^*_{L+4}
	20	π_H	$4p_y$			
1^3A_1	71	π_{H-1}	π^*_{L+4}	60	π_{H-1}	π^*_{L+4}
	17	π_{H-1}	$4p_y$	25	π_H	π^*_{L+11}
	7	π_H	π^*_{L+11}			
1^3B_2	51	π_H	σ^*_{L+10}	79	π_H	σ^*/p_x
	32	π_H	$4p_x$	7	π_{H-1}	$4s$
	9	π_H	$3d_{xz}$			
2^3A_2	59	π_{H-1}	σ^*_{L+10}	77	π_{H-1}	σ^*/p_x
	23	π_{H-1}	$4p_x$	7	π_{H-1}	$\sigma^*_{,}/p_x$
	10	π_{H-1}	$3d_{xz}$			
2^3A_1	75	π_H	π^*_{L+11}	43	π_H	π^*_{L+11}
	8	π_{H-3}	π^*_{L+4}	35	π_{H-1}	π^*_{L+4}
	6	π_{H-1}	π^*_{L+4}	18	π_{H-3}	π^*_{L+4}

The σ^*/p_x and $\sigma^*_{,}/p_x$ CASSCF orbitals are, respectively, positive and negative linear combinations of σ^* and p_x orbitals. In HF and DFT calculations these orbitals do not mix.

S4.6. *Quinoxaline*

Table S32. Experimental and computed DFT/MRCI, DFT/MRCI-R, MR-MP2(HF)and MR-MP2(BH-LYP) vertical excitation energies of **quinoxaline**. The oscillator strengths are given in the parentheses.

		Energies(eV)				
State	Dominant character	DFT/MRCI	DFT/MRCI-R	MRMP2 (HF)	MRMP2 (BH-LYP)	Experiment
1^1B_1	$n \to \pi^*$	3.54 (0.007)	3.63 (0.008)	3.24 (0.004)	3.24 (0.005)	
2^1A_1	$\pi \to \pi^*$	4.14 (0.080)	4.13 (0.094)	3.75 (0.060)	3.61 (0.064)	**3.96**^{a}
1^1B_2	$\pi \to \pi^*$	4.36 (0.052)	4.33 (0.059)	4.68 (0.033)	4.57 (0.025)	
1^1A_2	$n \to \pi^*$	4.75 (0)	4.93 (0)	4.68 (0)^1	4.56 (0)^1	
2^1A_2	$n \to \pi^*$	5.05 (0)	5.14 (0)	4.47 (0)^2	4.28 (0)^2	
1^3B_2	$\pi \to \pi^*$	3.06	3.02	3.00	2.88	
1^3B_1	$n \to \pi^*$	3.16	3.25	2.83	2.74	
1^3A_1	$\pi \to \pi^*$	3.70	3.63	3.72	3.59	
1^3A_2	$n \to \pi^*$	4.42	4.57	4.32	4.17^3	
2^3B_2	$\pi \to \pi^*$	4.53	4.41	4.22	4.10	

MRMP2(HF): $^1 2^1A_2$, $^2 1^1A_2$

MRMP2(BHLYP): $^1 2^1A_2$, $^2 1^1A_2$, $^3 2^3A_2$

[a] Vapor absorption maximum [16]

Table S33.: Calculated percentage of electron configurations in the excited states wave functions of **quinoxaline** obtained at the DFT/MRCI, MR-MP2(HF) and MR-MP2(BH-LYP) levels of theory. Only electron configurations with more than 2 percentage are presented.

	DFT/MRCI (BH-LYP)			MRMP2 (HF)			MRMP2 (BH-LYP)		
		Excitation			Excitation			Excitation	
State	%	from	to	%	from	to	%	from	to
1^1B_1	83	n_{H-2}	π^*_L	53	n_{H-2}	π^*_L	53	n_{H-2}	π^*_L
	5	n_{H-2}	π^*_{L+2}	5	n_{H-2}	π^*_{L+2}	4	n_{H-2}	π^*_{L+2}
	2	n_{H-3},π_H	π^*_L,π^*_L				2	n_{H-3},π_{H-4}	π^*_L,π^*_L
2^1A_1	63	π_{H-1}	π^*_L	41	π_{H-1}	π^*_L	40	π_{H-1}	π^*_L
	24	π_H	π^*_{L+1}	16	π_H	π^*_{L+1}	15	π_H	π^*_{L+1}
1^1B_2	83	π_H	π^*_L	53	π_H	π^*_L	51	π_H	π^*_L
	2	π_{H-1},π_H	π^*_L,π^*_L	4	π_{H-1}	π^*_{L+1}	3	π_{H-1},π_H	π^*_L,π^*_L
	2	π_{H-1}	π^*_{L+1}	3	π_{H-1},π_H	π^*_L,π^*_L	3	π_{H-1}	π^*_{L+1}
	2	π_H	π^*_{L+2}				2	π_H	π^*_{L+2}
1^1A_2	61	n_{H-3}	π^*_L	43	n_{H-3}	π^*_L	40	n_{H-3}	π^*_L
	11	n_{H-2}	π^*_{L+1}	4	n_{H-3}	π^*_{L+2}	6	n_{H-2},π_H	π^*_L,π^*_L
	8	n_{H-2},π_H	π^*_L,π^*_L	4	n_{H-2}	π^*_{L+1}	4	n_{H-2}	π^*_{L+1}
	4	n_{H-3}	π^*_{L+2}	4	n_{H-2},π_H	π^*_L,π^*_L	3	n_{H-3}	π^*_{L+2}
	3	n_{H-2}	π^*_{L+5}	2	π_{H-4},n_{H-2}	π^*_L,π^*_L	2	π_{H-4},n_{H-2}	π^*_L,π^*_L
	3	π_{H-4},n_{H-2}	π^*_L,π^*_L	2	n_{H-2}	π^*_{L+5}	2	n_{H-2}	π^*_{L+5}
2^1A_2	73	n_{H-2}	π^*_{L+1}	51	n_{H-2}	π^*_{L+1}	50	n_{H-2}	π^*_{L+1}
	8	n_{H-3}	π^*_L	3	n_{H-3}	π^*_L	3	n_{H-3}	π^*_L
	3	n_{H-2},π_H	π^*_L,π^*_L	2	n_{H-2},π_{H-1}	π^*_L,π^*_{L+1}	2	n_{H-2},π_{H-1}	π^*_L,π^*_{L+1}
	3	n_{H-2},π_{H-1}	π^*_L,π^*_{L+1}						
1^3B_2	83	π_H	π^*_L	52	π_H	π^*_L	50	π_H	π^*_L
	3	π_H	π^*_{L+2}	3	π_{H-1}	π^*_{L+1}	3	π_{H-1}	π^*_{L+1}
	3	π_{H-1}	π^*_{L+1}	3	π_H	π^*_{L+2}	3	π_H	π^*_{L+2}
	2	π_{H-4}	π^*_{L+2}	2	π_{H-4}	π^*_{L+2}	2	π_{H-4}	π^*_{L+2}
	2	π_{H-4}	π^*_L				2	π_{H-4}	π^*_L
1^3B_1	82	n_{H-2}	π^*_L	52	n_{H-2}	π^*_L	52	n_{H-2}	π^*_L
	8	n_{H-2}	π^*_{L+2}	6	n_{H-2}	π^*_{L+2}	5	n_{H-2}	π^*_{L+2}
	2	n_{H-3}	π^*_{L+5}	2	n_{H-3}	π^*_{L+5}	2	n_{H-3}	π^*_{L+5}
1^3A_1	85	π_{H-1}	π^*_L	54	π_{H-1}	π^*_L	52	π_{H-1}	π^*_L
	6	π_H	π^*_{L+1}	7	π_H	π^*_{L+1}	7	π_H	π^*_{L+1}
1^3A_2	69	n_{H-3}	π^*_L	45	n_{H-3}	π^*_L	44	n_{H-3}	π^*_L
	8	n_{H-3}	π^*_{L+2}	7	n_{H-3}	π^*_{L+2}	6	n_{H-3}	π^*_{L+2}
	6	n_{H-2}	π^*_{L+1}	4	n_{H-2}	π^*_{L+5}	4	n_{H-2}	π^*_{L+5}
	6	n_{H-2}	π^*_{L+5}	2	n_{H-2}	π^*_{L+1}	2	n_{H-2},π_H	π^*_L,π^*_L
	2	n_{H-2},π_H	π^*_L,π^*_L				2	n_{H-2}	π^*_{L+1}

The orbitals presented in the table are labeled according to the order obtained within the DFT theory.
In the following cases the ordering of the Hartree-Fock orbitals is different:
The n_{H-3} bh-lyp orbital corresponds to the n_{H-5} hf orbital;
The π_{H-4} bh-lyp orbital corresponds to the π_{H-3} hf orbital;
The π^*_{L+5} bh-lyp orbital corresponds to the π^*_{L+9} hf orbital;

S4.7. *Quinazoline*

Table S34. Experimental and computed DFT/MRCI, DFT/MRCI-R, MR-MP2(HF), MR-MP2(BH-LYP) vertical excitation energies of **quinazoline**. The oscillator strengths are given in the parentheses.

State	Dominant character	Energies(eV)				
		DFT/MRCI	DFT/MRCI-R	MRMP2 (HF)	MRMP2 (BH-LYP)	Experiment
1^1A$''$	$n \to \pi^*$	3.80 (0.007)	3.92 (0.008)	3.49 (0.004)	3.39 (0.004)	
2^1A$'$	$\pi \to \pi^*$	4.27 (0.032)	4.26 (0.040)	3.90 (0.019)	3.55 (0.018)	**4.07**[a]
3^1A$'$	$\pi \to \pi^*$	4.72 (0.063)	4.68 (0.067)	4.86 (0.049)	4.62 (0.034)	**4.66**[a]
2^1A$''$	$n \to \pi^*$	4.76 (0)	4.89 (0)	4.35 (0)	4.13 (0)	
3^1A$''$	$n \to \pi^*$	5.18 (0.001)	5.29 (0.001)	4.72 (0)	4.42 (0)	
1^3A$'$	$\pi \to \pi^*$	3.16	3.13	3.13	2.96	
1^3A$''$	$n \to \pi^*$	3.54	3.66	3.16	3.10	
2^3A$'$	$\pi \to \pi^*$	4.06	4.00	3.91	3.72	
3^3A$'$	$\pi \to \pi^*$	4.38	4.33	4.50[1]	4.27[1]	
2^3A$''$	$n \to \pi^*$	4.44	4.58	4.03	3.75	

MRMP2(HF):[1]4^3A$'$

MRMP2(BHLYP):[1]4^3A$'$

[a] Absorption maximum in cyclohexane and etylether [17]

Table S35.: Calculated percentage of electron configurations in the excited states wave functions of **quinazoline** obtained at the DFT/MRCI, MR-MP2(HF) and MR-MP2(BH-LYP) levels of theory. Only electron configurations with more than 2 percentage are presented.

	DFT/MRCI			MRMP2			MRMP2		
	(BH-LYP)			(HF)			(BH-LYP)		
		Excitation			Excitation			Excitation	
State	%	from	to	%	from	to	%	from	to
1^1A$''$	81	n_{H-2}	π^*_L	53	n_{H-2}	π^*_L	52	n_{H-2}	π^*_L
	6	n_{H-2}	π^*_{L+2}	5	n_{H-2}	π^*_{L+2}	4	n_{H-2}	π^*_{L+2}
3^1A$'$	52	π_H	π^*_L	32	π_H	π^*_L	38	π_H	π^*_L
	23	π_{H-1}	π^*_L	17	π_{H-1}	π^*_L	11	π_{H-1}	π^*_L
	12	π_H	π^*_{L+1}	9	π_H	π^*_{L+1}	5	π_H	π^*_{L+1}
				2	π_{H-1}	π^*_{L+1}	3	π_{H-1}	π^*_{L+1}
2^1A$''$	68	n_{H-2}	π^*_{L+1}	45	n_{H-2}	π^*_{L+1}	42	n_{H-2}	π^*_{L+1}
	13	n_{H-3}	π^*_L	9	n_{H-3}	π^*_L	10	n_{H-3}	π^*_L
	4	n_{H-2}	π^*_{L+5}	3	n_{H-2}	π^*_{L+5}	3	n_{H-2}	π^*_{L+5}
3^1A$''$	64	n_{H-3}	π^*_L	42	n_{H-3}	π^*_L	39	n_{H-3}	π^*_L
	15	n_{H-2}	π^*_{L+1}	11	n_{H-2}	π^*_{L+1}	12	n_{H-2}	π^*_{L+1}
	4	n_{H-3}	π^*_{L+2}	3	n_{H-3}	π^*_{L+2}	3	n_{H-3}	π^*_{L+2}
	2	n_{H-2},π_{H-1}	π^*_L,π^*_{L+1}				2	n_{H-2},π_{H-1}	π^*_L,π^*_{L+1}
1^3A$'$	81	π_H	π^*_L	52	π_H	π^*_L	53	π_H	π^*_L
	3	π_{H-4}	π^*_{L+2}	4	π_{H-1}	π^*_L	2	π_{H-4}	π^*_{L+2}
	3	π_{H-1}	π^*_L	2	π_{H-4}	π^*_{L+2}	2	π_H	π^*_{L+2}
	2	π_H	π^*_{L+1}	2	π_H	π^*_{L+1}	2	π_{H-1}	π^*_L
	2	π_{H-1}	π^*_{L+1}	2	π_H	π^*_{L+2}			
1^3A$''$	80	n_{H-2}	π^*_L	51	n_{H-2}	π^*_L	51	n_{H-2}	π^*_L
	8	n_{H-2}	π^*_{L+2}	6	n_{H-2}	π^*_{L+2}	5	n_{H-2}	π^*_{L+2}
	2	n_{H-3}	π^*_{L+5}						
2^3A$''$	49	n_{H-2}	π^*_{L+1}	25	n_{H-2}	π^*_{L+1}	24	n_{H-3}	π^*_L
	27	n_{H-3}	π^*_L	21	n_{H-3}	π^*_L	22	n_{H-2}	π^*_{L+1}
	8	n_{H-2}	π^*_{L+5}	7	n_{H-2}	π^*_{L+5}	7	n_{H-2}	π^*_{L+5}
	3	n_{H-3}	π^*_{L+2}	3	n_{H-3}	π^*_{L+2}	3	n_{H-3}	π^*_{L+2}

The orbitals presented in the table are labeled according to the order obtained within the DFT theory.
In the following cases the ordering of the Hartree-Fock orbitals is different:
The n_{H-3} bh-lyp orbital corresponds to the n_{H-4} hf orbital;
The π_{H-4} bh-lyp orbital corresponds to the π_{H-3} hf orbital;
The π^*_{L+5} bh-lyp orbital corresponds to the π^*_{L+10} hf orbital;

S4.8. *Pyranthione*

Table S36. Experimental and computed DFT/MRCI, DFT/MRCI-R, MR-MP2(HF) and MR-MP2(BH-LYP) vertical excitation energies of **pyranthione**. The oscillator strengths are given in the parentheses.

State	Dominant character	Energies(eV) DFT/MRCI	DFT/MRCI-R	MRMP2 (HF)	MRMP2 (BH-LYP)	Experiment
1^1A_2	$n \to \pi^*$	2.16 (0)	2.22 (0)	2.26 (0)	2.25 (0)	**2.25**[a]
1^1B_2	$n \to \pi^*$	3.76 (0)	3.66 (0)	3.95 (0.001)	3.85 (0)	
2^1A_1	$\pi \to \pi^*$	3.92 (0.497)	3.90 (0.544)	3.76 (0.495)	3.71 (0.482)	**3.78**[a]
1^1B_1	$\pi \to \pi^*$	4.32 (0.003)	4.35 (0.002)	4.39 (0.001)	4.30 (0.002)	
2^1B_1	$\pi \to \pi^*$	5.59 (0.107)	5.63 (0.121)	5.54 (0.082)	5.37 (0.067)	
1^3A_2	$n \to \pi^*$	2.05	2.08	2.15	2.16	
1^3A_1	$\pi \to \pi^*$	2.28	2.19	2.22	2.19	
1^3B_1	$\pi \to \pi^*$	3.70	3.71	3.57	3.49	
1^3B_2	$n \to \pi^*$	3.80	3.61	3.94	3.83	
2^3A_1	$\pi \to \pi^*$	4.85	4.82	4.74	4.66	

[a] Absorption maximum in 3-methylpentane [18]

Table S37.: Calculated percentage of electron configurations in the excited states wave functions of **pyranthione** obtained at the DFT/MRCI, MR-MP2(HF) and MR-MP2(BH-LYP) levels of theory. Only electron configurations with more than 2 percentage are presented.

	DFT/MRCI (BH-LYP)			MRMP2 (HF)			MRMP2 (BH-LYP)		
		Excitation			Excitation			Excitation	
State	%	from	to	%	from	to	%	from	to
1^1A_2	87	n_H	π^*_L	62	n_H	π^*_L	60	n_H	π^*_L
	6	π_{H-1},n_H	π^*_L,π^*_L	6	π_{H-1},n_H	π^*_L,π^*_L	7	π_{H-1},n_H	π^*_L,π^*_L
	2	π_{H-2},n_H	π^*_L,π^*_{L+1}						
1^1B_2	76	n_H	π^*_{L+1}	50	n_H	π^*_{L+1}	48	n_H	π^*_{L+1}
	12	π_{H-1},n_H	π^*_L,π^*_{L+1}	13	π_{H-1},n_H	π^*_L,π^*_{L+1}	13	π_{H-1},n_H	π^*_L,π^*_{L+1}
	5	π_{H-2},n_H	π^*_L,π^*_{L+1}	4	π_{H-2},n_H	π^*_L,π^*_L	5	π_{H-2},n_H	π^*_L,π^*_L
2^1A_1	81	π_{H-1}	π^*_L	55	π_{H-1}	π^*_L	53	π_{H-1}	π^*_L
	6	π_{H-1},π_{H-1}	π^*_L,π^*_L	6	π_{H-1},π_{H-1}	π^*_L,π^*_L	6	π_{H-1},π_{H-1}	π^*_L,π^*_L
	4	π_{H-2},π_{H-1}	π^*_L,π^*_{L+1}	2	π_{H-2},π_{H-1}	π^*_L,π^*_{L+1}	3	π_{H-2},π_{H-1}	π^*_L,π^*_{L+1}
							2	π_{H-3},π_{H-1}	π^*_L,π^*_L
1^1B_1	77	π_{H-1}	π^*_{L+1}	51	π_{H-1}	π^*_{L+1}	48	π_{H-1}	π^*_{L+1}
	10	π_{H-1},π_{H-1}	π^*_L,π^*_{L+1}	9	π_{H-1},π_{H-1}	π^*_L,π^*_{L+1}	11	π_{H-1},π_{H-1}	π^*_L,π^*_{L+1}
	3	π_{H-2},π_{H-1}	π^*_L,π^*_L	3	π_{H-2},π_{H-1}	π^*_L,π^*_L	3	π_{H-2},π_{H-1}	π^*_L,π^*_L
	2	π_{H-3},π_{H-1}	π^*_L,π^*_{L+1}	2	π_{H-3},π_{H-1}	π^*_L,π^*_{L+1}	3	π_{H-2}	π^*_L
1^3A_2	91	n_H	π^*_L	63	n_H	π^*_L	61	n_H	π^*_L
	3	π_{H-1},n_H	π^*_L,π^*_L	5	π_{H-1},n_H	π^*_L,π^*_L	5	π_{H-1},n_H	π^*_L,π^*_L
1^3A_1	94	π_{H-1}	π^*_L	66	π_{H-1}	π^*_L	65	π_{H-1}	π^*_L
				2	π_{H-2}	π^*_{L+1}	2	π_{H-2}	π^*_{L+1}
1^3B_1	71	π_{H-1}	π^*_{L+1}	40	π_{H-1}	π^*_{L+1}	42	π_{H-1}	π^*_{L+1}
	16	π_{H-2}	π^*_L	20	π_{H-2}	π^*_L	16	π_{H-2}	π^*_L
	2	π_{H-2}	π^*_{L+6}	4	π_{H-3}	π^*_{L+1}	3	π_{H-2}	π^*_{L+6}
	2	π_{H-3}	π^*_{L+1}	3	π_{H-2}	π^*_{L+6}	3	π_{H-3}	π^*_{L+1}
	2	π_{H-1},π_{H-1}	π^*_L,π^*_{L+1}	2	π_{H-1},π_{H-1}	π^*_L,π^*_{L+1}	2	π_{H-1},π_{H-1}	π^*_L,π^*_{L+1}
1^3B_2	81	n_H	π^*_{L+1}	51	n_H	π^*_{L+1}	49	n_H	π^*_{L+1}
	10	π_{H-1},n_H	π^*_L,π^*_{L+1}	13	π_{H-1},n_H	π^*_L,π^*_{L+1}	13	π_{H-1},n_H	π^*_L,π^*_{L+1}
	3	π_{H-2},n_H	π^*_L,π^*_L	4	π_{H-2},n_H	π^*_L,π^*_L	5	π_{H-2},n_H	π^*_L,π^*_L
2^3A_1	63	π_{H-2}	π^*_{L+1}	43	π_{H-2}	π^*_{L+1}	42	π_{H-2}	π^*_{L+1}
	18	π_{H-3}	π^*_L	15	π_{H-3}	π^*_L	15	π_{H-3}	π^*_L
	11	π_{H-1}	π^*_{L+6}	7	π_{H-1}	π^*_{L+6}	7	π_{H-1}	π^*_{L+6}
	2	π_{H-2},π_{H-1}	π^*_L,π^*_{L+1}						

The orbitals presented in the table are labeled according to the order obtained within the DFT theory.
In the following cases the ordering of the Hartree-Fock orbitals is different:
The n_H bh-lyp orbital corresponds to the n_{H-1} hf orbital;
The π_{H-1} bh-lyp orbital corresponds to the π_H hf orbital;
The π^*_{L+6} bh-lyp orbital corresponds to the π^*_{L+7} hf orbital.

S4.9. *Dithiin*

Table S38. Experimental and computed DFT/MRCI, DFT/MRCI-R, MR-MP2(HF) and MR-MP2(BH-LYP) vertical excitation energies of **dithiin**. The oscillator strengths are given in the parentheses.

State	Dominant character	Energies(eV)				
		DFT/MRCI	DFT/MRCI-R	MRMP2 (HF)	MRMP2 (BH-LYP)	Experiment
1^1B	$\pi \rightarrow \pi^*$	2.60 (0.001)	2.58 (0.001)	2.38 (0.001)	2.33 (0.001)	**2.74**[a]
2^1A	$\pi \rightarrow \pi^*$	4.36 (0.035)	4.36 (0.038)	4.17 (0.015)	4.01 (0.010)	**4.44**[a]
2^1B	$\pi \rightarrow \pi^*/\sigma^*$	4.54 (0.018)	4.52 (0.019)	4.26 (0.014)[1]	4.14 (0.009)[1]	**5.00**[a]
3^1B	$\pi \rightarrow \pi^*/\sigma^*$	4.73 (0.005)	4.69 (0.006)	4.20 (0.006)[2]	3.97 (0.005)[2]	
3^1A	$\pi^2 \rightarrow \pi^{*2}$	4.80 (0)	4.69 (0)	4.39 (0)	4.23 (0)	
1^3B	$\pi \rightarrow \pi^*$	2.00	2.06	1.86	1.84	
2^3B	$\pi \rightarrow \pi^*/\sigma^*$	3.31	3.40	2.88	2.85	
1^3A	$\pi \rightarrow \pi^*$	3.75	3.82	3.74	3.68	
3^3B	$\pi \rightarrow \pi^*/\sigma^*$	4.36	4.36	3.91	3.81	
2^3A	$\pi \rightarrow \pi^*$	4.77	4.88	4.37	4.24	

MR-MP2(HF): $^13^1$B,$^22^1$B

MR-MP2(BH-LYP): $^13^1$B,$^22^1$B

[a] UV-vis absorption maximum in CH_2Cl_2 [19]

Table S39. Calculated percentage of electron configurations in the excited states wave functions of **dithiin** obtained at the DFT/MRCI, MR-MP2(HF) and MR-MP2(BH-LYP) levels of theory. Only electron configurations with more than 2 percentage are presented.

	DFT/MRCI (BH-LYP)			MRMP2 (HF)			MRMP2 (BH-LYP)		
		Excitation			Excitation			Excitation	
State	%	from	to	%	from	to	%	from	to
1^1B	89	π_H	π^*_L	62	π_H	π^*_L	64	π_H	π^*_L
	3	π_H	σ^*_{L+1}	2	π_H	σ^*_{L+1}	2	π_H	σ^*_{L+1}
	2	π_{H-2}	π^*_L	2	π_{H-2}	π^*_L			
2^1A	83	π_{H-1}	π^*_L	54	π_{H-1}	π^*_L	55	π_{H-1}	π^*_L
	4	π_{H-1}	σ^*_{L+1}	4	π_{H-1}	σ^*_{L+1}	3	π_{H-1}	σ^*_{L+1}
				2	π_H	π^*_{L+4}			
2^1B	44	π_H	σ^*_{L+1}	28	π_{H-2}	π^*_L	30	π_{H-2}	π^*_L
	36	π_{H-2}	π^*_L	27	π_H	σ^*_{L+1}	29	π_H	σ^*_{L+1}
	7	π_{H-2}	σ^*_{L+1}	6	π_{H-2}	σ^*_{L+1}	4	π_{H-2}	σ^*_{L+1}
	5	π_H	π^*_L	5	π_H	π^*_L	2	π_H	π^*_L
3^1B	48	π_{H-2}	π^*_L	31	π_H	σ^*_{L+1}	31	π_H	σ^*_{L+1}
	40	π_H	σ^*_{L+1}	31	π_{H-2}	π^*_L	29	π_{H-2}	π^*_L
3^1A	81	π_H, π_H	π^*_L,π^*_L	49	π_H, π_H	π^*_L,π^*_L	49	π_H, π_H	π^*_L,π^*_L
	3	π_{H-2},π_H	π^*_L,σ^*_{L+1}	3	π_{H-2},π_H	π^*_L,σ^*_{L+1}	3	π_{H-2},π_H	π^*_L,σ^*_{L+1}
	2	π_{H-1},π_{H-1}	π^*_L,π^*_L	3	n_{H-3}	π^*_L	3	π_{H-2},π_H	π^*_L,π^*_L
				2	π_H	σ^*_{L+2}	2	n_{H-3}	π^*_L
				2	π_{H-1},π_{H-1}	π^*_L,π^*_L			
1^3B	92	π_H	π^*_L	64	π_H	π^*_L	61	π_H	π^*_L
	2	π_{H-2}	σ^*_{L+1}	2	π_{H-2}	σ^*_{L+1}	3	π_{H-2}	π^*_L
							3	π_{H-2}	σ^*_{L+1}
2^3B	52	π_{H-2}	π^*_L	33	π_{H-2}	π^*_L	32	π_{H-2}	π^*_L
	40	π_H	σ^*_{L+1}	30	π_H	σ^*_{L+1}	31	π_H	σ^*_{L+1}
							3	π_H	π^*_L
1^3A	84	π_{H-1}	π^*_L	43	π_{H-1}	π^*_L	42	π_{H-1}	π^*_L
	4	π_H	π^*_{L+4}	12	π_H	π^*_{L+4}	10	π_H	π^*_{L+4}
				4	n_{H-3}	π^*_L	5	n_{H-3}	π^*_L
				3	π_{H-2}	π^*_{L+4}	4	π_{H-2}	π^*_{L+4}
3^3B	49	π_H	σ^*_{L+1}	29	π_{H-2}	π^*_L	28	π_{H-2}	π^*_L
	39	π_{H-2}	π^*_L	28	π_H	σ^*_{L+1}	28	π_H	σ^*_{L+1}
				4	n_{H-4}	π^*_L	5	n_{H-4}	π^*_L
				2	n_{H-4}	σ^*_{L+1}	2	n_{H-4}	σ^*_{L+1}
2^3A	23	π_H	π^*_{L+4}	16	π_{H-1}	σ^*_{L+1}	17	π_{H-1}	σ^*_{L+1}
	21	π_H	σ^*_{L+2}	12	π_{H-1}	π^*_L	16	π_{H-1}	π^*_L
	18	π_{H-1}	σ^*_{L+1}	10	π_H	π^*_{L+4}	9	π_H	π^*_{L+4}
	17	n_{H-3}	π^*_L	8	n_{H-3}	π^*_L	9	n_{H-3}	π^*_L
	6	π_{H-6}	π^*_L	7	π_H	σ^*_{L+2}	6	π_{H-6}	π^*_L
	3	π_{H-2}	π^*_{L+4}	6	π_{H-6}	π^*_L	5	π_H	σ^*_{L+2}
				2	π_{H-2}	σ^*_{L+2}	3	π_{H-2}	π^*_{L+4}

The orbitals presented in the table are labeled according to the order obtained within the DFT theory. In the following cases the ordering of the Hartree-Fock orbitals is different:
The π_{H-2} bh-lyp orbital corresponds to the π_{H-1} hf orbital;
The π_{H-1} bh-lyp orbital corresponds to the π_{H-2} hf orbital;
The σ^*_{L+2} bh-lyp orbital corresponds to the σ^*_{L+3} hf orbital.
The Ry_{L+3} bh-lyp orbital corresponds to the Ry_{L+2} hf orbital.
The π^*_{L+4} bh-lyp orbital corresponds to the π^*_{L+5} hf orbital.

S4.10. *Bithiophene*

Table S40. Experimental and computed DFT/MRCI, DFT/MRCI-R, MR-MP2(HF) and MR-MP2(BH-LYP) vertical excitation energies of s-*trans* **bithiophene**. The oscillator strengths are given in the parentheses.

		Energies(eV)				
State	Dominant character	DFT/MRCI	DFT/MRCI-R	MRMP2 (HF)	MRMP2 (BH-LYP)	Experiment
1^1B	$\pi \rightarrow \pi^*$	4.17 (0.446)	4.15 (0.472)	4.02 (0.437)	3.93 (0.401)	3.86[a], 4.09 (**4.11**)[b]
2^1A	$\pi \rightarrow \pi^*$	4.81 (0.005)	4.87 (0.006)	4.66 (0.001)	4.39 (0)[1]	
2^1B	$\pi \rightarrow \pi^*$	4.95 (0.112)	5.00 (0.129)	4.58 (0.092)	4.18 (0.066)	**5.02**[b]
3^1A	$\pi \rightarrow \pi^*$	5.02 (0.003)	5.11 (0.004)	4.69 (0.003)	4.28 (0.002)[2]	
4^1A	$\pi \rightarrow \sigma^*$	5.34 (0.001)	5.39 (0.002)	5.27 (0.001)[1]	4.81 (0)[3]	
3^1B	$\pi \rightarrow \sigma^*$	5.42 (0.023)	5.46 (0.029)	5.44 (0.030)	4.92 (0.028)	
1^3B	$\pi \rightarrow \pi^*$	2.78	2.81	2.62	2.44	2.32[a]
1^3A	$\pi \rightarrow \pi^*$	3.72	3.79	3.50	3.25	
2^3A	$\pi \rightarrow \pi^*$	4.17	4.22	4.02	3.72	
2^3B	$\pi \rightarrow \pi^*$	4.21	4.26	3.98	3.71	
3^3B	$\pi \rightarrow \sigma^*$	5.09	5.14	5.03	4.55	
3^3A	$\pi \rightarrow \sigma^*$	5.09	5.14	5.35	4.76	
4^3B	$\pi \rightarrow \pi^*$	5.43	5.49	5.46	4.76	
4^3A	$\pi \rightarrow \pi^*$	5.45	5.39	5.38	4.92	

MRMP2(HF): [1]5^1A

MRMP2(BH-LYP):[1]3^1A, [2]2^1A, [3]5^1A

[a] PD-PES in the gas phase [20]

[b] Absorption maximum in dioxane. [21]

[b] Value in parentheses is for the spectra in methylcyclohexane [21]

Table S41.: Calculated percentage of electron configurations in the excited states wave functions of s-*trans* **bithiophene** obtained at the DFT/MRCI, MR-MP2(HF) and MR-MP2(BH-LYP) levels of theory. Only electron configurations with more than 2 percentage are presented.

	DFT/MRCI (BH-LYP)			MRMP2 (HF)			MRMP2 (BH-LYP)		
		Excitation			Excitation			Excitation	
State	%	from	to	%	from	to	%	from	to
1^1B	89	π_H	π^*_L	58	π_H	π^*_L	56	π_H	π^*_L
2^1A	54	π_{H-1}	π^*_L	21	π_H	π^*_{L+1}	21	π_H	π^*_{L+1}
	16	π_H	π^*_{L+1}	21	π_{H-1}	π^*_L	12	π_{H-1}	π^*_L
	4	π_{H-2}	π^*_{L+1}	8	π_H,π_H	π^*_L,π^*_L	12	π_H,π_H	π^*_L,π^*_L
	3	π_{H-3}	π^*_L	3	π_{H-3}	π^*_L	7	π_{H-3}	π^*_L
	3	π_H,π_H	π^*_L,π^*_L	2	π_{H-3},π_H	π^*_L, π^*_{L+1}	3	π_{H-3},π_H	π^*_L, π^*_{L+1}
	2	π_{H-2},π_H	π^*_L,π^*_L						
	2	π_H	σ^*_{L+2}						
2^1B	65	π_{H-2}	π^*_L	40	π_{H-2}	π^*_L	35	π_{H-2}	π^*_L
	5	π_H	π^*_{L+6}	5	π_H	π^*_{L+6}	8	π_H	σ^*_{L+3}
	5	π_H	σ^*_{L+3}	4	π_H	σ^*_{L+3}	5	π_H	π^*_{L+6}
	3	π_H,π_{H-1}	π^*_L, π^*_L	3	π_H,π_{H-1}	π^*_L, π^*_L	3	π_H,π_{H-1}	π^*_L, π^*_L
	3	π_{H-1}	π^*_{L+1}	2	π_H	Ry_{L+4}	2	π_H	Ry_{L+4}
	2	π_H	Ry_{L+4}						
1^3B	87	π_H	π^*_L	56	π_H	π^*_L	54	π_H	π^*_L
	5	π_{H-3}	π^*_{L+1}	5	π_{H-3}	π^*_{L+1}	6	π_{H-3}	π^*_{L+1}
1^3A	51	π_H	π^*_{L+1}	33	π_H	π^*_{L+1}	32	π_H	π^*_{L+1}
	37	π_{H-3}	π^*_L	24	π_{H-3}	π^*_L	25	π_{H-3}	π^*_L
2^3A	73	π_{H-1}	π^*_L	42	π_{H-1}	π^*_L	42	π_{H-1}	π^*_L
	11	π_{H-2}	π^*_{L+1}	10	π_{H-2}	π^*_{L+1}	10	π_{H-2}	π^*_{L+1}
	3	π_{H-3}	π^*_L	4	π_{H-3}	π^*_L	2	π_H	π^*_{L+7}
							2	π_{H-3}	π^*_L
2^3B	67	π_{H-2}	π^*_L	39	π_{H-2}	π^*_L	38	π_{H-2}	π^*_L
	14	π_{H-1}	π^*_{L+1}	12	π_{H-1}	π^*_{L+1}	11	π_{H-1}	π^*_{L+1}
	5	π_H	π^*_{L+6}	5	π_H	π^*_{L+6}	4	π_H	π^*_{L+6}
	2	π_H	σ^*_{L+3}	2	π_{H-3}	π^*_{L+1}	2	π_{H-3}	π^*_{L+1}
	2	π_H	Ry_{L+4}				2	π_H	σ^*_{L+3}
	2	π_{H-3}	π^*_{L+1}				2	π_H	Ry_{L+4}
3^3B	63	π_H	σ^*_{L+3}	15	π_H	σ^*_{L+3}	27	π_H	σ^*_{L+3}
	9	π_{H-3}	π^*_{L+1}	12	π_H	π^*_{L+6}	9	π_{H-3}	π^*_{L+1}
	7	π_{H-2}	π^*_L	11	π_{H-3}	π^*_{L+1}	8	π_{H-2}	π^*_L
	3	π_H	π^*_{L+6}	10	π_{H-2}	π^*_L	6	π_H	π^*_{L+6}
	2	π_{H-6}	π^*_L	7	π_H	Ry_{L+4}	3	π_{H-6}	π^*_L
				3	π_{H-6}	π^*_L	2	π_H	Ry_{L+4}
							2	π_H	π^*_L
3^3A	76	π_H	σ^*_{L+2}	22	π_H	σ^*_{L+2}	41	π_H	σ^*_{L+2}
	3	π_{H-3}	σ^*_{L+3}	12	π_H	Ry_{L+5}	4	π_{H-1}	π^*_L
	2	π_H	Ry_{L+5}	6	π_H	π^*_{L+7}	4	π_{H-3}	π^*_{L+6}
				5	π_{H-1}	π^*_L	3	π_H	Ry_{L+5}
				4	π_{H-3}	π^*_{L+6}	2	π_H	π^*_{L+7}
				3	π_H	Ry_{L+10}	2	π_{H-3}	Ry_{L+4}
				2	π_H	π^*_{L+1}			
				2	π_{H-3}	π^*_L			

Continued on next page

Table S41 – continued from previous page

	DFT/MRCI			MRMP2			MRMP2		
	(BH-LYP)			(HF)			(BH-LYP)		
		Excitation			Excitation			Excitation	
State	%	from	to	%	from	to	%	from	to
				2	π_{H-3}	Ry_{L+11}			
4^3B	33	π_H	π^*_{L+6}	20	π_H	σ^*_{L+3}	20	π_H	σ^*_{L+3}
	12	π_H	σ^*_{L+3}	11	π_H	Ry_{L+11}	15	π_H	π^*_{L+6}
	12	π_H	Ry_{L+4}	7	π_H	π^*_{L+6}	8	π_{H-3}	σ^*_{L+2}
	9	π_{H-3}	σ^*_{L+2}	4	π_{H-3}	σ^*_{L+2}	5	π_H	Ry_{L+4}
	9	π_{H-3}	π^*_{L+1}	4	π_{H-1}	Ry_{L+2}	3	π_{H-1}	Ry_{L+2}
	6	π_{H-2}	π^*_L	3	π_{H-3}	π^*_{L+1}	3	π_{H-3}	π^*_{L+1}
	4	π_{H-6}	π^*_L	3	π_H	Ry_{L+4}			
4^3A	34	π_{H-3}	π^*_L	17	π_H	σ^*_{L+2}	11	π_{H-3}	π^*_L
	27	π_H	π^*_{L+1}	12	π_{H-3}	π^*_L	11	π_H	π^*_{L+1}
	7	π_{H-1}	π^*_L	11	π_H	π^*_{L+1}	10	π_H	σ^*_{L+2}
	6	π_H	π^*_{L+7}	5	π_{H-3}	σ^*_{L+3}	7	π_H	π^*_{L+7}
	4	π_{H-3}	π^*_{L+6}	5	π_H	Ry_{L+10}	7	π_{H-3}	σ^*_{L+3}
	3	π_H	Ry_{L+5}				3	π_{H-1}	π^*_L
	3	π_{H-3}	σ^*_{L+3}				2	π_H	Ry_{L+5}
	2	π_H	Ry_{L+10}				2	π_H	Ry_{L+9}
	2	π_H	Ry_{L+9}				2	π_{H-3}	π^*_{L+6}
							2	π_H	Ry_{L+10}

The orbitals presented in the table are labeled according to the order obtained within the DFT theory. In the following cases the ordering of the Hartree-Fock orbitals is different:
The π^*_{L+7} bh-lyp orbital corresponds to the π^*_{L+8} hf orbital;
The Ry_{L+10} bh-lyp orbital corresponds to the Ry_{L+11} hf orbital;
The Ry_{L+11} bh-lyp orbital corresponds to the Ry_{L+10} hf orbital.

S4.11. *Nitromethane*

Table S42. Experimental and computed DFT/MRCI, DFT/MRCI-R, MR-MP2(HF) and MR-MP2(BH-LYP) vertical excitation energies of **nitromethane** using the valence basis. The oscillator strengths are given in the parentheses.

		Energies(eV)				
State	Dominant character	DFT/MRCI	DFT/MRCI-R	MRMP2 (HF)	MRMP2 (BH-LYP)	Experiment
$1^1A''$	$n \rightarrow \pi^*$	3.92 (0)	4.00 (0)	3.83 (0)	3.77 (0)	**4.25**[a]
$2^1A''$	$n \rightarrow \pi^*$	4.34 (0)	4.36 (0)	4.04 (0)	4.07 (0)	**4.50**[b], 4.45[c], 4.51[d], 4.59[e]
$2^1A'$	$\pi \rightarrow \pi^*$	6.39 (0.260)	6.44 (0.305)	6.46 (0.209)	6.47 (0.198)	**6.25**[b], 6.23[a,c] 6.29[d], 6.26[e]
$3^1A'$	$\pi \rightarrow \pi^*$	8.86 (0.093)	9.02 (0.045)†	8.60 (0.196)[1]	8.59 (0.260)[1]	
$4^1A'$	$\pi \rightarrow Ryd$	8.92 (0.007)	8.88 (0.002)	8.58 (0.019)[2]	8.54 (0.003)[2]	
$1^3A'$	$\pi \rightarrow \pi^*$	3.43	3.31	3.54	3.55	
$1^3A''$	$n \rightarrow \pi^*$	3.71	3.80	3.55	3.60	
$2^3A''$	$n \rightarrow \pi^*$	4.10	4.13	3.85	3.92	
$2^3A'$	$n, n \rightarrow \pi^{*2}$	7.51	6.25	8.66[3]	8.85[3]	
$3^3A'$	$\pi \rightarrow \pi^*$	7.98	8.13	8.27[4]	8.26[4]	
$4^3A'$	$\pi \rightarrow Ryd$	8.81	8.75	8.44[5]	8.40[5]	

†$5^1A'$

MRMP2(HF):[1]$4^1A'$,[2]$3^1A'$, [3]$4^3A'$, [4]$2^3A'$, [5]$3^3A'$

MRMP2(BHLYP):[1]$4^1A'$,[2]$3^1A'$, [3]$6^3A'$, [4]$2^3A'$, [5]$3^3A'$

[a] Electron energy-loss maximum in gas [22]

[b] Absorption maximum in gas [22]

[c] Electron energy-loss maximum in gas[23]

[d] Absorption maximum in gas [24]

[e] Absorption maximum in gas [25]

Table S43.: Calculated percentage of electron configurations in the excited states wave functions of **nitromethane** obtained at the DFT/MRCI, MR-MP2(HF) and MR-MP2(BH-LYP) levels of theory using the valence basis. Only electron configurations with more than 2 percentage are presented.

	DFT/MRCI (BH-LYP)			MRMP2 (HF)			MRMP2 (BH-LYP)		
		Excitation			Excitation			Excitation	
State	%	from	to	%	from	to	%	from	to
1^1A$''$	90	n_{H-1}	π^*_L	62	n_{H-1}	π^*_L	70	n_{H-1}	π^*_L
	7	n_{H-2},π_H	π^*_L,π^*_L	7	n_{H-2}	π^*_L	6	n_{H-2},π_H	π^*_L,π^*_L
				5	n_{H-2},π_H	π^*_L,π^*_L			
				2	n_{H-1}	Ry_{L+4}			
2^1A$''$	89	n_{H-2}	π^*_L	62	n_{H-2}	π^*_L	71	n_{H-2}	π^*_L
	8	n_{H-1},π_H	π^*_L,π^*_L	8	n_{H-1}	π^*_L	6	n_{H-1},π_H	π^*_L,π^*_L
				6	n_{H-1},π_H	π^*_L,π^*_L			
				2	n_{H-2}	Ry_{L+4}			
2^1A$'$	83	π_H	π^*_L	65	π_H	π^*_L	63	π_H	π^*_L
	6	π_{H-7},π_H	π^*_L,π^*_L	6	π_{H-7},π_H	π^*_L,π^*_L	9	π_{H-7},π_H	π^*_L,π^*_L
	4	π_{H-3},π_H	π^*_L,π^*_L	3	π_{H-3},π_H	π^*_L,π^*_L	3	π_{H-3},π_H	π^*_L,π^*_L
1^3A$'$	98	π_H	π^*_L	78	π_H	π^*_L	80	π_H	π^*_L
				2	π_H	Ry_{L+4}			
1^3A$''$	93	n_{H-1}	π^*_L	64	n_{H-1}	π^*_L	71	n_{H-1}	π^*_L
	3	n_{H-2},π_H	π^*_L,π^*_L	6	n_{H-2}	π^*_L	4	n_{H-2},π_H	π^*_L,π^*_L
				4	n_{H-2},π_H	π^*_L,π^*_L			
				2	n_{H-1}	Ry_{L+4}			
2^3A$''$	94	n_{H-2}	π^*_L	65	n_{H-2}	π^*_L	72	n_{H-2}	π^*_L
	4	n_{H-1},π_H	π^*_L,π^*_L	7	n_{H-1}	π^*_L	5	n_{H-1},π_H	π^*_L,π^*_L
				5	n_{H-1},π_H	π^*_L,π^*_L			
				2	n_{H-2}	Ry_{L+4}			

The orbitals presented in the table are labeled according to the order obtained within the DFT theory.
In the following cases the ordering of the Hartree-Fock orbitals is different:
The π_{H-7} bh-lyp orbital corresponds to the π_{H-6} hf orbital;
The n_{H-1} bh-lyp orbital corresponds to the n_{H-2} hf orbital;
The n_{H-2} bh-lyp orbital corresponds to the n_{H-1} hf orbital.

Table S44. Selected matrix elements (cm^{-1}) for **nitromethane** calculated with DFT/MRCI, DFT/MRCI-R, MR-MP2(HF) and MR-MP2(BH-LYP) methods using the valence basis.

	SOMEs(cm^{-1})			
	DFT/MRCI	DFT/MRCI-R	MRMP2 (HF)	MRMP2 (BH-LYP)
$\langle 1^3A' \vert \hat{\mathcal{H}}_{\mathrm{SO\ z}} \vert 1^1A' \rangle$	0.3	0.3	0.2	0.0
$\langle 1^3A'' \vert \hat{\mathcal{H}}_{\mathrm{SO\ x}} \vert 1^1A' \rangle$	33.9	32.8	31.8	36.6
$\langle 1^3A'' \vert \hat{\mathcal{H}}_{\mathrm{SO\ x}} \vert 2^1A' \rangle$	17.0	16.0	17.2	17.4
$\langle 1^3A'' \vert \hat{\mathcal{H}}_{\mathrm{SO\ y}} \vert 1^1A' \rangle$	16.5	16.7	22.8	18.0
$\langle 1^3A'' \vert \hat{\mathcal{H}}_{\mathrm{SO\ y}} \vert 2^1A' \rangle$	30.1	28.6	30.7	30.6
$\langle 1^3A' \vert \hat{\mathcal{H}}_{\mathrm{SO\ x}} \vert 1^1A'' \rangle$	23.8	23.3	22.3	23.7
$\langle 1^3A' \vert \hat{\mathcal{H}}_{\mathrm{SO\ x}} \vert 2^1A'' \rangle$	9.5	9.4	10.6	7.9
$\langle 1^3A' \vert \hat{\mathcal{H}}_{\mathrm{SO\ y}} \vert 1^1A'' \rangle$	41.1	40.5	42.1	41.5
$\langle 1^3A' \vert \hat{\mathcal{H}}_{\mathrm{SO\ y}} \vert 2^1A'' \rangle$	6.7	6.3	1.2	5.3
$\langle 1^3A'' \vert \hat{\mathcal{H}}_{\mathrm{SO\ z}} \vert 2^1A'' \rangle$	32.8	32.3	35.1	35.7
$\langle 1^3A'' \vert \hat{\mathcal{H}}_{\mathrm{SO\ x}} \vert 1^3A' \rangle$	22.6	23.1	22.3	23.5
$\langle 1^3A'' \vert \hat{\mathcal{H}}_{\mathrm{SO\ y}} \vert 1^3A' \rangle$	39.0	40.0	41.2	40.7
$\langle 2^3A'' \vert \hat{\mathcal{H}}_{\mathrm{SO\ z}} \vert 1^3A'' \rangle$	33.9	32.5	35.5	35.9

Table S45. Experimental and computed DFT/MRCI, DFT/MRCI-R, MR-MP2(HF), MR-MP2(BH-LYP), CASPT2 (8,7) and CASPT2 (8,6) vertical excitation energies of **nitromethane** using the augmented basis. The CASPT2 (8,7) active space consists of fallowing occupied/unoccupied orbitals: 2/2 $a^{'}$ and 2/1 $a^{''}$. The (8,6) active space has one $a^{'}$ orbital less. The oscillator strengths are given in the parentheses.

State	Dominant character	Energies(eV)						
		DFT/MRCI	DFT/MRCI-R	MRMP2 (HF)	MRMP2 (BH-LYP)	CASPT2 (8,7)	CASPT2 (8,6)	Experiment
1^1A″	$n \rightarrow \pi^*$	3.83 (0)	3.92 (0)	3.64 (0)	3.71 (0)	3.92 (0)	3.88 (0)	**4.25**^{a}
2^1A″	$n \rightarrow \pi^*$	4.26 (0)	4.28 (0)	3.97 (0)	4.03 (0)	4.32 (0)	4.33 (0)	**4.50**^{b}, 4.45^c, 4.51^d, 4.59^e
2^1A′	$\pi \rightarrow \pi^*$	6.30 (0.257)	6.34 (0.297)	6.18 (0.204)	6.31 (0.200)	6.38 (0.260)	5.63 (0.384)	**6.25**^{b}, 6.23^{a,c}, 6.29^d, 6.26^e
3^1A′	$n \rightarrow 3s$	7.74 (0.008)	7.66 (0.007)	7.55 (0.004)	7.49 (0.010)	7.07 (0.033)	7.42 (0.003)	
4^1A′	$n \rightarrow 3s$	8.00 (0.041)	7.87 (0.042)	7.62 (0.022)	7.72 (0.033)	7.55 (0.078)	7.80 (0)	
1^3A′	$\pi \rightarrow \pi^*$	3.36	3.30	3.54	3.57	3.65	3.70	
1^3A″	$n \rightarrow \pi^*$	3.61	3.72	3.42	3.52	3.66	3.66	
2^3A″	$n \rightarrow \pi^*$	4.01	4.06	3.80	3.93	4.15	4.16	
2^3A′	$n, n \rightarrow \pi^{*2}$	7.31	6.12	8.70^1	8.79^1	8.97	9.01	
3^3A′	$n \rightarrow 3s$	7.65	7.56	7.50^2	7.46^2	7.43	7.48	
4^3A′	$n \rightarrow 3s$	7.91	7.79	7.51^3	7.57^3	7.73	7.73	

MRMP2(HF):[1] 5^3A′, [2]2^3A′, [3]3^3A′

MRMP2(BH-LYP):[1] 8^3A′, [2]2^3A′, [3]3^3A′

[a] Electron energy-loss maximum in gas [22]

[b] Absorption maximum in gas [22]

[c] Electron energy-loss maximum in gas[23]

[d] Absorption maximum in gas [24]

[e] Absorption maximum in gas [25]

Table S46.: Calculated percentage of electron configurations in the excited states wave functions of **nitromethane** obtained at the DFT/MRCI, MR-MP2(HF) and MR-MP2(BH-LYP) levels of theory using the augmented basis. Only electron configurations with more than 5 percentage are presented.

	DFT/MRCI			MRMP2			MRMP2		
	(BH-LYP)			(HF)			(BH-LYP)		
		Excitation			Excitation			Excitation	
State	%	from	to	%	from	to	%	from	to
$1^1\text{A}''$	86	n_{H-1}	π^*_L	52	n_{H-1}	π^*_L	68	n_{H-1}	π^*_L
	6	n_{H-2},π_H	π^*_L,π^*_L	10	n_{H-1}	π^*/pz	5	n_{H-2},π_H	π^*_L,π^*_L
				6	n_{H-1}	$\pi^*/pz^{'}$			
$2^1\text{A}''$	86	n_{H-2}	π^*_L	52	n_{H-2}	π^*_L	68	n_{H-2}	π^*_L
	7	n_{H-1},π_H	π^*_L,π^*_L	10	n_{H-2}	π^*/pz	6	n_{H-1},π_H	π^*_L,π^*_L
				6	n_{H-2}	$\pi^*/pz^{'}$			
$2^1\text{A}'$	82	π_H	π^*_L	39	π_H	π^*_L	63	π_H	π^*_L
	6	π_{H-7},π_H	π^*_L,π^*_L	16	π_H	π^*/pz	8	π_{H-7},π_H	π^*_L,π^*_L
				11	π_H	$\pi^*/pz^{'}$			
$1^3\text{A}'$	94	π_H	π^*_L	62	π_H	π^*_L	77	π_H	π^*_L
				11	π_H	π^*/pz			
				6	π_H	$\pi^*/pz^{'}$			
$1^3\text{A}''$	89	n_{H-1}	π^*_L	54	n_{H-1}	π^*_L	68	n_{H-1}	π^*_L
				9	n_{H-1}	π^*/pz			
				6	n_{H-1}	$\pi^*/pz^{'}$			
$2^3\text{A}''$	90	n_{H-2}	π^*_L	54	n_{H-2}	π^*_L	69	n_{H-2}	π^*_L
				10	n_{H-2}	π^*/pz	5	n_{H-1},π_H	π^*_L,π^*_L
				6	n_{H-2}	$\pi^*/pz^{'}$			

The orbitals presented in the table are labeled according to the order obtained within the DFT theory.
In the following cases the ordering of the Hartree-Fock orbitals is different:
The π^*_L bh-lyp orbital corresponds to the π^*_{L+9} hf orbital;
The n_{H-1} bh-lyp orbital corresponds to the n_{H-2} hf orbital;
The n_{H-2} bh-lyp orbital corresponds to the n_{H-1} hf orbital.

Table S47.: Calculated percentage of electron configurations in the discussed wave functions of **nitromethane** obtained at the DFT/MRCI-R, CASPT2 (8,7) and CASPT2 (8,6) levels of theory using the augmented basis. Only electron configurations with more than 5 percentage are presented.

	DFT/MRCI-R			CASPT2 (8,7)			CASPT2 (8,6)		
		Excitation			Excitation			Excitation	
State	%	from	to	%	from	to	%	from	to
$1^1A''$	88	n_{H-1}	π^*_L	86	n_{H-1}	π^*_L	84	n_{H-1}	π^*_L
	5	n_{H-2},π_H	π^*_L,π^*_L	11	n_{H-2},π_H	π^*_L,π^*_L	16	n_{H-2},π_H	π^*_L,π^*_L
$2^1A''$	87	n_{H-2}	π^*_L	82	n_{H-2}	π^*_L	81	n_{H-2}	π^*_L
	6	n_{H-1},π_H	π^*_L,π^*_L	16	n_{H-1},π_H	π^*_L,π^*_L	19	n_{H-1},π_H	π^*_L,π^*_L
$2^1A'$	85	π_H	π^*_L	57	π_H	π^*_L	81	π_H	π^*_L
	5	π_{H-7},π_H	π^*_L,π^*_L	12	n_{H-1}	$3s$	15	π_{H-7},π_H	π^*_L,π^*_L
				10	n_{H-2}	$3s$			
				8	π_{H-7},π_H	π^*_L,π^*_L			
$1^3A'$	95	π_H	π^*_L	97	π_H	π^*_L	98	π_H	π^*_L
$1^3A''$	89	n_{H-1}	π^*_L	88	n_{H-1}	π^*_L	86	n_{H-1}	π^*_L
				9	n_{H-2},π_H	π^*_L,π^*_L	14	n_{H-2},π_H	π^*_L,π^*_L
$2^3A''$	89	n_{H-2}	π^*_L	84	n_{H-2}	π^*_L	83	n_{H-2}	π^*_L
	5	n_{H-1},π_H	π^*_L,π^*_L	13	n_{H-1},π_H	π^*_L,π^*_L	17	n_{H-1},π_H	π^*_L,π^*_L

S4.12. *Nitrobenzene*

Table S48. Experimental and computed DFT/MRCI, DFT/MRCI-R, MR-MP2(HF) and MR-MP2(BH-LYP) vertical excitation energies of **nitrobenzene**. The oscillator strengths are given in the parentheses.

State	Dominant character	Energies(eV)				
		DFT/MRCI	DFT/MRCI-R	MRMP2 (HF)	MRMP2 (BH-LYP)	Experiment
1^1A_2	$n \rightarrow \pi^*$	3.29 (0)	3.46 (0)	3.25 (0)	3.47 (0)	**3.65**[a]
1^1B_2	$n \rightarrow \pi^*$	3.88 (0)	3.91 (0)	3.82 (0)	3.76 (0)	
1^1B_1	$\pi \rightarrow \pi^*$	4.29 (0.004)	4.40 (0.021)	4.28 (0.006)	4.18 (0.004)	
2^1B_1	$\pi, \pi \rightarrow \pi^*, \pi^*$	4.63 (0.024)		7.19 (0.170)[1]	7.00 (0.198)[1]	
2^1A_1	$\pi \rightarrow \pi^*$	4.77 (0.249)	4.81 (0.311)	5.33 (0.246)	5.08 (0.243)	**5.17**[b]
1^3B_1	$\pi \rightarrow \pi^*$	2.84	2.93	3.35	3.35	
1^3A_2	$n \rightarrow \pi^*$	3.11	3.26	3.00	3.09	
1^3A_1	$\pi \rightarrow \pi^*$	3.66	3.65	3.62	3.51	
1^3B_2	$n \rightarrow \pi^*$	3.67	3.72	3.63	3.62	
2^3B_1	$\pi \rightarrow \pi^*$	4.01	4.01	4.34	4.18	
⋮						
4^3B_1	$\pi, \pi \rightarrow \pi^*, \pi^*$	5.88				

MR-MP2(HF): [1] 5^1B_1

MR-MP2(HF): [1] 5^1B_1

[a] Absorption maximum in n-hexane [26]

[b] Absorption maximum in gas phase [26]

Table S49. Calculated percentage of electron configurations in the excited states wave functions of **nitrobenzene** obtained at the DFT/MRCI, MR-MP2(HF) and MR-MP2(BH-LYP) levels of theory. Only electron configurations with more than 2 percentage are presented.

	DFT/MRCI			MRMP2			MRMP2		
	(BH-LYP)			(HF)			(BH-LYP)		
		Excitation			Excitation			Excitation	
State	%	from	to	%	from	to	%	from	to
1^1A_2	77	n_{H-3}	π^*_L	45	n_{H-3}	π^*_L	50	n_{H-3}	π^*_L
	12	n_{H-3}	π^*_{L+2}	12	n_{H-3}	π^*_{L+2}	7	n_{H-3}	π^*_{L+2}
	3	n_{H-4},π_{H-2}	π^*_L,π^*_L	3	n_{H-4},π_{H-2}	π^*_L,π^*_L	3	n_{H-4},π_{H-2}	π^*_L,π^*_L
				2	n_{H-4},π_{H-2}	π^*_L,π^*_{L+2}			
1^1B_2	76	n_{H-4}	π^*_L	45	n_{H-4}	π^*_L	50	n_{H-4}	π^*_L
	11	n_{H-4}	π^*_{L+2}	12	n_{H-4}	π^*_{L+2}	6	n_{H-4}	π^*_{L+2}
	4	n_{H-3},π_{H-2}	π^*_L,π^*_L	3	n_{H-3},π_{H-2}	π^*_L,π^*_L	4	n_{H-3},π_{H-2}	π^*_L,π^*_L
				2	n_{H-3},π_{H-2}	π^*_L,π^*_{L+2}	2	n_{H-3},π_{H-2}	π^*_L,π^*_{L+2}
1^1B_1	46	π_H	π^*_L	35	π_H	π^*_L	26	π_H	π^*_L
	26	π_{H-2},π_H	π^*_L,π^*_{L+1}	21	π_{H-1}	π^*_{L+1}	23	π_{H-1}	π^*_{L+1}
	5	π_{H-1}	π^*_{L+1}	4	π_H	π^*_{L+2}	8	π_H	π^*_{L+2}
	5	π_{H-2},π_{H-1}	π^*_L,π^*_L						
	4	π_{H-2},π_H	π^*_{L+1},π^*_{L+2}						
	3	π_{H-2}	π^*_L						
2^1B_1	33	π_{H-2},π_H	π^*_L,π^*_{L+1}	24	π_{H-2},π_H	π^*_L,π^*_{L+1}	28	π_{H-2},π_H	π^*_L,π^*_{L+1}
	25	π_H	π^*_L	10	π_{H-1},π_H	π^*_{L+1},π^*_{L+2}	6	π_{H-1},π_H	π^*_{L+1},π^*_{L+2}
	12	π_{H-1}	π^*_{L+1}	8	π_{H-2}	π^*_{L+2}	5	π_{H-2},π_{H-1}	π^*_L,π^*_L
	5	π_{H-2}	π^*_L	7	π_{H-2},π_{H-1}	π^*_L,π^*_L	5	π_{H-1}	π^*_{L+1}
	5	π_{H-2},π_{H-1}	π^*_L,π^*_L	3	π_{H-1}	π^*_{L+1}	4	π_{H-2}	π^*_{L+2}
2^1A_1	75	π_{H-1}	π^*_L	54	π_{H-1}	π^*_L	50	π_{H-1}	π^*_L
	5	π_{H-2},π_{H-1}	π^*_L,π^*_{L+1}	7	π_H	π^*_{L+1}	6	π_H	π^*_{L+1}
	3	π_{H-2},π_H	π^*_L,π^*_L						
	2	π_{H-2}	π^*_{L+1}						
	2	π_H	π^*_{L+1}						
1^3B_1	77	π_{H-2}	π^*_L	49	π_{H-2}	π^*_L	53	π_{H-2}	π^*_L
	15	π_{H-2}	π^*_{L+2}	16	π_{H-2}	π^*_{L+2}	10	π_{H-2}	π^*_{L+2}
	4	π_H	π^*_L						
1^3A_2	78	n_{H-3}	π^*_L	46	n_{H-3}	π^*_L	51	n_{H-3}	π^*_L
	13	n_{H-3}	π^*_{L+2}	13	n_{H-3}	π^*_{L+2}	7	n_{H-3}	π^*_{L+2}
	2	n_{H-4},π_{H-2}	π^*_L,π^*_L	2	n_{H-4},π_{H-2}	π^*_L,π^*_L	3	n_{H-4},π_{H-2}	π^*_L,π^*_L
1^3A_1	77	π_{H-1}	π^*_L	38	π_{H-1}	π^*_L	30	π_{H-1}	π^*_L
	9	π_{H-1}	π^*_{L+2}	15	π_H	π^*_{L+1}	17	π_H	π^*_{L+1}
	8	π_H	π^*_{L+1}	8	π_{H-1}	π^*_{L+2}	13	π_{H-1}	π^*_{L+2}
1^3B_2	78	n_{H-4}	π^*_L	46	n_{H-4}	π^*_L	51	n_{H-4}	π^*_L
	12	n_{H-4}	π^*_{L+2}	13	n_{H-4}	π^*_{L+2}	7	n_{H-4}	π^*_{L+2}
	2	n_{H-3},π_{H-2}	π^*_L,π^*_L	2	n_{H-3},π_{H-2}	π^*_L,π^*_L	4	n_{H-3},π_{H-2}	π^*_L,π^*_L
4^3B_1	55	π_{H-2},π_H	π^*_L,π^*_{L+1}						
	9	π_{H-1},π_H	π^*_{L+1},π^*_{L+2}						
	7	π_{H-2},π_{H-1}	π^*_L,π^*_L						
	6	π_{H-1}	π^*_{L+1}						

The orbitals presented in the table are labeled according to the order obtained within the DFT theory.
In the following cases the ordering of the Hartree-Fock orbitals is different:
The π^*_{L+2} bh-lyp orbital corresponds to the π^*_{L+3} hf orbital;

Table S50.: Calculated percentage of electron configurations in the excited states wave functions of **nitrobenzene** obtained at the DFT/MRCI, and DFT/MRCI-R levels of theory. Only electron configurations with more than 2 percentage are presented.

	DFT/MRCI			DFT/MRCI-R		
		Excitation			Excitation	
State	%	from	to	%	from	to
1^1A_2	77	n_{H-3}	π^*_L	78	n_{H-3}	π^*_L
	12	n_{H-3}	π^*_{L+2}	12	n_{H-3}	π^*_{L+2}
	3	n_{H-4},π_{H-2}	π^*_L,π^*_L	4	n_{H-4},π_{H-2}	π^*_L,π^*_L
1^1B_2	76	n_{H-4}	π^*_L	75	n_{H-4}	π^*_L
	11	n_{H-4}	π^*_{L+2}	10	n_{H-4}	π^*_{L+2}
	4	n_{H-3},π_{H-2}	π^*_L,π^*_L	5	n_{H-3},π_{H-2}	π^*_L,π^*_L
1^1B_1	46	π_H	π^*_L	73	π_H	π^*_L
	26	π_{H-2},π_H	π^*_L,π^*_{L+1}	14	π_{H-1}	π^*_{L+1}
	5	π_{H-1}	π^*_{L+1}			
	5	π_{H-2},π_{H-1}	π^*_L,π^*_L			
	4	π_{H-2},π_H	π^*_{L+1},π^*_{L+2}			
	3	π_{H-2}	π^*_L			
2^1B_1	33	π_{H-2},π_H	π^*_L,π^*_{L+1}			
	25	π_H	π^*_L			
	12	π_{H-1}	π^*_{L+1}			
	5	π_{H-2}	π^*_L			
	5	π_{H-2},π_{H-1}	π^*_L,π^*_L			
2^1A_1	75	π_{H-1}	π^*_L	86	π_{H-1}	π^*_L
	5	π_{H-2},π_{H-1}	π^*_L,π^*_{L+1}	2	π_H	π^*_{L+1}
	3	π_{H-2},π_H	π^*_L,π^*_L			
	2	π_{H-2}	π^*_{L+1}			
	2	π_H	π^*_{L+1}			
1^3B_1	77	π_{H-2}	π^*_L	79	π_{H-2}	π^*_L
	15	π_{H-2}	π^*_{L+2}	13	π_{H-2}	π^*_{L+2}
	4	π_H	π^*_L	4	π_H	π^*_L
1^3A_2	78	n_{H-3}	π^*_L	78	n_{H-3}	π^*_L
	13	n_{H-3}	π^*_{L+2}	12	n_{H-3}	π^*_{L+2}
	2	n_{H-4},π_{H-2}	π^*_L,π^*_L	3	n_{H-4},π_{H-2}	π^*_L,π^*_L
1^3A_1	77	π_{H-1}	π^*_L	77	π_{H-1}	π^*_L
	9	π_{H-1}	π^*_{L+2}	9	π_{H-1}	π^*_{L+2}
	8	π_H	π^*_{L+1}	7	π_H	π^*_{L+1}
1^3B_2	78	n_{H-4}	π^*_L	77	n_{H-4}	π^*_L
	12	n_{H-4}	π^*_{L+2}	11	n_{H-4}	π^*_{L+2}
	2	n_{H-3},π_{H-2}	π^*_L,π^*_L	4	n_{H-3},π_{H-2}	π^*_L,π^*_L
4^3B_1	55	π_{H-2},π_H	π^*_L,π^*_{L+1}			
	9	π_{H-1},π_H	π^*_{L+1},π^*_{L+2}			
	7	π_{H-2},π_{H-1}	π^*_L,π^*_L			
	6	π_{H-1}	π^*_{L+1}			

S4.13. *Dithiosuccinimide*

Table S51. Experimental and computed DFT/MRCI, DFT/MRCI-R, MR-MP2(HF) and MR-MP2(BH-LYP) vertical excitation energies of **dithiosuccinimide**. The oscillator strengths are given in the parentheses.

		Energies(eV)				
State	Dominant character	DFT/MRCI	DFT/MRCI-R	MRMP2 (HF)	MRMP2 (BH-LYP)	Experiment
1^1B_1	$n \rightarrow \pi^*$	2.66 (0)	2.73 (0)	2.58 (0)	2.45 (0)	**2.77**[a], 2.82[b]
1^1A_2	$n \rightarrow \pi^*$	2.85 (0)	2.93 (0)	2.80 (0)	2.66 (0)	**3.04**[a], 3.08[b]
1^1B_2	$\pi \rightarrow \pi^*$	4.13 (0.722)	4.09 (0.7222)	3.85 (0.585)	3.75 (0.544)	**3.96**[a], 3.87[b]
2^1A_2	$n \rightarrow \pi^*$	4.64 (0)	4.64 (0)	4.37 (0)	4.00 (0)	
2^1A_1	$n, n \rightarrow \pi^*, \pi^*$	4.71 (0)	3.40 (0)			
2^1B_1	$n \rightarrow \pi^*$	4.83 (0)	4.80 (0)	4.55 (0)	4.20 (0)	
⋮						
5^1A_1	$n^2 \rightarrow \pi^{*2}$	6.07 (0)	5.08 (0)[1]	5.51 (0)[1]	5.26(0) [1]	
1^3B_1	$n \rightarrow \pi^*$	2.44	2.57	2.42	2.42	**2.63**[a]
1^3A_2	$n \rightarrow \pi^*$	2.64	2.77	2.67	2.59	
1^3B_2	$\pi \rightarrow \pi^*$	2.77	2.84	2.67	2.55	
1^3A_1	$\pi \rightarrow \pi^*$	3.43	3.51	3.42	3.28	
2^3B_2	$n, n \rightarrow \pi^{*2}$	4.60	3.87	5.70[2]	5.29[2]	
2^3A_1	$n, n \rightarrow \pi^*, \pi^*$	4.68	3.36[2]	6.67[3]	6.55[3]	
2^3A_2	$n \rightarrow \pi^*$	4.70	4.60	4.38	4.03	
2^3B_1	$n \rightarrow \pi^*$	4.87	4.73	4.50	4.14	

DFT/MRCI-R: [1] 3^1A_1, [2] 1^3A_1
MRMP2(HF): [1] 4^1A_1, [2] 3^3B_2, [3] 4^3A_1
MRMP2(BH-LYP): [1] 4^1A_1, [2] 3^3B_2, [3] 5^3A_1
[a] Absorption maximum in cyclohexane [27]
[b] Absorption maximum in methanol [27]

Table S52.: Calculated percentage of electron configurations in the excited states wave functions of **dithiosuccinimide** obtained at the DFT/MRCI, MR-MP2(HF) and MR-MP2(BH-LYP) levels of theory. Only electron configurations with more than 2 percentage are presented.

	DFT/MRCI			MRMP2			MRMP2		
	(BH-LYP)			(HF)			(BH-LYP)		
		Excitation			Excitation			Excitation	
State	%	from	to	%	from	to	%	from	to
1^1B_1	81	n_H	π^*_L	53	n_H	π^*_L	50	n_H	π^*_L
	11	n_{H-1}	π^*_{L+1}	10	n_{H-1}	π^*_{L+1}	12	n_{H-1}	π^*_{L+1}
				2	n_{H-1},π_{H-2}	π^*_L,π^*_L	2	n_{H-1},π_{H-2}	π^*_L,π^*_L
1^1A_2	75	n_{H-1}	π^*_L	49	n_{H-1}	π^*_L	45	n_{H-1}	π^*_L
	16	n_H	π^*_{L+1}	14	n_H	π^*_{L+1}	17	n_H	π^*_{L+1}
	3	π_{H-2},n_H	π^*_L,π^*_L				2	π_{H-2},n_H	π^*_L,π^*_L
1^1B_2	88	π_{H-2}	π^*_L	58	π_{H-2}	π^*_L	56	π_{H-2}	π^*_L
	4	π_{H-3},π_{H-2}	π^*_L,π^*_L	4	π_{H-3},π_{H-2}	π^*_L,π^*_L	5	π_{H-3},π_{H-2}	π^*_L,π^*_L
				2	π_{H-3}	π^*_{L+1}	2	π_{H-3}	π^*_{L+1}
							2	π_{H-7},π_{H-2}	π^*_L,π^*_{L+1}
2^1A_2	61	n_H	π^*_{L+1}	35	n_H	π^*_{L+1}	29	n_H	π^*_{L+1}
	11	n_{H-1}	π^*_L	9	n_{H-1}	π^*_L	10	n_{H-1}	π^*_L
	9	π_{H-2},n_{H-1}	π^*_L,π^*_{L+1}	7	π_{H-2},n_H	π^*_L,π^*_L,	10	π_{H-2},n_H	π^*_L,π^*_L,
	8	π_{H-2},n_H	π^*_L,π^*_L,	7	π_{H-2},n_{H-1}	π^*_L,π^*_{L+1}	8	π_{H-2},n_{H-1}	π^*_L,π^*_{L+1}
2^1A_1	86	n_{H-1},n_H	π^*_L,π^*_{L+1}						
2^1B_1	63	n_{H-1}	π^*_{L+1}	36	n_{H-1}	π^*_{L+1}	30	n_{H-1}	π^*_{L+1}
	11	π_{H-2},n_H	π^*_L,π^*_{L+1}	7	π_{H-2},n_H	π^*_L,π^*_{L+1}	9	π_{H-2},n_{H-1}	π^*_L,π^*_L
	7	π_{H-2},n_{H-1}	π^*_L,π^*_L	7	π_{H-2},n_{H-1}	π^*_L,π^*_L	9	π_{H-2},n_H	π^*_L,π^*_{L+1}
	6	n_H	π^*_L	6	n_H	π^*_L	7	n_H	π^*_L
5^1A_1	49	n_H,n_H	π^*_L,π^*_L	32	n_H,n_H	π^*_L,π^*_L	31	n_H,n_H	π^*_L,π^*_L
	37	n_{H-1},n_{H-1}	π^*_L,π^*_L	25	n_{H-1},n_{H-1}	π^*_L,π^*_L	25	n_{H-1},n_{H-1}	π^*_L,π^*_L
1^3B_1	82	n_H	π^*_L	53	n_H	π^*_L	51	n_H	π^*_L
	12	n_{H-1}	π^*_{L+1}	12	n_{H-1}	π^*_{L+1}	13	n_{H-1}	π^*_{L+1}
1^3A_2	76	n_{H-1}	π^*_L	49	n_{H-1}	π^*_L	46	n_{H-1}	π^*_L
	18	n_H	π^*_{L+1}	15	n_H	π^*_{L+1}	17	n_H	π^*_{L+1}
				2	n_H	Ry_{L+5}			
1^3B_2	88	π_{H-2}	π^*_L	59	π_{H-2}	π^*_L	57	π_{H-2}	π^*_L
	8	π_{H-3}	π^*_{L+1}	8	π_{H-3}	π^*_{L+1}	10	π_{H-3}	π^*_{L+1}
1^3A_1	58	π_{H-3}	π^*_L	43	π_{H-3}	π^*_L	39	π_{H-3}	π^*_L
	36	π_{H-2}	π^*_{L+1}	23	π_{H-2}	π^*_{L+1}	26	π_{H-2}	π^*_{L+1}
				2	π_{H-2}	Ry_{L+5}			
2^3B_2	87	n_{H-1},n_H	π^*_L,π^*_L	58	n_{H-1},n_H	π^*_L,π^*_L	56	n_{H-1},n_H	π^*_L,π^*_L
	6	n_{H-1},n_H	π^*_{L+1},π^*_{L+1}	5	n_{H-1},n_H	π^*_{L+1},π^*_{L+1}	7	n_{H-1},n_H	π^*_{L+1},π^*_{L+1}
2^3A_1	89	n_{H-1},n_H	π^*_L,π^*_{L+1}	57	n_{H-1},n_H	π^*_L,π^*_{L+1}	57	n_{H-1},n_H	π^*_L,π^*_{L+1}
2^3A_2	65	n_H	π^*_{L+1}	33	n_H	π^*_{L+1}	30	n_H	π^*_{L+1}
	15	n_{H-1}	π^*_L	10	n_{H-1}	π^*_L	11	n_{H-1}	π^*_L
2^3B_1	69	n_{H-1}	π^*_{L+1}	35	n_{H-1}	π^*_{L+1}	32	n_{H-1}	π^*_{L+1}

Continued on next page

Table S52 – continued from previous page

	DFT/MRCI			MRMP2			MRMP2		
	(BH-LYP)			(HF)			(BH-LYP)		
		Excitation			Excitation			Excitation	
State	%	from	to	%	from	to	%	from	to
	9	n_H	π^*_L	9	π_{H-2},n_H	π^*_L,π^*_{L+1}	10	π_{H-2},n_H	π^*_L,π^*_{L+1}
	8	π_{H-2},n_H	π^*_L,π^*_{L+1}	7	n_H	π^*_L	8	n_H	π^*_L

The orbitals presented in the table are labeled according to the order obtained within the DFT theory. In the following cases the ordering of the Hartree-Fock orbitals is different:
The n_H bh-lyp orbital corresponds to the n_{H-1} hf orbital;
The n_{H-1} bh-lyp orbital corresponds to the n_{H-2} hf orbital;
The π_{H-2} bh-lyp orbital corresponds to the π_H hf orbital.

Table S53.: Calculated percentage of electron configurations in the excited states wave functions of **dithiosuccinimide** obtained at the DFT/MRCI, and DFT/MRCI-R levels of theory. Only electron configurations with more than 2 percentage are presented.

	DFT/MRCI			DFT/MRCI-R		
		Excitation			Excitation	
State	%	from	to	%	from	to
1^1B$_1$	81	n_H	π^*_L	82	n_H	π^*_L
	11	n_{H-1}	π^*_{L+1}	10	n_{H-1}	π^*_{L+1}
1^1A$_2$	75	n_{H-1}	π^*_L	75	n_{H-1}	π^*_L
	16	n_H	π^*_{L+1}	16	n_H	π^*_{L+1}
	3	π_{H-2},n_H	π^*_L,π^*_L	3	π_{H-2},n_H	π^*_L,π^*_L
1^1B$_2$	88	π_{H-2}	π^*_L	87	π_{H-2}	π^*_L
	4	π_{H-3},π_{H-2}	π^*_L,π^*_L	5	π_{H-3},π_{H-2}	π^*_L,π^*_L
2^1A$_2$	61	n_H	π^*_{L+1}	59	n_H	π^*_{L+1}
	11	n_{H-1}	π^*_L	12	π_{H-2},n_{H-1}	π^*_L,π^*_{L+1}
	9	π_{H-2},n_{H-1}	π^*_L,π^*_{L+1}	10	n_{H-1}	π^*_L
	8	π_{H-2},n_H	π^*_L,π^*_L,	6	π_{H-2},n_H	π^*_L,π^*_L,
2^1A$_1$	86	n_{H-1},n_H	π^*_L,π^*_{L+1}	87	n_{H-1},n_H	π^*_L,π^*_{L+1}
2^1B$_1$	63	n_{H-1}	π^*_{L+1}	60	n_{H-1}	π^*_{L+1}
	11	π_{H-2},n_H	π^*_L,π^*_{L+1}	16	π_{H-2},n_H	π^*_L,π^*_{L+1}
	7	π_{H-2},n_{H-1}	π^*_L,π^*_L	6	π_{H-2},n_{H-1}	π^*_L,π^*_L
	6	n_H	π^*_L	7	n_H	π^*_L
5^1A$_1$	49	n_H,n_H	π^*_L,π^*_L	49	n_H,n_H	π^*_L,π^*_L
	37	n_{H-1},n_{H-1}	π^*_L,π^*_L	34	n_{H-1},n_{H-1}	π^*_L,π^*_L
1^3B$_1$	82	n_H	π^*_L	82	n_H	π^*_L
	12	n_{H-1}	π^*_{L+1}	11	n_{H-1}	π^*_{L+1}
1^3A$_2$	76	n_{H-1}	π^*_L	76	n_{H-1}	π^*_L
	18	n_H	π^*_{L+1}	17	n_H	π^*_{L+1}
1^3B$_2$	88	π_{H-2}	π^*_L	89	π_{H-2}	π^*_L
	8	π_{H-3}	π^*_{L+1}	7	π_{H-3}	π^*_{L+1}
1^3A$_1$	58	π_{H-3}	π^*_L	58	π_{H-3}	π^*_L
	36	π_{H-2}	π^*_{L+1}	36	π_{H-2}	π^*_{L+1}
2^3B$_2$	87	n_{H-1},n_H	π^*_L,π^*_L	85	n_{H-1},n_H	π^*_L,π^*_L
	6	n_{H-1},n_H	π^*_{L+1},π^*_{L+1}	6	n_{H-1},n_H	π^*_{L+1},π^*_{L+1}
2^3A$_1$	89	n_{H-1},n_H	π^*_L,π^*_{L+1}	87	n_{H-1},n_H	π^*_L,π^*_{L+1}
2^3A$_2$	65	n_H	π^*_{L+1}	59	n_H	π^*_{L+1}
	15	n_{H-1}	π^*_L	12	n_{H-1}	π^*_L
2^3B$_1$	69	n_{H-1}	π^*_{L+1}	60	n_{H-1}	π^*_{L+1}
	9	n_H	π^*_L	6	n_H	π^*_L
	8	π_{H-2},n_H	π^*_L,π^*_{L+1}	17	π_{H-2},n_H	π^*_L,π^*_{L+1}

S4.14. *Methionine*

Table S54. Computed DFT/MRCI, DFT/MRCI-R, MR-MP2(HF) and MR-MP2(BH-LYP) vertical excitation energies of **methionine**. The oscillator strengths are given in the parentheses.

State	Dominant character	Energies(eV)			
		DFT/MRCI	DFT/MRCI-R	MRMP2 (HF)	MRMP2 (BH-LYP)
2^1A	$\pi \rightarrow \sigma^*/Ry$	5.12 (0)	5.32 (0)	5.99 (0)^1	5.24 (0)
3^1A	$n_O \rightarrow \pi^*$	5.48 (0.002)	5.71 (0.003)	5.97 (0.002)^2	5.54 (0.002)
1^3A	$\pi \rightarrow \sigma^*/Ry$	4.65	4.94	5.62	4.77
2^3A	$n_O \rightarrow \pi^*$	5.13	5.46	5.77	5.26
3^3A	$\pi \rightarrow \sigma^*/Ry$	5.74	6.00	6.74	5.74
4^3A	$\pi_{H-4} \rightarrow \pi^*$	6.06	6.31	7.01^3	6.24^1

MRMP2(HF):^{1}3^{1}A, $^2 2^1 A$, $^3 7^3 A$

MRMP2(BH-LYP):^{1}6^{3}A

Table S55.: Calculated percentage of electron configurations in the excited states wave functions of **methionine** obtained at the DFT/MRCI, MR-MP2(HF) and MR-MP2(BH-LYP) levels of theory. Only electron configurations with more than 2 percentage are presented.

	DFT/MRCI (BH-LYP)			MRMP2 (HF)†			MRMP2 (BH-LYP)		
		Excitation			Excitation			Excitation	
State	%	from	to	%	from	to	%	from	to
2^1A	44	π_H	$(\sigma^*/Ry)_{L+1}$	25	π_H	$(\sigma^*/Ry)_{L+1}$	29	π_H	$(\sigma^*/Ry)_{L+1}$
	20	π_H	$(\sigma^*/Ry)_{L+2}$	13	π_H	$(Ry/\sigma^*)_{L+2}$	16	π_H	$(\sigma^*/Ry)_{L+2}$
	13	π_H	$(Ry/\sigma^*)_{L+3}$	7	π_H	$(Ry/\sigma^*)_{L+6}$	8	π_H	$(Ry/\sigma^*)_{L+3}$
	5	π_H	$(Ry)_{L+4}$	7	π_H	$(\sigma^*/Ry)_{L+9}$			
				5	π_H	$(Ry/\sigma^*)_{L+5}$			
3^1A	61	$n(O)_{H-2}$	π^*_L	28	$n(O)_{H-3}$	π^*_{L+3}	48	$n(O)_{H-2}$	π^*_L
	7	$n(O)_{H-2}$	$(\sigma^*/Ry)_{L+1}$	18	$n(O)_{H-3}$	$(Ry)_{L+4}$			
	7	$n(S)_{H-3}$	π^*_L	6	$n(O)_{H-3}$	$(Ry/\sigma^*)_{L+5}$			
	5	$n(N)_{H-1}$	π^*_L						
1^3A	42	π_H	$(\sigma^*/Ry)_{L+1}$	24	π_H	$(\sigma^*/Ry)_{L+1}$	29	π_H	$(\sigma^*/Ry)_{L+1}$
	20	π_H	$(\sigma^*/Ry)_{L+2}$	13	π_H	$(Ry/\sigma^*)_{L+2}$	15	π_H	$(\sigma^*/Ry)_{L+2}$
	13	π_H	$(Ry/\sigma^*)_{L+3}$	8	π_H	$(Ry/\sigma^*)_{L+6}$	8	π_H	$(Ry/\sigma^*)_{L+3}$
	6	π_H	$(Ry)_{L+4}$	8	π_H	$(\sigma^*/Ry)_{L+9}$			
				6	π_H	$(Ry/\sigma^*)_{L+5}$			
2^3A	63	$n(O)_{H-2}$	π^*_L	29	$n(O)_{H-3}$	π^*_{L+3}	50	$n(O)_{H-2}$	π^*_L
	7	$n(O)_{H-2}$	$(\sigma^*/Ry)_{L+1}$	18	$n(O)_{H-3}$	$(Ry)_{L+4}$			
	7	$n(S)_{H-3}$	π^*_L	6	$n(O)_{H-3}$	$(Ry/\sigma^*)_{L+5}$			
	5	$n(N)_{H-1}$	π^*_L						
3^3A	33	π_H	π^*_L	15	π_H	$(Ry/\sigma^*)_{L+8}$	29	π_H	$(\sigma^*/Ry)_{L+7}$
	26	π_H	$(\sigma^*/Ry)_{L+7}$	13	π_H	$(Ry)_L$	11	π_H	$(Ry/\sigma^*)_{L+5}$
	12	π_H	$(Ry/\sigma^*)_{L+5}$	10	π_H	$(\sigma^*/Ry)_{L+9}$	8	π_H	π^*_L
	10	π_H	$(\sigma^*/Ry)_{L+2}$	8	π_H	$(Ry/\sigma^*)_{L+7}$	7	π_H	$(\sigma^*/Ry)_{L+2}$
4^3A	70	π_{H-4}	π^*_L	26	π_{H-4}	π^*_{L+3}	49	π_{H-4}	π^*_L
	8	π_{H-4}	$(\sigma^*/Ry)_{L+1}$	18	π_{H-4}	$(Ry)_{L+4}$			
				6	π_{H-4}	$(Ry/\sigma^*)_{L+5}$			
				5	σ_{H-5}	π^*_{L+3}			

† Since the BH-LYP virtual orbitals are very different compared to the HF orbitals for Methionine, in the table are presented HF orbitals in original ordering, without correlation with BH-LYP orbitals
Regarding the occupied orbitals, the $n(O)_{H-2}$ bh-lyp orbital corresponds to the $n(O)_{H-3}$ hf orbital;

S4.15. *Isoalloxazine*

Table S56. Experimental and computed DFT/MRCI, DFT/MRCI-R, MR-MP2(HF) and MR-MP2(BH-LYP) vertical excitation energies of **isoalloxazine**. The oscillator strengths are given in the parentheses.

		Energies(eV)				
State	Dominant character	DFT/MRCI	DFT/MRCI-R	MRMP2 (HF)	MRMP2 (BH-LYP)	Experiment
$2^1\mathrm{A}'$	$\pi \rightarrow \pi^*$	3.03 (0.287)	3.00 (0.311)	2.84 (0.230)	2.64 (0.253)	**2.85**[a]
$1^1\mathrm{A}''$	$n \rightarrow \pi^*$	3.16 (0.002)	3.28 (0.002)	3.52 (0)[1]	3.85 (0)[1]	
$2^1\mathrm{A}''$	$n \rightarrow \pi^*$	3.34 (0.001)	3.46 (0.001)	3.45 (0.002)[2]	3.11 (0.002)[2]	
$3^1\mathrm{A}''$	$n \rightarrow \pi^*$	3.90 (0)	4.00 (0)	3.87 (0)	3.76 (0)[3]	
$3^1\mathrm{A}'$	$\pi \rightarrow \pi^*$	3.94 (0.194)	3.94 (0.188)	3.98 (0.097)	3.71 (0.143)[4]	3.76[a]
$1^3\mathrm{A}'$	$\pi \rightarrow \pi^*$	2.31	2.27	2.60	2.29	
$1^3\mathrm{A}''$	$n \rightarrow \pi^*$	2.86	3.01	3.53	2.98	
$2^3\mathrm{A}'$	$\pi \rightarrow \pi^*$	3.12	3.13	3.31	2.84	
$2^3\mathrm{A}''$	$n \rightarrow \pi^*$	3.19	3.28	3.87	3.61[5]	

MRMP2(HF): [1] $2^1\mathrm{A}''$, [2] $1^1\mathrm{A}''$

MRMP2(BHLYP): [1] $4^1\mathrm{A}''$, [2] $1^1\mathrm{A}''$, [3] $2^1\mathrm{A}''$, [4] $6^1\mathrm{A}'$, [5] $3^3\mathrm{A}''$

[a] 8-methylisoalloxazine in ethanol [28]

Table S57.: Calculated percentage of electron configurations in the excited states wave functions of **isoalloxazine** obtained at the DFT/MRCI, MR-MP2(HF) and MR-MP2(BH-LYP) levels of theory. Only electron configurations with more than 2 percentage are presented.

	DFT/MRCI (BH-LYP)			MRMP2 (HF)			MRMP2 (BH-LYP)		
		Excitation			Excitation			Excitation	
State	%	from	to	%	from	to	%	from	to
2^1A′	83	π_H	π^*_L	48	π_H	π^*_L	45	π_H	π^*_L
				2	π_{H-1}	π^*_{L+1}	2	π_{H-1}	π^*_{L+1}
				2	π_{H-1}	π^*_L			
1^1A″	50	$n(O)_{H-2}$	π^*_L	36	$n(O)_{H-2}$	π^*_L	32	$n(O)_{H-2}$	π^*_L
	27	$n(N)_{H-4}$	π^*_L	4	$n(N)_{H-4}$	π^*_L	7	$n(O)_{H-5}$	π^*_L
	2	$n(N)_{H-7}$	π^*_L	2	$n(O)_{H-5}$	π^*_L	3	$n(O)_{H-2}$	π^*_{L+4}
				2	$n(O)_{H-5}$	π^*_{L+4}	2	$n(O)_{H-5}$	π^*_{L+4}
				2	$n(N)_{H-4}$	π^*_{L+4}	2	$n(N)_{H-4}$	π^*_L
2^1A″	45	$n(N)_{H-4}$	π^*_L	40	$n(N)_{H-4}$	π^*_L	37	$n(N)_{H-4}$	π^*_L
	21	$n(O)_{H-2}$	π^*_L	7	$n(N)_{H-7}$	π^*_L	7	$n(N)_{H-7}$	π^*_L
	8	$n(O)_{H-5}$	π^*_L	2	$n(O)_{H-2}$	π^*_L	5	$n(O)_{H-2}$	π^*_L
	5	$n(N)_{H-7}$	π^*_L	2	$n(N)_{H-4}$	π^*_{L+2}			
3^1A′	74	π_{H-1}	π^*_L	43	π_{H-1}	π^*_L	41	π_{H-1}	π^*_L
	4	π_H	π^*_{L+1}	5	π_H	π^*_{L+1}	4	π_H	π^*_{L+1}
	2	π_H	π^*_{L+4}	3	π_H	π^*_L	2	π_H	π^*_L
				2	π_H	π^*_{L+2}	2	π_H	π^*_{L+2}
1^3A′	85	π_H	π^*_L	45	π_H	π^*_L	43	π_H	π^*_L
	4	π_{H-1}	π^*_L	7	π_{H-1}	π^*_L	7	π_{H-1}	π^*_L
1^3A″	56	$n(N)_{H-4}$	π^*_L	36	$n(N)_{H-4}$	π^*_L	34	$n(N)_{H-4}$	π^*_L
	17	$n(O)_{H-2}$	π^*_L	11	$n(N)_{H-7}$	π^*_L	11	$n(N)_{H-7}$	π^*_L
	10	$n(N)_{H-7}$	π^*_L				5	$n(O)_{H-2}$	π^*_L
2^3A″	53	$n(O)_{H-2}$	π^*_L	29	$n(O)_{H-2}$	π^*_L	32	$n(O)_{H-2}$	π^*_L
	10	$n(N)_{H-4}$	π^*_L	7	$n(O)_{H-5}$	π^*_L	7	$n(O)_{H-5}$	π^*_L
	10	$n(O)_{H-5}$	π^*_L	4	$n(N)_{H-4}$	π^*_L	4	$n(O)_{H-2}$	π^*_{L+4}
	3	$n(O)_{H-2}$	π^*_{L+4}	4	$n(O)_{H-5}$	π^*_{L+4}	3	$n(O)_{H-5}$	π^*_{L+4}
	3	$n(N)_{H-7}$	π^*_L	4	$n(N)_{H-4}$	π^*_{L+4}			
	3	$n(O)_{H-5}$	π^*_{L+4}	2	$n(O)_{H-2}$	π^*_{L+4}			

The orbitals presented in the table are labeled according to the order obtained within the DFT theory. In the following cases the ordering of the Hartree-Fock orbitals is different:
The $n(O)_{H-2}$ bh-lyp orbital corresponds to the $n(O)_{H-4}$ hf orbital;
The $n(N)_{H-4}$ bh-lyp orbital corresponds to the $n(N)_{H-5}$ hf orbital;
The $n(O)_{H-5}$ bh-lyp orbital corresponds to the $n(O)_{H-6}$ hf orbital.
The π^*_{L+4} bh-lyp orbital corresponds to the π^*_{L+6} hf orbital.

Table S58. Isoalloxazine, SOMEs, RAS 16-11-2

	SOMEs(cm^{-1})		
	DFT/MRCI	MRMP2 (HF)	MRMP2 (BH-LYP)
$\langle 1^3A''\|\hat{\mathcal{H}}_{\mathrm{SO\ x}}\|1^1A'\rangle$	8.5	11.4	12.1
$\langle 1^3A''\|\hat{\mathcal{H}}_{\mathrm{SO\ x}}\|2^1A'\rangle$	6.0	3.1	3.0
$\langle 1^3A''\|\hat{\mathcal{H}}_{\mathrm{SO\ x}}\|3^1A'\rangle$	4.2	3.6	3.6
$\langle 2^3A''\|\hat{\mathcal{H}}_{\mathrm{SO\ x}}\|1^1A'\rangle$	10.3	6.8	7.2
$\langle 1^3A''\|\hat{\mathcal{H}}_{\mathrm{SO\ y}}\|1^1A'\rangle$	10.7	3.6	4.7
$\langle 1^3A''\|\hat{\mathcal{H}}_{\mathrm{SO\ y}}\|2^1A'\rangle$	2.0	0.4	0.3
$\langle 1^3A''\|\hat{\mathcal{H}}_{\mathrm{SO\ y}}\|3^1A'\rangle$	2.5	1.7	1.8
$\langle 2^3A''\|\hat{\mathcal{H}}_{\mathrm{SO\ y}}\|1^1A'\rangle$	23.0	24.7	25.7
$\langle 1^3A'\|\hat{\mathcal{H}}_{\mathrm{SO\ x}}\|1^1A''\rangle$	11.1	2.4	0.9
$\langle 1^3A'\|\hat{\mathcal{H}}_{\mathrm{SO\ x}}\|2^1A''\rangle$	2.4	7.4	7.8
$\langle 1^3A'\|\hat{\mathcal{H}}_{\mathrm{SO\ y}}\|1^1A''\rangle$	9.7	8.3	9.0
$\langle 1^3A'\|\hat{\mathcal{H}}_{\mathrm{SO\ y}}\|2^1A''\rangle$	7.3	2.3	3.1
$\langle 1^3A''\|\hat{\mathcal{H}}_{\mathrm{SO\ z}}\|1^1A''\rangle$	1.9	4.8	5.6
$\langle 1^3A''\|\hat{\mathcal{H}}_{\mathrm{SO\ z}}\|2^1A''\rangle$	3.2	0.5	0.8
$\langle 1^3A''\|\hat{\mathcal{H}}_{\mathrm{SO\ x}}\|1^3A'\rangle$	9.7	6.9	7.1
$\langle 1^3A''\|\hat{\mathcal{H}}_{\mathrm{SO\ y}}\|1^3A'\rangle$	4.4	1.8	2.1
$\langle 2^3A''\|\hat{\mathcal{H}}_{\mathrm{SO\ x}}\|1^3A'\rangle$	2.3	1.6	1.7
$\langle 2^3A''\|\hat{\mathcal{H}}_{\mathrm{SO\ y}}\|1^3A'\rangle$	10.3	8.1	8.3
$\langle 2^3A''\|\hat{\mathcal{H}}_{\mathrm{SO\ z}}\|1^3A''\rangle$	4.2	5.9	5.9

S5. Optimized geometries of all polyatomic molecules in Turbomole format

```
o-benzyne

$coord
    1.17436585005558      0.00000000000000     -2.91783955856904      c
   -1.17436585005558      0.00000000000000     -2.91783955856904      c
   -2.75209598591275      0.00000000000000     -0.84138302133317      c
   -1.32564422167504      0.00000000000000      1.40629603021343      c
    1.32564422167504      0.00000000000000      1.40629603021343      c
    2.75209598591275      0.00000000000000     -0.84138302133317      c
   -4.79588042002593      0.00000000000000     -0.84670344838957      h
   -2.31805929976997      0.00000000000000      3.19962999807835      h
    2.31805929976997      0.00000000000000      3.19962999807835      h
    4.79588042002593      0.00000000000000     -0.84670344838957      h
$user-defined bonds
$end

#######################################################################

Formaldehyde

$coord
    0.00000000000000      0.00000000000000     -1.13492173758470      c
    0.00000000000000      0.00000000000000      1.13487499210216      o
    0.00000000000000      1.77442119446536     -2.24490992799825      h
    0.00000000000000     -1.77442119446536     -2.24490992799825      h
$user-defined bonds
$end

#######################################################################

Thioformaldehyde

$coord
    0.00000000000000      0.00000000000000     -0.21272080063682  c
    0.00000000000000      0.00000000000000      2.83208049504587  s
   -1.74201265716538      0.00000000000000     -1.30967984720453  h
    1.74201265716538      0.00000000000000     -1.30967984720453  h
$user-defined bonds
$end

########################################################################
```

```
Furan

$coord
    0.00000000000000      0.00000000000000     -2.60951767812713      o
   -2.06944695013647      0.00000000000000     -1.07409817620120      c
   -1.35446631345745      0.00000000000000      1.38655862649115      c
    2.06944695013647      0.00000000000000     -1.07409817620120      c
    1.35446631345745      0.00000000000000      1.38655862649115      c
   -3.87275264412434      0.00000000000000     -2.01429504621195      h
   -2.58841049419110      0.00000000000000      3.00661787535332      h
    2.58841049419110      0.00000000000000      3.00661787535332      h
    3.87275264412434      0.00000000000000     -2.01429504621195      h
$user-defined bonds
$end

#########################################################################

Thiophene

$coord
    1.34566119550646      0.00000000000000     -2.48135783630059      c
   -1.34566119550646      0.00000000000000     -2.48135783630059      c
   -2.34140829359619      0.00000000000000     -0.10207603421092      c
    2.34140829359619      0.00000000000000     -0.10207603421092      c
    0.00000000000000      0.00000000000000      2.16998967240478      s
   -4.30322604139690      0.00000000000000      0.44859441791091      h
   -2.48480316694106      0.00000000000000     -4.17813269206495      h
    2.48480316694106      0.00000000000000     -4.17813269206495      h
    4.30322604139690      0.00000000000000      0.44859441791091      h
$user-defined bonds
$end

#########################################################################
```

```
Quinoxaline

coord
    0.00000000000000      1.34851448928290     -0.04308396822032      c
    0.00000000000000     -1.34851448928290     -0.04308396822032      c
    0.00000000000000      2.65971823554233      2.28673743415383      c
    0.00000000000000      1.33705869093915      4.51645111448426      c
    0.00000000000000     -1.33705869093915      4.51645111448426      c
    0.00000000000000     -2.65971823554233      2.28673743415383      c
    0.00000000000000     -2.67165472069636     -2.25056228491017      n
    0.00000000000000      2.67165472069636     -2.25056228491017      n
    0.00000000000000      1.33982622873228     -4.33893321844487      c
    0.00000000000000     -1.33982622873228     -4.33893321844487      c
    0.00000000000000      2.36641046716173     -6.11641565124786      h
    0.00000000000000     -2.36641046716173     -6.11641565124786      h
    0.00000000000000      4.70524646880327      2.23830739016897      h
    0.00000000000000      2.34078894813222      6.30069856802307      h
    0.00000000000000     -2.34078894813222      6.30069856802307      h
    0.00000000000000     -4.70524646880327      2.23830739016897      h
$user-defined bonds
$end

########################################################################

Quinazoline

$coord
   -1.36377830593764      0.02164891624333      0.00000000000000      c
    1.32358004466339     -0.00642782560434      0.00000000000000      c
   -2.67344557760090      2.35111102112969      0.00000000000000      c
   -1.34210560585668      4.57650051698381      0.00000000000000      c
    1.33118157888386      4.55054284673907      0.00000000000000      c
    2.64773551616107      2.31460626473841      0.00000000000000      c
    2.62027853734640     -2.23232554321978      0.00000000000000      n
   -2.55361790292543     -2.37354727839355      0.00000000000000      c
   -1.29008728275860     -4.50630971662982      0.00000000000000      n
    1.27443449300352     -4.30859688746912      0.00000000000000      c
   -4.60660305711199     -2.49662580101590      0.00000000000000      h
    2.29583861341275     -6.08655825695464      0.00000000000000      h
   -4.72287386788293      2.35172083639553      0.00000000000000      h
   -2.33128955432688      6.36844044222261      0.00000000000000      h
    2.34668983885953      6.32863938189363      0.00000000000000      h
    4.69249305982863      2.26136784419168      0.00000000000000      h
$user-defined bonds
$end

########################################################################
```

```
Pyranthione

$coord
    0.00000000000000      0.00000000000000     -5.41280084911143  s
    0.00000000000000      0.00000000000000     -2.27610234375952  c
    2.28239911071821      0.00000000000000     -0.77097741589196  c
   -2.28239911071821      0.00000000000000     -0.77097741589196  c
    2.19281770453302      0.00000000000000      1.76800159282312  c
   -2.19281770453302      0.00000000000000      1.76800159282312  c
    0.00000000000000      0.00000000000000      3.10029625536432  o
    4.09779134136361      0.00000000000000     -1.70846637180746  h
   -4.09779134136361      0.00000000000000     -1.70846637180746  h
    3.81569058976344      0.00000000000000      3.00574566362965  h
   -3.81569058976344      0.00000000000000      3.00574566362965  h
$user-defined bonds
$end

########################################################################

Dithiin

$coord
   -2.86580686520235      0.06685457466165     -0.58761113643798      c
   -1.74686625152159     -0.93439975340578     -3.58743246371355      s
    1.74686625152159      0.93439975340578     -3.58743246371355      s
    2.86580686520235     -0.06685457466165     -0.58761113643798      c
    1.34949386294333     -0.26465201376855      1.43325076748021      c
   -1.34949386294333      0.26465201376855      1.43325076748021      c
    4.88043546579430     -0.42046691325140     -0.47732257370807      h
    2.19170307049153     -0.81587368262624      3.21985735926151      h
   -2.19170307049153      0.81587368262624      3.21985735926151      h
   -4.88043546579430      0.42046691325140     -0.47732257370807      h
$user-defined bonds
$end

########################################################################
```

```
Bithiophene

coord
   -3.96988778421768      1.08891220762545      0.86140126635055      s
   -0.74152793302954      1.15246315166230      0.17136717343972      c
    0.02013601870388      3.59049859122632     -0.30037764090575      c
   -1.96658915178120      5.38569505078307     -0.13126800701727      c
   -4.23600721856751      4.31664305664117      0.46548485545081      c
    0.74152793302954     -1.15246315166230      0.17136717343972      c
   -0.02013601870388     -3.59049859122632     -0.30037764090575      c
    1.96658915178120     -5.38569505078307     -0.13126800701727      c
    4.23600721856751     -4.31664305664117      0.46548485545081      c
    3.96988778421768     -1.08891220762545      0.86140126635055      s
    6.04440759167992     -5.22731659581586      0.69687312532149      h
   -6.04440759167992      5.22731659581586      0.69687312532149      h
   -1.71756381233833      7.38826074025362     -0.45753873320741      h
    1.94373787470285      4.07268383409784     -0.79726048539097      h
   -1.94373787470285     -4.07268383409784     -0.79726048539097      h
    1.71756381233833     -7.38826074025362     -0.45753873320741      h
$user-defined bonds
$end

######################################################################

Nitromethane

$coord
    1.39335214705160     -0.76295979932813      0.00000000000000  n
    1.28450387612169     -3.06825847571066      0.00000000000000  o
    3.32868182243600      0.49273279279710      0.00000000000000  o
   -1.08606004843182      0.62725172762346      0.00000000000000  c
   -0.69904605232834      2.63955977340387      0.00000000000000  h
   -2.11071587242454      0.03583699060714     -1.68078913533078  h
   -2.11071587242454      0.03583699060714      1.68078913533078  h
$user-defined bonds
$end

######################################################################
```

```
Nitrobenzene

$coord
    0.00000000000000      0.00000000000000      1.60347294530390  c
    0.00000000000000      0.00000000000000     -3.59896025534619  c
    2.29878831137124      0.00000000000000      0.33655081995768  c
   -2.29878831137124      0.00000000000000      0.33655081995768  c
   -2.28322846111443      0.00000000000000     -2.28896805815391  c
    2.28322846111443      0.00000000000000     -2.28896805815391  c
    4.04004564954374      0.00000000000000      1.40275883089641  h
   -4.04004564954374      0.00000000000000      1.40275883089641  h
   -4.05541523981593      0.00000000000000     -3.31160564246933  h
    4.05541523981593      0.00000000000000     -3.31160564246933  h
    0.00000000000000      0.00000000000000     -5.64617215317262  h
    0.00000000000000      0.00000000000000      4.40465230335952  n
    2.04887036382285      0.00000000000000      5.47976762969691  o
   -2.04887036382285      0.00000000000000      5.47976762969691  o
$user-defined bonds
$end

########################################################################

Dithiosuccinimide

$coord
    0.00000000000000     -1.45666900594610     -1.66620418588077  c
    0.00000000000000     -2.21034538961508      1.10066498364750  c
    0.00000000000000      0.00000000000000      2.46084368279514  n
    0.00000000000000      2.21034538961508      1.10066498364750  c
    0.00000000000000      1.45666900594610     -1.66620418588077  c
    0.00000000000000      5.04724275757076      2.32512196784998  s
    0.00000000000000     -5.04724275757076      2.32512196784998  s
    0.00000000000000      0.00000000000000      4.37458631463165  h
    1.65477054116251     -2.26812361781069     -2.58864888216505  h
   -1.65477054116251     -2.26812361781069     -2.58864888216505  h
   -1.65477054116251      2.26812361781069     -2.58864888216505  h
    1.65477054116251      2.26812361781069     -2.58864888216505  h
$user-defined bonds
$end

########################################################################
```

```
Methionine

$coord
    4.76099430895915     -1.71333782672988      1.79001120037847      c
    4.44195060765592     -2.57337548311441      4.17681740779049      o
    6.73547550894334     -0.87343024066359      1.03129552889427      o
    6.03384721355275     -2.33959388425558      5.05836468986696      h
    2.33223111761168     -1.83336199077757      0.26252246897826      c
    3.01191601137541     -2.24565242658838     -2.37088018598580      n
    1.25452267943939     -3.46488828582037      0.93136353597730      h
    0.78326112962969      0.59026860172462      0.85795464483749      c
    1.50001951379748     -2.08106869788800     -3.52885842715726      h
    4.36762180027747     -1.00791439640966     -2.92238815854439      h
   -1.82234113037246      0.55764684457247     -0.37825550229080      c
    0.55704472603565      0.75684654251706      2.90554979877657      h
    1.85046680753457      2.23982186123099      0.21438436052467      h
   -3.58938225022865      3.40382269096334      0.48331018053293      s
   -1.66355429116183      0.50012898279821     -2.43637847953666      h
   -2.88850199322567     -1.10159950300212      0.23926972954955      h
   -6.46776499311525      2.85263434307328     -1.31680416127601      c
   -7.71857857571236      4.44536166753883     -0.94532193712846      h
   -6.07612816129063      2.77019011069814     -3.33892928668144      h
   -7.40310002970565      1.11750109013264     -0.71302740750607      h
$user-defined bonds
$end

#########################################################################
```

```
Isoalloxazine

$coord
    2.51988147835166     -1.36384049945196      0.00000000000000      c
    4.57172112766037     -2.70142876166231      0.00000000000000      n
    6.87887313585653     -1.46785020644587      0.00000000000000      c
    6.85196359523531      1.21173040580103      0.00000000000000      n
    4.79189986631520      2.81261547442180      0.00000000000000      c
    2.33542437604255      1.39534955869551      0.00000000000000      c
    0.24197822755524     -2.58712143575286      0.00000000000000      n
   -2.05105524911613     -1.36512882582954      0.00000000000000      c
   -2.00997620849890      1.31100618503416      0.00000000000000      c
    0.22684912824209      2.62521091683690      0.00000000000000      n
   -4.35206876488726     -2.66514536632553      0.00000000000000      c
   -6.58317892927744     -1.30417219401142      0.00000000000000      c
   -6.57340285963868      1.34837992430289      0.00000000000000      c
   -4.30974932946563      2.63989017414723      0.00000000000000      c
    8.88925948139859     -2.55529606892658      0.00000000000000      o
    4.97576345077364      5.09131875662744      0.00000000000000      o
   -8.34351156204724      2.37249377528319      0.00000000000000      h
    0.32588952491405     -4.50054276596776      0.00000000000000      h
   -8.36597009104112     -2.30989604609086      0.00000000000000      h
   -4.37233213191804     -4.71294314907122      0.00000000000000      h
   -4.22485476781693      4.68341199676864      0.00000000000000      h
    8.57651329975121      2.04188095074323      0.00000000000000      h
$user-defined bonds
$end

########################################################################
```

References

[1] C. Marian, Spin–orbit coupling in molecules, in *Reviews In Computational Chemistry*, edited by K. Lipkowitz and D. Boyd, Vol. 17, pp. 99–204, Wiley-VCH, Weinheim (2001).
[2] J.G.G. Simon, N. Mnzel and A. Schweig, Chem. Phys. Lett. **170** (23), 187 (1990).
[3] K.N. Walzl, C.F. Koerting and A. Kuppermann, J. Chem. Phys. **87**, 3796 (1987).
[4] S. Taylor, D.G. Wilden and J. Comer, Chem. Phys. **70**, 291 (1982).
[5] J.E. Mentall, E.P. Gentieu, M. Krauss and D. Neumann, J. Chem. Phys. **55**, 5471 (1971).
[6] P. Brint, J.P. Connerade, C. Mayhew and K. Sommer, J. Chem. Soc., Faraday Trans. 2 **81**, 1643 (1985).
[7] C. Drury and D. Moule, J. Mol. Spectrosc. **92**, 469 (1982).
[8] R. Judge, C. Drury-Lessard and D. Moule, Chem. Phys. Lett. **53**, 82 (1978).
[9] S.Y. Chiang and I.F. Lin, J. Chem. Phys. **122**, 094301 (2005).
[10] M.H. Palmer, I.C. Walker, C.C. Ballard and M.F. Guest, Chem. Phys. **192**, 111 (1995).
[11] K.R. Asmis, Ph.D. thesis, University of Freiburg, Switzerland 1996.
[12] W.M. Flicker, O.A. Mosher and A. Kuppermann, J. Chem. Phys. **64**, 1315 (1976).
[13] E.V. Veen, Chem. Phys. Lett. **41** (3), 535 (1976).
[14] J. Roebber, D. Gerrity, R. Hemley and V. Vaida, Chem. Phys. Lett. **75** (1980).
[15] M.H. Palmer, I.C. Walker and M.F. Guest, Chem. Phys. **241**, 275 (1999).
[16] R.W. Glass, L.C. Robertson and J.A. Merritt, J. Chem. Phys. **53**, 3857 (1970).
[17] J. Aaron, A. Tine, M. Gaye, C. Parkanyi, C. Boniface and T. Bieze, Spectrochim. Acta A: Mol. Spectrosc. **47**, 419 (1991).
[18] M. Szymanski, R. Steer and A. Maciejewski, Chem. Phys. Lett. **135**, 243 (1987).
[19] E. Block, M. Birringer, R. DeOrazio, J. Fabian, R.S. Glass, C. Guo, C. He, E. Lorance, Q. Qian, T.B. Schroeder, Z. Shan, M. Thiruvazhi, G.S. Wilson and X. Zhang, J. Am. Chem. Soc. **122**, 5052 (2000).
[20] S. Siegert, F. Vogeler, C.M. Marian and R. Weinkauf, Phys. Chem. Chem. Phys. **13**, 10350 (2011).
[21] R.S. Becker, J. Seixas de Melo, A.L. Maçanita and F. Elisei, J. Phys. Chem. **100**, 18683 (1996).
[22] I.C. Walker and M.A. Fluendy, Intern. J. Mass Spectrom. **205**, 171 (2001).
[23] W.M. Flicker, O.A. Mosher and A. Kuppermann, J. Chem. Phys. **72**, 2788 (1980).
[24] W.D. Taylor, T.D. Allston, M.J. Moscato, G.B. Fazekas, R. Kozlowski and G.A. Takacs, Int. J. Chem. Kinet. **12**, 231 (1980).
[25] S. Nagakura, Mol. Phys. **3**, 152 (1960).
[26] S. Nagakura, M. Kojima and Y. Maruyama, J. Mol. Spectrosc. **13**, 174 (1964).
[27] S.C. Meskers, T. Polonski and H.P. Dekkers, J. Phys. Chem. **99**, 1134 (1995).
[28] M. Sun, T.A. Moore and P.S. Song, J. Am. Chem. Soc. **94**, 1730 (1972).

THE JOURNAL OF
PHYSICAL CHEMISTRY C

Article

pubs.acs.org/JPCC

Singlet Fission in Quinoidal Oligothiophenes

Nikolai Elfers,[†] Igor Lyskov,[†] J. Dominik Spiegel,[†] and Christel M. Marian*,[†]

[†]Institute of Theoretical and Computational Chemistry, Heinrich Heine University Düsseldorf, Universitätsstrasse 1, D-40225 Düsseldorf, Germany

Supporting Information

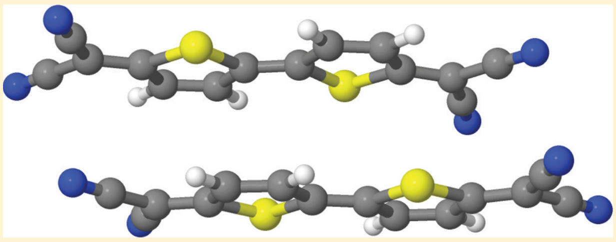

ABSTRACT: The electronic properties of quinoidal oligithiophenes make them interesting for applications in semiconductor technology. Because of their very large singlet−triplet splitting, they are promising candidates for singlet fission (SF), a process in which an initially excited singlet state is converted into two triplet excitons. Thus, the efficiency of solar cells could be increased to overcome the Shockley-Queisser limit. Here, we investigate the ability of a quinoidal bithiophene to undergo SF in solution. We calculated the ground state and low-lying excited states using a combined density functional theory and multireference configuration interaction approach including dispersion corrections. Potential energy curves along normal mode displacements were computed to detect avoided crossings between the initially excited bright singlet state and a dark doubly excited state which can be interpreted as a triplet pair overall coupled to a singlet ^{1}(TT). The studied quinoidal bithiophene meets the energetic requirement for SF. A path enabling *intramolecular* SF could not be found. In contrast, we were able to identify two vibrational modes relevant for an *intermolecular* SF process in the slip-stacked dimer: A promoting coordinate that couples a bright singlet state with the ^{1}(TT) state and a separating coordinate that localizes the triplet states on the respective monomers. These results elucidate the mechanism underlying the formation of a triplet pair and the separation of the triplet excitons after initial photoexcitation of the bright singlet state.

1. INTRODUCTION

Organic solar cells have attracted great interest as an alternative for conventional inorganic photovoltaics. Their key advantages are lower manufacturing costs, flexibility and transparency of the modules, as well as lower environmental impact.[1] Current research aims at improving their photochemical stability and increasing their efficiency. Higher efficiency can be reached by using materials in which multiple electron−hole pairs are generated after absorption of one photon. In organic semiconductors, this process is known as singlet fission (SF).[2] In SF, an initially excited singlet exciton is converted into two triplet excitons. It has been observed experimentally in molecular crystals such as tetracene[3] or pentacene[4] but also in conjugated polymer films such as polythiophene.[5] SF is a very fast process. For example, in pentacene crystals it occurs on a sub-200 fs time scale according to transient absorption studies.[6] It has been shown that the Shockley−Queisser limit of the efficiency of 33.7% for an ideal single-state solar cell[7] could theoretically be increased to 44.4%, if SF takes place.[8]

In the literature, different theoretical approaches toward describing the process of SF are found. A general mechanism is shown in Figure 1. After initial photon absorption to a bright singlet state (S_n), nonadiabatic transition leads to a dark multiexciton singlet state which can be interpreted as a triplet pair coupled overall to a singlet ^{1}(TT).[9] Therefore, SF is a spin-allowed process. The two triplet excitons can then diffuse apart in the crystal. The detailed photophysics of this process is yet little understood. So, it is difficult to devise general requirements for organic materials to be able to undergo SF. Concerning the molecular structure, alternant hydrocarbons as well as biradicaloids seem to be promising canditates.[10] As there are a lot of different decay channels in molecular crystals, SF has to be faster than competing processes such as internal conversion or fluorescence. To be exoergic or at least isoergic, the requirement $E(S_n) \geqslant 2E(T_1)$ has to be met. In tetracene crystals, where SF is endoergic but still highly efficient, the reverse process—triplet−triplet upconversion—readily follows, resulting in delayed fluorescence.[11,12]

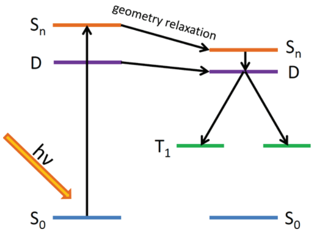

Figure 1. General mechanism of singlet fission according to ref 9.

While most studies to date have addressed SF processes in small-molecular crystals of films, a few reports have been dedicated to intermolecular and even intramolecular SF in

Received: March 3, 2016
Revised: May 15, 2016
Published: June 8, 2016

DOI: 10.1021/acs.jpcc.6b02263
J. Phys. Chem. C 2016, 120, 13901−13910

solution. Walker et al.,[13] for example, report the occurrence of singlet exciton fission in a 6,13-bis (triisopropylsilylethinyl)-pentacene (TIPS-pentacene) excimer in solution. By combining two TIPS-pentacene units via a covalent linker, even intramolecular SF, where two triplets are generated on one molecule, could be observed in solution.[14] Ultrafast SF occurs with a time constant below 100 fs also in aggregates of 2−6 astaxanthin molecules in solution.[15] The mechanism, proposed by Musser et al.,[15] is particularly interesting. According to these authors, the 1-photon-accessible 1^1B_u state no longer couples to the lower-lying 2^1A_g state upon aggregation. Instead, it converts directly into triplet pairs via SF.

In this work, we investigate the feasibility of SF in a quinoidal bithiophene (QBT, Figure 2) and in a π-stacked QBT dimer by means of quantum chemical methods. These systems are interesting canditates for SF because of their large singlet−triplet splitting.[16] Time-resolved spectroscopy of a QBT in dilute solution revealed the ultrafast formation of a long-lived species with high quantum yield.[17−19] While Wang and Kobayashi[17] as well as Chien et al.[19] come to the conclusion that the long-lived species is most probably the dark 2^1A_g state, Varnavski et al.[18] found indications in favor of the 1^3B_u state built on the subpicosecond time scale by an intramolecular SF process. Also benzoidal bithiophene is known to form triplets with very high quantum yields.[20] It exhibits a nonplanar gauche conformation in the electronic ground state but has a quinoidal structure in the 1-photon-accessible S_1 state. The ultrafast intersystem crossing in that system has been explained qualitatively by the accidental degeneracy of the 1^1B (S_1) and 1^3A (T_2) states and the heavy-atom effect due to the presence of the sulfur atoms.[21,22]

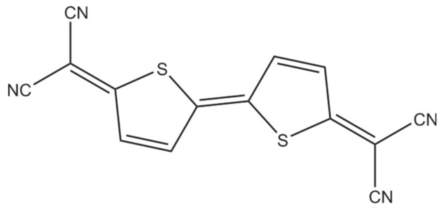

Figure 2. QBT.

A combined density functional theory and multireference configuration-interaction method (DFT/MRCI-R)[23] was employed to calculate the electronic states. First, we had to find out whether the method is suited for describing SF in this molecular system. The demands on the method are the following: (i) It has to yield a consistent description of the excited states of different spin multiplicity, (ii) monomers and dimers must be treated in a balanced manner, and (iii) the method should be applicable to extended molecular systems. Furthermore, dispersion interactions have to be taken account of, as we are looking at a noncovalently bound dimer. The results show that the redesigned DFT/MRCI-R method is able to tackle this problem. In particular, it is seen that the energetic requirement for SF is met in the QBT monomer as well as in the QBT dimer. While no pathway for intramolecular SF in the QBT monomer could be found, two vibrational modes have been identified in the dimer that promote the formation and disentanglement of the singlet-coupled triplet-pair state.

2. METHODS AND COMPUTATIONAL DETAILS

The geometry optimizations of the singlet ground state and the first triplet state of QBT were performed with Turbomole[24] using density functional theory (DFT) in conjunction with the B3LYP functional.[25,26] For the optimization of the excited singlet state, time-dependent density functional theory (TDDFT) was employed.[27] Throughout, the TZVP basis set[28] was utilized. The optimization of the π-stacked QBT dimer geometry requires the inclusion of dispersion interactions. For this purpose, we used the D3-correction by Grimme and co-workers.[29] To get a consistent picture, the D3-correction was also employed in the monomer calculations. All optimizations were carried out without symmetry constraints, except for the monomer, which was also optimized in C_{2h}-symmetry. Harmonic vibrational frequencies were computed using the Aoforce and Numforce programs implemented in Turbomole.[30] Energies and transition moments of the electronically excited singlet, triplet, and quintet states were obtained from a combined density functional theory and multiconfiguration interaction (DFT/MRCI) approach. In this semiempirical method, the dynamical correlation is described by DFT whereas the static correlation is treated with MRCI. The orignial DFT/MRCI ansatz[31] has been successfully applied to many excited-state problems with an error of less than 0.2 eV.[32,33] Unfortunately, it yields physically incorrect results for electronically excited dimers. Recently, the DFT/MRCI Hamiltonian has been redesigned by Lyskov et al.[23] The redesigned and reparameterized Hamiltonian, henceforth denoted by DFT/MRCI-R, has a confidence range comparable to the original ansatz for singly excited states but is, in addition, well-suited for bichromophoric systems, too.[23] The configurations in the MRCI expansion are built up from Kohn−Sham BHLYP[26,34] molecular orbitals (MOs) of a closed-shell reference state. The reference spaces of the MRCI expansions were determined iteratively. In a first step, all possible single and double excitations from the seven highest occupied orbitals to the seven lowest unoccupied orbitals were included. Then all configurations with a squared coefficient greater than 0.003 were added to the reference space. Unless noted otherwise, the standard parameterization in conjunction with a configuration selection threshold of 1 E_H was applied. Spin−orbit coupling calculations were performed using the SPOCK program developed in our laboratoy employing a mean-field approximation to the full Breit-Pauli spin−orbit Hamiltonian.[35]

3. RESULTS AND DISCUSSION

3.1. Monomer.

3.1.1. Geometric and Electronic Structure. Because of the nitrile substituents, QBT has a quinoidal structure in the electronic ground state; that is, the pattern of alternating single and double bonds is reversed with respect to benzoidal bithiophene (Figure 2). We can draw mesomeric structures of a quinoidal form and a biradical aromatic form. The ground-state geometry is well described by the quinoidal form, as the inter-ring bond length (137 pm) lies in the range of C−C-double-bonds. At the S_1 geometry a length of 140 pm is found for this bond, and for the T_1-geometry we find a length of 144 pm. These values lie in between typical values of single and double bonds. Also the two C−C-bonds that connect the rings and the $C(CN)_2$ groups are longer in the S_1 state compared to the ground-state geometry. When the first triplet state is optimized, these bond lengths increase even more. So, the aromatic character of QBT increases from the S_0 state over

S_1 to the T_1 state whereas the quinoidal character decreases. Coordinates of all optimized structures can be found in the Supporting Information (SI). As QBT has a singlet ground state, it is not a biradical, but with its very low triplet state with an adiabatic excitation energy of merely 0.62 eV, it has significant biradical character.

Details on the vertical excitation energies and the electronic structures of the QBT-monomer states at the S_0, S_1, and T_1 geometries are shown in Tables 1−3. For all three geometries, we find that the S_1 state is the bright 1^1B_u state with the HOMO → LUMO excitation as the main configuration. Its computed vertical excitation energy of 2.26 eV in the Franck−Condon (FC) region correlates very well with the band maximum (2.25 eV) observed in steady-state absorption spectra of the related QOT2 molecule in tetrahydrofuran solution.[18] (QOT2 differs from the QBT model studied in this and other theoretical work only by aliphatic rest groups that should have a minor effect on the spectroscopy.) Also, the calculated emission wavelength of 610 nm (2.03 eV) at the relaxed S_1 geometry and the radiative lifetime (competing nonradiative processes left aside) of approximately 15 ns agree well with experimental data. Varnavski et al.[18] report a time constant in the nanosecond regime for the fluorescence at 580 nm (2.14 eV). CASPT2 (10,8) calculations of the same authors yield excitation energies for this state (2.06 eV in absorption, 1.99 eV in emission) similar to our results, whereas the XMS-CASPT2 (10,8) calculations of Chien et al.[19] place the 1^1B_u state at higher energies (2.69 eV in absorption, 2.44 eV in emission). All three theoretical studies agree in that the 1^1B_u state is nearly degenerate with the optically dark 2^1A_g state. Our DFT/MRCI-R calculations at the (TD)DFT-optimized S_0 and S_1 geometries place the 2^1A_g state slightly above the 1^1B_u state (Tables 1 and 2). Proceeding to the T_1 minimum geometry deminishes the energy gap to merely 0.05 eV. The CASPT2 (10,8) calculations of Varnavski et al. predict a crossing of the potential energy surfaces along the relaxation path from the FC region to the S_1 minimum, whereas XMS-CASPT2 (10,8) places the 2^1A_g state slightly below the 1^1B_u state throughout. The multiconfigurational composition of the 2^1A_g state wave function is typical of polyenes. In short polyenes, it has two leading singly excited configurations, namely HOMO−1 → LUMO and HOMO → LUMO+1, that are augmented by a doubly excited configuration HOMO^2 → LUMO^2 in longer polyenes.[32] Although it has often been argued that the 2^1A_g state can be imagined as a coupled triplet-pair state,[36,37] we cannot find any indication in the analysis of its wave function that supports this characterization. Double excitations with four open shells are not present among the dominating configurations. As will be seen below, it is the 3^1A_g state that shows the desired charactersitics upon a simultaneous 90° twist about the terminal C═C double bonds. This state and the lowest-lying quintet state, which truely can be interpreted as a coupled triplet pair, 1^5A_g, are found approximately 1 eV above 2^1A_g.

Table 1. Low-Lying QBT Monomer States at the S_0 Geometry[a]

state	main configurations	c^2-value	ΔE_{vert} [eV]	nm	$f(L)$
1^1A_g	GS	0.90	0.00	-	-
1^1B_u	HOMO→LUMO	0.85	2.26	548	1.437
2^1A_g	HOMO^2→LUMO^2	0.30			
	HOMO−1→LUMO	0.25	2.49	497	0.000
	HOMO→LUMO+1	0.18			
3^1A_g	HOMO−3→LUMO	0.33			
	HOMO→LUMO+1	0.23	3.43	361	0.000
	HOMO−1→LUMO	0.21			
2^1B_u	HOMO−2→LUMO	0.42	3.50	354	0.063
1^3B_u	HOMO→LUMO	0.85	0.96	1297	-
1^3A_g	HOMO−1→LUMO	0.52	2.26	549	-
	HOMO→LUMO+1	0.33			
1^5A_g	(HOMO−1) (HOMO) →(LUMO) (LUMO+1)	0.85	3.28	378	-

[a] For the spin-allowed radiative transitions from S_0 also the oscillator strength $f(L)$ is given.

Table 2. Low-Lying QBT Monomer States at the S_1 Geometry[a]

state	main configurations	c^2-value	ΔE_{adia} [eV]	ΔE_{vert} [eV]	$f(L)$
1^1A_g	GS	0.82	0.11	0.00	-
1^1B_u	HOMO→LUMO	0.82	2.14	2.03	1.329
2^1A_g	HOMO^2→LUMO^2	0.33			
	HOMO−1→LUMO	0.25	2.28	2.17	0.000
	HOMO→LUMO+1	0.15			
2^1B_u	HOMO−2→LUMO	0.47	3.27	3.16	0.075
3^1A_g	HOMO−3→LUMO	0.50	3.31	3.20	0.000
1^3B_u	HOMO→LUMO	0.85	0.72	0.61	-
1^3A_g	HOMO−1→LUMO	0.59	2.24	2.13	-
	HOMO→LUMO+1	0.26			
1^5A_g	(HOMO−1) (HOMO) →(LUMO) (LUMO+1)	0.84	3.17	3.06	-

[a] For the spin-allowed radiative transitions to S_0 also the oscillator strength $f(L)$ is given.

Table 3. Low-Lying QBT Monomer States at the T_1 Geometry[a]

state	main configurations	c^2-value	ΔE_{adia} [eV]	ΔE_{vert} [eV]	$f(L)$
1^1A_g	GS	0.83	0.26	0.00	-
1^1B_u	HOMO→ LUMO	0.80	2.20	1.94	1.300
2^1A_g	HOMO^2→LUMO^2	0.33			
	HOMO−1→LUMO	0.25	2.25	1.99	0.000
	HOMO→LUMO+1	0.13			
2^1B_u	HOMO−2→LUMO	0.61	3.26	3.00	0.113
3^1A_g	HOMO−3→LUMO	0.57	3.30	3.04	0.000
1^3B_u	HOMO→LUMO	0.86	0.62	0.36	-
1^3A_g	HOMO−1→LUMO	0.65	2.41	2.15	-
	HOMO→LUMO+1	0.20			
1^5A_g	(HOMO−1) (HOMO) →(LUMO) (LUMO+1)	0.84	3.24	2.98	-

[a] For the spin-allowed radiative transitions to S_0 also the oscillator strength $f(L)$ is given.

The first triplet state originates from a HOMO → LUMO excitation. Because of the large exchange interaction of the electrons in the polyene-like π MOs (Figure 3), the 1^3B_u state is located at substantially lower excitation energies than the corresponding singlet state. The energetic requirement for SF, namely $E(S_1) \geqslant 2E(T_1)$, is met in the FC region and at the relaxed S_1 geometry. In contrast to the $1^{1,3}B_u$ pair of states, 2^1A_g and 1^3A_g are almost degenerate. This might be surprising at first glance, given that the exchange interaction should strongly favor the 1^3A_g state. The reason for the small singlet−triplet splitting is simply the fact that configuration interaction with

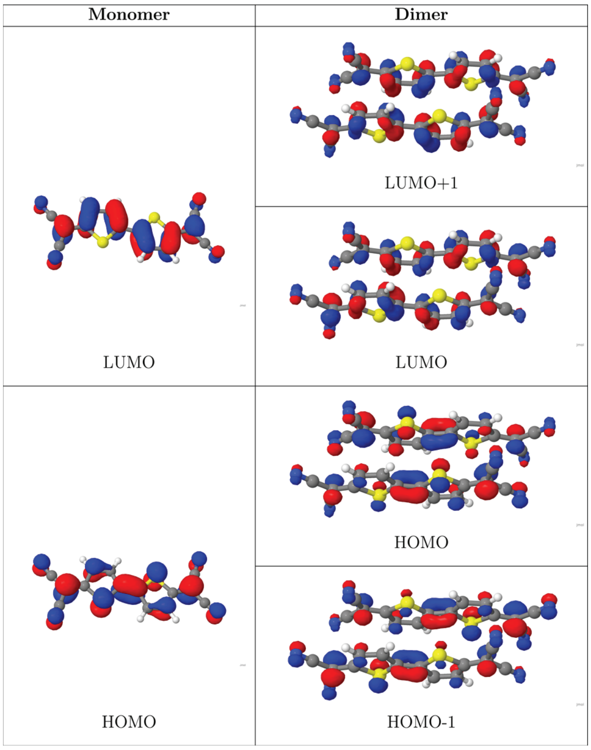

Figure 3. Monomer and dimer frontier orbitals.

the closed-shell HOMO^2 → LUMO^2 configuration stabilizes the 2^1A_g state, thus counteracting the exchange interaction.

3.1.2. Excited-State Absorption from a Long-Lived Species. In time-resolved pump−probe experiments on QOT2 in solution, Varnavski et al.[18] observed the buildup of a long-lived species (57 μs) at the picosecond time scale. This species gave rise to excited-state absorption (ESA) with maxima at 570 and 830 nm which they attributed to the absorption from a triplet-like species. From the intensity attenuation of their probe pulse and the computed oscillator strength of the $1^3B_u \rightarrow 1^3A_g$ absorption, they deduced a singlet−triplet conversion quantum efficiency of 1.76, thus indicating efficient SF. For comparison, they generated QOT2 triplet species by sensitization experiments. The lifetime of that triplet species is substantially longer (111 μs), and its ESA is red-shifted with respect to the spectrum originating from the pump−probe experiments. Further, Varnavski et al. employed a cost-efficient restricted active space spin flip (RAS-SF) approach to search for pathways that promote the disentanglement of the initial excitation into two fully separated triplets on the same molecule. However, the torsion about the central double bond as well as the simultaneous rotation of the C(CN)$_2$ groups are seen to require substantial activation energy for reaching the separated triplet states and are thus not compatible with the experimental kinetics. Chien et al.[19] carried out similar RAS-SF calculations for a torsion about the central bond and for a twist of only one of the dicyano groups. They conclude that out-of-plane rotational pathways are inoperative in QBT as internal conversion pathways. Based on their calculations, they give an alternative explanation for the experimental observations. Chien et al. propose the long-lived species responsible for the transient absorption strong signals to be the 2^1A_g state that is formed ultrafast through vibronic coupling with the bright 1^1B_u state. They argue that—given that the molar absorptivity of that state is high enough—the observed transmission drop might also be explained by the formation of a single exciton instead of two generated from an SF process.

While Varnavski et al.[18] as well as Chien et al.[19] base their discussion of the vertical excitation energies of the electronic states on high-level CASPT2 (10,8) or XMS-CASPT2 (10,8) results, they employ very approximate RAS-SF quantum chemical methods, lacking essentially all dynamic correlation effects, for the potential energy scans. In an attempt to get a consistent picture, we performed potential energy scans and computed ESA spectra at the same level of theory; that is, we used DFT/MRCI-R throughout.

Rigid scans along the torsional coordinates started from the relaxed planar 1^1B_u geometry. In the excited state, the central C−C bond and the C−C bonds connecting the dicyano groups with the thiophene rings are longer than in the electronic ground state, and thus, the barriers might be lower. For the conrotatory twist about the terminal double bonds (Figure 4), various groups of states emerge. The electronic ground state exhibits a torsional barrier of roughly 2.4 eV. The energy profile of the first excited triplet state (1^3B) increases less rapidly (by about 1.4 eV) upon the conrotatory twist and is seen to cross the ground-state potential at a rotational angle of approximately 55°. No such crossing is found in the RAS-SF energy profiles of Varnavski et al.,[18] presumably because of the longer C−C bond distance in their calculations. The energy profiles of the next group of states, consisting of the nearly degenerate 1^1B, 2^1A, and 1^3A states, are shifted by about 1.5 eV toward higher energies, but they run, in essence, parallel to the one of 1^3B. In contrast, the RAS-SF method finds a remarkably large energy gap of ≈1 eV between the 2^1A and 1^1B potentials.[18] The only states that do not show a substantial energy rise upon the conrotatory twist of the end groups are the components of the coupled triplet-pair state, namely 1^5A, 2^3A, and 3^1A. While the (HOMO−1) (HOMO) → (LUMO) (LUMO+1) configuration dominates the 1^5A wave function for all torsion angles, it becomes the leading term for 2^3A and 3^1A only at large twisting angles. Unfortunately, the coupled triplet-pair components are at least 1 eV higher in energy than the optically excited 1^1B state and its near-degenerate 2^1A and 1^3A partners. Hence, there is little chance for SF along this coordinate.

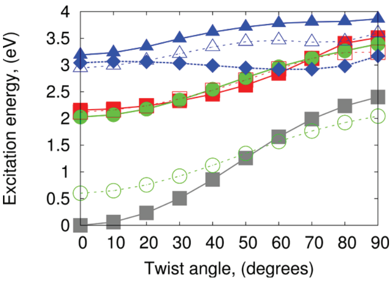

Figure 4. Energy profiles of the low-lying electronic states of the QBT monomer for a conrotatory twist of the dicyano end groups. Singlets: solid lines; triplets: dashed lines; quintets: dotted lines. Circles represent the lowest *B*-symmetric states; all other states transform according to the totally symmetric *A* irreducible representation. For clarity, the 2^1B and 2^3B states have been omitted.

The barriers for a torsion about the central C−C bond are found to be substantially smaller (Figure 5). As for the double torsion of the end groups, a curve crossing is observed between

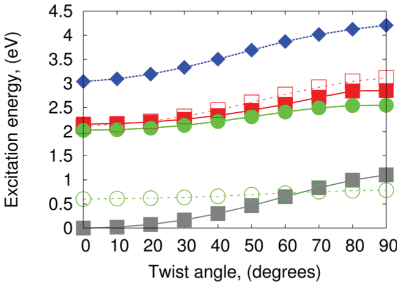

Figure 5. Energy profiles of low-lying electronic states of the QBT monomer for a torsion about the central C−C bond. Singlets: solid lines; triplets: dashed lines; quintets: dotted lines. Circles represent the lowest *B*-symmetric states; all other states transform according to the totally symmetric *A* irreducible representation. For clarity, the 2^1B, 2^3B, and 1^5B states have been omitted.

the lowest triplet state and the singlet ground state. For the 1^3B state, only a very small barrier of less than 0.2 eV is found for the *trans*−*cis*-isomerization, which will probably disappear completely if the remaining geometry parameters are relaxed. In qualitative agreement with Chien et al.,[19] we obtain a barrier height of 1.1 eV in the electronic ground state. In contrast, the energy profiles of the electronically excited singlet states differ markedly from the RAS-SF(4,4) results of Chien et al. In our DFT/MRCI-R calculations, the bright 1^1B state remains the first excited singlet at all angles. The activation barrier for the *trans*−*cis*-isomerization is lower (≈0.5 eV) than that in the ground state, in qualitative concordance with the single-bond character of the central bond in the HOMO → LUMO excited state. For the 2^1A state, we obtain a barrier of ≈0.7 eV along this path which should be considered an upper bound for a relaxed torsion. There is no indication for the formation of a decoupled triplet pair at large twisting angles in any of the low-lying singlet states. This finding is in line with the observation that the profile of the 1^5A (HOMO−1) (HOMO) → (LUMO) (LUMO+1) state runs in essence parallel to that of the ground state.

Because of the energetic proximity of the excited 1^1B, 2^1A, and 1^3A states, even mediocre spin−orbit coupling matrix elements (SOCMEs) could give rise to fast intersystem crossing (ISC). At planar C_{2h}-symmetric nuclear arrangements, the spin−orbit interaction between *gerade* and *ungerade* states is symmetry-forbidden, of course.[38] Due to the presence of the two sulfur atoms, even small distortions of the nuclear frame might, however, lead to a strong increase of spin−orbit coupling. It is beyond the scope of the present work to compute the ISC rate constants quantitatively. Here, we tested only the feasibilty of an ISC pathway from the excited singlet state to the triplet manifold. A torsion of QBT about the central bond by 20° requires an activiation energy of merely 370 cm^{-1} in the 1^1B state. For this nuclear arrangement, we find values of 2.3 and 1.4 cm^{-1} for the *x* and *y* components of the $\langle 1^3A|\hat{H}_{SO}|1^1B\rangle$, respectively. Numerous examples can be found where derivatives of this size lead to efficient ISC via vibronic spin−orbit coupling.[39] The SOCME for the coupling between the 2^1A and 1^3A pair of states is below 0.1 cm^{-1}. We therefore conclude that a possible pathway for triplet formation leads from 1^1B_u via ISC to 1^3A_g and from there via internal conversion to 1^3B_u.

The calculation of ESA spectra might help differentiate between the alternative pathways. Since analytical derivatives are not available for DFT/MRCI-R at present and TDDFT is not suited for the geometry optimization of the 2^1A_g state, we employed the XMS-CASPT2 geometry data provided by Chien et al.[19] for the ESA calculations. As may be seen from our data, collected in Tables 4 and 5, 2^1A_g and 1^3B_u exhibit strong ESA transitions in the desired energy regime. Within the confidence range of our method, the computed excitation energies of 2.27 eV for the 2^1A_g → 5^1B_u transition and of 2.37 eV for 1^3B_u → 2^3A_g agree with the experimental ESA spectrum peaking at approximately 570 nm (2.18 eV).[19]

Table 5. Excited-State Absorption of the QBT Monomer from the 1^3B_u State Employing Geometry Parameters from the Work of Chien et al.[19]

state	main configurations	c^2-value	ΔE_{vert} [eV]	nm	*f(L)*
1^3B_u	HOMO→LUMO	0.84	0.00	-	-
1^3A_g	HOMO−1→LUMO	0.64	1.49	831	0.145
	HOMO→LUMO+1	0.21			
2^3A_g	HOMO→LUMO+1	0.47	2.37	524	0.709
	HOMO−1→LUMO	0.16			
3^3A_g	HOMO−3→LUMO	0.63	2.59	479	0.187

3.2. Dimer.

The excited states of the π-stacking dimer can be interpreted in terms of the monomer states. First we look at a dimer with a monomer distance of 100 Å, where we have no interaction between the two molecules before we turn to the equilibrium structure of the slip-stacked dimer. Finally, we scan the potential energy surfaces of the low-lying excited state with

Table 4. Excited-State Absorption of the QBT Monomer from the 2^1A_g State Employing Geometry Parameters from the Work of Chien et al.[19]

state	main configurations	c^2-value	ΔE_{vert} [eV]	nm	*f(L)*
2^1A_g	HOMO^2→LUMO^2	0.31	0.00	-	-
	HOMO−1→LUMO	0.25			
	HOMO→LUMO+1	0.13			
2^1B_u	HOMO−2→LUMO	0.23	1.11	1121	0.042
	HOMO−4→LUMO	0.19			
	(HOMO−1) (HOMO)→LUMO^2	0.18			
3^1B_u	HOMO−2→LUMO	0.46	1.20	1030	0.024
4^1B_u	HOMO−7→LUMO	0.42	2.17	571	0.026
	(HOMO−8) (HOMO)→LUMO^2	0.19			
5^1B_u	HOMO−1→LUMO+1	0.27	2.27	547	0.627
	HOMO^2→(LUMO) (LUMO+1)	0.21			

DOI: 10.1021/acs.jpcc.6b02263
J. Phys. Chem. C 2016, 120, 13901−13910

Table 6. Excited States of the QBT Dimer at 100 Å

state	main configurations	c^2-value	ΔE [eV]	nm	$f(L)$
S_1	(HOMO−1) (HOMO)→(LUMO) (LUMO+1)	0.58	2.00	621	0.000
S_2	HOMO−1→LUMO+1	0.74	2.23	556	0.570
S_3	HOMO→LUMO	0.74	2.23	556	2.355
S_4	$(\text{HOMO}-1)^2 \rightarrow (\text{LUMO}+1)^2$	0.16	2.57	4 82	0.002
S_5	$\text{HOMO}^2 \rightarrow \text{LUMO}^2$	0.13	2.60	477	0.000
S_6	HOMO−1→LUMO	0.79	3.27	379	0.000
S_7	HOMO→LUMO+1	0.79	3.27	379	0.000
T_1	HOMO→LUMO	0.89	1.00	1240	-
T_2	HOMO−1→LUMO+1	0.80	1.00	1240	-
T_3	(HOMO−1) (HOMO)→(LUMO) (LUMO+1)	0.65	2.02	617	-
Q_1	(HOMO−1) (HOMO)→(LUMO) (LUMO+1)	0.76	2.00	620	-

Table 7. Excited States of the QBT Dimer at the Ground-State Equilibrium Geometry

state	main configurations	c^2-value	ΔE [eV]	nm	$f(L)$
S_1	HOMO→LUMO	0.54	1.69	734	0.005
S_2	(HOMO−1) (HOMO)→(LUMO) (LUMO+1)	0.22	1.98	625	0.007
	(HOMO)→(LUMO)	0.19			
S_3	HOMO−1→LUMO	0.63	2.00	620	0.387
S_4	HOMO−1→LUMO+1	0.24	2.21	562	0.008
	(HOMO−1) (HOMO)→(LUMO) (LUMO+1)	0.16			
S_5	$(\text{HOMO}-1)\ (\text{HOMO}) \rightarrow \text{LUMO}^2$	0.20	2.28	544	0.060
S_6	HOMO→LUMO+1	0.62	2.38	522	1.980
S_7	HOMO−1→LUMO+1	0.42	2.38	521	0.007
T_1	HOMO−1→LUMO	0.51	0.94	1319	-
T_2	HOMO→LUMO	0.54	0.94	1315	-
T_3	$(\text{HOMO}-1)\ (\text{HOMO}) \rightarrow \text{LUMO}^2$	0.20	1.77	700	-
Q_1	(HOMO−1) (HOMO)→(LUMO) (LUMO+1)	0.77	1.21	1023	-

the aim of finding modes that may promote the formation and fission of the singlet-coupled triplet pair, ^{1}(TT).

3.2.1. Large Monomer Distances. The orbitals of a slip-stacked dimer with a monomer distance of 100 Å are completely localized on one or the other monomer. Hence, it is easy to assign the excitations in the dimer to the monomer excitations (Table 6). We find two degenerate locally excited triplet states which relate to the 1^3B_u excitation in the monomer. They lie 1.00 eV above the singlet ground state at this intermolecular distance. Simultaneous excitation of the two monomer 1^3B_u states leads to a coupled triplet pair $T_1 \otimes T_1$ with singlet, triplet, or quintet multiplicity. As expected, for each of the three multiplicities we find a doubly excited state with four open shells. They are nearly degenerate and have twice the excitation energy of the lowest triplet. These results show that the DFT/MRCI-R method yields a consistent description of singlet, triplet, and quintet states in the monomer and the dimer, which is essential for the treatment of SF. The singlet-coupled triplet pair ^{1}(TT), which we are mainly interested in, is the S_1 state at this intermolecular separation. In the triplet manifold, ^{3}(TT) forms the T_3 state while ^{5}(TT) yields the lowest quintet state, Q_1. S_2 and S_3 (both at 2.23 eV) are linear combinations of local HOMO → LUMO excitations corresponding to the bright monomer 1^1B_u states. Although the states are energetically nearly degenerate at such long intermolecular separation, their transition dipole moments with respect to the ground state show tendencies typical of H-aggregates where the transition to the upper component is the stronger one. The corresponding dark charge-transfer (CT) HOMO → LUMO transitions from one monomer to the other are found at 3.27 eV in the singlet manifold (S_6 and S_7) and at 3.22 eV in the triplet manifold (T_6 and T_7). The S_4 and S_5 states related to the local 2^1A_g excitations appear at slightly higher energies compared to the monomer excitations. This holds true also for T_4 and T_5, which correlate with local 1^3A_g exciations on the monomers.

3.2.2. Slip-Stacked Minimum Geometry. The minimum on the dimer ground-state potential energy surface is found for a slip-stacked conformation with a binding energy of 0.59 eV, computed as the difference between the minimum energy and the energy of the supermolecule with the monomers 100 Å apart. The equilibrium distance of the two π-stacked monomers of 3.5 Å is a reasonable van der Waals distance compared to crystal structure data of similar compounds.[40] Here, the molecular orbitals are delocalized over both monomers, with HOMO and HOMO−1 resulting from the monomer HOMOs and with LUMO and LUMO+1 originating from the monomer LUMOs (Figure 3). In a four-electron−four-orbital model, four singly excited triplet and singlet states should arise, respectively. In the triplet case, these four states can be identified (T_1, T_2, T_4, T_5) whereas the singlet wave functions are strongly mixed with double excitations. Hence, it is not easy to make a correspondence between the dimer states and monomer states (Table 7).

Within the singlet manifold, transition dipole moment (TDM) vectors can aid the assignment. While the z axis of our coordinate system is chosen to be perpendicular to the molecular planes of the π-stacked momomers, the x and y axes run approximately parallel to the long (x) and short (y) molecular axes, respectively. Because of their large TDM vectors pointing essentially in the x direction, S_3 and S_6 can be identified as originating from the bright locally excited 1^1B_u

states. The S_1 state with a vertical excitation energy of 1.69 eV exhibits only a small TDM pointing in the y direction. In addition to its leading HOMO → LUMO configuration, its wave function shows substantial contributions from doubly excited configurations either with zero or four open shells, among them the four-open shell ^{1}(TT) configuration (HOMO−1) (HOMO) → (LUMO) (LUMO+1). The latter configuration is the leading term of the S_2 state at (1.98 eV) with the coefficient of the HOMO → LUMO excitation being only slightly smaller. Also S_4 and S_8 have pronounced contributions from (HOMO−1) (HOMO) → (LUMO) (LUMO+1). In addition, they mix in configurations related to 2^1A_g monomer excitations. As will be seen later in section 3.2.3, the composition of the excited-state wave functions varies markedly upon distortions of the nuclear frame. The general mechanism, sketched in Figure 1, will therefore have to be amended in such a way that it takes account of (avoided) curve crossings in the singlet manifold after initial photon absorption to the bright S_3 state.

The T_1 and T_2 states are clearly related to the locally excited 1^3B_u states of the monomers. The corresponding simultaneous CT excitations are found as the fourth and fifth triplet states at 2.08 and 2.12 eV, respectively. The triplet states arising from simultaneous single excitations on the monomers are found as T_3 and T_8 at this geometry. Here, T_3 is mainly composed of doubly excited configurations with two open shells. It arises from a mixture of the $^3(1^3B_u \otimes 1^3B_u)$ and the two $^3(1^3B_u \otimes 1^1B_u)$ dimer states that are stabilized when the monomers approach one another. The triplet state that is dominated by the four-open shell (HOMO−1) (HOMO) → (LUMO) (LUMO+1) configuration (T_8) is located at 2.47 eV with respect to the ground-state minimum.

The ^{5}(TT) state is the lowest among the coupled triplet-pair states with an excitation energy of merely 1.21 eV at the ground-state minimum. Taking into account the dimer binding energy of 0.59 eV and the excitation energy of the ^{5}(TT) state at 100 Å π-stacking distance (2.00 eV), we see that the ^{5}(TT) state is markedly stabilized upon aggregation. The next quintet state is located at substantially higher energies (2.58 eV) and should not play any role in the photophysics of the QBT dimer.

As mentioned above, the S_3 state is a bright singly excited state correlating with locally excited 1^1B_u monomer states. It is found at almost the same energy as the S_2 state. Hence, one can imagine fast relaxation from the initially populated S_3 state to the ^{1}(TT) state via nonadiabatic coupling. The S_6 state has the largest oscillator strength, and its excitation energy of 2.38 eV is in excellent agreement with experimental findings. A UV-spectrum of QBT in the solid state showed an absorption maximum at 2.35 eV.[41] Relaxation from the S_6 state to the ^{1}(TT) state has to take place via intermediate singlet states. The S_1 state is separated from the ^{1}(TT) state by about 0.80 eV according to our calculations. For SF to occur, the diffusion of the two triplet excitons in the ^{1}(TT) state has to be faster than the relaxation from the ^{1}(TT) state to the S_1 state.

3.2.3. Intermolecular Singlet Fission.

Potential energy curves were calculated for the ground and excited singlet and triplet states. First we calculated potential energy curves along the π-stacking coordinate of the two monomers (Figure 6). Between 3.5 and 4.0 Å we find an avoided crossing of the S_1 and the S_2 states. Here, the doubly excited ^{1}(TT) state and the HOMO → LUMO singlet state change order, so that at larger distances the ^{1}(TT) state is the lowest excited singlet state. The HOMO → LUMO excited state, which contains substantial contributions from CT terms, undergoes another curve crossing a little bit further out. Between 4.3 and 4.4 Å it changes order with the locally excited, bright HOMO → LUMO state. Over the whole range, the two lowest triplet states remain degenerate and have half of the excitation energy of the ^{1}(TT) state.

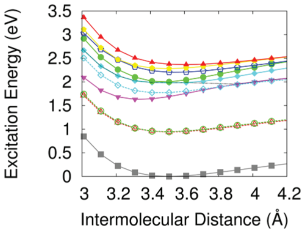

Figure 6. Ground- and excited-state potential energy curves of a π-stacked QBT dimer using DFT/MRCI-R including Grimme D3 dispersion corrections. Singlets are represented by filled symbols and solid lines, triplets by unfilled symbols and dashed lines. For clarity, only the three lowest triplet states are shown. The course of the diabatic singlet-coupled (TT) state is indicated by a black dotted line.

To understand the vibrational relaxation process of the dimer after photoexcitation, we calculated potential energy curves for the singlet and triplet states along the normal coordinates. We were looking for modes that couple the ^{1}(TT) state with a bright singlet state because this might give us a qualitative picture of how the initially excited singlet state relaxes into the singlet-coupled triplet pair via internal conversion. To get a quick overview, all modes except the H-stretching modes were scanned with a configuration selection threshold of 0.8 E_H for DFT/MRCI-R. These potential energy profiles can be found in the SI along with the characterization of the vibrational mode. Upon distortion along these normal coordinates, most of the relevant potential energy curves were seen to run essentially parallel. These modes are thus inactive with regard to SF. However, two interesting modes were found that could be classified as coupling modes. These modes are symmetric and antisymmetric linear combinations of a monomer mode that varies the bond length between the two thiophene rings. The symmetric mode (Figure 7) drives the coupling of the bright excited singlet state with the ^{1}(TT) state. The antisymmetric

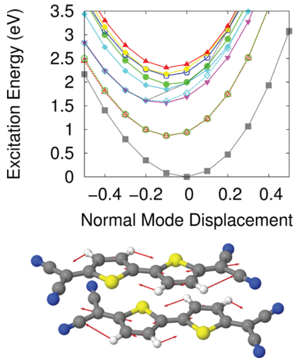

Figure 7. Ground- and excited-state potential energy curves of a π-stacked QBT dimer for the deformation of the nuclear framework in vibrational mode 113. The DFT/MRCI-R energies include Grimme D3 dispersion corrections. Singlets are represented by filled symbols and solid lines, triplets by unfilled symbols and dashed lines. For clarity, only the three lowest triplet states are shown. The course of the diabatic singlet-coupled (TT) state is indicated by a black dotted line.

mode (Figure 8) localizes the triplet exciton on one or the other monomer. Their energy profiles were recalculated with the standard configuration selection threshold of 1.0 E_H.

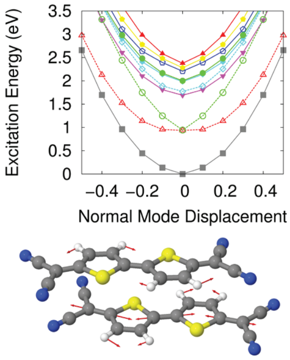

Figure 8. Ground- and excited-state potential energy curves of a π-stacked QBT dimer for the deformation of the nuclear framework in vibrational mode 114. The DFT/MRCI-R energies include Grimme D3 dispersion corrections. Singlets are represented by filled symbols and solid lines, triplets by unfilled symbols and dashed lines. For clarity, only the three lowest triplet states are shown. The degenerate T_1 and T_2 pair of states is seen to split up into a locally excited state (red unfilled triangles) and a charge-transfer state (green open circles) for distortions along this normal coordinate.

First we analyze the potential energy curves of the symmetric mode in Figure 7. We find an avoided crossing between the S_2 and S_3 states in the FC region. If we move from this point to the right side on the x axis, which refers to a decrease of the bond length between the two thiophene moieties in each monomer, we find that the ^{1}(TT) state is the S_3 state while S_2 is a bright singly excited state dominated by a HOMO−1 → LUMO configuration. On the left side of the crossing point, which means at larger inter-ring bond lengths, these two states interchange. When we go further in the left direction along the vibrational coordinate, we find a strong mixing between the S_2 and S_1 states that eventually leads to S_1 being the ^{1}(TT) state.

When we look at the potential energy curves of the antisymmetric mode in Figure 8, we see that the two lowest triplet states, which are degenerate at the equilibrium geometry of the electronic ground state, are strongly split as the nuclear frame is distorted along the normal coordinate. This behavior can be explained by inspection of the molecular orbitals involved in the excitation. At the equilibrium geometry, the orbitals are delocalized. Distortion along the vibrational coordinate means that the inter-ring bond length in one monomer is increased whereas the bond gets shorter in the other monomer. This distortion leads to localization of the orbitals. Now we see that the T_1 state, which is dominated by a HOMO → LUMO excitation, is a locally excited state, whereas the T_2 state with the HOMO−1 → LUMO excitation as the leading configuration is a charge-transfer state. This formation of a local triplet exciton from a delocalized state promotes the generation of two separate triplets from the ^{1}(TT) state.

Pictorially, the proposed SF mechanism is summarized in Figure 9: After photoexcitation of the bright S_3 state in the FC zone, the symmetric C−C stretching mode 113 conveys the excited-state population efficiently to the dark ^{1}(TT) state. Mediated by the antisymmetric C−C stretching mode 114, ^{1}(TT) may split into two separate triplet states. Energetically, SF is predicted to be a downhill process in the QBT dimer and should hence proceed facilely.

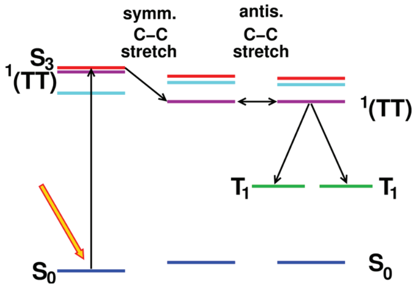

Figure 9. Proposed mechanism of singlet fission in the slip-stacked QBT excimer. While displacements of the nuclear frame along a symmetric stretching coordinate (mode 113) lead to a stabilization of the ^{1}(TT) state and fast nonradiative decay of the originally excited bright S_3 state, the antisymmetric stretching normal mode 114 promotes the splitting of the ^{1}(TT) state into two individual triplets.

4. CONCLUSIONS

In this work, we investigated a quinoidal oligothiophene with respect to its ability to undergo singlet fission. We found that the energetic requirement for SF, namely $E(S_n) \geqslant 2E(T_1)$, is met in this system. However, a path enabling *intramolecular* SF could not be identified. Comparison of computed excited-state absorption spectra with experimental data showed that both 2^1A_g and 1^3B_u qualify as candidates for the observed long-lived species. Because of the near-degeneracy of the dark 2^1A_g state and the optically bright 1^1B_u state, a fast equilibration of the excited-state populations via vibronic interaction is expected. Furthermore, we could show that even a small deviation from planarity, such as a torsion about the central bond by 20°, is sufficient to invoke fast intersystem crossing between the 1^1B_u state and the closeby 1^3A_g state.

In contrast, two vibrational modes relevant for an *intermolecular* SF process in the slip-stacked dimer could be identified. One of them drives the coupling between the photoexcited singlet state and the ^{1}(TT) state while the other one leads to the localization of the triplet excitons. For intermolecular SF to be efficient in this system, the separation of the two triplet excitons in the ^{1}(TT) state needs to be faster than the internal conversion to the S_1 state. Further studies of the excited-state dynamics have to be carried out to find out whether this is the case.

Our results show that the chosen DFT/MRCI-R method is suitable for describing the excimer states. When used in conjunction with the Grimme D3 dispersion correction, it yields a physically correct description of the van der Waals interactions of the π-stacked monomers, as a comparison with crystal structure data calculations shows. The calculations can be performed at relatively low computational cost. With regard to the excitation energy of the bright singlet state, we obtain excellent agreement with experimental findings. Furthermore, the DFT/MRCI-R method yields a consistent description of the singlet, triplet, and quintet states in the monomer and the dimer which is essential for the quantum chemical treatment of SF.

DOI: 10.1021/acs.jpcc.6b02263
J. Phys. Chem. C 2016, 120, 13901−13910

ASSOCIATED CONTENT

Supporting Information

The Supporting Information is available free of charge on the ACS Publications website at DOI: 10.1021/acs.jpcc.6b02263.

> Coordinates of all optimized structures, characterization of vibrational modes of the QBT dimer, and energy profiles of the low-lying QBT dimer states for distortions along selected normal coordinates (PDF)

AUTHOR INFORMATION

Corresponding Author

*E-mail: Christel.Marian@uni-duesseldorf.de.

Notes

The authors declare no competing financial interest.

ACKNOWLEDGMENTS

Financial support by the Deutsche Forschungsgemeinschaft through TA 725/1-1 and MA 1051/14-1 is gratefully acknowledged.

REFERENCES

(1) Scharber, M.; Sariciftci, N. Efficiency of Bulk-Heterojunction Organic Solar Cells. *Prog. Polym. Sci.* **2013**, *38*, 1929−1940.

(2) Smith, M. B.; Michl, J. Singlet Fission. *Chem. Rev.* **2010**, *110*, 6891−6936.

(3) Burdett, J. J.; Müller, A. M.; Gosztola, D.; Bardeen, C. J. Excited State Dynamics in Solid and Monomeric Tetracene: The Roles of Superradiance and Exciton Fission. *J. Chem. Phys.* **2010**, *133*, 144506.

(4) Thorsmølle, V. K.; Averitt, R. D.; Demsar, J.; Smith, D.; Tretiak, S.; Martin, R.; Chi, X.; Crone, B.; Ramirez, A.; Taylor, A. Morphology Effectively Controls Singlet-Triplet Exciton Relaxation and Charge Transport in Organic Semiconductors. *Phys. Rev. Lett.* **2009**, *102*, 017401.

(5) Guo, J.; Ohkita, H.; Benten, H.; Ito, S. Near-IR Femtosecond Transient Absorption Spectroscopy of Ultrafast Polaron and Triplet Exciton Formation in Polythiophene Films with Different Regioregularities. *J. Am. Chem. Soc.* **2009**, *131*, 16869−16880.

(6) Rao, A.; Wilson, M. W.; Hodgkiss, J. M.; Albert-Seifried, S.; Bassler, H.; Friend, R. H. Exciton Fission and Charge Generation via Triplet Excitons in Pentacene/C60 Bilayers. *J. Am. Chem. Soc.* **2010**, *132*, 12698−12703.

(7) Shockley, W.; Queisser, H. J. Detailed Balance Limit of Efficiency of p-n Junction Solar Cells. *J. Appl. Phys.* **1961**, *32*, 510−519.

(8) Hanna, M.; Nozik, A. Solar Conversion Efficiency of Photovoltaic and Photoelectrolysis Cells with Carrier Multiplication Absorbers. *J. Appl. Phys.* **2006**, *100*, 074510.

(9) Zimmerman, P. M.; Bell, F.; Casanova, D.; Head-Gordon, M. Mechanism for Singlet Fission in Pentacene and Tetracene: From Single Exciton to Two Triplets. *J. Am. Chem. Soc.* **2011**, *133*, 19944−19952.

(10) Smith, M. B.; Michl, J. Recent Advances in Singlet Fission. *Annu. Rev. Phys. Chem.* **2013**, *64*, 361−386.

(11) Burdett, J. J.; Bardeen, C. J. Quantum Beats in Crystalline Tetracene Delayed Fluorescence due to Triplet Pair Coherences Produced by Direct Singlet Fission. *J. Am. Chem. Soc.* **2012**, *134*, 8597−8607.

(12) Monahan, N.; Zhu, X.-Y. Charge Transfer-Mediated Singlet Fission. *Annu. Rev. Phys. Chem.* **2015**, *66*, 601−618.

(13) Walker, B. J.; Musser, A. J.; Beljonne, D.; Friend, R. H. Singlet Exciton Fission in Solution. *Nat. Chem.* **2013**, *5*, 1019−1024.

(14) Zirzlmeier, J.; Lehnherr, D.; Coto, P. B.; Chernick, E. T.; Casillas, R.; Basel, B. S.; Thoss, M.; Tykwinski, R. R.; Guldi, D. M. Singlet Fission in Pentacene Dimers. *Proc. Natl. Acad. Sci. U. S. A.* **2015**, *112*, 5325−5330.

(15) Musser, A. J.; Maiuri, M.; Brida, D.; Cerullo, G.; Friend, R. H.; Clark, J. The Nature of Singlet Exciton Fission in Carotenoid Aggregates. *J. Am. Chem. Soc.* **2015**, *137*, 5130−5139.

(16) Casado, J.; Ortiz, R. P.; Navarrete, J. T. L. Quinoidal Oligothiophenes: New Properties Behind an Unconventional Electronic Structure. *Chem. Soc. Rev.* **2012**, *41*, 5672−5686.

(17) Wang, Z.; Kobayashi, T. Electronic Relaxation and Vibrational Dynamics in a Thiophene Oligomer Studied Under the Same Experimental Condition with a sub-5 fs Laser. *New J. Phys.* **2008**, *10*, 123021.

(18) Varnavski, O.; Abeyasinghe, N.; Aragó, j.; Serrano-Pérez, J. J.; Ortí, E.; Lopez Navarrete, J. T.; Takimiya, K.; Casanova, D.; Casado, J.; Goodson, T., III High Yield Ultrafast Intramolecular Singlet Exciton Fission in a Quinoidal Bithiophene. *J. Phys. Chem. Lett.* **2015**, *6*, 1375−1384.

(19) Chien, A. D.; Molina, A. R.; Abeyasinghe, N.; Varnavski, O. P.; Goodson, T., III; Zimmerman, P. M. Structure and Dynamics of the 1 (TT) State in a Quinoidal Bithiophene: Characterizing a Promising Intramolecular Singlet Fission Candidate. *J. Phys. Chem. C* **2015**, *119*, 28258−28268.

(20) Becker, R. S.; de Melo, J. S.; Maçanita, A. L.; Elisei, F. Comprehensive Investigation of the Solution Photophysics and Theoretical Aspects of Oligothiophenes of 1−7 Rings. *Pure Appl. Chem.* **1995**, *67*, 9−16.

(21) Rubio, M.; Merchán, M.; Pou-AméRigo, R.; Ortí, E. The Low-Lying Excited States of 2,2′-Bithiophene: A Theoretical Analysis. *ChemPhysChem* **2003**, *4*, 1308−1315.

(22) Siegert, S.; Vogeler, F.; Marian, C. M.; Weinkauf, R. Throwing Light on Dark States of α-Oligothiophenes of Chain Lengths 2 to 6: Radical Anion Photoelectron Spectroscopy and Excited State Theory. *Phys. Chem. Chem. Phys.* **2011**, *13*, 10350−10363.

(23) Lyskov, I.; Kleinschmidt, M.; Marian, C. M. Redesign of the DFT/MRCI Hamiltonian. *J. Chem. Phys.* **2016**, *144*, 034104.

(24) *TURBOMOLE*, a Development of University of Karlsruhe and Forschungszentrum Karlsruhe GmbH; 1989−2007, TURBOMOLE GmbH, since2007, available from http://www.turbomole.com.

(25) Becke, A. D. Density-Functional Thermochemistry. III. The Role of Exact Exchange. *J. Chem. Phys.* **1993**, *98*, 5648−5652.

(26) Lee, C.; Yang, W.; Parr, R. G. Development of the Colle-Salvetti Correlation-Energy Formula into a Functional of the Electron Density. *Phys. Rev. B: Condens. Matter Mater. Phys.* **1988**, *B37*, 785−789.

(27) Furche, F.; Ahlrichs, R. Adiabatic Time-Dependent Density Functional Methods for Excited State Properties. *J. Chem. Phys.* **2002**, *117*, 7433−7447.

(28) Schäfer, A.; Huber, C.; Ahlrichs, R. Fully Optimized Contracted Gaussian Basis Sets of Triple Zeta Valence Quality for Atoms Li to Kr. *J. Chem. Phys.* **1994**, *100*, 5829−5835.

(29) Grimme, S.; Antony, J.; Ehrlich, S.; Krieg, H. A Consistent and Accurate ab initio Parametrization of Density Functional Dispersion Correction (DFT-D) for the 94 elements H-Pu. *J. Chem. Phys.* **2010**, *132*, 154104.

(30) Deglmann, P.; Furche, F.; Ahlrichs, R. An Efficient Implementation of Second Analytical Derivatives for Density Functional Methods. *Chem. Phys. Lett.* **2002**, *362*, 511−518.

(31) Grimme, S.; Waletzke, M. A Combination of Kohn-Sham Density Functional Theory and Multi-Reference Configuration Interaction Methods. *J. Chem. Phys.* **1999**, *111*, 5645−5655.

(32) Marian, C. M.; Gilka, N. Performance of the Density Functional Theory/Multireference Configuration Interaction Method on Electronic Excitation of Extended π-Systems. *J. Chem. Theory Comput.* **2008**, *4*, 1501−1515.

(33) Silva-Junior, M. R.; Schreiber, M.; Sauer, S. P. A.; Thiel, W. Benchmarks for Electronically Excited States: Time-Dependent Density Functional Theory and Density Functional Theory Based Multireference Configuration Interaction. *J. Chem. Phys.* **2008**, *129*, 104103.

(34) Becke, A. D. A New Mixing of Hartree-Fock and Local Density Functional Theories. *J. Chem. Phys.* **1993**, *98*, 1372−1377.

(35) Kleinschmidt, M.; Tatchen, J.; Marian, C. M. Spin-Orbit Coupling of DFT/MRCI Wavefunctions: Method, Test Calculations, and Application to Thiophene. *J. Comput. Chem.* **2002**, *23*, 824−833.

(36) Schulten, K.; Karplus, M. On the Origin of a Low-Lying Forbidden Transition in Polyenes and Related Molecules. *Chem. Phys. Lett.* **1972**, *14*, 305−309.

(37) Tavan, P.; Schulten, K. Electronic Excitations in Finite and Infinite Polyenes. *Phys. Rev. B: Condens. Matter Mater. Phys.* **1987**, *36*, 4337−4358.

(38) Marian, C. In *Reviews In Computational Chemistry*; Lipkowitz, K., Boyd, D., Eds.; Wiley-VCH: Weinheim, 2001; Vol *17*, pp 99−204.

(39) Marian, C. M. Spin-Orbit Coupling and Intersystem Crossing in Molecules. *WIREs Comput. Mol. Sci.* **2012**, *2*, 187−203.

(40) Janzen, D. E.; Burand, M. W.; Ewbank, P. C.; Pappenfus, T. M.; Higuchi, H.; da Silva Filho, D. A.; Young, V. G.; Brédas, J.-L.; Mann, K. R. Preparation and Characterization of π-Stacking Quinodimethane Oligothiophenes. Predicting Semiconductor Behavior and Bandwidths from Crystal Structures and Molecular Orbital Calculations. *J. Am. Chem. Soc.* **2004**, *126*, 15295−15308.

(41) Hernandez, V.; Casado, J.; Hotta, S.; Navarrete, J. L. Vibrational and Electronic Spectroscopic Study of Two Oligothiophene Materials Bearing a Heteroquinonoid Structure. *Synth. Met.* **1999**, *101*, 549−550.

Supporting Information for
Singlet Fission in Quinoidal Oligothiophenes

Nikolai Elfers[a], Igor Lyskov[a], Dominik Spiegel[a], and Christel M. Marian[a*]

[a]*Institute of Theoretical and Computational Chemistry, Heinrich Heine University Düsseldorf, Universitätsstr. 1, D-40225 Düsseldorf, Germany*

E-mail: Christel.Marian@uni-duesseldorf.de

---

[*] To whom correspondence should be addressed

QBT monomer, S_0 state

-2.29730167005089	2.82898359529355	0.00000000000000	c
-1.24981860986024	0.33217128094380	0.00000000000000	c
-3.73217119956455	-1.94961564890675	0.00000000000000	s
-6.03444640100795	0.46614065179245	0.00000000000000	c
-4.85606464910324	2.91113080479148	0.00000000000000	c
1.24981860986024	-0.33217128094380	0.00000000000000	c
3.73217119956455	1.94961564890675	0.00000000000000	s
6.03444640100795	-0.46614065179245	0.00000000000000	c
4.85606464910324	-2.91113080479148	0.00000000000000	c
2.29730167005089	-2.82898359529355	0.00000000000000	c
-5.96619110619450	4.62622909987997	0.00000000000000	h
-1.11195642430964	4.49477783099887	0.00000000000000	h
1.11195642430964	-4.49477783099887	0.00000000000000	h
5.96619110619450	-4.62622909987997	0.00000000000000	h
8.59040123770526	0.01363677984045	0.00000000000000	c
10.35093871840656	-2.01421035176208	0.00000000000000	c
9.54691992178156	2.52018407858914	0.00000000000000	c
10.26209642115361	4.58285267357961	0.00000000000000	n
11.74622906551883	-3.69261888892537	0.00000000000000	n
-8.59040123770526	-0.01363677984045	0.00000000000000	c
-9.54691992178156	-2.52018407858914	0.00000000000000	c
-10.35093871840656	2.01421035176208	0.00000000000000	c
-10.26209642115361	-4.58285267357961	0.00000000000000	n
-11.74622906551883	3.69261888892537	0.00000000000000	n

QBT monomer, S_1 state

-2.26063745644720	2.86753598572113	0.00085066225454	c
-1.26590166977445	0.39568721746446	0.00080734143884	c
-3.72475973916944	-1.86046151369959	0.00068101006587	s
-6.03355626296611	0.57279819115748	0.00040462087333	c
-4.86632298958355	2.97473682096555	0.00060506051551	c
1.26586188566150	-0.39583136542899	0.00050886328161	c
3.72467638329388	1.86037293310783	0.00025940408309	s
6.03354540273346	-0.57283456570553	-0.00015293549650	c
4.86636794509978	-2.97481912977191	-0.00009015868685	c
2.26065749441957	-2.86766564449830	0.00025030949591	c
-5.95701319877951	4.70083474975623	0.00048470095661	h
-1.06270670935828	4.52386892362739	0.00106910456220	h
1.06276044181705	-4.52402770627160	0.00029080959951	h
5.95711247147939	-4.70090358734482	-0.00034248220582	h
8.60752598568342	0.00269680607456	-0.00040221451158	c
10.40257927354381	-1.97763021997662	-0.00041406140909	c
9.48514414418591	2.52536412283914	-0.00052914999235	c
10.13848762491544	4.61348774889200	-0.00059541200719	n
11.81477322366325	-3.64765229632264	-0.00030020197369	n
-8.60754066880152	-0.00261592723554	-0.00016209316917	c
-9.48525932693498	-2.52522653823602	-0.00010203757537	c
-10.40249491924277	1.97776484250356	-0.00105893172040	c
-10.13868579420571	-4.61330984419039	-0.00003239044228	n
-11.81461354123290	3.64782999657271	-0.00202981793678	n

QBT monomer, T_1 state

-2.26653213802018	2.83070239462742	0.00558426224265	c
-1.30223327910371	0.39658591488708	-0.00025298585391	c
-3.74490846774722	-1.85124024562878	-0.00584535962885	s
-6.04516411006444	0.55691392768346	-0.00009259133305	c
-4.90629754382083	2.93499322010153	0.00594129984514	c
1.30222819940888	-0.39662739895173	-0.00188639190249	c
3.74488810233583	1.85121864104208	-0.00546916370275	s
6.04516046495006	-0.55692412270999	-0.00227148845647	c
4.90631012881480	-2.93501733612446	0.00051853536387	c
2.26654263581469	-2.83074386561779	0.00018257396726	c
-5.98775579583387	4.66815139203986	0.01068865582720	h
-1.08113862165947	4.49554207617152	0.01002926504532	h
1.08115979007368	-4.49559668693009	0.00179017768227	h
5.98778084296419	-4.66817325662607	0.00271833853346	h
8.66160808885641	0.00012728907907	-0.00206614616393	c
10.44742551055157	-1.98459886015046	0.00696927231083	c
9.56264587785419	2.51005564234171	-0.01002044469196	c
10.25864999632116	4.58481215024613	-0.01732599728011	n
11.87466233738489	-3.64212926585158	0.01572245703491	n
-8.66161617203046	-0.00010730647326	-0.00220477825751	c
-9.56267836496088	-2.51003536505884	-0.00637219170434	c
-10.44741195519383	1.98465693159377	0.00038057797945	c
-10.25870202948868	-4.58479647247680	-0.00914870300818	n
-11.87462349740684	3.64223060278618	0.00243082615113	n

QBT slip-stacked dimer, S_0 state

0.90139863514856	-2.52245737204846	-0.10005119239488	c
2.24917263581746	-0.17936058189218	-0.00024637219363	c
0.06701147766894	2.38963330473260	0.05685705946709	s
-2.51325926350740	0.27950832466723	-0.03095594560951	c
-1.65009156782069	-2.28942134788148	-0.12696271141969	c
4.80992567654216	0.17538653059237	0.05656468341874	c
6.98547430480478	-2.39199334713526	0.05945286095988	s
9.57109931032113	-0.27772692355880	0.17312047964683	c
8.70320470164823	2.29507309139532	0.19653112660421	c
6.15569082612350	2.52781651992845	0.14360899931680	c
-2.96480191901486	-3.85103872137600	-0.19445094980281	h
1.87301082214653	-4.32076856522842	-0.15546426941780	h
5.18549043278446	4.32632492177843	0.17117090134738	h
10.01063244300969	3.86185137376515	0.29047826355703	h
12.03557791922476	-1.08663241400996	0.25891165897237	c
14.04677132328646	0.68790364857705	0.38937835370776	c
12.64003419429373	-3.70119400279569	0.23372581006554	c
13.03641023326391	-5.84644494465469	0.18772701040979	n
15.64615072914051	2.16815769672168	0.49155392949436	n
-4.98894532477571	1.08136398723942	0.03302474273522	c
-5.59569873708581	3.68109575516570	0.27527958480071	c
-6.99535438038852	-0.69757885842839	-0.02922247768640	c
-5.99345686601873	5.81117482738095	0.54469581262699	n
-8.59439734272386	-2.18333984496999	-0.03580862971052	n
-2.37648001879562	2.53248287111511	6.45974649470802	c
-1.03034685613217	0.18039134613041	6.54776202277997	c

-3.20557489348399	-2.38725183693395	6.55257710783890	s
-5.79172089213355	-0.27335433951901	6.44315607421841	c
-4.92411190310700	2.29947984905142	6.41368208931193	c
1.53050927104984	-0.17396794888075	6.60258140976324	c
3.71235856422078	2.39518906485285	6.54149414477747	s
6.29284568287320	0.28564121180554	6.63764016959270	c
5.42989633162825	-2.28322916917028	6.73708219541579	c
2.87849071175131	-2.51663989016230	6.70758025183890	c
-6.23195351209429	3.86599390520753	6.32072273315310	h
-1.40654796043811	4.33103793663788	6.42700626335759	h
1.90710865981786	-4.31497017135909	6.76556419757977	h
6.74468757518296	-3.84453943380881	6.81001228070284	h
8.76853708446383	1.08776592678978	6.57783746200083	c
10.77508038534122	-0.69067858582168	6.64903335637435	c
9.37541402951964	3.68723437365320	6.33309799593039	c
9.77331269233681	5.81704147196142	6.06186717128093	n
12.37442107452671	-2.17600472475975	6.66386338609809	n
-8.25639632325093	-1.08258499012377	6.36611497627411	c
-8.86050598385907	-3.69718864171521	6.39602535759194	c
-10.26829049769467	0.69163535648037	6.24178761141448	c
-9.25655618566841	-5.84245671535646	6.44578053136666	n
-11.86837292143307	2.17164007596045	6.14606115012814	n

Table 1: Classification of the normal modes

Mode	**Classification**
1	libration
2	slip stack
3	butterfly
4	shearing
5	torsion of C(CN)2
6	torsion
7	deformation
8	deformation
9	torsion
10	tilting
11	wagging
12	frustrated translation of pi-stack
13	butterfly
14	in plane rocking
15	in plane rocking
16	rocking
17	twisting
18	twisting
19	twisting
20	scissoring
21	scissoring
22	twisting
23	twisting
24	scissoring
25	scissoring
113-122	C-C-stretch

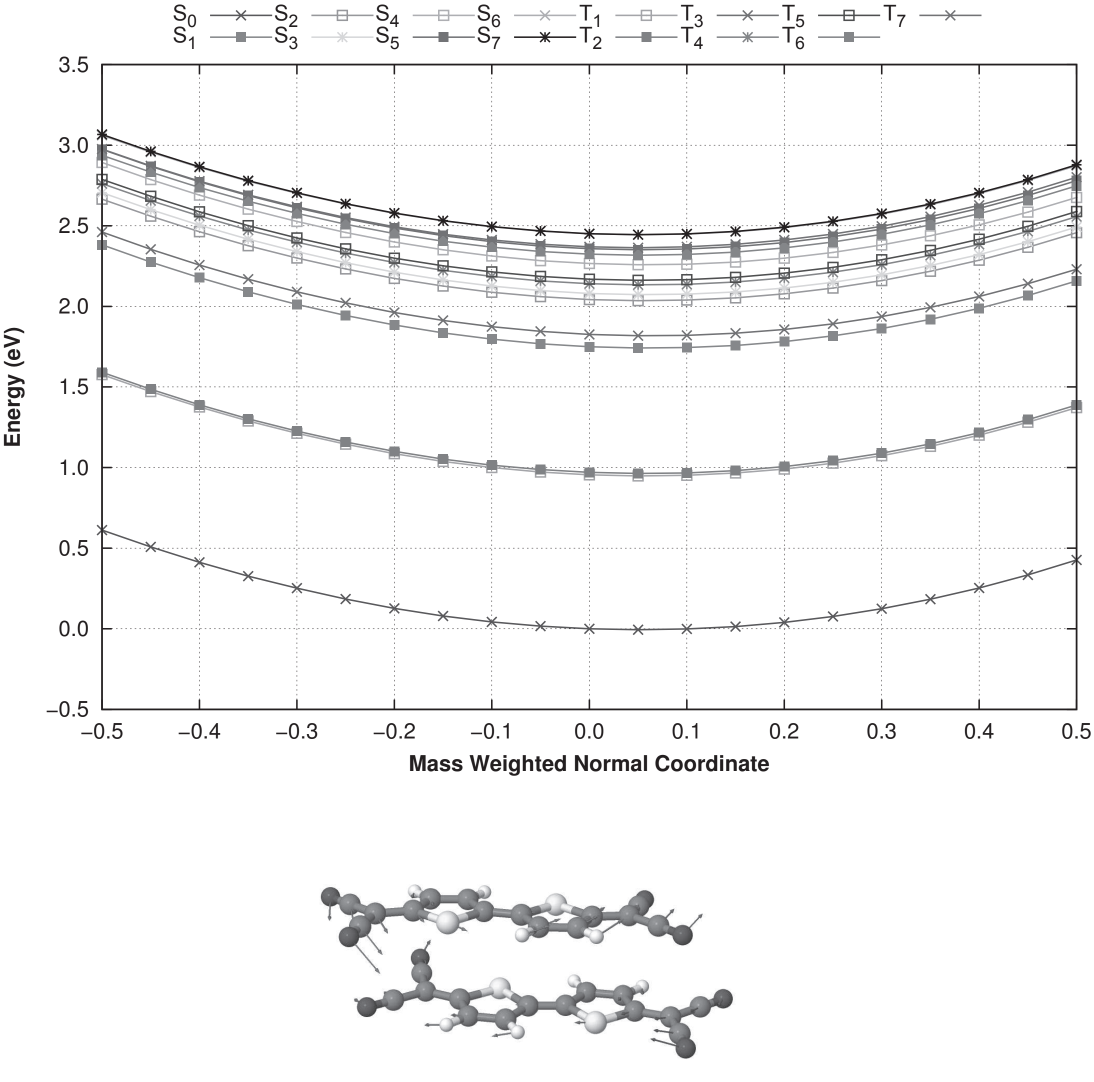

Figure 1: Mode 1

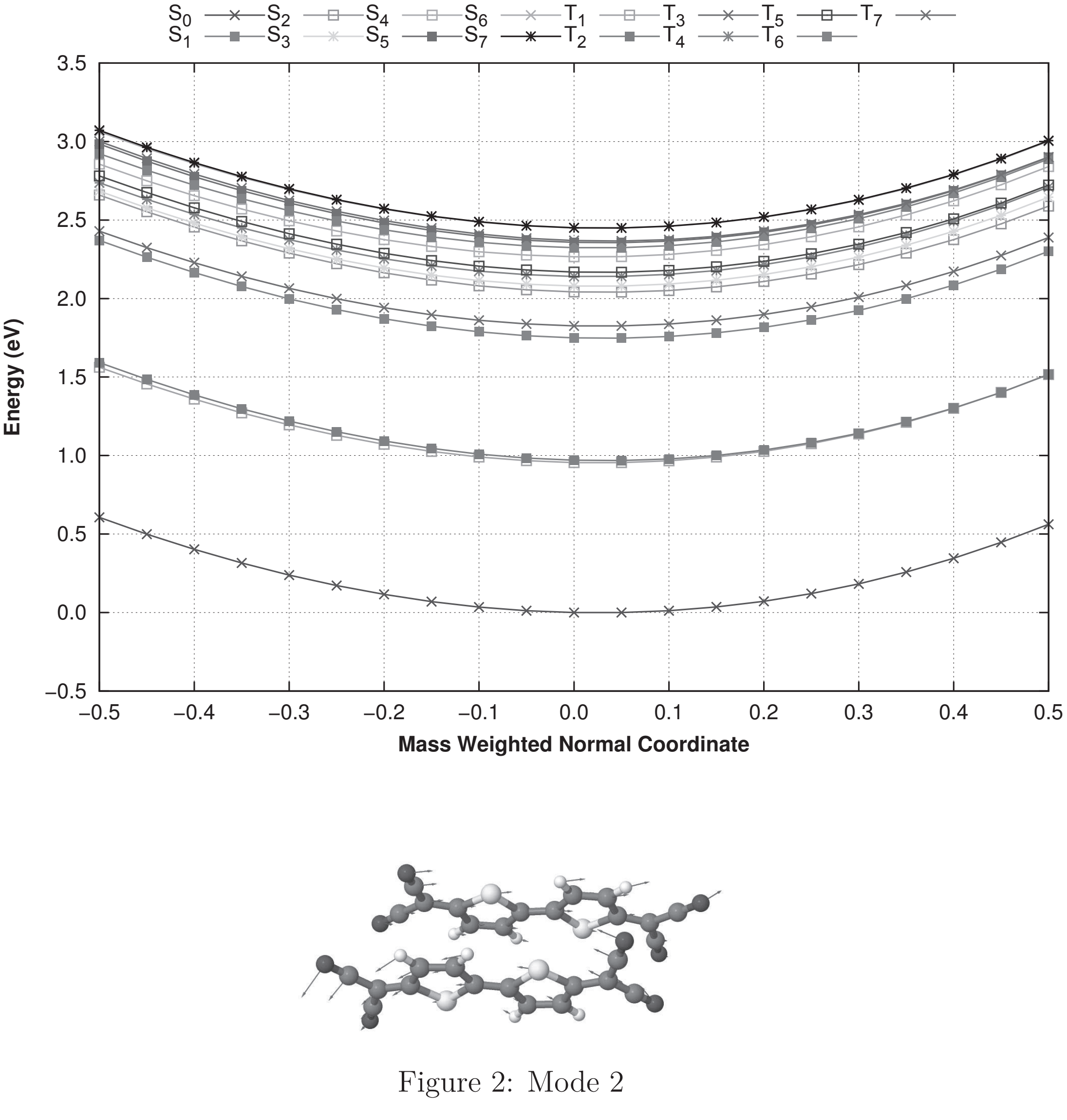

Figure 2: Mode 2

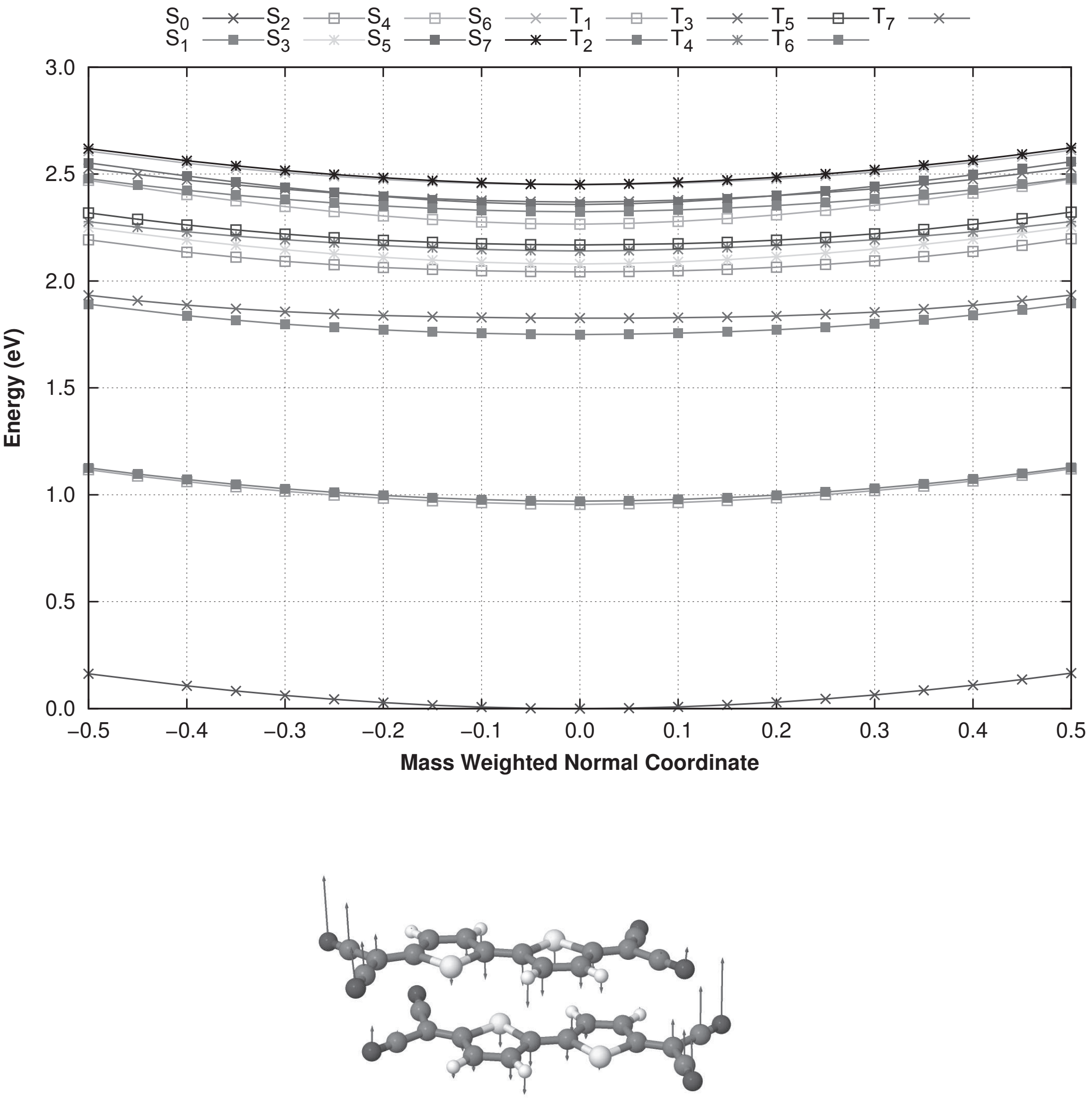

Figure 3: Mode 3

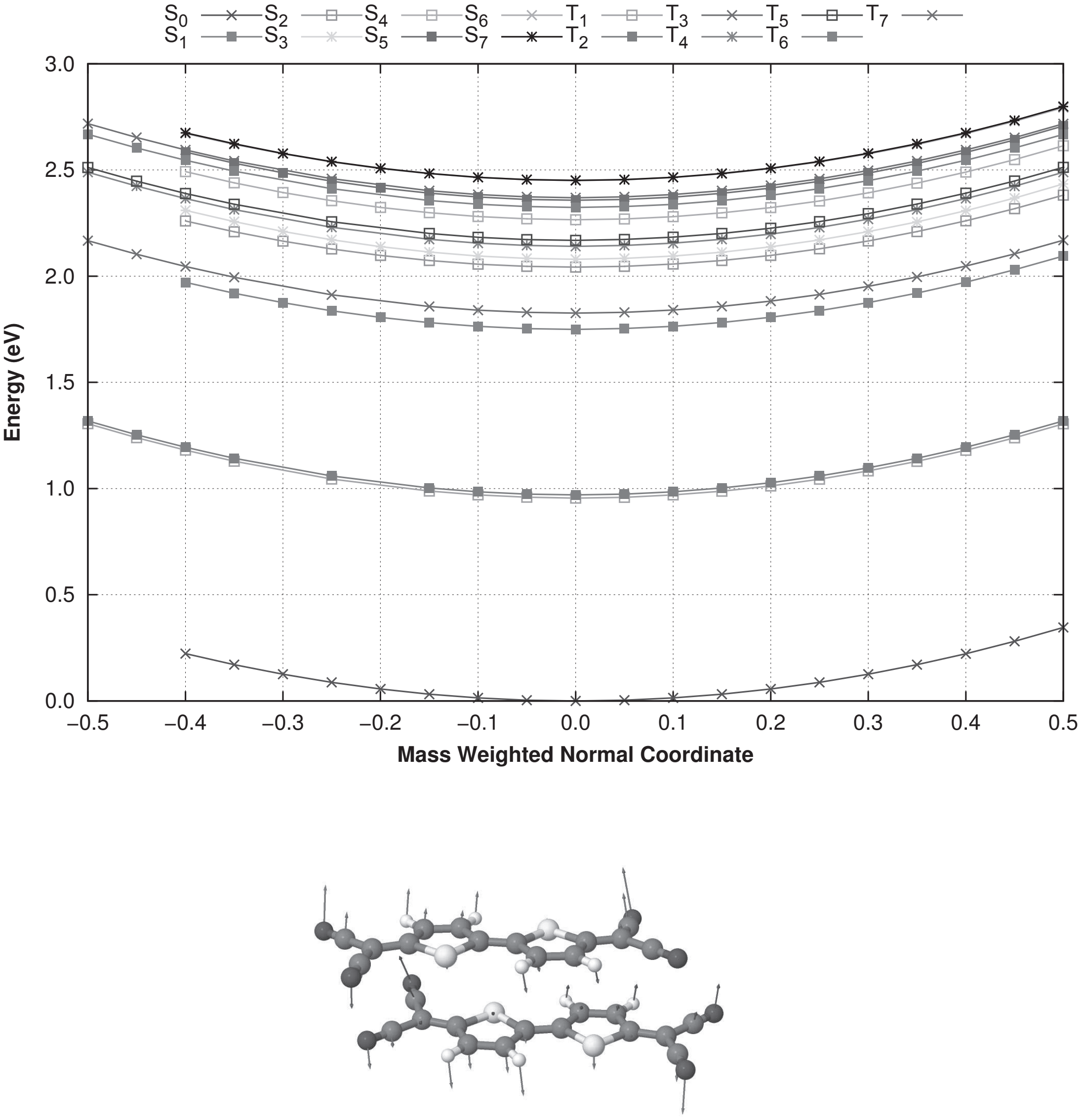

Figure 4: Mode 4

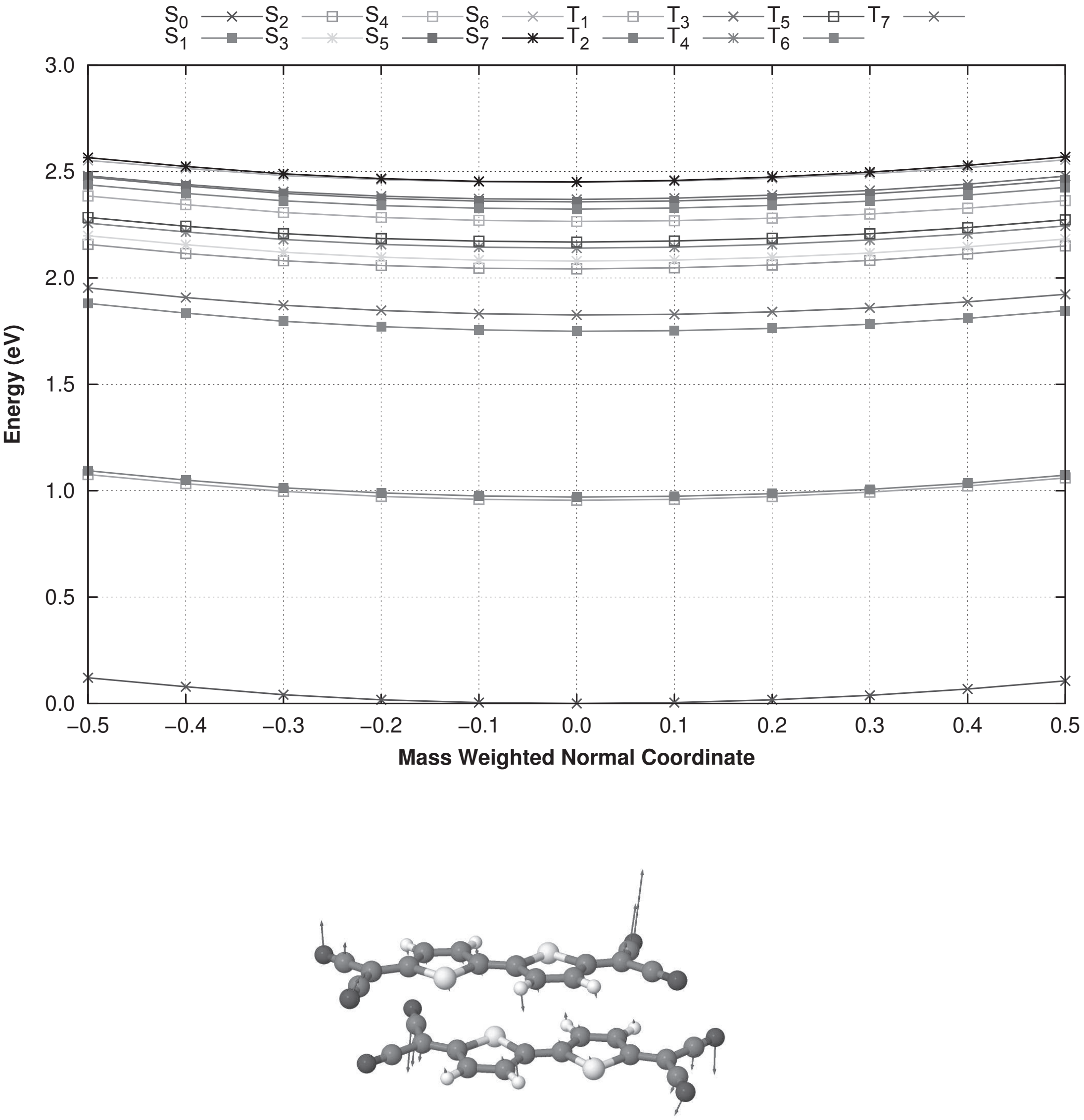

Figure 5: Mode 6

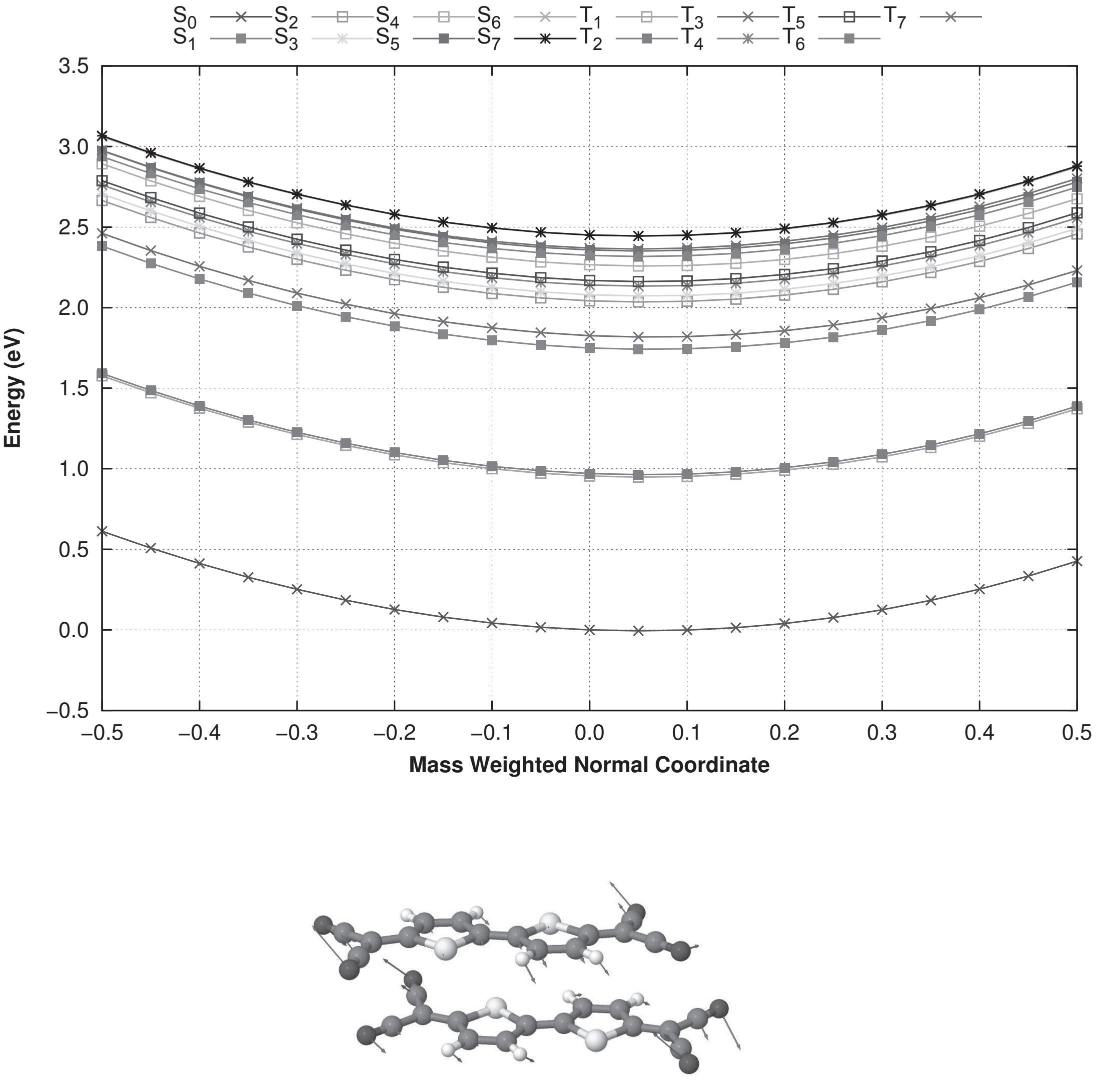

Figure 6: Mode 7

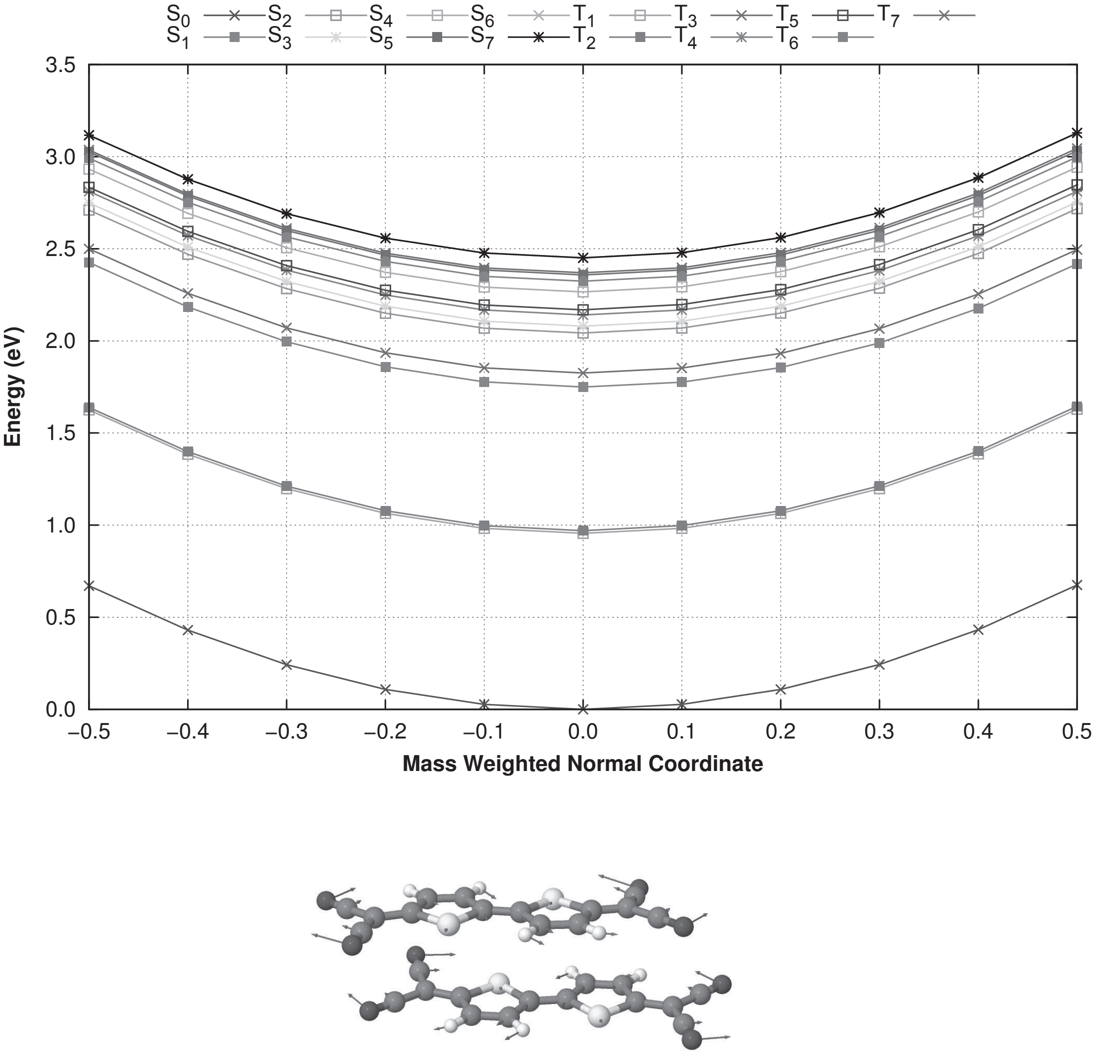

Figure 7: Mode 8

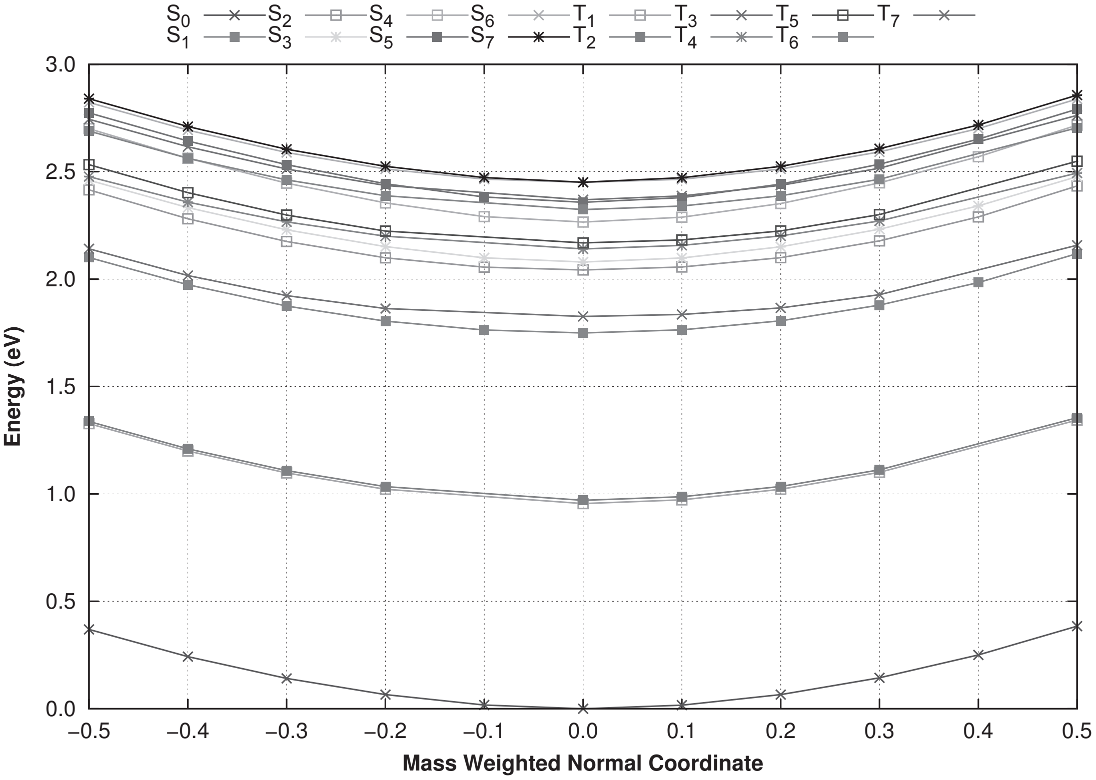

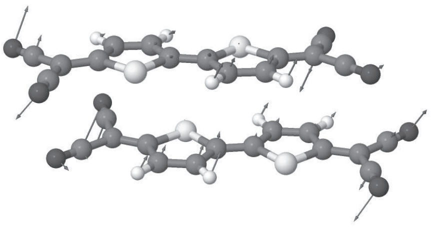

Figure 8: Mode 9

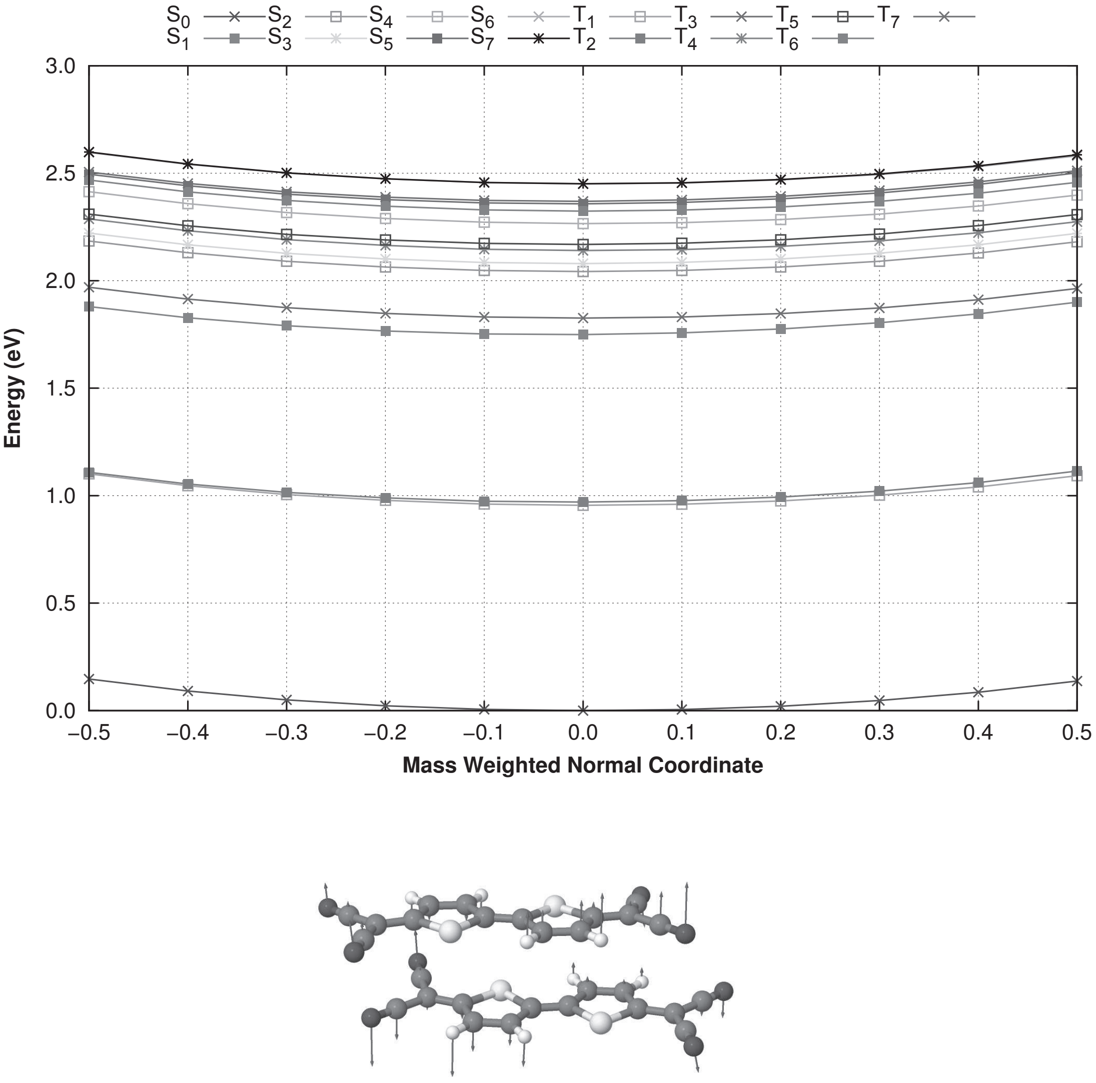

Figure 9: Mode 10

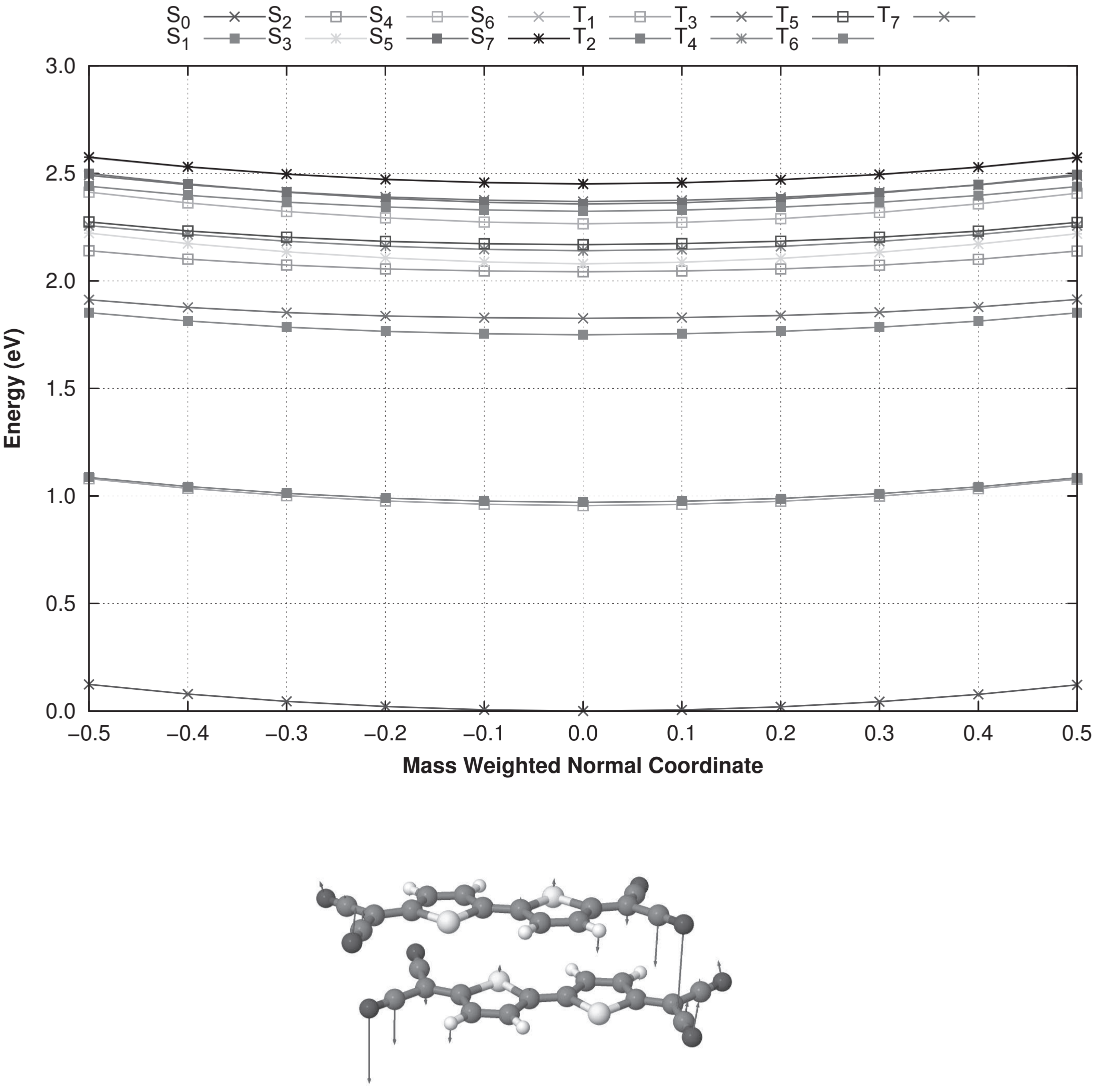

Figure 10: Mode 11

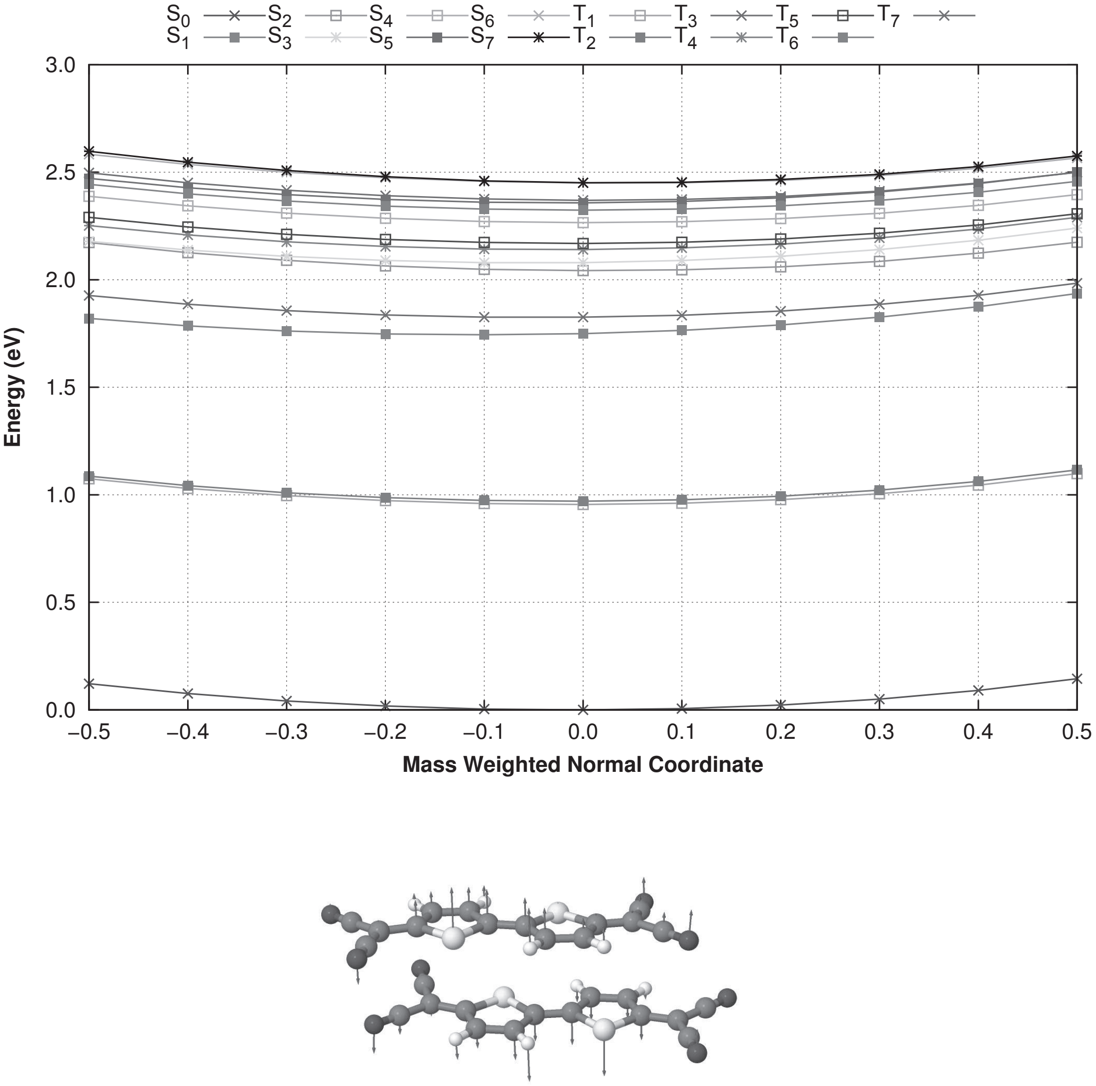

Figure 11: Mode 12

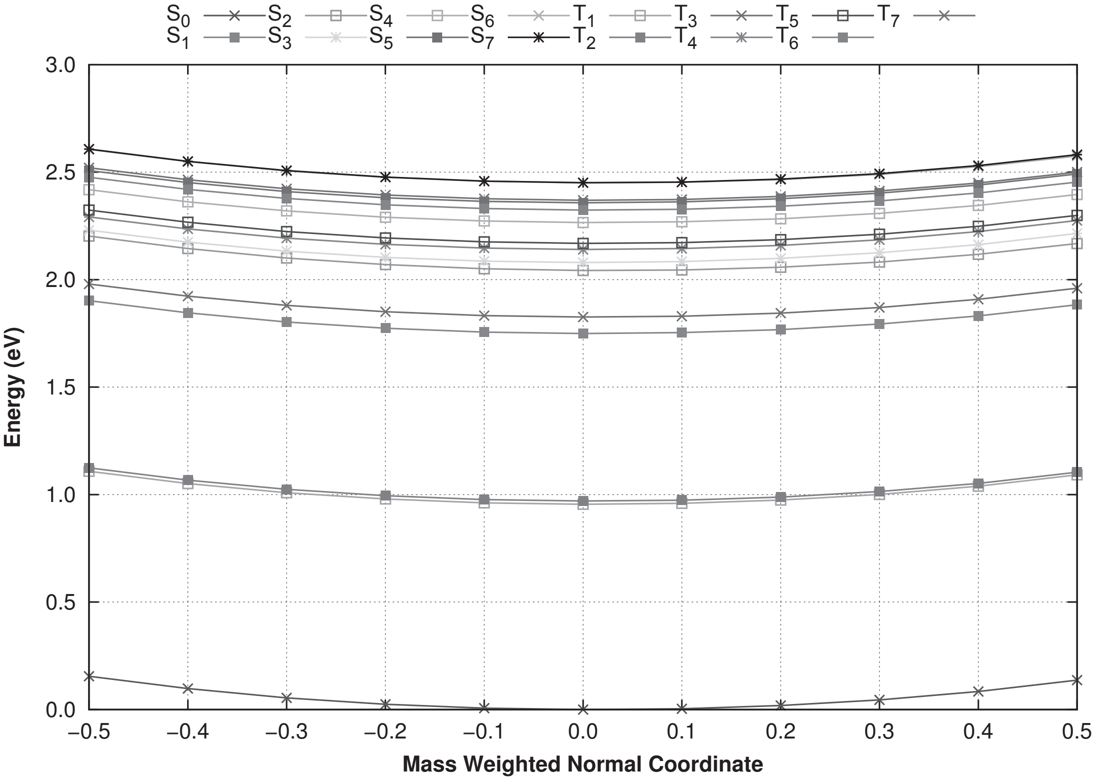

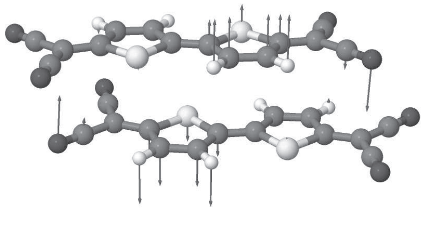

Figure 12: Mode 13

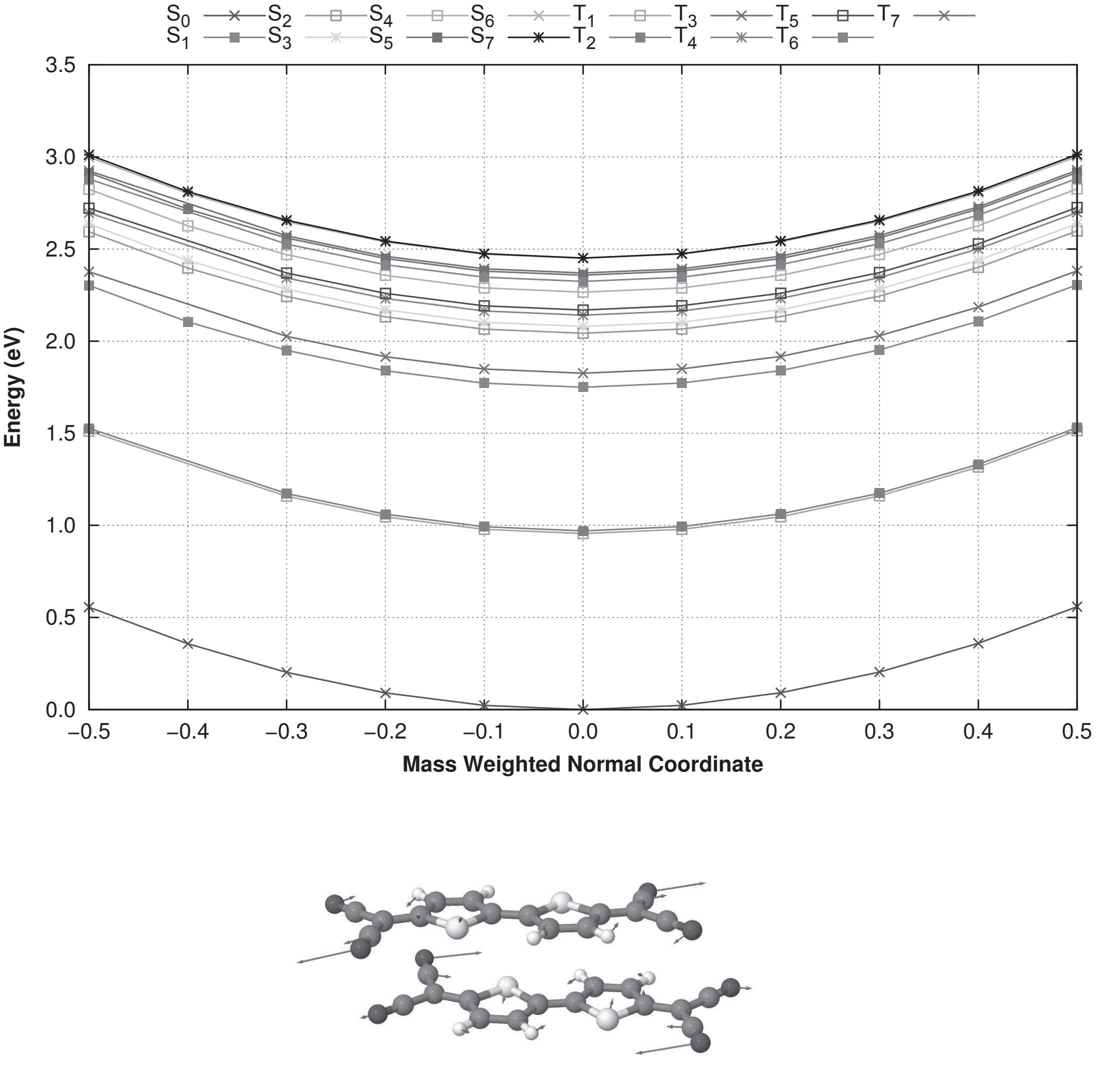

Figure 13: Mode 14

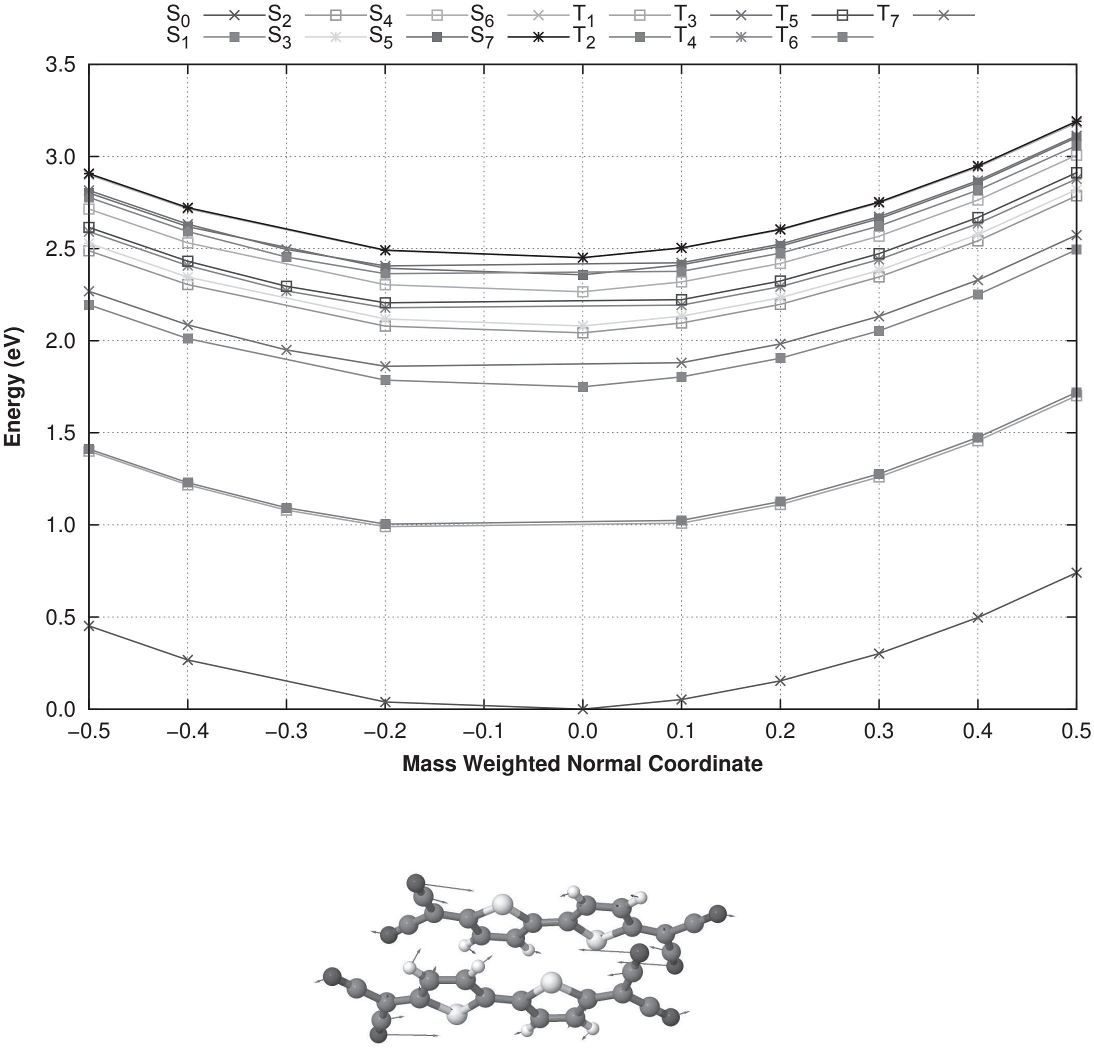

Figure 14: Mode 15

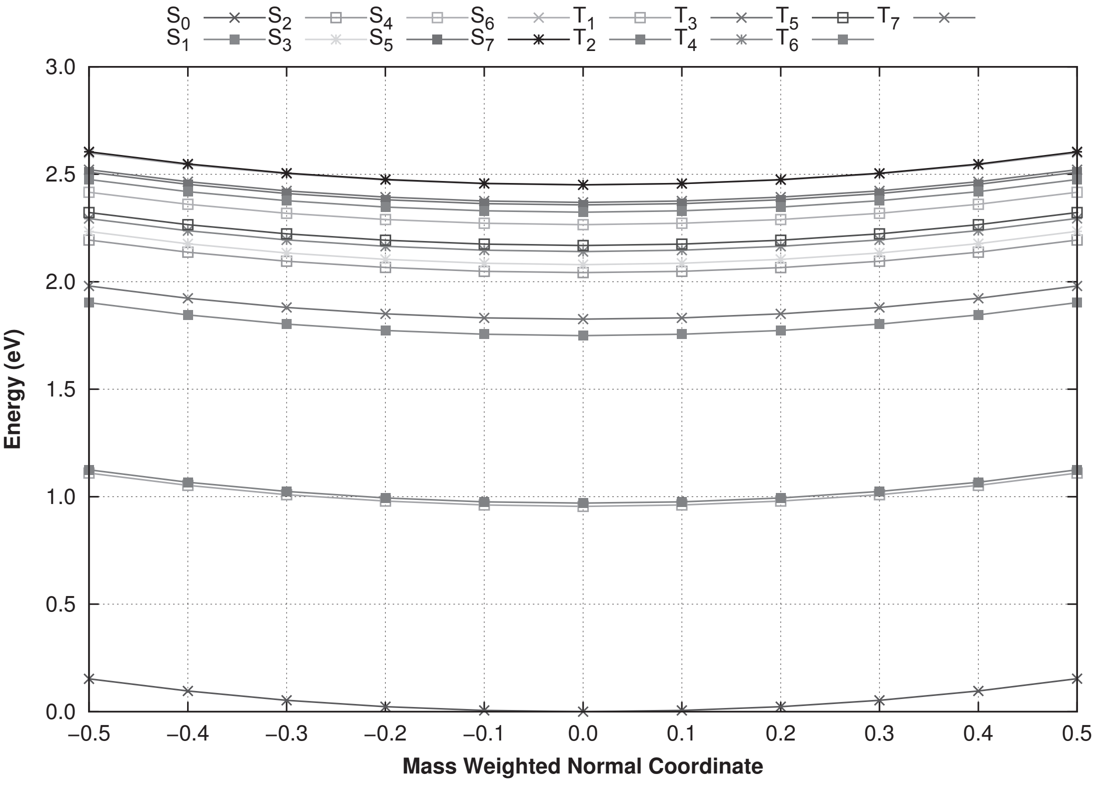

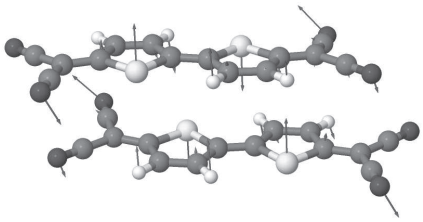

Figure 15: Mode 17

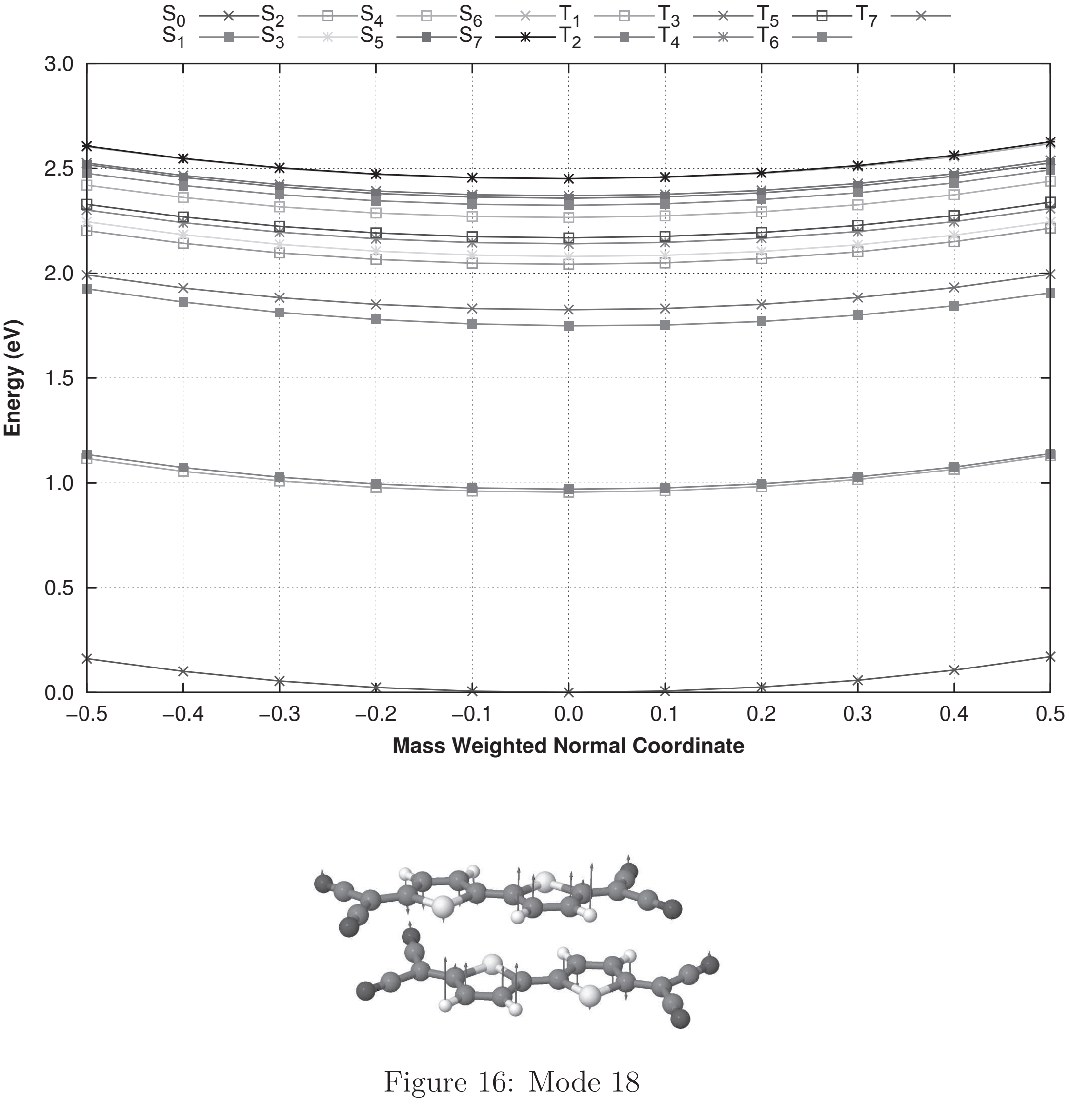

Figure 16: Mode 18

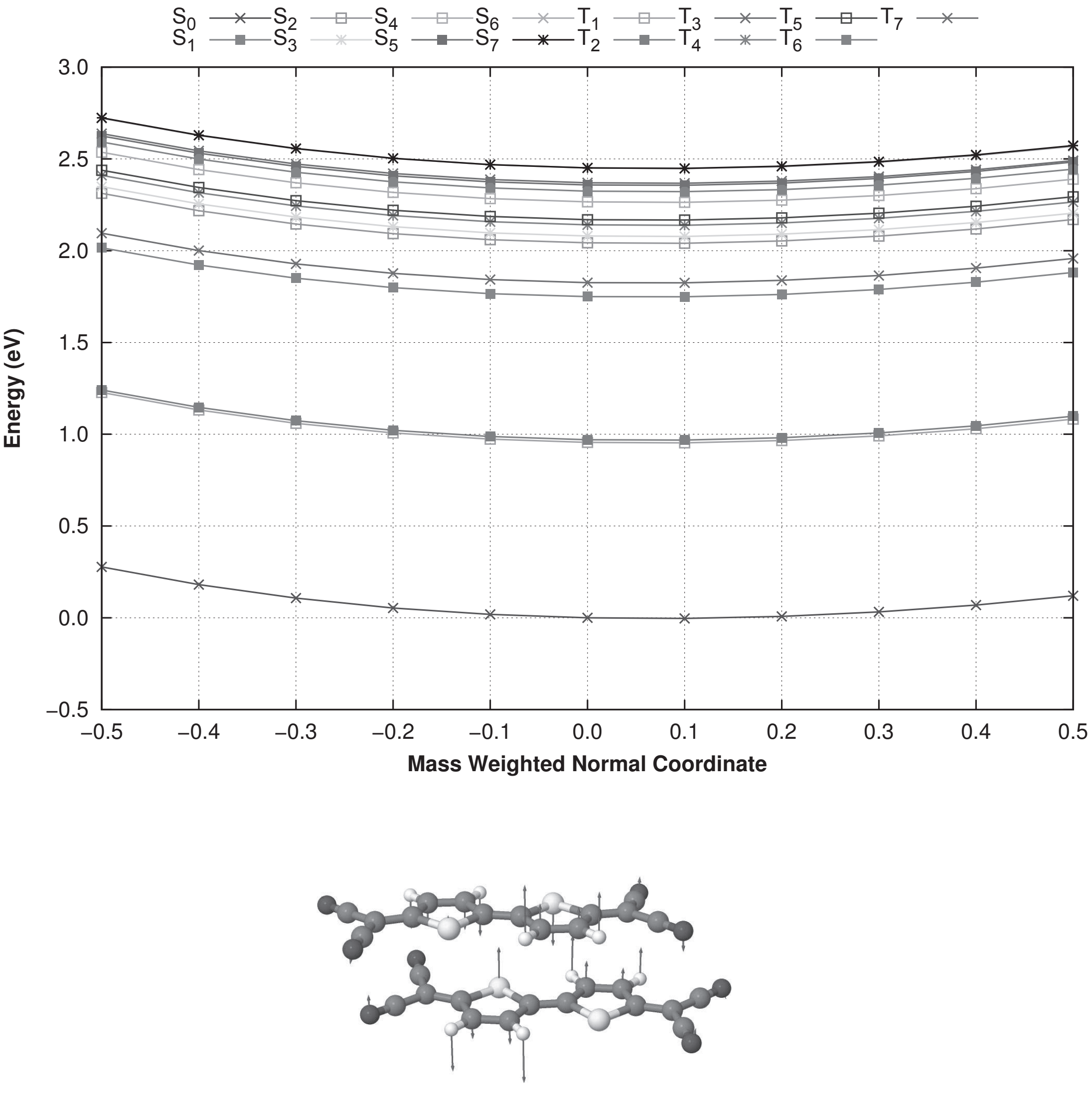

Figure 17: Mode 19

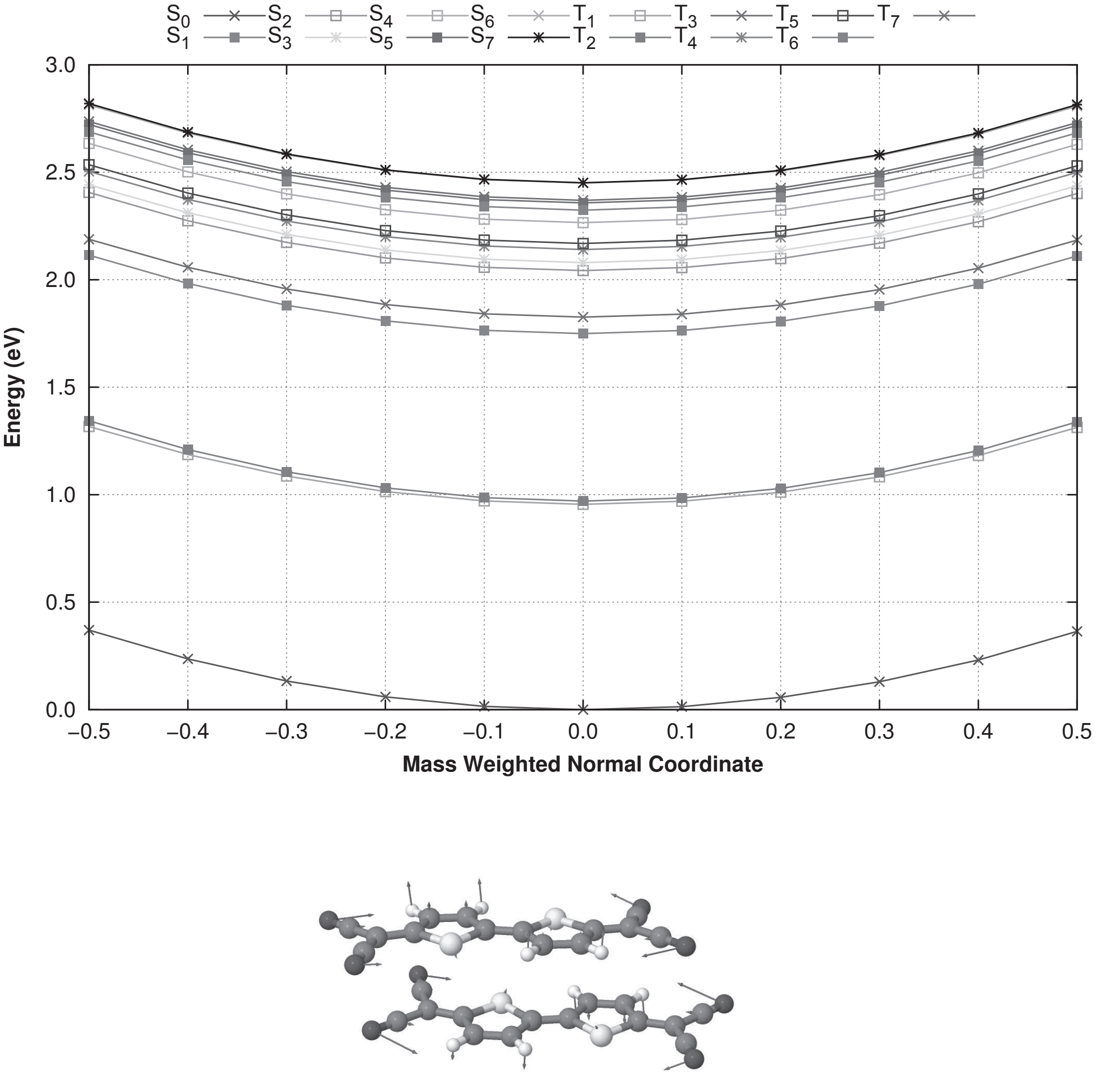

Figure 18: Mode 20

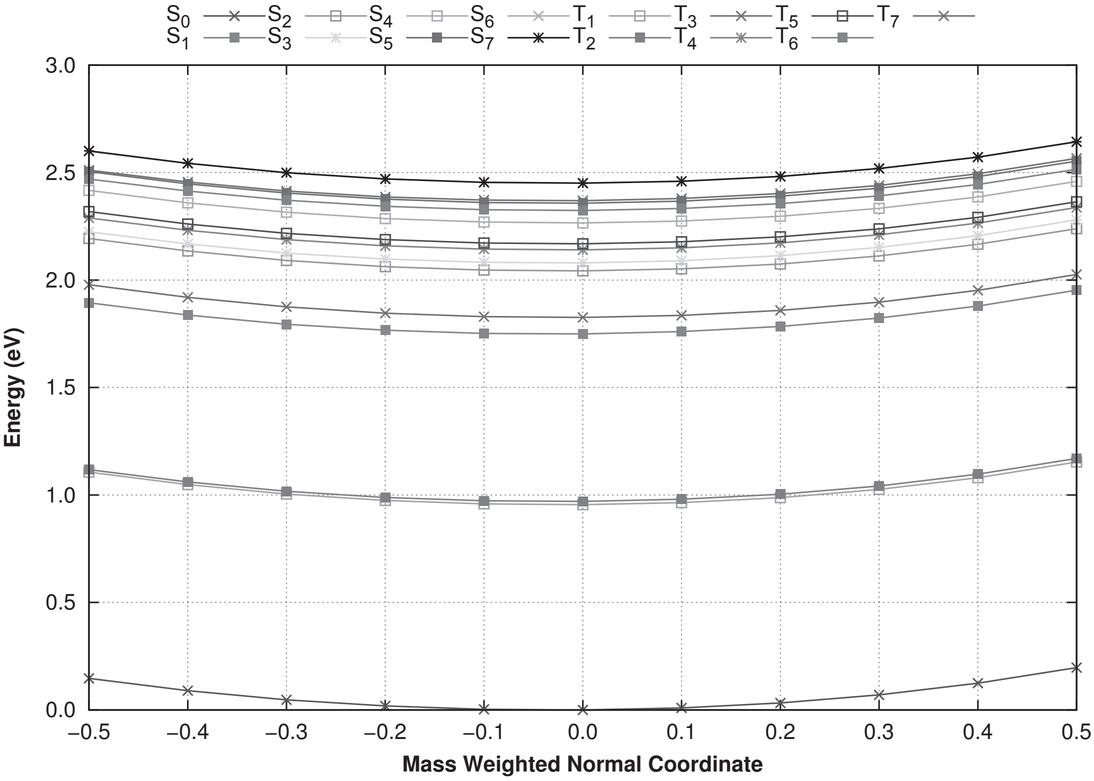

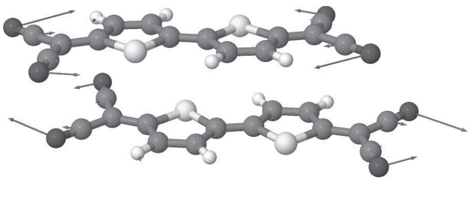

Figure 19: Mode 21

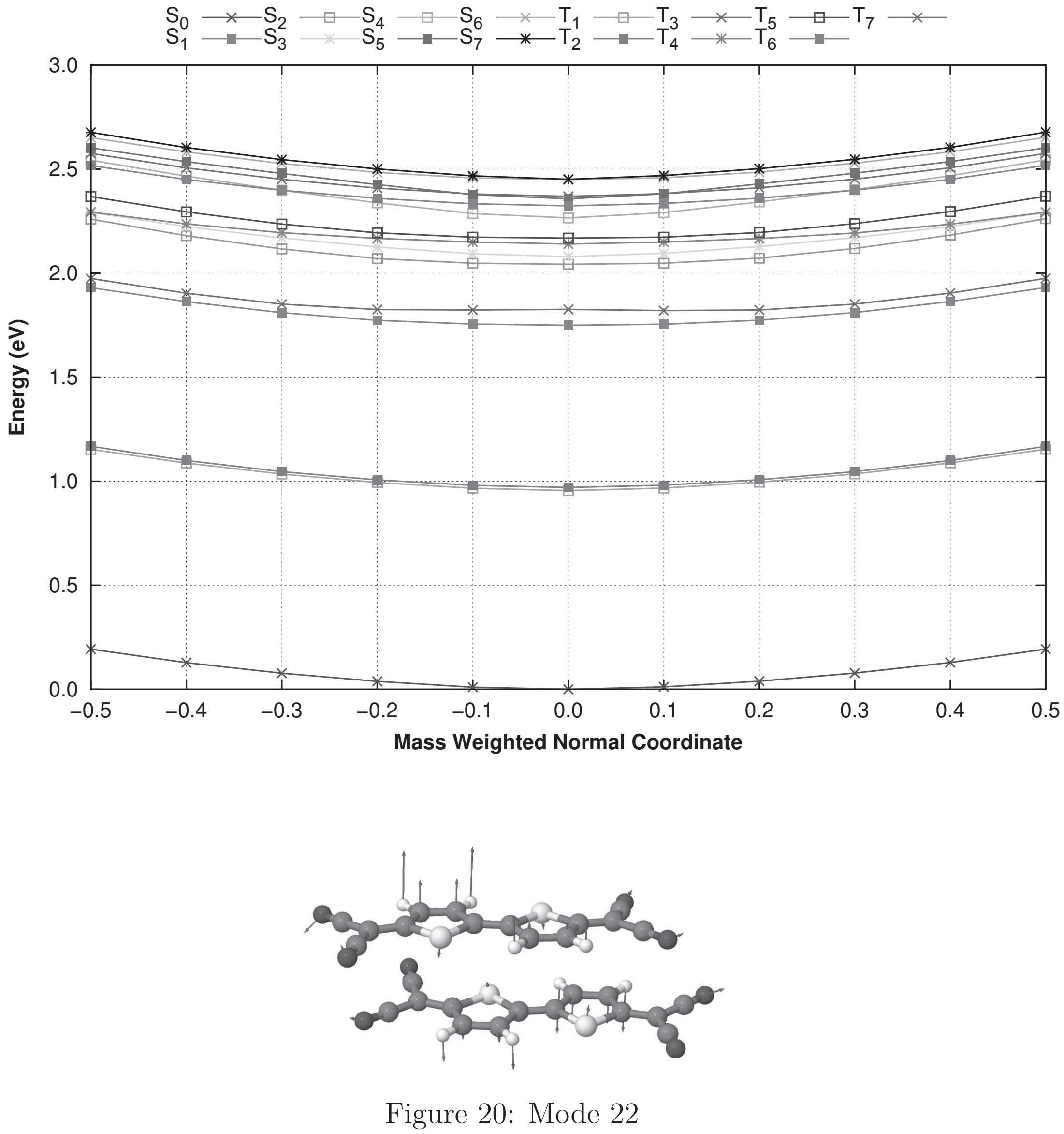

Figure 20: Mode 22

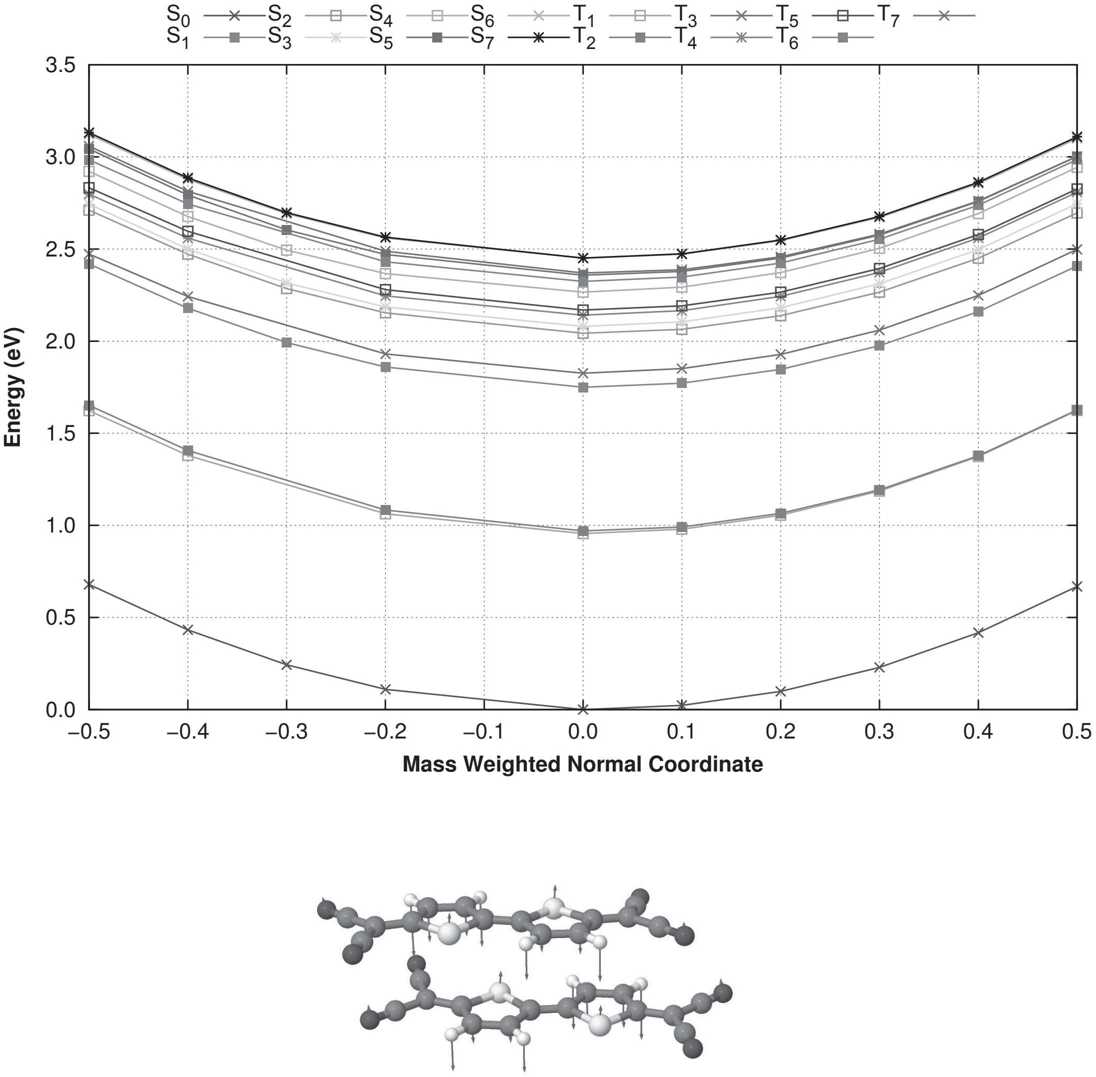

Figure 21: Mode 23

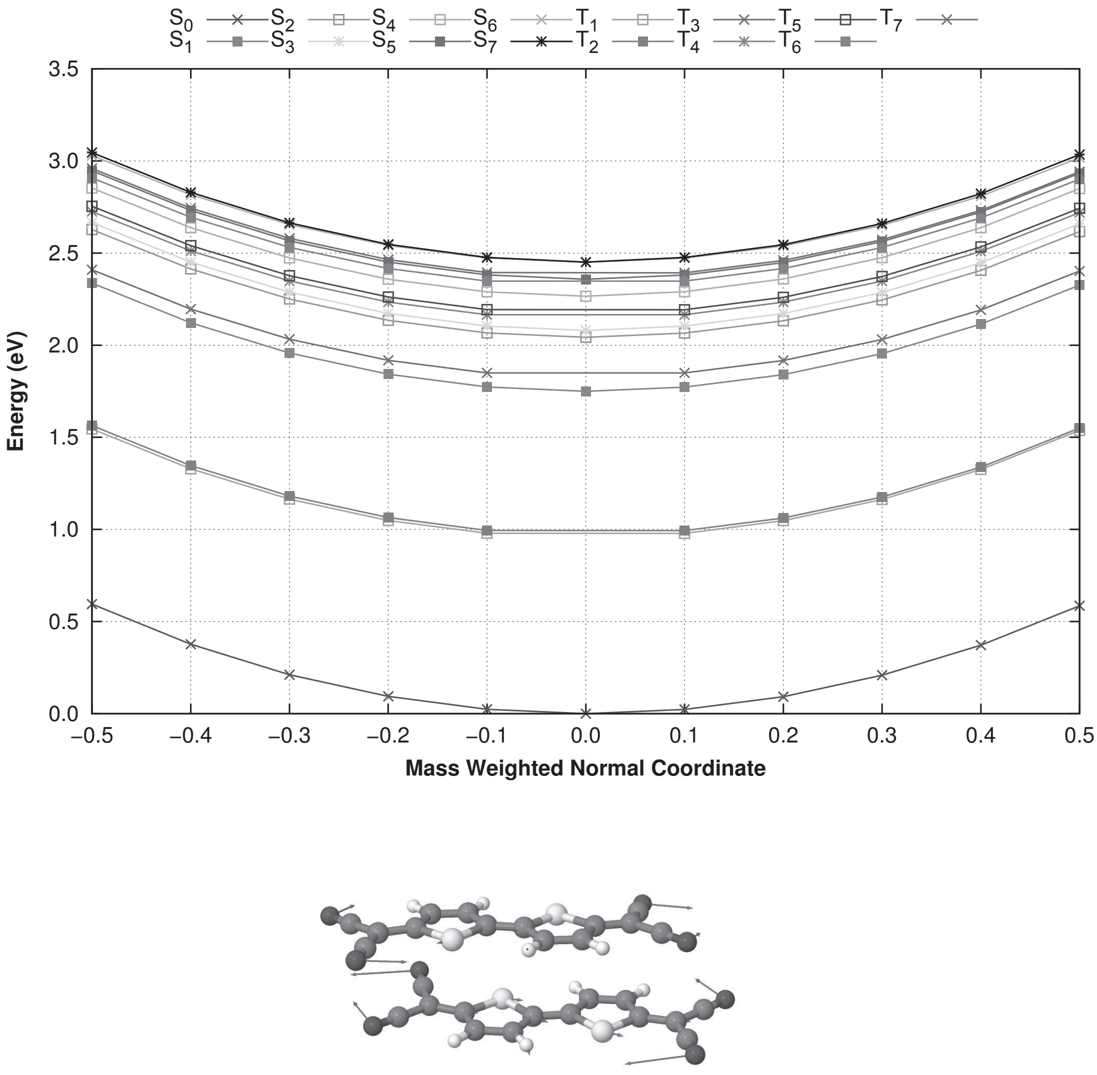

Figure 22: Mode 24

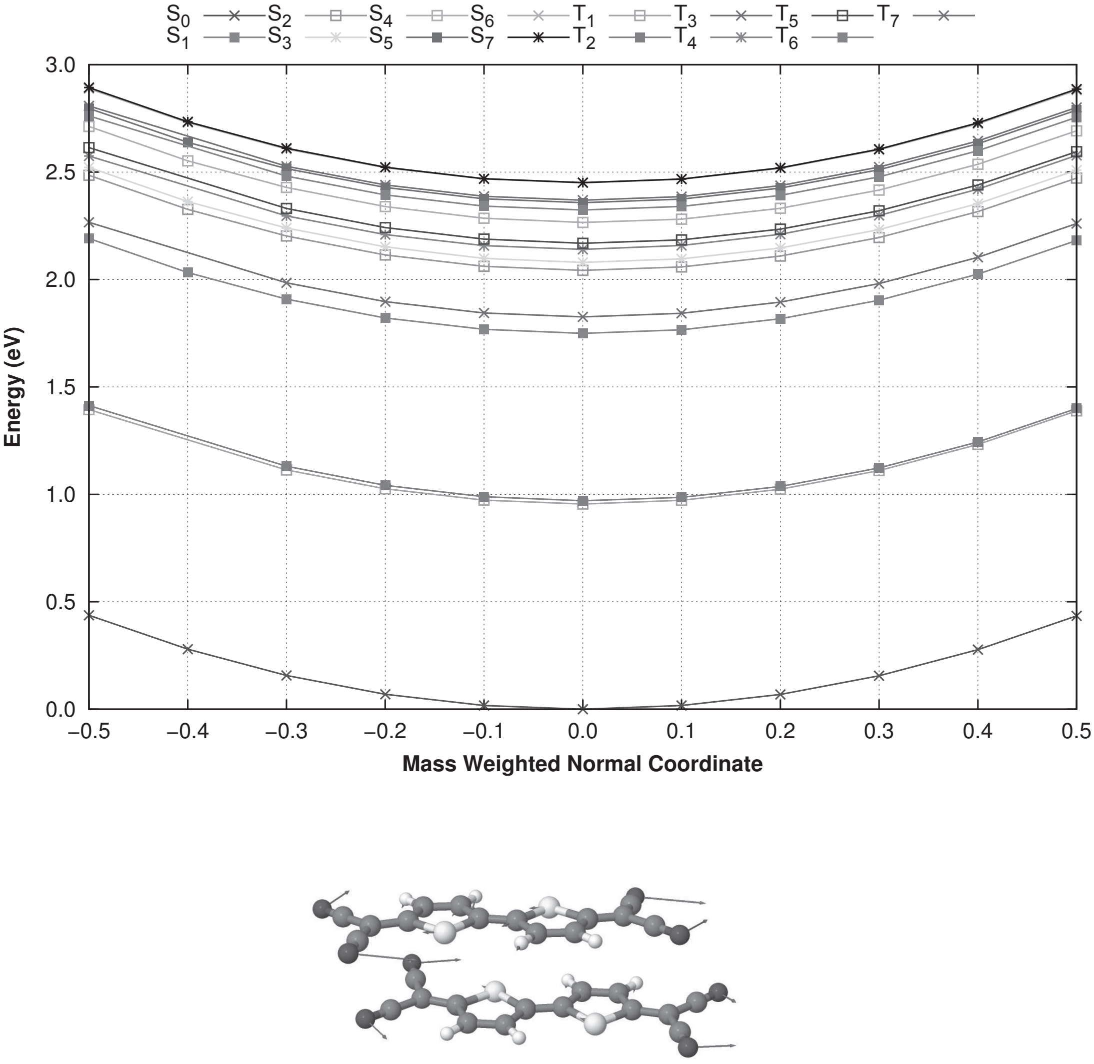

Figure 23: Mode 25

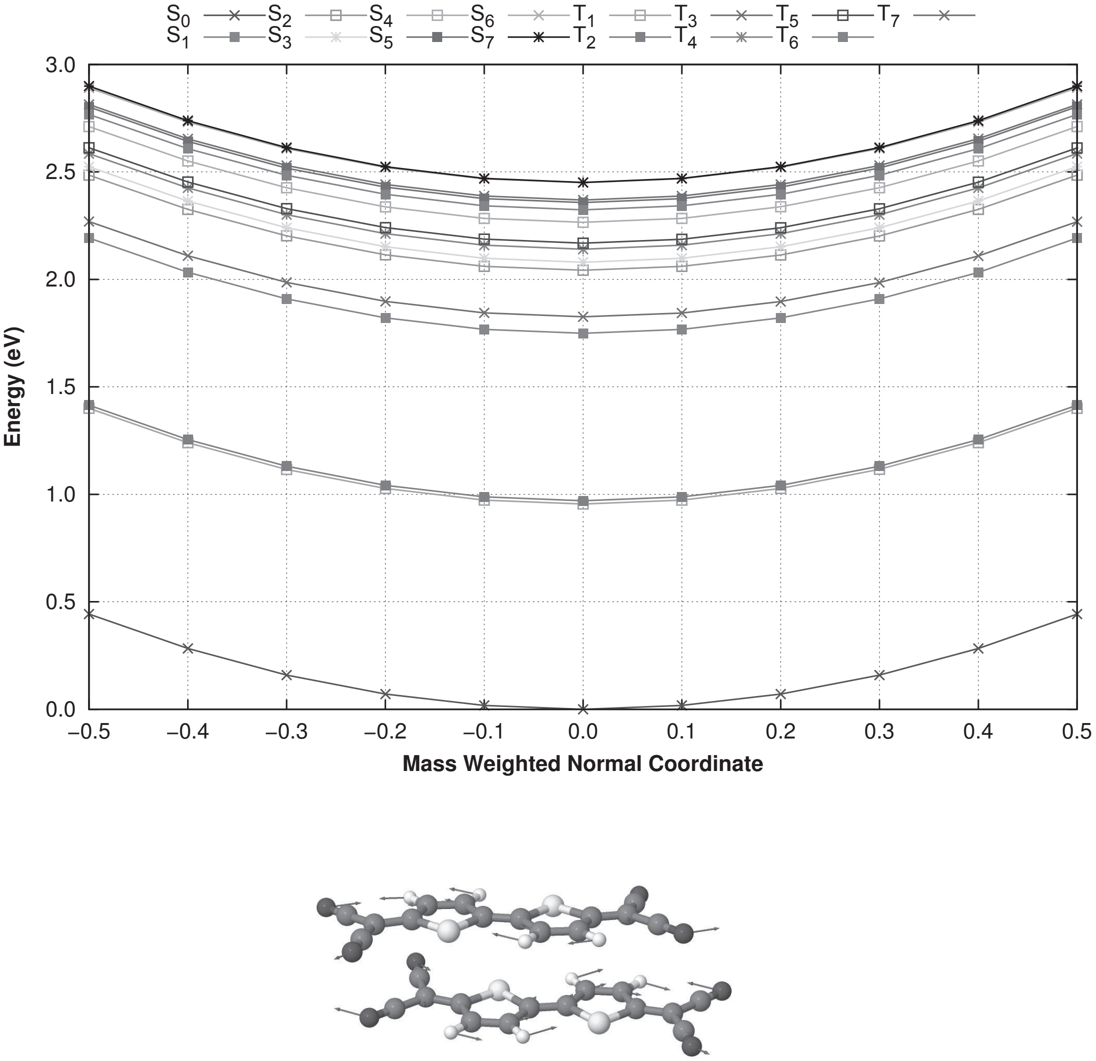

Figure 24: Mode 26

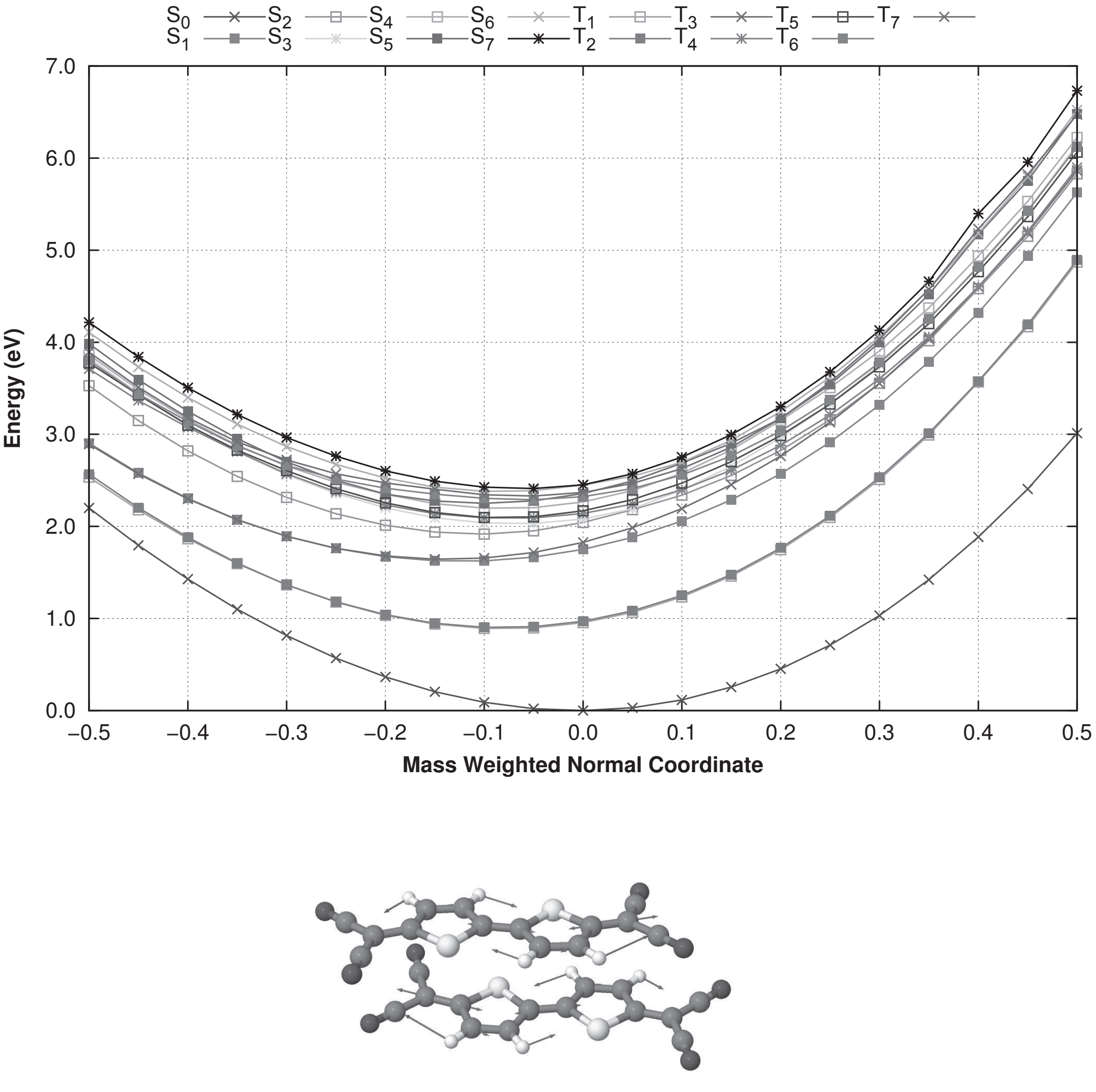

Figure 25: Mode 113

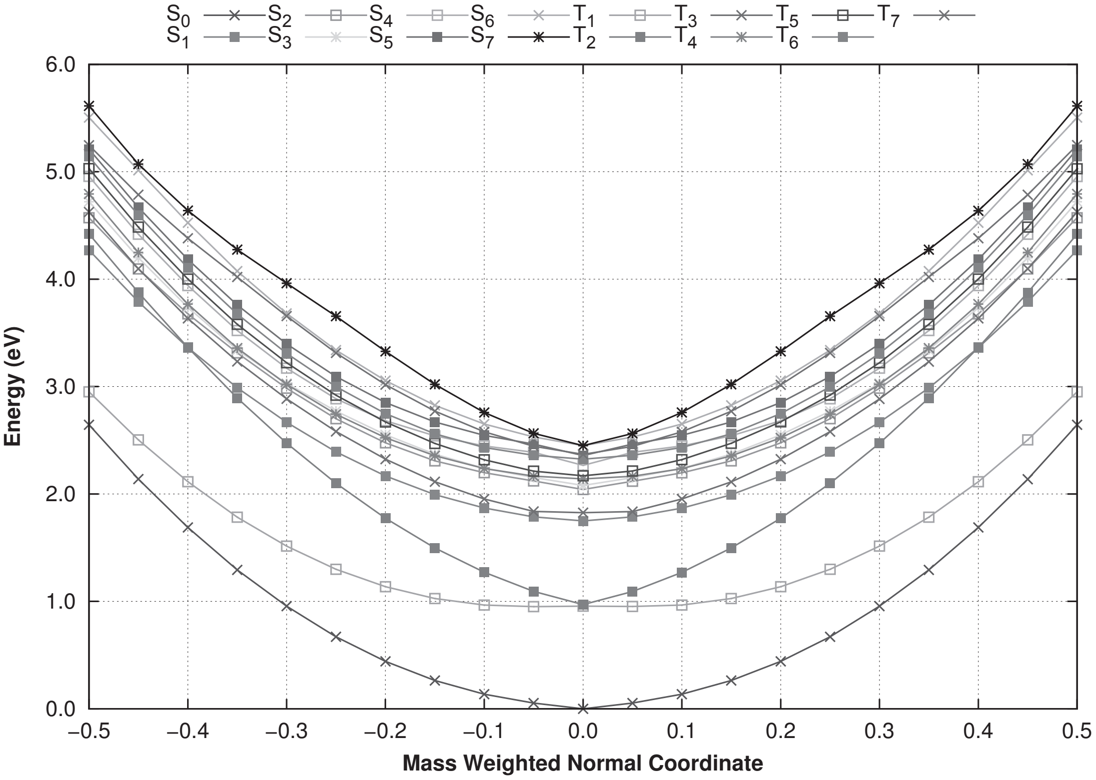

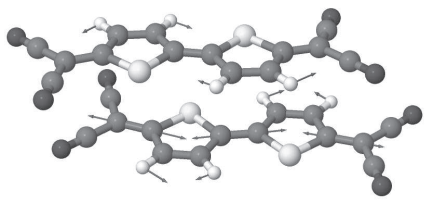

Figure 26: Mode 114

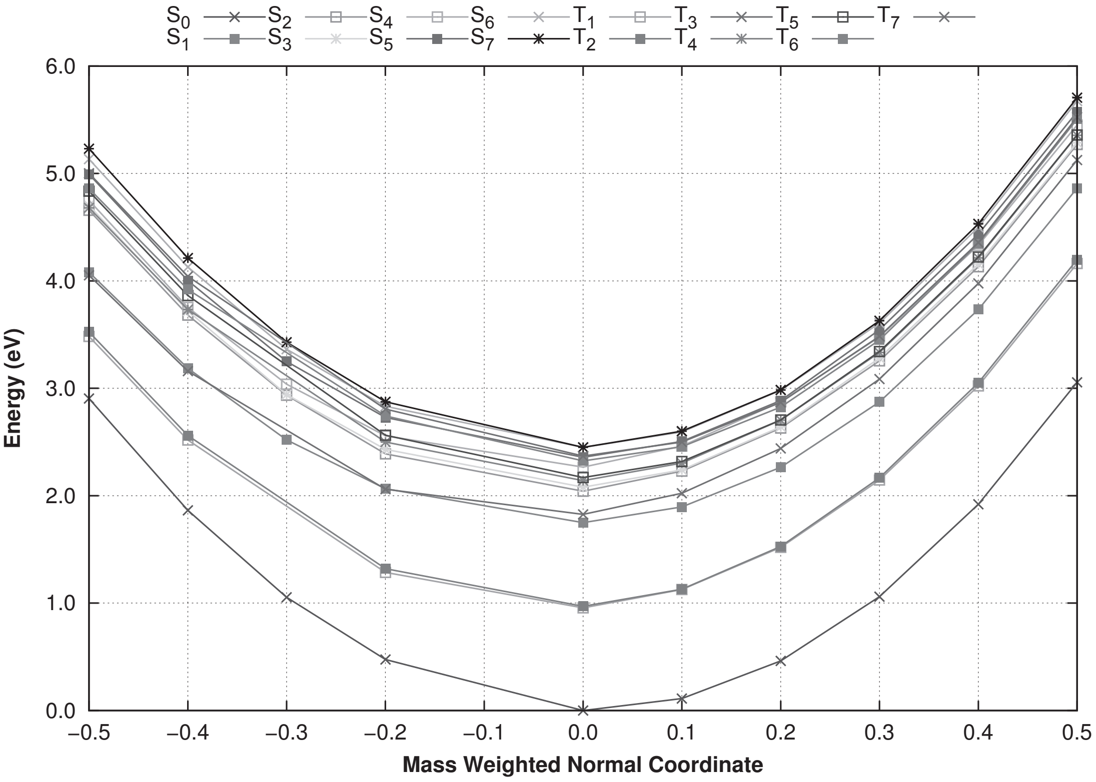

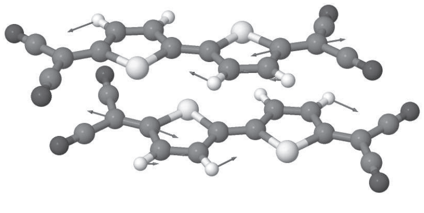

Figure 27: Mode 115

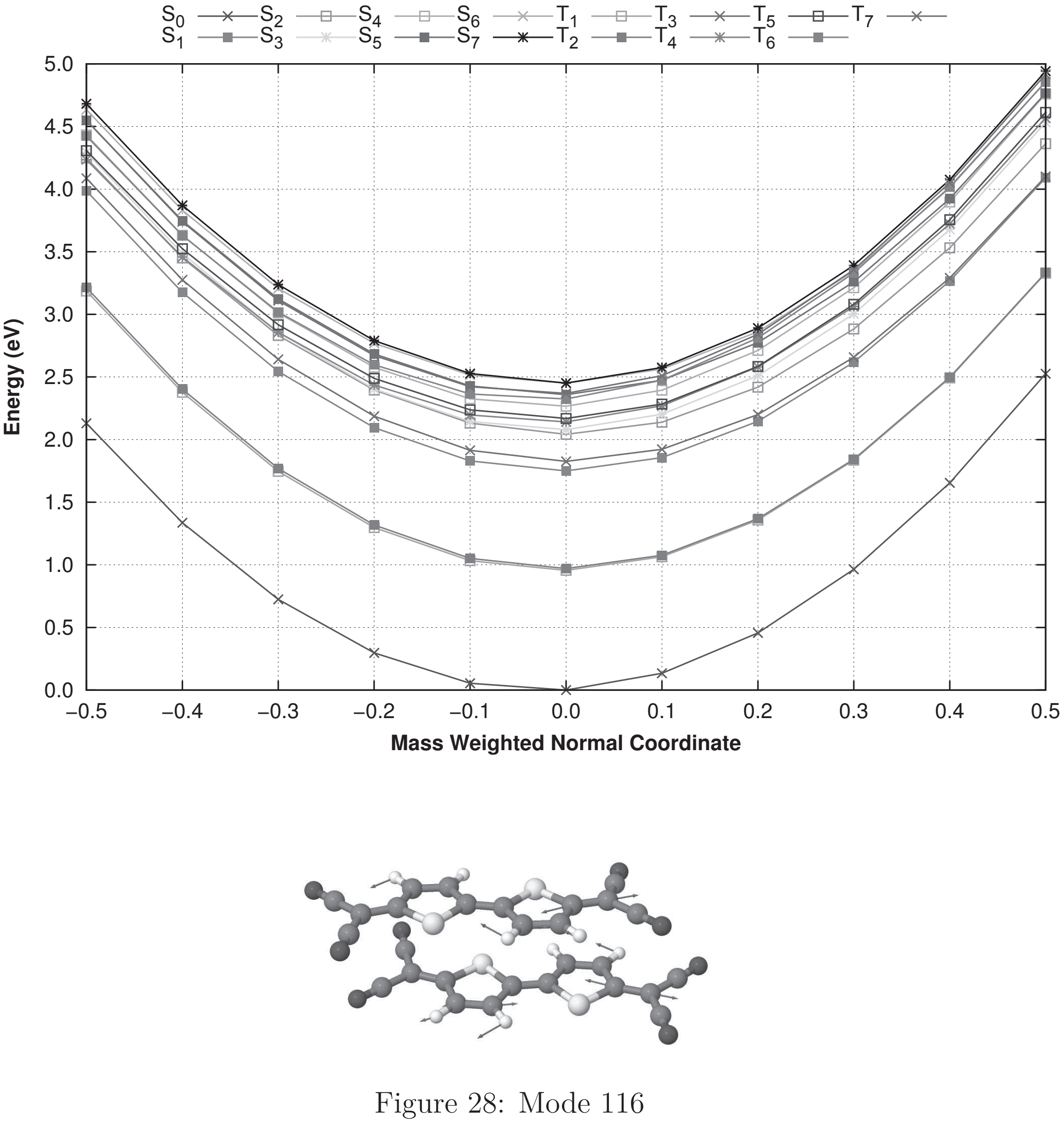

Figure 28: Mode 116

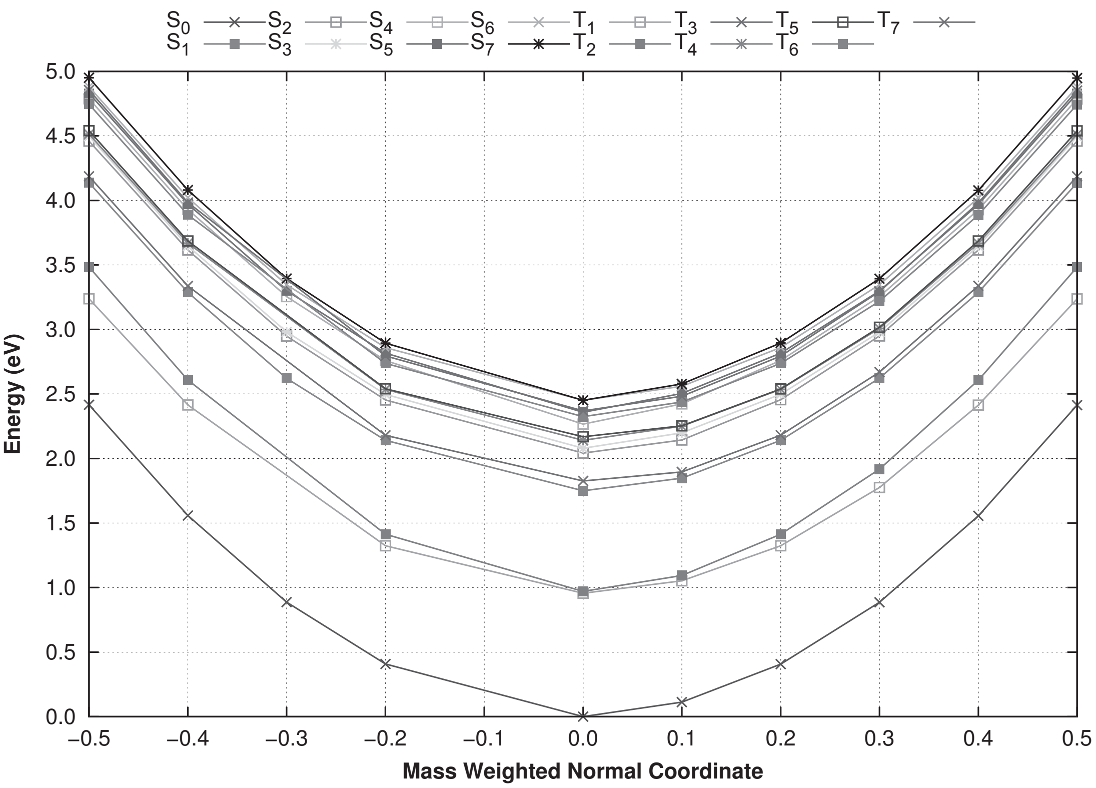

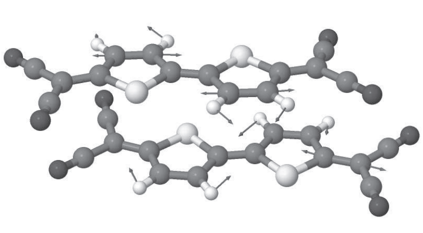

Figure 29: Mode 117

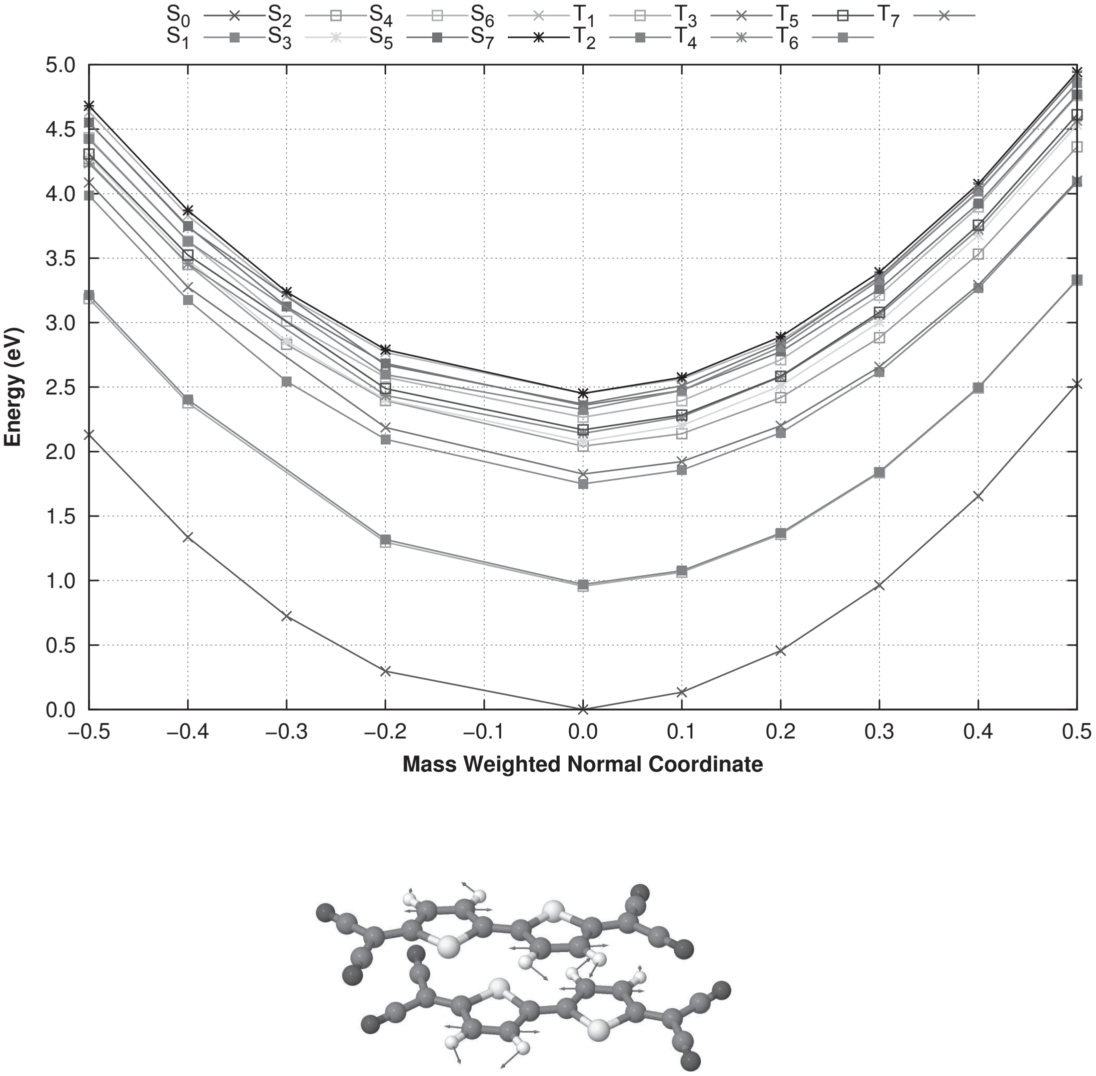

Figure 30: Mode 118

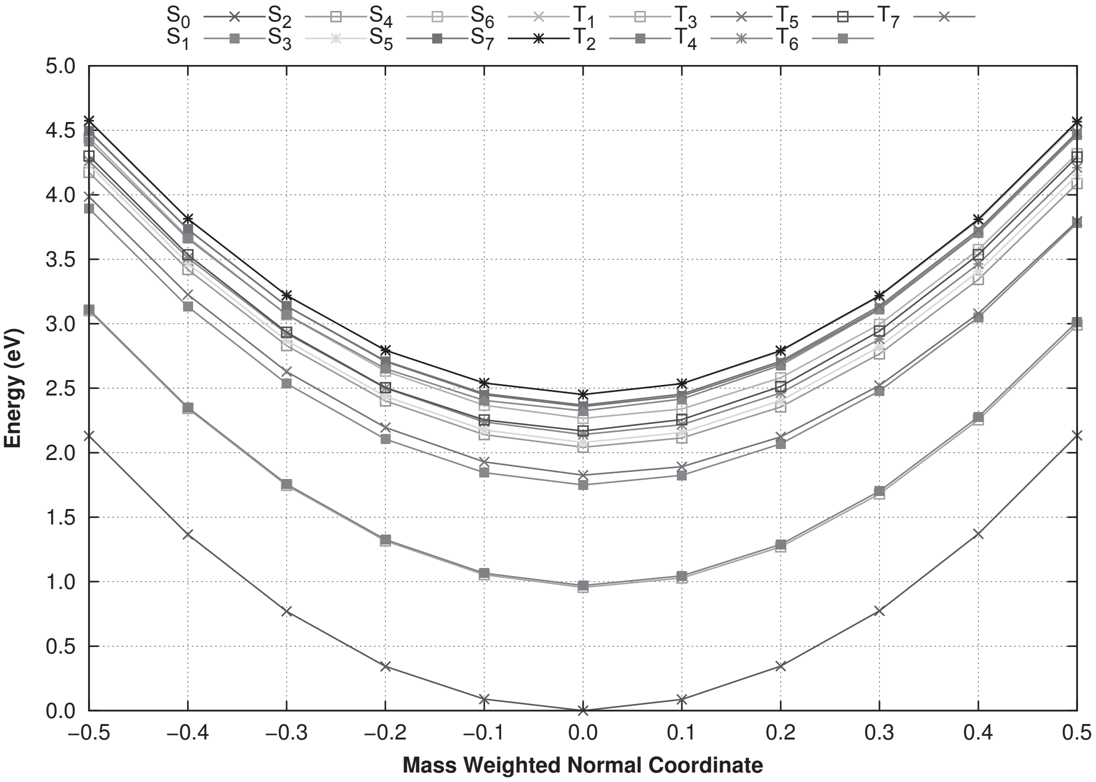

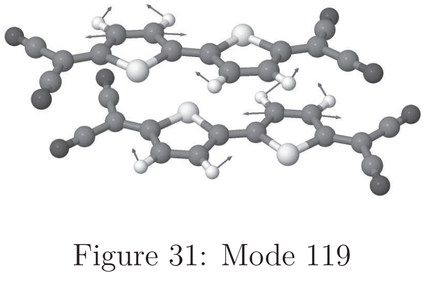

Figure 31: Mode 119

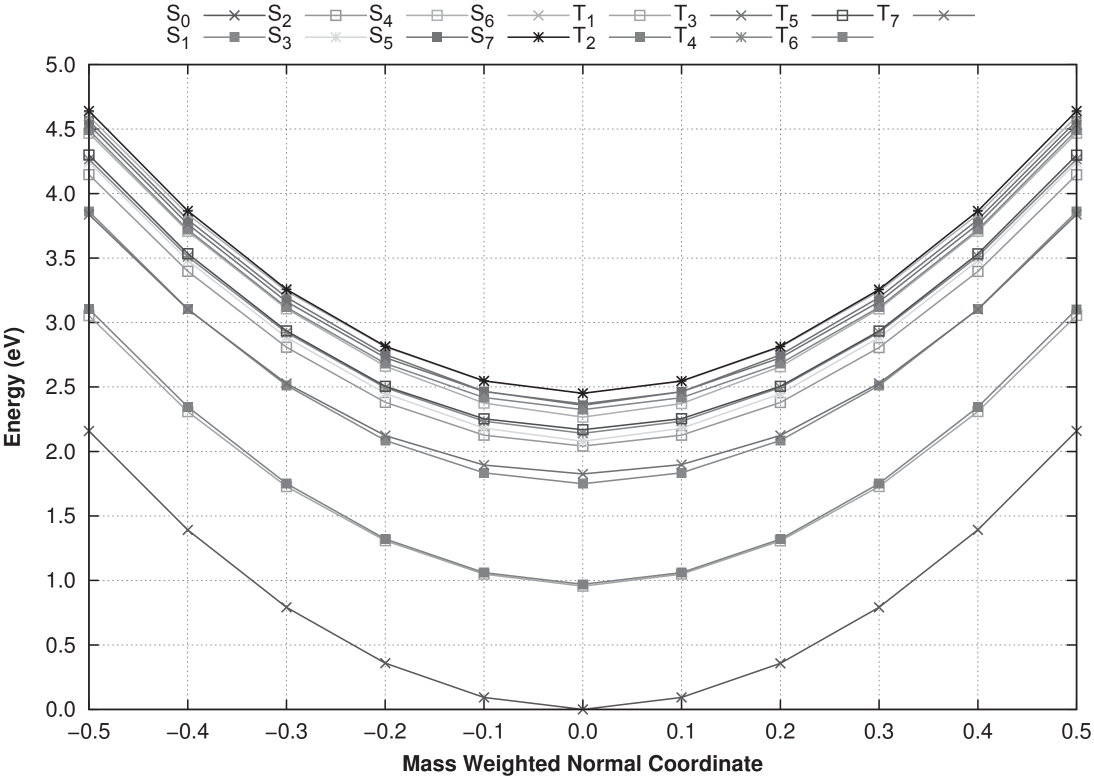

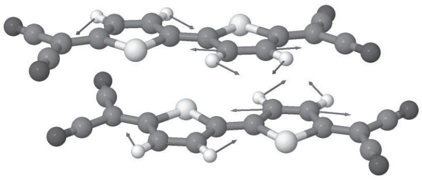

Figure 32: Mode 120

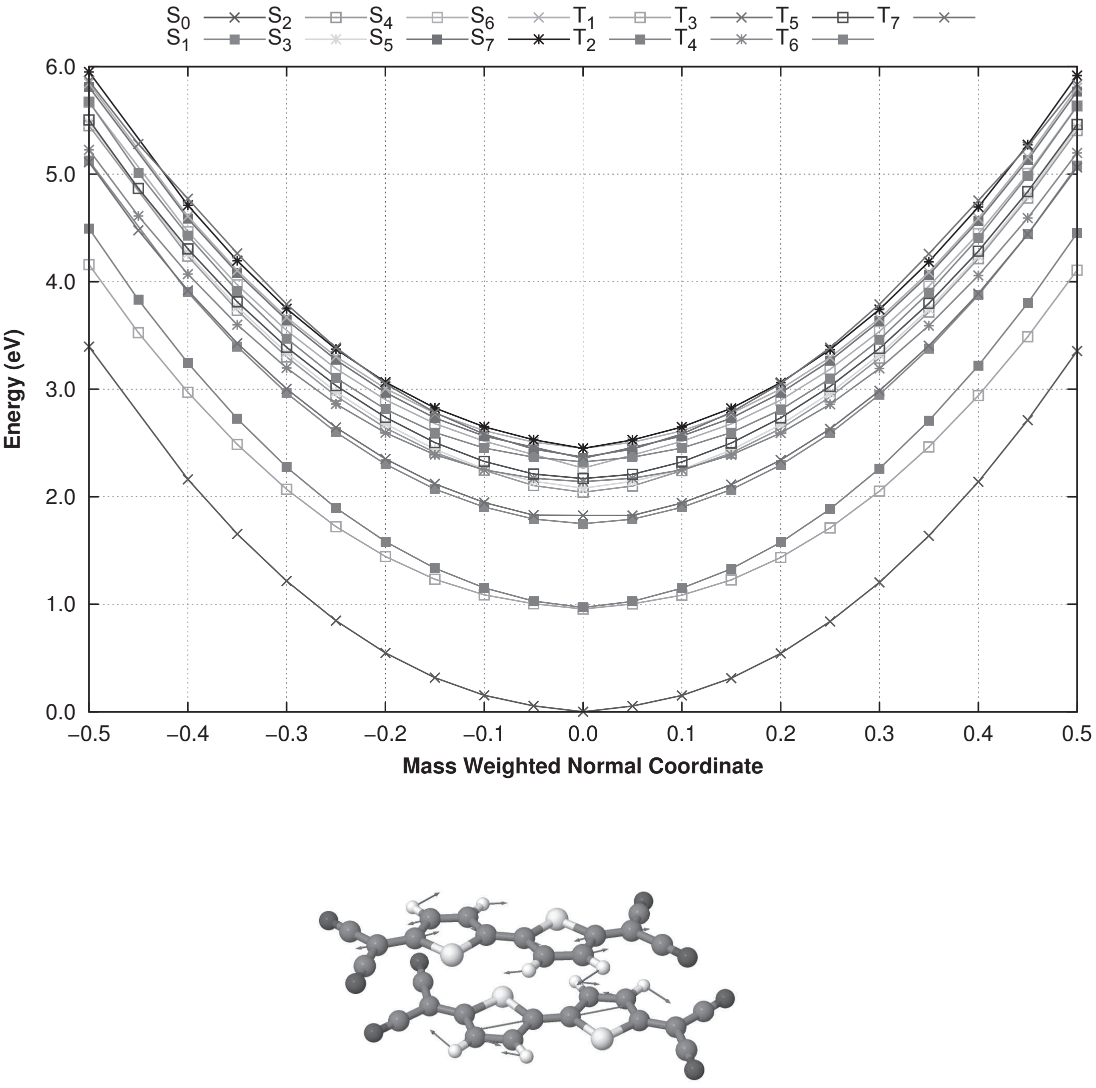

Figure 33: Mode 121

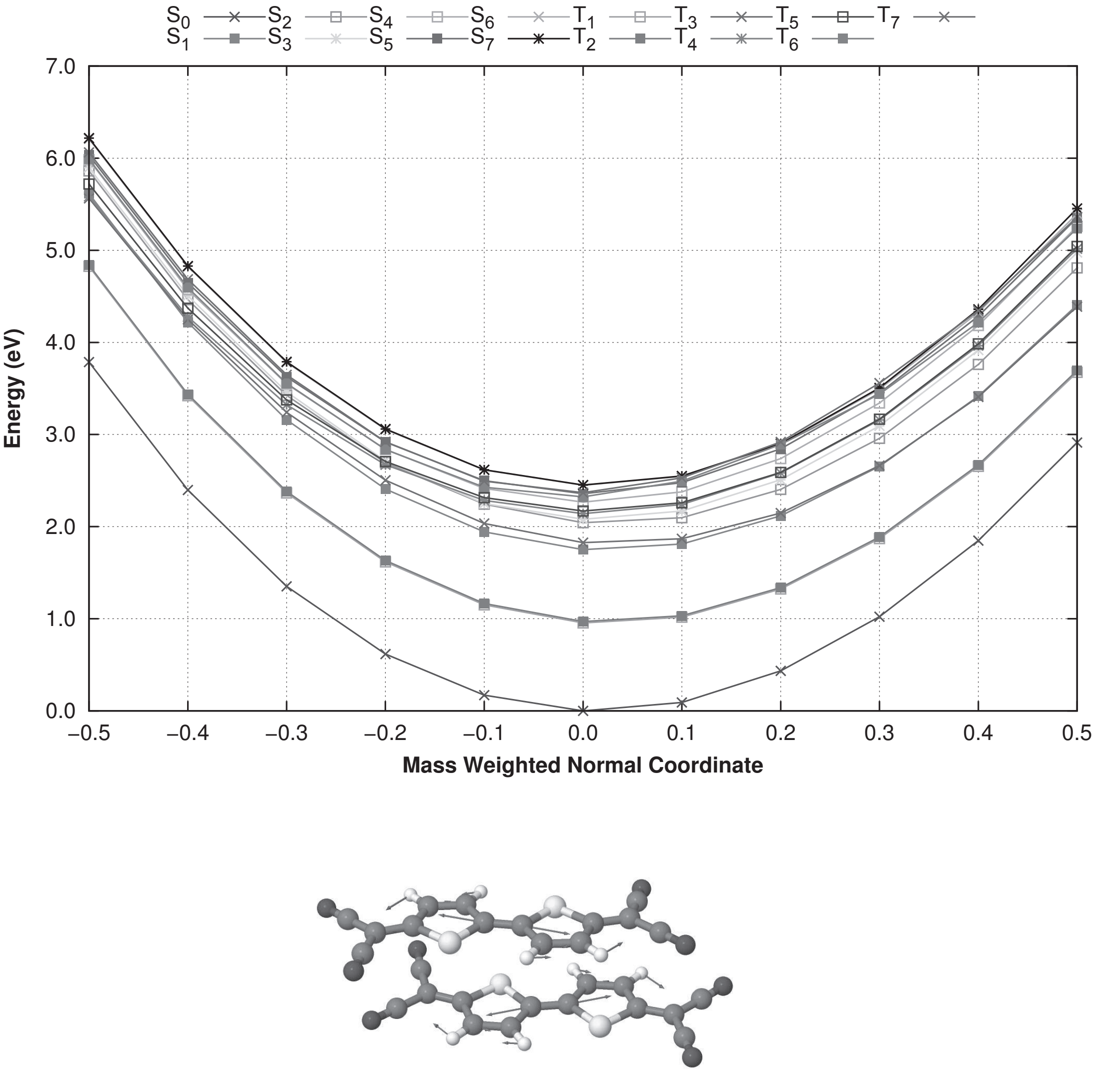

Figure 34: Mode 122

Cite this: DOI: 10.1039/xxxxxxxxxx

Nonadiabatic photodynamics and UV absorption spectrum of all-trans-octatetraene.[†]

Igor Lyskov[a], Horst Köppel[b], and Christel M. Marian[a,*]

Received Date
Accepted Date

DOI: 10.1039/xxxxxxxxxx

www.rsc.org/journalname

The short-time molecular quantum dynamics of all-*trans*-octatetraene after electronic excitation to the first bright valence state is theoretically investigated. A semiempirical approach of a multireference configuration interaction based on density functional theory, the so called hybrid DFT/MRCI, in both its original and redesigned formulations, is used for treating the electronic part of the problem. The nuclear kinetic part is defined with the help of symmetry-adapted internal coordinates also suitable for a large amplitude displacement. By incorporating ten in-plane and two out-of-plane nuclear degrees of freedom in the underlying Hamiltonian, the results of the time evolution of the excited wave packet are discussed. We show that the population transfer between the two coupled low-lying states in all-*trans*-octatetraene occurs in a 100-200 fs time regime. The calculated UV absorption spectra describe the main vibronic features correctly except for the band associated with the single-bond stretching motion which lacks intensity. The possible products of the photoisomerization in terms of symmetry-adapted coordinates are also discussed.

Introduction

Linear polyenes have been the subject of various spectroscopical and theoretical investigations due to the non-trivial photophysical properties of their electronically excited states and relaxation processes. A biologically important class of polyenes are the carotenoids, which play a big role in light harvesting complexes[1–3] and chemical quenching of singlet oxygen[4–6]. Also, the knowledge of linear π-systems with alternating single and double bonds can serve as a basis for elucidating the mechanisms of photodynamics in visual pigments[6–9].

It is well known that for short polyenes with two and three double bonds the valence 2^1A_g state is located vertically higher than the ionic 1^1B_u state. These two states describe the electron-hole interaction of the π-manifold and possess different physical natures from the point of view of static correlation. The dark multiconfigurational 2^1A_g state manifests itself as a two-photon state which is characterized by three electronic configurations, whereas the optically bright 1^1B_u is generated by a one-electron excitation from the highest bonding orbital to the lowest unoccupied antibonding orbital. The amplitude of the bosonic configuration $\pi^2 \rightarrow \pi^{*2}$ in the wave function of the valence state is enhanced relative to the other two leading configurations upon increasing the number of double bonds[10,11]. The absorption spectra of polyenes show non-trivial band structures as a result of the interaction between the 1^1B_u and 2^1A_g states. An extension of the π-framework gradually reduces the $E(2^1A_g)-E(1^1B_u)$ energy difference and shifts the absorption spectrum toward the infrared region[11–14]. The energetic position and the coupling strength between two low-lying states 1^1B_u and 2^1A_g guide the wave packet evolution after the excitation in the UV/vis range.

Following our previous studies of butadiene and hexatriene, in the present work we extend the conjugation length of the linear polyene, focusing on all-*trans*-octatetraene (OT). The primary step of the mechanism of the excitation quenching $S_2 \rightsquigarrow S_0$ involves a coherent population of the S_1 caused by vibronic interactions. As has been experimentally and theoretically shown before,[15–22] the depopulation time of the 1^1B_u state becomes longer when going from a two- to four-double-bond system. Since the population transfer crucially depends on the electronic parameters of a system such as the vertical interstate energy gap at the ground state geometry and the magnitude of vibronic coupling between the interacting electronic states, the quantum dynamics treatment will be carried out utilizing electronic potentials computed by two different formulations of DFT/MRCI. As will be shown later, the two DFT/MRCI parameterizations deliver distinctively different key characteristics for OT with regard to the aforementioned parameters, the internal conversion process is sensitive to. For this reason, we decided to construct a vibronic Hamiltonian separately for each of the cases to arrive subsequently at a

---

[a] *Institute of Theoretical and Computational Chemistry, Heinrich-Heine-University Düsseldorf, Universitätsstraße 1, 40225 Düsseldorf, Germany, Fax: +49-211-8113446. Tel.: +49-211-8113209. E-mail: Christel.Marian@hhu.de*

[b] *Physikalisch-Chemisches Institut, Universität Heidelberg, Im Neuenheimer Feld 229, D-69120 Heidelberg, Germany*

[†] Electronic Supplementary Information (ESI) available: 1D cuts of excited states potential energy surfaces. See DOI: 10.1039/b000000x/

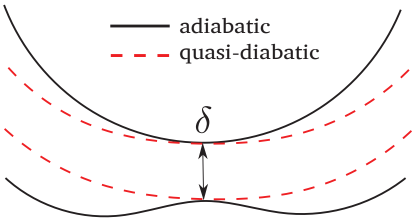

Fig. 1 Quasi-diabatic state potentials along a coupling mode in the LVC model.

comprehensive picture of the nonadiabatic dynamics.

Calculation details

Vibronic Hamiltonian

All *trans*-polyenes belong to the C_{2h} molecular point group and their entire set of vibrational modes $\mathbf{Q}$ spans over the a_g, b_g, a_u and b_u irreducible representations (irreps). Apparently, the light absorption populates the bright 1^1B_u state at first. However, a model for the calculation of a vibronically resolved excitation spectrum needs to be adjusted in a way that it should be able to account for effects due to the presence of the close-lying 2^1A_g dark state. Generally speaking, the quantum Hamiltonian must encompass both the interaction caused by nuclear motions within electronic states (intrastate) as well as the coupling between two electronic states (interstate). Following the well-established notations, all vibrations of the first type will be called tuning $\mathbf{Q}_{tune}$ and vibrations of the second type as coupling $\mathbf{Q}_{coup}$ modes. Use of symmetry-adapted internal coordinates makes the definition of two sets $\mathbf{Q}_{tune}$ and $\mathbf{Q}_{coup}$ feasible and straightforward. The non-vanishing interstate coupling modes are those for which the product of the irreps yields the totally symmetric representation:

$$\Gamma_1 \otimes \Gamma_{\mathbf{Q}_{coup}} \otimes \Gamma_2 \supset \Gamma_{\mathrm{sym}} \tag{1}$$

where Γ_1 and Γ_2 are the irreps of the two electronic states considered and $\Gamma_{\mathbf{Q}_{coup}}$ is the irrep of a mode coupling the electronic states. By analogy, the intrastate coupling motions for each of the states ($\Gamma_1=\Gamma_2$) must obey following relationship:

$$\Gamma_{\mathbf{Q}_{tune}} = \Gamma_{\mathrm{sym}} \tag{2}$$

In the context of this paper, $\mathbf{V}_{coup}$ and $\mathbf{V}_{tune}$ are considered as electronic potentials for the displacement of the nuclear framework along $\mathbf{Q}_{coup}$ and $\mathbf{Q}_{tune}$ correspondingly. By the symmetry constraint imposed in Equation (1), it is clear that all $\mathbf{Q}_{coup}$ modes should possess b_u symmetry. Such vibrations break the C_2 generator of C_{2h} and retain the mirror plane. An interaction of electronic configurations with b_u distortions reduces the symmetry of the wave functions, such that the 1^1B_u and 2^1A_g states transform under the same irrep A' of the C_s point group. The evaluation of electronic potentials $\mathbf{V}_{tune}$ along the $\mathbf{Q}_{tune}$ set appears to be trivial and does not require additional computational work, unlike the $\mathbf{V}_{coup}$ potentials. One of the simplest solutions to overcome the diabatization problem is the linear vibronic coupling scheme (LVC)[23–25].

At the ground state geometry ($\mathbf{Q}_0$), the wave functions of the states transform under different irreps and it is assumed that quasi-diabatic and adiabatic state energies are identical. The LVC model[25] postulates that in a two-level system, in the presence of a b_u deformation, generated by the coupling mode $q_i \subset \mathbf{Q}_{coup}$, the quasi-diabatic potentials can be expressed with the help of a coupling function $\mu(q_i)$ as:

$$\mathbf{V}_{coup}(q_i) = \begin{bmatrix} \overline{\mathrm{U}}(q_i) + \frac{\delta}{2} & \mu(q_i) \\ \mu(q_i) & \overline{\mathrm{U}}(q_i) - \frac{\delta}{2} \end{bmatrix} \tag{3}$$

where δ is the interstate energy spacing between two levels at $\mathbf{Q}_0$. The solution of the secular Equation (3) brings back the adiabatic potentials $\varepsilon_{1,2}(q_i)$ as a function of an applied distortion q_i:

$$\varepsilon_{1,2}(q_i) = \overline{\mathrm{U}}(q_i) \pm \sqrt{\frac{\delta^2}{4} + \mu^2(q_i)} \tag{4}$$

From Equation (4) it is seen that $\overline{\mathrm{U}}(q_i)$ represents an average curve of two adiabatic potentials. In this way, the two surfaces are topologically nested and shifted with respect to each other by δ in the quasi-diabatic representation. They remain equidistant along the complete range of the coupling coordinate q_i as graphically represented in Figure 1. The knowledge of $\varepsilon_{1,2}(q_i)$ allows to estimate the quasi-coupling $\mu(q_i)$ by the least-squares-fit of Equation (4).

For setting up the vibronic Hamiltonian, the kinetic energy operator which describes the nuclear motions needs to be set up. Employment of the FG matrix technique[26,27] yields the full Hamiltonian:

$$\mathbf{H} = \mathrm{T}\mathbf{1}_2 + \mathbf{V}_{tune}(\mathbf{Q}_{tune}) + \mathbf{V}_{coup}(\mathbf{Q}_{coup}) + \varepsilon_v(\mathbf{Q}_0) \tag{5}$$

with the kinetic energy

$$2\mathrm{T} = \sum_{i,j} \mathbf{p}_j^{\top} \mathbf{G}_{ij} \mathbf{p}_i \tag{6}$$

where $\mathbf{p}_i$ refers to the momentum conjugate to the symmetry coordinate q_i. The last term ε_v of Equation (5) denotes a two-by-two diagonal matrix with elements equal to the vertical energies at the Franck-Condon (FC) point. The second and third terms describe the sum of 1D-cuts through quasi-diabatic potential energy surfaces (PESs) of the two considered states relative to their energies at $\mathbf{Q}_0$ along the tuning (a_g) and the coupling (b_u) modes, respectively:

$$\mathbf{V}_{tune} = \sum_{\mathbf{Q}_{tune}} \begin{bmatrix} \mathrm{U}_1(q_i) & 0 \\ 0 & \mathrm{U}_2(q_i) \end{bmatrix} \qquad \mathbf{V}_{coup} = \sum_{\mathbf{Q}_{coup}} \begin{bmatrix} \overline{\mathrm{U}}(q_i) & \mu(q_i) \\ \mu(q_i) & \overline{\mathrm{U}}(q_i) \end{bmatrix} \tag{7}$$

The kinetic energy in Equation (6) was built with the help of the $\mathbf{G}_{ij}$-matrix, the elements of which are analytically tabulated in Ref.[28]. Kinetic energy coefficients for momenta $\mathbf{p}_i$ and $\mathbf{p}_j$ conjugate to two distinct symmetric internal coordinates q_i and q_j (as will be defined later) represent a sum of factored pairwise interactions of all local momenta the $\mathbf{p}_i$ and $\mathbf{p}_j$ are composed of. The Hamiltonian (5) for the two-level system was treated within the fully quantal, time-dependent scheme of wave packet propagation as formulated in MCTDH (see below).

Electronic structure

For computations of the PESs the semiempirical hybrid DFT/MRCI method was employed in its original formulation[29] (later denoted as DFT/MRCI-S) and the recently redesigned parameterization[30] (DFT/MRCI-R). The correlation-consistent polarized valence triple-ζ cc-pVTZ[31,32] basis set for hydrogen and carbon was used. A set of one-electron wave functions for configuration interaction has been obtained by the DFT branch of Turbomole[33–35] employing the semi-local BHLYP[36] exchange-correlation functional. The reference space for MRCI was generated by including all electronic configurations with expansion coefficients greater than 0.003 in the intermediately generated DFT/MRCI wave function within the reference space of a RAS(10,10) electron-orbital window. To avoid a double count of dynamic electron correlation arising in the MRCI expansion, off-diagonal matrix elements were attenuated by multiplication with a damping function and all configurations with an energy higher than 1.0 E_h compared to the highest reference energy were discarded. The calculation of four-index two-electron integrals between the Kohn-Sham orbitals was performed with cc-pVTZ[37] auxiliary basis sets from the standard RI-MP2 Turbomole library.

Wave packet propagation

The quantal motion of the nuclei of a molecule is described by the time-dependent Schrödinger equation. If the Hamiltonian $\hat{H}$ is time-independent, the propagated wave packet (WP) may be expressed as:

$$\psi(t) = \sum_j a_j e^{-iE_j t} \phi_j \tag{8}$$

where ϕ_j is a set of eigenstates of the Hamiltonian

$$\hat{H}\phi_j = E_j \phi_j \tag{9}$$

and the expansion coefficients a_j are defined through the initial wave packet $\psi(0)$ as:

$$a_j = \langle \phi_j | \psi(0) \rangle \tag{10}$$

The standard approach for solving the time-dependent Schrödinger equation is the numerically exact propagation of a WP represented in a time-independent product basis set. In the MCTDH[38–40] scheme, the wave function which describes the molecular dynamics of a system with f degrees of freedom is written as a linear combination of Hartree products as follows:

$$\Psi(q_1, \ldots, q_f, t) = \sum_{j_1}^{n_1} \cdots \sum_{j_f}^{n_f} A_{j_1 \ldots j_f}(t) \prod_{k=1}^{f} \phi_{j_k}^{(k)}(q_k, t) \tag{11}$$

Here $q_1, \ldots, q_f$ are a set of the nuclear coordinates, $A_{j_1 \ldots j_f}$ denote the time-dependent expansion coefficients, and $\phi_{j_k}^{(k)}(q_k, t)$ are a set of time-dependent single-particle functions (SPFs) combined to give the Hartree product Φ_J. In turn, SPFs are expressed in a time-independent basis set:

$$\phi_{j_k}^{(k)}(q_k, t) = \sum_{i_1=1}^{N_k} c_{i_k}^{(k, j_k)}(t) \chi_{i_k}^{(k)}(q_k) \tag{12}$$

where $\chi_{i_k}^{(k)}(q_k)$ are primitive basis functions of the k-th degree of freedom that depend on the particle coordinate q_k. The accuracy of MCTDH depends on the number of primitive functions $N_1, \ldots, N_f$ and the number of SPFs $n_1, \ldots, n_f$. Since both the coefficients and the basis functions in Equation (11) are time-dependent, they both are optimized using a variational principle. The equations of motion are derived from the Dirac-Frenkel variational principle, which leads to:

$$\begin{aligned} i\dot{A}_J &= \sum_L \langle \Phi_J | H | \Phi_L \rangle A_L - \sum_k^f \sum_l^{n_k} g_{j_k l}^{(k)} A_{J_l^k} \\ i\dot{\phi}^{(k)} &= g^{(k)} \mathbf{1}_{n_k} \phi^{(k)} + (1 - P^{(k)}) \Big[(\rho^{(k)})^{-1} \langle H \rangle^{(k)} - g^{(k)} \mathbf{1}_{n_k} \Big] \phi^{(k)} \end{aligned} \tag{13}$$

$\rho^{(k)}$ denotes the density matrix, $\langle H \rangle^{(k)}$ the matrix of mean field operators, and $g^{(k)}$ the constraint operator[39,41].

To account for the coupling between different excited states, one extra degree of freedom has to be introduced to represent the electronic manifold. The multi-set formalism, used hereafter, employs different sets of SPFs for each state. In this formulation, the wave function is written

$$\Psi(t) = \sum_\alpha^{n_s} \Psi_\alpha(t) |\alpha\rangle \tag{14}$$

where the summation index α denotes the electronic states. The SPFs are optimized separately for each electronic state with the advantage that fewer coefficients are needed for the expansion of the wave function. This advantage of MCTDH results in a contraction effect which speeds up the calculation without loss of accuracy[39,41].

The MCTDH calculation was performed in similar fashion as in previous studies[15,42]. At first, the MCTDH wave function was relaxed in the precalculated DFT/MRCI ground state potentials of the twelve symmetry-adapted internal coordinates which are specified in Table 4. The resulting WF is then lifted vertically upward to the potential energy curve of the optically bright state. Assuming the Fermi golden rule for the direct transition from the initial to the final state[25,43], the absorption spectrum is obtained by inverse Fourier transformation of the autocorrelation function:

$$P(E) \propto \int e^{iEt} c(t) dt \tag{15}$$

with

$$c(t) = \langle \Psi(0) | \Psi(t) \rangle = \left\langle 0 \middle| \tau^\dagger e^{-i\mathbf{H}t} \tau \middle| 0 \right\rangle = \langle \Psi(t/2)^* | \Psi(t/2) \rangle \tag{16}$$

In these equations, $|0\rangle$ stands for the vibrational ground state of the initial electronic ground state, $\tau^\dagger$ denotes the vector of the individual transition dipole matrix elements between the two states involved in the transition. The wave packet evolves subsequently in time on the PESs of the two coupled electronic states. The autocorrelation function represents the overlap of the time-evolving WP with the initial one.

Table 1 CASPT2 optimized geometry[a] of 1^1A_g, 2^1A_g, 1^1B_u states of all-*trans*-octatetraene. For abbreviations see Figure 2.

	$r_{11'}$	r_{12}	r_{23}	r_{34}	$\phi_{1'12}$	ϕ_{123}	ϕ_{234}	$\tau_{2'1'12}$	$\tau_{1'123}$	τ_{1234}
1^1A_g	1.448	1.372	1.454	1.361	123.9	123.7	123.8	180.0	180.0	180.0
Exp.[b]	1.451	1.327	1.451	1.336	125.3	125.1	124.7	180.0	180.0	180.0
2^1A_g	1.398	1.456	1.392	1.427	123.8	124.2	124.5	180.0	180.0	180.0
1^1B_u	1.396	1.400	1.413	1.373	124.7	124.2	125.3	180.0	180.0	180.0
AC1[c]	1.419	1.506	1.400	1.420	123.3	122.3	126.5	121.7	130.0	184.8
		1.490	1.456	1.368	94.8	126.2	125.0		-102.7	181.6
AC2[c]	1.359	1.485	1.393	1.439	126.7	123.8	126.9	177.3	177.3	178.7
		1.493	1.450	1.498	123.9	127.1	93.6		189.0	-121.7

[a] MS(3)-CASPT2(8,8)/cc-pVDZ from Ref.[44]

[b] X-ray diffraction from Ref.[45]

[c] S_1/S_0 adiabatic crossing by DFT/MRCI-R with cc-pVTZ basis

Results and discussions

Ground state geometry and vertical excitation energies

Not surprisingly, the ground-state geometry of all-*trans*-octatetraene is arranged in a planar chain. As in all polyenes, except for infinitely large carbon chains with vanishing alternation[46,47], the equilibrium geometry $\mathbf{Q}_0$ shows different lengths for single and double C–C bonds as a balance effect of π-conjugation. The single-bond parameters, as predicted by the CASPT2 optimization including all π-orbitals in the active space, look remarkably good compared to the measured parameters for crystalline OT (Table 1). In contrast, the double bonds overshoot the experimental values, although X-ray diffraction is known to underestimate their quantity. Slightly less satisfactory agreement was obtained for the C–C–C angles. The CASPT2 values are smaller by $\sim 1^\circ$ which can be attributed to the tight packing effects of the measured structure. The geometry of 1^1B_u state, and even so more 2^1A_g, changes the spirit of bond alternation. Due to the nodal structure of the frontier orbitals, the HOMO-LUMO excitation compresses the nominally single bonds and elongates the nominally double bonds of the ground state $\mathbf{Q}_0$. Therefore, single-double bond alternation is smoothed at the 1^1B_u state minimum accompanied by a slight increase of the bond angles. In turn, the dark state minimum swaps the double bonds to the single bonds and vice versa. Let us also stress that the excited-state geometries retain the C_{2h} symmetry.

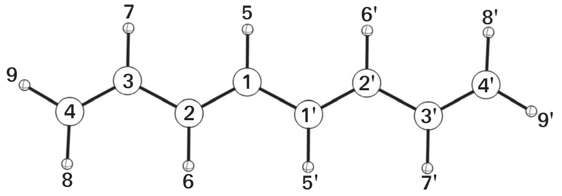

Fig. 2 Atom numbering of all-*trans*-octatetraene.

Numerous theoretical works have reported the results of semiempirical schemes[12,13,48], *ab initio* multireference[10,11,49–51] and density functional based[52,53] methods which often ambiguously predict the order and energy of the first two excited singlet states (see the surveys in Ref.[48,49,53]). Besides the fact that the excitation energy is highly dependent on the ground-state geometry[13], the challenge is the different nature of these states which deserves a different consideration in the computational treatment. The character of 2^1A_g necessitates an appropriate description of the doubly excited HOMO^2-LUMO^2 electron configuration, making linear response-based DFT questionable. On the other hand, for a proper description of 1^1B_u, one must take into account σ-π^* correlation[54] which, in combination with a reliable basis set, dramatically increases the computation time of the electronic potentials $\mathbf{V}_{coup}$ and $\mathbf{V}_{tune}$ for multireference methods. These time demands are alleviated in DFT/MRCI due to the effective truncation of the configuration expansion. A vibronic progression of the recorded spectra complicates the assignment of the vertical excitation energies, although for OT it is well established experimentally that the dark state lies vertically lower than the bright one[22,55]. The experimental estimate of 4.43 eV for the 1^1B_u state[55] agrees very well with the value of 4.41 eV obtained at the MS(3)-CASPT2(12,12)/cc-pVDZ level[44]. The same holds also for the dark state — 4.1 eV estimated from the experiment[56,57] compared to 4.18 eV from theory[44]. Trusting the convergence, the interstate gap at $\mathbf{Q}_0$ is in the range of $\sim$0.3 eV.

The DFT/MRCI-R vertical excitation of 4.05 eV is somewhat too small for the dipole allowed state when compared to the best estimated value by at least 0.35 eV (Table 2). The calculated position of the 0-0 origin and the emission energy are also red shifted by the same energy. The fact, that a perfect match of DFT/MRCI-R/cc-pVTZ energy (5.94 eV) with the experiment (5.92 eV[61]) was found for 1^1B_u in *trans*-butadiene, and the slightly worse agreement (0.23 eV below the experimental value of 5.08 eV[62]) in linear hexatriene suggests that the latter method is unable to accurately describe the properties of the bright state upon extending the conjugation length owing to an incorrect scaling. Presumably, DFT/MRCI-R inherits the methodological drawbacks from DFT which is known to systematically underestimate the energies of ionic states for polyenes of longer chain length[63]. Apart from this, DFT/MRCI-R yields a qualitatively good energy of 4.10 eV for 2^1A_g which is indeed close to what is expected. The mapping of the calculated transition origin with measured values also corroborates this finding. As a result, the two states are almost isoenergetic at $\mathbf{Q}_0$ with a gap $E(1^1B_u)-E(2^1A_g)$ of -0.05 eV. Although

Table 2 Excitation energies (in eV) of first valence states in all-*trans*-octatetraene. Experimental values for vertical excitations are estimated.

	CASPT2[a]	MRMP[b]	DFT/MRCI-R	DFT/MRCI-S	Exp.
			vertical transitions		
1^1B_u	4.42	4.66	4.05	4.16	∼4.4[m]
2^1A_g	4.38	4.47	4.10	3.85	∼4.1[n]
			0-0 transitions		
1^1B_u	4.35	4.34	3.67	3.80	3.98[c,k] 4.40[d] 4.41[f,h,l]
2^1A_g	3.61	3.50	3.44	3.30	3.55[c] 3.59[e] 3.54[k]
			emission maxima		
1^1B_u	4.14	3.80	3.74	3.87	4.12[h] 4.20[d] 4.31[g]
2^1A_g	2.95	2.80	2.92	2.60	∼3.1[l]

[a] CASPT2 from Ref.[50]
[b] MRMP form Ref.[11]
[c] 77K in hexane from Ref.[59]
[d] gas phase from Ref.[59]
[e] jet from Ref.[56]
[m] estimated from Ref.[55]
[f] jet from Ref.[21]
[g] 4.2K in n-hexane from Ref.[58]
[h] jet from Ref.[55]
[k] 4.2K in n-octane from Ref.[60]
[l] vapor from Ref.[22]
[n] estimated from Ref.[56,57]

both states are offset by 0.25 eV in DFT/MRCI-S with regard to the experiment (Table 2), they are both shifted downward consistently. Thus, contrary to DFT/MRCI-R, the standard parameterization perfectly maintains the experimental splitting of 0.3 eV for the CASPT2 geometry.

Like the absorption, the emission intensities exhibit systematic variations with the polyene length[22]. In contrast to smaller linear polyenes, all-*trans*-octatetraene shows detectable emission with a quantum yield depending on both thermodynamic (pressure, temperature) and environment (solvent, impurity) conditions of the measurements[56,59,64]. Because the transition to the ground state from 2^1A_g is dipole forbidden, it is assumed that the signal originates from 1^1B_u. However, the emission from the dark state has been assigned in fluorescence excitation spectra in free jet[56,60] and fluorescence of vapor at room temperature[22] placing the maximum of the broad peak at 3.1 eV. The fact that the emission spectrum from 1^1B_u overlaps with the allowed absorption[22] indicates that no significant geometry relaxation occurs. So, it is likely that an influence of the in-plane a_g distortions $\mathbf{Q}$ dominates the vibronic spectra.

Potential energy surfaces

At the ground-state geometry, the vibrational modes of all-*trans*-octatetraene transform under

$$\Gamma_{\mathbf{Q}} = 17a_g \oplus 8a_u \oplus 7b_g \oplus 16b_u \tag{17}$$

The a_u vibrational modes reduce the molecular symmetry to C_2, whereas the b_g and b_u — to C_i and C_s, respectively. Based on previous MCTDH studies of butadiene[15] and hexatrienes[42], high-intensity peaks in the vibrational spectrum are impelled by the movements of the carbon atoms. Exhaustive analysis of all distortions $\mathbf{Q}$ reveals three symmetrized single and double carbon-carbon bond elongations q_1, q_2, q_4 and q_6 to be the coordinates modulating the interstate energy gap. As it is seen in Figure 3, the DFT/MRCI-R and DFT/MRCI-S potentials exhibit different behaviour near the Franck-Condon zone. As expected, the single-bond shortening and the double-bond elongation stabilize 2^1A_g more rapidly than the one-photon state. The differences between the state minima for PESs along q_2, q_4 and q_6 are in the range of 0.45-0.5 eV for DFT/MRCI-S and 0.05-0.1 for DFT/MRCI-R. The adiabatic energy difference seems consistent with regard to the energy splitting observed at the ground state geometry. As long as 2^1A_g and 1^1B_u do not interact, the curvature and the steepness of the PESs along the FC active modes are almost identical. Moreover, the excited state minima are equally displaced along these distortions as predicted by different parameterizations. Therefore, the discrepancy mainly originates from the different vertical shifts of the individual potential manifolds. However, it is worthwhile to note that the energy gap together with the coordinate at which the PESs cross are immensely important for the dynamics picture. In addition to the stretching modes, we included three modes to describe symmetric bond-angle deformations of the carbon framework, i.e. q_8, q_{10} and q_{12} as documented in ESI. Unlike the bond stretches, they do not diminish the energy gap but their incorporation is motivated by the spectral assignment in the experiments near the band origin.

The second class of distortions are coupling modes. As has been mentioned above, the LVC approach allows to estimate the coupling strength produced by a given perturbation q_i of the nuclear framework. To lowest order, the coupling μ can be defined as a function linearly dependent on the coordinate $\mu(q_i) = \mu \cdot q_i$. Taking into account the second nonvanishing term of the Taylor expansion, we define the coupling as:

$$\mu(q_i) = \mu^{(1)} \cdot q_i + \mu^{(3)} \cdot q_i^3 \tag{18}$$

where $\mu^{(1)}$ and $\mu^{(3)}$ are parameters for the numerical fit in Equation (4). Preliminary comparative examination of all b_u in-

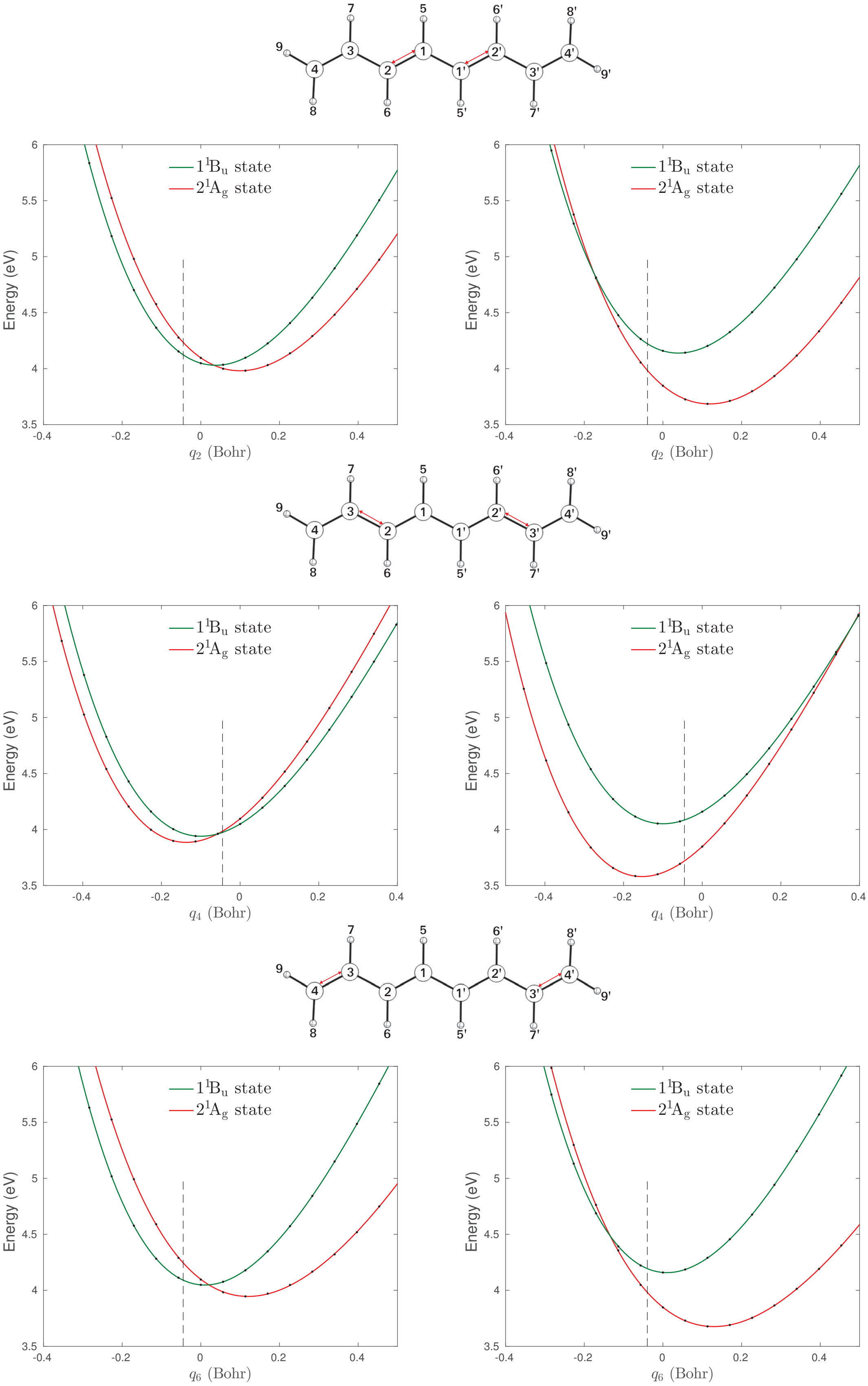

Fig. 3 DFT/MRCI-R (left) and DFT/MRCI-S (right) potential cuts along the symmetric bond alternation modes. The origin of the x-axes corresponds to the CASPT2 ground state geometry, whilst vertical dashed lines indicate the respective coordinates of the Franck-Condon point.

ternal coordinates spotted the strongest vibronic coupling constants arising due to carbon chain deformation. DFT/MRCI-S and DFT/MRCI-R electronic potentials yield slightly different pictures upon the $\mathbf{Q}_{coup}$ perturbation, as Table 3 implies. In case of DFT/MRCI-R, the bond alternations induce relatively small coupling constants compared to those from the angle alternations. An exception might be the terminal bond stretch with a fitted linear $\mu^{(1)}$ value of 0.30 eV/Bohr in DFT/MRCI-R, however the interaction of the potentials along q_7 is rather complicated and cannot be thoroughly captured by the applied vibronic model. In contrast to this, DFT/MRCI-S indicates that q_3, q_5 and q_7 are non-negligible motions, which is likely a result of a different interaction of the excited state electron densities. Based on the hierarchy of $\mu^{(1)}$ parameters, three $\mathrm{b_u}$ modes were selected for the dynamical treatment. In this way, the antisymmetric deformations of the inner and middle bond angles q_9 and q_{11} are included for both vibronic Hamiltonians. In addition, the $\mathbf{Q}_{coup}$ set is supplemented by the terminal bond alternation q_{13} for DFT/MRCI-R and by the q_7 stretching for DFT/MRCI-S. The distortions along these modes mimic double minima on adiabatic potential surfaces, which is often interpreted as a consequence of a second-order Jahn-Teller effect. The deeper the minimum drops energetically down, the stronger the repulsion μ is estimated in the LVC approach. Lets us state here that, within the $\mathrm{C_{2h}}$ molecular point group, the dipole moment transforms as the $\mathrm{a_u} \oplus 2\mathrm{b_u}$ representation, and, therefore, $\mathbf{Q}_{coup}$ modes result in pronounced dipole moments even at small nuclear displacements (see ESI). The above mentioned phenomenon of sudden polarization in polyenes[65–68] and its role in visual chromophores[69,70] is based on a highly unbalanced charge distribution, originating from an interplay of distorted σ- and π-orbitals. Consequently, the Coulomb interaction of the $1^1\mathrm{B_u}$ and $2^1\mathrm{A_g}$ polarized electron densities is one of the mechanisms responsible for a non-zero vibronic coupling strength.

Table 3 Coupling constants $\mu^{(1)}$ (eV/rad. or eV/Bohr) and $\mu^{(3)}$ (eV/rad.^{3} or eV/Bohr^3) of LVC model with respect to the CASPT2 ground state geometry.

Mode	Motion	DFT/MRCI-R		DFT/MRCI-S	
		$\mu^{(1)}$	$\mu^{(3)}$	$\mu^{(1)}$	$\mu^{(3)}$
q_3	$\frac{1}{2}(r_{12} - r_{1'2'})$	0.02	0.23	0.37	0.44
q_5	$\frac{1}{2}(r_{23} - r_{2'3'})$	0.02	0.05	0.26	0.45
q_7	$\frac{1}{2}(r_{34} - r_{3'4'})$	0.30	0.07	0.75	-0.16
q_9	$\frac{1}{2}(\phi_{1'12} - \phi_{11'2'})$	0.75	0.28	0.60	0.62
q_{11}	$\frac{1}{2}(\phi_{123} - \phi_{1'2'3'})$	0.58	0.08	0.42	0.39
q_{13}	$\frac{1}{2}(\phi_{234} - \phi_{2'3'4'})$	0.31	0.08	0.02	0.68

Table 4 Definition of internal coordinates used in the dynamical treatment. m - order of polynomial expansion, N - number of Hermite primitives in DVR representation, n - number of SPFs in multiset formalism.

Mode	Sym.	Motion	m	N	n
q_1	$\mathrm{a_g}$	$r_{11'}$	1-6	60	30:30
q_4	$\mathrm{a_g}$	$\frac{1}{2}(r_{23} + r_{2'3'})$	1-6	60	
q_2	$\mathrm{a_g}$	$\frac{1}{2}(r_{12} + r_{1'2'})$	1-6	60	30:30
q_6	$\mathrm{a_g}$	$\frac{1}{2}(r_{34} + r_{3'4'})$	1-6	60	
q_8	$\mathrm{a_g}$	$\frac{1}{2}(\phi_{1'12} + \phi_{11'2'})$	1-6	40	20:20
q_{10}	$\mathrm{a_g}$	$\frac{1}{2}(\phi_{123} + \phi_{1'2'3'})$	1-6	40	
q_{12}	$\mathrm{a_g}$	$\frac{1}{2}(\phi_{234} + \phi_{2'3'4'})$	1-6	40	
q_9	$\mathrm{b_u}$	$\frac{1}{2}(\phi_{1'12} - \phi_{11'2'})$	2,4,6	40	20:20
q_{11}	$\mathrm{b_u}$	$\frac{1}{2}(\phi_{123} - \phi_{1'2'3'})$	2,4,6	40	
q_{13}	$\mathrm{b_u}$	$\frac{1}{2}(\phi_{234} - \phi_{2'3'4'})$	2,4,6	40	
q_7	$\mathrm{b_u}$	$\frac{1}{2}(r_{34} - r_{3'4'})$			
q_{19}	$\mathrm{a_u}$	$\frac{1}{8}(\tau_{2348} + \tau_{2349} + \tau_{7348} + \tau_{7349} + \tau_{2'3'4'8'} + \tau_{2'3'4'9'} + \tau_{7'3'4'8'} + \tau_{7'3'4'9'})$	2,4,6	50	25:25
q_{20}	$\mathrm{b_g}$	$\frac{1}{8}(\tau_{2348} + \tau_{2349} + \tau_{7348} + \tau_{7349} - \tau_{2'3'4'8'} - \tau_{2'3'4'9'} - \tau_{7'3'4'8'} - \tau_{7'3'4'9'})$	2,4,6	50	

Finally, as it was emphasized in previous works on polyenes, the out-of-plane motions of the $\mathrm{CH_2}$ group play a significant role. We added the two motions q_{19} and q_{20} to represent the symmetric and antisymmetric methylene torsions about the terminal C=C double bonds. Therefore, these twelve symmetry-adapted internal coordinates were used to construct the potential energy matrix as formulated in Equation (7). To generate smooth quasi-diabatic PES, 1D-cuts were interpolated by 6-th order polynomial expressions:

$$\mathrm{U}_{1,2}(q_i) = \sum_{j}^{m} \zeta^{(j)} q_i^j \qquad (19)$$

omitting odd powers for symmetric potentials. As shown in Table 4, specific modes were grouped together to represent in total five MCTDH-particles as follows: combinations of single- and double-bond elongation, combination of all bond-angle alternation modes, all coupling $\mathrm{b_u}$ modes and finally the combination of the two out-of-plane motions. The relevant single-particle functions then describe multi-mode particles rather than a single degree of freedom, justified by the moderate time demands of the propagation computation.

Vibrationally resolved spectra

In order to simulate the experimental line broadening, the autocorrelation function is damped by further multiplication with a Gaussian function, which contains a damping parameter denoted in the following chapter as dephasing time. In this spirit, results of the simulation are presented in its high-resolution description utilizing a dephasing time of 1000 fs and a low-resolution form with a dephasing time of 30 fs. The absorption spectra of OT in the UVA region are shown in Figure 4. The intensities of all peaks are normalized to the maximum peak height corresponding to the origin. For comparison, the high-resolution absorption spectrum, recorded in a jet-cooled experiment, is presented in Figure 4. Similar to the polyenes of smaller lengths, the main features are well described by two principal vibrational modes. The most promi-

Table 5 First overtones of main absorption bands in all-*trans*-octatetraene. Deviation from the harmonic expansion are in parentheses.

Modes	Band	Position (cm^{-1})			
		Exp.[a]	Exp.[b]	DFT/ MRCI-R	DFT/ MRCI-S
origin	ν_0	35553	35523	29882	30644
q_1, q_4	ν_1	1235	1246		
q_2, q_6	ν_2	1645	1666	1727	1736
	$2\nu_1$	2477	2482		
		(+7)	(-10)		
	$\nu_1+\nu_2$	2872	2888	2846	2839
		(-8)	(-24)		
	$2\nu_2$	3281	3290	3446	3446
		(-9)	(-42)	(-8)	(-26)

[a] argon jet from Ref.[21]
[b] gas phase from Ref.[59]

nent mode (denoted by ν_2) with the most intense progression is associated with the carbon-carbon double-bond stretchings q_2 and q_6. The linear combinations of these two motions give rise to vibrations with almost degenerate frequency in the ground state[18,21]. DFT/MRCI-R places the peak at 1727 cm^{-1} to the right of the origin (denoted by ν_0), whereas DFT/MRCI-S — at 1736 cm^{-1}. Both methods here overshoot by $\sim$70 cm^{-1} the reported values of 1645 cm^{-1} measured in the jet-cooled experiment[21] and 1666 cm^{-1} in the gas phase[59]. However, because the minimum of the PES of the dark state lies below the minimum of the PES of the bright state, the position of the calculated peak is very similar to the 2^1A_g C–C frequency of 1754 cm^{-1} measured in one- and two-photon experiments[60].

The peak displayed at 1235 cm^{-1} (assigned to ν_1) in the jet-cooled spectrum gives rise to the secondary vibrational progression and is attributed to the symmetric single C–C bond alternations q_1 and q_4. This band appears with very low intensity in both the DFT/MRCI-R spectrum and the DFT/MRCI-S spectrum. Because its presence is corroborated by many other spectra measured under various conditions (see for example Ref.[21,22,59,64]), this lack of intensity is obviously a failure either of the model defined according to Equations (5, 7) or of the DFT/MRCI potentials being incapable to reproduce one of the principal features in the absorption spectrum of OT. The ν_1 and ν_2 spawned by symmetric bond alternation modes and their vibronic progressions give the largest Franck-Condon factors in the absorption spectrum of OT. The most intense peaks for the $1^1B_u \leftarrow 1^1A_g$ transition fit the series

$$\nu_{m,n} = \nu_0 + m\cdot\nu_1 + n\cdot\nu_2 \qquad m,n \geqslant 0 \tag{20}$$

with uncertainties as listed in Table 5. These uncertainties are the result of the vibronic interaction of 1^1B_u and 2^1A_g multidimensional potential manifolds and their curvilinear nature, which violate the harmonic expansion (20). Despite the almost dark ν_1 peak, DFT/MRCI-R and DFT/MRCI-S feature the $\nu_{1,1}$ overtone at 2846 cm^{-1} and 2839 cm^{-1} respectively, whilst the low-

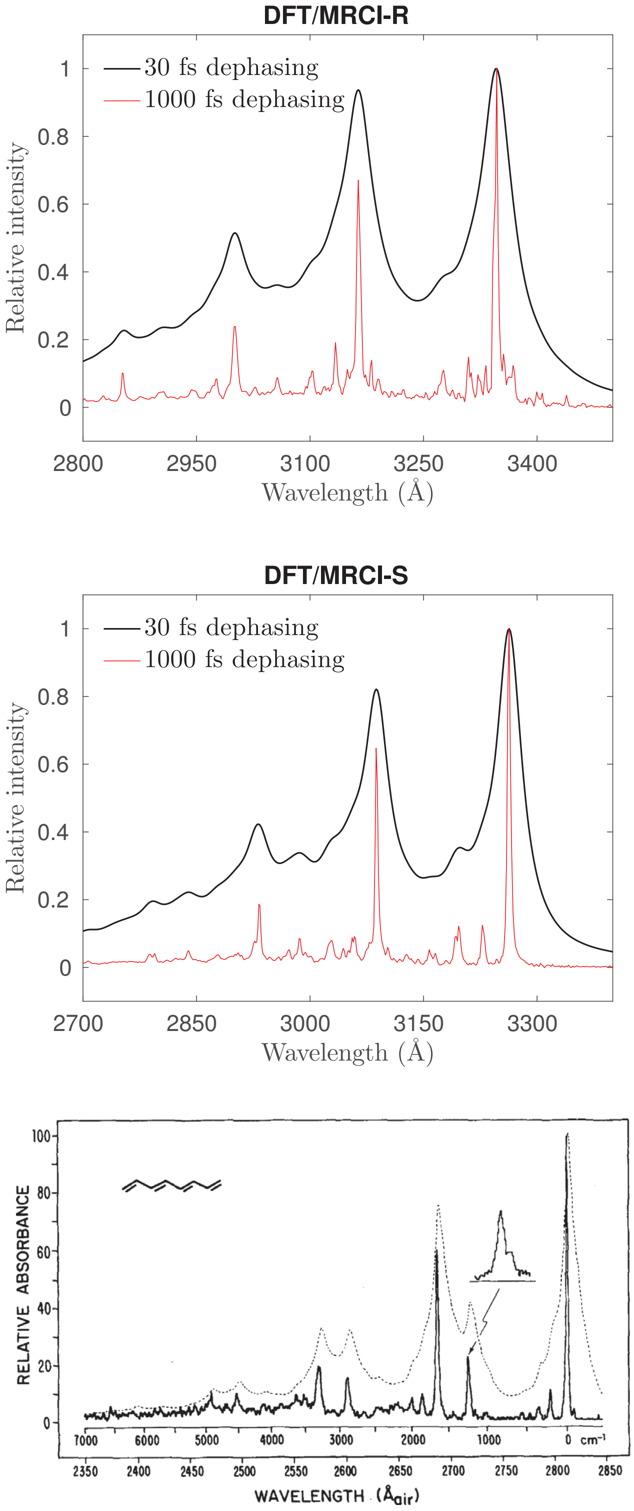

Fig. 4 Calculated (upper) and experimental (lower) $1^1B_u \leftarrow 1^1A_g$ absorption spectra of all-*trans*-octatetraene. Supersonic argon jet spectrum was reprinted from J. Chem. Phys. **81**, 4210 (1984) with the permission of AIP Publishing.

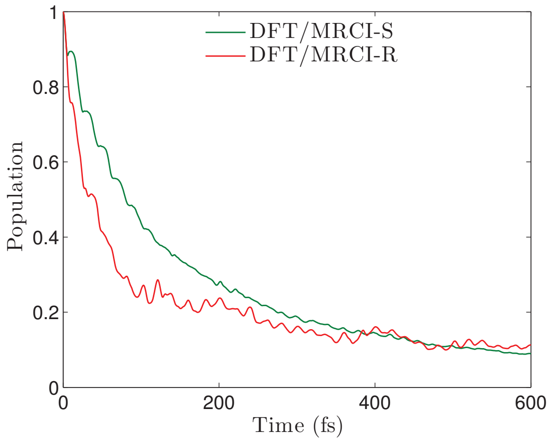

Fig. 5 Population decay following the 1^1B_u excitation.

temperature experimental value is 2872 cm^{-1}. All aforementioned overtones $v_{m,n}$ appear with low frequency shoulders, which are caused by symmetic in-plane angle bending q_8, q_{10} and q_{12} motions detected experimentally at 197 cm^{-1}, 348 cm^{-1}, 547 cm^{-1} [21]. The activity of these modes is also apparent in the simulated spectra, however the positions of minor bands are difficult to precisely locate due to the intricate low-intensity structure.

Time-dependent Electronic Population

The initially excited wave packet was propagated over 600 femtoseconds in the 1^1B_u and 2^1A_g potential manifolds. Figure 5 shows the population dynamics of the bright state utilizing DFT/MRCI-R and DFT/MRCI-S PESs. As in the *trans*-1,3-butadiene and *trans*-1,3,5-hexatriene, the energy transfer to 2^1A_g in octatetraene proceeds on the sub-picosecond time scale. DFT/MRCI-S completes the first step of photodynamics within τ=157 fs after the excitation to the bright state, as estimated from the curve fit to the exponential function $exp(-t/\tau)$. The population curve of the ionic state decays monotonously, with 10% of the entire wave packet remaining localized on the 1^1B_u surfaces. This outcome is in good agreement with the value of ~0.3 ps deduced from the experimentally observed 0-0 bandwidth for excitation at the origin[21,22]. DFT/MRCI-R predicts a slightly different picture with exponentially fitted lifetime τ=95 fs. The 1^1B_u population abruptly sweeps down and the wave packet reaches its quasi-stationary average among the two manifolds after 100 fs of propagation time yielding 70% of its density to the dark state. Hereafter, the remaining half is lost in the next 200 fs. This is somewhat too fast for OT compared to what is experimentally estimated. However, one can understand this effect considering the negligible energy splitting between the states at the ground state geometry as the pivotal quantity in the internal conversion process. Moreover, the coordinates of the crossing point of the 1D-potentials almost coincide with the FC center at the DFT/MRCI-R level (Figure 3). This explains the very steep slope of the DFT/MRCI-R population curve, and therefore the nonradiative lifetime of the bright state is clearly underrated. The slower decay of the DFT/MRCI-S population in Figure 5 indicates that the S_2/S_1 conical intersection and the FC point are located further apart. Following the recent theoretical studies on all-*trans*-octatetraene[20,52,71], the local skeletal torsion about the r_{12} bond mediates the conical intersection between 1^1B_u and 2^1A_g states. On this ground, incorporation of two symmetric modes q_{15} and q_{16} (conrotatory and disrotatory twists $\tau_{1'123} \pm \tau_{11'2'3'}$ correspondingly) into $\mathbf{Q}$ for MCTDH treatment will open a new decay channel which may alleviate the transition dynamics. Based on adiabatic surface hopping methods driven by MRCI(8,8)-S/6-31G* excited state surfaces, the time constant of 1^1B_u was estimated as 251 fs finishing with 15% of all trajectories on the bright state[20]. Although an activation of out-of-plane distortions of the carbon chain should facilitate an energy transfer, by now we assume that no inverse population will occur and the rest of the energy belonging to the ionic state is converted to the emission of radiation. In this framework, the fluorescence quantum yield of 0.10±0.08 measured in vapor phase at 295 K[59] accurately matches to the 1^1B_u population for both DFT/MRCI-R and DFT/MRCI-S after 600 fs of WP propagation. The vibrational structure of the emission spectra of the ionic state of OT suggests the presence of long-lived components[22,55,56,72].

Emission from 2^1A_g to the ground state of OT in the vapor phase occurs with a quantum yield of 0.06 relative to the emission from 1^1B_u.[22] This is a fairly tiny part of the entire 2^1A_g population after the first step of photodynamics has been accomplished. The dominating channel of energy dissipation in octatetraene involves the nonradiative decay to the ground state[56,64,71,73,74]. It was proposed that all-*trans*- to *cis,trans*- isomerization occurs nonadiabatically in cooled jet experiment[56]. The observed energy barrier of 2100 cm^{-1} for the activation of the photoisomerization finds an agreement with theoretical calculations[71]. This excess energy can be borrowed from the nuclear kinetic component by exciting hot vibrational bands or the process can be activated thermally in glassy matrices[64]. In such a way the system will arrive at the conical intersection of the S_1/S_0 potentials. Besides the *cis-trans*- product, Kohler[64] observed a non-centrosymmetric conformer by irradiation into the 2^1A_g origin in an n-octane matrix at 4.2 K and assigned this species to 2-s-*cis*-octatetraene. In contrast, extended irradiation leads to the formation of a centrosymmetric species assigned to *trans,trans*-octatetraene. The former reaction occurs also non-adiabatically with a transition state energy of 3500 cm^{-1} above the S_1 minimum[71].

At present we can only qualitatively speak about possible products of the photoreaction. Numerical minimization of the DFT/MRCI-R S_1-S_0 energy gap starting from the transition state geometry[71] reveals a Hula-twist[75] of center 1′ as decisive motion to reach the crossing of the adiabatic potentials (see AC1 in Table 1). In terms of symmetry-adapted coordinates, the Hula-twist encompasses the skeletal torsion about the middle bond and the already mentioned torsions about the inner double bonds. Simultaneous rotation about the middle bond $\tau_{2'1'12}$ and conrotatory twists about the $r_{1'2'}$ and r_{12} bonds bring the system to the *cis-trans*- photoproduct of octatetraene following the steepest descent of the S_0 potential energy (see Figure 6 left). In turn, a positive combination of $\tau_{2'1'12}$ and disrotatory twists $(\tau_{1'123} - \tau_{11'2'3'})$ will stabilize the all-*trans*-isomer (see Figure 6 middle). The sec-

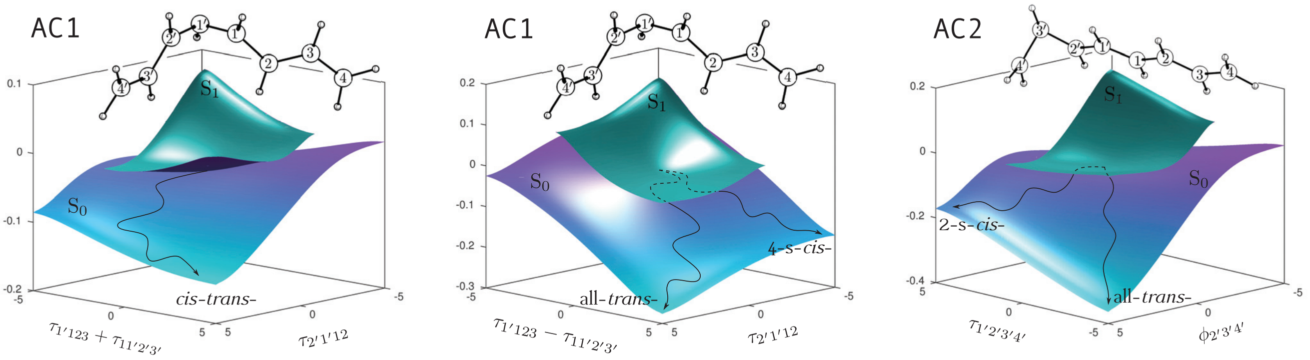

Fig. 6 Adiabatic potential energy surfaces near the S_1/S_0 crossing point and possible isomerization pathways towards various photoproducts of octatetraene.

ond S_1/S_0 crossing point (see AC2 in Table 1) near the transition state of the all-*trans*- to 2-s-*cis*- isomerization[71] reveals the terminal C–C–C bending and the rotation about the $r+2'3'$ bond as the most vivid deformations of the internal coordinates. In this case, the 2-s-*cis*– confomer can be formed by increasing the $\tau_{1'2'3'4'}$ dihedral angle (Figure 6 right). For a fair assessment of the formation of the photoproducts, the vibronic Hamiltonian (5) needs to be extended to the ground state potentials with inclusion of appropriate vibronic coupling constants. Furthermore, the MCTDH wave function (11) has to incorporate additional a_u and b_g out-of-plane modes. The rates of the photoisomerization are determined by the vibronic coupling among three states, such that the process finishes with the vibrational relaxation to the ground-state manifold. We leave a more complete treatment of the internal conversion to the electronic ground state for future work.

Conclusions

In this paper we have described the nonadiabatic quantum dynamics of all-*trans*-octatetraene followed by light absorption in the UV energy range. By employing the extended LVC model for calculation of the excited wave packet evolution among two potential manifolds of energetically close-lying excited states, we analyzed the computed spectra and the nonradiative transition process $1^1B_u \rightsquigarrow 2^1A_g$. The electronic potential energy surfaces were evaluated employing both formulations of the hybrid semiempirical DFT/MRCI Hamiltonians and the overall results were critically compared with experimental findings.

We found that the depopulation time of the bright state in OT occurs in the sub-picosecond time regime — 157 fs as follows from DFT/MRCI-S and 95 fs from DFT/MRCI-R. This is consistently longer than previously reported values of nonadiabatic dynamics studies for shorter length polyenes — *trans*-butadiene and *trans*-hexatriene. The outcome of the standard parameterization for the lifetime of the bright state is in better agreement with the experimental estimation. In this regard, the population curve of DFT/MRCI-R is not very different. Its steeper decay is explained by the nearby location of the crossing point of the two potentials along the tuning modes at the Franck-Condon center, and therefore almost no kinetic component is needed for the energy dissipation to 2^1A_g.

The application of either DFT/MRCI approach to generate potentials for the 1^1B_u and 2^1A_g states yields computed absorption spectra which describe the key features and their vibronic progressions due to Franck-Condon effects well in general. However, the band associated with carbon-carbon single bond length changes is lacking intensity, which might be the result of the additivity assumption of the multidimensional potential energy surface. To remedy this shortcoming, we suggest to account for the vibronic interaction between the symmetric single and double bond stretchings in the framework of a bilinear coupling model. At the end, we shall stress that the family of excited polyenes represents a big challenge for computational chemistry due to the different nature of the two low-lying valence states. They require an accurate and balanced description at and near the FC zone to model the absorption spectrum and nonradiative internal conversion dynamics properly.

Acknowledgments

The authors are grateful to A. Komainda for useful discussions and sharing results prior to publication. Financial support by the *Deutsche Forschungsgemeinschaft* (DFG) through projects MA1051/14-1 and KO945/19-1 are gratefully acknowledged.

References

1 G. Cerullo, D. Polli, G. Lanzani, S. De Silvestri, H. Hashimoto and R. J. Cogdell, *Science*, 2002, **298**, 2395–2398.
2 X. Hu, A. Damjanović, T. Ritz and K. Schulten, *Proc. Natl. Acad. Sci.*, 1998, **95**, 5935–5941.
3 X. Hu and K. Schulten, *Phys. Today*, 1997, **50**, 28–34.
4 R. Schmidt, *J. Phys. Chem. A*, 2004, **108**, 5509–5513.
5 P. D. Mascio, S. Kaiser and H. Sies, *Arch. Biochem. Biophys.*, 1989, **274**, 532 – 538.
6 O. Hirayama, K. Nakamura, S. Hamada and Y. Kobayasi, *Lipids*, 1994, **29**, 149–150.
7 R. S. Becker, *Photochem. Photobiol.*, 1988, **48**, 369–399.
8 O. Weingart, *J. Am. Chem. Soc.*, 2007, **129**, 10618–10619.
9 D. Polli, P. Altoe, O. Weingart, K. M. Spillane, C. Manzoni, D. Brida, G. Tomasello, G. Orlandi, P. Kukura, R. A. Mathies, M. Garavelli and G. Cerullo, *Nature*, 2010, **467**, 440–443.
10 J. H. Starcke, M. Wormit, J. Schirmer and A. Dreuw, *Chem.*

Phys., 2006, **329**, 39 – 49.

11 K. Nakayama, H. Nakano and K. Hirao, *Int. J. Quantum Chem.*, 1998, **66**, 157–175.

12 P. Tavan and K. Schulten, *J. Chem. Phys.*, 1979, **70**, 5407–5413.

13 C. M. Marian and N. Gilka, *J. Chem. Theory Comput.*, 2008, **4**, 1501–1515.

14 R. McDiarmid, *Adv. Chem. Phys.*, 2007, **110**, 177–214.

15 A. Komainda, B. Ostojić and H. Köppel, *J. Phys. Chem. A*, 2013, **117**, 8782–8793.

16 A. Komainda, I. Lyskov, C. M. Marian and H. Köppel, *J. Phys. Chem. A*, 2016, **120**, 6541–6556.

17 A. B. Myers and K. S. Pranata, *J. Phys. Chem.*, 1989, **93**, 5079–5087.

18 D. G. Leopold, R. D. Pendley, J. L. Roebber, R. J. Hemley and V. Vaida, *J. Chem. Phys.*, 1984, **81**, 4218–4229.

19 X. Ci and A. B. Myers, *J. Chem. Phys.*, 1992, **96**, 6433–6442.

20 Z. Qu and C. Liu, *J. Chem. Phys.*, 2013, **139**, 244304.

21 D. G. Leopold, V. Vaida and M. F. Granville, *J. Chem. Phys.*, 1984, **81**, 4210–4217.

22 W. G. Bouwman, A. C. Jones, D. Phillips, P. Thibodeau, C. Friel and R. L. Christensen, *J. Phys. Chem.*, 1990, **94**, 7429–7434.

23 L. Cederbaum, W. Domcke, H. Köppel and W. V. Niessen, *Chem. Phys.*, 1977, **26**, 169 – 177.

24 L. S. Cederbaum and W. Domcke, *Adv. Chem. Phys.*, 2007, **36**, 205–344.

25 H. Köppel, W. Domcke and L. S. Cederbaum, *Adv. Chem. Phys.*, 1984, **57**, 59–246.

26 E. B. Wilson, *J. Chem. Phys.*, 1939, **7**, 1047–1052.

27 E. B. Wilson, J. C. Decius and P. C. Cross, *Molecular Vibrations - the Theory of Infrared and Raman Vibrational Spectra*, McGraw-Hill Book Company, Inc, 1955.

28 J. H. Frederick and C. Woywod, *J. Chem. Phys.*, 1999, **111**, 7255–7271.

29 S. Grimme and M. Waletzke, *J. Chem. Phys.*, 1999, **111**, 5645–5655.

30 I. Lyskov, M. Kleinschmidt and C. M. Marian, *J. Chem. Phys.*, 2016, **144**, 034104.

31 T. H. Dunning, *J. Chem. Phys.*, 1989, **90**, 1007–1023.

32 D. E. Woon and T. H. Dunning, *J. Chem. Phys.*, 1995, **103**, 4572–4585.

33 R. Ahlrichs, M. Bär, M. Häser, H. Horn and C. Kölmel, *Chem. Phys. Lett.*, 1989, **162**, 165 – 169.

34 O. Treutler and R. Ahlrichs, *J. Chem. Phys.*, 1995, **102**, 346–354.

35 *TURBOMOLE V6.5 2013, a development of University of Karlsruhe and Forschungszentrum Karlsruhe GmbH, 1989-2007, TURBOMOLE GmbH, since 2007; available from* `http://www.turbomole.com`.

36 A. D. Becke, *J. Chem. Phys.*, 1993, **98**, 1372–1377.

37 F. Weigend, A. Köhn and C. Hättig, *J. Chem. Phys.*, 2002, **116**, 3175–3183.

38 H.-D. Meyer, U. Manthe and L. Cederbaum, *Chem. Phys. Lett.*, 1990, **165**, 73 – 78.

39 M. Beck, A. Jäckle, G. Worth and H.-D. Meyer, *Phys. Rep.*, 2000, **324**, 1 – 105.

40 G. A. Worth, M. H. Beck, A. Jäckle, O. Vendrell and H.-D. Meyer, The MCTDH Package, Version 8.2, (2000). H.-D. Meyer, Version 8.3 (2002), Version 8.4 (2007). O. Vendrell and H.-D. Meyer Version 8.5 (2013). Version 8.5 contains the ML-MCTDH algorithm. Current versions: 8.4.12 and 8.5.5 (2016). See http://mctdh.uni-hd.de/.

41 H.-D. Meyer, F. Gatti and G. Worth, *Multidimensional Quantum Dynamics. MCTDH Theory and Applications*, WILEY-VCH Verlag GmbH & Co., 2009.

42 A. Komainda, A. Zech and H. Köppel, *J. Mol. Spectrosc.*, 2015, **311**, 25 – 35.

43 R. Schinke, *Photodissociation Dynamics*, Cambridge University Press, 1991.

44 J. Heuser, *MSc thesis*, Universität Heidelberg, 2015.

45 R. Baughman, B. Kohler, I. Levy and C. Spangler, *Synth. Met.*, 1985, **11**, 37–52.

46 C. Neiss, E. Trushin and A. Görling, *ChemPhysChem*, 2014, **15**, 2497–2502.

47 R. R. Tykwinski, *Chem. Rec.*, 2015, **15**, 1060–1074.

48 M. R. Silva-Junior and W. Thiel, *J. Chem. Theory Comput.*, 2010, **6**, 1546–1564.

49 M. Schreiber, M. R. Silva-Junior, S. P. A. Sauer and W. Thiel, *J. Chem. Phys.*, 2008, **128**, 134110.

50 L. Serrano-Andres, R. Lindh, B. O. Roos and M. Merchan, *J. Phys. Chem.*, 1993, **97**, 9360–9368.

51 C. Angeli and M. Pastore, *J. Chem. Phys.*, 2011, **134**, 184302.

52 J. Catalán and J. L. G. de Paz, *J. Chem. Phys.*, 2006, **124**, 034306.

53 M. R. Silva-Junior, M. Schreiber, S. P. A. Sauer and W. Thiel, *J. Chem. Phys.*, 2008, **129**, 104103.

54 R. J. Cave and E. R. Davidson, *J. Phys. Chem.*, 1987, **91**, 4481–4490.

55 L. A. Heimbrook, B. E. Kohler and I. J. Levy, *J. Chem. Phys.*, 1984, **81**, 1592–1597.

56 H. Petek, A. J. Bell, Y. S. Choi, K. Yoshihara, B. A. Tounge and R. L. Christensen, *J. Chem. Phys.*, 1993, **98**, 3777–3794.

57 R. L. Christensen, M. G. I. Galinato, E. F. Chu, J. N. Howard, R. D. Broene and H. A. Frank, *J. Phys. Chem. A*, 2008, **112**, 12629–12636.

58 J. R. Ackerman, B. E. Kohler, D. Huppert and P. M. Rentzepis, *J. Chem. Phys.*, 1982, **77**, 3967–3973.

59 R. M. Gavin, C. Weisman, J. K. McVey and S. A. Rice, *J. Chem. Phys.*, 1978, **68**, 522–529.

60 M. F. Granville, G. R. Holtom and B. E. Kohler, *J. Chem. Phys.*, 1980, **72**, 4671–4675.

61 O. A. Mosher, W. M. Flicker and A. Kuppermann, *J. Chem. Phys.*, 1973, **59**, 6502–6511.

62 T. Fujii, A. Kamata, M. Shimizu, Y. Adachi and S. Maeda, *Chem. Phys. Lett.*, 1985, **115**, 369 – 372.

63 M. Wanko, M. Garavelli, F. Bernardi, T. A. Niehaus, T. Frauenheim and M. Elstner, *J. Chem. Phys.*, 2004, **120**, 1674–1692.

Nonadiabatic photodynamics and UV absorption spectrum of all-trans-octatetraene: Supplementary Information

Igor Lyskov[a], Horst Köppel[b], and Christel M. Marian[a,*]

[a]Institute of Theoretical and Computational Chemistry,
Heinrich-Heine-University Düsseldorf, Universitätsstraße 1,
40225 Düsseldorf, Germany,
Tel.: +49-211-8113209. Fax: +49-211-8113446.
E-mail: Christel.Marian@hhu.de

[b] Physikalisch-Chemisches Institut,
Universität Heidelberg, Im Neuenheimer Feld 229,
D-69120 Heidelberg, Germany

October 8, 2016

Figure 1: DFT/MRCI-R (left) and DFT/MRCI-S (right) 1D cuts of excited states potential energy surface for all-trans-octatetraene.

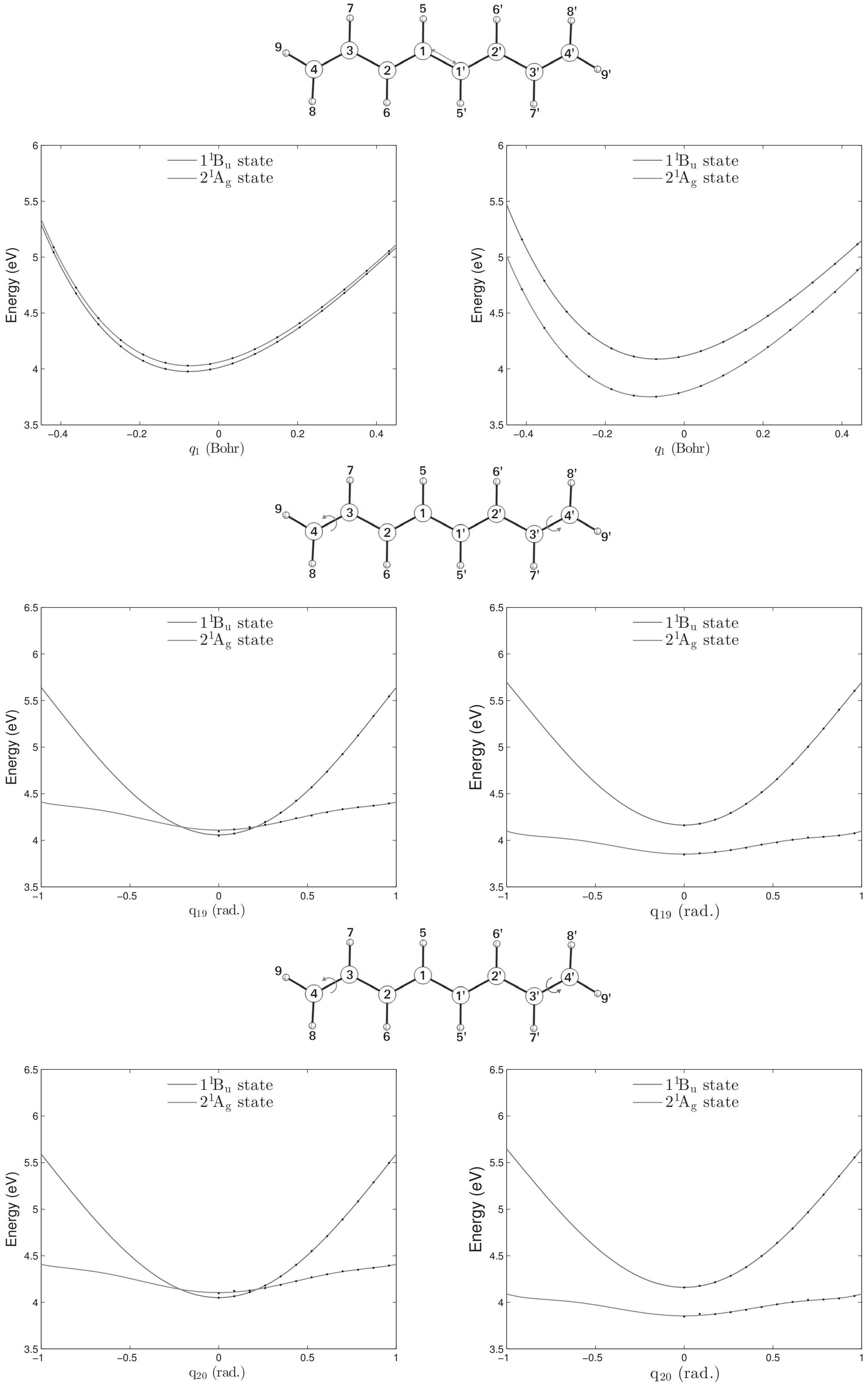

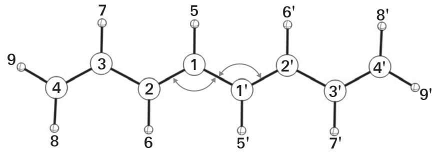
7
5
6'
8'
9
3
1
2'
4'
4
2
1'
3'
9'
8
6
5'
7'

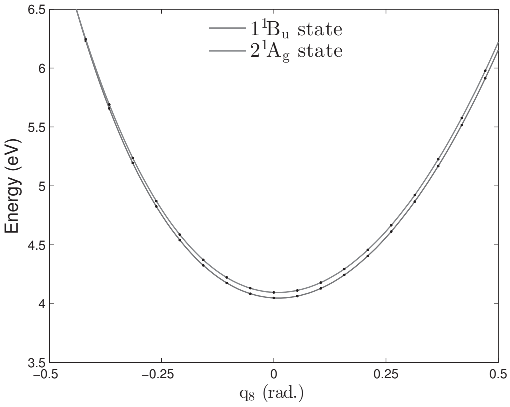
1^1B_u state
2^1A_g state
Energy (eV)
6.5
6
5.5
5
4.5
4
3.5
−0.5
−0.25
0
0.25
0.5
q_8 (rad.)

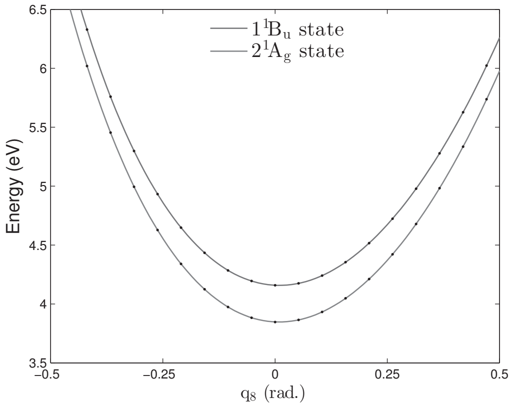
1^1B_u state
2^1A_g state
Energy (eV)
6.5
6
5.5
5
4.5
4
3.5
−0.5
−0.25
0
0.25
0.5
q_8 (rad.)

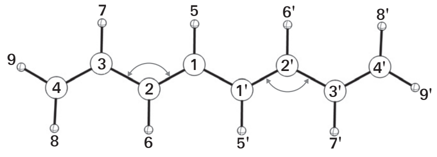
7
5
6'
8'
9
3
1
2'
4'
4
2
1'
3'
9'
8
6
5'
7'

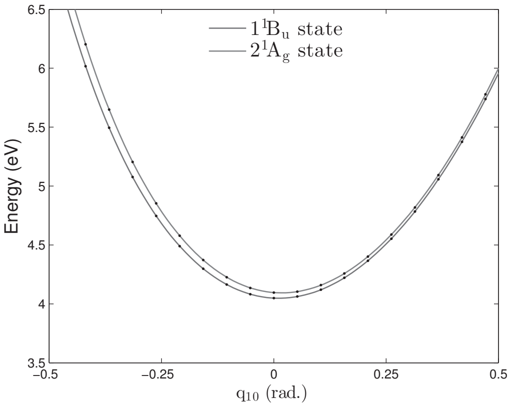
1^1B_u state
2^1A_g state
Energy (eV)
6.5
6
5.5
5
4.5
4
3.5
−0.5
−0.25
0
0.25
0.5
q_{10} (rad.)

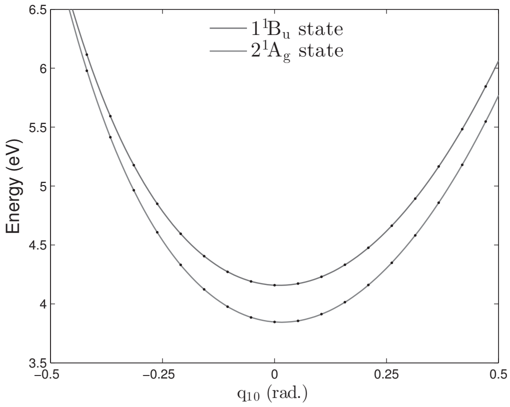
1^1B_u state
2^1A_g state
Energy (eV)
6.5
6
5.5
5
4.5
4
3.5
−0.5
−0.25
0
0.25
0.5
q_{10} (rad.)

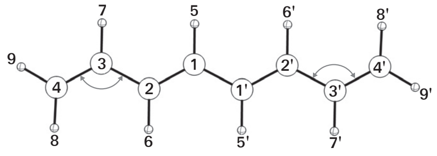
7
5
6'
8'
9
3
1
2'
4'
4
2
1'
3'
9'
8
6
5'
7'

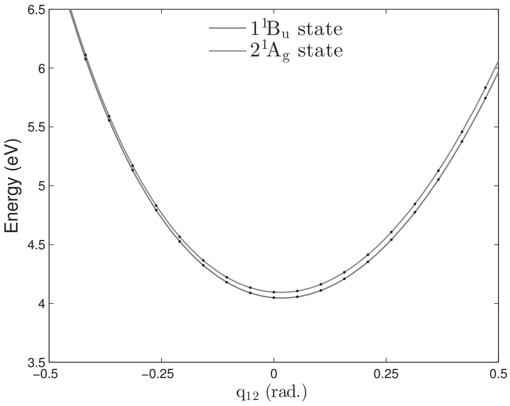
1^1B_u state
2^1A_g state
Energy (eV)
6.5
6
5.5
5
4.5
4
3.5
−0.5
−0.25
0
0.25
0.5
q_{12} (rad.)

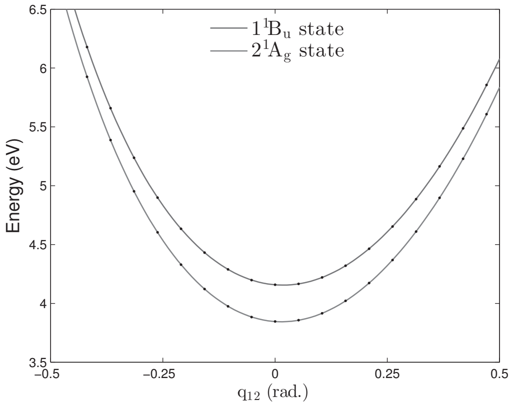
1^1B_u state
2^1A_g state
Energy (eV)
6.5
6
5.5
5
4.5
4
3.5
−0.5
−0.25
0
0.25
0.5
q_{12} (rad.)

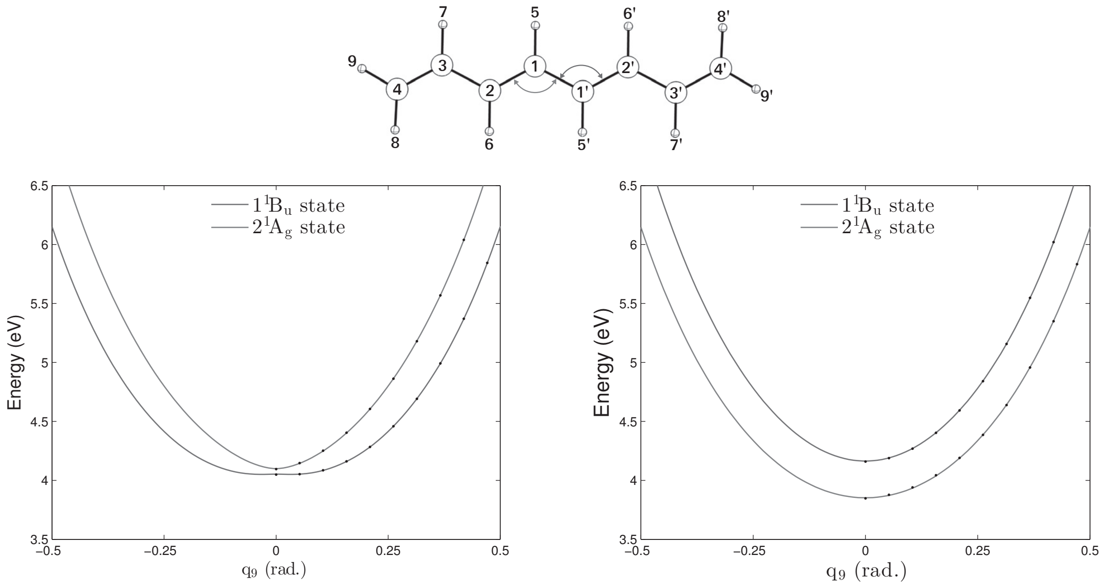

9
4
8
7
3
2
6
5
1
1'
5'
6'
2'
3'
7'
8'
4'
9'
Energy (eV)
1^1B_u state
2^1A_g state
q_9 (rad.)

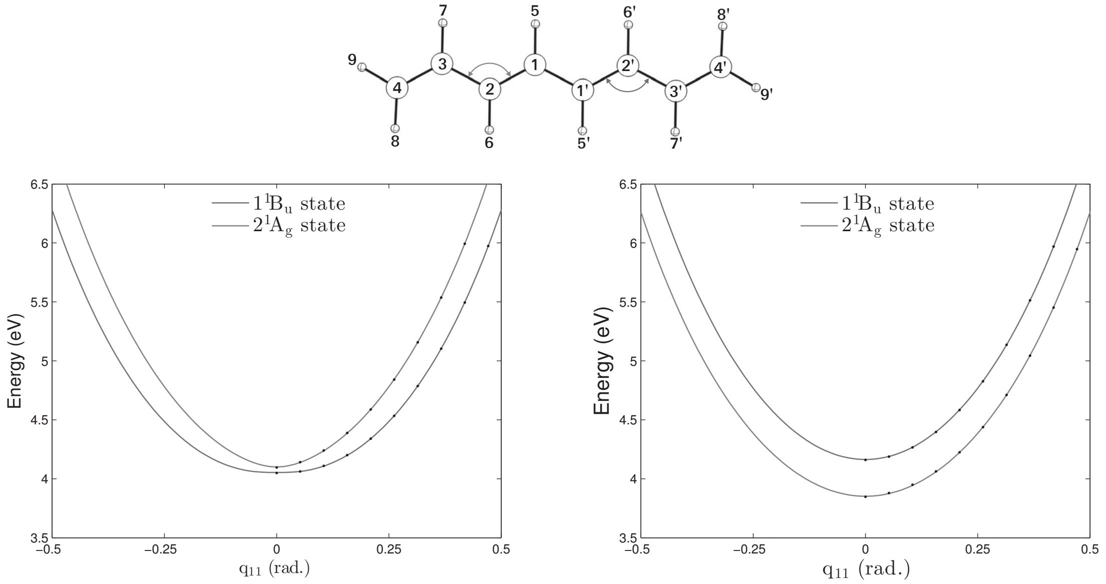

9
4
8
7
3
2
6
5
1
1'
5'
6'
2'
3'
7'
8'
4'
9'
Energy (eV)
1^1B_u state
2^1A_g state
q_{11} (rad.)

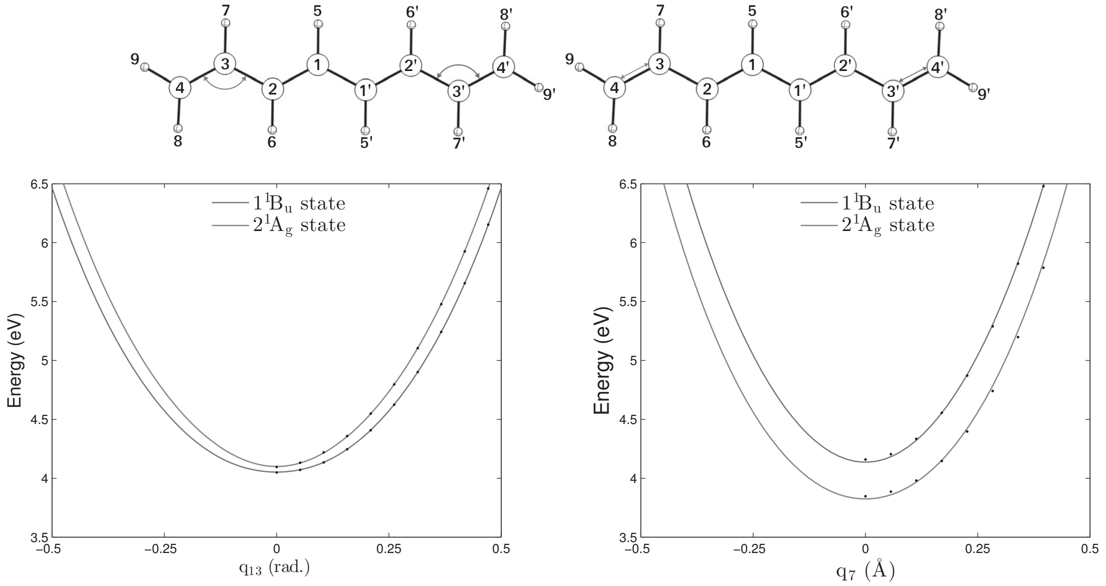

Energy (eV)
1^1B_u state
2^1A_g state
q_{13} (rad.)
q_7 (Å)

Figure 2: Magnitude of the dipole moment of $1^1\mathrm{B_u}$ and $2^1\mathrm{A_g}$ states modulated by q_9 ($\mathrm{b_u}$) and q_{15} ($\mathrm{a_u}$) symmetry adapted distortions. For illustration, positive-negative combination indicates that two vectors are anticollinear near FC region.

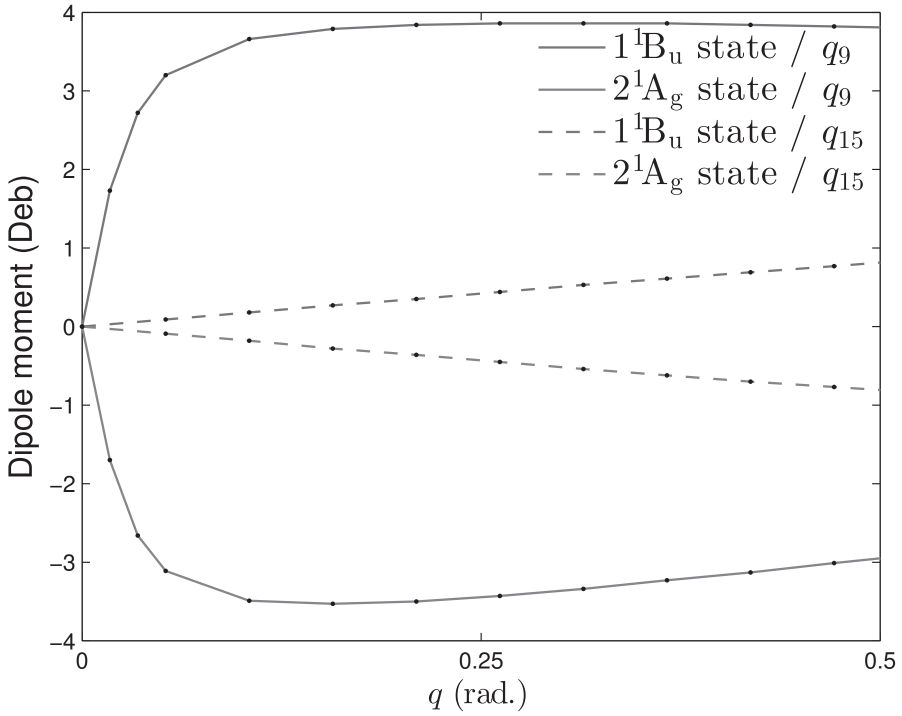

THE JOURNAL OF
PHYSICAL CHEMISTRY A

Article

pubs.acs.org/JPCA

Ab Initio Benchmark Study of Nonadiabatic S_1–S_2 Photodynamics of *cis*- and *trans*-Hexatriene

A. Komainda,[†] I. Lyskov,[‡] C. M. Marian,[‡] and H. Köppel*,[†]

[†]Physikalisch-Chemisches Institut, Universität Heidelberg, Im Neuenheimer Feld 229, D-69120 Heidelberg, Germany

[‡]Institut für Theoretische Chemie und Computerchemie, Universität Düsseldorf, Universitätsstraße 1, D-40225 Düsseldorf, Germany

Supporting Information

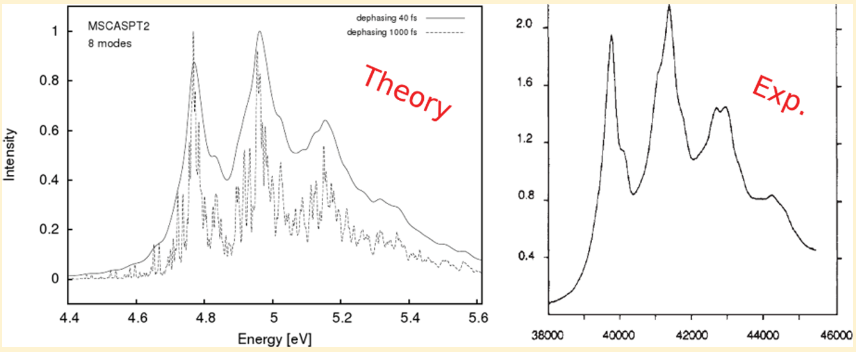

ABSTRACT: The dynamics of the nonadiabatically coupled lowest singlet excited states of *cis*- and *trans*-hexatriene are studied theoretically, in a comprehensive electronic structure and quantum dynamical investigation. At the ground state equilibrium geometry the relevant S_2 and S_1 states carry the A_1 (A_g) and B_2 (B_u) symmetry labels, for the *cis* (*trans*) isomer. Various high-level electronic structure methods are used, including the recently reparametrized DFT/MRCI method, and the results are critically compared. Key parameters of interest are the vertical energy gap and the strength of vibronic coupling between the interacting electronic states. To estimate their influence, suitable comparison calculations are performed. The results are used as the basis for quantum dynamical calculations on the UV absorption spectrum and electronic population transfer involving the S_1 and S_2 states. Up to nine nonseparable degrees of freedom are included in the calculations. The experimental UV absorption spectrum in the 5–5.2 eV energy range can be very well reproduced. The time-dependent wavepacket propagations reveal a population transfer on the order of 30–50 fs, which becomes increasingly complete with more degrees of freedom included in the calculation. The results are briefly compared with analogous data for the *s-trans*-butadiene system treated by some of us recently.

I. INTRODUCTION

Linear polyenes are of major importance in many biological systems, such as carotenoids, for the process of vision, and in materials science.[1−5] Despite numerous experimental and theoretical investigations key issues for electronically excited species are still unresolved.[6−14] This holds even for the smallest systems, such as butadiene and also the hexatriene isomers on which we focus here. The complexity in part stems from the close energetic proximity of the two lowest excited singlet states, which leads to complicated vibronic interactions.[6,8,15−17] These result in complex spectral structures, such as very broad bands in the UV absorption spectrum, even under jet-cooled conditions. See, for example, refs 6 and 18−22 for more details and further references.

The theoretical analysis is hampered by the complicated electronic wave functions of the excited electronic states. For the ease of later reference we give here their symmetry labels for both isomers (the labeling *cis* and *trans* refers to the central double bond). There is an A state that is optically dark and multiconfigurational in character, with a substantial double excitation contributing.[23−25] A nearby B state consists essentially of a HOMO−LUMO excitation, and the transition from the ground state is strongly allowed.[6,26] For the *trans*-HT isomer (C_{2h} point group) the symmetry labels of the states are $2A_g$ and $1B_u$; for the *cis*-HT isomer (C_{2v} point group) they are $2A_1$ and $1B_2$. The ordering of the two states and the behavior of their potential energy surfaces (PES) in and near the FC zone has been a matter of year-long debate in the literature.[27−30] The same holds for the photophysical and photochemical properties of HT in these states.[31,32] Because only singlet states are dealt with in this work, the spin multiplicity will be suppressed in what follows.

Recently, we have started an ab initio-based theoretical investigation of the UV absorption spectrum of *cis*- and *trans*-hexatriene (HT).[33] A vibronic coupling Hamiltonian was set up extending the well-known linear vibronic coupling model[34] and

Received: May 20, 2016
Revised: August 3, 2016
Published: August 3, 2016

DOI: 10.1021/acs.jpca.6b04971
J. Phys. Chem. A 2016, 120, 6541−6556

Table 1. Definition of the Symmetry-Adapted Internal Coordinates, Employed in Our Dynamical Study of *cis*- and *trans*-Hexatriene[a]

in-plane		out-of-plane	
S_1	$\frac{1}{2}(\Delta r_{1,2} + \Delta r_{5,6})$	S_{10}	$\frac{1}{4}(\Delta\tau_{2,3,4,5} + \Delta\tau_{9,3,4,11} + \Delta\tau_{2,3,4,11} + \Delta\tau_{9,3,4,5})$
S_2	$\frac{1}{2}(\Delta r_{2,3} + \Delta r_{4,5})$	S_{13}	$\frac{1}{8}(\Delta\tau_{7,1,2,10} + \Delta\tau_{8,1,2,3} + \Delta\tau_{8,1,2,10} + \Delta\tau_{7,1,2,3} + \Delta\tau_{4,5,6,13} + \Delta\tau_{12,5,6,14} + \Delta\tau_{12,5,6,13} + \Delta\tau_{4,5,6,14})$
S_3	$\Delta r_{3,4}$	S_{14}	$\frac{1}{8}(\Delta\tau_{7,1,2,10} + \Delta\tau_{8,1,2,3} + \Delta\tau_{8,1,2,10} + \Delta\tau_{7,1,2,3} - \Delta\tau_{4,5,6,13} + \Delta\tau_{12,5,6,14} + \Delta\tau_{12,5,6,13} + \Delta\tau_{4,5,6,14})$
S_5	$\frac{1}{2}(\Delta r_{2,3} - \Delta r_{4,5})$		
S_6	$\frac{1}{2}(\Delta\phi_{1,2,3} + \Delta\phi_{4,5,6})$		
S_9	$\frac{1}{2}(\Delta\phi_{2,3,4} - \Delta\phi_{3,4,5})$		

[a] The meaning of the algebraic expressions, relating the symmetry-adapted to the local internal coordinates, is reiterated in the main text below eq 2. For the atom numbering used to characterize the local coordinates, see Figure 1.

six planar degrees of freedom included in the ab initio and dynamical treatments. Applying a suitable (phenomenological) broadening, the experimental spectral profiles of both isomers could be well reproduced.[20,22] The underlying high-resolution spectra show a highly complex and irregular peak structure owing to the mixing of the electronic states and the nonseparability of the vibrational modes. The phenomenological line broadening applied is considerably smaller than the apparent line width observed experimentally. This shows that a substantial part of the complicated line broadening mechanisms operative in the UV spectra has been captured in the microscopic treatment.

In the present paper we want to systematically extend this earlier line of work, primarily by covering also the time-dependent dynamics, that is, the ultrafast electronic population transfer (internal conversion processes) between the coupled electronic states. Because these populations often depend more sensitively on the system parameters than the absorption spectra, we will also reconsider the vibronic Hamiltonian to be adopted in the theoretical treatment and reassess the ab initio determination of the system parameters. Alongside other reasons, which will become apparent below, the investigation includes (i) an extended comparison of various electronic structure methods for computing, e.g., the vertical excitation energies and potential energy surfaces. This includes, in particular, the highly cost-efficient DFT/MRCI method originally developed by Grimme and Waletzke[35] and recently reparametrized by two of us.[36] (ii) These methods will also be compared regarding the strength of vibronic coupling along the relevant vibrational (b_2 or b_u symmetric) vibrational modes. (iii) The uncertainty of the aforementioned key quantities (such as vertical excitation energies and vibronic coupling constants) for the dynamics will be estimated by a series of comparison calculations for the dynamical quantities addressed under (iv) and (v). (iv) The results will be used to recompute the UV absorption spectrum in the 5 eV energy range for both *cis*- and *trans*-HT. Up to nine curvilinear degrees of freedom will be included in the calculations, suitable also for large amplitude displacements. For the first time, out-of-plane coordinates are considered in a quantum study of this molecule (two for the terminal CH_2 torsional modes and one for the central C−C−C-C (or skeletal) torsion). (v) Using similar methodology, the electronic population dynamics is computed and analyzed for different numbers of coordinates (6 and 8) and the results for different electronic structure methods are compared. In this way we hope to gain a comprehensive overview over relevant scenarios for the nonadiabatic excited state dynamics of *cis*- and *trans*-hexatriene.

This paper is organized as follows. In section II we briefly explain the theoretical methodology employed in our work. This relates to the construction of the underlying vibronic Hamiltonian and to the electronic structure as well as quantum dynamical computations. The results are presented in section III, first regarding the electronic structure data for ground and excited states, followed by the quantum dynamical results, namely, vibronic structure of the UV absorption spectrum and time-dependent electronic populations. The significance of these findings and their relation to corresponding experimental quantities is also discussed. Finally, section IV concludes.

II. THEORETICAL METHODOLOGY

IIA. Vibronic Hamiltonian. The vibronic Hamiltonian is constructed in a similar way as in our previous work on hexatriene, see ref 33, and *s*-*trans*-butadiene, see ref 37. *cis*-HT belongs to the molecular point group C_{2v} and its 36 vibrational modes transform as follows:

$$\Gamma_{\text{vib}}^{\text{cis}} = 13a_1 + 5b_1 + 12b_2 + 6a_2 \tag{1}$$

For *trans*-HT (point group C_{2h}) the analogous symmetry labels read

$$\Gamma_{\text{vib}}^{\text{trans}} = 13a_g + 5b_g + 12b_u + 6a_u \tag{2}$$

To describe the nuclear degrees of freedom, symmetry-adapted internal coordinates are used. Previous works[10,11,33,38] indicate that the most important vibrations to describe the absorption spectrum involve the movement of the carbon atoms. The nine symmetry adapted internal coordinates applied in this work are listed in Table 1. The atom numbering is defined in Figure 1 for both isomers. Four of these modes transform as the totally symmetric representation (a_1 for *cis*, a_g for *trans*). Explicitly, the totally symmetric coordinate S_1 (Table 1) is the symmetric stretching of the two terminal double bonds. S_2 represents the symmetric stretching of the single bonds. The third important coordinate is the stretching of the central double bond (in this work referred to as S_3). The last relevant totally symmetric mode is the symmetric angle deformation of the angles $\varphi_{1,2,3}$ and $\varphi_{6,5,4}$, denoted as S_6. The b_2 (b_u) modes lead to a coupling of the $2A_1$ and $1B_2$ ($2A_g$ and $1B_u$) excited electronic states in first order. We include two of

DOI: 10.1021/acs.jpca.6b04971

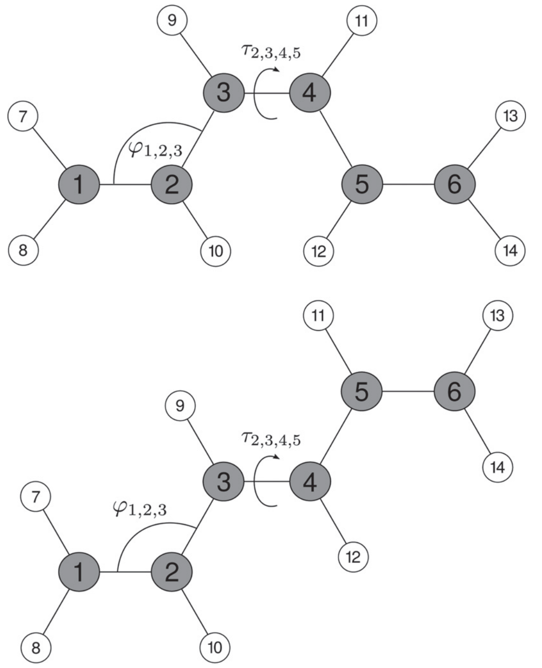

Figure 1. Atom numbering for *cis-* (upper panel) and *trans*-hexatriene (lower panel).

either type of mode. For the coupling b_2 (b_u) modes, the antisymmetric stretching of the single bonds S_5 and the antisymmetric angle deformation of $\varphi_{2,3,4}$ and $\varphi_{5,4,3}$ (denoted as S_9) were used. Furthermore, extending the work of ref 33, we include three out-of-plane modes with b_1 (b_g) and a_2 (a_u) symmetry for the first time in our quantum dynamical treatment. For the out-of-plane modes with b_2 (b_u) symmetry S_{13} we used the disrotatory torsion of the terminal CH_2 groups. S_{14} denotes the conrotatory twisting of the CH_2 groups a_2 (a_u) symmetry). Finally, we include the torsion of the C−C−C−C skeleton about $r_{C_3C_4}$, S_{10} in Table 1. To set up the vibronic Hamiltonian, we need to define expressions for the kinetic energy of the nuclear motion. To this end, we employ the familiar **G**-matrix technique of Wilson[39,40] and use the **G**-matrix elements for the localized internal coordinates of hexatriene as tabulated by Frederick and Woywod.[41] Especially for the out-of-plane modes, a large number of terms have to be evaluated. With these terms it is possible to write the well-established vibronic coupling Hamiltonian as follows:[34]

$$\mathbf{H} = T_N \mathbf{1} + \mathbf{W}(\mathbf{S}) \tag{3}$$

with the kinetic energy

$$2T_N = \mathbf{p}^T \mathbf{G} \mathbf{p} \tag{4}$$

Here **p** refers to the vector of momenta conjugate to the above symmetry coordinates and **1** denotes the 2 × 2 unit matrix. Note that the matrices **1** and **W** refer to electronic function space, whereas within T_N boldface notation refers to nuclear coordinate space. In eq 3 a (quasi)diabatic electronic basis is used and the potential energy matrix is constructed as follows:

$$\mathbf{W}(\mathbf{S}) = \begin{pmatrix} W_a(S) & W_{ab}(S) \\ W_{ba}(S) & W_b(S) \end{pmatrix} \qquad W_{ab} = W_{ba} \tag{5}$$

The potentials along the aforementioned coordinates enter the potential energy matrix of the vibronic Hamiltonian. The diagonal elements W_a and W_b representing the diabatic $2A_1$ and $1B_2$ ($2A_g$ and $1B_u$) electronic states are taken as sums of the 1D potential energies along the coordinates S_i.

$$W_{a,b} = \sum_{i=1-3,5,6,9,10,13,14} V_{a,b}(S_i) \tag{6}$$

To fit the potential energy data, we used polynomials up to the fourth order following the general expression:

$$V_\alpha = \sum_{\substack{k=0 \\ i=1,2,3,6}}^{4} V_{\alpha,i}^{(k)} S_i^k \qquad (\alpha = a, b) \tag{7}$$

For $V_{\alpha,5}$, $V_{\alpha,9}$ see below. In eq 7 the zeroth-order term equals the vertical excitation energy E_v. Because E_v is included in every 1D potential energy expression, it has to be suitably subtracted in the summation of eq 6 to avoid overcounting. For the out-of-plane modes we employed cosine functions.

$$V_\alpha = \sum_{\substack{k=0 \\ i=10,13,14}}^{8} \cos(k_\alpha S_i) \qquad (\alpha = a, b) \tag{8}$$

Finally, the off-diagonal elements were taken to be sums of the linear and cubic vibronic coupling elements of the b_2 (b_u) coordinates S_i considered:

$$W_{ab} = \sum_{i=5,9} (\lambda_i S_i + \mu_i S_i^3) \tag{9}$$

Due to the coupling nature of the b_2 (b_u) coordinates, the fit functions follow the vibronic coupling model:[34]

$$V_\pm = \bar{V}(S_i) \pm \sqrt{\Delta^2 + (\lambda S_i + \mu S_i^3)^2} \tag{10}$$

Here $\bar{V}$ stands for the average potential of the two electronic states considered and is fitted with even polynomials up to fourth order. Δ is the half-difference of the vertical excitation energies of the two states considered at the ground state minimum.

The above approach represents a substantial extension of the so-called linear vibronic coupling approach well established in the literature.[34,42] This holds, especially given the analytical expressions for the diagonal elements according to eqs 7 and 8, and should provide an adequate basis of the subsequent theoretical treatment.

IIB. Electronic Structure Details. *a. CAS-Based Methods.*

In the work presented here, we apply two different electronic structure methods in a comparative manner, on the one hand second-order perturbation theory (PT2) and on the other hand a combination of density functional theory (DFT) and multireference configuration interaction (MRCI),[35] which will be described later. The PT2 calculations rely on complete active space self-consistent field (CASSCF)[43,44] reference wave functions.[45,46] For the calculation of the potential energy surfaces we investigated several CAS spaces and compared the results with our previous work on the hexatriene isomers.[33] In the first CAS space six electrons in the six lowest π-orbitals were included, denoted CAS(6,6) in our nomenclature. This CAS(6,6) includes three orbitals of a_2 (a_u) symmetry and three orbitals of b_1 (b_g) symmetry. The second CAS space CAS(8,8) includes four electrons in π type orbitals, namely, two orbitals of a_2 (a_u) and two of b_1 (b_g) symmetry. Additionally, four σ

DOI: 10.1021/acs.jpca.6b04971
J. Phys. Chem. A 2016, 120, 6541−6556

type of orbitals (from which two are occupied) were included, namely, two orbitals of a_1 (a_g) symmetry, and two belonging to the b_2 (b_g) representation. The third CAS space CAS(10,10) is an extension of CAS(6,6) with four electrons in four σ-type orbitals. Like in CAS(8,8), two orbitals of a_1 (a_g) symmetry and two orbitals of b_2 (b_g) symmetry were included. The inclusion of σ type orbtials is motivated by the work of Cave and Davidson,[47] emphasizing the importance of σ−π correlation for a better description of the $1B_2$ ($1B_u$) excited state with a single-reference character. The CASSCF computation is performed within the framework of state averaging with the three states of interest. The ground state is optimized with MP2 and additionally with PT2 using the corresponding CAS space. The energies of the CASSCF calculation were afterward corrected by single state CASPT2 (SSCASPT2), multistate CASPT2 (MSCASPT2),[48] or the extended multiconfiguration quasi-degenerate perturbation theory (XMCQDPT2) of Granovsky.[49] For all computations, the correlation-consistent polarized valence triple-ζ basis set for hydrogen and carbon is used.[50,51] To perform SSCASPT2 and MSCASPT2 computations, we used the MOLCAS suite of programs,[52−54] for the XMCQDPT2 calculations we employed the Firefly Quantum Chemistry Package,[55] which is partly based on the GAMESS (US)[56] source code.

b. DFT/MRCI. Due to the fact that at distorted geometries of polyenes the doubly excited configurations play an important role, we used a new formulation of DFT/MRCI specially attuned for treating their effect.[36] A set of molecular orbitals (MOs) as one-electron basis for CI has been obtained by the DFT branch of Turbomole[57,58] employing the semilocal BHLYP[59] exchange-correlation functional. The reference space for MRCI was generated by including all electronic configurations with expansion coefficients greater than 0.003 in the intermediately generated DFT/MRCI wave function within the reference space of the RAS(10,10) electron-orbital window. To avoid a double count of dynamic electron correlation arising in the MRCI expansion, off-diagonal matrix elements were attenuated by multiplication with a damping function and all configurations with an energy higher than 1.0 E_h compared to the highest reference energy were discarded. The calculation of four-index two-electron MO integrals was performed with cc-pVTZ[60] auxiliary basis sets from the standard RI-MP2 Turbomole library.

IIC. Quantum Dynamical Treatment.

The above Hamiltonian is used to obtain the absorption spectra and time-dependent electronic populations by the multiconfiguration time-dependent Hartree (MCTDH) method.[61−66] Its efficiency rests on the use of variationally optimized single-particle functions (SPFs) for the various degrees of freedom. The latter are expanded in an underlying set of "primitive" time-independent basis functions such as harmonic oscillator wave functions or else. These expansion coefficients are detemined by a Dirac−Frenkel variational principle to keep the expansion optimally short. The efficiency is further enhanced by two features which are also exploited in the current work. First, each coordinate (called particle Q_i) in the integration scheme can comprise more than a single physical coordinate S_i. Second, for systems with several interacting electronic states like here, the wave function reads as

$$\Psi(t) = \sum_{\alpha}^{n_s} \Psi_\alpha(t)|\alpha\rangle \tag{11}$$

and the SPFs are optimized for each state separately (so-called multiset formalism). All these features combined result in a shortening of the WP expansion (also called MCTDH contraction effect) by about a factor of 10^8 in typical applications in this work. This is documented in Table 8, to be further discussed below.

Given the time-dependent WP of eq 11, the dynamical quantities of interest are directly obtained, such as the electronic spectrum $P(E)$ and the electronic populations of the coupled surfaces. According to eq 12, the former can be obtained directly from the WP as the Fourier transform of the autocorrelation function $C(t)$. The underlying vertical transition follows Fermi's golden rule:[34,67]

$$P(E) \propto \int e^{iEt} C(t)\, dt \tag{12}$$

with

$$C(t) = \langle\Psi(0)|\Psi(t)\rangle = \langle 0|\boldsymbol{\tau}^\dagger e^{-i\mathbf{H}t}\boldsymbol{\tau}|0\rangle \tag{13}$$

$$= \langle\Psi(t/2)^*|\Psi(t/2)\rangle \tag{14}$$

In these equations, $|0\rangle$ stands for the vibrational ground state of the initial electronic ground state (for the hexatriene isomers $1A_1$ and $1A_g$, respectively). $\boldsymbol{\tau}^\dagger$ denotes the vector of the individual transition dipole matrix elements $\boldsymbol{\tau}_{\boldsymbol{\alpha}}$ between the excited state labeled by α and the ground state. The computation of the ground state WF is carried out by a relaxation scheme (propagation on the computed ground state PES in imaginary time).[64,68] The resulting WP is used as the initial state for a propagation on the bright B state (principle of vertical transition) subject to the coupling to the dark A state. In other words only $\boldsymbol{\tau}_{\boldsymbol{\alpha}}$ for the 1B state is nonzero. The autocorrelation function $C(t)$ is then obtained by evaluating the overlap of the time-evolving WP with the initial one. Because the Hamiltonian applied is Hermitian and the initial WP is real, it is possible with the aid of eq 14 to reduce the propagation time by a factor of 2.[69,70] To reduce artifacts arising from the so-called Gibbs phenomenon,[71] it is necessary to multiply the autocorrelation function by a damping function $\cos^2(\pi t/2T)$.[64,72] To simulate the experimental line broadening, the autocorrelation function is damped by further multiplication with a Gaussian function $\exp[-(t/\tau_d)^2]$. In this function τ_d is the damping parameter denoted in the following chapters as dephasing time. The result of this damping is a convolution of the spectrum with a Gaussian with a full width at half-maximum (fwhm) of $(4(\ln 2)^{1/2}/\tau_d)$. All time-dependent WP calculations have been performed with the Heidelberg MCTDH package.[73]

III. RESULTS AND DISCUSSION

IIIA. Ground State Geometry and Vertical Excitation Energies.

The optimized geometries obtained for *cis*- and *trans*-HT in their electronic GS are presented in Tables 2 and 3, respectively, and compared there with representative data from the literature. For both isomers the overall agreement with the literature data is considered rather good. Also the agreement between the three optimization methods is very good, yielding only very small deviations. It is noteworthy to point out that our calculated values for the terminal double bond lengths are somewhat longer than the experimental ones, whereas the computed single bond lengths are somewhat shorter than the experimental data. This finding leads to a smaller bond length alternation character. With these geometries at hand, we proceed to calculate the vertical excitation energies with the

DOI: 10.1021/acs.jpca.6b04971
J. Phys. Chem. A 2016, 120, 6541−6556

Table 2. Key Structural Parameters of the Ground State Equilibrium Geometry of *cis*-Hexatriene (Bond Lengths r in Å and Bond Angles φ in deg)

			MP2	MSCAS(6,6) PT2	MSCAS(8,8) PT2
	exp[a]	exp[b]	cc-pVTZ	cc-pVTZ	cc-pVTZ
$r_{C_1C_2}$	1.336	1.340	1.343	1.345	1.346
$r_{C_2C_3}$	1.462	1.450	1.449	1.449	1.449
$r_{C_3C_4}$	1.362	1.350	1.353	1.355	1.355
$\varphi_{C_1C_2C_3}$	122.1	122.8	122.8	122.7	122.7
$\varphi_{C_2C_3C_4}$	125.9	126.3	126.2	126.2	126.3
$r_{C_1H_7}$	1.090	1.083	1.082	1.081	1.081
$r_{C_1H_8}$	1.090	1.080	1.080	1.079	1.079
$\varphi_{C_2C_1H_7}$	124.0	121.0	120.9	121.0	121.0
$\varphi_{C_2C_1H_8}$	124.0	121.5	121.4	121.5	121.5
$r_{C_2H_{10}}$	1.090	1.088	1.082	1.081	1.081
$r_{C_3H_9}$	1.090	1.085	1.085	1.083	1.083
$\varphi_{C_2C_3H_9}$	118.0	117.9	115.9	115.8	115.8
$\varphi_{C_3C_2H_{10}}$	121.0	118.0	118.5	118.4	118.4

[a] Reference 85. [b] Reference 9.

Table 3. Key Structural Parameters of the Ground State Equilibrium Geometry of *trans*-Hexatriene (Bond Lengths r in Å and Bond Angles φ in deg)

			MP2	MSCAS(6,6) PT2	MSCAS(8,8) PT2
	exp[a]	theory[b]	cc-pVTZ	cc-pVTZ	cc-pVTZ
$r_{C_1C_2}$	1.337	1.350	1.342	1.345	1.347
$r_{C_2C_3}$	1.458	1.446	1.446	1.446	1.445
$r_{C_3C_4}$	1.368	1.343	1.350	1.352	1.355
$\varphi_{C_1C_2C_3}$	121.7	123.7	123.7	123.7	123.7
$\varphi_{C_2C_3C_4}$	124.4	123.7	123.7	123.7	123.7
$r_{C_1H_7}$	1.104	1.082	1.082	1.081	1.081
$r_{C_1H_8}$	1.104	1.080	1.080	1.079	1.079
$\varphi_{C_2C_1H_7}$	120.5	120.9	120.9	121.0	121.0
$\varphi_{C_2C_1H_8}$	120.5	121.4	121.4	121.5	121.5
$r_{C_2H_{10}}$	1.104	1.085	1.085	1.084	1.084
$r_{C_3H_9}$	1.104	1.086	1.086	1.085	1.085
$\varphi_{C_2C_3H_9}$	115.0	119.0	116.9	116.8	116.9
$\varphi_{C_3C_2H_{10}}$	121.3	116.9	117.3	117.2	117.3

[a] Reference 85. [b] Reference 86.

Table 4. Vertical Excitation Energies of the $1B_2$ and $2A_1$ States of *cis*-Hexatriene Obtained with Various Methods and the cc-pVTZ Basis Set[a]

method	$E_v(1B_2)$	$E_v(2A_1)$	$E_v(2A_1) - E_v(1B_2)$
SSCAS(6,6)PT2	5.20	5.43	0.23
SSCAS(8,8)PT2	5.20	5.42	0.22
MSCAS(6,6)PT2	5.16	5.41	0.25
MSCAS(8,8)PT2	5.16	5.41	0.25
MSCAS(10,10)PT2	5.18	5.40	0.22
XMCQDPT2(CAS(6,6))	5.22	5.33	0.11
DFT/MRCI	4.87	5.15	0.28
SS-CASPT2[74]	5.75	5.41	−0.34
SS-CASPT2[11]	5.50	5.03	−0.47
MS-CASPT2[30]	5.12	5.20	0.08
MRMP[8]	5.10	5.09	−0.01
exp[22]	5.16		
exp[21]	5.16		
exp[32]		4.27 (ad.)	

[a] Entries without a reference denote results obtained in the present work. All quantities are in electronvolts.

CAS spaces applied. For *cis*-HT our results are collected in Table 4. SSCASPT2, MSCASPT2, and XMCQDPT2 place the B_2 excited state at a vertical excitation energy of 5.16−5.22 eV, independent of the CAS space applied. These results agree very well with each other and with the experimental value of 5.16 eV.[21,22] The DFT/MRCI level of theory yields a vertical excitation energy of 4.87 eV. This seems somewhat too small, but this finding can be explained by the small bond length alternation obtained by the MP2 ground state geometry optimization and used in the DFT/MRCI calculation of the vertical excitation energies. Because the minimum geometry of the $1B_2$ state exhibits nearly equalized C−C bond lengths, a small bond length alternation preferentially stabilizes the $1B_2$ state, as was reported in previous work.[14] A similar argument holds in the case of the $2A_1$ state, where the positions of single and double bonds are interchanged. For the $2A_1$ excited state the results for the vertical excitation energy range from 5.40 to 5.43 eV applying SSCASPT2 and MSCASPT2 level of theory (Table 4). The XMCQDPT2 method gives 5.33 eV as the value for the vertical excitation energy. The excitation energy for the DFT/MRCI method is again somewhat smaller with 5.15 eV. For the $2A_1$ state there is no reliable experimental data concerning the vertical excitation energy. In our calculations SSCASPT2, MSCASPT2, and DFT/MRCI yield similar energetic gaps between the two excited states. With these levels of theory the value for $E_v(2A_1) - E_v(1B_2)$ ranges between 0.22 and 0.30 eV. Only XMCQDPT2 shows a smaller energetic gap of the vertical excitation energies with 0.11 eV. It is noteworthy that our results for *cis*-HT show a different ordering of the excited states than in our previous work[33] and in some of the theory data in Table 4.[11,74] We emphasize that the present CAS(6,6) orbital space comprises the six frontier π-orbitals whereas in the earlier work also higher-energy π-type orbitals were included.[33] The finding that the various levels of theory applied in the present work lead to the same energetic ordering of the two excited states gives us confidence that these new results (with reversed energetic ordering than before) are trustworthy.

The analogous results for *trans*-hexatriene are presented in Table 5. Again, for the $1B_u$ excited state SSCASPT2 and MSCASPT2 show very similar results with values ranging from 5.15 to 5.20 eV. This is also in line with the experimental values of 5.15[20] and 5.17 eV.[26] XMCQDPT2 places the $1B_u$ state at a higher vertical excitation energy of 5.31 eV, whereas the DFT/MRCI computations yield 4.85 eV. In our calculations the $2A_g$ excited state is predicted at a vertical excitation energy of 5.45−5.46 eV, applying the SSCASPT2 and MSCASPT2 levels of theory with different CAS spaces. With the XMCQDPT2 method we obtain a vertical excitation energy of 5.39 eV. Compared to the experimental result of 5.21 eV by Fujii et al.,[18] the CAS-based results lead to somewhat too big vertical excitation energies for the $2A_g$ excited state. The results of the DFT/MRCI computations for this state show a better agreement with experiment, resulting in a vertical excitation

Table 5. Same as Table 4, but for *trans*-Hexatriene

method	$E_v(1B_u)$	$E_v(2A_g)$	$E_v(2A_g) - E_v(1B_u)$
SSCAS(6,6)PT2	5.16	5.45	0.29
SSCAS(8,8)PT2	5.20	5.46	0.26
MSCAS(6,6)PT2	5.15	5.45	0.30
MSCAS(8,8)PT2	5.18	5.46	0.28
MSCAS(10,10)PT2	5.19	5.45	0.26
XMCQDPT2(CAS(6,6))	5.31	5.39	0.08
DFT/MRCI	4.85	5.22	0.37
SS-CASPT2[7]	5.10	5.20	0.10
SS-CASPT2[9]	5.42	4.92	−0.50
MS-CASPT2[87]	5.31	5.42	0.11
CC3[75]	5.58	5.72	0.14
CCSDR(3)[88]	5.56	6.04	0.48
TD-DFT[17]	5.16	5.21	0.05
exp[20]	5.15		
exp[26]	5.17		
exp[18]	5.08	5.21	0.13

energy of 5.22 eV. For the $E_v(2A_g) - E_v(1B_u)$ energetic gap SSCASPT2, MSCASPT2, and DFT/MRCI agree quite well with each other (Table 5). Again, XMCQDPT2 shows a smaller gap of 0.11 eV. The theoretical literature places the $2A_g$ excited state mostly energetically above the $1B_u$ excited state (but see ref 33), but still the magnitude of the energetic gap remains uncertain. Compared to recent studies[17,75] and the experimental data,[18] our data for the energetic gap seem somewhat too big. For the quantum dynamics this magnitude might be important concerning the population dynamics and the calculated spectra.

IIIB. Potential Energy Matrix for the S_1 and S_2 States.

The computation of the potential energy surfaces used in this work was performed at the MSCAS(6,6)PT2 and DFT/MRCI levels of theory. The analysis of the above results of the vertical excitation energies (Tables 4 and 5) shows that the MSCASPT2 and SSCASPT2 calculations do not depend strongly on the CAS space applied. We therefore decided to carry out the potential energy surfaces computations with the cheap and efficient CAS(6,6) space. The 1D PE curves for both levels of theory were fitted to polynomials of fourth order (eq 7) for the in-plane modes. The out-of-plane modes were fitted by series of cosine functions as shown in eq 8. The values for the fits of the different coordinates can be found in the Supporting Information. From previous dynamical calculations it is well-known that the most important vibrational coordinate for the population dynamics and envelope of the absorption spectra is the elongation of the terminal double bonds[10,12,33] (S_1 according to Table 1). The resulting 1D-PES for the *cis* isomer are depicted in Figure 2 (left panel MSCAS(6,6)PT2 and right panel DFT/MRCI). The potentials obtained with both methods are in quite good agreement with each other, ignoring the different values for the vertical excitation energies. For both methods the energetic minima for the two states occur in the same range of displacements of S_1. For the $1B_1$ state (green curve in Figure 2) this occurs near $S_1 = 0.03{-}0.04$ Å and for the $2A_2$ state (red curve in Figure 2) near $S_1 = 0.1$ Å. Also the intersection point of both potential curves is located at a similar value for S_1. In Figure 3 analogous results for the 1D potentials along S_1 are presented for *trans*-hexatriene. Again, the two methods result in qualitatively similar potentials. The minima of the excited states for the $1B_u$ and $2A_g$ state are located at approximately the same values for S_1. But in contrast to *cis*-hexatriene, in *trans*-hexatriene the two levels of theory show a small difference. In *trans*-HT the MSCASPT2 method locates the minimum for the $2A_g$ excited state along S_1 at a lower energy than for the $1B_u$ state, whereas the DFT/MRCI potentials result in nearly the same energies for both minima. So in MSCASPT2 the $2A_g$ state is energetically more strongly relaxed than in DFT/MRCI, which can lead to different dynamical results. In contrast to our previous work on hexatriene[33] we are able to calculate the potentials along totally symmetric b_1 (b_g) modes and nontotally symmetric b_2 (b_u) modes at the same level of theory. (In the older work we had to switch to the CASMRCI method for the nontotally symmetric modes, but this leads to wrong vertical excitation energies.) The antisymmetric b_2 (b_u) modes were fitted well, as presented in eq 9. The fitting values for both isomers can be found in Tables 6 and 7 and in the Supporting Information. An example fit for a coupling mode in *cis*-HT can be found in Figure 4. In this figure the potential along the coupling mode S_9 is presented for MSCAS(6,6)PT2 and DFT/MRCI. The two levels of theory lead to different shapes of the potentials. The MSCAS(6,6)PT2 result exhibits a well-defined double-minimum for this coordinate (see left panel of Figure 4), whereas the DFT/MRCI potentials do not show this feature (see right panel of Figure 4). Consequently, the coupling parameters for the MSCAS(6,6)PT2 potentials shown in Table 6 are substantially bigger than the ones obtained at the DFT/MRCI level of theory. From the repulsion of the B_2 (B_u) and A_1 (A_g) PE curves along the coupling mode coordinates we infer

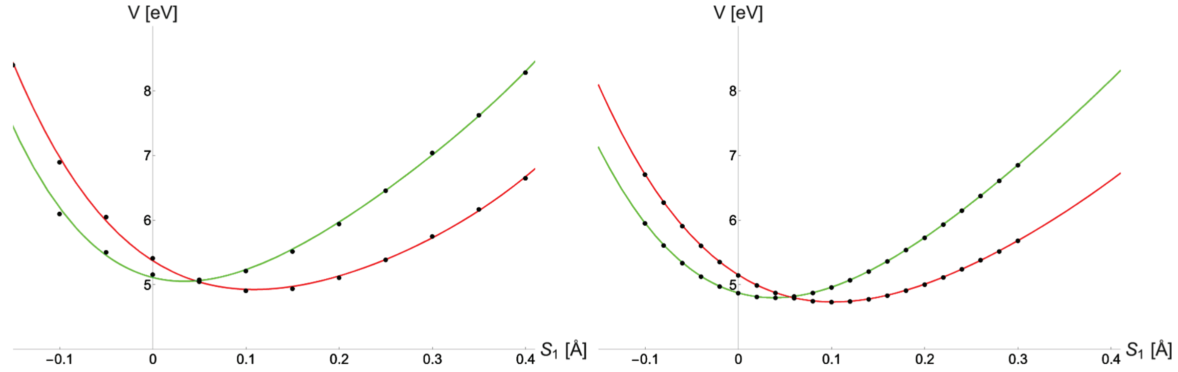

Figure 2. Excited state potential curves for *cis*-hexatriene along the a_1 mode S_1, computed at the MSCAS(6,6)PT2 (left panel) and DFT/MRCI (right panel) level of theory. In green the $1B_2$ state and in red the $2A_1$ state is shown.

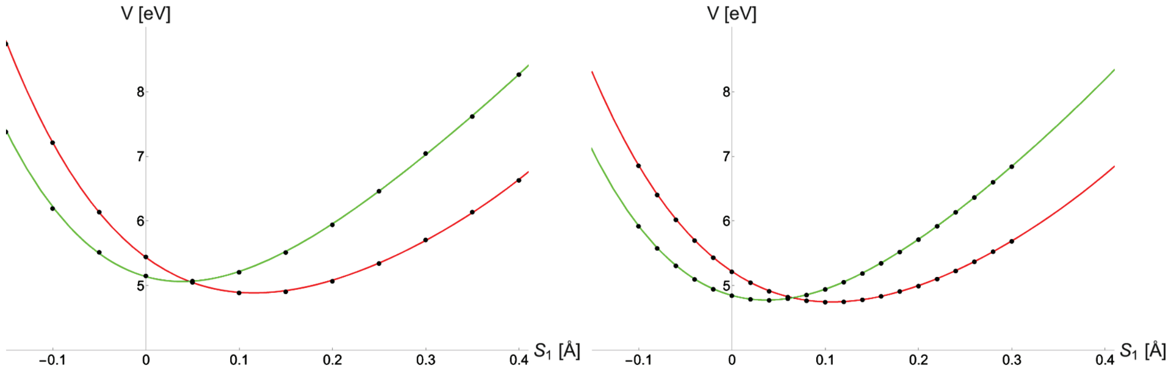

Figure 3. Excited state potential curves for *trans*-hexatriene along the a_g mode S_1, computed at the MSCAS(6,6)PT2 (left panel) and DFT/MRCI (right panel) level of theory. In green the $1B_u$ state and in red the $2A_g$ state is shown.

Table 6. $1B_2$−$2A_1$ Coupling Parameters for *cis*-Hexatriene Obtained by Different Levels of Theory for the b_2 Modes S_9 and S_5

	S_9		S_5	
method	λ [eV/rad]	μ [eV/rad^3]	λ [eV/Å]	μ [eV/Å^3]
MSCAS(6,6)PT2	1.72	0.42	0.26	0.12
MSCAS(8.8)PT2	1.86	0.60	0.27	0.11
CAS(4,4)MRCI[33]	1.34			
CAS(6,6)MRCI[33]	1.34			
DFT/MRCI	1.00	0.39	0.27	0.20
XMCQDPT2	1.10	0.51	0.19	

Table 7. $1B_u$−$2A_g$ Coupling Parameters for *trans*-Hexatriene Obtained by Different Levels of Theory for the b_u Modes S_9 and S_5

	S_9		S_5	
method	λ [eV/rad]	μ [eV/rad^3]	λ [eV/Å]	μ [eV/Å^3]
MSCAS(6,6)PT2	1.82	0.96	0.42	2.68
MSCAS(8.8)PT2	1.78	0.61	0.22	
CAS(4,4)MRCI[33]	1.20			
CAS(6,6)MRCI[33]	1.30			
DFT/MRCI	0.91	0.53	0.23	
XMCQDPT2	1.08		0.12	

that the interaction of the singlet excited state is stronger along the S_9 coordinate than along S_5 (for 1D potential energy curves along S_5 see the Supporting Information). In more detail, the MSCASPT2 level of theory with the two CAS spaces CAS(6,6) and CAS(8,8) leads to the biggest values for the coupling term λ, which is the leading (first-order) coupling term. With λ = 1.00 eV/rad the results for the DFT/MRCI calculations are the smallest entries in Table 6, but the other values for λ obtained by the XMCQDPT2 and CASMRCI method (from our previous work[33]) are rather close. Like in the case of *trans*- and *cis*-butadiene,[76] it appears that the MSCASPT2 results are overestimating the coupling terms. For the weak coupling mode S_5 all values for λ and μ agree very well with each other in the order of magnitude and confirm the weak coupling observed in the potential curves (see two right columns in Table 6). The 1D-potential energy curves along S_9 for *trans*-hexatriene are depicted in Figure 5. Like in the case of the *cis* isomer, the PES obtained by the MSCAS(6,6)PT2 method features a double minimum and the DFT/MRCI potential curve along this mode also exhibits a repulsion between the two excited states, but without a double minimum. The stronger coupling is again quantified in Table 7 in which the MSCASPT2 level of theory, regardless of the CAS space applied, yields the biggest values for the dominant coupling parameter λ. For *trans*-HT the coupling term λ obtained by MSCASPT2 (1.82 eV/rad) is twice as big as the one computed with DFT/MRCI (0.91 eV/rad). The values for the other methods employed are located between these aforementioned parameter values. Again we conclude that the MSCASPT2 method might overshoot the magnitude of the coupling parameter λ. Save for CAS(6,6), the coupling parameters for

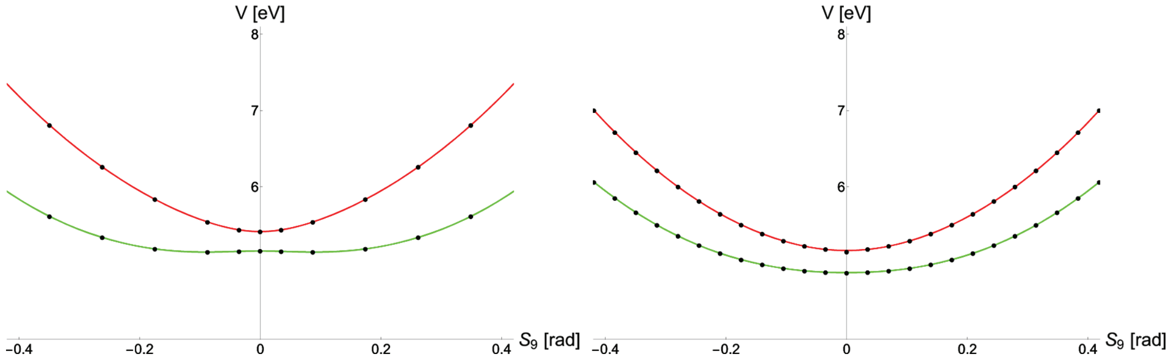

Figure 4. Potential along the b_2 mode S_9, computed at the MSCAS(6,6)PT2 (left panel) and DFT/MRCI (right panel) level of theory. In green the $1B_2$ state and in red the $2A_1$ state is shown.

DOI: 10.1021/acs.jpca.6b04971
J. Phys. Chem. A 2016, 120, 6541−6556

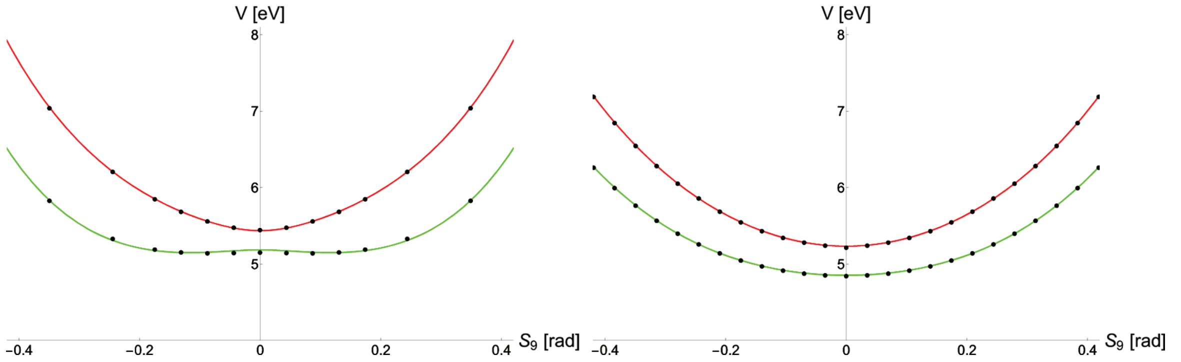

Figure 5. Potential along the b_u mode S_9, computed at the MSCAS(6,6)PT2 (left panel) and DFT/MRCI (right panel) level of theory. In green the $1B_u$ state and in red the $2A_g$ state is shown.

the weaker coupling along S_5 are again quite small and in the same range for the different methods (Table 7).

IIIC. Vibronic Structure of the Absorption Spectrum. We now apply the various levels of theory to investigate the UV absorption spectrum of *cis*- and *trans*-hexatriene in the 5 eV spectral range, corresponding to the $1A_1$ $(1A_g) \rightarrow 1B_2$ $(1B_u)$ electronic transition. Because the inclusion of out-of-plane modes is new in the present study, we reveal their influence by comparing results with only in-plane and different numbers of out-of-plane modes (six to nine vibrational degrees of freedom). The number of single particle functions (SPF) and primitive basis size are presented in Table 8. These numbers lead to the aforementioned MCTDH contraction effect of 1.1 × 10^8, reducing the basis size from 2 × 10^{14} to 1.8 × 10^6. In Figure 6 the calculated UV spectra using the MSCAS(6,6)PT2 ab initio results are shown and compared with the experimental spectrum by Wilbrandt et al.[22] The experimental spectrum features three major bands at 39 760 cm^{-1} (≙4.93 eV), 41 390 (≙5.13 eV), and 43 000 cm^{-1} (≙5.33 eV), the second one being strongest, followed by the first. The third band exhibits two overlapping peaks. Besides, near 44 000 cm^{-1} a shoulder can be seen. The upper left panel of Figure 6 shows our result from the quantum dynamical calculation using six in-plane modes. Like in all calculated spectra presented below, the full line shows the "low-resolution spectrum", whereas the dotted line denotes the "high-resolution" spectrum. With "low-resolution" we refer to a phenomenological broadening such that the calculated spectrum resembles the experiment. Effects of experimental resolution as well as further, e.g., rotational, broadening are thus included in the "effective" line widths. The term "high-resolution" is used for a minimum broadening, i.e., maximum value for the dephasing time consistent with our WP propagation time (mostly 1000 fs). This should be close to the discrete (line) spectrum emerging from the present (bound state) dynamical treatment. Due to convergence issues arising of long propagation times, the high-resolution spectrum is not given for the nine-mode cases.

Table 8. Number of Basis Functions for the Primitive as Well as the Time-Dependent (SPF) Basis Used in the MCTDH Calculations for the Excited Electronic States of Both Isomers of Hexatriene[a]

modes	primitive basis	SPF basis
(S_1, S_5)	(70, 60)	[42, 42]
(S_9, S_3)	(60, 60)	[37, 37]
(S_6, S_2)	(60, 60)	[35, 35]
(S_{13}, S_{14})	(60, 60)	[33, 33]

[a] For all modes harmonic primitive basis functions were used.

With the six in-plane modes and a dephasing time of 25 fs we achieve a satisfactory overall agreement with the experimental spectrum for *cis*-hexatriene. The intensity distribution of the bands and their energetic positions agree with experiment, although we need to add that the fine structure of the bands with the observed shoulders and double peaks is not reproduced well. Furthermore, the bands in the calculated spectrum seem to be somewhat broader compared to experiment. The spectrum with the two additional (out-of-plane) modes S_{13} and S_{14} is presented in the lower left panel of Figure 6. The low-resolution spectrum could be obtained with a weaker dephasing of τ_d = 40 fs. Again, the agreement with the experiment by Wilbrandt et al.[22] is quite good. The intensity distribution of the peaks is correct, as well as their energetic position. But still, with eight modes included in the quantum dynamical computation the calculated spectrum displays somewhat too broad bands. The same holds for the nine-mode spectrum (see lower right panel) where the "skeletal" distortion S_{10} has been additionally included. Like in our result with six modes, the high-resolution spectrum for eight modes shows a lot of structure. This finding might be caused by the rather big value for the coupling constant λ_{S_9} overestimating the interaction between the two states. Because of this finding, we repeated the calculations with best estimate values for the coupling constant λ_{S_9} and also for the energetic gap $E_v(2A_1) - E_v(1B_2)$ (in view of the uncertainty of the correct vertical excitation energy for the $2A_1$ excited state). For the coupling constant we compared the data of Table 6 and selected an average value for the linear coupling constant λ_{S_9} = 1.3 eV/rad. The energetic gap $E_v(2A_1) - E_v(1B_2)$ was decreased to 0.15 eV. The resulting spectra are depicted in Figure 7. The upper left panel shows the result using the 6 in-plane modes. The agreement with experiment is better than in Figure 6 (six-mode calculation with the ab initio data). The ordering of band intensities is correct, as are their energetic positions. The low-resolution spectra of the eight- and nine-mode propagations with a dephasing time of 40 fs show an even better agreement with experiment. The bands are not as broad as in the six-mode case and the shoulder of the first band, visible in the experimental spectrum, can be reproduced. Additionally, the double peak for the third band is indicated. The high-resolution spectrum for eight modes shows a little bit less lines than with the ab initio values of λ_{S_9} = 1.76 eV/rad and $E_v(2A_1) - E_v(1B_2)$

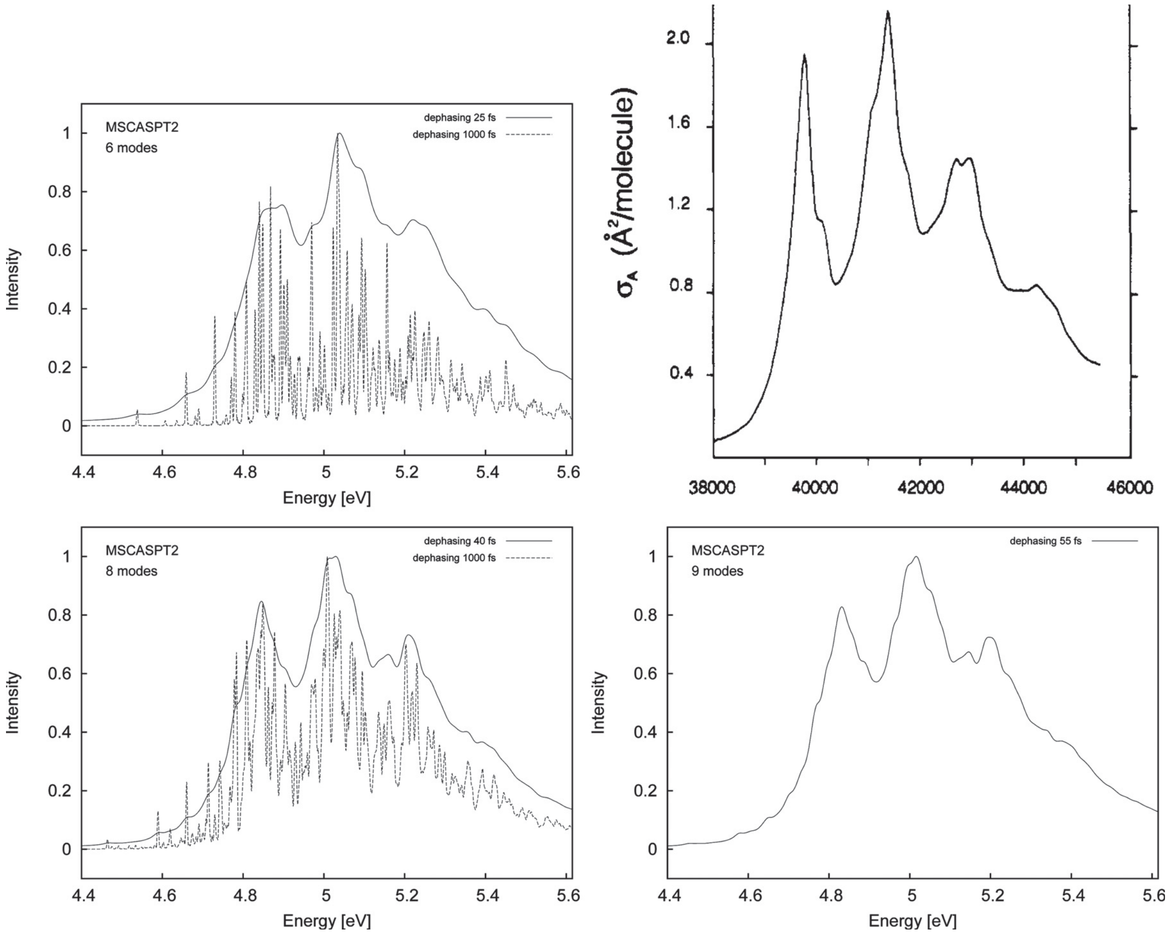

Figure 6. Calculated absorption spectra of *cis*-hexatriene using the MSCAS(6,6)PT2 potentials. The upper left panel shows the spectra using 6 modes. The lower left panel contains the spectra with 8 modes considered, whereas the lower right one shows the 9-mode spectrum. The upper right panel shows the experimental spectrum by Wilbrandt et al.[22]

= 0.25 eV. This suggests that the coupling constants obtained from the MSCASPT2 computations might be somewhat too big. The spectra obtained by using the DFT/MRCI potentials for the dynamical calculations are presented in Figure 8. The low-resolution spectrum of the six-mode propagation depicted in the upper left panel of Figure 8 is dephased by 30 fs and again a qualitatively good agreement with the experiment[22] is visible. The intensity of the bands is in the right range, only the third band seems to have a somewhat too big intensity and shows no feature of a double peak. Interestingly, the high-resolution spectra in this figure show many fewer lines than the high-resolution spectra using the MSCAS(6,6)PT2 parameters. The small DFT/MRCI value for λ_{S_9} of 1.00 eV/rad might be an explanation for this difference. The result of the eight-mode calculation in the lower left panel of Figure 8 is also in good agreement with the experiment. The bands are quite narrow and even the shoulder of the first band is visible. As in the six-mode case the third band seems a little bit too intense. The high-resolution DFT/MRCI spectrum exhibits more lines than in the six-mode calculation, but much less than the eight-mode spectrum using the MSCAS(6,6)PT2 level of theory. The spectra using the DFT/MRCI potentials are shifted to lower energies, due to the smaller vertical excitation energy of the $1B_2$ excited state.

The analogous spectra for the *trans* isomer, using again the MSCAS(6,6)PT2 level of theory, are depicted in Figure 9 and compared there with the experimental recording by Myers et al.[20] In the latter spectrum the most intense band is the first one at 39 900 cm^{-1} ($\hat{=}$4.95 eV), followed by the second one at 41 500 cm^{-1} ($\hat{=}$5.15 eV) and then the third band at 43 100 cm^{-1} ($\hat{=}$5.34 eV). The third band shows a double peak feature. The upper left panel in Figure 9 depicts the spectrum obtained with the six in-plane modes. The low-resolution spectrum is based on a dephasing time of 30 fs and shows a good agreement with the experiment. The relative peak intensities are reproduced well and the third band even shows the double peak feature. Only in the second band the shoulder, visible in the experiment, is missing. The inclusion of the two out-of-plane modes in the eight-mode case yields a better agreement with the experiment, although the shoulder in the second band is still missing. Here the low-resolution spectrum has been obtained with a dephasing time of 40 fs. The high-resolution spectrum exhibits, like in the *cis* isomer, a lot of structure. The addition of the skeletal torsion S_{10} in the nine-mode spectrum (lower right panel in Figure 9) shows a remarkable result. The low-resolution spectrum can be obtained with only a very small phenomenological broadening with a dephasing time as long as 80 fs. This is a bigger value for τ_d than in any of our related calculations[33,37,77] before. Still, the low-resolution spectrum is

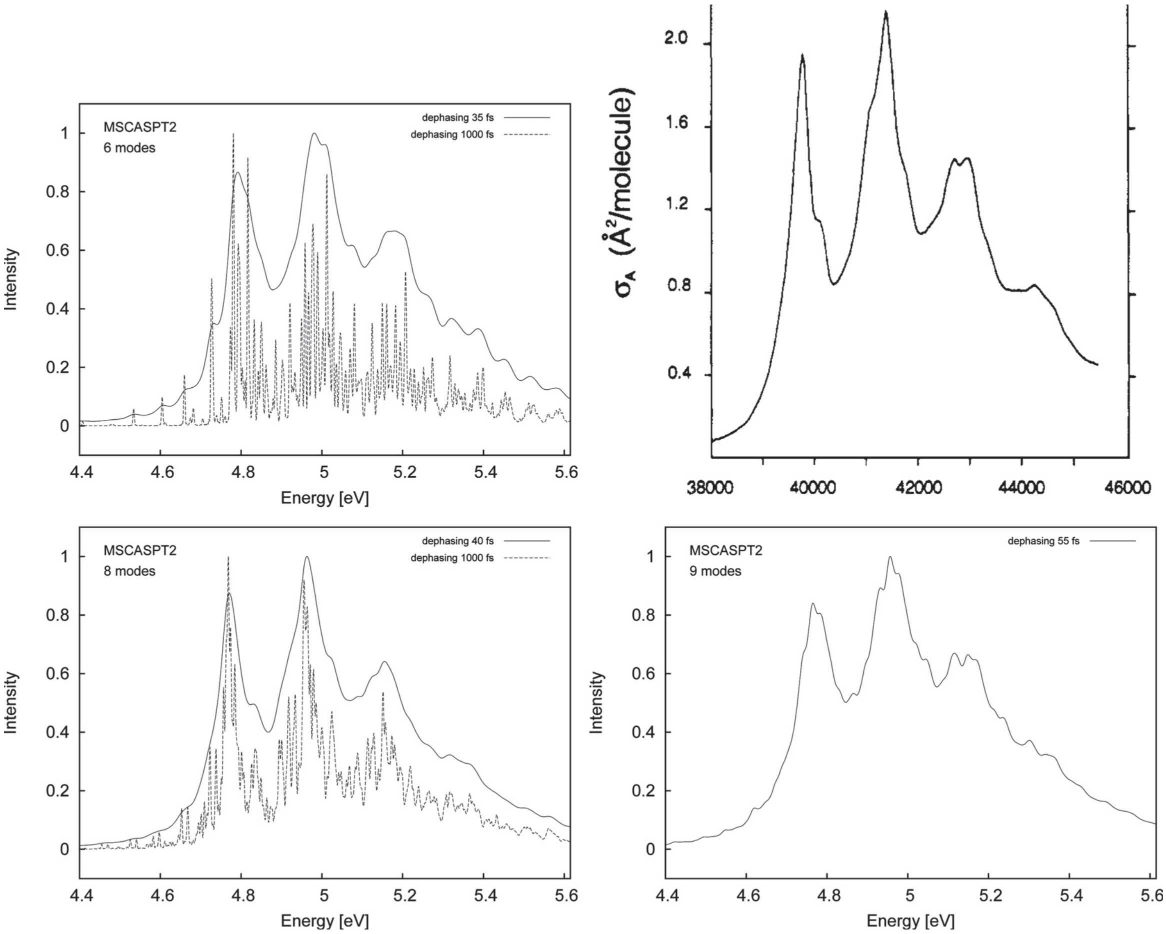

Figure 7. Calculated absorption spectra of *cis*-hexatriene using MSCAS(6,6)PT2 potentials with the best estimates for the vertical excitation energies and coupling parameters. The upper left panel shows the spectra using 6 modes. The lower left panel contains the spectra with 8 modes considered, whereas the lower right one shows the 9-mode spectrum. The upper right panel shows the experimental spectrum by Wilbrandt et al.[22]

in a good agreement with experiment. The bands and their corresponding intensities are very well reproduced. Some small peaks between the main bands are visible, as is an indication of a shoulder at the second band. In comparison with the theoretical study on the photodynamics of *trans*-hexatriene by Woywod et al.[10] our calculated spectra show a better agreement with experiment. This emphasizes the importance of the out-of-plane modes, included in our study. The spectra of *trans*-hexatriene obtained from the quantum dynamical calculations with the DFT/MRCI potentials are depicted in Figure 10. Again we present the six-, eight-, and nine-mode cases. The low-resolution spectrum in the six-mode case can be obtained with a phenomenological dephasing time of 30 fs. The calculated spectrum seems to look like the experimental one by Myers et al.,[20] but some differences are detectable. The first band is not the most intense one in the six mode as well as in the eight- and nine-mode cases (left and bottom panels of Figure 10) but rather the second one. Both the low-resolution and the high-resolution spectra show more structure in the eight-mode case than in the six-mode case, but still some features of the experiment are missing. Finally, the issue of overestimated MSCASPT2 coupling constants for *cis*-hexatriene appears to be mitigated in the *trans* isomer (cf. Figures 6 and 9), and we therefore do not compare here with best estimate results as given in Figure 7.

Summarizing, we have presented and compared results for the UV absorption spectrum of both hexatriene isomers based on two different electronic strucure methods and for various dimensionalities of the calculation. The experimental gas phase recordings could be generally well reproduced, although the vibrational excitation predicted by the DFT/MRCI potential energy surfaces appears to be slightly too strong for the *trans* isomer. The progressions of bands are dominated by the potentials along the bond stretching coordinate S_1 and, to a smaller extent, by S_2 and S_3. We obtain an energetic gap between the first two bands of approximately 0.2 eV ($\hat{=}$1600 cm^{-1}). This in line with the experimental values and identifies the terminal double bonds (coordinate S_1) as being most important for the progression of the absorption spectrum. Comparing spectra of different dimensionality, we find that with more degrees of freedom included, less phenomenological broadening is needed to reproduce the experimental absorption spectra. This shows that more details of the complicated broadening mechanism underlying the spectra are captured in the microscopic treatment.

IIID. Time-Dependent Electronic Populations. In the same manner as before we present and analyze now the time-dependent electronic populations following an excitation from the $1A_1$ ($1A_g$) ground state to the $1B_2$ ($1B_u$) excited state. They are displayed for the first 500 fs for *cis*-HT in Figure 11. The

DOI: 10.1021/acs.jpca.6b04971
J. Phys. Chem. A 2016, 120, 6541−6556

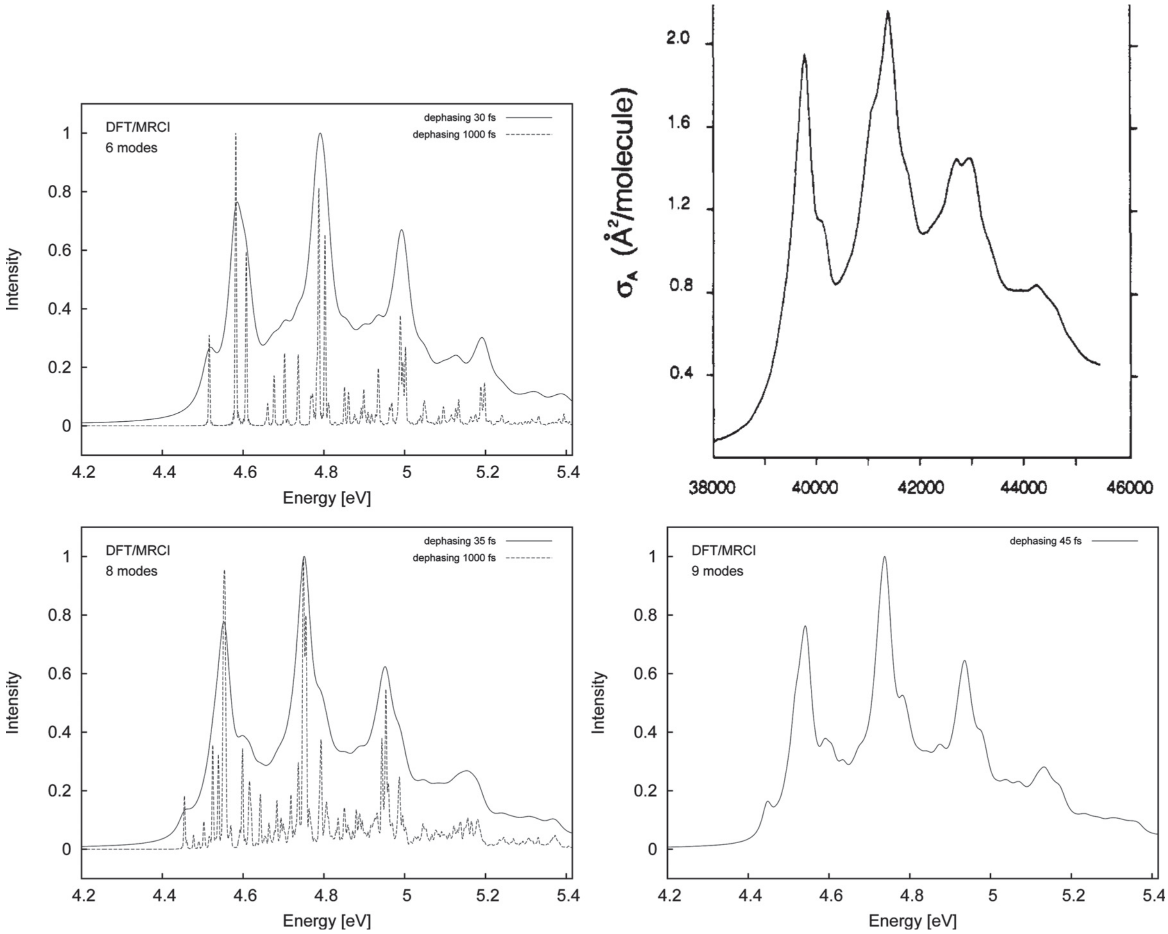

Figure 8. Calculated absorption spectra of *cis*-hexatriene using the DFT/MRCI potentials. The upper left panel shows the spectra using 6 modes. The lower left panel contains the spectra with 8 modes considered, whereas the lower right one shows the 9-mode case. The upper right panel shows the experimental spectrum by Wilbrandt et al.[22]

dynamical calculations are based on the MSCAS(6,6)PT2 potentials with the ab initio values obtained for the linear coupling constant λ_{S_9} and the energetic gap $E_v(2A_1) - E_v(1B_2)$ (same ab initio data as the absorption spectra depicted in Figure 6). The plots in Figure 11 show the population decay for the six and eight mode cases (red and blue lines, respectively). The curves show an ultrafast transfer from the $1B_2$ state to the $2A_1$ state, proceeding on a time scale of 15 fs. In the six-mode calculation 25% of the population remains in the B_2 state after 500 fs. Including the additional out-of-plane modes yields a more efficient population transfer and less than 10% population remains in the B_2 state after the same time. In addition, the population shows less fluctuations than with six modes. This finding is in line with our previous work on butadiene,[37] showing that the inclusion of out-of-plane modes smoothens the time-dependent populations. In Figure 12 the same plot is shown using the DFT/MRCI potentials for the dynamical calculations. The population transfer is again ultrafast, proceeding on a time scale of ∼25 fs. Compared to the results of Figure 11, the population transfer is less complete. In the six-mode calculation (red line) 40% of the population remains in the B_2 state after 500 fs, and only 15% for the eight-mode case (blue line). The somewhat less efficient transfer (compared to the CASPT2 data) may be related to the smaller coupling constant for the S_9 coordinate (Figure 4 and Table 6). Additionally, the vertical energy gap $E_v(2A_1) - E_v(1B_2)$ is larger in the DFT/MRCI than in the CASPT2 data. Again, for the dynamical computations using the DFT/MRCI potentials, the inclusion of the out-of-plane modes reduces the fluctuations in the population dynamics. Still, the results with both underlying electronic structure methods show a more efficient population transfer than in the work of Woywod et al.,[12] using up to 10 in-plane modes. After 500 fs the B_2 state shows a population of 30% or 60% in this work, depending on the energy gap used by these authors. Our results show furthermore a faster transfer than in ref 12.

In Figures 13 analogous results are shown for *trans*-HT. On the basis of the MSCAS(6,6)PT2 ab initio results, the six-mode (red line) and eight-mode (blue line) cases confirm an ultrafast population transfer from the B_u to the $2A_g$ state, proceeding on a slightly slower time scale of 25 fs. After 500 fs the six-mode propagation gives a population of about 20% in the B_u state, whereas the eight-mode case shows less than 10% population in this state. In the first 30−40 fs the two time-dependent populations almost coincide, but subsequently, the dynamical calculation with just in-plane modes exhibits more oscillations. The analogous populations using the DFT/MRCI potentials are presented in Figure 14. Like in the case of the *cis* isomer, the population transfer based on the DFT/MRCI potentials is somewhat slower (50 fs) and also less efficient than with the

DOI: 10.1021/acs.jpca.6b04971
J. Phys. Chem. A 2016, 120, 6541−6556

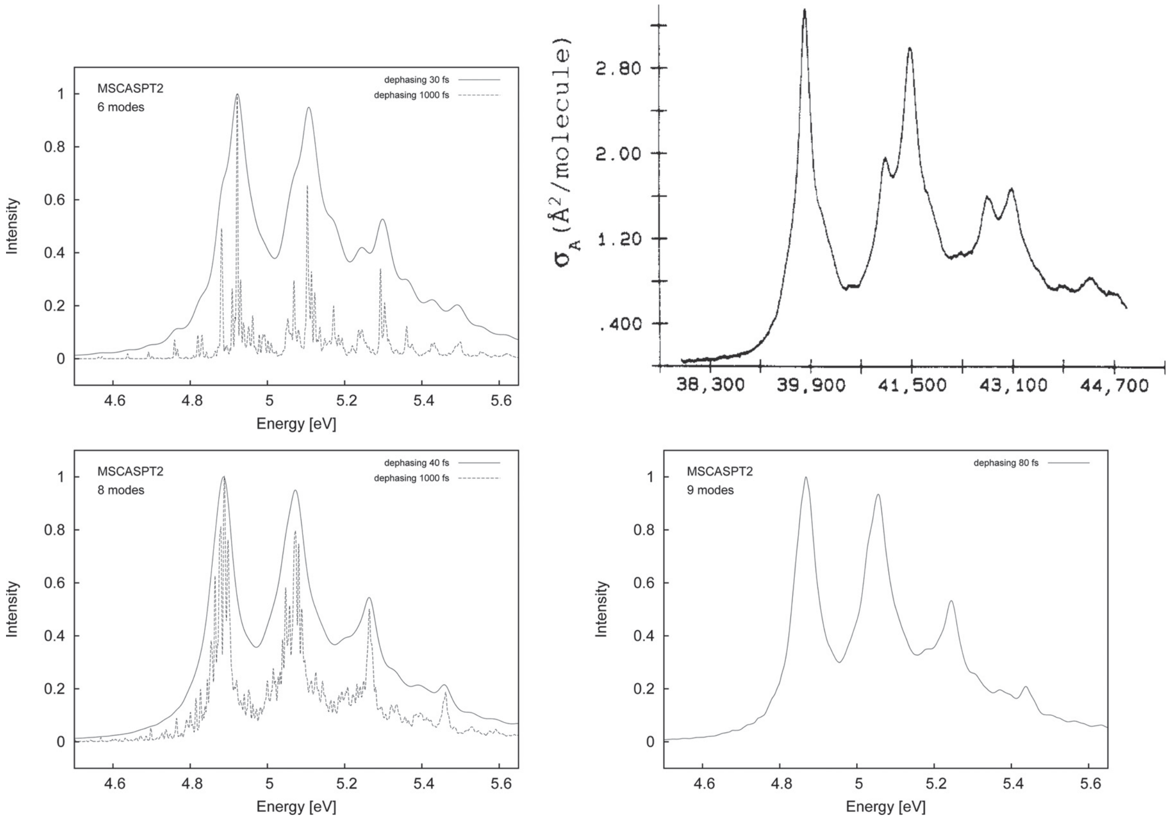

Figure 9. Calculated absorption spectra of *trans*-hexatriene using the MSCAS(6,6)PT2 potentials. The upper left panel shows the spectra using 6 modes. The lower left panel contains the spectra with 8 modes considered, whereas the lower right one shows the 9-mode case. The upper right panel shows the experimental spectrum by Myers et al.[20]

MSCASPT2 potentials. For the six-mode case (red line) the B_u state has a population of approximately 40% after 500 fs, whereas the eight-mode calculation shows a population of 15% after this time. Again the reason for this finding is the presumably smaller coupling constant along the S_9 coordinate (Figure 5 and Table 7). These results are in line with those of Woywod et al.[10] using up to 10 in-plane modes with an energetic gap $E_v(2A_g) - E_v(1B_u) = -0.1$ eV. In their calculations, after 500 fs 20% of the population remains in the B_u state, which is a less complete transfer.

All calculations presented above agree on an ultrafast B_2−A_1 (B_u−A_g) population transfer in both hexatriene isomers, proceeding on a time scale of 20−30 fs for the *cis* isomer and 30−50 fs for the *trans* isomer. These numbers, and also the difference between the two isomers, agree very well with experimental estimates on the population decay time of the optically bright (B) state of 15−21 fs (for *cis*-HT)[20,26] and 33−55 fs (for *trans*-HT).[26,78] Quite generally, such a time scale is much faster than the ns time scale of dipole-allowed emission. If complete, the population transfer thus suppresses emission (fluorescence) which cannot compete (see, for example, refs 79 and 80). In our cases the population transfer (nonradiative decay) is not strictly complete owing to the finite number of vibrational modes included (and the ensuing finite density of states involved). It is nevertheless rather efficient with long-time averages as small as 0.05−0.06 in the MSCASPT2 calculations. In other words, similarly to the calculations on the absorption spectra, a major part of the complexity (and irreversibility) of the system dynamics is captured by the dynamical simulations, especially with eight or nine vibrational degrees of freedom. Although the CASPT2 and DFT/MRCI data result in very similar short-time dynamics, the long-time average of the former drops systematically below that of the latter. This trend can be further rationalized with the aid of density of states arguments: at the vertical excitation energy of the B_2 (B_u) state, the density of A_1 (A_g) vibrational levels is to be compared to that of B_2 (B_u) levels. These densities are approximated by those of harmonic oscillators with equal frequencies in the two states. Then only their dependence on the excess energy ΔE_A and ΔE_B in the $2A_g$ and $1B_u$ state remains, which leads to the following expression for the relative density in question:[81]

$$g_{rel} = \frac{1}{1 + (\Delta E_A/\Delta E_B)^{(f-1)}} \tag{15}$$

Here f is the number of relevant (totally symmetric, see ref 82) vibrational modes, which we have taken to be $f = 4$. Extracting the excess energies from Tables 4 and 5 and from the energy lowering due to structural relaxation (such as seen in Figures 2 and 3), their ratio is found to be smaller for the DFT/MRCI than for the CASPT2 potential energy data. This holds uniformly for all relevant values of f and nicely reflects the observed trends in Figures 11−14.

As already mentioned, the nonradiative decay, if complete, suppresses fluorescence in the hexatrienes. Indeed, *trans*-hexatriene, like *s-trans*-butadiene is a nonfluorescent species,[8,83] fully in line with the above conjecture. *cis*-Hexatriene, however, exhibits detectable emission, though only a very weak one and

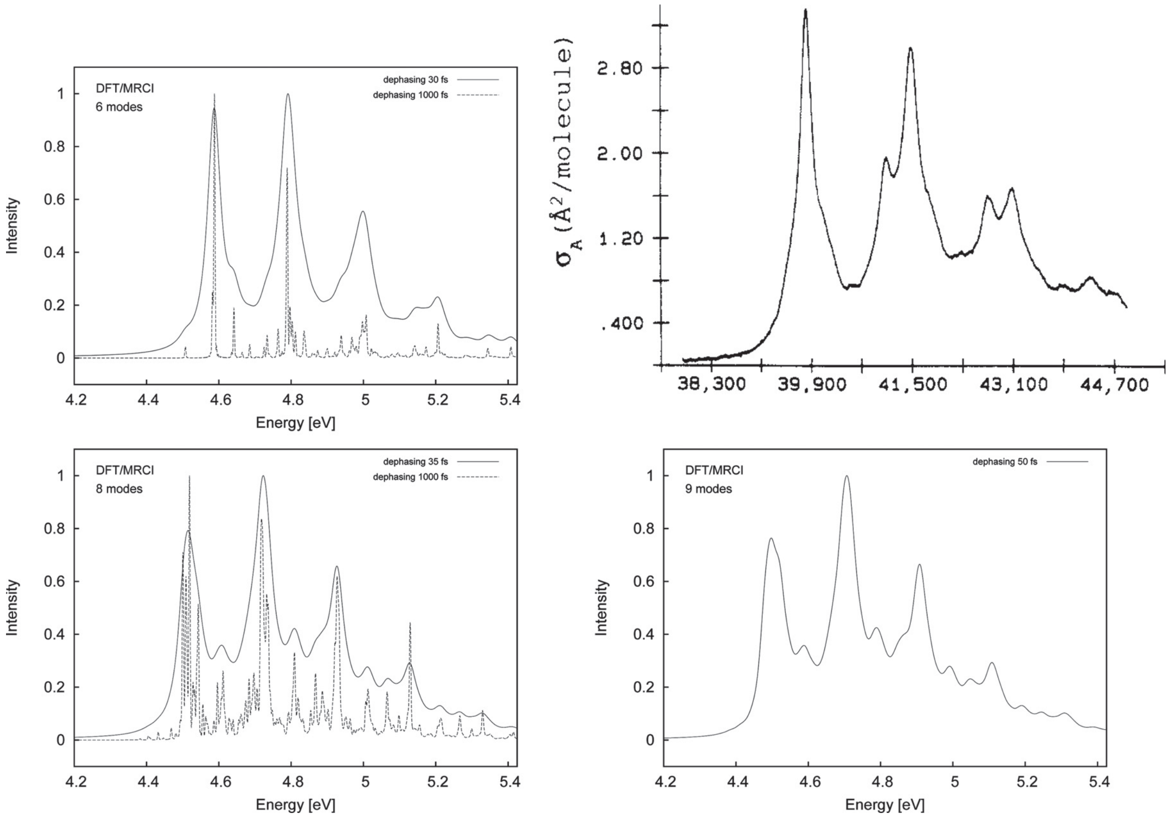

Figure 10. Calculated absorption spectra of *trans*-hexatriene using the DFT/MRCI potentials. The upper left panel shows the spectra using 6 modes. The lower left panel contains the spectra with 8 modes considered, whereas the lower right one shows the 9-mode case. The upper right panel shows the experimental spectrum by Myers et al.[20]

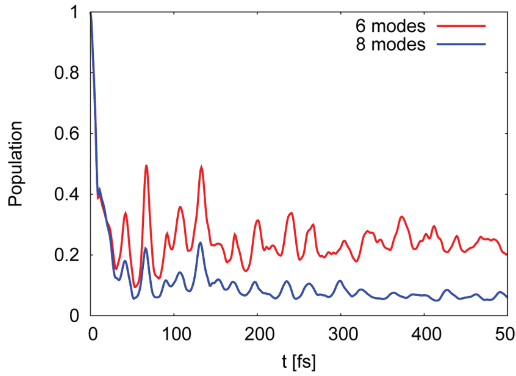

Figure 11. Population dynamics of the coupled $1B_2$−$2A_1$ excited states of *cis*-hexatriene using the MSCAS(6,6)PT2 potentials following a vertical excitation to the $1B_2$ state. The red line shows the result for 6 modes, and the blue one, for 8 modes.

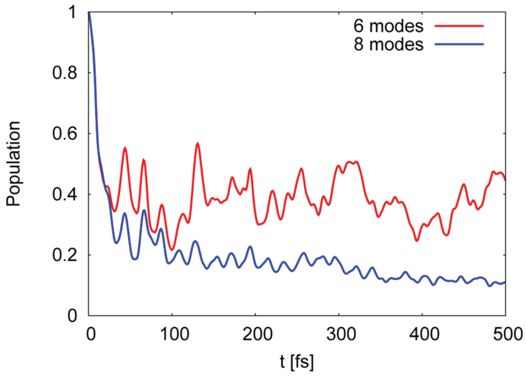

Figure 12. Population dynamics of the coupled $1B_2$−$2A_1$ excited states of *cis*-hexatriene using the DFT/MRCI potentials following a vertical excitation to the $1B_2$ state. The red line shows the result for 6 modes, and the blue one, for 8 modes.

only for low excitation energies.[32,84] In principle, this is also consistent with the above findings, given the finite long-time average populations discussed above. Nevertheless, the difference between the two isomers cannot be captured quantitatively with the present dynamical treatment, presumably owing to the simplified model approach (additivity assumption) underlying our Hamiltonian, eqs 5−8. A more complete treatment is left to future work.

IV. CONCLUSIONS

In this paper we have presented a combined ab initio and quantum dynamical study of the nonadiabatic photodynamics of *cis*-and *trans*-HT in their two lowest excited singlet states. Two different electronic structure methods have been employed, and their results have been systematically compared. The DFT/MRCI semiempirical method is an inexpensive and reliable tool to compute in a straightforward fashion excited state energies also of larger molecular systems. For the short

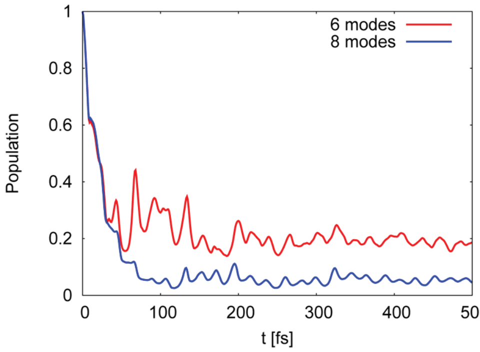

Figure 13. Population dynamics of the coupled $1B_u-2A_g$ excited states of *trans*-hexatriene using the MSCAS(6,6)PT2 potentials following a vertical excitation to the $1B_u$ state. The red line shows the result for 6 modes, and the blue one, for 8 modes.

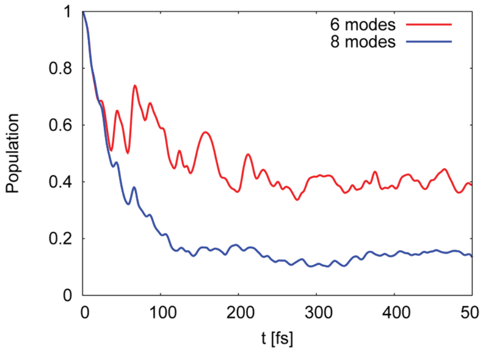

Figure 14. Population dynamics of the coupled $1B_u-2A_g$ excited states of *trans*-hexatriene using the DFT/MRCI potentials following a vertical excitation to the $1B_u$ state. The red line shows the result for 6 modes, and the blue one, for 8 modes.

polyenes under consideration in this work, also the CAS scheme, augmented with second-order perturbation theory for dynamical electron correlation, is well tractable computationally. Regarding the spectral intensity distribution, where a comparsion with experiment is possible, the CASPT2 scheme seems to perform better than DFT/MRCI for the potential energy curves of some totally symmetric modes, especially the coordinate S_1 in the *trans* isomer. The latter method, however, was found to provide better vibronic couplings between the excited states in the *cis* isomer which can be recast as leading to more accurate potential energy curves along the coupling mode S_9.

Apart from these two specific differences the methods agree in the key features of the potential energy surfaces and photodynamics. The typical progression of the terminal C−C stretching mode, which is substantially excited in the first dipole-allowed transition, is reproduced for both isomers. The large widths of the vibrational bands are interpreted as being due to strong intramolecular couplings arising from substantial out-of-plane distortions and torsional excitation on the one hand and strong nonadiabatic B_2-A_1 (B_u-A_g) interactions on the other hand. In our "high-resolution" spectra these show up as highly erractic and dense "line" spectra mimicked by many narrow and closely spaced peaks. The nonadiabatic interactions lead to a B_2-A_1 (B_u-A_g) electronic population decay proceeding on the order of 15−25 fs for the *cis* isomer and 25−50 fs for the *trans* isomer.

In conclusion, we have arrived at a more complete theoretical description of the nonadiabatic photodynamics of these prototype small polyenes. Out-of-plane (torsional) degrees of freedom have been included for the first time in a quantum dynamical treatment. Spectroscopic and photophysical (fluorescence) properties have been covered in a unified fashion. Extension to longer polyenes (*all-trans*-octatetraene) is underway in our groups, whereas a more accurate modeling, going beyond the additivity assumption of eq 6, is left to future work. In combination with a similar, ongoing investigation on *s-cis*-butadiene, we thus hope to arrive at a coherent picture of the nonadiabatic excited state dynamics of these intriguing systems.

■ ASSOCIATED CONTENT

Ⓢ Supporting Information

The Supporting Information is available free of charge on the ACS Publications website at DOI: 10.1021/acs.jpca.6b04971.

Equations for the potential energy surfaces, potential energy curves along S_5, and potential energy curves along S_{10} (PDF)

■ AUTHOR INFORMATION

Corresponding Author

*H. Köppel. E-mail: horst.koeppel@pci.uni-heidelberg.de. Phone: +49 6221/545214.

Notes

The authors declare no competing financial interest.

■ ACKNOWLEDGMENTS

The authors are grateful to A. Dreuw for stimulating discussions and to H.-D. Meyer for help with the MCTDH calculations. This work has been supported financially by the Deutsche Forschungsgemeinschaft under grant numbers KO 945/19-1 and MA 1051/14-1.

■ REFERENCES

(1) Levine, B. G.; Martinez, T. Isomerization Through Conical Intersections. *Annu. Rev. Phys. Chem.* **2007**, *58*, 613−634.

(2) Dugave, C.; Demange, L. Cis-Trans Isomerization of Organic Molecules and Biomolecules: Implications and Applications. *Chem. Rev.* **2003**, *103*, 2475−2532.

(3) Bernardi, F.; Olivucci, M.; Robb, M. A. Potential Energy Surface Crossings in Organic Photochemistry. *Chem. Soc. Rev.* **1996**, *25*, 321−328.

(4) Schoenlein, R. W.; Peteanu, L. A.; Mathies, R. A.; Shank, C. V. The First Step in Vision: Femtosecond Isomerization of Rhodopsin. *Science* **1991**, *254*, 412−415.

(5) Rosenfeld, T.; Honig, B.; Ottolenghi, M.; Hurley, J.; Ebrey, T. G. Cis-Trans Isomerization in the Photochemistry of Vision. *Pure Appl. Chem.* **1977**, *49*, 341−351.

(6) Orlandi, G.; Zerbetto, F.; Zgierski, M. Z. Theoretical Analysis of Spectra of Short Polyenes. *Chem. Rev.* **1991**, *91*, 867−891.

(7) Serrano-Andrés, L.; Nebot-Gil, I.; Lindh, R.; Roos, B. Towards an accurate molecular orbital theory for excited states: Ethene, butadiene, and hexatriene. *J. Chem. Phys.* **1993**, *98*, 3151−3162.

(8) Nakayama, K.; Nakano, H.; Hirao, K. The Study of the π-π^* Excited States of Linear Polyenes: The Energy Gap Between 1 $^1B_u^+$ and 1 ^1A_g States and Their Characters. *Int. J. Quantum Chem.* **1998**, *66*, 157−175.

(9) Woywod, C.; Livingood, W. C.; Frederick, J. H. S_1-S_2 vibronic coupling in *trans*-1,3,5-hexatriene. I. Electronic structure calculations. *J. Chem. Phys.* **2000**, *112*, 613−625.

(10) Woywod, C.; Livingood, W. C.; Frederick, J. H. S_1-S_2 vibronic coupling in *trans*-1,3,5-hexatriene. II. Theoretical investigation of

absorption and resonance Raman spectra. *J. Chem. Phys.* **2000**, *112*, 626–640.

(11) Woywod, C.; Livingood, W. C.; Frederick, J. H. S_1-S_2 vibronic coupling in *cis*-1,3,5-hexatriene. I. Electronic structure calculations. *J. Chem. Phys.* **2001**, *114*, 1631–1644.

(12) Woywod, C.; Livingood, W. C.; Frederick, J. H. S_1-S_2 vibronic coupling in *cis*-1,3,5-hexatriene. II. Theoretical investigation of absorption and resonance Raman spectra. *J. Chem. Phys.* **2001**, *114*, 1645–1662.

(13) Grimme, S.; Nonnenberg, C.; Frank, I. Restricted open-shell Kohn-Sham theory for π-π^* transitions: I. Polyenes, cyanines and protonated imines. *J. Chem. Phys.* **2003**, *119*, 11574–11584.

(14) Marian, C. M.; Gilka, N. Performance of the Density Functional Theory/ Multireference Configuration Interaction Method on Electronic Excitation of Extended π-Systems. *J. Chem. Theory Comput.* **2008**, *4*, 1501–1515.

(15) Lim, E. Ed. *Excited States*; Academic Press: London, 1982.

(16) Fuß, W.; Haas, Y.; Zilberg, S. Twin states and conical intersection in linear polyenes. *Chem. Phys.* **2000**, *259*, 273–295.

(17) Mazur, G.; Makowski, M.; Włodarczyk, R.; Aoki, Y. Dressed TDDFT Study of Low-Lying Electronic Excited States in Selected Linear Polyenes and Diphenylopolyenes. *Int. J. Quantum Chem.* **2011**, *111*, 819–825.

(18) Fujii, T.; Kamata, A.; Shimizu, M.; Adachi, Y.; Maeda, S. Two Photon Absorbtion Study of 1,3,5-Hexatriene by CARS and CSRS. *Chem. Phys. Lett.* **1985**, *115*, 369–372.

(19) Sabljic, A.; McDiarmid, R. The lower Rydberg states of *trans*-hexatriene. *J. Chem. Phys.* **1985**, *82*, 2559–2565.

(20) Myers, A. B.; Pranata, K. S. Excited State Geometry and Dynamics of *trans*-Hexatriene: A Resonance Raman Intensity Study. *J. Phys. Chem.* **1989**, *93*, 5079–5087.

(21) Hemley, R. J.; Lasaga, A. C.; Vaida, V.; Karplus, M. Theoretical Analysis of the 1 $^1B_u^+$ ($^1B_1^+$) ← 1 $^1A_g^-$ ($^1A_1^-$) of *trans*- and *cis*-1,3,5-Hexatriene. *J. Phys. Chem.* **1988**, *92*, 945–954.

(22) Amstrup, B.; Langkilde, F. W.; Bajdor, K.; Wilbrandt, R. Resonance Raman Spectra and Excitation Profiles of (*Z*-1,3,5-Hexatriene Vapor. *J. Phys. Chem.* **1992**, *96*, 4794–4801.

(23) Cave, R. J.; Davidson, E. R. Theoretical Investigation of Several Low-Lying States of *trans,trans*-1,3,5-Hexatriene. *J. Phys. Chem.* **1988**, *92*, 614–620.

(24) Starcke, J. H.; Wormit, M.; Schirmer, J.; Dreuw, A. How much double excitation character do the lowest excitation states of linear polyenes have? *Chem. Phys.* **2006**, *329*, 39–49.

(25) Mikhailov, I. A.; Tafur, S.; Masunov, A. E. Double excitations and state-to state transition dipoles in π-π^* excited singlet states of linear polyenes: Time-dependent density functional theory versus multiconfigurational methods. *Phys. Rev. A: At., Mol., Opt. Phys.* **2008**, *77*, 012510.

(26) Leopold, D. G.; Pendley, R. D.; Roebber, J. L.; Hemley, R. J.; Vaida, V. Direct absorption spectroscopy of jet-cooled polyenes. II. The 1 $^1B_u^+$ - 1 $^1A_g^-$ transitions of butadienes and hexatrienes. *J. Chem. Phys.* **1984**, *81*, 4218–4229.

(27) Westerfield, C.; Myers, A. B. The 2 $^1A_1$ state of *cis*-hexatriene vapor: resonance Raman spectra. *Chem. Phys. Lett.* **1993**, *202*, 409–414.

(28) Hayden, C. C.; Chandler, D. W. Femtosecond Time-Delayed Photoionization Studies of Ultrafast Internal Conversion in 1,3,5-Hexatriene. *J. Phys. Chem.* **1995**, *99*, 7897–7903.

(29) Cyr, D. R.; Hayden, C. C. Femtosecond time-resolved photoionization and photoelectron spectroscopy studies of ultrafast internal conversion in 1,3,5-hexatriene. *J. Chem. Phys.* **1996**, *104*, 771–774.

(30) Fuß, W.; Schikarski, T.; Schmid, W.; Trushin, S.; Hering, P.; Kompa, K. Spectroscopy and ultrafast dynamics of the $2A_1$ state of Z-hexatriene in gas phase. *J. Chem. Phys.* **1997**, *106*, 2205–2211.

(31) Buma, W. J.; Kohler, B. E.; Song, K. Location of the 2 ^1A_g state in hexatriene. *J. Chem. Phys.* **1990**, *92*, 4622–4623.

(32) Petek, H.; Bell, A. J.; Christensen, R. L.; Yoshihara, K. Fluorescence excitation spectra of the S_1 states of isolated trienes. *J. Chem. Phys.* **1992**, *96*, 2412–2415.

(33) Komainda, A.; Zech, A.; Köppel, H. Ab initio quantum study of UV absorption spectra of *cis*-and trans-hexatriene. *J. Mol. Spectrosc.* **2015**, *311*, 25–35.

(34) Köppel, H.; Domcke, W.; Cederbaum, L. S. Multimode Molecular-Dynamics Beyond the Born-Oppenheimer Approximation. *Adv. Chem. Phys.* **1984**, *57*, 59–246.

(35) Grimme, S.; Waletzke, M. A combination of Kohn-Sham density functional theory and multi-reference configuration interaction methods. *J. Chem. Phys.* **1999**, *111*, 5645–5655.

(36) Lyskov, I.; Kleinschmidt, M.; Marian, C. Redesign of the DFT/ MRCI Hamiltonian. *J. Chem. Phys.* **2016**, *144*, 034104.

(37) Komainda, A.; Ostojić, B.; Köppel, H. Ab Initio Quantum Study of Nonadiabatic S_1-S_2 Photodynamics of *s-trans*-Butadiene. *J. Phys. Chem. A* **2013**, *117*, 8782–8793.

(38) Zech, A. Ab initio study of potential energy surfaces of low-lying electronic states in cis-hexatriene. *Master thesis*. Ruprecht-Karls-Universität: Heidelberg, 2014.

(39) Wilson, E. B. A Method of Obtaining the Expanded Secular Equation for the Vibration Frequencies of a Molecule. *J. Chem. Phys.* **1939**, *7*, 1047–1052.

(40) Wilson, E. B.; Decius, J.; Cross, P. C. *Molecular Vibrations - The Theory of Infrared and Raman Vibrational Spectra*; Dover Publications: New York, 1980.

(41) Frederick, J. H.; Woywod, C. General formulation of the vibrational kinetic energy operator in internal bond-angle coordinates. *J. Chem. Phys.* **1999**, *111*, 7255–7271.

(42) Domcke, W., Yarkony, D., Köppel, H., Eds. *Conical intersections: Electronic Structure, Dynamics and Spectroscopy*; World Scientific: Singapore, 2004.

(43) Werner, H. J.; Knowles, P. J. A second order multiconfiguration SCF procedure with optimum convergence. *J. Chem. Phys.* **1985**, *82*, 5053–5063.

(44) Knowles, P. J.; Werner, H. J. An efficient second-order MC SCF method for long configuration expansions. *Chem. Phys. Lett.* **1985**, *115*, 259–267.

(45) Andersson, K.; Malmqvist, P. A.; Sadlej, A.; Wolinski, K.; Roos, B. O. Second-order perturbation theory with a CASSCF reference function. *J. Phys. Chem.* **1990**, *94*, 5483–5488.

(46) Andersson, K.; Malmqvist, P. A.; Roos, B. O. Second-order perturbation theory with a complete active space self-consistent field reference function. *J. Chem. Phys.* **1992**, *96*, 1218–1226.

(47) Cave, R. J.; Davidson, E. R. A theoretical investigation of some low-lying singlet states of 1,3-butadiene. *J. Phys. Chem.* **1987**, *91*, 4481–4490.

(48) Finley, J.; Malmqvist, P. A.; Roos, B. O.; Serrano-Andrés, L. The multi state CASPT2 method. *Chem. Phys. Lett.* **1998**, *288*, 299–306.

(49) Granovsky, A. Extended multi-configuration quasi-degenerate perturbation theory: The new approach to multi state multi-reference perturbation theory. *J. Chem. Phys.* **2011**, *134*, 214113.

(50) Dunning, T. H. Gaussian basis sets for use in correlated molecular calculations. I. The atoms boron through neon and hydrogen. *J. Chem. Phys.* **1989**, *90*, 1007–1023.

(51) Woon, D. E.; Dunning, T. H. Gaussian basis sets for use in correlated molecular calculations. V. Core-valence basis sets for boron through neon. *J. Chem. Phys.* **1995**, *103*, 4572–4585.

(52) Aquilante, F.; et al. MOLCAS 7: The Next Generation. *J. Comput. Chem.* **2010**, *31*, 224–257.

(53) Veryazov, V.; Widmark, P. O.; Serrano-Andrés, L.; Lindh, R.; Roos, B. 2MOLCAS as a development platform for quantum chemistry software. *Int. J. Quantum Chem.* **2004**, *100*, 626–635.

(54) Karlström, G.; et al. MOLCAS: a program package for computational chemistry. *Comput. Mater. Sci.* **2003**, *28*, 222–239.

(55) Granovsky, A. A. *Firefly* version 8, http://classic.chem.msu.su/gran/firefly/index.html.

(56) Schmidt, M.; et al. General atomic and molecular electronic structure system. *J. Comput. Chem.* **1993**, *14*, 1347–1363.

(57) Ahlrichs, R.; Bår, M.; Håser, M.; Horn, H.; Kölmel, C. Electronic structure calculations on workstation computers: The program system turbomole. *Chem. Phys. Lett.* **1989**, *162*, 165−169.

(58) Treutler, O.; Ahlrichs, R. Efficient molecular numerical integration schemes. *J. Chem. Phys.* **1995**, *102*, 346−354.

(59) Becke, A. D. A new mixing of Hartree-Fock and local density functional theories. *J. Chem. Phys.* **1993**, *98*, 1372−1377.

(60) Weigend, F.; Köhn, A.; Hättig, C. Efficient use of the correlation consistent basis sets in resolution of the identity MP2 calculations. *J. Chem. Phys.* **2002**, *116*, 3175−3183.

(61) Meyer, H. D.; Manthe, U.; Cederbaum, L. S. The multi-configurational time-dependent approach. *Chem. Phys. Lett.* **1990**, *165*, 73−78.

(62) Manthe, U.; Meyer, H. D.; Cederbaum, L. S. Wave-packet dynamics within the multiconfiguraton Hartree framework: General aspects and application to NOCl. *J. Chem. Phys.* **1992**, *97*, 3199−3213.

(63) Worth, G. A.; Meyer, H. D.; Cederbaum, L. S. The effect of a model environment on the S_2 absorption spectrum of pyrazine: A wave packet study treating all 24 vibrational modes. *J. Chem. Phys.* **1996**, *105*, 4412−4426.

(64) Beck, M.; Jäckle, A.; Worth, G. A.; Meyer, H. D. The Multiconfiguration Time-dependent Hartree (MCTDH) Method: A Highly Efficient Algorithm for Propagating Wavepackets. *Phys. Rep.* **2000**, *324*, 1−105.

(65) Meyer, H. D.; Worth, G. A. Quantum molecular dynamics: propagating wavepackets and density operators using the multi-configuration time-dependent Hartree method. *Theor. Chem. Acc.* **2003**, *109*, 251−267.

(66) Meyer, H. D.; Gatti, F.; Worth, G. A. *Multidimensional Quantum Dynamics: MCTDH Theory and Applications*; Wiley-VCH: Weinheim, 2009.

(67) Schinke, R. *Photodissociation Dynamics*; Cambridge University Press: Cambridge, U.K., 1991.

(68) Kosloff, R.; Tal-Ezer, H. A direct relaxation method for calculating eigenfunctions and eigenvalues of the Schrödinger equation on a grid. *Chem. Phys. Lett.* **1986**, *127*, 223−230.

(69) Manthe, U.; Meyer, H. D.; Cederbaum, L. S. Multiconfigurational time-dependent Hartree study of complex dynamics: Photodissociation of NO_2. *J. Chem. Phys.* **1992**, *97*, 9062−9071.

(70) Engel, V. The calculation of autocorrelation functions for spectroscopy. *Chem. Phys. Lett.* **1992**, *189*, 76−78.

(71) Jerri, A. J. *The Gibbs Phenomenon in Fourier Analysis, Splines and Wavelet Approximations*; Kluwer: New York, 1998.

(72) Raab, A.; Worth, G. A.; Meyer, H. D.; Cederbaum, L. S. Molecular dynamics of pyrazine after excitation to the S_2 electronic state using a realistic 24-mode model Hamiltonian. *J. Chem. Phys.* **1999**, *110*, 936−946.

(73) Worth, G. A.; Beck, M. H.; Jäckle, A.; Meyer, H. D. *The MCTDH Package*, Version 8.2 (2000). H.-D. Meyer, Version 8.3 (2002), Version 8.4 (2007). O. Vendrell and H.-D. Meyer 8.5 (2011) See http://mctdh.uni-hd.de/.

(74) Serrano-Andrés, L.; Roos, B. O.; Merchán, M. Theoretical study of the electronic spectra of *cis*-1,3,5-hexatriene and *cis*-1,3-butadiene. *Theoret. Chim. Acta* **1994**, *87*, 387−402.

(75) Kánnár, D.; Szalay, P. Benchmarking Coupled Cluster Methods on Valence Singlet Excited States. *J. Chem. Theory Comput.* **2014**, *10*, 3757−3765.

(76) Komainda, A.; Köppel, H. Unpublished work 2016.

(77) Krawczyk, R. P.; Malsch, K.; Hohlneicher, G.; Gillen, R. C.; Domcke, W. 1 ^1B_u-2 ^1A_g conical intersection in *trans*-butadiene: ultrafast dynamics and optical spectra. *Chem. Phys. Lett.* **2000**, *320*, 535−541.

(78) Anderson, N.; Durfee, C.; Murnane, M.; Kapteyn, H.; Sension, R. The internal conversions of *trans*- and *cis*-1,3,5-hexatriene in cyclohexane solution studied with sub-50 fs UV pulses. *Chem. Phys. Lett.* **2000**, *323*, 365−371.

(79) Köppel, H.; Döscher, M.; Baldea, I.; Meyer, H. D.; Szalay, P. Multistate vibronic interactions in the benzene radical cation: II Quantum dynamical simulations. *J. Chem. Phys.* **2002**, *117*, 2657−2671.

(80) Faraji, S.; Meyer, H. D.; Köppel, H. Multistate vibronic interactions in difluorobenzene radical cations: II Quantum dynamical simulations. *J. Chem. Phys.* **2008**, *129*, 074311.

(81) Steinfeld, J.; Francisco, J.; Hase, W. *Chemical Kinetics and Dynamics*; Prentice Hall: Englewood Cliffs, NJ, 1999.

(82) Köppel, H. Ultrafast non-radiative decay via conical intersections of molecular potential-energy surfaces: $C_2H_4^+$. *Chem. Phys.* **1983**, *77*, 359−375.

(83) Zerbetto, F.; Zgierski, M. Z. The missing fluorescence of s-trans butadiene. *J. Chem. Phys.* **1990**, *93*, 1235−1245.

(84) Buma, W. J.; Kohler, B. E.; Song, K. Lowest energy excited singlet state of isolated *cis*-hexatriene. *J. Chem. Phys.* **1991**, *94*, 6367−6376.

(85) Trætteberg, M.; Cyvin, S. J.; Olofsson, B.; Nielsen, P. H. The Single and Double Bonds between sp2-Hybridized Carbon Atoms, as Studied by the Gas Electron Diffraction Method. III. The Molecular Structure of 1,3,5-cis-Hexatriene. *Acta Chem. Scand.* **1968**, *22*, 2294−2304.

(86) Craig, N. C.; Chen, Y.; Fuson, H. A.; Tian, H.; van Besien, H.; Conrad, A. R.; Tubergen, M. J.; Rudolph, H. D.; Demaison, J. Microwave spectra of the Deuterium Isotopologues of *cis*-hexatriene and a Semiexperimental Equilibrium structure. *J. Phys. Chem. A* **2013**, *117*, 9391−9400.

(87) Schreiber, M.; Silva-Junior, M.; Sauer, S.; Thiel, W. Benchmarks for electronically excited states: CASPT2 CC2, CCSD and CC3. *J. Chem. Phys.* **2008**, *128*, 134110−1.

(88) Sauer, S.; Schreiber, M.; Silva-Junior, M.; Thiel, W. Benchmarks for Electronically Excited States: A Comparison of Noniterative and Iterative Triples Correction in Linear Response Coupled Cluster Methods: CCSDR(3) versus CC3. *J. Chem. Theory Comput.* **2009**, *5*, 555−564.

DOI: 10.1021/acs.jpca.6b04971
J. Phys. Chem. A 2016, 120, 6541−6556

Supporting Information - Ab Initio Benchmark Study of Nonadiabatic S_1-S_2 Photodynamics of cis- and trans-Hexatriene

A. Komainda[1], I. Lyskov[2], C. M. Marian[2], and H. Köppel[1]

[1] *Physikalisch-Chemisches Institut, Universität Heidelberg,*
Im Neuenheimer Feld 229, D-69120 Heidelberg, Germany and
[2] *Institut für Theoretische Chemie und Computerchemie,*
Universität Düsseldorf, Universitätsstr. 1, D-40225 Düsseldorf, Germany

I. EXPLICIT FORM OF EQS. (5-8) FOR THE POTENTIAL ENERGY MATRIX

A. *Cis*-Hexatriene

a. MSCAS(6,6)PT2

$$
\begin{aligned}
V_a(S_1) =&\ 5.4137 - 9.1759S_1 + 57.0018S_1^2 - 105.1059S_1^3 + 100S_1^4 \\
V_a(S_2) =&\ 5.4137 + 5.3095S_2 + 33.1631S_2^2 - 74.2958S_2^3 + 84.7526S_2^4 \\
V_a(S_3) =&\ 5.4137 - 4.5508S_3 + 27.8718S_3^2 - 47.7190S_3^3 + 23.8921S_3^4 \\
V_a(S_5) =&\ 5.4137 + 36.8770S_5^2 - 93.6597S_5^4 \\
V_a(S_6) =&\ 5.4137 + 0.6459S_6 + 7.2431S_6^2 - 2.8576S_6^3 + 3.6527S_6^4 \\
V_a(S_9) =&\ 5.4137 + 7.3077S_9^2 + 2.1954S_9^4 \\
V_a(S_{10}) =&\ 4.9807 + 0.0071\cos(S_{10}) + 0.5408\cos(2S_{10}) - 0.0392\cos(3S_{10}) \\
&-0.0771\cos(4S_{10}) + 0.0157\cos(5S_{10}) - 0.0584\cos(6S_{10}) + 0.0157\cos(7S_{10}) \\
V_a(S_{13}) =&\ -77.1567 + 148.6869\cos(S_{13}) - 107.6306\cos(2S_{13}) + 60.7974\cos(3S_{13}) \\
&-25.1860\cos(4S_{13}) + 6.8463\cos(5S_{13}) - 0.9359\cos(6S_{13}) \\
V_a(S_{14}) =&\ 5.4137 - 0.0176S_{14}^2 - 0.4355S_{14}^4 + 0.6747S_{14}^6 - 0.5157S_{14}^8 + 0.1755S_{14}^{10}
\end{aligned}
$$

$$
\begin{aligned}
V_b(S_1) = {} & 5.1603 - 3.5935S_1 + 58.9621S_1^2 - 120.2313S_1^3 + 112.8539S_1^4 \\
V_b(S_2) = {} & 5.1603 + 3.3711S_2 + 33.3509S_2^2 - 73.6916S_2^3 + 85.4558S_2^4 \\
V_b(S_3) = {} & 5.1603 - 3.7382S_3 + 30.0443S_3^2 - 51.5822S_3^3 + 34.6104S_3^4 \\
V_b(S_5) = {} & 5.1603 + 36.8770S_5^2 - 93.6597S_5^4 \\
V_b(S_6) = {} & 5.1603 + 0.4786S_6 + 5.7125S_6^2 - 6.1152S_6^3 + 10.0779S_6^4 \\
V_b(S_9) = {} & 5.1603 + 7.3077S_9^2 + 2.1954S_9^4 \\
V_b(S_{10}) = {} & 4.9837 + 0.0190\cos(S_{10}) + 0.2728\cos(2S_{10}) + 0.0090\cos(3S_{10}) \\
& -0.0323\cos(4S_{10}) - 0.0004\cos(5S_{10}) - 0.0112\cos(6S_{10}) + 0.0091\cos(7S_{10}) \\
V_b(S_{13}) = {} & -6.0954 + 0.0051\cos(S_{13}) - 1.1162\cos(2S_{13}) + 0.0018\cos(3S_{13}) \\
& +0.2234\cos(4S_{13}) - 0.0030\cos(5S_{13}) - 0.0587\cos(6S_{13}) \\
& +0.0492\cos(8S_{13}) + 0.0015\cos(9S_{13}) \\
V_b(S_{14}) = {} & 5.1603 + 2.2506S_{14}^2 - 2.5310S_{14}^4 + 1.9817S_{14}^6 - 0.4772S_{14}^8
\end{aligned}
$$

b. DFT/MRCI

$$
\begin{aligned}
V_a(S_1) = {} & 5.1505 - 8.9859S_1 + 56.1863S_1^2 - 86.9040S_1^3 + 63.8169S_1^4 \\
V_a(S_2) = {} & 5.1505 + 4.2167S_2 + 33.6494S_2^2 - 69.2768S_2^3 + 55.1018S_2^4 \\
V_a(S_3) = {} & 5.1505 - 3.7270S_3 + 28.2265S_3^2 - 43.1630S_3^3 + 29.9282S_3^4 \\
V_a(S_5) = {} & 5.1505 + +37.1082S_5^2 - 59.0942S_5^4 \\
V_a(S_6) = {} & 5.1505 + 0.0683S_6 + 8.5373S_6^2 - 2.5953S_6^3 + 3.6792S_6^4 \\
V_a(S_9) = {} & 5.1505 + 9.0491S_9^2 + 5.7513S_9^4 \\
V_a(S_{10}) = {} & 5.1728 - 0.0009\cos(S_{10}) + 0.0657\cos(2S_{10}) - 0.0025\cos(3S_{10}) \\
& -0.1186\cos(4S_{10}) + 0.0037\cos(5S_{10}) + 0.0801\cos(6S_{10}) \\
& +0.0027\cos(7S_{10}) - 0.0526\cos(8S_{10}) \\
V_a(S_{13}) = {} & 5.1505 + 0.0648S_{13}^2 - 0.2596S_{13}^4 - 0.1038S_{13}^6 + 0.3420S_{13}^8 - 0.1017S_{13}^{10} \\
V_a(S_{14}) = {} & 5.1505 + 0.2612S_{14}^2 - 1.0554S_{14}^4 + 0.8943S_{14}^6 - 0.1663S_{14}^8 - 0.0121S_{14}^{10}
\end{aligned}
$$

$$
\begin{aligned}
V_b(S_1) =&\ 4.8733 - 3.9947S_1 + 57.6893S_1^2 - 94.9505S_1^3 + 68.1370S_1^4\\
V_b(S_2) =&\ 4.8733 + 3.9867S_2 + 33.6705S_2^2 - 62.9717S_2^3 + 42.6804S_2^4\\
V_b(S_3) =&\ 4.8733 - 2.9879S_3 + 28.3876S_3^2 - 50.4400S_3^3 + 38.4954S_3^4\\
V_b(S_5) =&\ 4.8733 + 37.1082S_5^2 - 59.0942S_5^4\\
V_b(S_6) =&\ 4.8733 - 0.4215S_6 + 9.2473S_6^2 - 3.2203S_6^3 + 3.7073S_6^4\\
V_b(S_9) =&\ 4.8733 + 9.0491S_9^2 + 5.7513S_9^4\\
V_b(S_{10}) =&\ 4.8733 - 0.3757S_{10}^2 + 0.1233S_{10}^4 - 0.0139S_{10}^6 + 0.0005S_{10}^8\\
V_b(S_{13}) =&\ 4.8733 + 1.4918S_{13}^2 - 1.2895S_{13}^4 + 1.9085S_{13}^6 - 1.1148S_{13}^8 + 0.2182S_{13}^{10}\\
V_a(S_{14}) =&\ 4.8733 + 0.7740S_{14}^2 + 0.9092S_{14}^4 - 0.9890S_{14}^6 + 0.4750S_{14}^8 - 0.0841S_{14}^{10}
\end{aligned}
$$

B. *Trans*-Hexatriene

c. MSCAS(6,6)PT2

$$
\begin{aligned}
V_a(S_1) =&\ 5.4486 - 10.5738S_1 + 61.0801S_1^2 - 102.1803S_1^3 + 86.1209S_1^4\\
V_a(S_2) =&\ 5.4486 + 5.6558S_2 + 31.5873S_2^2 - 77.0590S_2^3 + 99.9949S_2^4\\
V_a(S_3) =&\ 5.4486 - 4.8549S_3 + 30.3709S_3^2 - 48.8046S_3^3 + 29.5091S_3^4\\
V_a(S_5) =&\ 5.4486 + 34.2285S_5^2 + 74.1713S_5^4\\
V_a(S_6) =&\ 5.4486 - 0.0802S_6 + 7.9802S_6^2 - 1.4925S_6^3 + 2.0964S_6^4\\
V_a(S_9) =&\ 5.4486 + 5.7979S_9^2 + 28.3563S_9^4\\
V_a(S_{10}) =&\ 5.0949 + 0.0002\cos(S_{10}) + 0.4829\cos(2S_{10}) + 0.0048\cos(3S_{10}) - 0.1407\cos(4S_{10})\\
V_a(S_{13}) =&\ -31.6458 + 66.9013\cos(S_{13}) - 48.7587\cos(2S_{13}) + 27.5695\cos(3S_{13})\\
&-11.1037\cos(4S_{13}) + 2.8277\cos(5S_{13}) - 0.3418\cos(6S_{13})\\
V_a(S_{14}) =&\ -76.9245 + 148.9749\cos(S_{14}) - 109.3880\cos(2S_{14}) + 63.1157\cos(3S_{14})\\
&-26.7495\cos(4S_{14}) + 7.4271\cos(5S_{14}) - 1.0071\cos(6S_{14})
\end{aligned}
$$

$$
\begin{aligned}
V_b(S_1) =&\ 5.1538 - 4.0327S_1 + 57.2213S_1^2 - 97.5121S_1^3 + 71.5010S_1^4 \\
V_b(S_2) =&\ 5.1538 + 2.9781S_2 + 32.0042S_2^2 - 65.9972S_2^3 + 80.8630S_2^4 \\
V_b(S_3) =&\ 5.1538 - 3.0019S_3 + 29.5260S_3^2 - 58.9396S_3^3 + 46.1062S_3^4 \\
V_b(S_5) =&\ 5.1538 + 34.2285S_5^2 + 74.1713S_5^4 \\
V_b(S_6) =&\ 5.1538 + 0.3298S_6 + 5.5318S_6^2 - 4.1136S_6^3 + 7.9585S_6^4 \\
V_b(S_9) =&\ 5.1538 + 5.7979S_9^2 + 28.3563S_9^4 \\
V_b(S_{10}) =&\ 4.9376 - 0.0179\cos(S_{10}) + 0.2823\cos(2S_{10}) - 0.0302\cos(3S_{10}) \\
&-0.0126\cos(4S_{10}) - 0.0038\cos(5S_{10}) - 0.0002\cos(6S_{10}) \\
V_b(S_{13}) =&\ -10.8431 + 30.7560\cos(S_{13}) - 23.8125\cos(2S_{13}) + 13.3099\cos(3S_{13}) \\
&-5.6856\cos(4S_{13}) + 1.6976\cos(5S_{13}) - 0.2591\cos(6S_{13}) \\
V_b(S_{14}) =&\ -18.5990 + 44.5542\cos(S_{14}) - 33.9480\cos(2S_{14}) + 19.5212\cos(3S_{14}) \\
&-8.5882\cos(4S_{14}) + 2.6426\cos(5S_{14}) - 0.4280\cos(6S_{14})
\end{aligned}
$$

d. DFT/MRCI

$$
\begin{aligned}
V_a(S_1) =&\ 5.2172 - 9.6437S_1 + 57.8474S_1^2 - 90.0047S_1^3 + 72.9053S_1^4 \\
V_a(S_2) =&\ 5.2172 + 4.0522S_2 + 33.9319S_2^2 - 66.6097S_2^3 + 47.9959S_2^4 \\
V_a(S_3) =&\ 5.2172 - 3.7144S_3 + 27.9297S_3^2 - 43.8073S_3^3 + 31.9884S_3^4 \\
V_a(S_5) =&\ 5.2172 + 32.8045S_5^2 + 72.6014S_5^4 \\
V_a(S_6) =&\ 5.2172 - 0.0977S_6 + 9.0688S_6^2 - 3.4722S_6^3 + 3.2924S_6^4 \\
V_a(S_9) =&\ 5.2172 + 8.05363S_9^2 + 8.9404S_9^4 \\
V_a(S_{10}) =&\ -1.6087 + 12.7718\cos(S_{10}) - 10.2228\cos(2S_{10}) + 7.0511\cos(3S_{10}) \\
&-4.0993\cos(4S_{10}) + 1.7256\cos(5S_{10}) - 0.3933\cos(6S_{10}) \\
V_a(S_{13}) =&\ 5.2686 + 0.0009\cos(S_{13}) - 0.1681\cos(2S_{13}) + 0.0005\cos(3S_{13}) \\
&+0.2255\cos(4S_{13}) + 0.0007\cos(5S_{13}) - 0.1108\cos(6S_{13}) \\
&+0.0009\cos(7S_{13}) + 0.0365\cos(8S_{13}) \\
V_a(S_{14}) =&\ 5.2434 + 0.0003\cos(S_{14}) - 0.1433\cos(2S_{14}) + 0.0001\cos(3S_{14}) + 0.2124\cos(4S_{14}) \\
&+0.0002\cos(5S_{14}) - 0.1124\cos(6S_{14}) + 0.0004\cos(7S_{14}) + 0.0303\cos(8S_{14})
\end{aligned}
$$

$$
\begin{aligned}
V_b(S_1) =&\ 4.8465 - 3.9067S_1 + 57.7812S_1^2 - 97.1947S_1^3 + 73.5690S_1^4 \\
V_b(S_2) =&\ 4.8465 + 3.9094S_2 + 34.2150S_2^2 - 66.0007S_2^3 + 47.8265S_2^4 \\
V_b(S_3) =&\ 4.8465 - 2.7620S_3 + 27.8433S_3^2 - 49.3151S_3^3 + 36.7786S_3^4 \\
V_b(S_5) =&\ 4.8465 + 32.8045S_5^2 + 72.6014S_5^4 \\
V_b(S_6) =&\ 4.8465 - 0.2402S_6 + 9.1777S_6^2 - 3.6297S_6^3 + 3.2569S_6^4 \\
V_b(S_9) =&\ 4.8465 + 8.05363S_9^2 + 8.9404S_9^4 \\
V_b(S_{10}) =&\ 5.2172 - 0.1932S_{10}^2 + 0.0245S_{10}^4 + 0.0063S_{10}^6 - 0.0011S_{10}^8 + 0.0001S_{10}^{10} \\
V_b(S_{13}) =&\ 5.8157 + 0.0010\cos(S_{13}) - 1.1596\cos(2S_{13}) + 0.0009\cos(3S_{13}) + 0.2792\cos(4S_{13}) \\
&+0.0010\cos(5S_{13}) - 0.1207\cos(6S_{13}) + 0.0010\cos(7S_{13}) + 0.0731\cos(8S_{13}) \\
V_b(S_{14}) =&\ 5.7098 + 0.0006\cos(S_{14}) - 1.0645\cos(2S_{14}) + 4.2002\cos(3S_{14}) + 0.2710\cos(4S_{14}) \\
&+0.0004\cos(5S_{14}) - 0.0962\cos(6S_{14}) + 0.0004\cos(7S_{14}) + 0.0424\cos(8S_{14})
\end{aligned}
$$

II. POTENTIAL ENERGY CURVES FOR MODE S_5

A. Cis-hexatriene

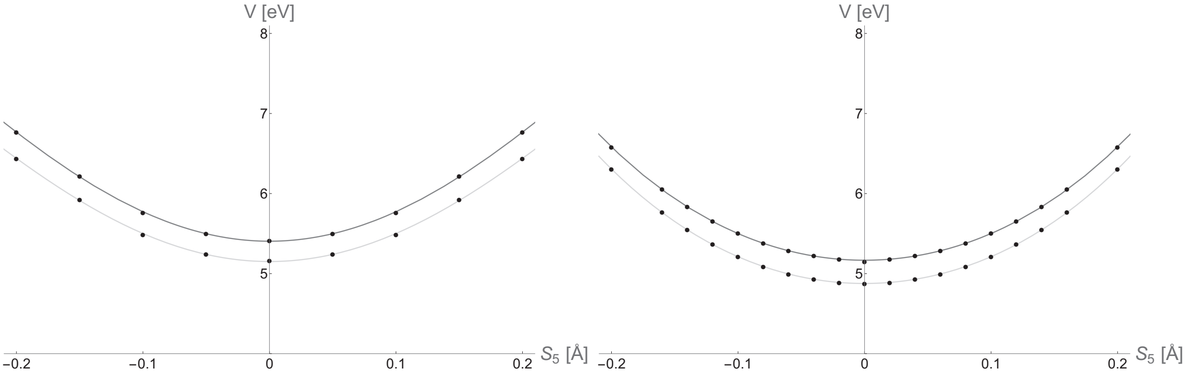

Figure 1: Potential energy along the b_2 mode S_5, computed at the MSCAS(6,6)PT2 (left panel) and DFT/MRCI (right panel) level of theory. In green the $1B_2$ state and in red the $2A_1$ state is shown.

B. Trans-hexatriene

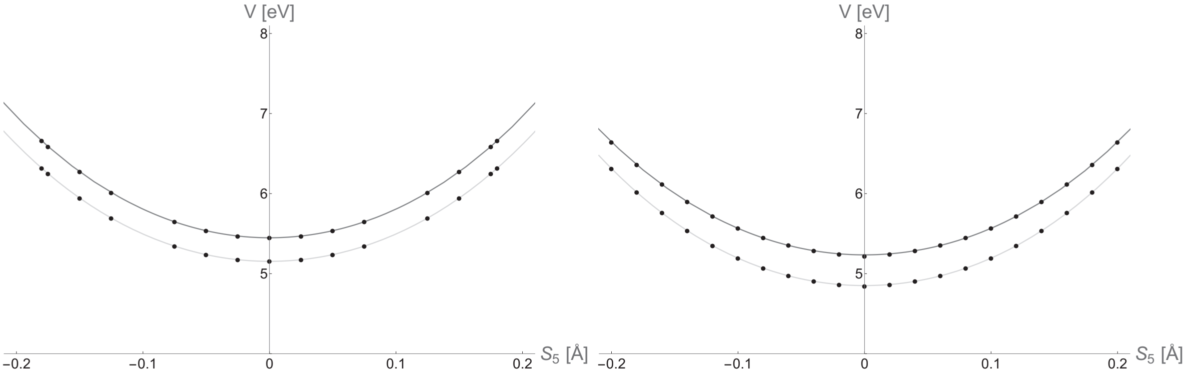

Figure 2: Potential energy along the b_u mode S_5, computed at the MSCAS(6,6)PT2 (left panel) and DFT/MRCI (right panel) level of theory. In green the $1B_u$ state and in red the $2A_g$ state is shown.

III. POTENTIAL ENERGY CURVES FOR MODE S_{10}

A. Cis-hexatriene

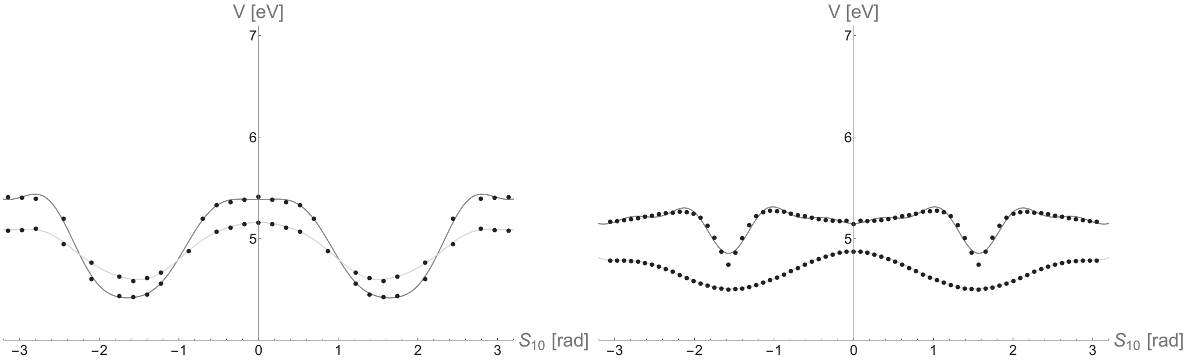

Figure 3: Potential energy along the mode S_{10}, computed at the MSCAS(6,6)PT2 (left panel) and DFT/MRCI (right panel) level of theory. In green the $1B_2$ state and in red the $2A_1$ state is shown. The analogous potential energy curves for the *trans*-isomer differ only by the slightly different bond lengths and angles (apart from an offset in the origin of the torsional coordinate). They are very similar to the curves shown here and thus not displayed for brevity